ΕΘΝΙΚΟ ΜΕΤΣΟΒΙΟ ΠΟΛΥΤΕΧΝΕΙΟ
Σχολή Πολιτικών Μηχανικών
Εργαστήριο Εδαφομηχανικής

NATIONAL TECHNICAL UNIVERSITY
School of Civil Engineering
Soil Mechanics Laboratory

DOCTORAL DISSERTATION

Experimental and Numerical Simulation of Buried Pipelines subjected to Large Permanent Ground Displacements: Fault Rupture and Landslides

Angelos Tsatsis

Diploma in Civil Engineering
National Technical University of Athens - 2010

Supervised by: ***Professor George Gazetas***

Athens, May 2017

ΕΘΝΙΚΟ ΜΕΤΣΟΒΙΟ ΠΟΛΥΤΕΧΝΕΙΟ
Σχολή Πολιτικών Μηχανικών
Εργαστήριο Εδαφομηχανικής

NATIONAL TECHNICAL UNIVERSITY
School of Civil Engineering
Soil Mechanics Laboratory

ΔΙΔΑΚΤΟΡΙΚΗ ΔΙΑΤΡΙΒΗ

Πειραματική και Αριθμητική Προσομοίωση Αγωγών έναντι Μεγάλων Εδαφικών Μετακινήσεων: Τεκτονική Διάρρηξη, Κατολίσθηση

Άγγελου Τσάτση

Διπλωματούχου Πολιτικού Μηχανικού
Εθνικού Μετσόβιου Πολυτεχνείου - 2010

Επιβλέπων: ***Καθηγητής Γεώργιος Γκαζέτας***

Αθήνα, Μάϊος 2017

ΔΙΔΑΚΤΟΡΙΚΗ ΔΙΑΤΡΙΒΗ

Πειραματική και Αριθμητική Προσομοίωση Αγωγών έναντι Μεγάλων Εδαφικών Μετακινήσεων: Τεκτονική Διάρρηξη, Κατολίσθηση

Εκτενής Περίληψη

Εισαγωγή

Σύγχρονα επιστημονικά ευρήματα (π.χ. O'Rourke & Palmer (1996), Takada et al. (1999), Tang (2000), Uzarski & Arnold (2001), Liang & Sung (2000), O'Rourke & Liu (2011), O'Rourke et al. (2015)), έχουν αναδείξει την ευπάθεια των υπογείων αγωγών στις μεγάλες εδαφικές μετατοπίσεις. Αυτές μπορεί να προκληθούν είτε από κατολίσθηση, είτε από εκδήλωση επιφανειακή τεκτονικής διάρρηξης, είτε από οριζόντια εδαφική εξάπλωση λόγω ρευστοποίησης ή και από εκτεταμένη καθίζηση του εδάφους πλησίον του αγωγού. Παρότι, οι σύγχρονες κανονιστικές διατάξεις ενθαρρύνουν την αποφυγή πιθανών 'επισφαλών' περιοχών, η ραγδαία επέκταση των δικτύων μεταφοράς και διανομής (που ανέρχονται πλέον σε εκατομμύρια χιλιομέτρων αγωγών), η εκθετική αύξηση των αστικών περιοχών και οι αυστηροί περιβαλλοντικοί περιορισμοί, δημιουργούν σημαντικούς περιορισμούς στην χάραξη των δικτύων ώστε πολύ συχνά καθίσταται αναπόφευκτη η διασταύρωση του αγωγού με περιοχές επιρρεπείς στους παραπάνω γεωλογικούς/γεωτεχνικούς κινδύνους. Ως εκ τούτο η μελέτη επάρκειας του αγωγού θα πρέπει να εξασφαλίζει καί την ασφαλή ανάληψη μεγάλων εδαφικών μετακινήσεων.

Σήμερα ο σχεδιασμός των αγωγών γίνεται ως επί το πλείστον με χρήση αναλυτικών επιλύσεων ή απλοποιημένων ελατηριωτών προσομοιωμάτων (π.χ. Takada et al. (2001), Karamitros et al. (2007), Gantes et al. (2008), Randolph et al. (2010), Trifonov & Cherniy (2012), Zhang et al. (2016), Melissianos et

al. (2016)) όπου ο αγωγός προσομοιώνεται ως δοκός ενώ το έδαφος αναπαρίσταται από ανεξάρτητα μεταξύ τους μη-γραμμικά ελατήρια (ASCE 1984, ALA 2001, IITK-GSDMA 2007, PRCI 2004). Παρά την δεδομένη χρησιμότητα των μεθόδων αυτών, πολλοί ερευνητές έχουν εγείρει ερωτήματα σε σχέση με την αξιοπιστία τους (Phillips et al. (2004), Yimsiri et al (2004), Guo (2005), Hsu et al. (2006), Cocchetti et al. (2009), Daiyan et al. (2009, 2010), Pike et al. 2011). Οι Zhang et al. (2002) και οι Di Prisco et al. (2004) τόνισαν πως η αγνόηση της αλληλεπίδρασης των εδαφικών ελατηρίων υπεραπλουστεύει την "πραγματικότητα" κατά την οποία κάθε συνιστώσα μετακίνησης και στροφής του αγωγού εξαρτάται από την περίπλοκη συζευγμένη συσχέτιση όλων των συνιστωσών δυνάμεων που δρουν επί αυτού. Επιπλέον οι Nobahar and Kenny (2007) εντόπισαν σημαντικές αδυναμίες των ελατηριωτών προσεγγίσεων σε καθεστώς μεγάλων εδαφικών μετακινήσεων. Τέλος, οι Konuk et al. (2006) συγκρίνοντας ελατηριωτά προσομοιώματα με εμπεριστατωμένα προσομοιώματα συνεχούς μέσου παρήγαγαν αντικρουόμενα συμπεράσματα: η χρήση των ελατηριωτών προσομοιωμάτων άλλοτε οδηγούσε σε συντηρητικό σχεδιασμό, ενώ εντοπίστηκαν και περιπτώσεις όπου τα ελατηριωτά προσομοιώματα υποτιμούσαν τις αναπτυσσόμενες παραμορφώσεις και μετακινήσεις.

Ο πλέον αποτελεσματικός τρόπος σχεδιασμού υπογείων αγωγών έναντι μεγάλων εδαφικών μετακινήσεων είναι η αριθμητική προσομοίωση με πεπερασμένα στοιχεία συνεχούς μέσου, τα οποία να μπορούν να λάβουν υπόψη την μη-γραμμική συμπεριφορά του αγωγού και του περιβάλλοντος εδάφους, αλλά και το σύνολο των φαινομένων που σχετίζονται με την αλληλεπίδρασή τους. Στόχος της παρούσας διατριβής είναι η κατάρτιση πρωτότυπης και πλήρους τεκμηριωμένης αριθμητικής μεθοδολογίας για την ανάλυση της συμπεριφοράς υπογείων μεταλλικών αγωγών μεταφοράς φυσικού αερίου υποβαλλομένων σε:

(α) τεκτονική διάρρηξη κατακόρυφης βύθισης (κανονικά και ανάστροφα ρήγματα) και

(β) περιστροφικές κατολισθήσεις.

Η παρούσα Διδακτορική Διατριβή περιλαμβάνει δύο κύριες ενότητες. Η πρώτη ενότητα είναι αφιερωμένη στην απόκριση υπογείων αγωγών υποβαλλόμενων σε τεκτονική διάρρηξη κατακόρυφης βύθισης (κανονικά και ανάστροφα ρήγματα). Στόχος μας είναι η πλήρης προσομοίωση της διάδοσης της διάρρηξης από το βραχώδες υπόβαθρο έως την επιφάνεια του εδάφους και η ταυτόχρονη μελέτη της δομητικής απόκρισης του αγωγού. Πλέον της ανελαστικής ανάλυσης του εδάφους και των συνθηκών επαφής εδάφους-αγωγού, ιδιαίτερη έμφαση δίδεται στην ορθή ανάλυση της εντόνως μη-γραμμικής απόκρισης του μεταλλικού κελύφους. Η δεύτερη ενότητα αναφέρεται στην απόκριση υπογείων αγωγών

υποβαλλόμενων σε μεγάλες εδαφικές μετακινήσεις λόγω ενεργοποίησης εδαφικής κατολίσθησης. Και για τις δύο (2) φορτίσεις καταρτήθηκε κατάλληλη αριθμητική μεθοδολογία η οποία εν συνεχεία βαθμονομήθηκε και επαληθεύτηκε έναντι πειραμάτων της βιβλιογραφίας και πειραμάτων μικρής κλίμακας που διεξήχθησαν στο Εργαστήριο Εδαφομηχανικής του Ε.Μ.Π.

Α' Μέρος

Συμπεριφορά αγωγών υποβαλλόμενων σε κανονική και ανάστροφη διάρρηξη

Ως γνωστόν οι τοπικές εδαφικές συνθήκες επηρεάζουν την διαδρομή (rupture path) και την εμφάνιση (outcrop) του σεισμικού ρήγματος στην ελεύθερη επιφάνεια του εδάφους (e.g. Cole and Lade (1984), Bray et al. (1994), Anastasopoulos et al. (2007, 2009)). Εν προκειμένω, (όπως σχηματικά παρουσιάζεται στο **Σχ. 1**) η σχεδόν σημειακή διαφορική μετακίνηση (δ_{fault}) στο επίπεδο του βράχου, καθώς μεταδίδεται προς τα άνωθεν, διαχέεται εντός του ενδόσιμου εδάφους σχηματίζοντας έναν ηπιότερο αναβαθμό. Αυτό ακριβώς το κινηματικό πεδίο καλείται να παραλάβει ο μεταλλικός αγωγός. Δανειζόμενοι την ορολογία της σχετικής βιβλιογραφίας (Wang & Yeh (1985), Chiou et al (1994), Trifonov & Cherniy (2010), Karamitros et al. (2011)), η απόκριση του αγωγού μπορεί να διαχωριστεί ως εξής:

(α) **3-Δ απόκριση πλησίον της ζώνης διάρρηξης (ή "εγγύς πεδίου" απόκριση)**: Στην περιοχή αυτή ο αγωγός κάμπτεται εντόνως προκειμένου να παραλάβει την διαφορική μετακίνηση των δύο τεμάχων (του σταθερού και του κινούμενου τεμάχους) ενώ ταυτόχρονα υπόκειται σε σημαντική αξονική δύναμη λόγω της επιβεβλημένης μεταβολής του συνολικού του μήκους.

(β) **1-Δ απόκριση (ή απόκριση "μακρινού πεδίου")** : Εκατέρωθεν του "εγγύς πεδίου", ο αγωγός τείνει να "συμμορφωθεί" με την εδαφική μετατόπιση και η απόκρισή του εκφυλίζεται σε αποκλειστικώς αξονική (μονοδιάστατη).

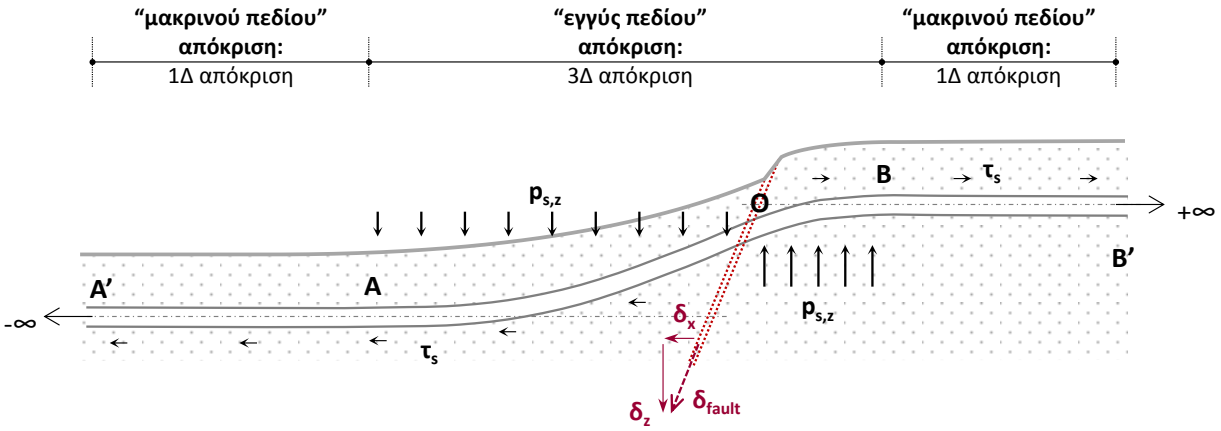

Σχήμα 1. Ποιοτική απεικόνιση της απόκρισης υπογείου απειρομήκους αγωγού υποβαλλόμενου σε κανονική διάρρηξη.

Αριθμητικό Προσομοίωμα και Επικύρωση Αριθμητικής Μεθοδολογίας

Ο διαχωρισμός της συμπεριφοράς του αγωγού σε "εγγύς πεδίου" και "μακρινού πεδίου" υιοθετείται και στην προτεινόμενη αριθμητική μεθοδολογία. Εν προκειμένω, η "εγγύς πεδίου" προσομοίωση περιλαμβάνει 3-Δ κάνναβο πεπερασμένων στοιχείων (Π.Σ.) όπου το έδαφος προσομοιώνεται με στοιχεία συνεχούς μέσου και ο αγωγός με στοιχεία κελύφους. Ειδικός αλγόριθμος επαφής χρησιμοποιείται για να περιγράψει την διεπιφάνεια αγωγού-εδάφους, που επιτρέπει την αποκόλληση του αγωγού από το έδαφος αλλά και την ανάπτυξη τριβής. Η μη-γραμμική συμπεριφορά του χάλυβα περιγράφεται μέσω του καταστατικού προσομοίωμα von Mises, ενώ για την ρεαλιστική απεικόνιση της εδαφικής συμπεριφοράς (διάδοση της διάρρηξης, συγκέντρωση παραμορφώσεων στο επίπεδο αστοχίας, πτώση της αντοχής για διαστολικά εδάφη κλπ.) υιοθετείται ένα ελαστοπλαστικό καταστατικό προσομοίωμα με κριτήριο αστοχίας Mohr-Coulomb και συμπεριφορά χαλάρωσης (Anastasopoulos et al. 2007). Μία άποψη του αριθμητικού προσομοιώματος που υιοθετείται στην απεικόνιση του "εγγύς πεδίου" παρουσιάζεται στο **Σχ. 2α**. Η προσομοίωση της 1-Δ περιοχής υλοποιείται κατά τα γνωστά με ένα απλουστευμένο προσομοίωμα beam-on-springs, όπου ο αγωγός προσομοιώνεται ως δοκός εδραζόμενη επί ελατηριωτού εδάφους τύπου Winkler (**Σχ. 2β**). Τα ελατήρια Winkler περιγράφουν την εδαφική αντίδραση στην αντίστοιχη κύρια κατεύθυνση και βαθμονομούνται έναντι αριθμητικών πειραμάτων μονοαξονικής μετατόπισης του αγωγού.

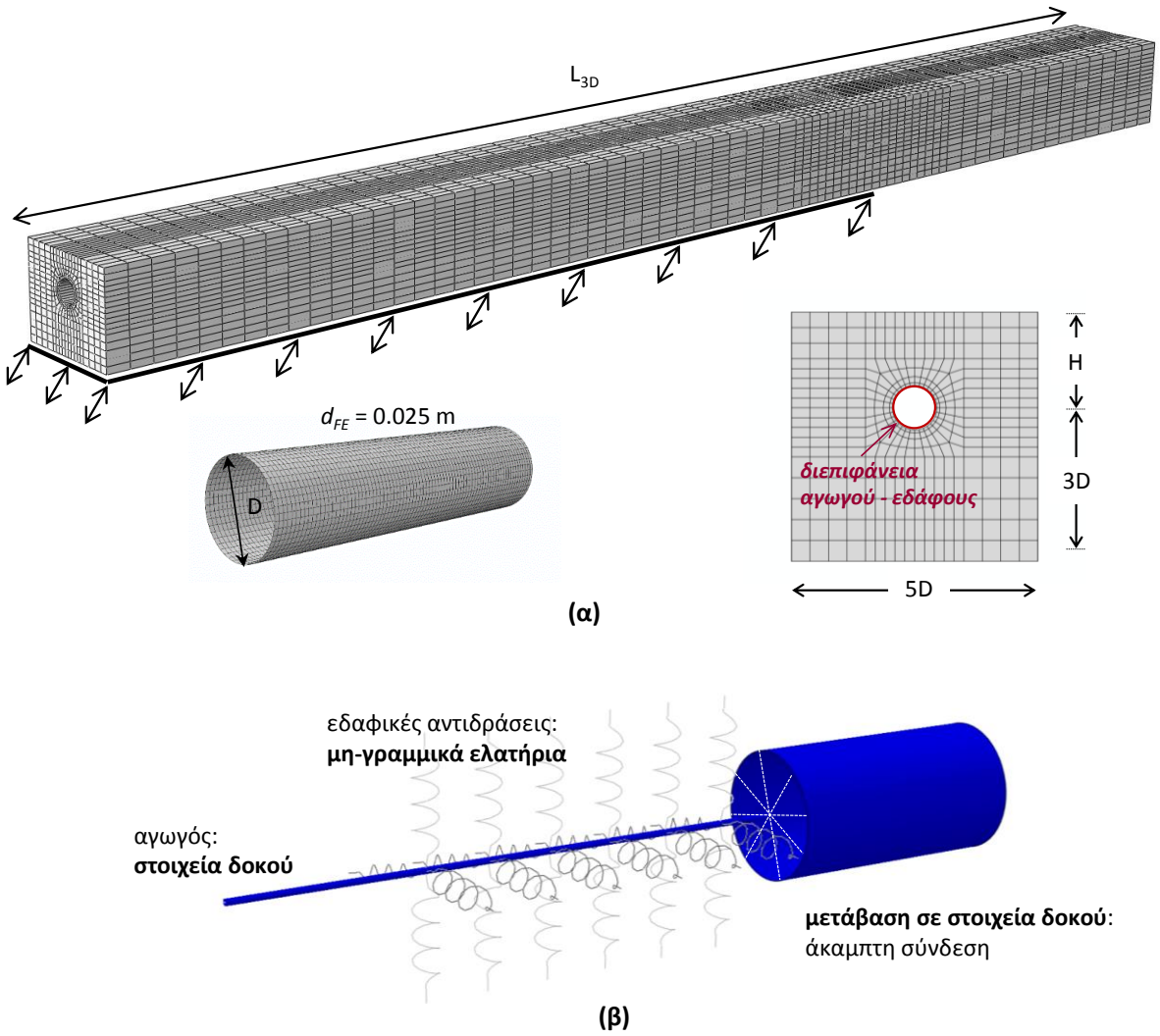

Σχήμα 2. Σχηματική παρουσίαση της προτεινόμενης αριθμητικής μεθοδολογίας: (α) 3-Δ προσομοίωση για την «εγγύς πεδίου» απόκριση και (β) προσομοίωση της «μακρινού πεδίου» με γραμμικά στοιχεία δοκού για τον αγωγό και ελατήρια για το έδαφος.

Για την τεκμηρίωση της προτεινόμενης αριθμητικής μεθοδολογίας αξιοποιήθηκε σημαντικό πλήθος πειραμάτων. Αρχικώς, χρησιμοποιήθηκαν τα αποτελέσματα πειραμάτων μονοαξονικής μετατόπισης αγωγού εντός εδάφους (μικρής και μεγάλης κλίμακας) με στόχο την επαλήθευση/βαθμονόμηση του εδαφικού καταστατικού προσομοιώματος. Το **Σχ. 3** παρουσιάζει ενδεικτικές συγκρίσεις των αριθμητικών αποτελεσμάτων με τα αντίστοιχα πειραματικά για οριζόντια (Trautmann & O'Rourke (1985)) κατακόρυφη προς τα πάνω (Cheuk, et al (2008)) και αξονική (Wijewickreme, et al 2009) μετατόπιση του αγωγού.

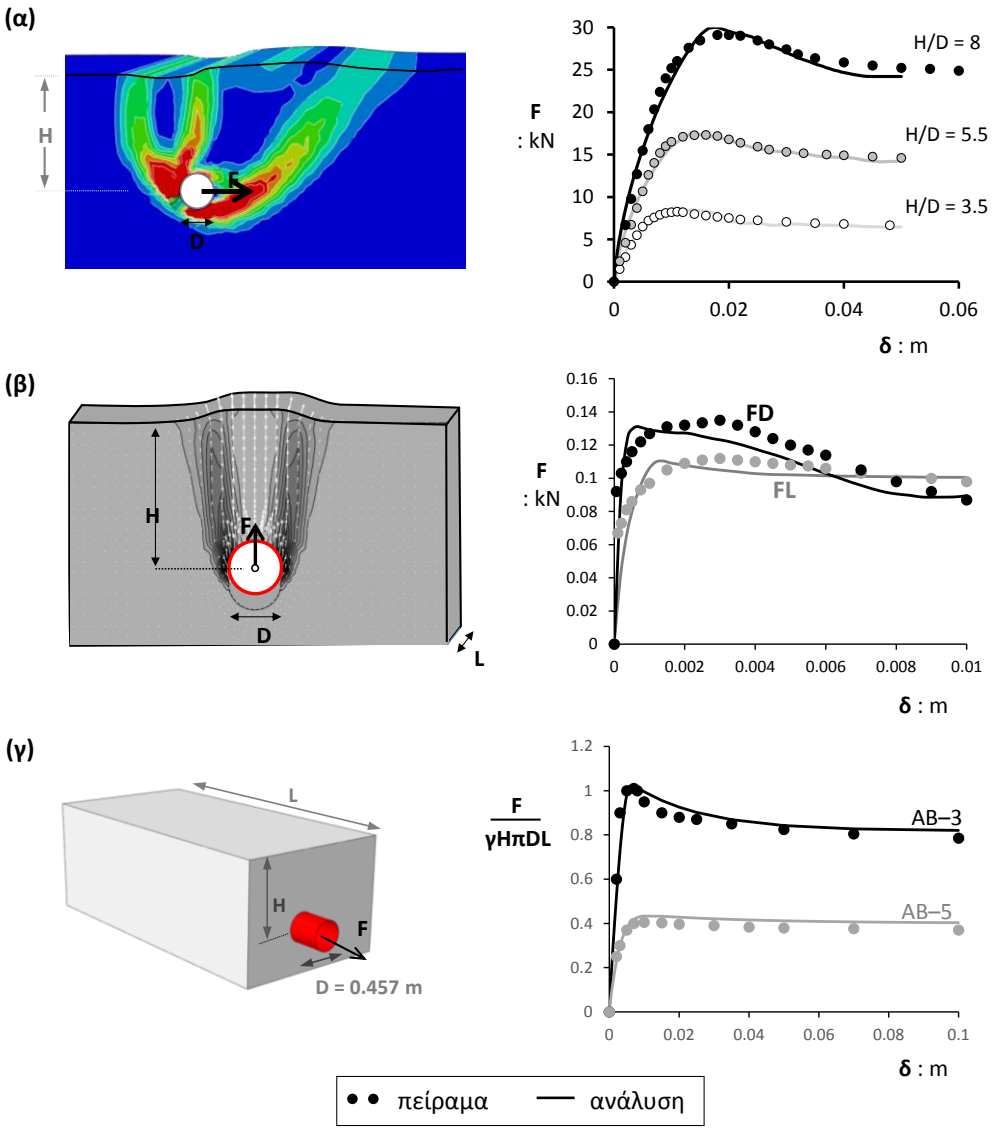

Σχήμα 3. συγκρίσεις των αριθμητικών αποτελεσμάτων με τα αντίστοιχα πειραμάματα μονο-αξονικής μετατόπισης του αγωγού: (α) οριζόντια μετατόπιση του αγωγού (Trautmann and O'Rourke 1985) (β) κατακόρυφη προς τα πάνω (Cheuk et al 2008) και (γ) αξονική μετατόπιση (Wijewickreme et al 2009).

Επιπλέον, ελέγχθηκε η ικανότητα του αριθμητικού μας προσομοιώματος να αναπαράγει ρεαλιστικώς την απόκριση μεταλλικού κελύφους σε καθαρή κάμψη. Προς τούτο προσομοιώθηκε αριθμητικά σειρά πειραμάτων (Van Es, et al (2014)) σε μεταλλικούς αγωγούς με και χωρίς εσωτερική πίεση. Τα αποτελέσματα της σύγκρισης αποτυπώνονται στο **Σχ. 4**.

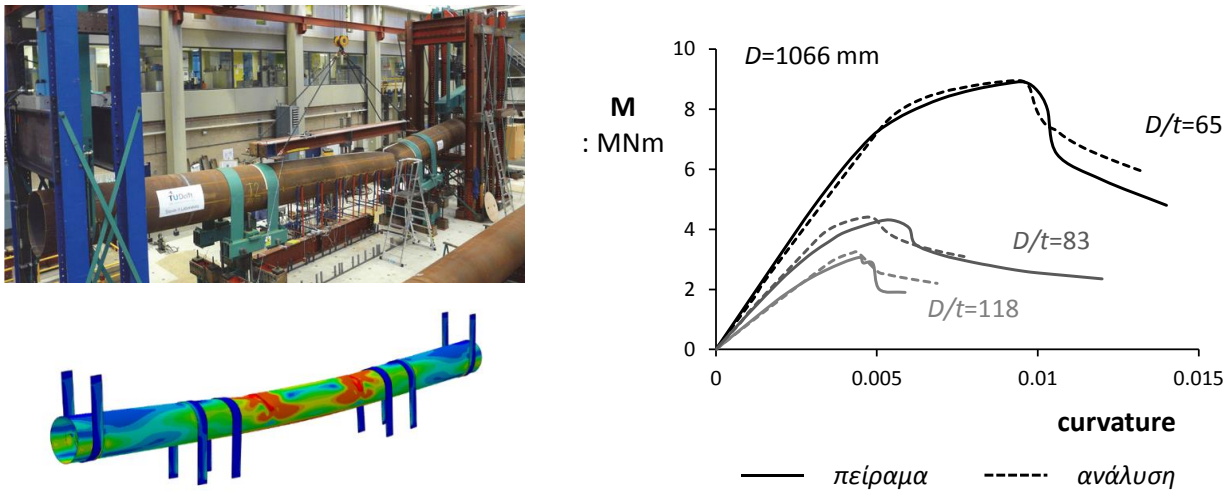

Σχήμα 4. Μεταλλικός αγωγός σε καθαρή κάμψη: Σύγκριση πειραμάτων (van Es et al 2014) και αριθμητικών αποτελεσμάτων.

Τέλος, για την πειραματική διερεύνηση της αλληλεπίδρασης αγωγού με κανονική και ανάστροφη διάρρηξη διεξήχθησαν πειράματα μικρής κλίμακας στο Εργαστήριο Εδαφομηχανικής. Σε σύνολο 26 πειραμάτων που έλαβαν χώρα (στο κουτί προσομοίωσης διάρρηξης) μελετήθηκε η επιρροή του τύπου της διάρρηξης (κανονική ή ανάστροφη), η επιρροή του βάθους εγκιβωτισμού και η γεωμετρία του αγωγού (D/t) στην ευπάθεια του αγωγού. Τα πειραματικά αποτελέσματα αξιοποιήθηκαν και για την επικύρωση της «εγγύς πεδίου» αριθμητικής μεθοδολογίας. Προηγήθηκε λεπτομερή βαθμονόμηση του καταστατικού προσομοιώματος της άμμου μέσω δοκιμών απ' ευθείας διάτμησης, ενώ για την αξιόπιστη αναπαραγωγή της πραγματικής καμπύλης τάσης-παραμόρφωσης του υλικού των αγωγών διενεργήθηκαν δοκιμές μονοαξονικού εφελκυσμού σε τυπικά δοκίμια αγωγών. Στα **Σχ. 5** και **Σχ. 6** παρουσιάζονται δύο ενδεικτικά αποτελέσματα όπου χαλύβδινος αγωγός διαμέτρου D=35 mm και πάχους t=0.5 mm υποβάλλεται σε κανονική και ανάστροφη τεκτονική διάρρηξη. Η αριθμητική μεθοδολογία περιγράφει ικανοποιητικά την διάδοση της διάρρηξης μέσω του εδαφικού σχηματισμού (παρατηρείστε την πρόβλεψη τόσο της κύριας και της αντιθετικής διάρρηξης όσο και της δευτερεύουσας διάρρηξης σε μικρές μετατοπίσεις στην περίπτωση κανονικού ρήγματος), ενώ προβλέπει με ακρίβεια την κάμψη του αγωγού υπό τις εδαφικές ωθήσεις και τον σχηματισμό τοπικού λυγισμού.

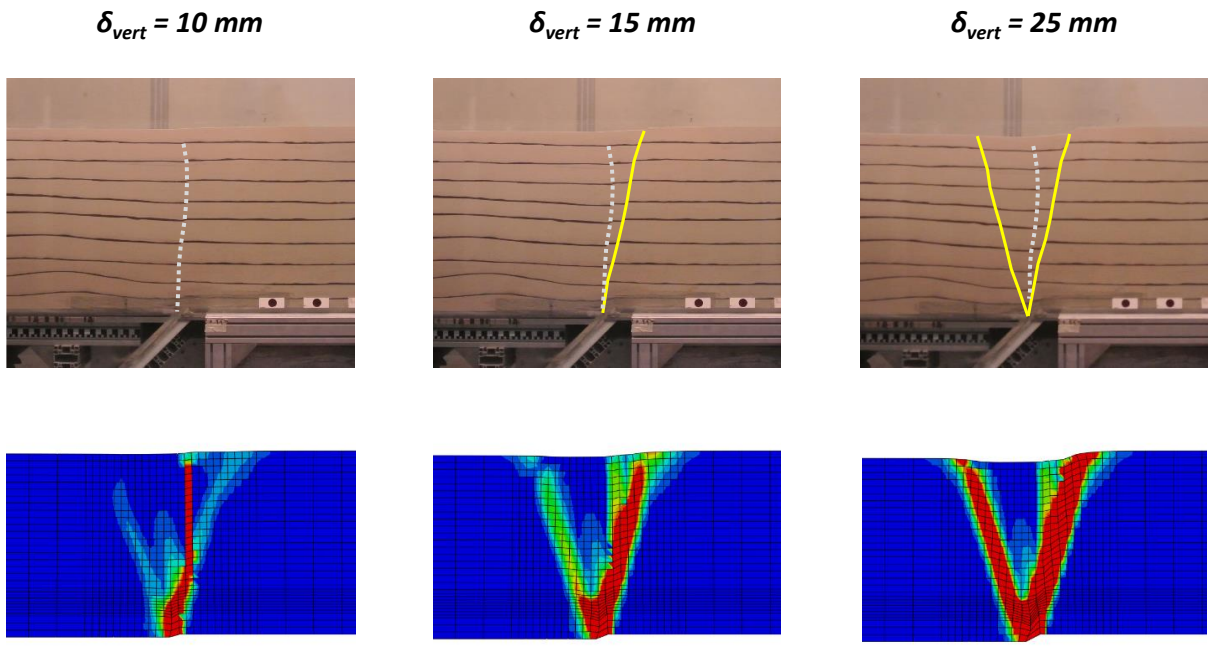

(α)

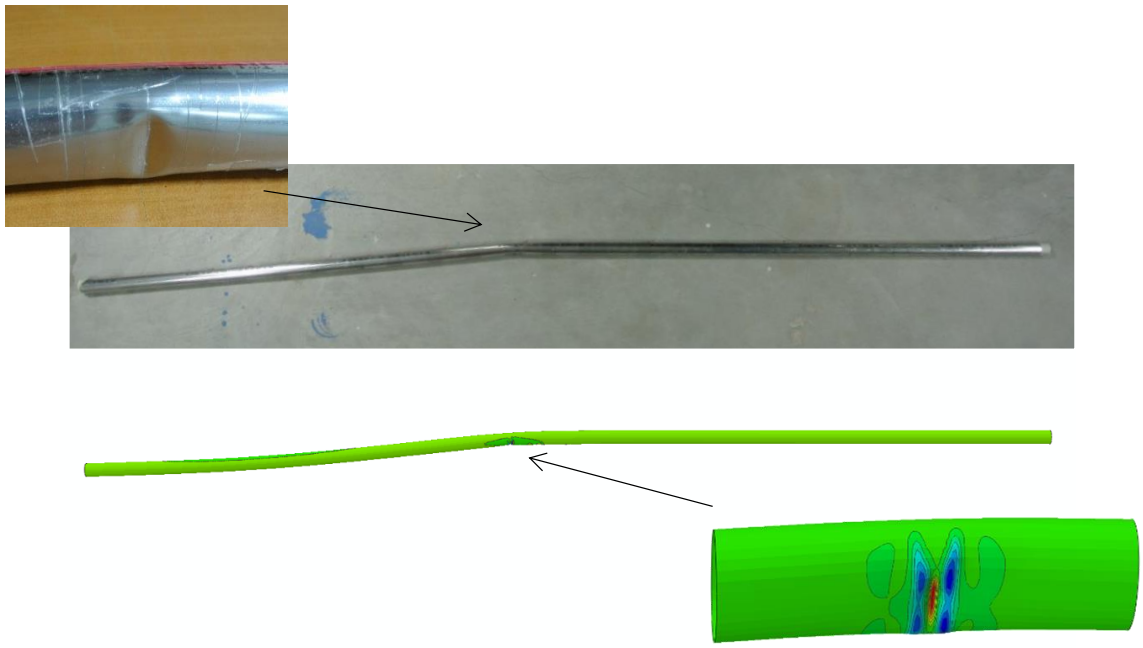

(β)

Σχήμα 5. Σύγκριση αριθμητικών και πειραματικών αποτελεσμάτων για την περίπτωση αγωγού υποβαλλόμενου σε κανονική διάρρηξη: (α) διάδοση της διάρρηξης και (β) παραμόρφωση του αγωγού.

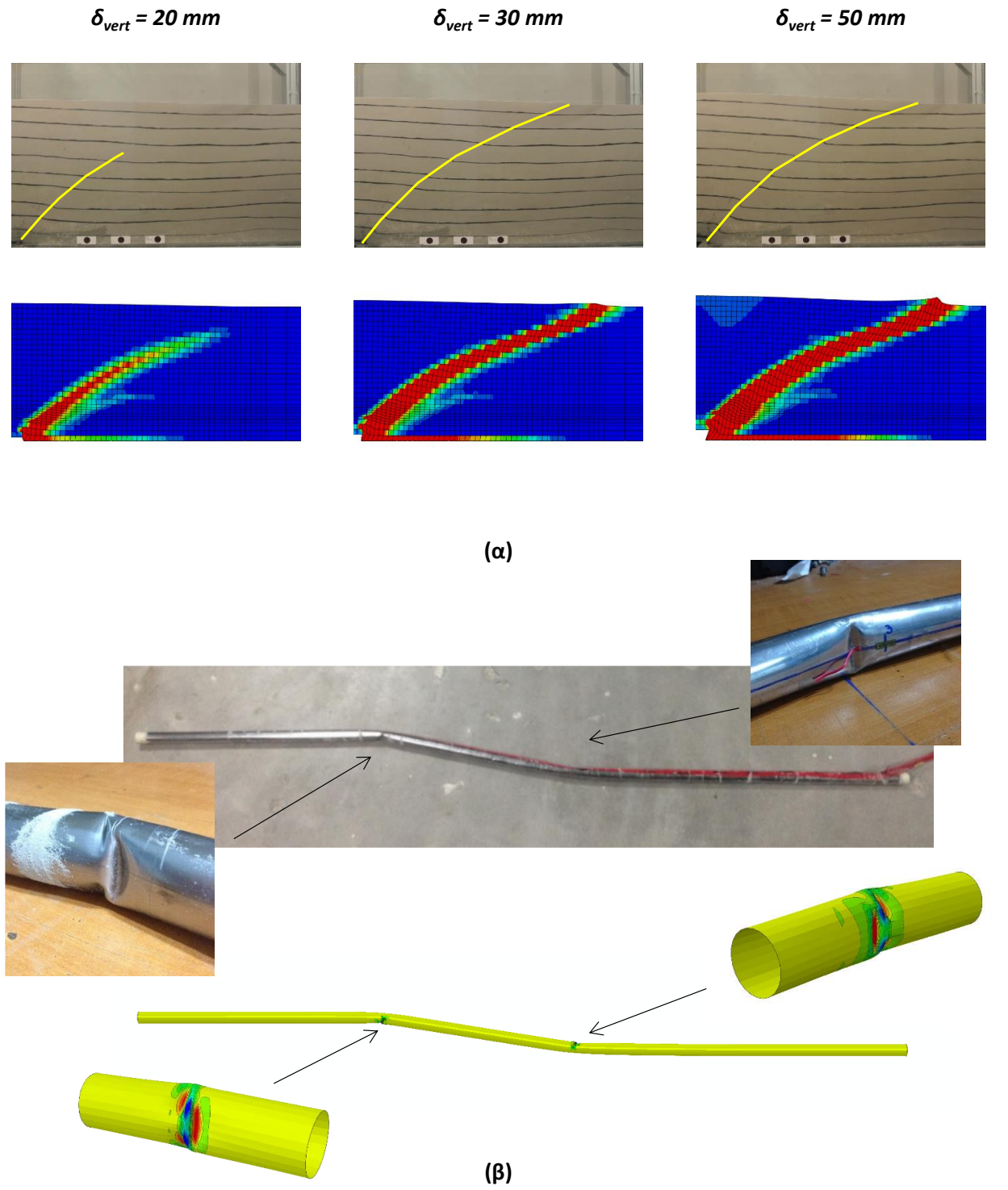

Σχήμα 6. Σύγκριση αριθμητικών και πειραματικών αποτελεσμάτων για την περίπτωση αγωγού υποβαλλόμενου σε ανάστροφη διάρρηξη: (α) διάδοση της διάρρηξης και (β) παραμόρφωση του αγωγού.

Για την επαλήθευση της μεθοδολογίας προσομοίωσης της συμπεριφοράς «μακρινού πεδίου», αξιοποιήθηκαν πειράματα εξόλκευσης αγωγού μεγάλης κλίμακας. Ιδιαίτερη έμφαση δόθηκε στην επίδραση της διαστολικότητας του εδάφους. Όπως σχηματικά απεικονίζεται στο Σχ. 7(α), κατά την εξόλκευση του αγωγού, το περιβάλλον σε αυτόν έδαφος αντιστέκεται με την ανάπτυξη διατμητικών τάσεων στην διεπιφάνεια αγωγού-εδάφους. Σε περίπτωση διαστολικού εδάφους η διάτμηση αυτή συνοδεύεται από τάση για διόγκωση της ζώνης διάτμησης, η οποία ωστόσο περιορίζεται εκατέρωθεν από τον αγωγό και το έδαφος. Ο περιορισμός αυτός της τάσης διόγκωσης μεταφράζεται σε επιπρόσθετες κάθετες τάσεις στην διεπιφάνεια αγωγού-εδάφους (επιπλέον των αρχικών γεωστατικών) οι οποίες τελικώς συνεισφέρουν στην αύξηση της δύναμης αντίστασης. Για την ποσοτικοποίηση της επίδρασης αυτής αναπτύχθηκε πρωτότυπη απλοποιημένη μεθοδολογία που λαμβάνει υπόψη την αύξηση της ορθής τάσης στην διεπιφάνεια αγωγού-εδάφους εξαιτίας της εμποδιζόμενης τάσης για διόγκωση. Το μέγεθος της διόγκωσης της ζώνης διάτμησης δz αρχικώς εκτιμάται μέσω δοκιμών απευθείας διάτμησης. Οι αυξημένες $\Delta\sigma_n$ στην διεπιφάνεια αγωγού εδάφους εκτιμώνται μέσω μιας δοκιμής διεύρυνσης της κοιλότητας (δηλαδή της ακτίνας του αγωγού) κατά δz. Η κατανομή αυτή της αυξημένη κάθετης τάσης στην διεπιφάνεια αγωγού-εδάφους λαμβάνεται υπόψη έμμεσα με την χρήση ενός κατάλληλα αυξημένου συντελεστή οριζοντίων ωθήσεων $K_{0,equiv}$. Τέλος, υπό την επίδραση αυτού του συντελεστή $K_{0,equiv}$ επιβάλλεται αξονική μετακίνηση στον αγωγό για τον υπολογισμό της αξονικής δύναμης αντίδρασης του περιβάλλοντος εδάφους. Η μεθοδολογία αυτή εφαρμόζεται για την προσομοίωση των αποτελεσμάτων πειραμάτων αξονικής μετατόπισης αγωγού (GIPIPE 2015). Στο **Σχ. 7β** εμφανίζονται τα αποτελέσματα της μεθοδολογίας σε σύγκριση με τα αντίστοιχα πειραματικά αποτελέσματα, ενώ παράλληλα σημειώνεται και η εκτίμηση της μέγιστης αξονικής δύναμης σύμφωνα με τους ισχύοντες κανονισμούς. Καθώς οι ισχύοντες κανονισμοί αγνοούν την επίδραση της διαστολικότητας στην αύξηση της αξονικής εδαφικής αντίστασης, η απόκλιση της πρόβλεψής τους είναι θεαματική. Αντιθέτως, εφαρμόζοντας την ανωτέρω μεθοδολογία μπορούμε να προβλέψουμε ικανοποιητικά την πραγματική αξονική αντίδραση του εδάφους.

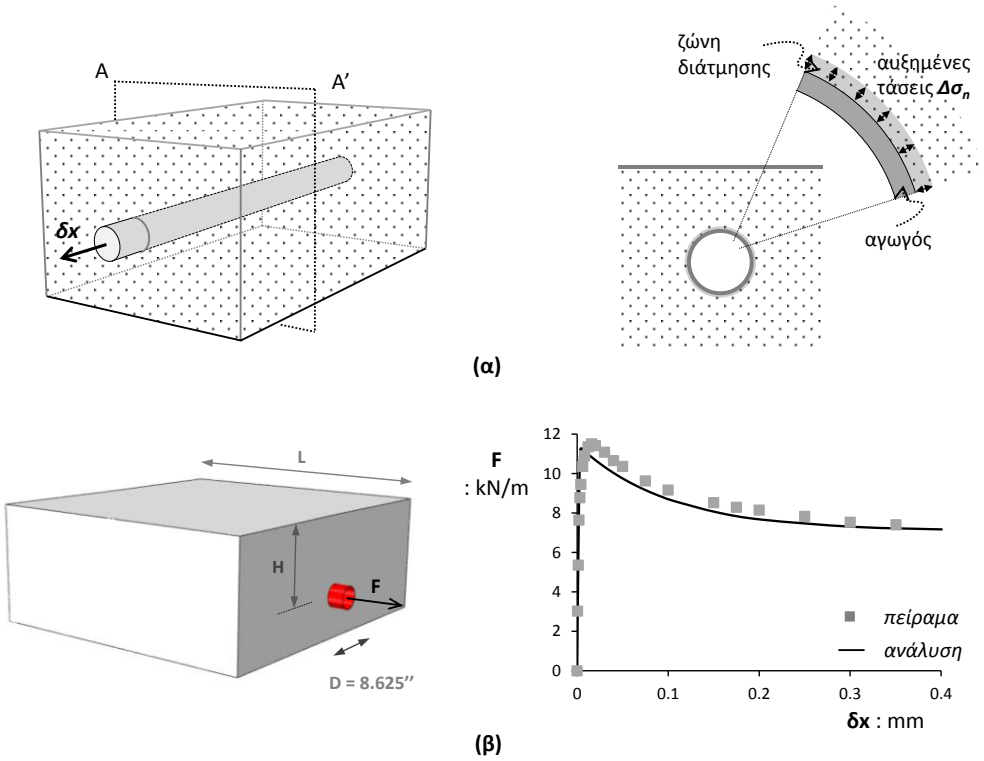

Σχήμα 7. (α) Ποιοτική απεικόνιση της επίδρασης της διαστολικότητας στην αύξηση της αξονικής αντίστασης. (β) Σύγκριση αριθμητικών και πειραματικών αποτελεσμάτων για την περίπτωση αξονικής μετατόπισης του αγωγού λαμβάνοντας υπόψη την επίδραση της διαστολικότητας

Διερεύνηση Συμπεριφοράς Υπογείου Αγωγού σε Τεκτονική Διάρρηξη

Εν συνεχεία, έχοντας βαθμονομήσει και επαληθεύσει την αριθμητική μεθοδολογία, μελετάται παραμετρικώς η δομητική συμπεριφορά υπογείων χαλύβδινων αγωγών απείρου μήκους υποβαλλόμενων σε κανονική και ανάστροφη διάρρηξη. Επιλέγονται γεωμετρίες αντιπροσωπευτικές αγωγών μεταφοράς υδρογονανθράκων σχετικώς μεγάλων διαμέτρων (η διάμετρος κυμαίνεται από D=28” έως D=48”) και λόγο διαμέτρου προς πάχος τοιχώματος D/t≈70, και μελετάται η συμπεριφορά τους μέχρι την αστοχία, εξετάζοντας την επίδραση των εδαφικών παραμέτρων (αντοχή, διαστολικότητα, μέτρο ελαστικότητας) και του βάθους εγκιβωτισμού. Οι τιμές των παραμέτρων που εξετάζονται στα πλαίσια της παραμετρικής διερεύνησης εμφανίζονται στο **Σχ. 8**.

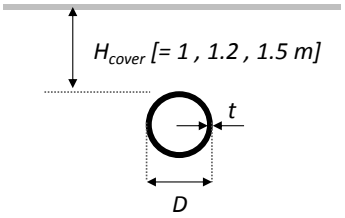

(α)

D *(in)*	***t*** *(in)*	***D/t***
28	0.375	74.7
36	0.5	72
40	0.562	71.2
48	0.688	69.8

(β)

φ *(deg)*	φ_{res} *(deg)*	ψ *(deg)*	δ_{xyield} *(mm)*	δ_{xpeak} *(mm)*	δ_{xres} *(mm)*	δ_z *(mm)*	ρ *(Mg/m³)*
45	35	15	0.5	1.25	4.5	0.70	1.8
40	32	10	0.85	1.75	5.0	0.46	1.7
35	30	5	1.15	2.0	5.5	0.24	1.6
30	30	0	1.5	-	-	-	1.5

(γ)

Σχήμα 8. Οι τιμές των παραμέτρων που εξετάζονται στα πλαίσια της παραμετρικής διερεύνησης: (α) βάθος κάλυψης του αγωγού, (β) γεωμετρικά χαρακτηριστικά των αγωγών και (γ) χαρακτηριστικά των εδαφών που λαμβάνονται υπόψη (αποτελέσματα δοκιμών απευθείας διάτμησης).

Το **Σχ. 9α** αφορά σε ένα χαρακτηριστικό πρόβλημα: αγωγός (από χάλυβα X65) διαμέτρου D=40” και πάχους t=0.562” εγκιβωτισμένος εντός στρώματος ξηρής άμμου (με γωνία τριβής φ=40^o και γωνία διαστολικότητας ψ=10^o) σε βάθος H_{cover}=1.2m υποβάλλεται σε κανονική διάρρηξη. Παρουσιάζεται η εξέλιξη της έντασης στον αγωγό σε όρους μέγιστης αναπτυσσόμενης εφελκυστικής παραμόρφωσης (ανεξαρτήτως θέσης εμφάνισης) με την αύξηση του πλάτους της διάρρηξης, και ο παραμορφωμένος κάνναβος του τμήματος του αγωγού το οποίο υφίσταται την μέγιστη καταπόνηση (με σημειωμένες τις ισοϋψείς των αξονικών παραμορφώσεων) σε χαρακτηριστικά στιγμιότυπα. Διακρίνονται τρεις (3) περιοχές απόκρισης. Συγκεκριμένα, για δ_{fault} < 0.5m η μέγιστη αναπτυσσόμενη εφελκυστική παραμόρφωση (που οφείλεται στον συνδυασμό καμπτικής και αξονικής καταπόνησης) δεν ξεπερνά το όριο διαρροής του χάλυβα και ο αγωγός συμπεριφέρεται ελαστικά. Καθώς το μέγεθος της επιβαλλόμενης μετακίνησης αυξάνει ο αγωγός εισέρχεται στην πλαστική του περιοχή και ο ρυθμός συσσώρευσης παραμόρφωσης αυξάνεται σημαντικά (Περιοχή II — Πλαστική Συμπεριφορά). Για πλάτος τεκτονικής διάρρηξης δ_{fault} < 1.9 m η μέγιστη αναπτυχθείσα παραμόρφωση είναι καμπτικής προέλευσης και ως εκ τούτου απαντάται στην θέση μέγιστης καμπυλότητας. Για μεγαλύτερες τιμές δ_{fault}, η κυρίαρχη μορφή καταπόνησης και η θέση της μέγιστης παραμόρφωσης αλλάζει (Περιοχή III) – ο αγωγός πλέον

καταπονείται αξονικά και τελικώς η θραύση του αγωγού (σχηματισμός λαιμού) λαμβάνει χώρα σε διατομή πλησίον της διάρρηξης (ήτοι στο τμήμα του αγωγού με τις εντονότερες αξονικές παραμορφώσεις).

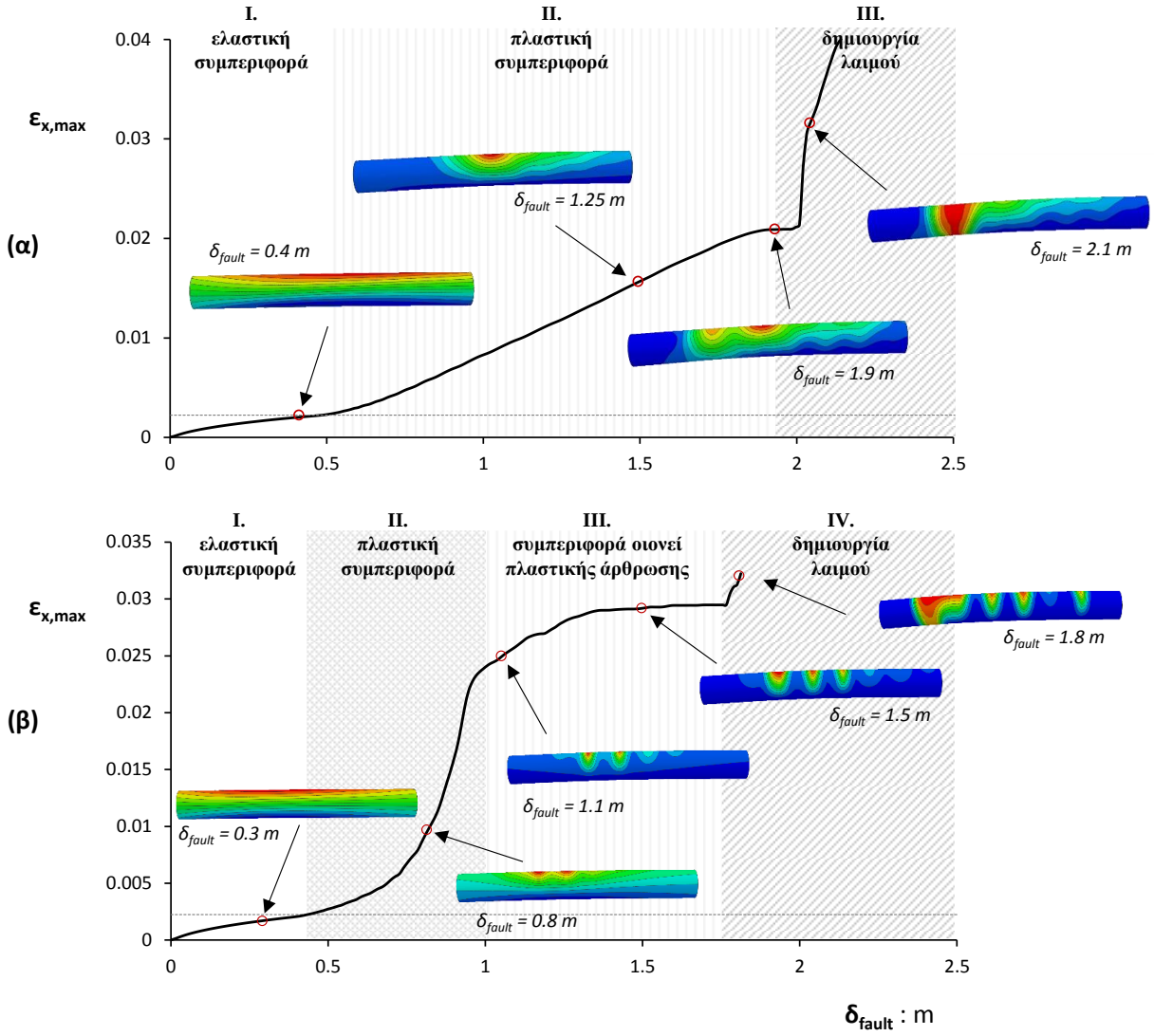

Σχήμα 9. Απόκριση αγωγού σε κανονική διάρρηξη: αγωγός διαμέτρου D=40" και πάχους t=0.562" εγκιβωτισμένος σε βάθος H_{cover}=1.2 m εντός πυκνής άμμου με γωνία τριβής φ=40°: Εξέλιξη της μέγιστης εφελκυστικής παραμόρφωσης με την αύξηση της μετακίνησης διάρρηξης με θεώρηση (α) p_{oper}=0 MPa και (β) $p_{oper}=p_{max}$=9 MPa.

Στο **Σχ. 9β** παρουσιάζεται η εξέλιξη της καταπόνησης του ίδιου αγωγού στην περίπτωση που λειτουργεί υπό την μέγιστη πίεση για την οποία σχεδιάστηκε p_{max}= 9 MPa η οποία υπολογίζεται ως:

$$p_{max} = 0.72\left(\frac{2\sigma_y t}{D}\right)$$

Η ύπαρξη της εσωτερικής πίεσης οδηγεί σε αισθητή διαφοροποίηση της συμπεριφοράς του αγωγού. Πρώτον, όπως αναμένετο, ο αγωγός διαρρέει σε (ελαφρώς) μικρότερη μετακίνηση από τον αντίστοιχο χωρίς πίεση αγωγό (δ_{yield} ≈ 0.4 m αντί δ_{yield} ≈ 0.5 m). Δεύτερον, ο ρυθμός συσσώρευσης παραμόρφωσης στην πλαστική περιοχή αυξάνει σημαντικά (Περιοχή II). Αξίζει να σημειωθεί ότι στην πλέον εντεινόμενη διατομή η αξονική παραμόρφωση της άνω ίνας αγγίζει το 2.5% για επιβληθείσα μετακίνηση ρήγματος μόλις 1m. Τρίτον, η καμπύλη της εξέλιξης της μέγιστης εφελκυστικής παραμόρφωσης με την αύξηση της μετατόπισης της διάρρηξης εμφανίζει έναν οριζόντιο κλάδο: η αύξηση της μετατόπισης (δηλαδή της καμπυλότητας του κρίσιμου τμήματος) δεν προκαλεί αύξηση στο μέγεθος της παρατηρούμενης παραμόρφωσης στην πλέον εντεινόμενη διατομή, ένδειξη πως ο αγωγός έχει εξαντλήσει την πλαστική ροπή αντοχής του (Περιοχή III). Τελικώς, και στην περίπτωση του υπό πίεση αγωγού επέρχεται μια μετατόπιση όπου ο εφελκυσμός γίνεται κρίσιμος και έχουμε τη δημιουργία λαιμού.

(α)

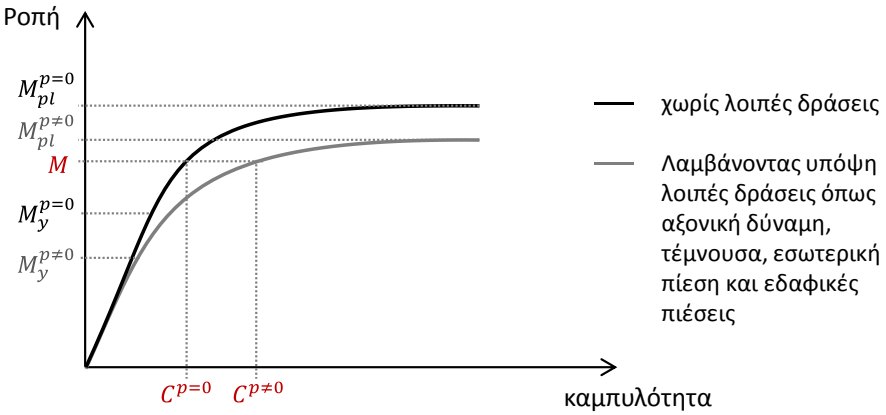

(β)

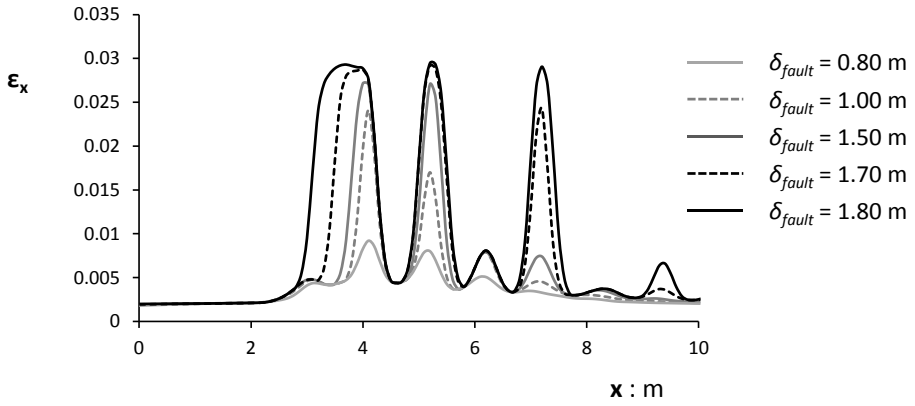

Σχήμα 10. (α) Διάγραμμα ροπής – καμπυλότητας για ευθύγραμμο αγωγό σύμφωνα με τον EN1993-4-3 Ευρωκώδικα. (α) Κατανομή της αξονικής παραμόρφωσης κατά μήκος της εφελκυστικής πλευράς του κρίσιμου τμήματος του αγωγού για διάφορα μεγέθη μετατόπισης ρήγματος.

Οι παραπάνω διαφοροποιήσεις στην συμπεριφορά του αγωγού υπό πίεση αποδίδονται στην μείωση της καμπτικής αντοχής του αγωγού με την ταυτόχρονη δράση της εσωτερικής πίεσης. Στην κίνηση του εδάφους λόγω της εμφάνισης της διάρρηξης αντιστέκεται ο αρχικώς ευθύγραμμος αγωγός. Ως αποτέλεσμα, εδαφικές ωθήσεις αναπτύσσονται στον αγωγό, οι οποίες και δημιουργούν καμπτική καταπόνηση. Ας θεωρήσουμε για λόγους απλούστευσης πως για την ίδια μετατόπιση ρήγματος αναπτύσσονται περίπου ίσες εδαφικές πιέσεις κάθετα στον άξονα του αγωγού και τελικώς παρόμοιες καμπτικές ροπές τόσο στην περίπτωση του υπό πίεση όσο και σε αυτήν του χωρίς πίεση αγωγού. Παράλληλα, στο **Σχ. 10α** εμφανίζεται σε ποιοτικούς όρους η επίδραση της εσωτερικής πίεσης στην συμπεριφορά του αγωγού σε όρους ροπής-καμπυλότητας, σύμφωνα με τον EN 1993-4-3 Ευρωκώδικα: για ευθύγραμμο αγωγό υπό καθαρή κάμψη, η αρχικώς ελαστική απόκριση μέχρι τη ροπή διαρροής $M_y^{p=0}$ ακολουθείται από μια σταδιακή μείωση της δυσκαμψίας μέχρι την εξάντληση της πλαστικής ροπής αντοχής $M_{pl}^{p=0}$ όπου το σύνολο της διατομής έχει πλαστικοποιηθεί. Όπως γλαφυρά αποτυπώνεται στο διάγραμμα αυτό, υπό την ταυτόχρονη δράση της εσωτερικής πίεσης τόσο η αντίστοιχη ροπή διαρροής $M_y^{p\neq0}$ όσο και πλαστική ροπή διαρροής $M_{pl}^{p\neq0}$ μειώνονται. Υπό αυτό το πρίσμα, γίνεται κατανοητή η γρηγορότερη πλαστικοποίηση του υπό πίεση αγωγού. Το διάγραμμα του **Σχ. 10α** είναι αρκετά διαφωτιστικό για να ερμηνεύσει και την αύξηση του ρυθμού συσσώρευσης πλαστικών παραμορφώσεων. Ας θεωρήσουμε πως η μετατόπιση της διάρρηξης οδηγεί σε απαίτηση σε ροπή Μ μεγαλύτερη από την ροπή διαρροής τόσο του χωρίς $M_y^{p=0}$ όσο και του υπό πίεση αγωγού $M_y^{p\neq0}$. Η συγκεκριμένη ροπή Μ οδηγεί τον υπό πίεση αγωγό σε μεγαλύτερη καμπυλότητα (και επομένως παραμόρφωση). Επιπλέον, μια αύξηση της ροπής αυτής ΔΜ θα οδηγήσει σε μεγαλύτερη αύξηση καμπυλότητας ΔC τον υπό πίεση αγωγό, καθώς αυτός βρίσκεται πιο βαθιά στην πλαστική περιοχή και χαρακτηρίζεται από μικρότερη δυσκαμψία από τον αντίστοιχο χωρίς πίεση αγωγό. Επομένως, είναι κατανοητή η αύξηση του ρυθμού συσσώρευσης παραμόρφωσης στην πλαστική περιοχή για τον υπό πίεση αγωγό. Με το ίδιο σκεπτικό εξηγείται εμμέσως και η τρίτη διαφοροποίηση στην συμπεριφορά: ο οριζόντιος κλάδος στην εξέλιξη των αξονικών παραμορφώσεων. Η μειωμένη πλαστική ροπή αντοχής σε συνδυασμό με τον αυξημένο ρυθμό συσσώρευσης πλαστικών παραμορφώσεων οδηγούν στην εξάντληση της πλαστικής ροπής αντοχής του υπό πίεση αγωγού σε μετατόπιση ρήγματος αρκετά μικρότερη από τον χωρίς πίεση αγωγό. Όταν ο αγωγός φτάσει την πλαστική ροπή αντοχής του δεν παρατηρείται αύξηση της μέγιστης παραμόρφωσης (καθώς δεν μπορεί να αυξηθεί περεταίρω η ροπή στην κρίσιμη διατομή), αλλά αντιθέτως επέρχεται μια ανακατανομή της έντασης. Στο **Σχ. 10β** όπου εμφανίζεται η κατανομή της αξονικής παραμόρφωσης στην εφελκυστική πλευρά του κρίσιμου τμήματος του αγωγού, επιχειρείται μια απεικόνιση της ανακατανομής αυτής. Στην κυματοειδή κατανομή του

σχήματος ξεχωρίζουν τρεις κορυφές, όπου οι εφελκυστικές παραμορφώσεις μεγιστοποιούνται. Αρχικώς η μέγιστη τιμή των τριών αυτών κορυφών αυξάνεται με την αύξηση της μετατόπισης ρήγματος. Για μετατοπίσεις όμως μεγαλύτερες της $\delta_{fault} \approx 1$ m, η μέγιστη τιμή τους πρακτικώς παραμένει σταθερή. Αντιθέτως, ο μηχανισμός παραλαβής του έργου της επιβαλλόμενης καμπυλότητας αλλάζει: το πλάτος της πρώτης κορυφής ($x = 4$ m) αυξάνει σταδιακά προς τα αριστερά. Επομένως, η επιπλέον επιβαλλόμενη ένταση παραλαμβάνεται από την κινητοποίηση μεγαλύτερης έκτασης του κρίσιμου τμήματος του αγωγού και όχι μέσω αύξησης της έντασης της κρίσιμης διατομής – περίπτωση ανακατανομής της έντασης. Η συμπεριφορά αυτή θυμίζει τη συμπεριφορά πλαστικής άρθρωσης. Αντιθέτως, δεν παρατηρείται στον χωρίς πίεση αγωγό γιατί αυτός χαρακτηρίζεται από μεγαλύτερη πλαστική ροπή αντοχής και μικρότερο ρυθμό συσσώρευσης πλαστικών παραμορφώσεων με αποτέλεσμα να επέρχεται πρώτα ο σχηματισμός λαιμού.

Ίσως η πιο εμφανής αλλαγή στην απόκριση του υπό πίεση αγωγού (όπως εμφανίζεται και στο **Σχ. 9**) είναι η διαφοροποίηση της κατανομής της αξονικής παραμόρφωσης κατά μήκος της εφελκυστικής πλευράς του κρίσιμου τμήματος. Ο χωρίς πίεση αγωγός αρχικώς αναπτύσσει μια πρακτικώς ομοιόμορφη κατανομή αξονικών παραμορφώσεων στην ελαστική περιοχή, η οποία όμως συγκεντρώνεται γύρω από το σημείο μέγιστης καμπυλότητας καθώς ο αγωγός εισέρχεται στην πλαστική περιοχή. Αντιθέτως, η αρχικώς ομοιόμορφη κατανομή του υπό πίεση αγωγού μεταβάλλεται σε μια κυματοειδή κατανομή καθώς αυτός εισέρχεται στην πλαστική περιοχή, η οποία χαρακτηρίζεται περισσότερα του ενός μεγίστου (κορυφές) στα οποία η συγκέντρωση τάσεων είναι πιο τοπική. Αυτή η συμπεριφορά θα πρέπει να αποδοθεί στην επιρροή των φαινομένων 2ας τάξης. Συγκεκριμένα, καθώς ο αγωγός εισέρχεται στην πλαστική περιοχή, η καμπύλωσή του αρχίζει και γίνεται σημαντική. Η εφελκυόμενη πλευρά του αγωγού αυξάνει σε μήκος, ενώ η θλιβόμενη συρρικνώνεται. Η δράση της εσωτερικής πίεσης στις δύο αυτές πλευρές έχει ως αποτέλεσμα μια συνισταμένη παρασιτική πίεση που δρα κάθετα στην εφελκυστική πλευρά με φορά τέτοια που τείνει να μειώσει την καμπυλότητα του αγωγού (**Σχ. 11α**). Η παρασιτική αυτή πίεση αυξάνει με την αύξηση της καμπυλότητας του αγωγού. Η ύπαρξή της μαρτυράται από την τάση να ισιώσει κάποιες διατομές κατά μήκος του καμπύλου τμήματος (**Σχ. 11β**), με αποτέλεσμα την συγκέντρωση παραμορφώσεων στις διατομές αυτές και τελικώς τη δημιουργία της χαρακτηριστικής κυματοειδούς κατανομής.

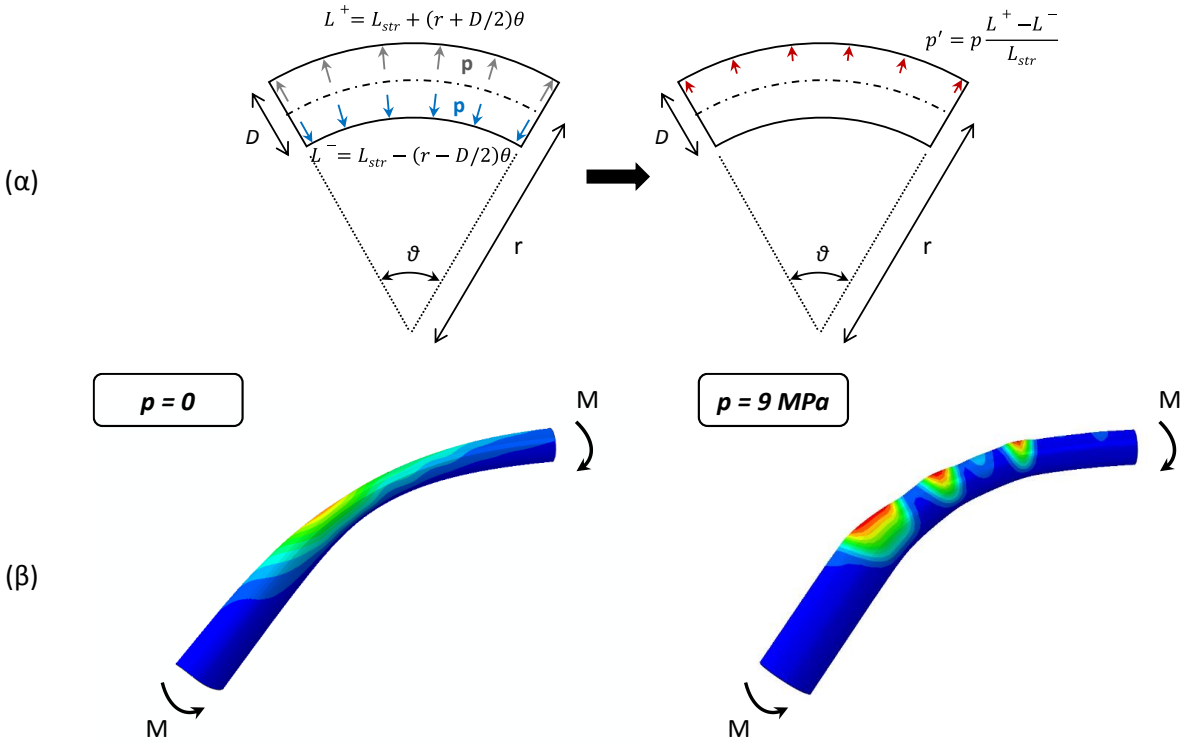

Σχήμα 11. (α) Σχηματική απεικόνιση της επίδρασης της εσωτερικής πίεσης λόγω των φαινομένων 2ας τάξης. (β) Το παραμορφωμένο κρίσιμο τμήμα του αγωγού με ισοϋψείς αξονικών παραμορφώσεων απουσία και παρουσία εσωτερικής πίεσης (συντελεστής μεγέθυνσης 20).

Το **Σχ. 12** συνοψίζει τα αποτελέσματα της παραμετρικής διερεύνησης για αγωγούς υποβαλλόμενους σε κανονική διάρρηξη. Τα αποτελέσματα παρουσιάζονται υπό την μορφή μέγιστης εφελκυστικής παραμόρφωσης στον αγωγό (ανεξαρτήτως θέσης εμφάνισης) συναρτήσει της κανονικοποιημένης μετακίνησης ρήγματος δ_{fault}/D για τα τέσσερα αμμώδη εδάφη και τα τρία χαρακτηριστικά βάθη εγκιβωτισμού θεωρώντας δύο σενάρια πίεσης: (α) αγωγοί χωρίς εσωτερική πίεση και (β) αγωγοί που λειτουργούν υπό την εσωτερική πίεση σχεδιασμού τους p_{max}. Ιδιαίτερο ενδιαφέρον παρουσιάζει το γεγονός πως ανεξαρτήτως διαμέτρου *D* η απόκριση του αγωγού δύναται να ομαδοποιηθεί για δεδομένο λόγο διαμέτρου προς πάχος (*D/t*), δεδομένες εδαφικές ιδιότητες (*φ*, *ψ*, *E*) και δεδομένο βάθος κάλυψης (H_{cover}) μετρούμενο από την επιφάνεια ως την στέψη του αγωγού.

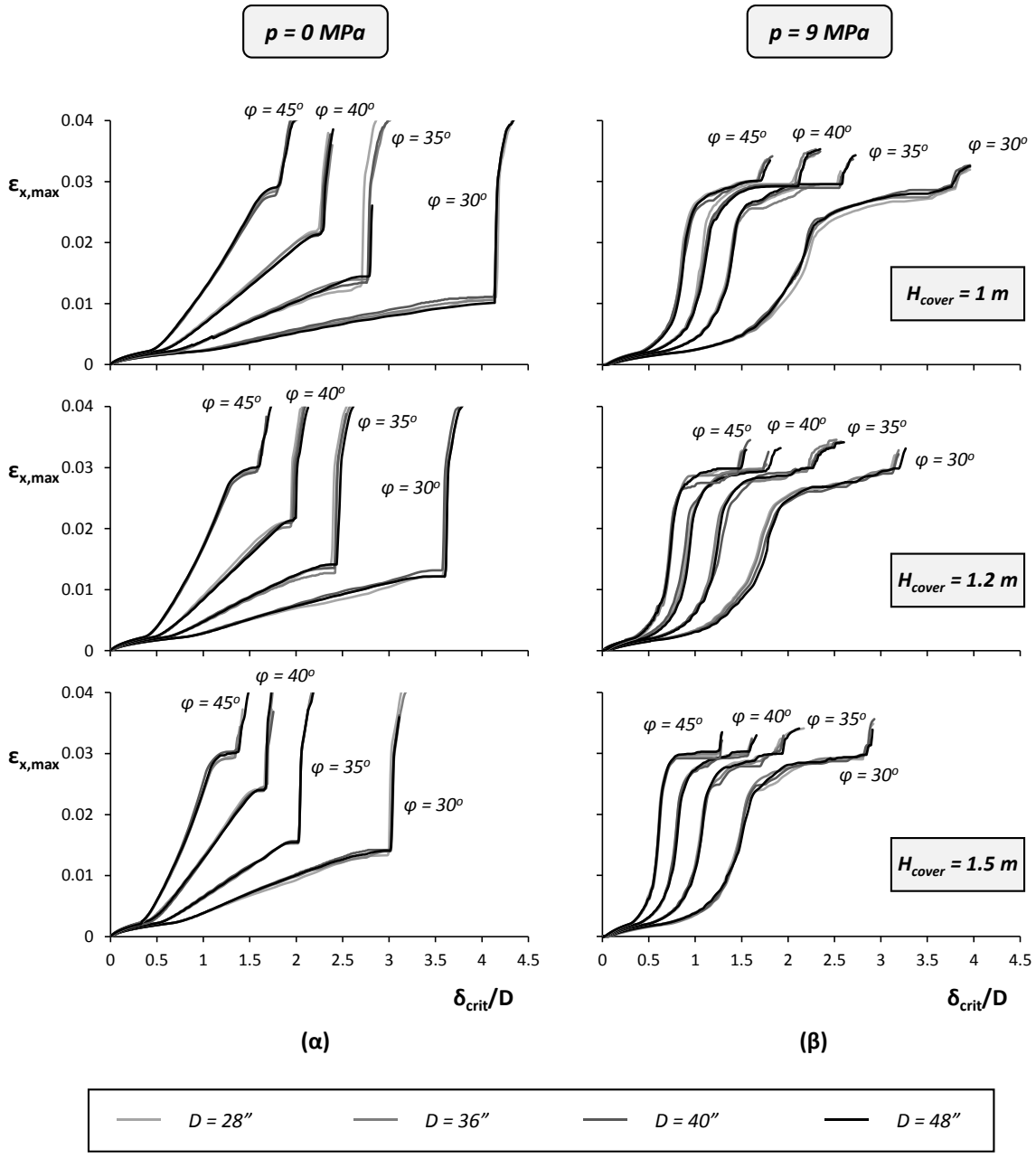

Σχήμα 12. Απόκριση υπογείων αγωγών (D/t≈70) εγκιβωτισμένων εντός αμμώδους εδάφους (γωνίας τριβής φ) υποβαλλόμενων σε κανονική διάρρηξη, θεωρώντας εσωτερική πίεση λειτουργίας (α) p_{oper}=0 και (β) p_{oper}=9 MPa: εξέλιξη της μέγιστης εφελκυστικής παραμόρφωσης με την αύξηση της κανονικοποιημένης μετακίνησης διάρρηξης.

Αντιστοίχως ομαδοποιείται και η απόκριση αγωγών υποβαλλόμενων σε ανάστροφη διάρρηξη. Στο **Σχ.13** παρουσιάζεται η κρίσιμη κανονικοποιημένη μετακίνηση ρήγματος δ_{crit}/D (ικανή να προκαλέσει τοπικό λυγισμό στα τοιχώματα του αγωγού) συναρτήσει της γωνίας τριβής του εδάφους φ και του βάθους εγκιβωτισμού, για αγωγούς με και χωρίς πίεση. Παρατηρείται ότι η κανονικοποιημένη κρίσιμη

μετατόπιση μειώνεται με την αύξηση της εδαφικής αντοχής και την αύξηση του βαθμού εγκιβωτισμού: και οι δύο αυτοί παράγοντες οδηγούν σε αύξηση της σχετικής δυσκαμψίας του εδάφους και επομένως σε πιο ενδόσιμη συμπεριφορά αγωγού.

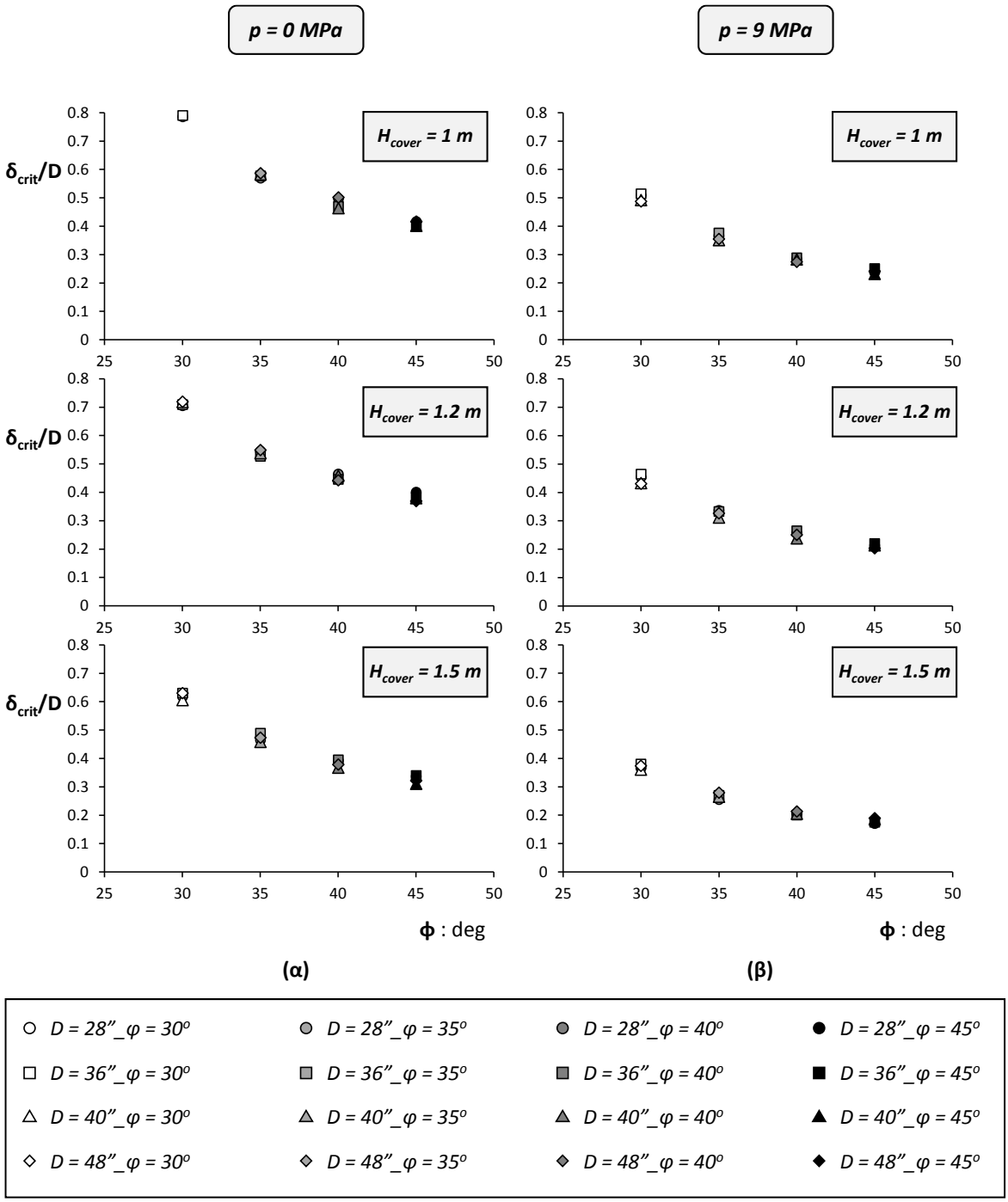

Σχήμα 13. Απόκριση υπογείων αγωγών διαμέτρου D και πάχους t (D/t≈70) εγκιβωτισμένων εντός αμμώδους εδάφους (γωνίας τριβής ϕ) υποβαλλόμενων σε ανάστροφη διάρρηξη, θεωρώντας εσωτερική πίεση λειτουργίας (α) p_{oper}=0 και (β) p_{oper}=9 MPa: κρίσιμη (κανονικοποιημένη ως προς της διάμετρο του αγωγού D) μετατόπιση ρήγματος συναρτήσει της γωνίας τριβής του εδάφους.

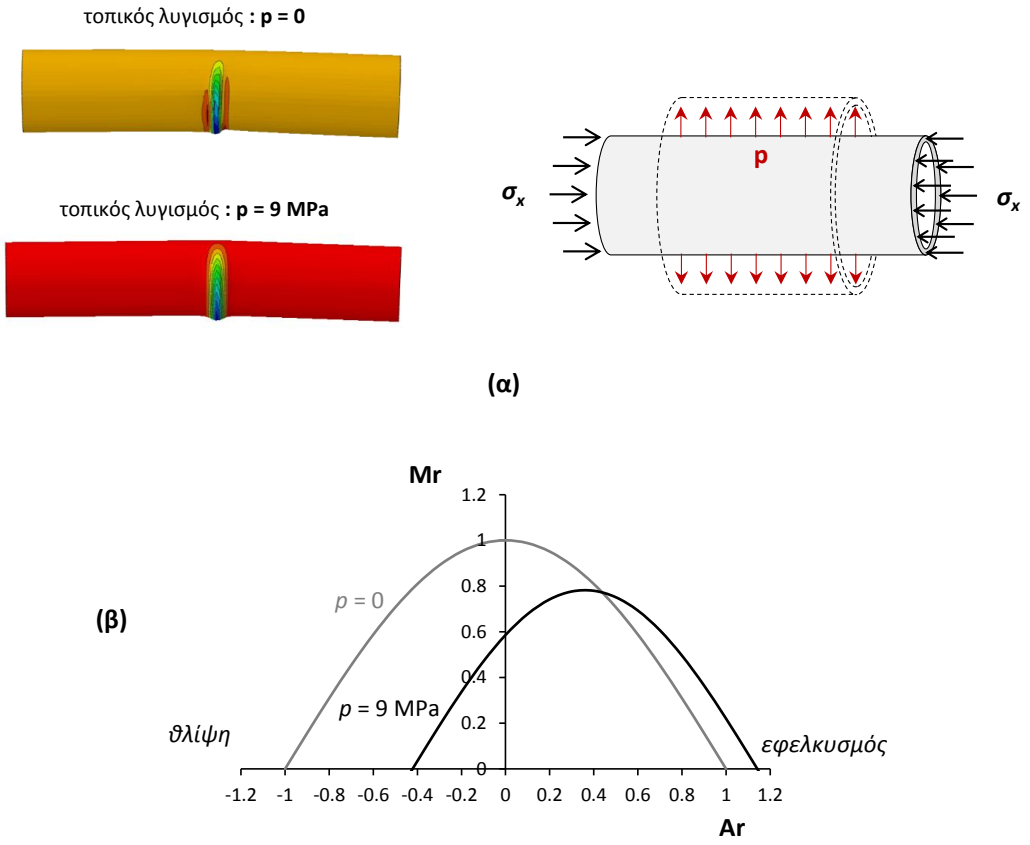

Σχήμα 14. (α) Ποιοτική απεικόνιση της συνδυασμένης δράσης θλίψης και εσωτερικής πίεσης στην απόκριση του αγωγού. (β) Διάγραμμα αλληλεπίδρασης ροπής – αξονικής δύναμης για αγωγό (D/t=70) με και χωρίς πίεση κατά Mohareb (2002)

Ενδιαφέρον επίσης παρουσιάζει η επίδραση της εσωτερικής πίεσης η οποία, αντίθετα με την διαισθητικώς αναμενόμενη συμπεριφορά, δεν προωθεί την ευστάθεια της διατομής, αλλά αντιθέτως μειώνει εμφανώς τα περιθώρια ασφαλείας. Μία απόπειρα σχηματικής επεξήγησης της ιδιάζουσας αυτής συμπεριφοράς παρουσιάζεται στο **Σχ. 14α**. Ας θεωρήσουμε αρχικώς τον αγωγό χωρίς πίεση: υπό την επίδραση της θλιπτικής δύναμης η διατομή έχει την τάση να διογκωθεί πλευρικά (φαινόμενο Poisson), ενώ με την αύξηση αυτής (και σε συνδυασμό με την ταυτόχρονη δράση ροπής) ο αγωγός τελικώς θα λυγίσει σχηματίζοντας το χαρακτηριστικό τσαλάκωμα, το οποίο θα έχει φορά προς τα έξω, μιας και αυτή είναι πιο ευπαθής πλευρά λόγω της τάσης για διόγκωση. Όταν το τμήμα αυτό του αγωγού βρεθεί υπό ταυτόχρονη δράση εσωτερικής πίεσης, στην τάση για διόγκωση λόγω Poisson προστίθεται και αυτή λόγω της πίεσης. Έτσι, η αντίσταση στην προκαλούμενη από την εσωτερική πίεση παραμόρφωση πηγάζει από τους ίδιους μηχανισμούς που αντιστέκονται στον σχηματισμό τοπικού λυγισμού και επομένως δρα ανταγωνιστικά προς αυτούς – η αύξηση της πίεσης οδηγεί σε μείωση της αντοχής. Μακροσκοπικά, η

παραπάνω συμπεριφορά αποτυπώνεται ξεκάθαρα στο **Σχ. 14β** όπου παρουσιάζεται διάγραμμα αλληλεπίδρασης σε όρους ροπής M_r (ροπή αντοχής προς πλαστική ροπή αντοχής M_p) και αξονικής A_r (αξονική δύναμη Α προς μέγιστη αξονική αντίσταση A_y) για αγωγό (D/t=70) με και χωρίς πίεση κατά Mohareb (2002). Πράγματι, υπό καθεστώς συνδυαζόμενης ροπής και θλίψης, η παρουσία υψηλής εσωτερικής πίεσης μειώνει την αντοχή της διατομής του αγωγού και έως εκ τούτου την δυνατότητα του να παραλάβει τεκτονική μετακίνηση.

Σύγκριση Προτεινόμενης Μεθοδολογίας με Ελατηριωτά Προσομοιώματα

Αντί επιλόγου του Μέρος Α', επιχειρείται και μία σύντομη αξιολόγηση της αξιοπιστίας των ευρέως χρησιμοποιούμενων ελατηριωτών προσομοιωμάτων. Επιλέχθηκαν δύο τυπικές διατάξεις υπογείων αγωγών οι οποίες υπεβλήθησαν σε κανονική και ανάστροφη διάρρηξη και επιλύθηκαν: (α) με χρήση της εμπεριστατωμένης αριθμητικής μεθοδολογίας και (β) με χρήση ελατηριωτού προσομοιώματος. Για την δεύτερη κατηγορία επίλυσης αξιολογήθηκαν δύο εναλλακτικές προσεγγίσεις. Στην πρώτη τα εδαφικά ελατήρια έχουν προκύψει από αναλύσεις πεπερασμένων στοιχείων, ενώ στην δεύτερη τα εδαφικά ελατήρια δίνονται από τις ημι-εμπειρικές συσχετίσεις των κανονιστικών διατάξεων (ALA 2001). Συμπεραίνεται ότι στις περιπτώσεις κανονικής διάρρηξης τα ελατηριωτά προσομοιώματα (ανεξαιρέτως προσέγγισης) τείνουν να υπερεκτιμούν την εδαφική αντίσταση (καθώς αγνοούν την μείωση της αντοχής του εδάφους λόγω των συνθηκών ενεργητικής αστοχίας), με αποτέλεσμα τη σημαντική υπερεκτίμηση της καμπτικής παραμόρφωσης του αγωγού (**Σχ. 15α**). Επιπλέον, σε περιπτώσεις σημαντικής εσωτερικής πίεσης, η προσομοίωση του αγωγού με στοιχεία δοκού υποεκτίμα σημαντικά τις αναπτυσσόμενες παραμορφώσεις (**Σχ. 15β**), καθώς αγνοεί την όχι αμελητέα παραμόρφωση στο επίπεδο της διατομής και τα συνεπαγόμενα φαινόμενα 2ας τάξης που οδηγούν σε μείωση της δυσκαμψίας του αγωγού. Ανάστροφο ρήγμα

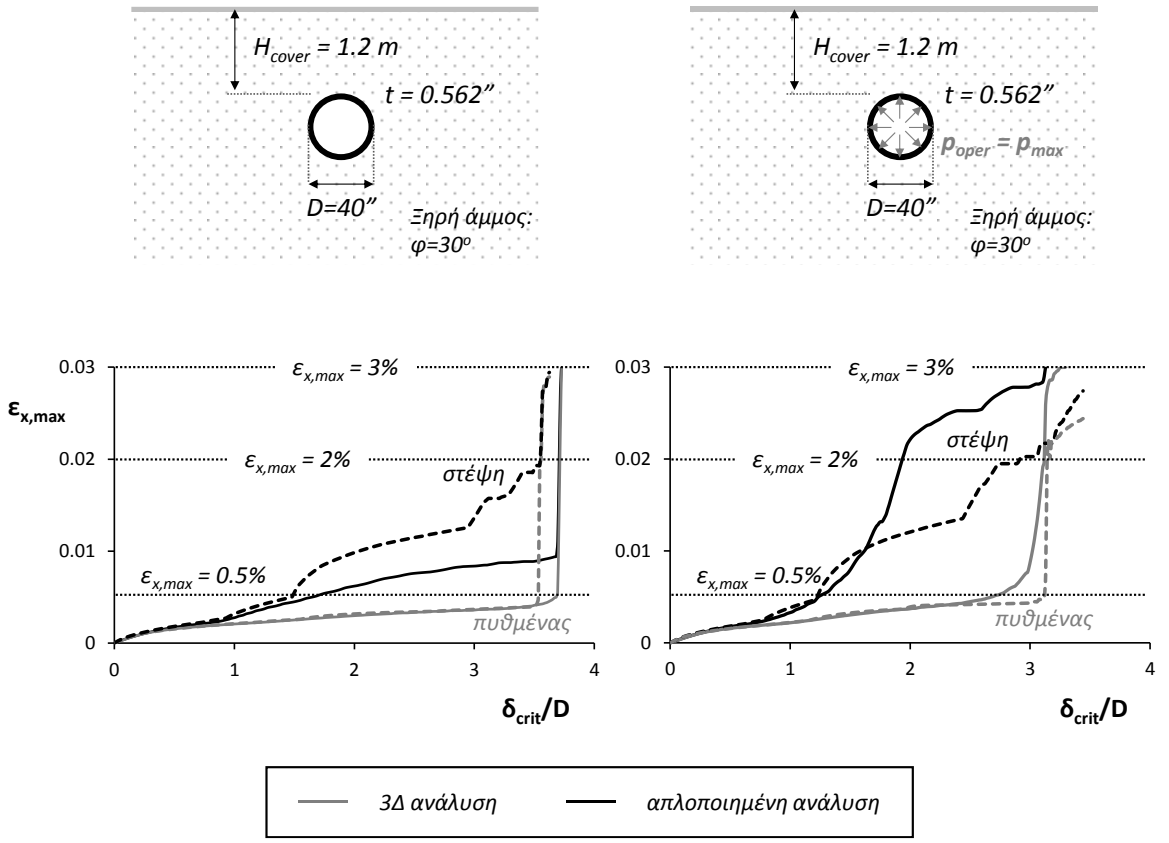

Σχήμα 15. Σύγκριση των αποτελεσμάτων της 3Δ ανάλυσης με τα αποτελέσματα απλοποιημένης ανάλυσης τύπου δοκού επί ελατηριωτού εδάφους: εξέλιξη της μέγιστης εφελκυστικής παραμόρφωσης με την αύξηση της κανονικοποιημένης μετατόπισης της διάρρηξης θεωρώντας εσωτερική πίεση λειτουργίας p_{oper}=0 και p_{oper}=9 MPa.

Β' Μέρος

Απόκριση αγωγών υποβαλλόμενων σε μετακινήσεις λόγω κατολίσθησης

Στην δεύτερη ενότητα της Διδακτορικής διατριβής ερευνάται η απόκριση απειρομήκους υπογείου αγωγού υποβαλλόμενου σε μεγάλες εδαφικές μετακινήσεις προκαλούμενων από εκδήλωση περιστροφικής κατολίσθησης. Μια από τις σημαντικότερες προκλήσεις στην προσομοίωση του φαινομένου απορρέει από την αναντιστοιχία των διαστάσεων μεταξύ αγωγού και κατολίσθησης. Αφενός, η λεπτομερής προσομοίωση του αγωγού και των πιθανών φαινομένων τοπικής αστάθειας (π.χ. τοπικός λυγισμός, οβαλοποίηση) απαιτεί την χρήση πεπερασμένων στοιχείων πολύ μικρών διαστάσεων

(της τάξεως λίγων εκατοστών), αφετέρου, η προσομοίωση κατολισθητικών φαινομένων απαιτεί κατά κανόνα προσομοιώσεις μεγάλων διαστάσεων. Ο συγκερασμός των δύο απαιτήσεων οδηγεί σε γιγαντιαία, δύσχρηστα και εξαιρετικά απαιτητικά προσομοιώματα. Εναλλακτικά, προτείνεται και υιοθετείται μια μεθοδολογία δύο βημάτων (**Σχ. 16**). Αρχικώς αναλύεται η εξέλιξη της κατολίσθησης στο ελεύθερο πεδίο (δηλ. αγνοώντας την ύπαρξη του αγωγού). Από την ανάλυση αυτή εξάγεται το πεδίο των μετακινήσεων, το οποίο στο δεύτερο βήμα χρησιμοποιείται ως συνοριακή συνθήκη στον πυθμένα και στα πλευρικά σύνορα ενός τοπικού προσομοιώματος που περιλαμβάνει τον αγωγό και ένα εδαφικό πρίσμα περί αυτού.

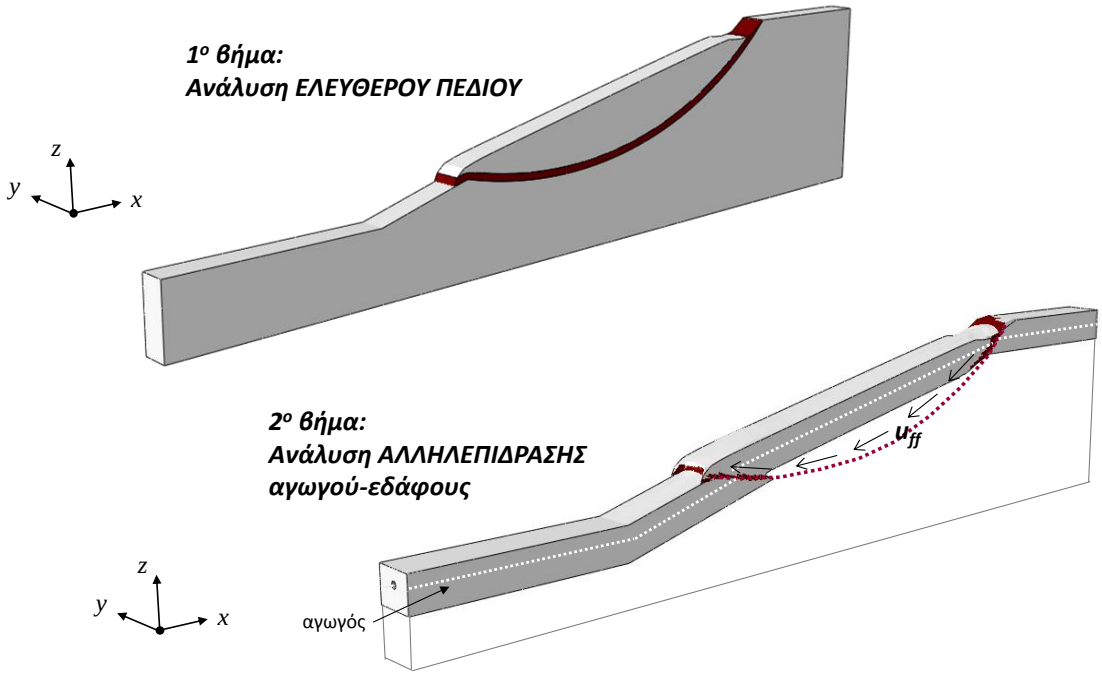

Σχήμα 16. Μεθοδολογία δύο βημάτων για την ανάλυση της συμπεριφοράς υπογείου αγωγού υποβαλλόμενου σε μεγάλες εδαφικές μετακινήσεις λόγω κατολίσθησης.

Με την χρήση της ως άνω μεθοδολογίας μελετάται αριθμητικά η απόκριση υπογείου χαλύβδινου όταν: (α) ο αγωγός διασχίζει κάθετα το πρανές και επομένως είναι παράλληλος στην κίνηση της κατολισθαίνουσας μάζας και (β) ο αγωγός είναι παράλληλος στην στέψη του πρανούς και η εδαφική ολίσθηση λαμβάνει χώρα κάθετα στον άξονά του.

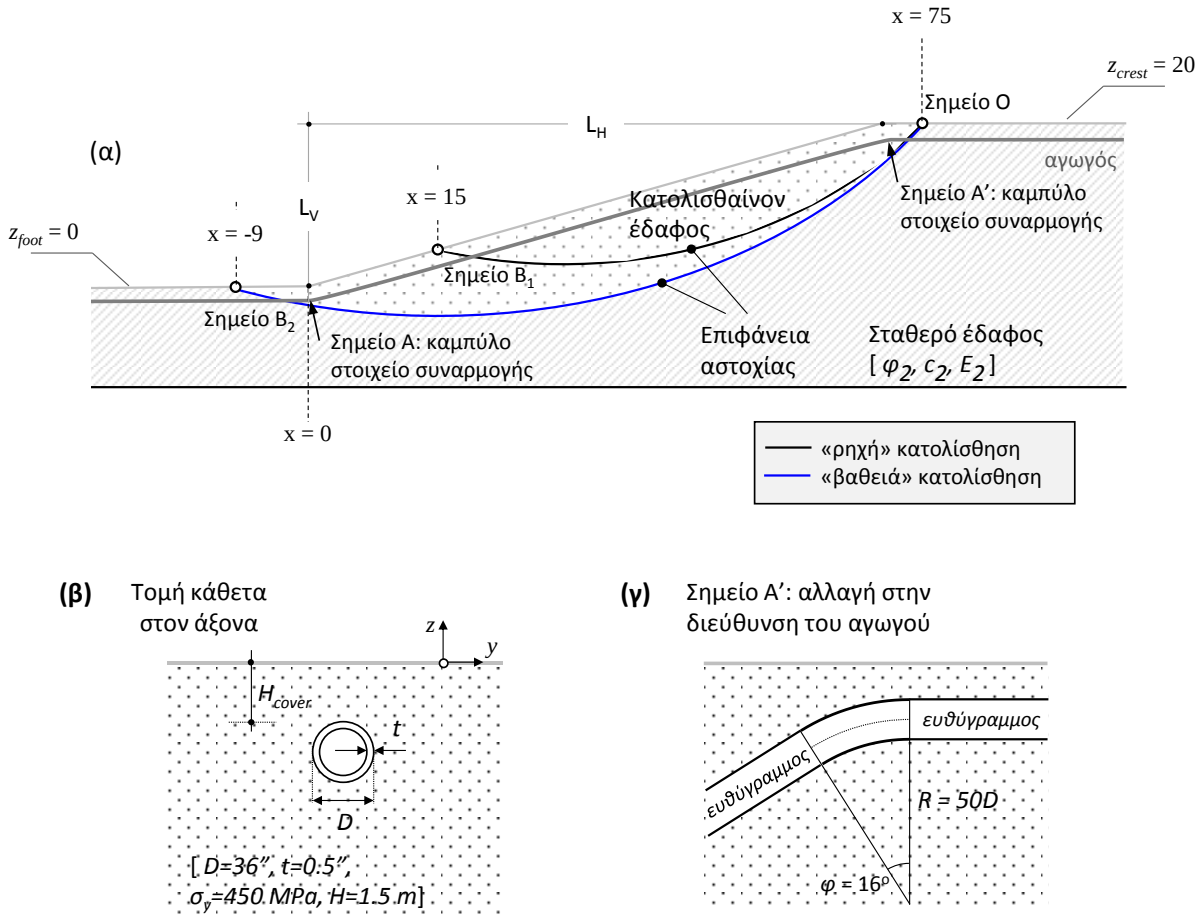

Σχήμα 17. Γραφική απεικόνιση του προβλήματος αγωγού υποβαλλόμενου σε μετακινήσεις λόγω κατολίσθησης παράλληλα στον άξονά του. (α) Η γεωμετρία του πρανούς και τα δύο υπό εξέταση σενάρια κατολίσθησης, (β) γεωμετρία του αγωγού και (γ) το καμπύλο στοιχείο συναρμογής.

Για την μελέτη της πρώτης περίπτωσης υιοθετήθηκε το παράδειγμα του **Σχ. 17**. Χαλύβδινος αγωγός (χάλυβας X65) διαμέτρου D=36" και πάχους t=0.5" με βάθος κάλυψης H_{cover}=1.5 m διασχίζει πρανές μήκους L_H=75 m και υψομετρικής διαφοράς πόδα-στέψης L_V=20 m. Για την υλοποίηση της μεταβολής στον άξονα του αγωγού χρησιμοποιούνται καμπύλα στοιχεία συναρμογής. Η απόκριση του αγωγού μελετάται παραμετρικά θεωρώντας δύο σενάρια κατολίσθησης: (α) ένα σχετικώς ρηχό σενάριο κατολίσθησης που δεν επηρεάζει το στοιχείο συναρμογής στην βάση του πρανούς και (β) ένα βαθύ σενάριο κατολίσθησης κατά το οποίο η κινητοποιούμενη εδαφική μάζα συμπαρασύρει το στοιχείο συναρμογής.

Μία άποψη του αριθμητικού προσομοιώματος του ελευθέρου πεδίου παρουσιάζεται στο **Σχ.18α**. Το σταθερό έδαφος (υποκείμενο της επιφάνειας ολίσθησης έδαφος) προσομοιώνεται ως πυκνή άμμος με μέτρο ελαστικότητας E_2 ≈ 17 MPa, γ = 20 kN/m^3 και ακολουθεί κριτήριο αστοχίας Mohr-Coulomb με

συμπεριφορά χαλάρωσης, για τον προσδιορισμό της οποίας υποθέτονται φ_p = 45°, φ_{res} = 37°, ψ = (φ_p - φ_{res})/0.8 = 10°, γ_y= 0.01, γ_p = 0.03 and γ_f = 0.07. Η κατολισθαίνουσα μάζα θεωρείται μια χαλαρή άμμος αποτελούμενη από αποθέσεις προηγούμενων επεισοδίων κατολίσθησης. Το ειδικό βάρος της λαμβάνεται 17 kN/m^3 και το μέτρο ελαστικότητας E = 4.5 MPa. Το υλικό του κινούμενου εδάφους δεν επιδεικνύει συμπεριφορά χαλάρωσης και ως εκ τούτου, για την περιγραφή της συμπεριφοράς του λαμβάνεται γωνία τριβής φ_p = 34°, γωνίας διαστολικότητας ψ = 5° και διατμητική παραμόρφωση διαρροής γ_y = 0.03. Μεταξύ των δύο παρεμβάλλεται μια λεπτή στρώση εδάφους (διεπιφάνεια) μικρής αντοχής και δυσκαμψίας. Το έναυσμα της κατολίσθησης δίνεται τεχνητά μειώνοντας σταδιακά την αντοχή της διεπιφάνειας. Χαρακτηριστικά στιγμιότυπα της παραμόρφωσης της ολισθαίνουσας μάζας από το έναυσμα έως την απόθεση παρουσιάζονται στο **Σχ. 18β.**

Άποψη του τοπικού προσομοιώματος αγωγού-κατολίσθησης δίνεται στο **Σχ.18γ**. Τα σύνορα του προσομοιώματος τοποθετούνται σε απόσταση *d'=3D* από τον αγωγό. Η συνοριακή αυτή συνθήκη προέκυψε μετά από σειρά αναλύσεων ευαισθησίας με στόχο να βρεθεί ο κατάλληλος συμβιβασμός ανάμεσα στην ακρίβεια των αποτελεσμάτων και στην αποδοτικότητα της ανάλυσης. Η προσομοίωση της συμπεριφορά του αγωγού πέρα των ορίων του 3-Δ προσομοιώματος υλοποιείται μέσω υβριδικών συνόρων αντίστοιχα με αυτά που αναπτύχθηκαν για την περίπτωση της διάρρηξης.

Στο **Σχ. 19** αποτυπώνεται η απόκριση του αγωγού υποβαλλόμενου στο σχετικώς «ρηχό» σενάριο κατολίσθησης. Στο **Σχ. 19α** παρουσιάζεται ο παραμορφωμένος κάνναβος του αγωγού με ισοϋψείς τάσεων για μετατόπιση του πόδα της κατολίσθησης U_{soil} =2 m. Η εδαφική μετακίνηση στην βάση της κατολίσθησης (**Σχ. 19β**)αναλύεται σε μια παράλληλη και μια κάθετη συνιστώσα στον άξονα του αγωγού. Η παράλληλη συνιστώσα προκαλεί θλίψη του αγωγού, ενώ η κάθετη προς τα πάνω συνιστώσα εκτρέπει τον αγωγό από την αρχική του θέση προκαλώντας έντονη κάμψη. Τελικά ο αγωγός αστοχεί με σχηματισμό τοπικού λυγισμού πλησίον της θέσης μέγιστης μετακίνησης.

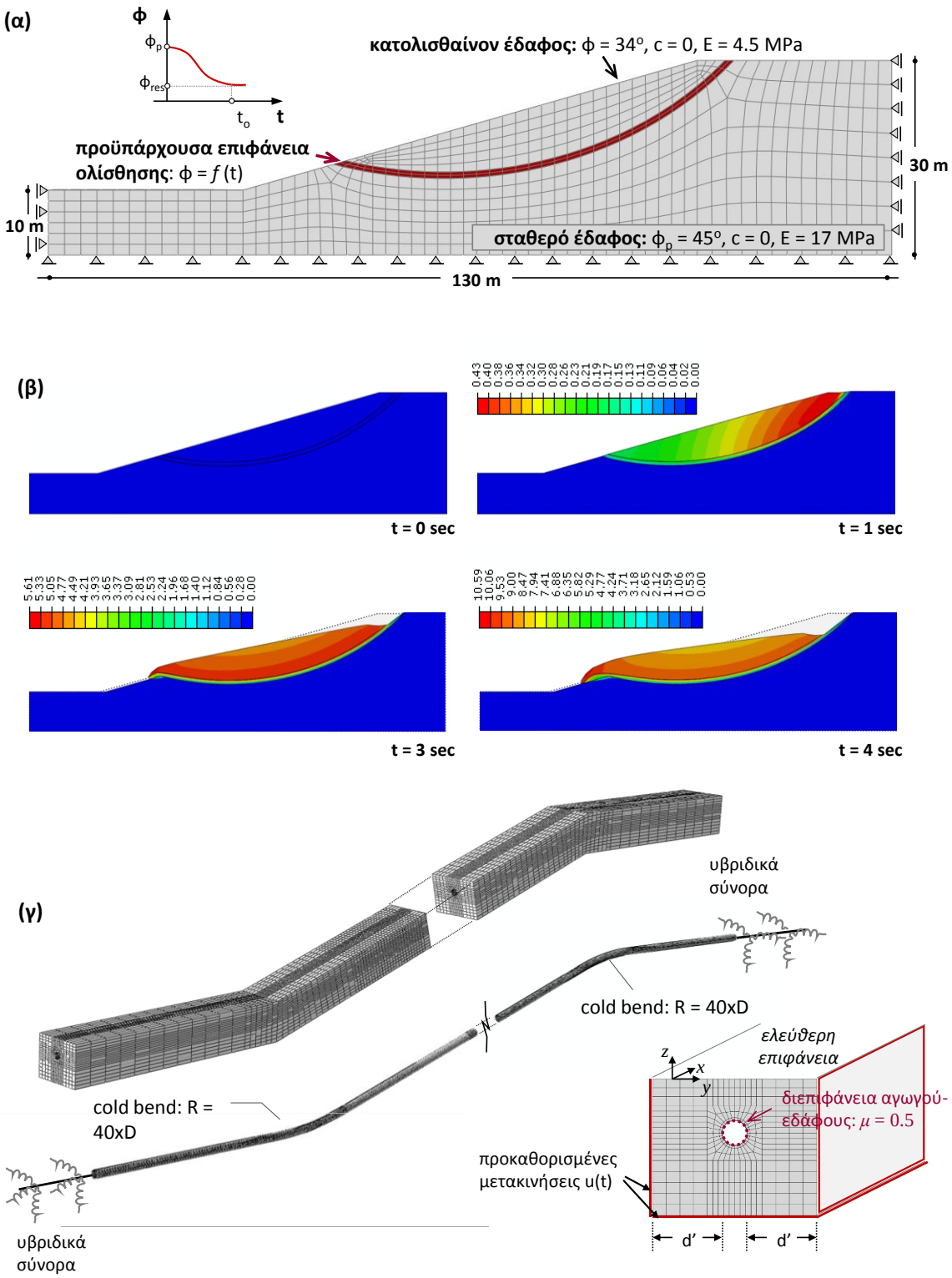

Σχήμα 18. (α) Το προσομοίωμα ελευθέρου πεδίου και (β) στιγμιότυπα του παραμορφωμένου καννάβου με ισοϋψείς μετακινήσεων σε χαρακτηριστικές στιγμές. (γ) Το προσομοίωμα αλληλεπίδρασης αγωγού-εδάφους για εδαφική μετακίνηση παράλληλα στον άξονα του αγωγού

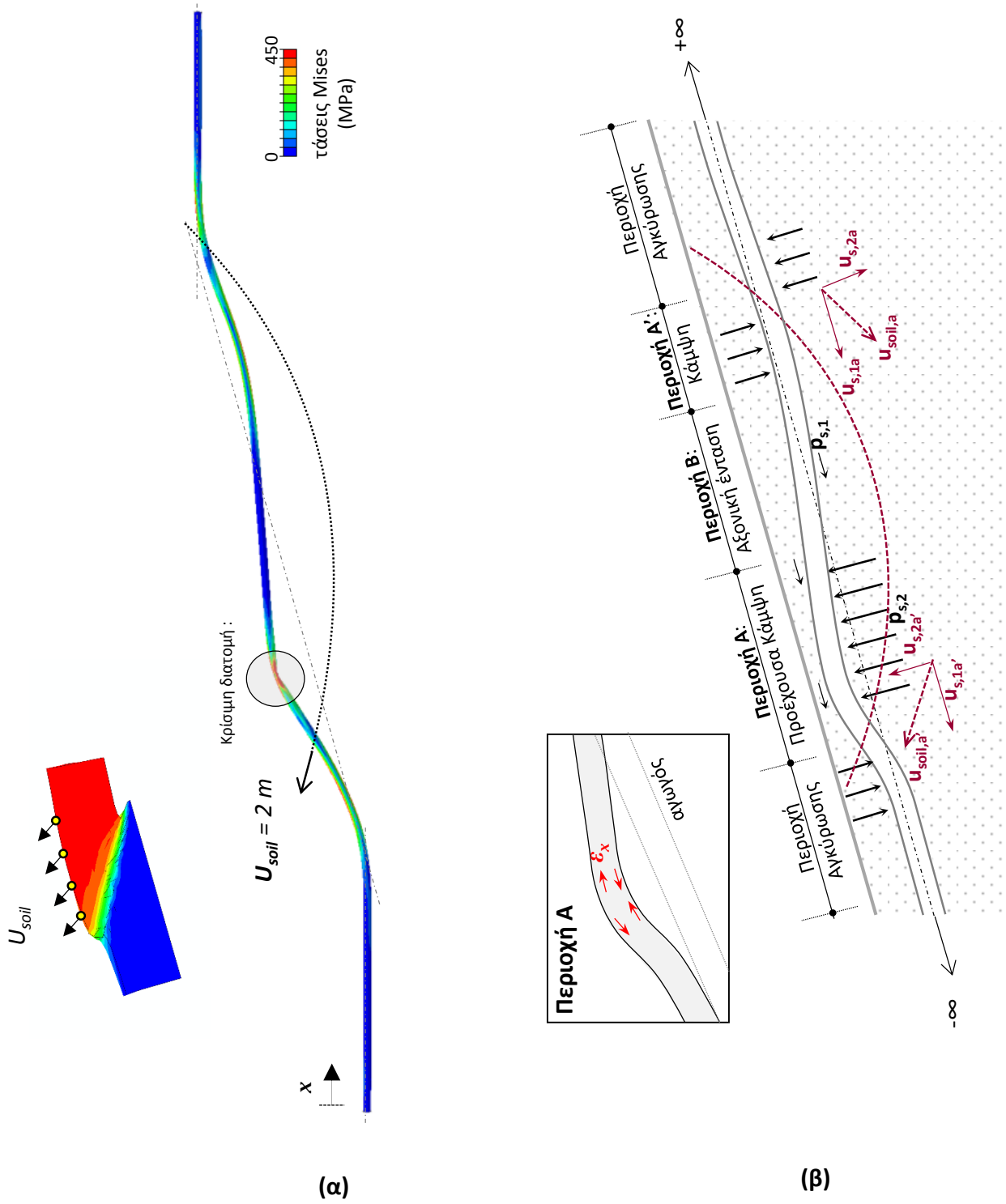

Σχήμα 19. Αγωγός υποβαλλόμενος στο «ρηχό» σενάριο κατολίσθησης: (α) Παραμορφωμένος αγωγός με ισοϋψείς τάσεων (χρωματισμένα κόκκινα τα τμήματα υπό μεγάλη καμπτική καταπόνηση), (β) ποιοτική αποτύπωση των μηχανισμών απόκρισης.

Στο βαθύ σενάριο κατολίσθησης **(Σχ. 20)** οι μηχανισμοί παραλαβής των εδαφικών μετακινήσεων παραμένουν ποιοτικώς ίδιοι με προηγουμένως: και εδώ ο αγωγός βρίσκεται υπό θλίψη λόγω της κίνησης του εδάφους προς τα κατάντη ενώ ταυτοχρόνως κάμπτεται λόγω της κίνησης του εδάφους προς τα άνω. Η κάμψη αυτή παραλαμβάνεται με την ανάπτυξη καμπτικών ροπών αντίθετης φοράς στο τμήμα του αγωγού που βρίσκεται εντός του σταθερού εδάφους (περιοχή αγκύρωσης). Στο σενάριο της βαθιάς κατολίσθησης, η αγκύρωση υλοποιείται στο καμπύλο τμήμα της συναρμογής και μεταφράζεται σε σημαντική θλίψη. Ως αναμένετο, η προκύπτουσα θλίψη στο τμήμα της συναρμογής καθιστά τον αγωγό ιδιαιτέρως ευάλωτο σε τοπικό λυγισμό.

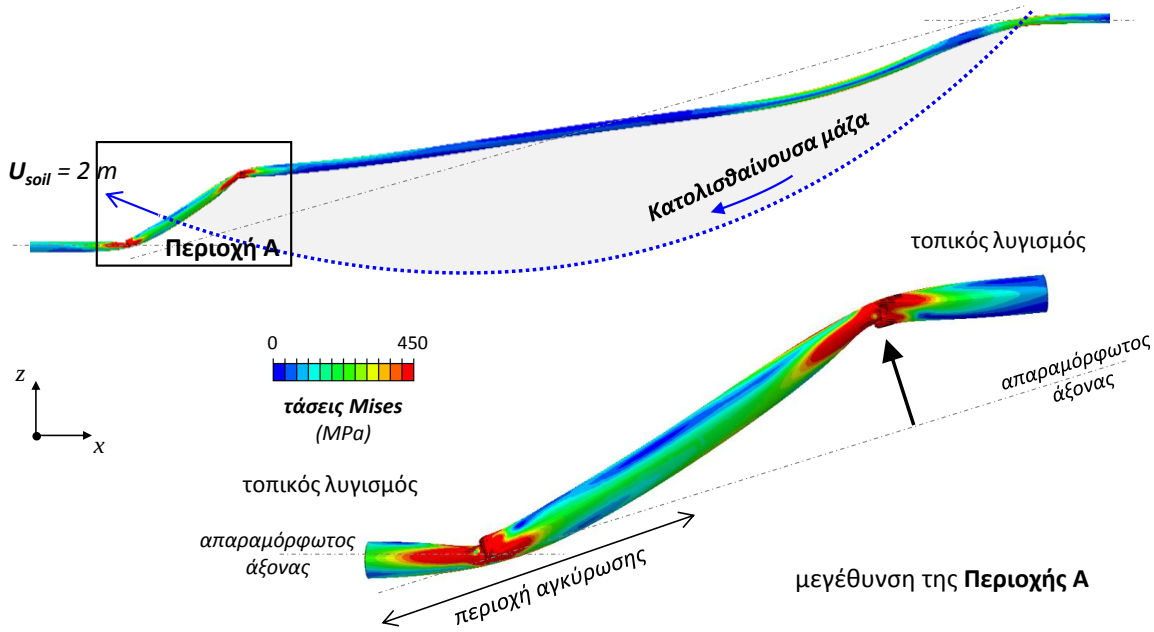

Σχήμα 20. Απόκριση αγωγού στο «βαθύ» σενάριο κατολίσθησης (παράλληλα στον άξονά του): παραμορφωμένος αγωγός με ισοϋψείς τάσεων για εδαφική μετατόπιση U_{soil} = 2 m.

Η ύπαρξη της εσωτερικής πίεσης έχει διπλή επίδραση. Πρώτον, σταθεροποιεί την διατομή που βρίσκεται υπό μεγάλη καμπυλότητα επιβραδύνοντας ή ακόμα και αποτρέποντας τον σχηματισμό τοπικού λυγισμού. Δεύτερον, μεταβάλλει την κατανομή και κυρίως το μέγεθος των παραμορφώσεων δακτυλίου ε_θ στο επίπεδο της διατομής. Εν προκειμένω, λόγω της κάμψης στη διαμήκη διεύθυνση, δημιουργείται τάση προς συστολή (ανάπτυξη αρνητικών ε_θ) στο τμήμα της διατομής που βρίσκεται υπό εφελκυσμό, και τάση προς διαστολή (ανάπτυξη θετικών ε_θ) σε αυτό που βρίσκεται υπό θλίψη. Η ύπαρξη της εσωτερικής πίεσης τείνει να μειώσει τις αρνητικές παραμορφώσεις ενώ ταυτόχρονα αυξάνει τις θετικές

παραμορφώσεις δακτυλίου. Ωστόσο για μεγάλες τιμές της εσωτερικής πίεσης *p* η αύξηση των (θετικών) παραμορφώσεων δακτυλίου δύναται να γίνει κρίσιμη ($\varepsilon_\theta \rightarrow \varepsilon_{max}$=3%). Ένα τέτοιο παράδειγμα αποτελεί η περίπτωση του αγωγού που παρουσιάζεται στο **Σχ.21** –αγωγός υπό την πίεση υποβαλλόμενος στο ρηχό σενάριο κατολίσθησης.

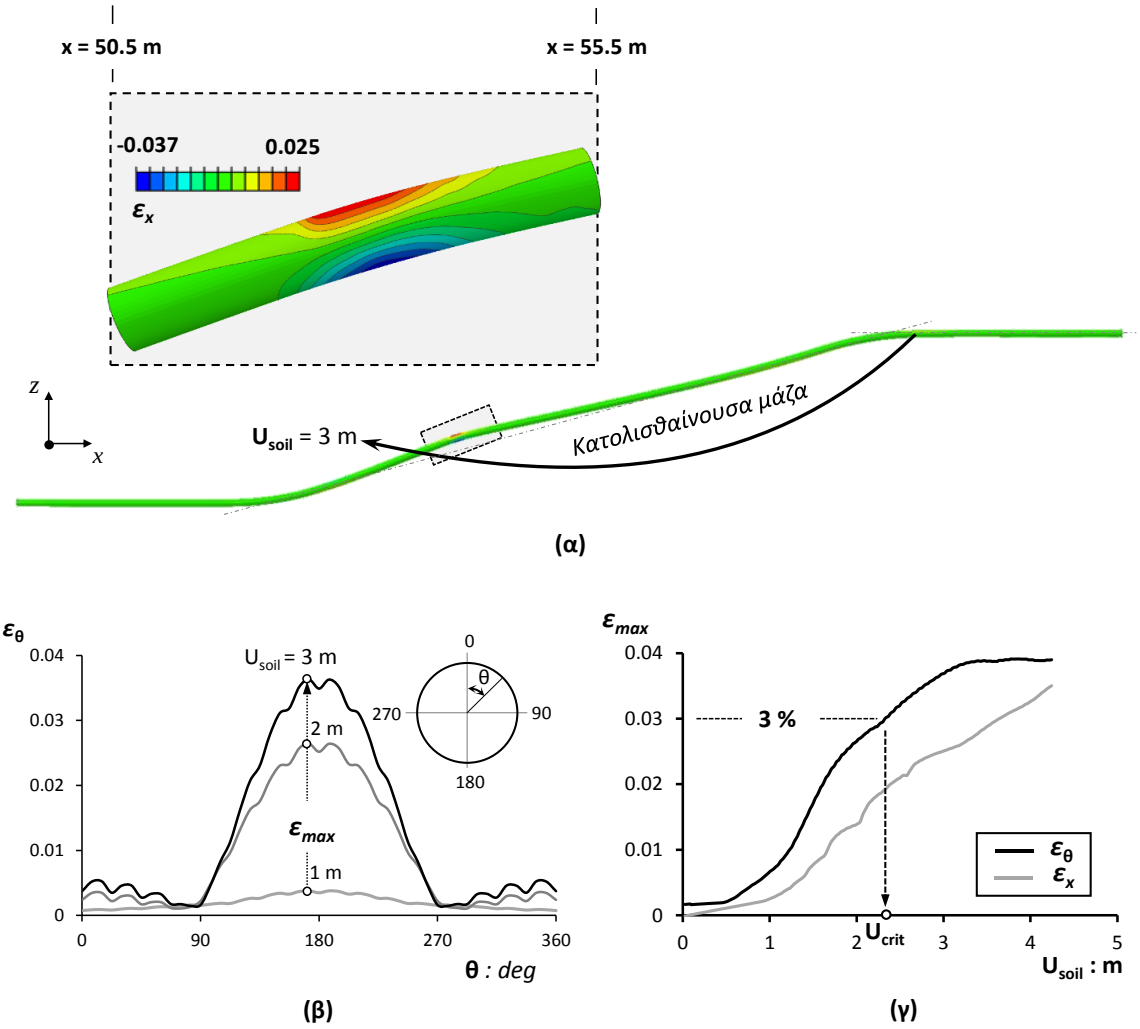

Σχήμα 21. Αγωγός υπό την πίεση σχεδιασμού του υποβάλλεται στην «ρηχή» κατολίσθησης κατανομή της (α) αξονικής παραμόρφωσης (ε_x) κατά μήκος του αγωγού, (β) της παραμόρφωσης δακτυλίου (ε_θ) στην κρίσιμη διατομή και (γ) εξέλιξη της μέγιστης παραμόρφωσης αξονικής και δακτυλίου με την μετατόπιση εδάφους.

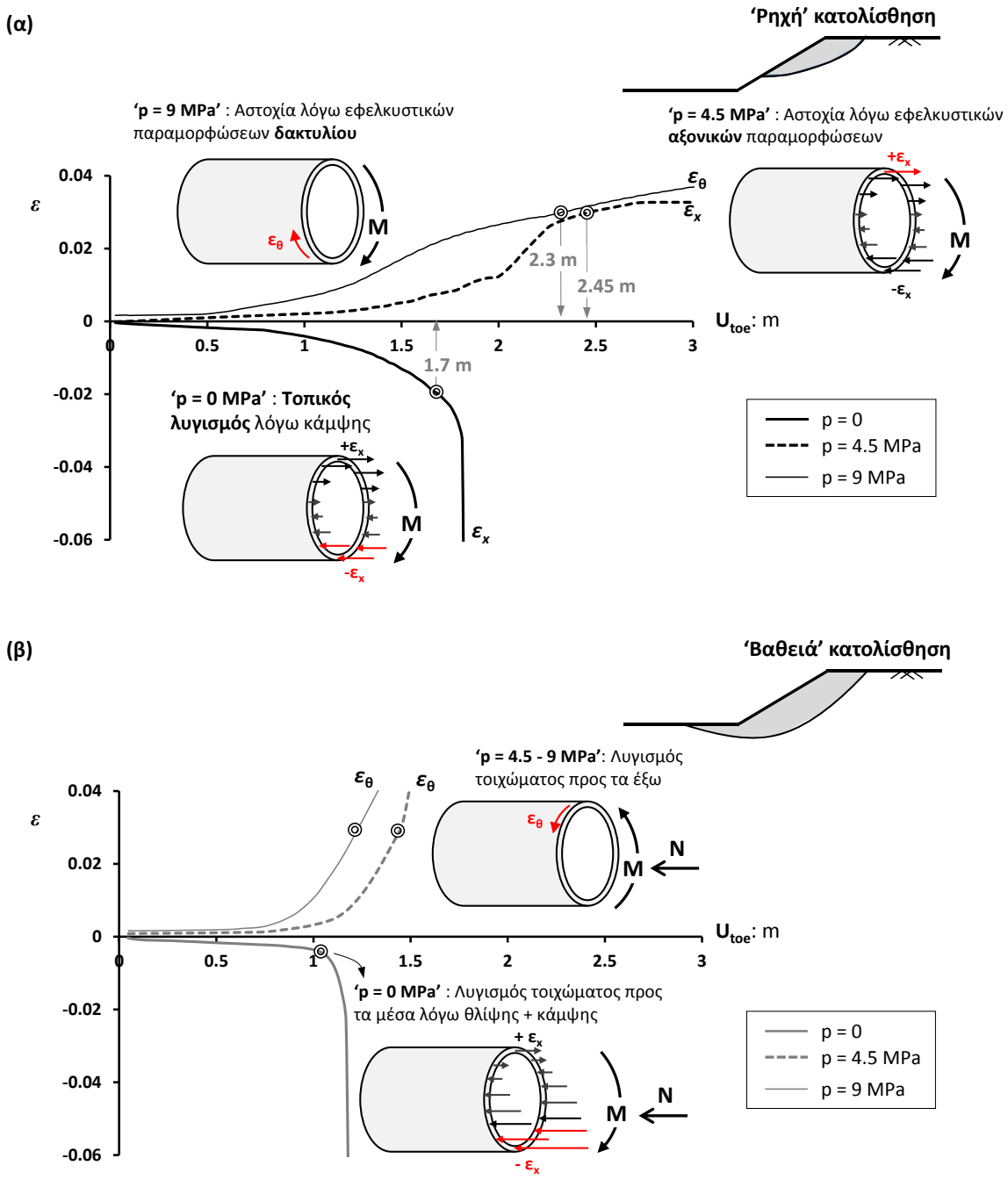

Σχήμα 22. Τα περιθώρια ασφαλείας του αγωγού μέχρι την αστοχία αναλόγως της εσωτερικής πίεσης (α) για το «ρηχό» σενάριο κατολίσθησης και (β) για το «βαθύ» σενάριο κατολίσθησης.

Στο **Σχ. 22** συνοψίζεται η συμπεριφορά του αγωγού υποβαλλόμενου σε μετακινήσεις λόγω κατολίσθησης παράλληλα στον άξονά του. Η γεωμετρία της κατολίσθησης εμφανίζεται να διαδραματίζει καθοριστικό ρόλο στην απόκριση του αγωγού. Στην περίπτωση της βαθιάς κατολίσθησης που επηρεάζει το κάτω στοιχείο συναρμογής τα περιθώρια ασφαλείας ελαχιστοποιούνται (για τους αγωγούς που εξετάστηκαν

υπό πίεση η μείωση των περιθωρίων ασφαλείας είναι της τάξης του 50%). Επιπλέον, τόσο η παρουσία όσο και το μέγεθος της εσωτερικής πίεσης επηρεάζουν καταλυτικά την απόκριση και τα περιθώρια ασφαλείας του αγωγού. Η ύπαρξη της πίεσης εμφανίζεται να καθυστερεί ή ακόμα και να αποτρέπει την εκδήλωση λυγισμού (όπως στο σενάριο ρηχής κατολίσθησης). Ωστόσο, τα αποτελέσματα δείχνουν πως η ευμενής αυτή συμπεριφορά δεν ακολουθεί μονοτονική συσχέτιση με το μέγεθος της πίεσης (και για τα δύο σενάρια τα περιθώρια ασφαλείας είναι μεγαλύτερα για αγωγό με p=4.5 MPa σε σχέση με p=9 MPa).

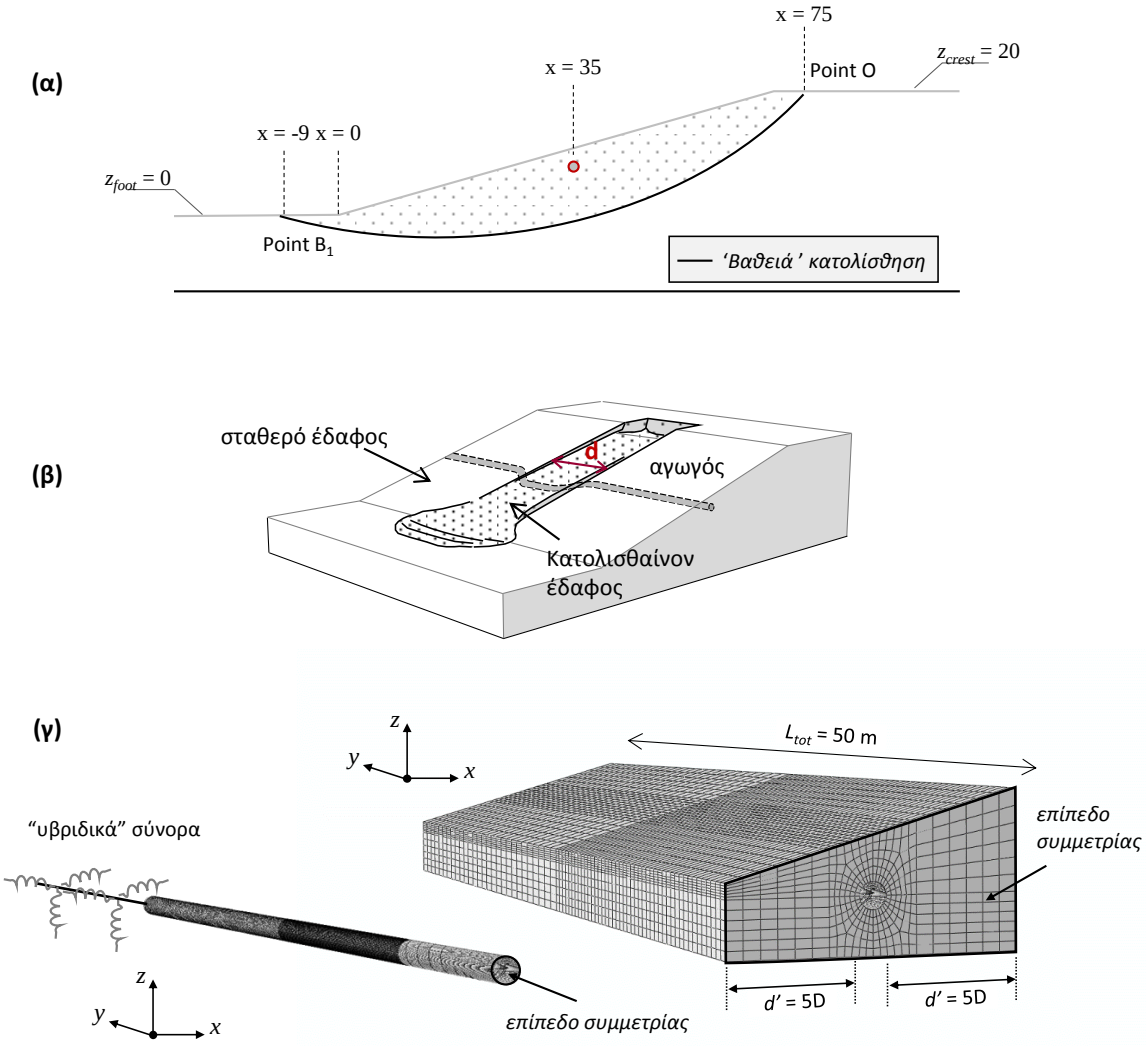

Σχήμα 23. (α) Τομή κάθετη στον άξονα του αγωγού: γεωμετρία πρανούς και κατολίσθησης. (β) Εξετάζεται παραμετρικά η εκτός επιπέδου έκταση *d* της κατολίσθησης. (γ) Λεπτομέρειες του προσομοιώματος αλληλεπίδρασης αγωγού-εδάφους.

Στη συνέχεια εξετάζεται η απόκριση του αγωγού για μετακινήσεις λόγω κατολίσθησης κάθετα στον άξονα του αγωγού. Ο άξονας του αγωγού διαπερνά το μέσο του πρανούς (στην θέση *x*=35 m) και

παράλληλα στην στέψη αυτού (**Σχ. 23α)**. Η βαθειά κατολίσθηση της προηγούμενης διερεύνησης λαμβάνεται ως πιθανό σενάριο εδαφικής κινητοποίησης. Εξετάζεται παραμετρικά η επίδραση της εκτός επιπέδου έκταση της κατολίσθησης *d* στην απόκριση του αγωγού (**Σχ. 23β**) μέσω δύο σεναρίων: (α) ενός σεναρίου «διευρυμένης» κατολίσθησης με πλάτος *d*=40 m και (β) ενός «στενού» σεναρίου με πλάτος *d*=20 m. Ομοίως με προηγουμένως η απόκριση του αγωγού μελετάται υιοθετώντας την προτεινόμενη μεθοδολογία δύο βημάτων (**Σχ. 23γ**). Εκμεταλλευόμενοι την συμμετρία του προβλήματος προσομοιώνεται το μισό μήκος αγωγού. Τα κάθετα όρια στα οποία επιβάλλονται οι μετακινήσεις ελευθέρου πεδίου τοποθετούνται σε απόσταση *5D* από τον αγωγό.

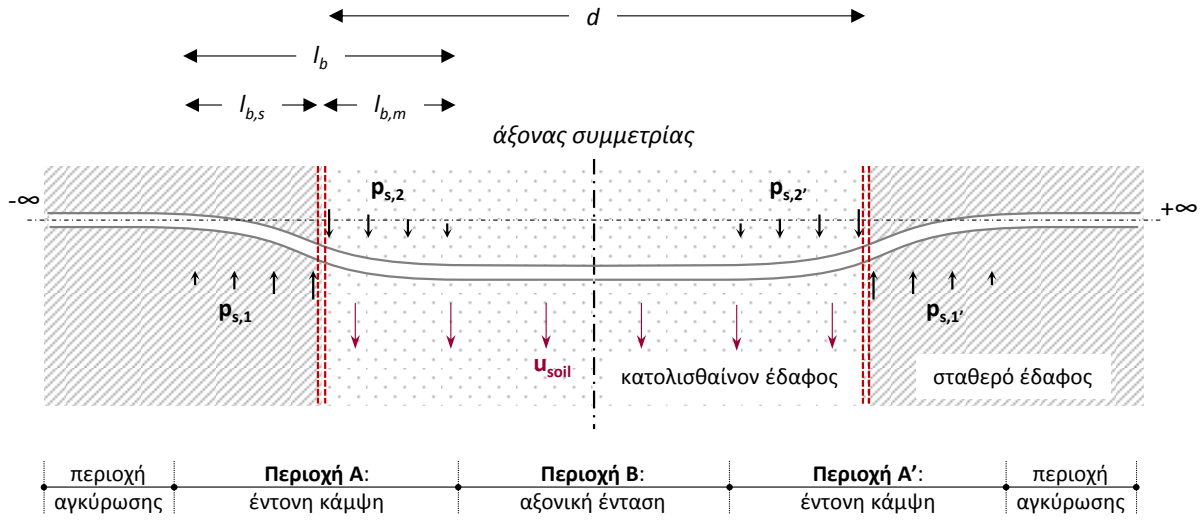

Σχήμα 24. Ποιοτική απεικόνιση των μηχανισμών απόκρισης υπογείου αγωγού που υπόκειται σε εδαφικές μετακινήσεις λόγω κατολίσθησης κάθετα στον άξονα του.

Η απόκριση του αγωγού στην κίνηση του εδάφους κάθετα στον άξονα του αποτυπώνεται σχηματικά στο **Σχ. 24**. Οι εδαφικές μετακινήσεις λόγω της ολίσθαινουσας μάζας δημιουργούν σχετική μετακίνηση του ακλόνητου άκρου του αγωγού που βρίσκεται στο σταθερό έδαφος και του άξονα συμμετρίας. Η διαφορική αυτή κίνηση παραλαμβάνεται μέσω κάμψης του αγωγού σε μια περιορισμένη μεταβατική ζώνη στην εγγύτητα του πέρατος της κατολίσθησης (η οποία σημειώνεται ως l_b). Το μήκος της μεταβατικής αυτής ζώνης καθορίζεται από την σχετική δυσκαμψία αγωγού-εδάφους. Πέραν αυτής της ζώνης, τόσο προς το σταθερό έδαφος όσο και προς το εσωτερικό της κατολίσθησης, η ένταση του αγωγού εκφυλίζεται σε πρακτικώς εφελκυστική εξαιτίας της τάσης για αύξηση το μήκος του. Για να αναπτυχθεί πλήρως η παραπάνω συμπεριφορά θα πρέπει το ημιπλάτος της κατολίσθησης ($d/2$) να είναι επαρκώς μεγαλύτερο από το μήκος της μεταβατικής ζώνης (l_b). Όσο το πλάτος της κατολισθαίνουσας μάζας μικραίνει (περίπτωση κατολίσθησης περιορισμένης έκτασης), το διαθέσιμο μήκος δεν επαρκεί να

παραλάβει τη παραμορφωμένη κατάσταση του αγωγού. Επιπλέον, η μεσαία διατομή του αγωγού υποχρεωτικά διατηρεί την καθετότητά της στην διεύθυνση της εδαφικής κίνησης λόγω συμμετρίας. Ο συνδυασμός των δύο συνοριακών συνθηκών συνεπάγεται την ανάπτυξη μεγάλης καμπυλότητας στην μεσαία διατομή —μεγαλύτερης από αυτήν που θα αναπτυσσόταν σε περίπτωση μιας διευρυμένης κατολίσθησης. Τελικώς, η μεγάλη καμπυλότητα που αναπτύσσεται στην μεσαία διατομή οδηγεί στον σχηματισμό τοπικού λυγισμού.

Στο **Σχ. 25** συνοψίζεται η συμπεριφορά του αγωγού υποβαλλόμενου σε μετακινήσεις λόγω κατολίσθησης κάθετα στον άξονά του. Ομοίως με την περίπτωση της εδαφικής κίνησης παράλληλα στον άξονα αυτού, έτσι και στην παρούσα περίπτωση η γεωμετρία της κατολίσθησης καθορίζει την απόκριση του αγωγού: η εφελκυστική αστοχία που συναντάται στην περίπτωση της διευρυμένης κατολίσθησης μετατρέπεται σε θλιπτική (τοπικός λυγισμός) καθώς το πλάτος της ολισθαίνουσας μάζας μειώνεται δραστικά. Και εδώ η παρουσία της εσωτερικής πίεσης καθορίζει το μηχανισμό αστοχίας του χαλύβδινου κελύφους και επομένως την ευπάθεια του αγωγού.

Συνοψίζοντας η ανάλυση αγωγών έναντι κατολίσθησης θα πρέπει να λαμβάνει υπόψη όλα τα πιθανά σενάρια εδαφικής μετακίνησης καταλήγοντας στο πιο κρίσιμο εξ αυτών. Εξίσου σημαντική είναι η μελέτη της απόκρισης στην θέση των στοιχείων συναρμογής. Τα καμπύλα αυτά τμήματα αποδεικνύονται τα πλέον ευαίσθητα στοιχεία του αγωγού και είναι αυτά που κρίνουν την αστοχία ή μη του αγωγού. Τέλος, η παρουσία της εσωτερικής πίεσης εμφανίστηκε να διαδραματίζει σημαντικό ρόλο στον υπολογισμό των περιθωρίων ασφαλείας: αναδείχθηκαν περιπτώσεις που η δράση της αποδεικνύεται ωφέλιμη (π.χ. «ρηχό» σενάριο κατολίσθησης παράλληλα στον άξονα του αγωγού) ενώ σε άλλες περιπτώσεις η παρουσία πίεσης μειώνει σημαντικά το περιθώριο παραλαβής εδαφικών μετακινήσεων (π.χ. «διευρυμένο» σενάριο κατολίσθησης κάθετα στον άξονα του αγωγού).

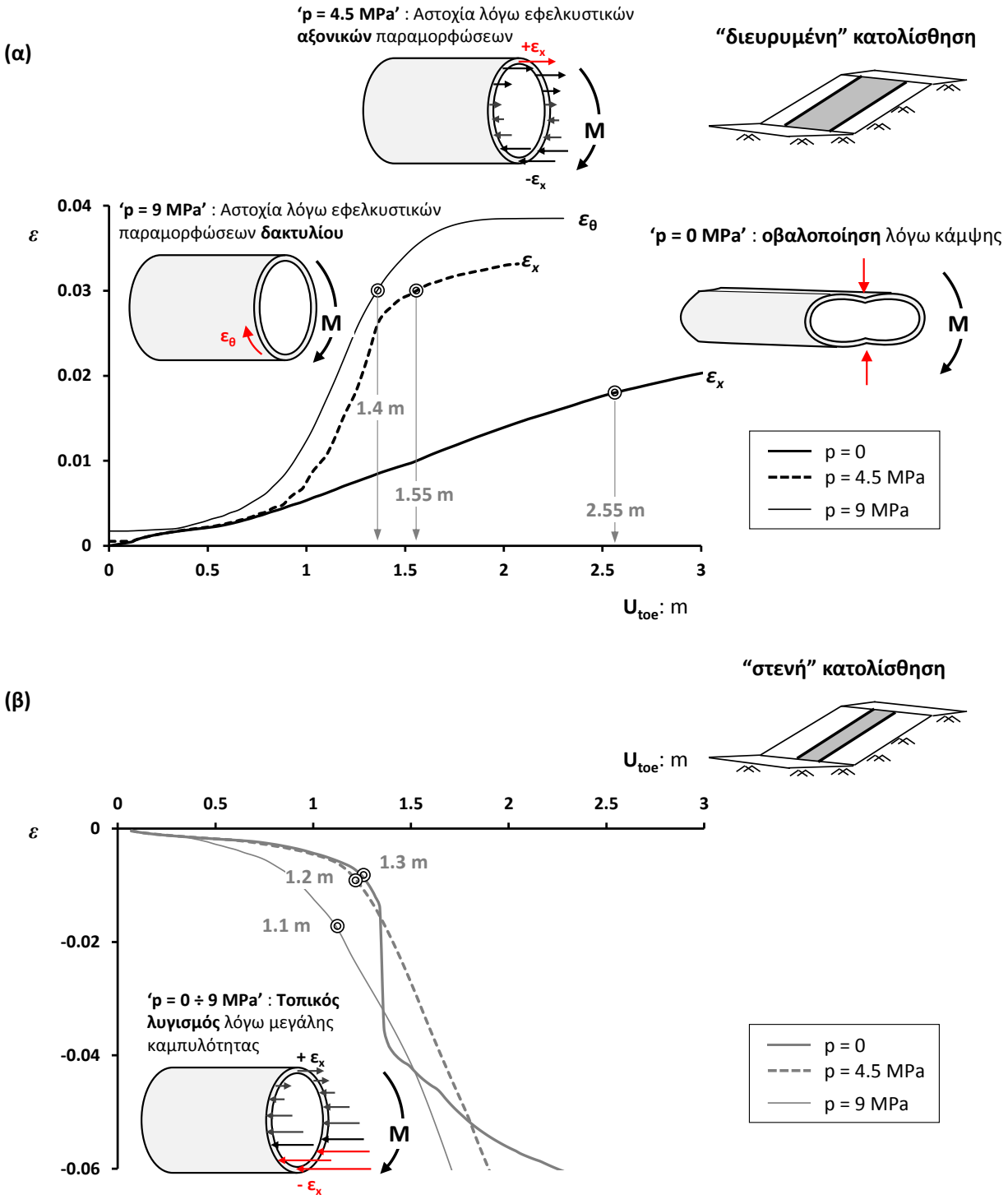

Σχήμα 25. Τα περιθώρια ασφαλείας του αγωγού μέχρι την αστοχία αναλόγως της εσωτερικής πίεσης (α) για το «πλατύ» σενάριο κατολίσθησης και (β) για το «στενό» σενάριο κατολίσθησης..

Βιβλιογραφική αναφορά

Alliance, A. L. (2001). Guidelines for the design of buried steel pipe. American Society of Civil Engineers.

Anastasopoulos, I., Gazetas, G., Bransby, M. F., Davies, M. C. R., & El Nahas, A. (2007). Fault rupture propagation through sand: finite-element analysis and validation through centrifuge experiments. *Journal of Geotechnical and Geoenvironmental Engineering, 133*(8), 943-958.

Anastasopoulos, I., Gerolymos, N., Gazetas, G., & Bransby, M. F. (2008). Simplified approach for design of raft foundations against fault rupture. Part I: free-field. *Earthquake Engineering and Engineering Vibration*, 7(2), 147-163.

ASCE, (1984) "Guidelines for the seismic design of oil and gas pipeline systems." Committee on Gas and Liquid Fuel Lifelines, ASCE, New York.

Bray, J. D., Seed, R. B., Cluff, L. S., & Seed, H. B. (1994). Earthquake fault rupture propagation through soil. *Journal of Geotechnical Engineering*, 120(3), 543-561.

Cheuk, C. Y., White, D. J., & Bolton, M. D. (2008). Uplift mechanisms of pipes buried in sand. *Journal of Geotechnical and Geoenvironmental Engineering*, 134(2), 154-163.

Chiou, Y. J., Chi, S. Y., & Chang, H. Y. (1994). A study on buried pipeline response to fault movement. *Journal of pressure vessel technology, 116*(1), 36-41.

Cocchetti, G., di Prisco, C., Galli, A., & Nova, R. (2009). Soil-pipeline interaction along unstable slopes: a coupled three-dimensional approach. Part 1: Theoretical formulation. *Canadian Geotechnical Journal, 46*(11), 1289-1304.

Cole Jr, D. A., & Lade, P. V. (1984). Influence zones in alluvium over dip-slip faults. *Journal of Geotechnical Engineering*, 110(5), 599-615.

Daiyan, N., Kenny, S., Phillips, R., & Popescu, R. (2009). Parametric study of lateral-vertical pipeline/soil interaction in clay. *1st Int Eng. Mechanics and Material Specialty Conf.* St. John's, NL, Canada.

Daiyan, N., Kenny, S., Phillips, R., & Popescu, R. (2010). Numerical investigation of oblique pipeline/soil in sand. *8th Int Pipeline Conf.*, Calgary, Alberta, Canada.

Dash, S. R., & Jain, S. K. (2007). IITK-GSDMA Guidelines for seismic design of buried pipelines: provisions with commentary and explanatory examples. *National Information Center of Earthquake Engineering, Kanpur, India.*

di Prisco, C., Nova, R. & Corengia, A. (2004). A model for landslide-pipe interaction analysis. *Soils Found. 44*, No. 3, 1–12.

European Commission, Directorate-General for Research and Innovation (2015), "*Safety of buried steel pipelines under ground-induced deformations (GIPIPE)*", ISBN: 978-92-79-54040-0

Gantes, C.J., Bouckovalas, G.D., and Koumousis, V.K., "Slope Failure Verification of Buried Steel Pipelines", *10th International Conference on Applications of Advanced Technologies in Transportation, Athens*, Greece, May 27- 31, 2008.

Guo, P. J., & Stolle, D. F. E. (2005). Lateral pipe–soil interaction in sand with reference to scale effect. *Journal of Geotechnical and Geoenvironmental Engineering*, 131(3), 338-349.

Hsu, T. W., Chen, Y. J., & Hung, W. C. (2006). Soil restraint to oblique movement of buried pipes in dense sand. *Journal of transportation engineering*, 132(2), 175-181.

Karamitros, D. K., Bouckovalas, G. D., & Kouretzis, G. P. (2007). Stress analysis of buried steel pipelines at strike-slip fault crossings. *Soil Dynamics and Earthquake Engineering,* 27(3), 200-211.

Karamitros, D. K., Bouckovalas, G. D., Kouretzis, G. P., & Gkesouli, V. (2011). An analytical method for strength verification of buried steel pipelines at normal fault crossings. *Soil Dynamics and Earthquake Engineering, 31*(11), 1452-1464.

Konuk, I., Yu, S. and Fredj, A. (2006). 'Do Winkler Models Work: A Case Study for Ice Scour Problem' Proc. *25th International Conference on Offshore Mechanics and Arctic Engineering*, Hamburg, Germany, June 2006.

Liang J. and Sung S. (2000) "Site effects on seismic behavior of pipelines: a review." *Journal Pressure Vessel Technology 122*(4), 469-475

Melissianos, V. E., Korakitis, G. P., Gantes, C. J., & Bouckovalas, G. D. (2016). Numerical evaluation of the effectiveness of flexible joints in buried pipelines subjected to strike-slip fault rupture. *Soil Dynamics and Earthquake Engineering*, 90, 395-410.

Mohareb, M. (2002). Plastic interaction relations for pipe sections. *Journal of engineering mechanics, 128*(1), 112-120.

Nobahar, A., and Kenny, S. (2007). 'Analysis and design of buried pipeline for displacement controlled hazards: A probabilistic approach.' *J. OMAE. Vol.129*, pp.219-228.

O'Rourke T.D. & Palmer M.C. (1996) Earthquake performance of gas transmission pipelines. *Earthquake Spectra, 12*(3), 493-527.

O' Rourke, T.D., (2009), "The 49th Rankine Lecture: Geohazards & Large Geographically Distributed Systems", *Geotechnique, 60*(7), 505-543.

O'Rourke, M. J., & Liu, X. (2012). Seismic design of buried and offshore pipelines. *MCEER Monograph MCEER-12-MN04*.

O'Rourke, M., Filipov, E., & Uçkan, E. (2015). Towards robust fragility relations for buried segmented pipe in ground strain areas. *Earthquake Spectra, 31*(3), 1839-1858.

Phillips, R., Nobahar, A., and Zhou, J. (2004). Combined axial and lateral pipe-soil interaction relationship, *5th Int. Pipeline Conf*., Calgary, Alberta, Canada.

Pike, K., Seo, D., & Kenny, S. (2011). Continuum modelling of ice gouge events: Observations and assessment. In *OTC Arctic Technology Conference. Offshore Technology Conference*.

PRCI, (2004), "Guidelines for the Seismic Design and Assessment of Natural Gas and Liquid Hydrocarbon Pipelines, Pipeline Design, Construction and Operations", Edited by Honegger, D. G., and Nyman D. J., Technical Committee of Pipeline Research Council International (PRCI) Inc, October 2004

Randolph, M. F., Seo, D., & White, D. J. (2010). Parametric solutions for slide impact on pipelines. *Journal of Geotechnical and Geoenvironmental Engineering*, 136(7), 940-949.

Takada S, Nakayama M, Ueno J, Tajima C. Report on Taiwan Earthquake. RCUSS, Earthquake Laboratory of Kobe University, 1999. p. 2–9.

Takada S, Hassani N, Fukuda K. (2001) "A new proposal for simplified design of buried steel pipes crossing active faults". *Earthquake Engineering and Structural Dynamics*, Vol. 30: 1243-1257.

Tang A.K (ed.) (2000). *Izmit (Kocaeli), Turkey, Earthquake of August 1999 Including Duzce Earthquake of November12, 1999: Lifeline Performance* (Vol. 17). ASCE Publications.

Trautmann C.H., and O'Rourke T.D. (1985) "Lateral force – displacement response of buried pipe." *Journal of Geotechnical Engineering, ASCE*, Reston, VW, Vol 111, No 9, pp 1077 – 1092.

Trifonov, O. V., & Cherniy, V. P. (2010). A semi-analytical approach to a nonlinear stress–strain analysis of buried steel pipelines crossing active faults. *Soil Dynamics and Earthquake Engineering, 30*(11), 1298-1308.

Trifonov, O. V., & Cherniy, V. P. (2012). Elastoplastic stress–strain analysis of buried steel pipelines subjected to fault displacements with account for service loads. *Soil Dynamics and Earthquake Engineering*, 33(1), 54-62.

Uzarski j. & Arnold C. (Eds). (2001). *Chi-Chi, Taiwan earthquake of September 21, 1999: reconnaissance report* (Vol. 17). Earthquake Engineering Research Institute.

Van Es, S. H. J., Gresnigt, A. M., Kolstein, M. H., & Bijlaard, F. S. K. (2014, August). Strain based design of spirally welded pipes, local buckling in 4-point bending. In *The Twenty-fourth International Ocean and Polar Engineering Conference*. International Society of Offshore and Polar Engineers.

Wang LRL, Yeh YA. A refined seismic analysis and design of buried pipeline for fault movement. *Earthquake Engineering and Structural Dynamics* 1985;13:75–96.

Wijewickreme D., Karimian H., and Honegger D.G. (2009). "Response of buried steel pipelines subjected to relative axial soil movement" *Canadian Geotechnical Journal*, 46: 735-752.

Yimsiri, S., Soga, K., Yoshizaki, K., Dasari, G.R., and O'Rourke, T.D. (2004). "Lateral and upward soil-pipeline interactions in sand for deep embedment conditions", *Journal of Geotechnical and Geoenvironmental Engineering, ASCE*, 130(8): 830-842.

Zhang, J., Stewart, D. P., & Randolph, M. F. (2002). Modeling of shallowly embedded offshore pipelines in calcareous sand. *Journal of Geotechnical and Geoenvironmental Engineering, 128*(5), 363-371.

Zhang, L., Zhao, X., Yan, X., & Yang, X. (2016). Elastoplastic Analysis of Mechanical Response of Buried Pipelines under Strike-Slip Faults. *International Journal of Geomechanics*, 04016109.

TABLE OF CONTENTS

Introduction

Excessive ground displacements may perhaps be characterized as the most astonishing cause of failure related with civil engineering. Their consequences are unfortunately not a local property but rather notoriously familiar all around the globe: from the most developed countries to the most secluded regions. For the latter case, their effects are auspiciously beyond our interest. In all other scenarios, excessive ground movements will only by fortune not result in the engineers' main concern: losses. Their sort, distribution and magnitude will define the scale of the disaster which may reach up to the most appalling scenario of several human casualties.

Recognition of our inherent inability to control nature (especially when resources are limited) has led the engineering community –driven by the earthquake engineering discipline– to pursue resilience (*Bruneau & Reinhorn, 2007; Chang & Shinozuka, 2004; O'Rourke, 2007; FEMA, 2009*) as the most viable strategy to minimize the cost of the inevitable disaster. Design for resilience is ramified in pre-event measures (summarized in the concept of opting for structural robustness) and past-event actions (focusing on technical and societal preparedness to recover functionality).

This concept appears indeed to be life-preserving in terms of community endurance but may perhaps be inappropriate for the design or retrofitting of critical infrastructure utilities, such as pipelines. In these cases excessive ground displacements may produce severe failures, while disruption of service for recovery (if possible) will result in shattering loss of assets.

Unlike most of our civil infrastructure (whose lifespan exceeds 50-100 years or even more at a quite reasonable cost and where effects of failure are usually contained), construction of power-related infrastructure requires abundant resources – the lack of which certainly limits their robustness thereby curtailing their life-expectancy (e.g. due to accumulation of deformation or fatigue). But even during their limited lifetime, they may indeed fail as a result of natural phenomena such as earthquakes, slope instability or large differential settlements provoking a plethora of cascading effects not only on the interrelated components of such facilities (e.g. pumping stations, tanks) but also on the very endurance of communities (lack of power supply to homes and industries, immediate effect on energy prices, environmental consequences etc), let alone the human casualties.

In an attempt to address the above issues in the design and retrofitting of critical pipeline systems, the present study presents a new method for the numerical simulation of the response of buried pipelines under large permanent ground displacements.

Three are the main compelling reasons for such an attempt:

1. *Traversing areas of intolerable slope displacements or active fault zones is often unavoidable*, especially when it comes to structures of considerable length such as pipelines. In case the unstable area is a priori known, abandoning initial planning in order to avoid it is a commonly adopted solution, which however may often question the financial survivability of the project.
2. *The rapid expansion of today's cities which is unavoidably pursued by the need to enlarge the size and population of infrastructure*. The growth of urbanized regions calls for increasing the dimensions of infrastructure in order to satisfy the augmented needs for energy production and transmission, thus challenging the capacities of conventional foundations.
3. *The need to limit empiricism and conservatism* in the design of pipelines and rather propose a more rigorous analysis methodology that will ultimately form the basis of more economical design.

Although several incidents of pipeline failures of larger or smaller intensity have indeed been reported, it is the cases of successful performance of such structures that have motivated the present research by providing evidence to suggest that proper design may prove a very effective technique for hindering failure.

It is in this context that, the present study has been oriented towards the ***investigation of the interplay between the pipeline and the surrounding soil in order to identify the phenomena that govern the pipeline's response***. Through an in-depth analysis of the problem mechanics, it is envisaged that a practical methodology can be provided to enhance the existing knowledge regarding the design of pipelines to sustain large ground displacements.

CHAPTER 1

Pipelines subjected to large ground deformations: the current state of knowledge

1.1. Introduction

Based on the damage mechanism of buried pipelines, permanent ground deformations such as fault deformation, landslide, liquefaction-induced soil movements and settlements constitute a substantial threat to the structural integrity of buried pipelines (e.g**. Jennings [1971], MaCaffrey and O'Rourke [1983], Desmod et al. [1995], Nakata and Hasuda [1995], Takada et al. [1999], Youd et al. [2000], Liang and Sun [2000], O'Rourke and Liu [2011], O'Rourke et al. [2014]**). Therefore, the scientific community has placed significant effort on the investigation of the performance of buried pipelines subjected to permanent ground displacements. Many approaches were employed to enhance our knowledge about the soil-pipeline interaction including numerical and physical modeling. In the ensuing, a brief review of the research conducted on the fields of pipeline-fault and pipeline-landslide interaction is presented with emphasis on the approach method.

1.2. Faults

The investigation of the pipeline response subjected to fault-induced displacements comprises mainly two approaches analytical solutions, and numerical methods ranging from simplified analyses to sophisticated 3D numerical models. In addition, there is an abundancy of experimental studies aiming to provide the physical evidence for the calibration verification of the analysis methods.

1.2.1. Analytical methods

Newmark and Hall [1975] were one of the first to develop simplified analysis methods for the fault crossing problem. This method assumed the pipeline to be subjected to direct tension due to the fault

motion and ignored lateral resistance of the soil. Hence, the analysis of the pipeline was performed by assuming it to be a cable deforming in straight line. **Kennedy et al. [1977 and 1983]** revised the Newmark–Hall method by incorporating (a) bending of the pipeline near the fault crossing point considering the soil lateral forces and (b) pipe-soil friction nonlinearity. The pipe model of elastic beam was adopted by **Vougioukas et al. [1979]** to account for the vertical and horizontal fault movements. **Wang and Yeh [1985]** suggested modifications to the closed-form analytical model of the Kennedy et al. [1977]. As shown in Fig.1.1, they proposed a localized large deflection beam model according to which the pipe near the fault intersection is modeled as a constant curvature curved segment and the remaining small deflection pipe as a semi-infinite beam on elastic foundation. The model used by Wang and Yeh included the bending rigidity of the pipe, a shear force at the point of inflection of the curved pipe crossing the fault zone, and a boundary condition related to semi-infinite beam on elastic foundation at some distance from the fault zone. **Chiou et al. [1994]** realized that the hypothesis of a constant curvature at the fault zone is a simplification that leads to overestimation of the stiffness of the buried pipe and underestimation of its strain. **Karamitros et al. [2007]** maintained assumptions in existing analytical methodologies, but introduced refinements to achieve a wider range of application. The pipeline was partitioned into four segments (Fig.1.2). Two pipeline segments in the high curvature zone on both sides of the fault trace were analyzed using elastic-beam theory with the objective of identifying the location of the most unfavorable combination of axial and bending strains. The segments outside the high curvature zone were treated as beams-on-elastic-foundation and the actual stress distribution on the pipe cross-section was considered so as to account for the effect of curvature on axial strains and to determine the maximum strain. The approach was later extended by **Karamitros et al. [2011]** to estimate maximum strains due to normal faulting. Extending the analytical methodology proposed in Karamitros et al. (2007), **Trifonov and Cherniy [2010]** presented a semi-analytical approach to analyze the mechanical behavior of buried pipelines, which comprehensively considered the nonlinearities of material, large displacement and pipe/soil interaction. In this work three modifications were made concerning (a) the lack of symmetry condition in the intersection point (wide range of fault types), (b) the incorporation of axial force in the equations of pipe motion in high curvature segments, in order to have a direct effect on bending stiffness and (c) the contribution of the transverse displacement to the axial elongation. The aforementioned work has been further extended by **Trifonov and Cherniy [2012**] in an attempt to refine the analytical model for inelastic material behavior of the steel pipeline. Along with the longitudinal stresses and strains arising from combined bending and tension due to fault displacements, additional hoop and axial stresses and strains resulting from the internal pressure and temperature variation were taken into account within a two-

dimensional elastoplastic model based on the plastic flow theory. The proposed model was validated through comparison of the obtained solutions to the results of numerical simulations of the finite-element beam-type and shell-type models in the finite-element software ANSYS for the case of strike-slip fault at different crossing angles. **Wang et al. [2011]** proposed a refined strain analytical methodology, taking the nonlinear characteristics of soil–pipeline interaction and pipe steel into account. Based on the elastic-beam and beam-on-elastic-foundation theories, the position of pipe potential destruction and the strain and deformation distributions along the pipeline were derived. Compared with existing analytical methods and finite element analysis, the maximum axial strains on the pipe derived from the analytical methodology are in good agreement with the finite element results at small and intermediate fault movements and become gradually more conservative at large fault displacements. **Zhang et al. [2016]** further modified the previous analytical models to account for the internal pressure and temperature variation, improving the calculation accuracy by introducing (a) an elastoplastic beam theory to analyze the bending moment and the bending strain and (b) a refined analysis of the axial force in the high-curvature zone, considering the friction force, the lateral resistance of soils and the curvature of the pipeline.

1.2.2. Numerical methods

The analytical approach remains a helpful tool during the preliminary design stage of a pipeline project. The pipeline-soil interaction complexity, however, requires the implementation of advanced numerical models that are capable of considering all pertinent parameters, such as geometrical and material non-linearity, cross-section ovalization and complex soil behavior. To address the complexity of the pipeline-soil interaction phenomenon a number of numerical methods were established.

Winkler-type models

To begin with, there are the **Winkler-type** numerical methods, where the soil is modeled with independent translational springs in four directions (axial, lateral, vertical upward and vertical downward) as schematically shown in Fig.1.3. The pipeline is generally meshed with beam-type finite elements that can model the axial, shear and bending deformation and can provide stresses and strains at cross-section integration points along the pipe. This numerical approach is also adopted by Standards and Regulations such as **Eurocode8**, **ALA** and **ASCE**. **Shakib and Zia-Tohidi [2004]** examined the effect of various parameters on the response of buried pipeline crossing the oblique-fault movements. The parameters

they studied were the anchored length of pipeline, buried depth of pipe, frictional angle of soil-pipe system, geometrical characteristics of pipe, fault displacement, crossing angle of pipe with the fault, and the fault slope angle. A Winkler-based finite element model, which uses beam elements for the pipeline and discrete nonlinear springs for the soil, has been adopted by **Joshi et al [2011]**, to analyze buried pipeline subjected to reverse fault motion. Results of their parametric study suggested that the pipeline's capacity to accommodate reverse fault offset can be increased significantly by choosing a near-parallel orientation in plan with respect to the fault line. Further improvement in the response of the pipeline is possible by adopting loose backfill, smooth and hard surface coating, and shallow burial depth in the fault crossing region. **Erami et al. [2014]** utilized the beam Winkler-type model to investigate the applicability of the pipe-soil interaction equations suggested by currently used pipeline seismic design codes to segmented pipelines. They compared the results predicted by finite element analyses to those obtained from full-scale experiments on a segmented ductile iron pipelines. Likewise, **Melissianos et al. [2016]** used the simplified Winkler-based finite element model to evaluate a kind of flexible joint as an innovative mitigating measure against the consequences of strike-slip faulting on pipelines. Despite the usefulness of the beam Winkler-type models deriving from their simplicity, they come with a significant drawback: the use of beam-type finite elements does not allow the direct estimation of local buckling, cross-section ovalization and detailed stress-strain distributions around the circumference of the pipe.

To study in a more rigorous way the pipe behavior at large deformations, and to realistically account for the response of the pipe at its section plane, the **shell Winkler-type** model was introduced. **Ariman et al. [1987, 1992]** used a shell model to investigate the tensile and bending behavior of pipelines subjected to abrupt fault displacements. A series of parametric studies were carried out to understand the effect of key variables such as the crossing of pipeline-fault intersection, burial depth, pipe diameter and soil properties. **Takada et al. [1998]** introduced a simplified method for the maximum axial strain in steel pipes, which are crossing active faults, considering the deformation of the pipe cross-section (Fig. 1.4). To that end, a shell model of pipe was analyzed under the normal and reverse displacement. The shell model was used for FEM analysis of fault-crossing pipe in order to consider the effect of local buckling and section deformation. Subsequently, they enhanced their methodology by adopting a beam-shell hybrid model (Fig. 1.5.b) to account for the response of the pipeline at large distance from the fault, and utilized it to develop a simplified method for obtaining the maximum strain in pipeline crossing active faults considering the section deformation of the pipe (**Takada et al. [2001]**). **Liu et al [2004]** proposed an equivalent boundary for the shell FEM method to analyze the large deformation of buried pipeline under fault movement that can be applied to the ends of shell model using nonlinear spring elements (Fig. 1.5c).

Xie et al. [2011] studied the response of buried HDPE pipelines subjected to strike-slip faulting through numerical analyses, where a hybrid beam-shell-type model was used for the pipe and springs were used to simulate the soil. Their numerical predictions were compared with experimental data obtained from small-scale split-box testing, as well as with results from large-scale tests. **Gantes and Bouckovalas [2013]** used a Winkler-type model to study the effects of activation of faults induced by seismic activity on the High Pressure Natural Gas Pipeline Komotini–Alexandroupolis–Kipi, in Northeastern Greece. The pipeline was modeled with shell elements at the area of interest, while an appropriate nonlinear material law for the pipeline steel and an elastic–perfectly plastic law for the soil springs was adopted. They also investigated the appropriate pipeline length to be included in the model which proved to be of the order of 2 km. However, the use of Winkler-type models

Continuum modelling

Notwithstanding the practical value of Winkler-type methodologies, the latter are as accurate as the assumed p-y springs formulations, while they completely ignore any load transfer effects between the adjacent soil springs. Many researchers have raised questions on the capability of the Winkler-type models to realistically capture the pipeline response subjected to permanent ground displacements. For example, **Zhang et al. [2002]** and **Di Prisco et al. [2004]** highlighted that assuming the soil springs to behave independently is an oversimplification of the fact that the each displacement and rotation component of the pipe depend on the complex, coupled relationship between all the load components acting on it. Hence, they promoted the use of interaction diagrams similar to those for rigid foundations. **Cocchetti et al. [2008]** tackled the problem of soil-pipe interaction along active faults following a numerical displacement-based approach. The interaction was analyzed by means of lumped coupled elastoplastic springs on elastic beam, whose failure locus was expressed as:

$$f = \left(\frac{N}{N_{5,6}}\right)^{\delta} + \left(\frac{H}{H_{3,4}}\right)^{\alpha} - \left(\frac{V_2 - V}{V_2}\right)^{2\gamma} * \left(\frac{V_1 - V}{V_1}\right)^{2\beta} = 0$$

where $V_{1,2}$ $H_{3,4}$ $N_{5,6}$ are the limit loads in V, H, N directions respectively and α, β, γ and δ define the shape of the elastic interaction domain. The 3D interaction domain (Fig. 1.6) was linearized piece-wise in a form such that a linear complementarity problem can be formulated. In addition, studies undertaken by **Konuk et al. [2006]** and **Nobahar and Kenny [2007]** in the arctic region particularly for ice scour problems revealed some deficiencies with the use of the Winkler approach for modelling pipe-soil interaction. The major deficiency concerns poor modelling of the realistic soil behavior for large deformation events. Their

research also noted that the conservatisms in the Winkler model could be removed by using the continuum approach for modelling the appropriate boundary value problem. **Konuk et al. [2006]** showed that the use of Winkler models for pipe-soil interaction produced contradicting results, i.e. can sometimes lead to a conservative design (which may result in substantial cover requirements) or sometimes predict strains and displacements less than those predicted by the continuum models. The most efficient way to account for the nonlinear response of the pipeline, the complex behavior of the soil and the interaction phenomena between the two is to employ sophisticated continuum modelling, where the pipe is discretized into shell finite elements and the surrounding soil into 3D solid elements. This approach may increase modeling complexity, nonlinearity and computational effort, yet it is capable of rigorously account for the coupled behavior of the loading components, for the formation of local instability phenomena on the pipe (local buckling, ovalization etc.), as well as any nonlinear phenomena on the pipe-soil interface (sliding, detachment) by using contact elements.

The initial attempts to employ the continuum model were presented in **Kokavessis and Anagnostidis [2006]** where the use of contact elements is proposed for the coupling of pipeline with the surrounding soil. Using the experimental results of Trautmann and O'Rourke [1985], **Yimsiri et al. [2004]** calibrated a finite element model to investigate the soil-pipeline interactions in sand under lateral and upward movements in a deep embedment condition. **Phillips et al. [2004]** presented a 3-dimensional finite element parametric study of pipe-soil interaction under combined axial and lateral loading. **Guo and Stolle [2005]** used a 2-dimensional continuum finite element methodology to investigate the pipe-soil interaction associated with relative pipe movements in the lateral direction. **Odina and Tan [2009]** discussed the application of continuum FE methods to model the fully coupled seabed-buried pipeline interaction events subject to ground movements at active seismic faults. A three-dimensional (3D) continuous soil representation was adopted by **Vazouras et al. [2010, 2012]** for the analysis of the strike-slip fault-crossing problem (Fig. 1.7). The model took into account the elastoplastic behavior of soil, the contact interaction between the soil and the pipe, large inelastic strains in the steel pipeline, and the distortion of the pipeline cross section and local buckling formation. Recently, **Vazouras et al. [2015]** analyzed the pipeline behavior of pipelines under the strike- slip fault using a refined finite element model that combined the detailed numerical model with mathematical solutions. **Cheong et al. [2011]** performed a series of 3-dimensional finite element analyses to investigate the interaction between soil and pipeline in sand subjected to lateral ground displacements with emphasis on the peak force exerted to a bended elbow-pipe. Both opening and closing modes of the elbow section for different initial pipe bending angles were investigated. **Seo et al. [2011]** investigated the yield envelopes for axial-lateral

oblique pipeline-soil interaction in cohesive soil with particular attention to the pipe oblique angle and the pipe burial depth ratio on the basis of LS-DYNA/Explicit ALE formulation. Based on this approach, the soil failure mechanisms were examined as a function of pipe oblique angle. **Roy et al. [2014 and 2015]** investigated the pipeline-soil interaction for lateral loading using the Arbitrary Lagrangian-Eulerian (ALE) method for plane-strain finite element modelling. **Zhang et al. [2014]** investigated the buckling behavior of buried gas pipeline under strike-slip fault displacement using the finite element method. Emphasis was placed on the effects of internal pressure, radius-thickness ratio and fault displacement on buckling mode and axial strain of buried pipeline. **Trifonov et al. [2014]** performed 3D numerical analyses of a buried steel pipeline crossing an active strike-slip fault with emphasis on the pipeline-soil interaction and mathematical representation of the fault. Different soil properties were specified for the parts of the soil volume representing the trench backfill and the native soil. The influence of the fault model on the predicted stress-strain state of the pipeline was analyzed using two different types of fault representation (Fig. 1.8). The first approach was based on the continuous representation of the fault; in the second approach, two separate soil blocks interacting along the fault plane were introduced. The effect of the fault representation on the stress-strain evolution and limit state initiation was not critical and did not result in substantial differences in limit state predictions and critical fault offset estimates. Additionally, the developed numerical model was compared to the analytical fault-crossing model of the papers by Trifonov and Cherniy [2010, 2012]. In the case of a consistent choice of input parameters, a generally good correspondence between the analytical and numerical models was established for small and moderate fault offsets. **Mokhtari and Alavi Nia [2015]** used the continuum finite element method to investigate the efficiency of FRP wraps as a means of reinforcement for buried steel pipelines subjected to strike-slip faulting. **Uckan [2015]** performed 3D finite element analyses and proposed a simplified numerical model for buried steel pipes crossing perpendicularly strike-slip faults. **Naeini et al. [2015]** analyzed the response of buried HDPE pipelines subjected to normal faults by means of finite element analyses. The pipe edges were assumed fixed in the longitudinal direction. By comparing the numerical predictions with the experimental results obtained from geotechnical centrifuge tests of Ha et al. 2008, they observed a good comparison for low fault offsets, although discrepancies of the order of 34% appeared for large fault deformations. They also examined the effect of the pipeline burial depth, pipe diameter and thickness, friction angle and density of the soil surrounding the pipe on the maximum bending strain as well as on the bending strain distribution along the pipeline. **Banushi [2015]** performed 3D finite element analyses, accounting for the pipe-soil system nonlinearity, to assess the seismic performance of a straight 36" diameter X65 steel grade pipeline subjected to strike-slip faulting. More specifically, the pipe was

modelled with four-node reduced integration shell elements (S4R), while the clayey soil, described by a Mohr Coulomb failure criterion, was modelled using eight-node linear brick continuum elements with reduced integration (C3D8R). The part of the soil-pipe system away from the fault was modeled as a single equivalent axial spring, connected to the pipe shell elements through appropriate constraints. The force displacement relationship of the equivalent spring was obtained analytically by subjecting the pipeline statically to a uniform axial displacement. **Zhang et al [2016]** proposed a finite element model to analyze the displacement and strain of the pipeline under strike-slip faults considering equivalent boundary springs. The purpose of introducing equivalent boundary springs was to simulate the interaction of the pipeline-soil more sufficiently, since the dimension of current models was far smaller than the actual one of the interaction of the pipeline-soil. Subsequently, a closed-form solution was derived to obtain the stiffness coefficient of equivalent boundary springs.

Other numerical methods have also been utilized to study the pipe–soil interaction. For example **Calvetti et al. [2004]** used the distinct element method, while **Karimian [2006]**, used the finite-difference method. Most notably, **Rahman et al. [2015]** combined the discrete element (DEM) and the finite element method (FEM) for use in the field of buried pipelines subjected to fault movement. The numerical model consisted of elastic three-dimensional beam elements to represent the pipe and spherical granular particles with diameter of 1.1 cm for the soil. The pipe had a diameter (D) of 150mm and a diameter-to-thickness ratio (D/t) equal to 30. The examined faults included a pure strike-slip fault at a dip angle of 90^o and a 60^o reverse fault, while the simulated pipe anchor length was equal to 30D. Emphasis was given on the force–displacement relation between pipes and particles in the axial and vertical directions for fault movement. The force response increased gradually with distance from the rupture point, confirming the critical points near the fault line. In addition, the force revealed a strain softening behavior, since it initially increased with relative displacement, and then entered a residual state after yielding of particles.

1.2.3. Physical modeling

The scientific community has placed significant effort on the understanding of pipeline-soil interaction for the case of permanent ground deformation. To that end, extensive experimental research has been performed by numerous researchers to quantify the soil-pipeline interaction effects due to the displacement of a pipeline relative to its surrounding soil. Scientific attention was attracted by two major topics: (a) the quantification of soil restrain against uniaxial movement of the pipe in order to realistically

calibrate the p-y curves attributed to the uniaxial springs for the Winkler-type models, and (b) the experimental investigation of the pipeline-soil interaction as a whole in order to present evidence of the pipeline response subjected to permanent ground deformation and to be used as a benchmark for the calibration and verification of existing analysis methods.

Uniaxial pipe displacement tests

Experimental research in the means of small scale, full scale and centrifuge tests was performed by numerous researchers. To the author's knowledge the first well-documented tests on buried pipes were performed by **Audibert and Nyman [1975, 1977]** who investigated the soil restraint against vertical and horizontal motion of steel pipes. During the next decades many researchers investigated the pipeline-soil interaction due to lateral displacement of a pipe. **Trautmann and O'Rourke [1985]** performed a full-scale experimental program to assess the response of buried pipes to lateral ground movements. They investigated the effects of pipe depth, soil density, pipe diameter and pipe roughness using various configurations of pipe diameter, burial depth and soil density for dry sands. They concluded that the force-displacement relationship can be modeled by the rectangular hyperbola:

$$F'' = \frac{Y''}{(0.17 + 0.83Y'')}$$

in which $F''=(F/\gamma HDL)/N_h$ the normalized force and $Y''=(Y/D)/(Y_f/D)$ the normalized displacement. Values for the factors N_h (maximum dimensionless force) and Y_f/D (and the corresponding dimensionless displacement) can be selected using design plots such as the one shown in Fig. 1.9. **Hsu [1993]** extended the work of Trautmann and O'Rourke [1985] performing an experimental series of 120 full-scale tests of pipe lateral movement within dry sand. In addition to pipe diameter, sand density and burial depth they also examined the effect of the relative velocity on the lateral soil restraint. The test results indicated that the maximum soil restraints and the corresponding displacements exhibited the power law the power law relationship with the pipe velocity. On the other hand, **Turner [2004]** investigated the influence of loading rate on the soil–pipe interaction with moist sand backfill at three loading rates of 0.03, 0.3, and 25 mm/s and found that the influence of loading rate is almost negligible. **Calvetti et al. [2004]** performed a series of small-scale tests of lateral displacement of pipes buried in fully saturated sand. **Karimian et al. [2006]** performed three full scale experiments to study the performance of buried pipelines subjected to transverse ground movement. Steel pipes of different diameters were used to account for different embedment ratios, placed within dry sand of relative density Dr = 70%. **Almahakeri et al. [2012, 2013]** experimentally investigated the longitudinal bending when pulled laterally through dense sand of (a) steel

and (b) Glass-Fiber-Reinforced-Polymer composite pipes. Subsequently they conducted the simulation of these experimental series using 3D finite element analysis (**Almahakeri et al. [2016]**). The mobilization of lateral soil restraint on buried steel pipelines under different trench backfill conditions was investigated by **Wijewickreme et al. [2014]** using full-scale soil-pipe interaction testing. In particular, they examined the development of lateral soil loads on pipes buried in dense moist sand, crushed sand and gravel, and crushed limestone. The results suggest that the peak normalized lateral soil restraint (N_{qh}) values estimated based on state-of-practice guidelines are in good agreement with those measured from full-scale testing.

Other researchers explored the performance of buried pipelines subjected to relative soil movements in the axial direction through pullout tests. **Capalletto et al. [1998]** and **Honegger [1999]** performed a series of field tests on pipes in cohesive and granular material. **Paulin et al. [1998]** conducted full-scale axial pullout tests buried in sand and clay. Interestingly, they observed that the axial load on pipe in loose sand is lower, and in dense sand is much higher than those predicted by the guidelines. This observation was pointed out by other researchers as well. **Scarpelli et al. [2003]** performed a number of tests both in the field at full scale and in the laboratory, to examine the axial pipe-soil interaction accounting for a variety of soil materials. **Anderson [2005]** conducted a series of pullout tests performed on straight and branched buried HDPE pipes in loose and dense sand. The results of these tests also indicated that the simplified formula suggested by **ASCE [1984]**, **ALA [2001]** and **PRCI [2004]** did not adequately predict the axial loads on pipe. **Wijewickreme et al. [2009]** explored the performance of buried steel pipelines subjected to relative soil movements in the axial direction using a full-scale pullout testing. Measured axial soil loads from pullout testing of pipes buried in loose dry sand were comparable to those predicted using guidelines commonly used in practice. The peak values of axial pullout resistance observed on pipes buried in dense dry sand were several-fold higher than the predictions from guidelines. **Smith and White [2014]** performed a large scale axial test on soft clay highlighting the effect of volumetric hardening on the soil around the pipe: the resistance to axial movement of the pipe increases over time on soft clays due to the repeated shearing during expansion and contraction; this shearing causes failure, positive excess pore pressure and subsequent volumetric hardening leading to an increase in the undrained strength of the surrounding clay.

Scientific attention was also attracted by the soil-pipeline interaction when the pipeline is subjected to vertical displacement. Since a very important issue in the designing of pipelines is the potential upheaval buckling due to axial expansion under high temperature of the containment, much effort was

concentrated on exploring the upward soil restrain. . Researchers have explored the uplift soil restrain both considering dry conditions accounting for onshore pipelines (e.g**. Trautmann et al [1985]**, **Bransby et al. [2001]**, **Chin et al. [2006]**, **Cheuk et al [2008], Wang et al. [2012]**) and saturated soils under drained and undrained conditions (e.g. **White et al. [2001]**, **Palmer et al. [2003]**, **Schupp et al. [2006]**, **Bransby and Ireland [2009]**, **Jung et al. [2013]**, **Williams et al. [2013], Wang et al. [2015]**) accounting for offshore pipelines. Finally, a few researchers have addressed experimentally the issue of vertical bearing capacity of buried pipelines (e.g. **Nagaoka [2007]**).

Oblique displacement tests

Di Prisco et al. [2006] investigated the coupling effect among the different loading components in the V-H-N space, based on both plain-strain experiments, finite element and distinct element analyses. They observed a remarkable coupling existing between vertical and horizontal loading directions, while the axial one was substantially independent of the others. **Hsu et al. [2006]** investigated the soil restraint to oblique pipe movement ranging from an axial-longitudinal to a lateral-transversal direction. Model pipes 0.61 m long with diameters of 152.4, 228.6, and 304.8 mm were tested at shallow burial depth. **Hodder and Cassidy [2010]** investigated experimentally the undrained behavior of a rigid pipe in clay soils when subjected to combined vertical and horizontal loading. The testing was conducted within the University of Western Australia's geotechnical drum centrifuge, and it served the purpose of establishing the parameters of a plasticity model for predicting the vertical and lateral behavior of pipelines in clay soils. **Daiyan et al. [2011]** investigated experimentally and numerically the axial-lateral interaction of pipes with dense sand. A series of centrifuge tests were conducted (Fig. 1.11), with a rigid pipeline displaced in the horizontal plane in a cohesionless bed. The ultimate axial and lateral soil loading was found to be dependent on the angle of attack for relative movement between the pipe and soil. **Tian et al [2011]** used 20 geotechnical centrifuge tests of a 1 m prototype diameter pipe in silty sand, collected from the seabed on Australia's North West Shelf as a benchmark to enhance a pipe-soil interaction model that describes the load-displacement behavior of a pipe subjected to a combined vertical and horizontal loading. **O'Rourke et al. [2015]** investigated the fundamental mechanics of soil-pipe interaction through normal surface stresses measured with tactile pressure sensors during large-scale tests on HDPE pipes. Based on this approach, they concluded that the maximum downward pipe force is only about one-third the maximum force determined with conventional bearing capacity equations, as well as that neglecting the coupled interaction between normal and frictional forces in the numerical modeling of soil-pipe

interaction leads to unconservative results for axial strain. **Monroy et al. [2015]** examined the soil restraint to oblique lateral movement corresponding to ground displacement imposed by a reverse fault.

Pipeline-fault interaction modeling

Yoshizaki et al. [2003] carried out large scale tests in which PGD effects were taken into account on steel pipelines with elbows. A 100mm-diameter pipeline with 4.1mm wall thickness and internal pressure of 0.1MPa was embedded in soil at 0.9m depth and subjected to 1m of ground displacement simulating PGD. It was composed of two straight pipes welded to a 90-degree elbow. Four experiments were conducted at different water contents. The first attempt to use centrifuge modelling to determine pipe strains induced by PGD was described by **O' Rourke et al [2005]**. Two aluminum buried in dry sand pipes with prototype diameters of 0.63 m and 0.95 m subjected to 0.6 and 2 m of full scale strike-slip fault offsets were tested at the Rensselaer Geotechnical centrifuge facility. **Choo et al [2007]** tested HDPE pipes subjected to tensile and compressive strike slip fault using centrifuge, exploring the idea of a remediation technique using expanded polystyrene (EPS) geofoam blocks as low-density backfill. The pipe had an outside diameter of 407.5mm and a wall thickness of 24mm in prototype scale. Three initial pipe–fault angles (-63.5^o, -85^o, 60^o) were considered, and for each angle, tests with and without remediation were done in order to evaluate the effectiveness of remediation. **Bransby et al. [2007]** conducted a series of centrifuge model tests to investigate the response of buried flexible, elastic, continuous pipelines running perpendicular to the strike of reverse faults. The test results showed that significant pipeline bending occurred as the fault-rupture propagated. Hogging and sagging moments were generated on either side of the fault crossing and because different sections of the pipeline moved towards or away from the soil surface, these were not anti-symmetric unlike that expected during strike-slip faulting. **Ha et al. [2008a]** adopted the use of high-density polyethylene (HDPE) pipes to model the prototype pipe and conducted centrifuge tests designed to investigate the differences in their behavior subjected to normal and strike-slip faulting. By combing the data from strain gauges and tactile pressure sensors, transverse force–deformation relations or p–y relations for the pipe were determined and compared with the relationships suggested by the ASCE Guidelines (1984). It was found that for the case of strike-slip faulting the experimental p-y relationship is generally compatible to the ASCE Guidelines suggested values. In contrast, for the case of normal faulting the experimental p-y relationship is much softer than the ASCE Guidelines suggested values. The same researchers (**Ha et al. [2008b]**) also explored the influence of pipe – fault orientation on pipe behavior under strike slip faulting using HDPE pipes. The test results showed that pipe axial strain was strongly influenced by the pipe-fault orientation angle, whereas the effect on

pipe bending strain was minor. In the work of **O'Rourke et al. [2008]** and **O'Rourke [2010]** full-scale strike-slip tests conducted in Cornell University for HDPE pipelines in the course of NEES-SG project were described (Fig. 1.13). HDPE pipes of 400mm and 250mm diameter and 24mm wall thickness were tested. All pipes were 12.2 m long and embedded in partially saturated sand. The pipelines were fixed at the two ends of the test basin by electrofusion couplings that were thermally welded to the pipe. Eight specimens were tested in tension strike-slip conditions and one in compression. **Abdoun et al. [2009]** conducted five pairs of centrifuge tests designed to investigate the influence of various factors on the behavior of HDPE pipes subjected to strike slip faulting at crossing angle of $\beta=26.5^{o}$ (Fig. 1.14); such factors are the fault offset rate, soil moisture content, burial depth ratio, and pipe diameter. 1-g small scale experiments were conducted in the Geotechnical Engineering Laboratory, University of Tokyo, where **Sim et al. [2012]** imposed simultaneously dynamic loading and quasi-static strike-slip fault movement in order to record the response of acrylic 20mm-diameter model pipes buried in dry sand. **Rojhani et al. [2012]** conducted four centrifuge tests investigating the behavior of continuous buried steel pipelines that were subjected to reverse faulting. They also investigated is the influence of factors such as faulting offset, burial depth, and pipe diameter on the axial and bending strain of pipelines and on the ground soil failure and pipeline deformation pattern. **Moradi et al. [2013]** experimentally investigated the behavior of continuous buried steel pipelines subjected to normal faulting through centrifuge testing. The influence of factors such as faulting offset, burial depth and pipe diameter on the axial and bending strains of pipes and on ground soil failure and pipeline deformation patterns are also investigated. **Jalali et al. [2016]** conducted full-scale experiments as well as finite element analyses of 4" and 6" buried steel gas pipelines under reverse faulting. A large 8.5 x 1.7 x 2 m split-box test basin with a fault-dip angle equal to 61° were constructed to test a number of 9 m long steel pipes (Fig. 1.15). The pipelines that were considered to have a burial depth of 1 m, in well graded sand (SW), were subjected to an offset of 0.6 m along the faulting plane.

1.3. Landslides

In the past, the design of pipelines positioned in landslide susceptible locations was conducted based on the distress caused by drag forces applied by the sliding soil on the pipeline, using simplified structural models such as those in Fig. 1.16 (**Georgiadis [1991]**). Therefore, the most important consideration was the assessment of the load exerted by the landslide on the pipeline. Studies into the impact force as slide

material flows around a pipeline fall into two categories based broadly on a solid mechanics approach where the loading is a function of primarily the soil shear strength and flow velocity (**Marti [1976]**; **Schapery and Dunlap [1978]**; **Towhata and Al-Hussaini [1988]**; **Georgiadis [1991]**) or a fluid mechanics approach with more direct focus on the yield stress and viscosity of the flowing debris and resulting drag coefficients (**Pazwash and Robertson [1973]**; **Bruschi et al. [2006]**). A review of work in this area and results of recent sophisticated experiments and numerical analysis are reported by **Zakeri [2009]** and **Zakeri et al. [2008, 2009]**. However, as the computational capability increased, the design of pipelines subjected to landslide-induced actions followed a more integrated approach, accounting simultaneously for the soil and the pipe response. Currently, two kinds of approaches are widely employed to analyze the pipeline behavior subjecting to landslides, namely the finite element method (FEM) and the analytical method.

1.3.1. Analytical Solutions

O'Rourke et al. [1995] and **Liu and O'Rourke [1997]** presented a simplified analytical approach to estimate the peak axial strains developed on the pipeline subjected to longitudinal and transversal permanent ground displacement respectively. **Parker et al. [2008]** developed a simple closed form solution, modeling the pipe as an elastic cable, the landslide as a distributed load and the soil as a rigid-plastic resistance, assuming a parabolic shape for the deformed pipeline. **Randolph et al. [2010]** established a simple analytical model to evaluate the deformation response of pipelines when encountering the landslide, initially for slides acting normal to the pipeline but later extended to general conditions with the slide impacting the pipeline at some angle. **Yuan et al. [2012a, 2012b]** proposed an analytical model to estimate the failure of surface and buried steel pipelines under the landslide, assuming the axial force of pipelines as a constant (Fig. 1.17). An elastoplastic semi-analytical method was proposed by **Zhang et al. [2015]** to deal with the plastic mechanical behavior of buried pipelines subjecting to landslides based on the plane stress condition, considering the inner pressure and the temperature variation. To verify the proposed model, they compared results from the proposed method with finite element analyses.

1.3.2. Finite Element modeling

As with other types of permanent ground displacement, the effect of landslide-induced actions on buried pipelines is most usually addressed with simplified Winkler-type models. Though the computational power has increased dramatically in the recent years, the simplified Winkler-type models are still employed to describe the pipeline-soil interaction mainly due to their practicality. **Gantes et al. [2008]** proposed a methodology for the evaluation of the effects of down-slope ground movements on buried pipelines based on the finite element method: the pipe was modelled with shell or beam elements and the soil with appropriate discrete springs in orthogonal directions. On the other hand, **Cocchetti et al. [2009a, 2009b]** recognized the coupling among the different loading components and introduced the use of macroelements to reproduce the pipeline-soil interaction that account for the interaction among the vertical, horizontal and axial soil reactions. **Zhu and Randolph [2010]** established a numerical approach, based on the finite-element method but using remeshing, to simulate large flow deformation of debris from a landslide and to quantify the loads and displacements imposed on pipelines embedded in the seabed. A simple two-dimensional elastic perfectly plastic soil model with plane strain conditions was employed in this analysis. **Liu et al. [2010]** established a 3D finite element model of the pipeline and soil to perform the failure analysis of natural gas buried X65 steel pipeline under deflection load. The pipeline is assumed to be loaded in a parabolic deflection displacement along the axial direction. **Zheng et al. [2012]** investigated the response of a buried X65 pipeline due to non-uniform deflection of landslide process, using 3D finite element modelling. Both pipeline and the surrounding soil were modelled with solid elements, with the behavior of the latter assumed linear elastic (Fig. 1.18). The pipeline was laid at the toe of the landslide and a quartic polynomial displacement was applied on the soil of landslide field. Investigating the effects of the surrounding soil, internal pressure, pipeline geometry and landslide width, they found that the D/t ratio and the width of the landslide had greater effect on the limited deflection displacement of the pipeline, compared with the internal pressure under normal operation. **Jafarzadeh et al. [2012]** numerically analyzed the behavior of a 24" diameter buried pipeline, located in a cemented slope and excited by dynamic loading of probable earthquakes in North Tehran area using 3D finite elements. **Han et al. [2012]** investigated buried pipelines subjected to landslides representing the pipe-soil interaction with two types of contact elements; elastoplastic axial, horizontal and vertical springs according to ASCE guidelines were used for the region outside the landslide, while for the pipeline inside the landslide, the pipe-soil interaction (PSI) was simulated with PSI elements, which have only 1-degree-of-freedom of displacements on nodes. **Yuan et al. [2014]** provided two alternatives methods to analyze pipeline behavior under the impact of landslides: the first was a refined analytical method that adopts a

better assumption of tension at the sliding zone, while the second was a vector-form intrinsic finite element method which can address asymmetric conditions and model the dynamic process. **Chen et al. [2014]** conducted stress analyses of an X80 steel buried gas pipeline subjected to transverse and longitudinal landslide thrust using one-dimensional finite element modeling. They concluded that the case where the pipe longitudinally traverses a sliding mass is more detrimental in terms of stress concentration, compared to the laterally traversing case. **Wu et al. [2014]** compared by means of 3D numerical analyses the response of pipelines across the leading and the trailing edge of a landslide. An X70 steel pipe with diameter of 1.016 m and internal pressure of 5 MPa was modelled in FLAC software. **Fredj et al. [2015]** presented an application of the Smoothed-Particle-Hydrodynamics (SPH) method for the 3D continuum modeling of a pipeline system subjected to large ground displacements. They validated their approach against published experimental data of large-scale tests model, and subsequently used it to characterize a slope movement geotechnical hazard and its rate of progress on the accumulation of strains on the pipeline. **Fredj et al. [2016]** employed a discrete element method (DEM) to establish a three-dimensional pipe-soil interaction model. The model was validated through comparison with medium-scale physical pipe-soil interaction tests. **Li et al. [2016]** established a three-dimensional model for the prediction of landslide hazards to gas pipeline using the strength reduction method for the landslide triggering.

1.3.3. Experimental Studies

Attempts to experimentally investigate the response of buried pipelines subjected to landslide-induced actions have also been made. **Kefang et al [2011]** experimentally investigated the effect of a transverse landslide on a 219 mm diameter buried pipeline by means of a full-scale landslide model. The landslide was induced by front edge excavation and posterior edge water injection. The results showed that free-face conditions of side-slope front edges and underground water were the key factors to affect pipeline landslide stability. **Feng et al. [2015]** examined the response of a gas pipeline crossing a landslide by conducting a large-scale field-test at Chengdu University of Technology (Fig. 1.20). The pipeline was 32 m long, and each end reached at least 10 m outside the landslide boundary. The diameter was 325 mm and the wall thickness was 8 mm. The pipeline, with normal internal pressure of 2.5 MPa, was buried at a depth of 1.5 m in a ditch perpendicular to the slide direction. The test was divided into 6 stages: 1) preliminary observation and measuring; 2) observation and measuring of the first excavation of the retaining wall (1st excavation) to decrease the Safety Factor; 3) complete removal of the retaining wall (2nd excavation) to create a free face for the potential landslide; 4) Infiltration of water in the back scarp

to promote sliding; 5) excavation of the collapsed material (3rd excavation), which hindered the development of the landslide; and 6) complete removal of the collapsed free face material (4th excavation). It was found that the pipeline stresses change in close relation with the displacement of the landslide, which can be described with an exponential function. The most critical stresses on the pipeline were concentrated on both sides of the landslide border and in the central part of the landslide.

References

Abdoun, T. H., Ha, D., O'Rourke, M. J., Symans, M. D., O'Rourke, T. D., Palmer, M. C., & Stewart, H. E. (2009). Factors influencing the behavior of buried pipelines subjected to earthquake faulting. *Soil Dynamics and Earthquake Engineering*, *29*(3), 415-427.

Ariman T, Lee BJ, Chen G. "Failure of buried pipelines under large ground deformations. Recent Advances in Lifeline Earthquake Engineering". 1987; Elsevier, Amesterdam: 63-75.

Ariman T, Lee BJ. "Tension/Bending behaviour of buried pipe-lines subjected to fault movements in Earthquake". Proceeding 10th World Conference on Earthquake Engineering, 1992; Madrid:5423-5426.

Alliance, A. L. (2001). Guidelines for the design of buried steel pipe. American Society of Civil Engineers.

Almahakeri, M., Fam, A., & Moore, I. D. (2012). Longitudinal bending and failure of GFRP pipes buried in dense sand under relative ground movement. *Journal of Composites for Construction*, *17*(5), 702-710.

Almahakeri, M., Fam, A., & Moore, I. D. (2013). Experimental investigation of longitudinal bending of buried steel pipes pulled through dense sand. *Journal of Pipeline Systems Engineering and Practice*, *5*(2), 04013014.

Almahakeri, M., Moore, I. D., & Fam, A. (2016). Numerical Study of Longitudinal Bending in Buried GFRP Pipes Subjected to Lateral Earth Movements. *Journal of Pipeline Systems Engineering and Practice*, 04016012.

Anderson, C., Wijewickreme, D., Ventura, C., & Mitchell, A. (2005). FULL-SCALE LABORATORTY TESTING OF SOIL-PIPE INTERACTION IN BRANCHED POLYETHYLENE PIPELINES. *Experimental Techniques*, *29*(2), 33-37.

ASCE, (1984) "Guidelines for the seismic design of oil and gas pipeline systems." Committee on Gas and Liquid Fuel Lifelines, ASCE, New York.

Audibert, J. M., & Nyman, K. J. (1975, December). Coefficients of subgrade reaction for the design of buried piping. In *Structural Design of Nuclear Plant Facilities* (pp. 109-141). ASCE.

Audibert, J. M., & Nyman, K. J. (1977). Soil restraint against horizontal motion of pipes. *Journal of the Geotechnical Engineering Division*, *103*(10), 1119-1142.

Banushi, G. (2015, June). Seismic Analysis of Buried Steel Pipeline Subjected to Ground Deformation with Emphasis on the Numerical Modelling Optimization. In *10th Pipeline Technology Conference 2015*. EITEP Institute.

Bransby, M. F., Nahas, E., Turner, E., & Davies, M. C. R. (2007). The interaction of reverse faults with flexible continuous pipelines. *International Journal of Physical Modelling in Geotechnics*, *7*(3), 25-40.

Bransby, M. F., Newson, T. A., Brunning, P., and Davies, M. C. R. (2001). "Numerical and centrifuge modeling of the upheaval resistance of buried pipelines." Proc., 20th Int. Conf. on Offshore Mechanics and Arctic Engineering, Rio de Janeiro, Brazil.

Bransby, M. F. & Ireland, J. (2009). Rate effects during pipeline upheaval buckling in sand. Proc. ICE – Geotech. Engng 162, No. 5, 247–256

Bruschi, R., Bughi, S., Spinazze, M., Torselletti, E., and Vitali, L. (2006). "Impact of debris flows and turbidity currents on seafloor structures." *Norw. J. Geol.*, 86, 317–337.

Cappelletto, A., Tagliaferri, R., Giurlani, G., Andrei, G., Furlani, G., & Scarpelli, G. (1998). Field full scale tests on longitudinal pipeline-soil interaction. In *PROC INT PIPELINE CONF IPC, ASME, FAIRFIELD, NJ,(USA), 1998,* (Vol. 2, pp. 771-778).

Calvetti, F., Di Prisco, C., & Nova, R. (2004). Experimental and numerical analysis of soil-pipe interaction. *Journal of geotechnical and geoenvironmental engineering*, *130*(12), 1292-1299.

Chiou, Y. J., Chi, S. Y., & Chang, H. Y. (1994). A study on buried pipeline response to fault movement. *Journal of pressure vessel technology*, *116*(1), 36-41.

Cheuk, C. Y., White, D. J., & Bolton, M. D. (2008). Uplift mechanisms of pipes buried in sand. Journal of geotechnical and geoenvironmental engineering, 134(2), 154-163.

Chin, E. L., Craig, W. H., and Cruickshank, M. (2006). "Uplift resistance of pipelines buried in cohesionless soil." Proc., 6th Int. Conf. on Physical Modelling in Geotechnics. Ng, Zhang, and Wang, eds., Vol. 1, Taylor & Francis Group, London, 723–728.

Choo, Y. W., Abdoun, T. H., O'Rourke, M. J., & Ha, D. (2007). Remediation for buried pipeline systems under permanent ground deformation. *Soil Dynamics and Earthquake Engineering*, *27*(12), 1043-1055.

Cocchetti, G., di Prisco, C., Galli, A., & Nova, R. (2009). Soil-pipeline interaction along unstable slopes: a coupled three-dimensional approach. Part 1: Theoretical formulation. *Canadian Geotechnical Journal*, *46*(11), 1289-1304.

Cocchetti, G., di Prisco, C., & Galli, A. (2009). Soil-pipeline interaction along unstable slopes: a coupled three-dimensional approach. Part 2: numerical analyses. *Canadian Geotechnical Journal*, *46*(11), 1305-1321.

Chen, L. Q., Wu, S. J., Lu, H. F., Huang, K., Lv, Y. T., & Wu, J. L. (2014). Stress analysis of buried gas pipeline traversing sliding mass. *Open Civil Engineering Journal*, *8*, 239-243.

Cheong, T. P., Soga, K., & Robert, D. J. (2011). 3D FE analyses of buried pipeline with elbows subjected to lateral loading. *Journal of Geotechnical and Geoenvironmental Engineering*, *137*(10), 939-948.

Desmod TP, Power MS, Taylor CL, Lau RW. Behavior of large-diameter pipeline at fault crossings. ASCE, TCLEE 1995(6):296–303.

di Prisco, C., Nova, R. & Corengia, A. (2004). A model for landslide-pipe interaction analysis. Soils Found. 44, No. 3, 1–12.

di Prisco, C., & Galli, A. (2006, May). Soil-pipe interaction under monotonic and cyclic loads: experimental and numerical modelling. In *Proceedings of the First Euro Mediterranean Symposium in Advances on Geomaterials and Structures. Hammamet, Tunisia* (pp. 3-5).

Daiyan, N., Kenny, S., Phillips, R., & Popescu, R. (2011). Investigating pipeline–soil interaction under axial–lateral relative movements in sand. *Canadian Geotechnical Journal*, *48*(11), 1683-1695.

de Normalisation, C. E. (1998). Eurocode 8, Part 4: Silos, tanks and pipelines. *CEN EN*, *4*.

Erami, M. H., Miyajima, M., Kaneko, S., Toshima, T., & Kishi, S. (2014). Pipe–soil interaction for segmented buried pipelines subjected to dip faults. *Earthquake Engineering & Structural Dynamics*, *44*(3), 403-417.

Fredj, A., Dinovitzer, A., & Sen, M. (2015). Application of the SPH Finite Element Method to Evaluate Pipeline Response to Slope Instability and Landslides. In *10th European LS-DYNA Conference 2015, Wurzburg, Germany*.

Fredj, A., Dinovitzer, A., Hassannejadasl, A., Gailing, R., & Sen, M. (2016). Application of the Discrete Element Method (DEM) to Evaluate Pipeline Response to Slope Movement. In *2016 11th International Pipeline Conference* (pp. V002T06A013-V002T06A013). American Society of Mechanical Engineers.

Feng, W., Huang, R., Liu, J., Xu, X., & Luo, M. (2015). Large-scale field trial to explore landslide and pipeline interaction. *Soils and Foundations*, *55*(6), 1466-1473.

Gantes, C. J., & Bouckovalas, G. (2013). Seismic Verification of the High Pressure Natural Gas Pipeline Komotini–Alexandroupoulis–Kipi in Areas of Active Fault Crossings. *Structural Engineering International*, *23*(2), 204-208.

Georgiadis, M., 1991. Landslide drag forces on pipelines. Soils and Foundations 31 (1), 156–161.

Gantes, C.J., Bouckovalas, G.D., and Koumousis, V.K., "Slope Failure Verification of Buried Steel Pipelines", 10th International Conference on Applications of Advanced Technologies in Transportation, Athens, Greece, May 27- 31, 2008.

Guo, P. J., & Stolle, D. F. E. (2005). Lateral pipe–soil interaction in sand with reference to scale effect. *Journal of geotechnical and geoenvironmental engineering*, *131*(3), 338-349.

Ha, D., Abdoun, T., O'Rourke, M., Symans, M., O'Rourke, T., Palmer, M., & Stewart, H. (2008). Buried Hdpe Pipelines Subjected to Normal Faulting-a Centrifuge Approach. *Canadian Geotechnical Journal*, *45*, 1733-1742.

Ha, D., Abdoun, T. H., O'Rourke, M. J., Symans, M. D., O'Rourke, T. D., Palmer, M. C., & Stewart, H. E. (2008). Centrifuge modeling of earthquake effects on buried high-density polyethylene (HDPE) pipelines crossing fault zones. *Journal of Geotechnical and Geoenvironmental Engineering*, *134*(10), 1501-1515.

Han, B., Wang, Z., Zhao, H., Jing, H., & Wu, Z. (2012). Strain-based design for buried pipelines subjected to landslides. *Petroleum Science*, *9*(2), 236-241.

Hodder, M. S., & Cassidy, M. J. (2010). A plasticity model for predicting the vertical and lateral behaviour of pipelines in clay soils. *Géotechnique*, *60*(4), 247-263.

Honegger D.G. (1999) "Field measurements of axial soil friction forces on buried pipelines." Technical Council on Lifeline Earthquake Engineering Monograph, 16, 703-710.

Hsu, T.W. 1993. Rate effect on lateral soil restraint of pipelines. Soils and Foundations, 33: 159–169.

Hsu, T. W., Chen, Y. J., & Hung, W. C. (2006). Soil restraint to oblique movement of buried pipes in dense sand. *Journal of transportation engineering*, *132*(2), 175-181.

Jennings, P.C., 1971. Engineering features of the San Fernando earthquake February 9, 1971, California Institute of Technology Report, EERL 71–02, Pasedena, CA.

Joshi, S., Prashant, A., Deb, A., & Jain, S. K. (2011). Analysis of buried pipelines subjected to reverse fault motion. *Soil Dynamics and Earthquake Engineering*, *31*(7), 930-940.

Jalali, H. H., Rofooei, F. R., Attari, N. K. A., & Samadian, M. (2016). Experimental and finite element study of the reverse faulting effects on buried continuous steel gas pipelines. *Soil Dynamics and Earthquake Engineering*, *86*, 1-14.

Jafarzadeh, F., Jahromi, J. F., Yoosefi, S., Sehizadeh, M., Joshaghani, M., & Alavi, M. (2012). Dynamic Response of Buried Gas Pipelines Due to Earthquake Induced Landslides by Nonlinear Numerical Modeling. In *The 15 th World Conference on Earthquake Engineering, Beijing, China (15WCEE)*.

Jung, J. K., O'Rourke, T. D., & Olson, N. A. (2013). Uplift soil–pipe interaction in granular soil. *Canadian Geotechnical Journal*, *50*(7), 744-753.

Karimian, H., Wijewickreme, D., & Honegger, D. (2006, January). Buried pipelines subjected to transverse ground movement: Comparison between full-scale testing and numerical modeling. In *25th International Conference on Offshore Mechanics and Arctic Engineering* (pp. 73-79). American Society of Mechanical Engineers.

Kennedy RP, Chow AW, Williamson RA. Fault movement effects on buried oil pipeline. ASCE Journal of Transportation Engineering 1977;103:617–33.

Kennedy, R.P., Kincaid,, R.H. . Fault crossing design for buried gas oil pipelines. ASME, PVP conference 1983;77:1–9.

Karamitros DK, Bouckovalas GD, Kouretzis GP. Stress analysis of buried steel pipelines at strike-slip fault crossings. Soil Dynamics and Earthquake Engineering 2007;27:200–11.

Karamitros, D. K., Bouckovalas, G. D., Kouretzis, G. P., & Gkesouli, V. (2011). An analytical method for strength verification of buried steel pipelines at normal fault crossings. *Soil Dynamics and Earthquake Engineering*, *31*(11), 1452-1464.

Kefang, L. I. N. D. L. E. I. Y., Min, H. R. Z. H. U. Y. L. U., & Hongwei, T. A. O. (2011). An experiment on the effect of a transverse landslide on pipelines [J]. *Acta Petrolei Sinica*, *4*, 028.

Kokavessis NK, Anagnostidis GS. Finite element modelling of buried pipelines subjected to seismic loads: soil structure interaction using contact elements. In: Proceedings, ASME PVP conference, Vancouver, BC, Canada, 2006.

Konuk, I., Yu, S. and Fredj, A. (2006). 'Do Winkler Models Work: A Case Study for Ice Scour Problem.' Proc. 25th International Conference on Offshore Mechanics and Arctic Engineering, Hamburg, Germany, June 2006.

Li, G., Zhang, P., Li, Z., Ke, Z., & Wu, G. (2016). Safety Length Simulation of Natural Gas Pipeline Subjected to Transverse Landslide. *Electronic Journal of Geotechnical Engineering*, *21*, 4387-4399.

Liang, J., & Sun, S. (2000). Site effects on seismic behavior of pipelines: a review. *Journal of pressure vessel technology*, *122*(4), 469-475.

Liu, A. W., Hu, Y. X., Zhao, F. X., Li, X. J., Takada, S., & Zhao, L. (2004). An equivalent-boundary method for the shell analysis of buried pipelines under fault movement. *Acta Seismologica Sinica*, *17*(1), 150-156.

Liu, P. F., Zheng, J. Y., Zhang, B. J., & Shi, P. (2010). Failure analysis of natural gas buried X65 steel pipeline under deflection load using finite element method. *Materials & Design*, *31*(3), 1384-1391.

MaCaffrey MA, O'Rourke TD. Buried pipeline response to reverse faulting during the 1971 San Fernando Earthquake. ASME, PVP conference 1983;77: 151–9.

Melissianos, V. E., Korakitis, G. P., Gantes, C. J., & Bouckovalas, G. D. (2016). Numerical evaluation of the effectiveness of flexible joints in buried pipelines subjected to strike-slip fault rupture. *Soil Dynamics and Earthquake Engineering*, *90*, 395-410.

Monroy, M., Wijewickreme, D., Nyman, D. J. and Honegger, D. G. 2015. "Soil restraint on steel buried pipelines under reverse fault displacement." Proc. 6th Int. Conf. on Earthquake Geotech. Eng. Christchurch.

Moradi, M., Rojhani, M., Galandarzadeh, A., & Takada, S. (2013). Centrifuge modeling of buried continuous pipelines subjected to normal faulting. *Earthquake Engineering and Engineering Vibration*, *12*(1), 155-164.

Mokhtari, M., & Nia, A. A. (2015). The influence of using CFRP wraps on performance of buried steel pipelines under permanent ground deformations. *Soil Dynamics and Earthquake Engineering*, *73*, 29-41.

Marti, J. (1976). "Lateral loads exerted on offshore piles by subbottom movements." Ph.D. dissertation, Dept. of Civil Engineering, Texas A&M Univ., Rep. No. MM 3008-76-5.

Nagaoka S. "The interaction of earthquake faults with foundations and pipelines," PhD thesis, University of Dundee, UK, 2007

Nobahar, A., and Kenny, S. (2007). 'Analysis and design of buried pipeline for displacement controlled hazards: A probabilistic approach.' J. OMAE. Vol.129, pp.219-228.

Nakata T, Hasuda K. Active fault I 1995 Hyogoken Nanbu earthquake. Kagaku 1995;65:127–42.

Newmark NM, Hall WJ. Pipeline design to resist large fault displacement. In: Proceedings of U.S. national conference on earthquake engineering, 1975. p. 416–25.

Naeini, S. A., Mahmoudi, E., Shojaedin, M. M., & Misaghian, M. (2015). Mechanical response of buried high-density polyethylene pipelines under normal fault motions. *KSCE Journal of Civil Engineering*, 1-9.

Odina, L., & Tan, R. (2009, January). Seismic fault displacement of buried pipelines using continuum finite element methods. In *ASME 2009 28th International Conference on Ocean, Offshore and Arctic Engineering* (pp. 617-625). American Society of Mechanical Engineers.

O'Rourke MJ, Liu X. Seismic Design of Buried and Offshore Pipelines, MCEER-12-MN04; 2011.

O'Rourke M, Filipov E, Uçkan E. Towards robust fragility relations for buried segmented pipe in ground strain areas, Earthq Spectra

O'Rourke, T. D., Jung, J. K. and Argyrou, C. 2015. "Underground infrastructure response to earthquake-induced ground deformation." Proc. 6th Int. Conf. on Earthquake Geotech. Eng. Christchurch.

O'rourke, M., Gadicherla, V., & Abdoun, T. (2005). Centrifuge modeling of PGD response of buried pipe. *Earthquake Engineering and Engineering Vibration*, *4*(1), 69-73.

O'Rourke, T. D., Jezerski, J. M., Olson, N. A., Bonneau, A. L., Palmer, M. C., Stewart, H. E., ... & Abdoun, T. (2008). Geotechnics of pipeline system response to earthquakes. In *Geotechnical earthquake engineering and soil dynamics IV* (pp. 1-38).

O'ROURKE, T. D. (2010). Geohazards and large, geographically distributed systems. *Géotechnique*, *60*(7), 505.

Palmer, A. C., White, D. J., Baumgard, A. J. et al. (2003). Uplift resistance of buried submarine pipelines: comparison between centrifuge modelling and full scale tests. Geotechnique 53, No. 10, 877–833

Phillips, R., Nobahar, A., and Zhou, J. (2004). Combined axial and lateral pipe-soil interaction relationship, 5th Int. Pipeline Conf., Calgary, Alberta, Canada.

Paulin M.J., Phillips R., Clark J.I., Trigg A., and Konuk I. (1998) "A full-scale investigation into pipeline-soil interaction" Proceedings, International Pipeline Conference, Calgary, AB, ASME, 779-779.

PRCI, (2004), "Guidelines for the Seismic Design and Assessment of Natural Gas and Liquid Hydrocarbon Pipelines, Pipeline Design, Construction and Operations", Edited by Honegger, D. G., and Nyman D. J., Technical Committee of Pipeline Research Council International (PRCI) Inc, October 2004

Pazwash, H., and Robertson, J. M. (1973). "Forces on bodies in Bingham fluids." *J. Hydraul. Res.*, 13(1), 35–53.

Rahman, M. A., & Taniyama, H. (2015). Analysis of a buried pipeline subjected to fault displacement: A DEM and FEM study. *Soil Dynamics and Earthquake Engineering*, *71*, 49-62.

Rojhani, M., Moradi, M., Galandarzadeh, A., & Takada, S. (2012). Centrifuge modeling of buried continuous pipelines subjected to reverse faulting. *Canadian Geotechnical Journal*, *49*(6), 659-670.

Roy, K., Hawlader, B., & Kenny, S. (2014, June). Influence of Low Confining Pressure in Modeling of Lateral Pipeline/Soil Interaction in Dense Sand. In *ASME 2014 33rd International Conference on Ocean, Offshore and Arctic Engineering* (pp. V06BT04A050-V06BT04A050). American Society of Mechanical Engineers.

Roy, K., Hawlader, B., Kenny, S., & Moore, I. (2015). Finite element modeling of lateral pipeline–soil interactions in dense sand. *Canadian Geotechnical Journal*, *53*(3), 490-504.

Scarpelli, G., Sakellariadi, E., & Furlani, G. (2003). Evaluation of soil–pipeline longitudinal interaction forces. *Rivista Italiana di Geotecnica*, *37*(4), 24-41.

Seo, D., Kenny, S., Hawlader, B., & Phillips, R. (2011). Yield Envelopes for Oblique Pipeline/Soil Interaction in Cohesive Soil Using ALE Procedure. In *Proc. Pan-Am CGS Geotechnical Conf*.

Schupp, J., Byrne, B. W., Eacott, N., Martin, C. M., Oliphant, J., Maconochie, A., and Cathie, D. (2006). "Pipeline unburial behaviour in loose sand." Proc., 25th Int. Conf. on Offshore Mechanics and Arctic Engineering, Hamburg, Germany, OMAE2006-92541.

Shakib, H., & Zia-Tohidi, R. (2004, August). Response of steel buried pipelines to three-dimensional fault movements by considering material and geometrical non-linearities. In *Proceedings of the 13th World Conference on Earthquake Engineering, Vancouver, BC, Canada* (pp. 1-6).

Sim, W. W., Towhata, I., Yamada, S., & Moinet, G. M. (2012). Shaking table tests modelling small diameter pipes crossing a vertical fault. *Soil Dynamics and Earthquake Engineering*, *35*, 59-71.

Schapery, R. A., and Dunlap, W. A. (1978). "Prediction of storm-induced sea bottom movements and platform forces." *Proc., Offshore Technology Conf.*, Houston, Paper OTC3259.

Smith, V. B., & White, D. J. (2014, March). Volumetric Hardening in Axial Pipe Soil Interaction. In *Offshore Technology Conference-Asia*. Offshore Technology Conference.

Takada, S., Liang, J. W., & Li, T. (1998). Shell-mode response of buried pipelines to large fault movements. *Journal of Structural Engineering*, *44*, 1637-1646.

Tian, Y., & Cassidy, M. J. (2011). Pipe-soil interaction model incorporating large lateral displacements in calcareous sand. *Journal of Geotechnical and Geoenvironmental Engineering*, *137*(3), 279-287.

Takada S, Nakayama M, Ueno J, Tajima C. Report on Taiwan Earthquake. RCUSS, Earthquake Laboratory of Kobe University, 1999. p. 2–9.

Takada S, Hassani N, Fukuda K. "A new proposal for simplified design of buried steel pipes crossing active faults". Earthquake Engineering and Structural Dynamics, 2001; Vol. 30: 1243-1257.

Towhata, I., and Al-Hussaini, T. M. (1988). "Lateral loads on offshore structures exerted by submarine mudflows." *Soils Found.*, 28(3), 26–34.

Trautmann, C. H., & O'Rourke, T. D. (1985). Lateral force-displacement response of buried pipe. *Journal of Geotechnical Engineering*, *111*(9), 1077-1092.

Trifonov, O. V., & Cherniy, V. P. (2010). A semi-analytical approach to a nonlinear stress–strain analysis of buried steel pipelines crossing active faults. *Soil Dynamics and Earthquake Engineering*, *30*(11), 1298-1308.

Trautmann, C. H., O'Rourke, T. D., and Kulhawy, F. H. (1985). "Uplift force-displacement response of buried pipe." Journal of Geotechnical Engineering., 111(9), 1061–1076.

Trifonov, O. V., & Cherniy, V. P. (2012). Elastoplastic stress–strain analysis of buried steel pipelines subjected to fault displacements with account for service loads. *Soil Dynamics and Earthquake Engineering*, *33*(1), 54-62.

Trifonov, O. V. (2014). Numerical stress-strain analysis of buried steel pipelines crossing active strike-slip faults with an emphasis on fault modeling aspects. *Journal of Pipeline Systems Engineering and Practice*, *6*(1), 04014008.

Turner JE. Lateral force–displacement behavior of pipes in partially saturated sand. MS thesis, Cornell University, Ithaca, NY; 2004.

Uckan, E., Akbas, B., Shen, J., Rou, W., Paolacci, F., & O'Rourke, M. (2015). A simplified analysis model for determining the seismic response of buried steel pipes at strike-slip fault crossings. *Soil Dynamics and Earthquake Engineering*, *75*, 55-65.

Vazouras, P., Karamanos, S. A., & Dakoulas, P. (2010). Finite element analysis of buried steel pipelines under strike-slip fault displacements. *Soil Dynamics and Earthquake Engineering*, *30*(11), 1361-1376.

Vazouras, P., Karamanos, S. A., & Dakoulas, P. (2012). Mechanical behavior of buried steel pipes crossing active strike-slip faults. *Soil Dynamics and Earthquake Engineering*, *41*, 164-180.

Vazouras, P., Dakoulas, P., & Karamanos, S. A. (2015). Pipe–soil interaction and pipeline performance under strike–slip fault movements. *Soil Dynamics and Earthquake Engineering*, *72*, 48-65.

Vougioukas EA, Theodossis C, Carydis PG. Seismic analysis of buried pipelines subjected to vertical fault movement. ASCE Journal of Technical Councils 1979;105(TCI):432–441.

Wang, B., Li, X., & Zhou, J. (2011). Strain analysis of buried steel pipelines across strike-slip faults. *Journal of Central South University of Technology*, *18*, 1654-1661.

Wijewickreme D., Monroy M., Nyman D.J., and Honegger D.G. (2014). "Response of buried pipelines subjected to ground displacements under different trench backfill conditions" Proceedings of the 10th U.S. National Conference on Earthquake Engineering, Anchorage, Alaska, 2014.

Wijewickreme D., Karimian H., and Honegger D.G. (2009). "Response of buried steel pipelines subjected to relative axial soil movement" Canadian Geotechnical Journal, 46: 735-752.

Wu, R., Mei, Y., Deng, Q., Pang, C., & Fu, M. (2014, December). Comparative Analysis by Numerical Simulation on Natural Gas Pipelines in Different Positions of Landslide. In *International Conference on Pipelines and Trenchless Technology 2014 (ICPTT)*.

White, D. J., Barefoot, A. J., and Bolton, M. D. (2001). ''Centrifuge modeling of upheaval buckling in sand.'' Int. J. Phys. Model. Geotech., 1(2), 19–28.

Williams, E. S., Byrne, B. W. & Blakeborough, A. (2013). Pipe uplift in saturated sand: rate and density effects. Geotechnique 63, No. 11, 946–956.

Wang LRL, Yeh YA. A refined seismic analysis and design of buried pipeline for fault movement. Earthquake Engineering and Structural Dynamics 1985;13:75–96.

Wang, J., Haigh, S. K., Forrest, G., & Thusyanthan, N. I. (2012). Mobilization distance for upheaval buckling of shallowly buried pipelines. *Journal of Pipeline Systems Engineering and Practice*, *3*(4), 106-114.

Wang, J., Haigh, S. K., & Thusyanthan, N. I. (2015, January). Pipe-soil interaction mechanism during pipeline upheaval buckling in loose saturated sand. In *Frontiers in Offshore Geotechnics III-Proceedings of the 3rd International Symposium on Frontiers in Offshore Geotechnics, ISFOG 2015* (pp. 459-464).

Xie, X., Symans, M. D., O'Rourke, M. J., Abdoun, T. H., O'Rourke, T. D., Palmer, M. C., & Stewart, H. E. (2011). Numerical modeling of buried HDPE pipelines subjected to strike-slip faulting. *Journal of Earthquake Engineering*, *15*(8), 1273-1296.

Youd, T. L., Bardet, J. P., & Bray, J. D. (2000). Kocaeli, Turkey, earthquake of August 17, 1999 reconnaissance report. *Earthquake Spectra, 16*.

Yimsiri, S., Soga, K., Yoshizaki, K., Dasari, G.R., and O'Rourke, T.D. (2004). "Lateral and upward soil-pipeline interactions in sand for deep embedment conditions", *J. of Geotech. and Geoenviron. Eng., ASCE*, 130(8): 830-842.

Yuan, F., Li, L., Guo, Z., & Wang, L. (2014). Landslide impact on submarine pipelines: analytical and numerical analysis. *Journal of Engineering Mechanics*, *141*(2), 04014109.

Yoshizaki, K., O'Rourke, T. D., & Hamada, M. (2003). Large scale experiments of buried steel pipelines with elbows subjected to permanent ground deformation. *Structural Engineering/Earthquake Engineering*, *20*(1), 1S-11S.

Zhang, L., Zhao, X., Yan, X., & Yang, X. (2016). Elastoplastic Analysis of Mechanical Response of Buried Pipelines under Strike-Slip Faults. *International Journal of Geomechanics*, 04016109.

Zakeri, A. (2009). "Review of state-of-the-art: Drag forces on submarine pipelines and piles caused by landslide or debris flow impact." *J. Offshore Mech. Arct. Eng.*, 131(1), 014001.

Zakeri, A., Hoeg, K., and Nadim, F. (2008). "Submarine debris flow impact on pipelines—Part I: Experimental investigation." *Coastal Eng.*, 55(12), 1209–1218.

Zakeri, A., Hoeg, K., and Nadim, F. (2009). "Submarine debris flow impact on pipelines—Part II: Numerical analysis." *Coastal Eng.*, 56(1), 1–10.

Zhu, H., & Randolph, M. F. (2009). Large deformation finite-element analysis of submarine landslide interaction with embedded pipelines. *International Journal of Geomechanics*, *10*(4), 145-152.

Zheng, J. Y., Zhang, B. J., Liu, P. F., & Wu, L. L. (2012). Failure analysis and safety evaluation of buried pipeline due to deflection of landslide process. *Engineering Failure Analysis*, *25*, 156-168.

Zhang, J., Stewart, D. P., & Randolph, M. F. (2002). Modeling of shallowly embedded offshore pipelines in calcareous sand. *Journal of geotechnical and geoenvironmental engineering*, *128*(5), 363-371.

Zhang, J., Liang, Z., & Han, C. J. (2014). Buckling behavior analysis of buried gas pipeline under strike-slip fault displacement. *Journal of Natural Gas Science and Engineering*, *21*, 921-928.

Zhang, L., Zhao, X., Yan, X., & Yang, X. (2016). A new finite element model of buried steel pipelines crossing strike-slip faults considering equivalent boundary springs. *Engineering Structures*, *123*, 30-44.

Figures

of Chapter 1

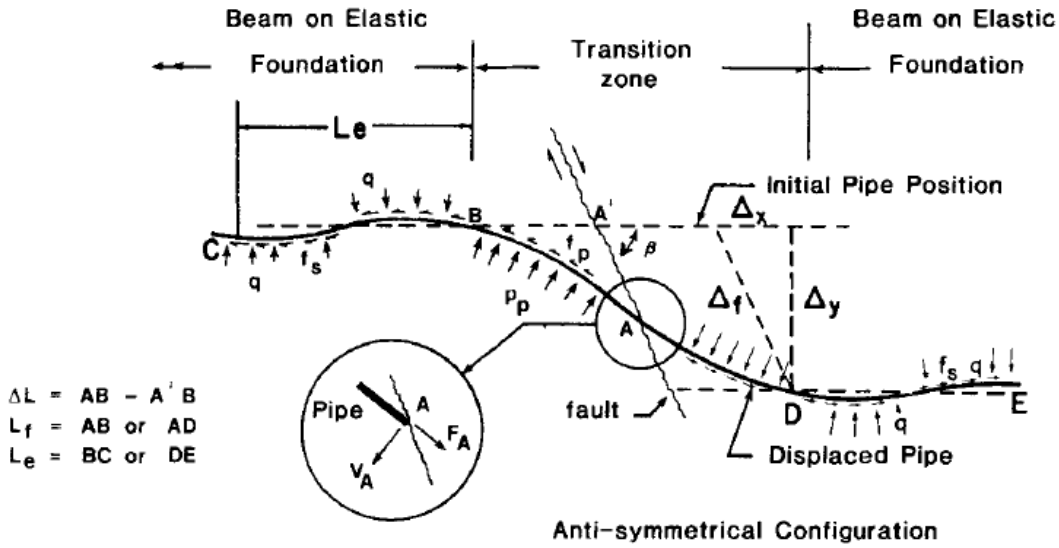

Fig. 1.1. The proposed analysis model for buried pipeline subjected to large strike-slip fault movement according to **Wang and Yeh [1985]**. The pipe near the fault intersection is modeled as a constant curvature curved segment and the remaining small deflection pipe as a semi-infinite beam on elastic foundation. [adapted from **Wang and Yeh** 1985]

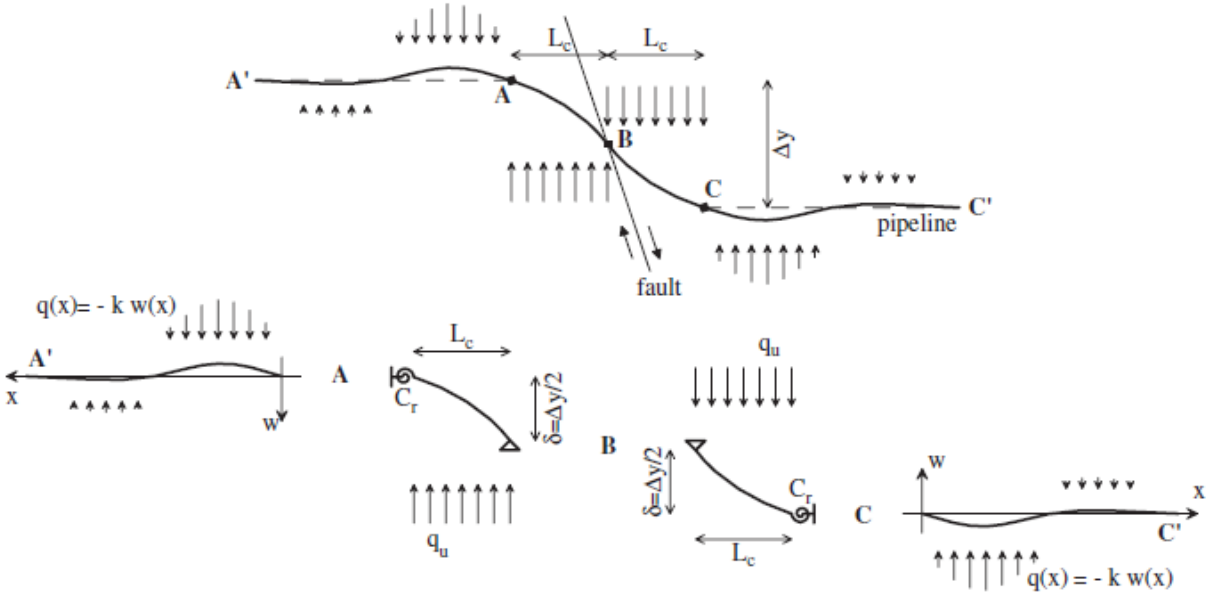

Fig. 3. Partitioning of the pipeline into four segments.

Fig. 1.2. Partitioning of the pipeline into four segments according to the proposed analytical method by Karamitros et al. [2007]. Two pipeline segments in the high curvature zone on both sides of the fault trace were analyzed using elastic-beam theory, while the segments outside the high curvature zone were treated as beams-on-elastic-foundation. [adapted from Karamitros et al. 2007]

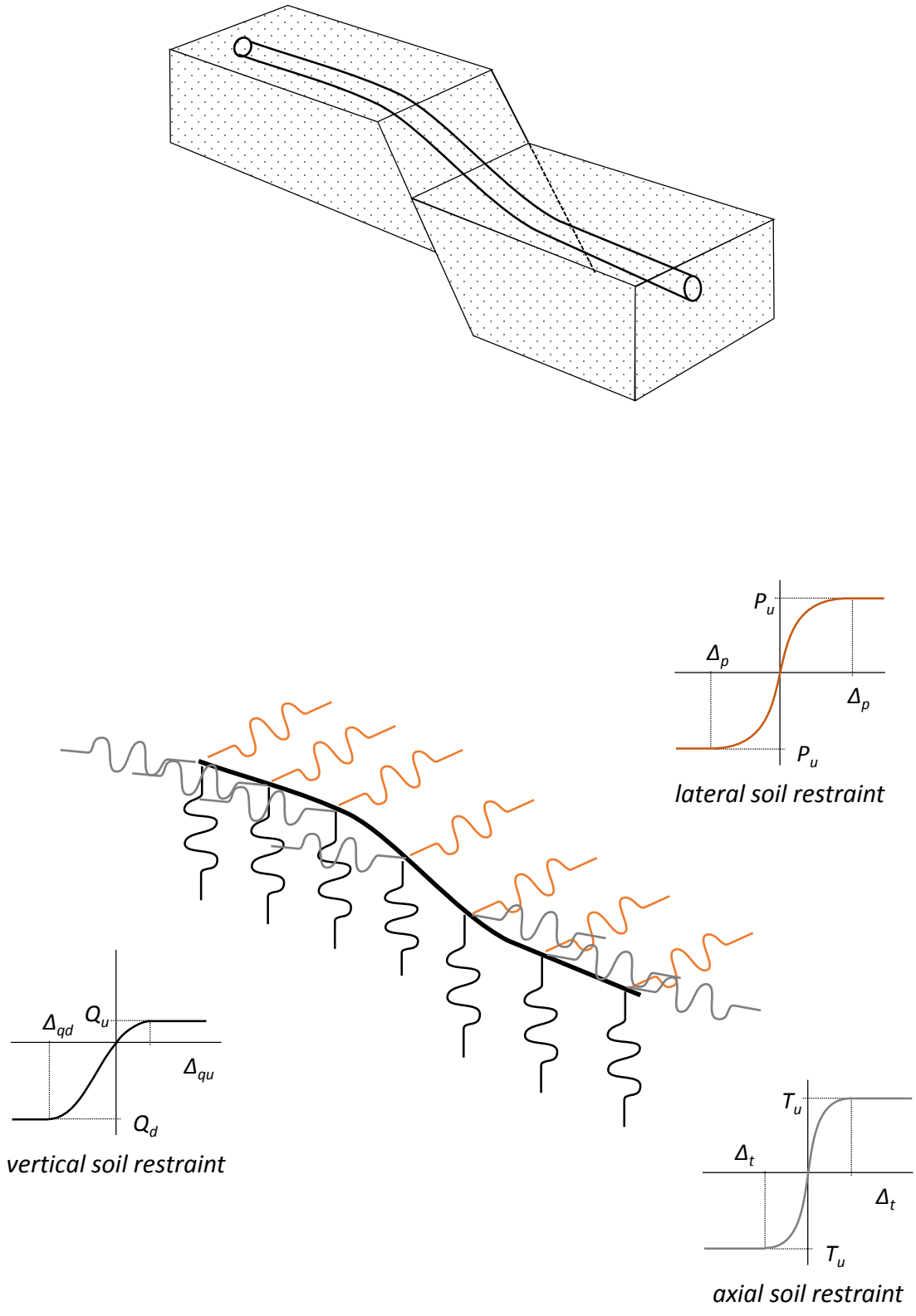

Fig. 1.3. Winkler-type numerical models: the soil is modeled with independent translational springs in the three orthogonal directions, while the fault offset is modeled with the dislocation of the support of the appropriate springs.

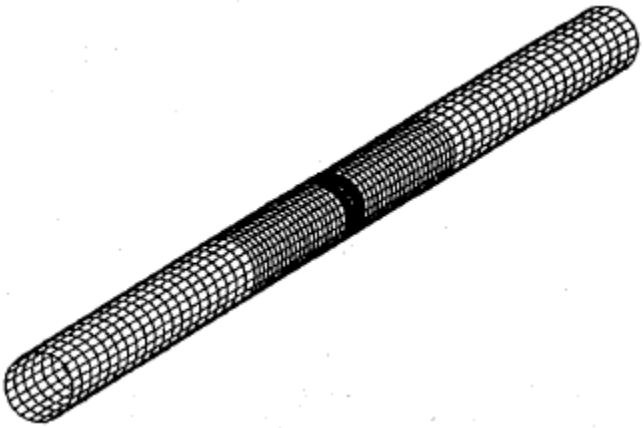

(a)

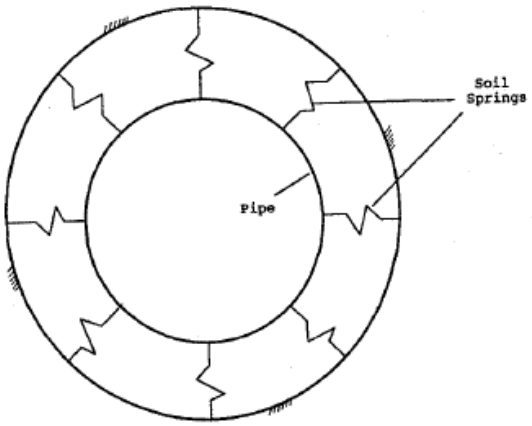

(b)

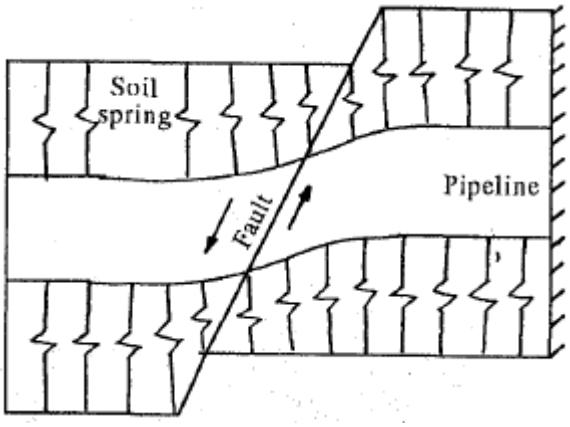

(c)

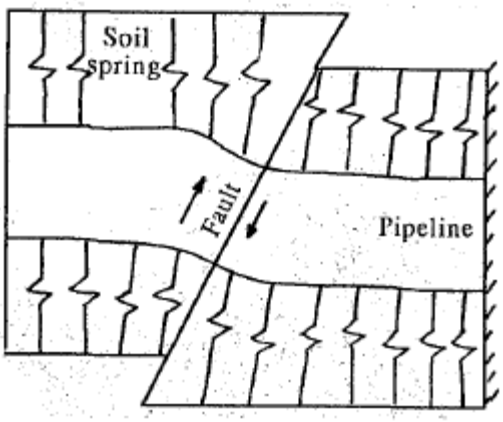

(d)

Fig. 1.4. The shell Winkler-type model by Takada et al. [1998]. (a) The pipe is modeled with shell elements. (b) Cross-section of the numerical model. (c) Simulation of pipeline intersection with a normal fault and (d) with a reverse fault. [adapted from Takada et al. 1998]

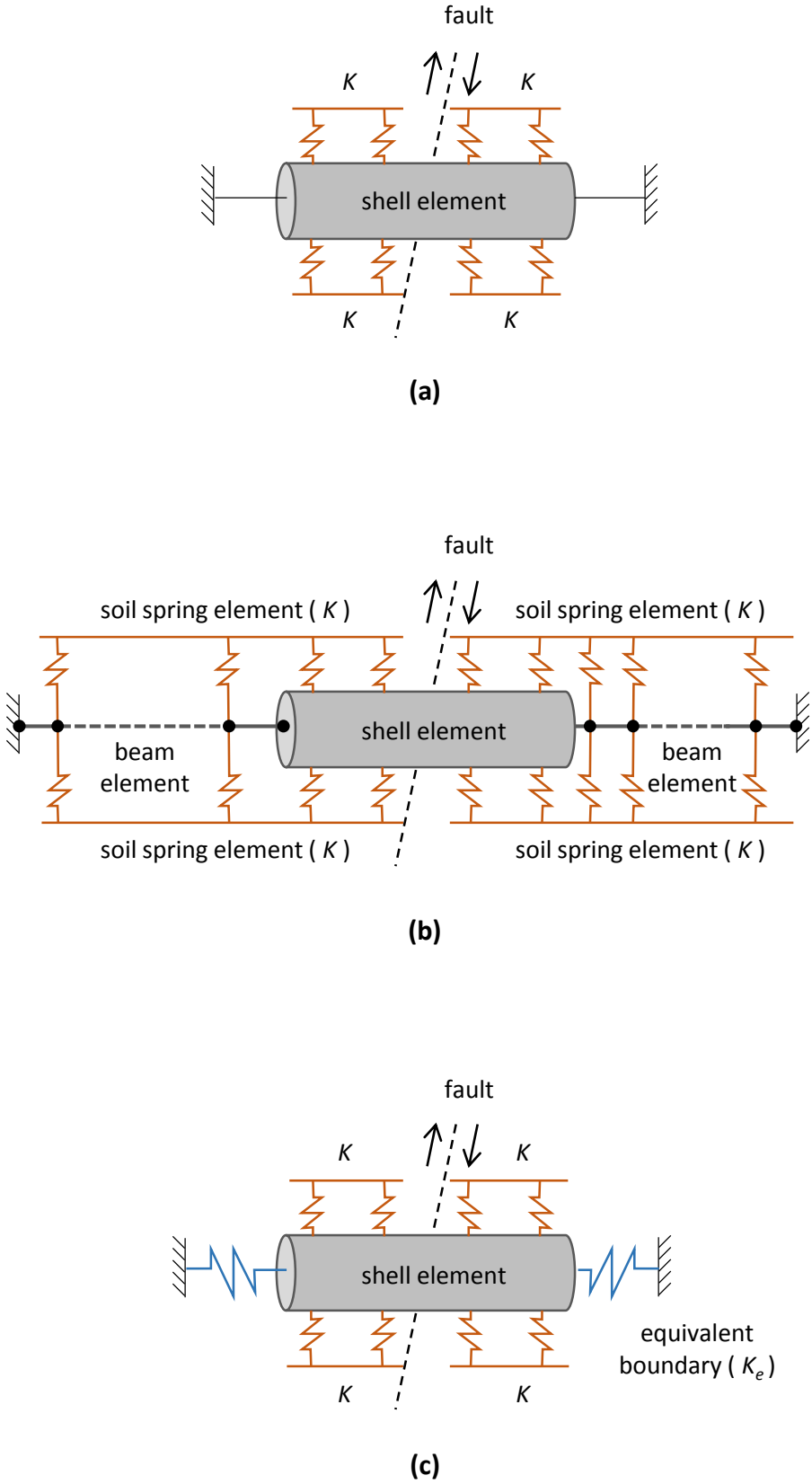

Fig. 1.5. Shell Winkler-type models for a fault-crossing pipeline: (a) Shell Winkler-type model with fixed boundaries after Takada et al. [1998]. (b) Shell-beam hybrid Winkler-type model after Takada et al. [2001]. (c) Shell Winkler-type model with equivalent boundaries after Liu et al. [2004].

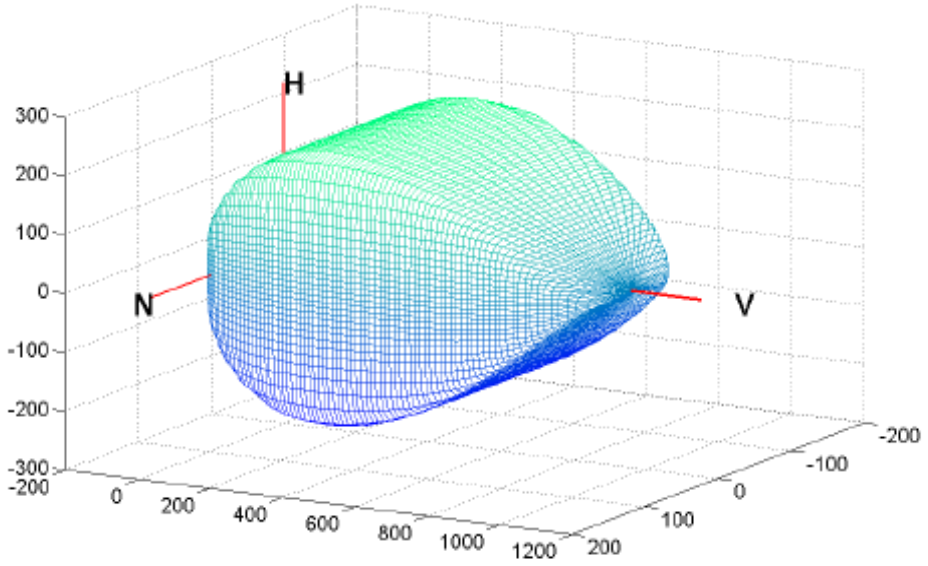

Fig. 1.6. The interaction domain for the coupled elastoplastic springs adopted by Cocchetti at al. [2008].[adapted from Cocchetti et al. 2008]

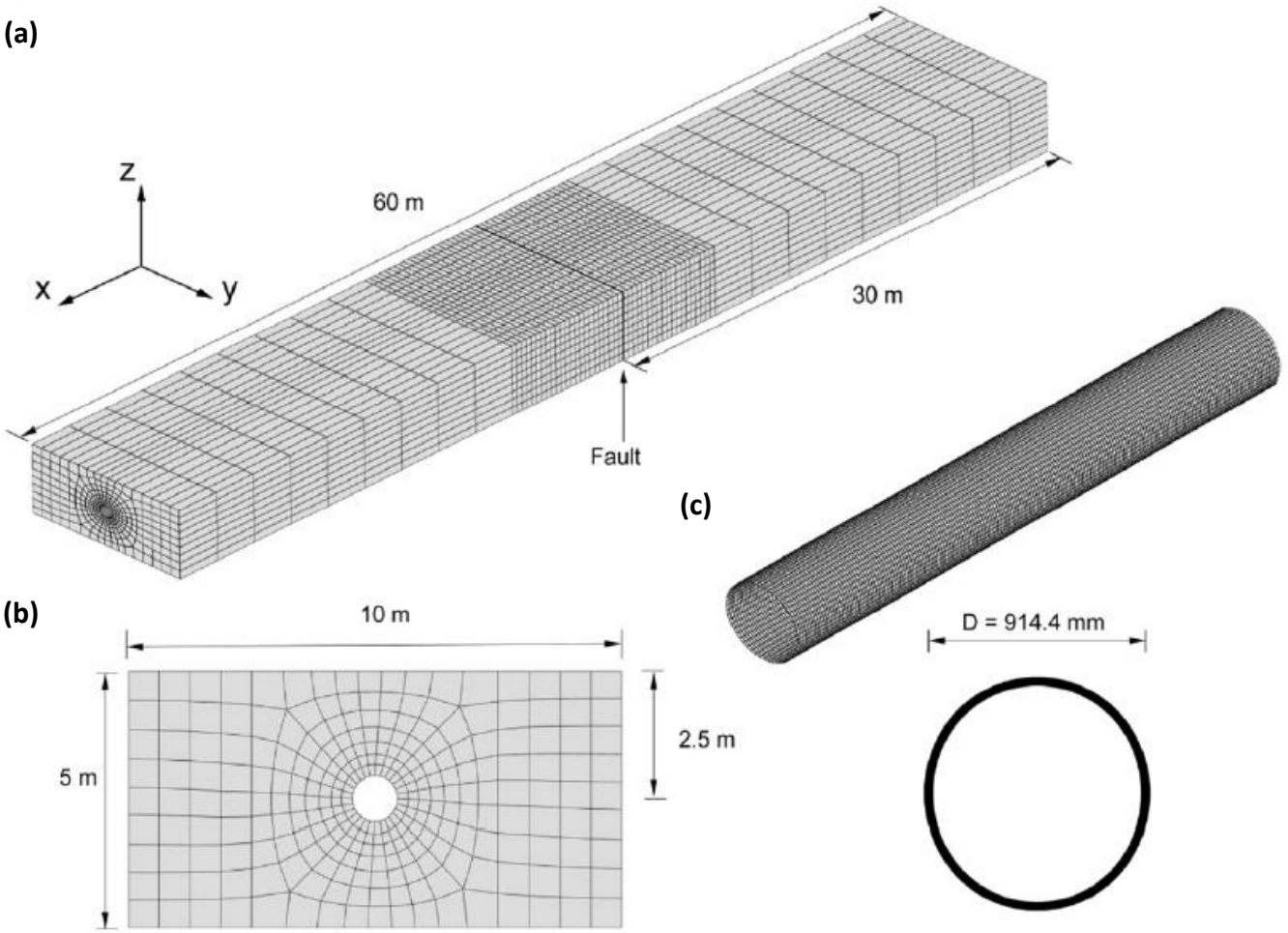

Fig. 1.7. Three-dimensional continuum modeling of the pipeline-strike slip fault interaction problem after Vazouras et al. [2010]: (a) A segment of the pipeline of total length of 60 m at the vicinity of the fault is modeled. (b) Cross-section of the model and (c) the pipeline mesh. [adapted from Vazouras et al. 2010]

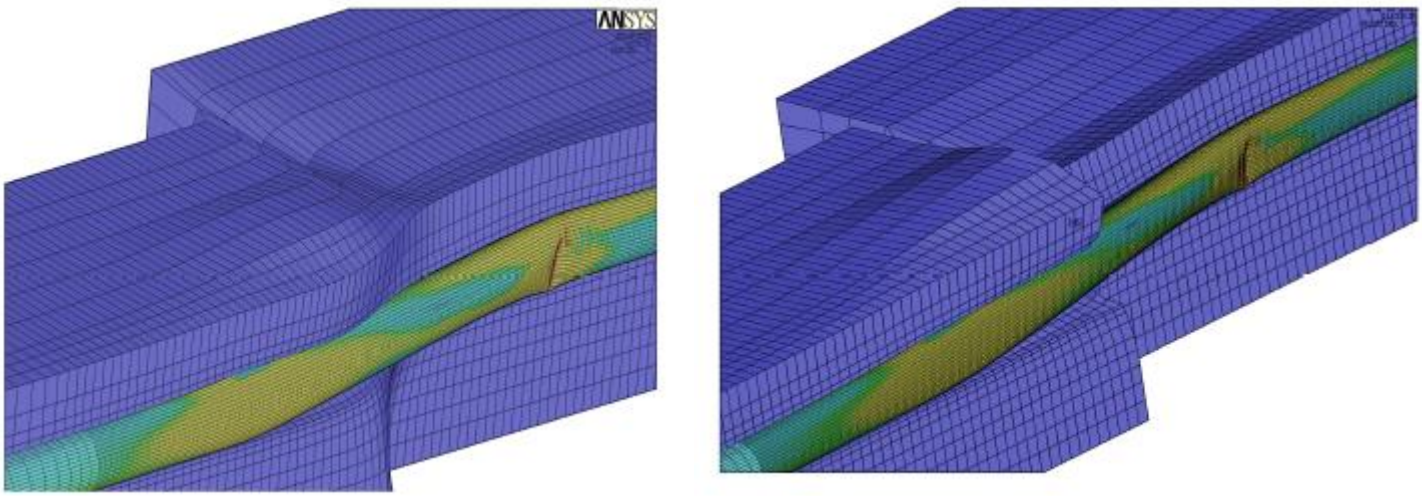

Fig. 1.8. Numerical analysis of a buried steel pipeline crossing an active fault with emphasis on the representation of the fault according to Trifonov et al [2014]: (a) continuous representation of the fault and (b) simulation of the fault with two separate blocks. [adapted from Trifonov et al. 2014]

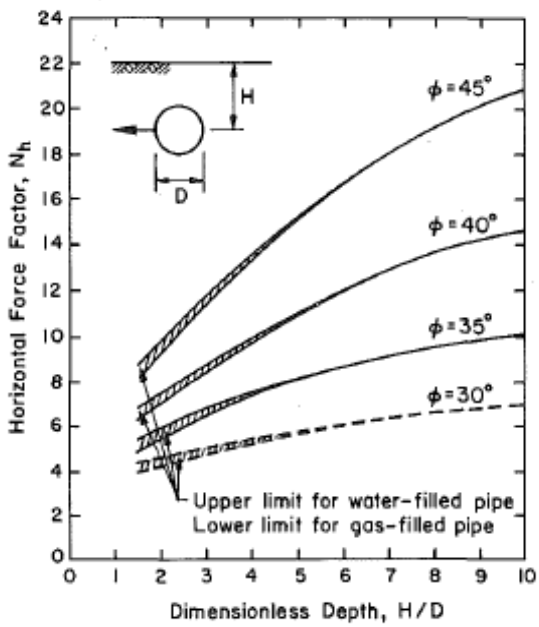

Fig. 1.9. Plot of the maximum dimensionless horizontal reaction force N_h versus H/D for pipeline design after the experimental work of Trautmann and O'Rourke [1985]. [adapted from Trautmann and O'Rourke 1985]

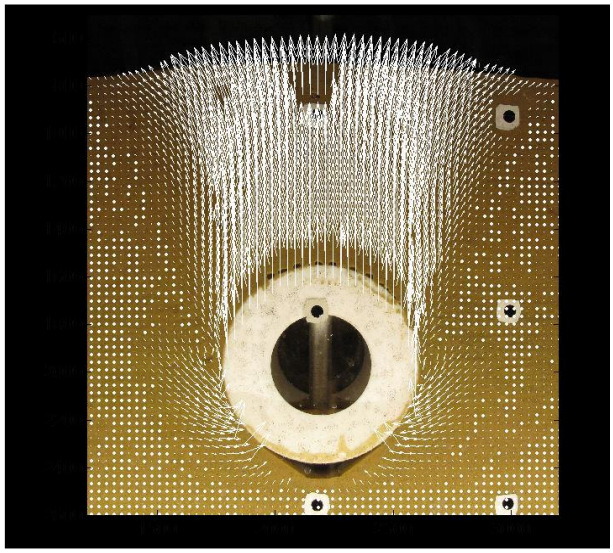

Fig. 1.10. Displacement vectors derived from one of the eight full-scale vertical pullout tests conducted by Wang et al. [2015]. [adapted from Wang et al. 2015]

Fig. 1.11. (a) Plan view and (b) elevation view of the test box used by Daiyan et al. [2011] to investigate the soil restrain to oblique axial-lateral pipe displacements. [adapted from Daiyan et al. 2011]

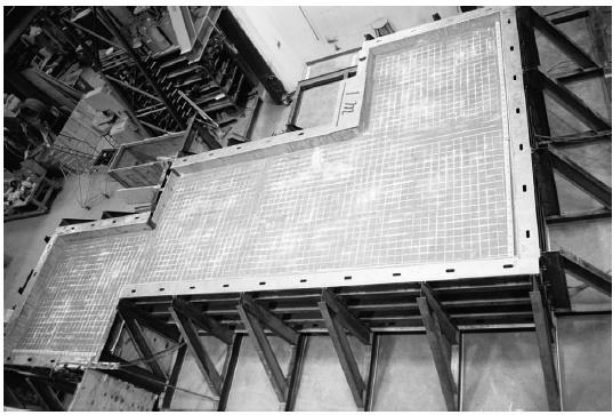

(a)

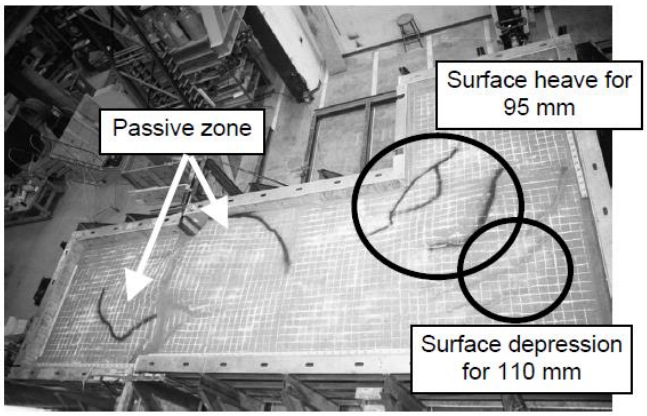

(b)

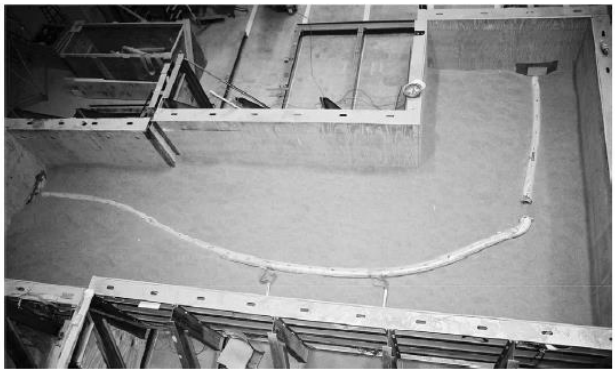

(c)

Fig. 1.12. Pictures from the experimental work of Yoshizaki et al. [2003]: (a) the soil compartment used to simulate the lateral soil displacement before the experiment and (b) after the experiment. (c) View of the deformed pipe after the experiment. [adapted from Yoshizaki et al. 2003]

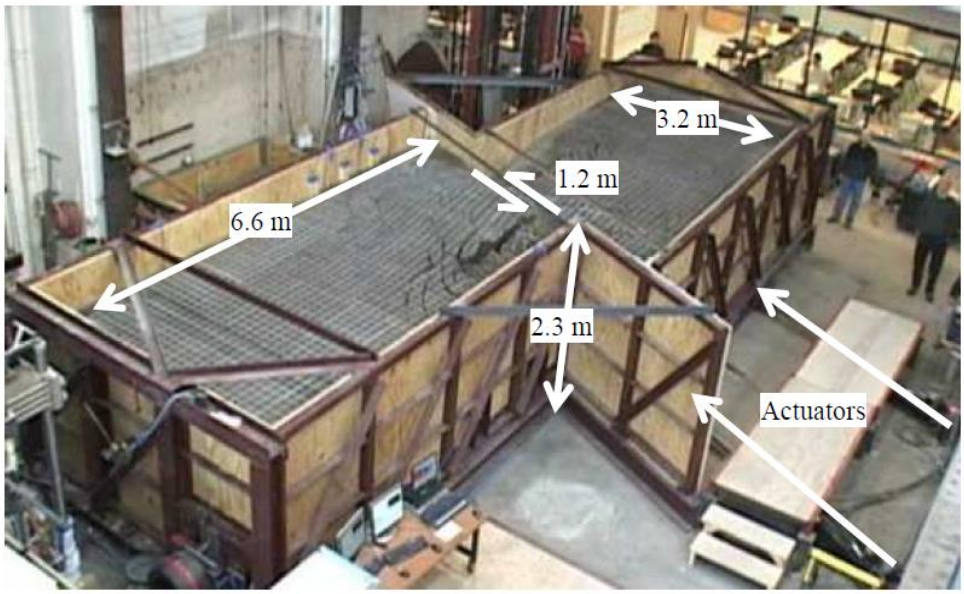

Fig. 1.13. Picture of the large-scale lateral soil displacement tests conducted at the Cornell University by O'Rourke et al. [2008]. [adapted from O'Rourke et al. 2008]

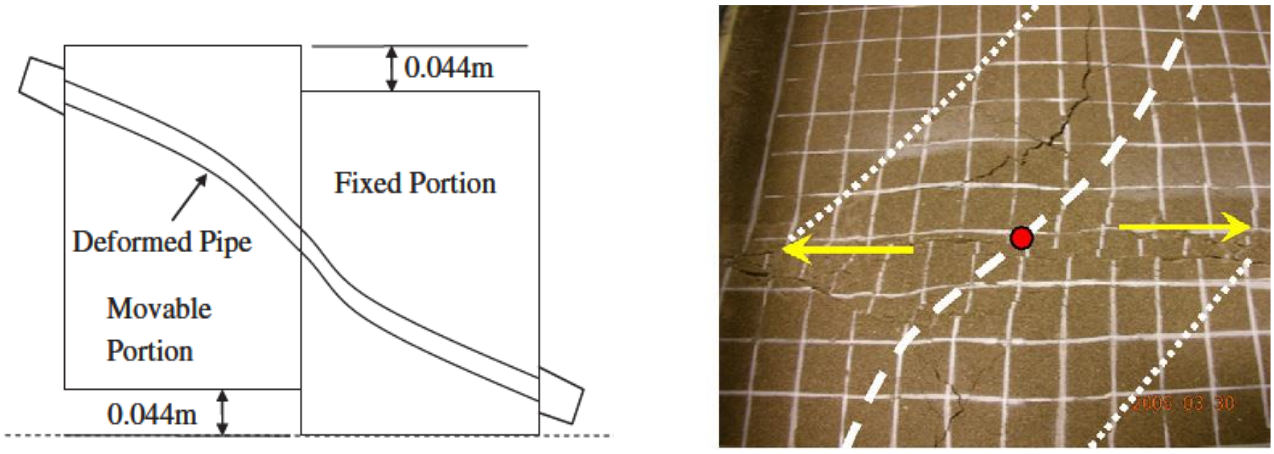

Fig. 1.14. Centrifuge experiments of buried HDPE pipelines subjected to strike-slip fault conducted by Abdoun et al. [2009]. (a) Plan view of the centrifuge model after offset. (b) Representative picture of a post-test surface condition. [adapted from Abdoun et al. 2009]

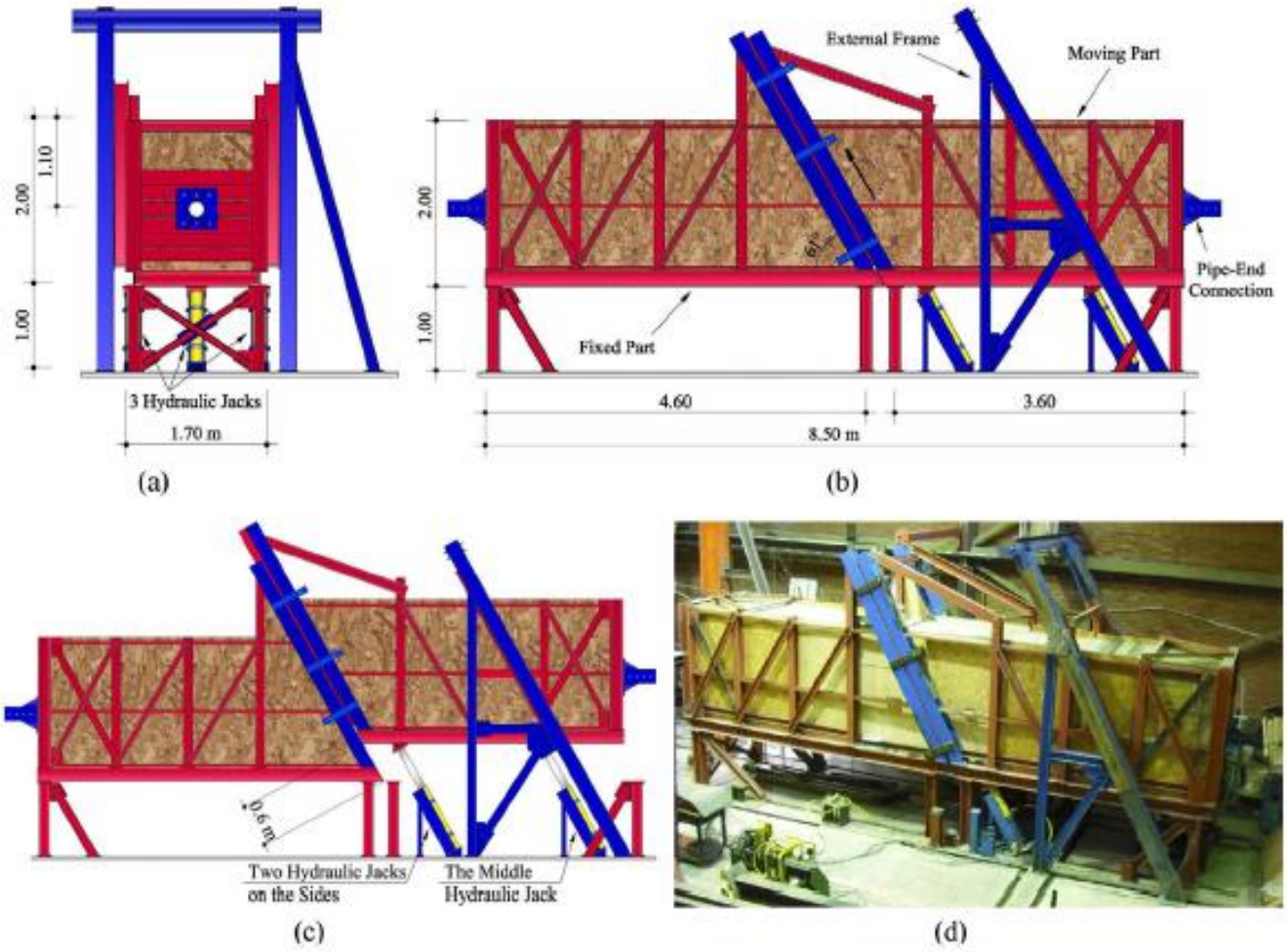

Fig. 1.15. Experimental study of the reverse faulting effects on buried pipelines conducted by Jalali et al. [2016]. Sketch of the split-box test basin used in the experiments (a) front view, (b) side view before and (c) after the fault offset. (d) Picture of the split-box during the experiment. [adapted from Jalali et al. 2016]

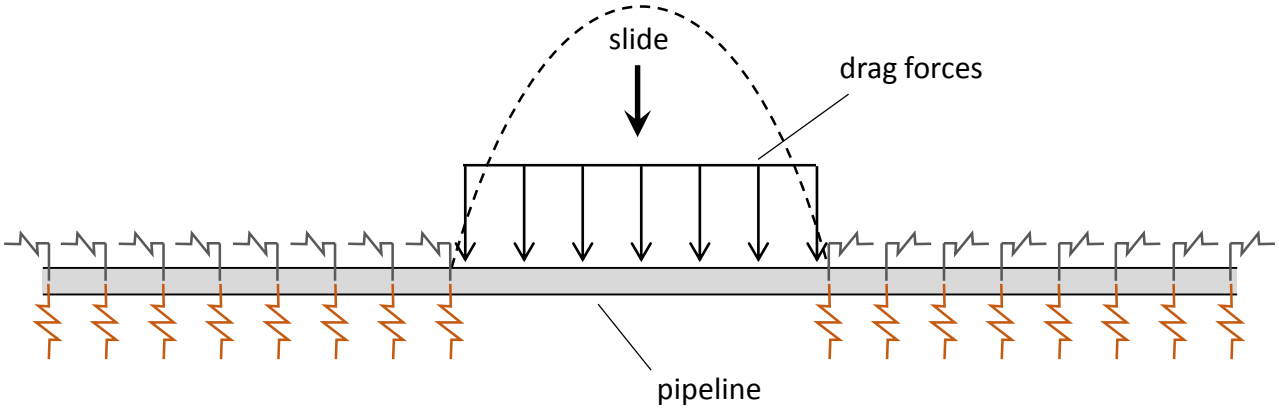

Fig. 1.16. A representative simplified structural model used in the past for the design of buried pipelines against landslide-induced actions based on the estimation of the drag forces induced by the landslide. [after Georgiadis et al. 1991]

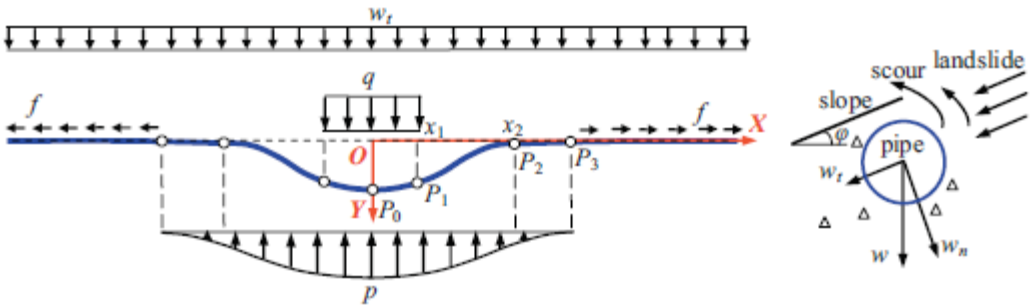

(a)

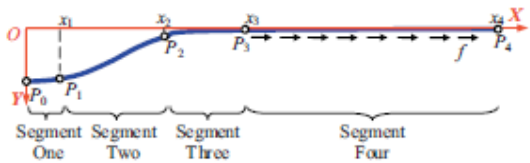

(a)

Fig. 1.17. (a) Sketch of the analytical model used by Yuan et al. [2012a,b] to describe the response of surface pipeline in deepwater under the impact of a landslide. (b) The pipeline is divided into four segments according to different loading conditions. [after Yuan et al. 2012]

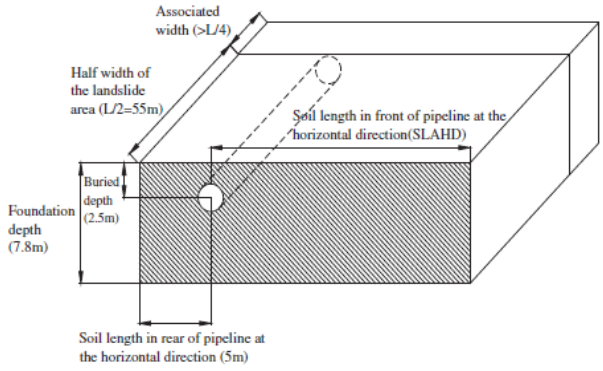

(a)

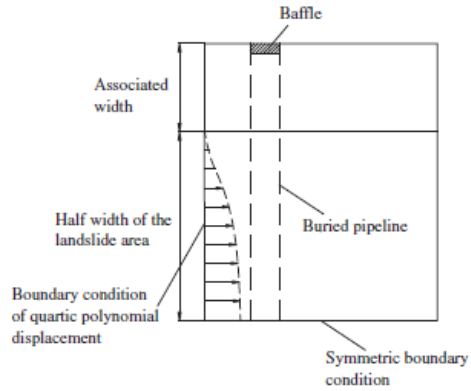

(b)

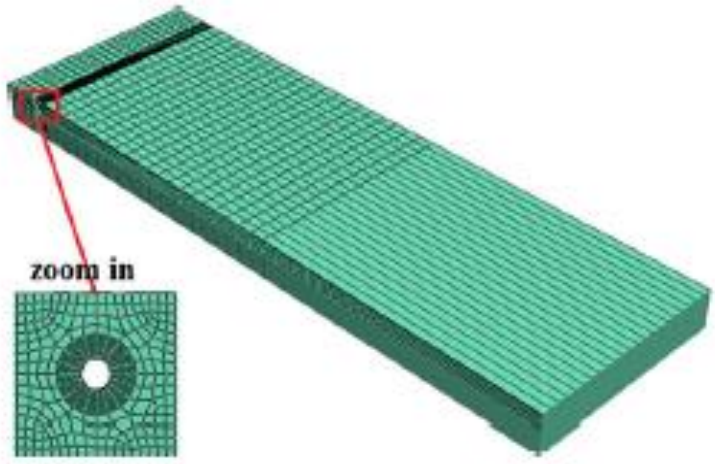

(c)

Fig. 1.18. Finite element analysis of a pipeline subjected to landslide-induced actions by Zheng et al. [2012]. Sketch of the finite element model showing the geometric features: (a) 3D view and (b) plan view. (c) The numerical model used in the analysis. [adapted from Zheng et al. 2012]

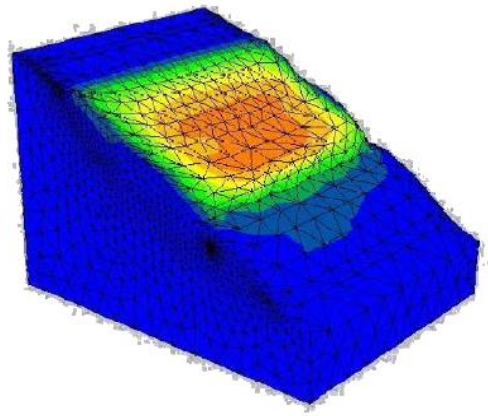

Fig. 1.19. Deformed mesh of the numerical model used for the simulation of a gas pipeline response subjected to the Baishiping landslide, China by Wu et al. [2014]. [after Wu et al. 2014]

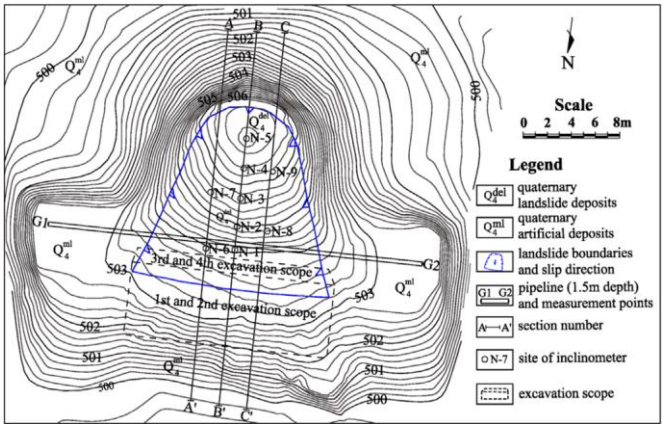

(a)

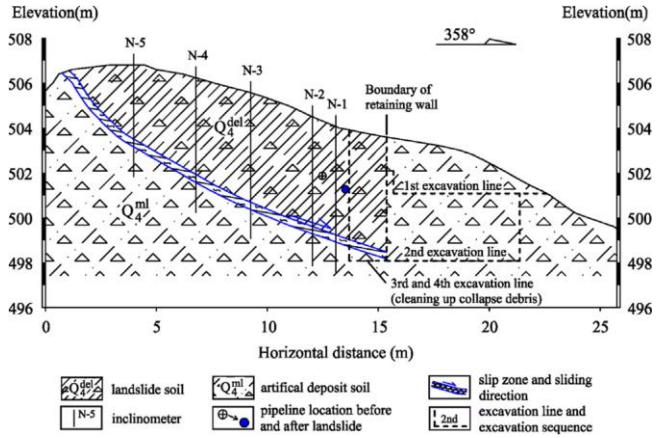

(b)

(c)

Fig. 1.20. Large-scale field test of a buried pipeline subjected to landslide-induced actions conducted by Feng et al. [2015] . (a) plan view of the landslide and pipeline model. (b) Geological cross section of the landslide model. (c) Picture of the landslide and pipeline model after the experiment. [adapted from Feng et al. 2015]

Chapter 2

Numerical Simulation of a buried Pipeline subjected to dip-slip faulting

2.1. Problem statement

Buried pipelines often cross tectonically active areas and may cross active faults capable of producing large earthquakes and large ground deformations. There are various examples of earthquakes that have caused severe damage to buried pipelines, such as the earthquakes of San Fernando 1971, Managua 1972, Haicheng 1975, Tang-shan 1976, Miyagiken-Oki 1978, Northridge 1994, Kobe 1995, Chi-Chi 1999, Kocaeli 1999 and more recently Chile 2010, Christchurch 2010-2011, and Japan 2011. Based on the observed damage mechanisms of buried pipelines, seismic effects can be caused either by transient strain and curvature due to traveling wave effects (Liang and Sun 2000), or permanent ground deformation due to seismic faulting, landsliding, or liquefaction-induced lateral spreading [e.g. O'Rourke and Palmer (1996), Uzarski end Arnold (2001)]. Among them, faulting-induced ground deformation can have the most severe effects on buried pipelines. In fact, there are only a few cases of pipeline damage purely due to wave propagation [Mexico City 1985, Michoacan earthquake, Pineda and Ordaz (2004)]. In contrast to shaking – related effects which are dynamic and transient, faulting generates permanent quasi-static deformations that may provoke significant damage.

An active fault can be seen as a discontinuity of the earth crust, along which relative displacement takes place. Three main fault types can be distinguished depending on the movement of the dislocating block. Strike-slip faults primarily exhibit horizontal movement, parallel to the strike of the fault (**Fig. 2.1a**). Strike-slip faults can be further categorized as "right-lateral" (dextral) or "left-lateral" (sinistral) depending on the direction of movement of the moving block. Dip slip faults are characterized by vertical displacement along the dip of the fault, and are further categorized to normal (**Fig. 2.1b**) and reverse (**Fig. 2.1c**), depending on the direction of movement of the hanging-wall. Normal faults are typically associated with a downward movement of the hanging wall (i.e., the moving block) relative to the footwall (i.e., the stationary block), mainly due to extension of the crust of the earth. Reverse faults are exactly the opposite: the hanging wall moves upwards relative to the footwall due to compression. When the horizontal component is dominant (i.e., when the fault dip is relatively low) the term thrust fault is usually applied.

Finally, when a fault combines a dip-slip and a strike-slip component, it is described as an oblique-slip fault (**Fig. 2.1d**). While most faults combine dip and strike slip, defining a fault as oblique requires both components to be measurable and significant.

This study focuses on the response of a buried continuous steel pipeline subjected to dip-slip faulting (normal and reverse fault). The primary goal is to develop a numerical analysis methodology that may accurately describe the non-linear soil behavior, the structural pipeline response and the soil-pipeline interaction.

2.2. Numerical methodology

2.2.1. Description of the numerical model

Pipelines are typically very elongated structures that may run for thousands of miles. Although an active fault will induce displacements that are concentrated on the fault trace (near-field region), the fault-induced effects may extend to a very large distance away from the fault (far-field). Hence, to realistically simulate the response of an infinitely long continuous buried pipeline subjected to faulting a quite extensive pipeline length should be accounted for. On the other hand, pipeline modeling simulation an extremely fine discretization of the pipe section to capture strain-sensitive phenomena (such as local buckling initiation or cross-section distortion). In order to meet the aforementioned requirements we would end up with a massive and computationally demanding numerical model.

To overcome this obstacle a hybrid procedure is adopted that employs different numerical strategies in the near and far-field. Namely, in the near-field, where the maximum stresses and strains are expected), the problem is modeled in 3 dimensions in order to rigorously capture all the complex phenomena related with soil-pipe interaction. **Fig. 2.2** presents the elements of this near-field. A soil prism around the pipe is considered modeled with 8-node continuum elements. The pipe is modeled with shell elements, with a total of 48 elements around the circumference and a maximum length of d_{FE} = 0.025 m. The contact between the pipe and the soil is simulated with interface elements that allows separation of the pipe and the surrounding soil, and accounts for interface friction through friction coefficient μ.

At the far-field, the simulation reduces to “beam-on-spring” model as portrayed in **Fig. 2.3**). Here, the pipe is simulated with beam elements (namely pipe elements that have one additional variable relating to hoop

strain). The soil response is idealized by discrete non-linear soil springs acting on all three directions. Uniaxial push tests are performed to derive the non-linear law of the discrete soil springs. In particular, the subgrade reactions are calculated through a downwards push, the reaction to upward movement through an uplift test, while the lateral and longitudinal reaction through transversal push test and a pullout test respectively.

2.2.2. Soil constitutive model

A key aspect of the numerical methodology is the rigorous simulation of the soil behavior. In cases where the soil failure is accompanied by a localization of shearing in discrete surfaces, it is necessary to realistically account for the shearing behavior of the soil in a more accurate manner. A soil specimen resists to shearing through the interlocking of its particles, and because of this interlocking it may display increase (dilative behavior) or decrease (contractive behavior) of its volume. Soils with large void ratios at large confinement stresses exhibit contractive behavior, since during shearing the void ratio decreases. On the other hand, in case of small void ratios or small confinement stresses soil particles tend to spread apart from each while sheared and the soil volume increases (**Fig. 2.4**).

Moreover, when dilative soil specimens are subjected to large deformations tend to exhibit a pronounced post-peak softening behavior. In fact, several experimental and numerical studies have shown that this post-peak soil behavior may be a decisive factor on fault rupture propagation and on its possible emergence on the ground surface (Cole and Lade 1984; Lade et al. 1984). Scott and Schoustra (1974) utilizing the FE method and an elastic–perfectly plastic constitutive soil model with Mohr–Coulomb failure criterion, produced results contradicting both reality and experiments. Walters and Thomas (1982) employed a more elaborate nonlinear incremental constitutive model with Drucker–Prager failure criterion, non-associated flow rule, and strain softening to simulate reverse fault rupture propagation through cohesionless soil. Comparing their analysis results with benchmark small-scale tests, they proved that (laboratory) reality could only be reproduced with a non-associated flow rule and strain softening. Bray (1990) and Bray et al. (1994a,b), utilizing a FE code with a hyperbolic nonlinear elastic constitutive law, also achieved satisfactory agreement with experiments (Bray et al. 1993). Also successful were the analyses performed by Roth et al. (1982), White et al. (1994), Nakai et al. (1995), Loukidis (1999), and Erickson et al. (2001), all of which made use of the finite-difference (FD) method with an elastoplastic constitutive model, Mohr–Coulomb failure criterion, and strain softening.

To account for all the aforementioned shearing mechanisms, an elastoplastic Mohr–Coulomb constitutive model with isotropic strain softening is utilized [Anastasopoulos et al., (2007)].

Strain softening is introduced by reducing the mobilized friction angle ψ_{mob} and the mobilized dilation angle φ_{mob} with the increase of octahedral plastic shear strain

$$\varphi_{mob} = \begin{cases} \varphi_p - \dfrac{\varphi_p - \varphi_{res}}{\gamma_f^p}\gamma_{oct}^p & \text{for } 0 \le \gamma_{\mathrm{oct}}^{\mathrm{p}} \le \gamma_{\mathrm{f}}^{\mathrm{p}} \\ \varphi_{res} & \text{for } \gamma_{\mathrm{oct}}^{\mathrm{p}} \ge \gamma_{\mathrm{f}}^{\mathrm{p}} \end{cases}$$

$$\psi_{mob} = \begin{cases} \psi_p \left(1 - \dfrac{\gamma_{oct}^p}{\gamma_f^p}\right) & \text{for } 0 \le \gamma_{\mathrm{oct}}^{\mathrm{p}} \le \gamma_{\mathrm{f}}^{\mathrm{p}} \\ \psi_{res} & \text{for } \gamma_{\mathrm{oct}}^{\mathrm{p}} \ge \gamma_{\mathrm{f}}^{\mathrm{p}} \end{cases}$$

where φ_{mob} and φ_{res} = ultimate mobilized friction angle and its residual (or critical state) value; ψ_p = ultimate dilation angle; and γ_f^p = plastic octahedral shear strain at which softening has been completed.

The constitutive model parameters are calibrated through direct shear test results; not only the shearing of a specimen during a direct shear test is quite similar to the shearing of a soil element during most permanent ground deformation cases, but it is also a very simple and easily done test.

The model is incorporated in the finite-element code ABAQUS through a user subroutine. Constitutive model parameters are calibrated through the results of direct shear tests. Soil response can be divided in four characteristic phases (Anastasopoulos et al. 2007):

(a) Quasi-elastic behavior: The soil deforms quasi-elastically (Jewell and Roth 1987), up to a horizontal displacement δx_y.

(b) Plastic behavior: The soil enters the plastic region and dilates, reaching peak conditions at horizontal displacement δx_p.

(c) Softening behavior: Right after the peak, a single horizontal shear band develops (Jewell and Roth 1987; Gerolymos et al. 2007).

(d) Residual behavior: Softening is completed at horizontal displacement δx_f ($\delta_y/\delta_x \approx 0$). Then, deformation is accumulated along the developed shear band.

Quasi-elastic behavior is modeled as linear elastic, with secant modulus GS linearly increasing with depth:

$$G_s = \frac{\tau_y}{\gamma_y}$$

where τ_y and γ_y = the shear stress and strain at first yield, directly measured from test data.

After peak conditions are reached, it is assumed that plastic shear deformation takes place within the shear band, while the rest of the specimen remains elastic (Shibuya et al. 1997). Scale effects have been shown to play a major role in shear localization problems (Stone and Muir Wood 1992; Muir Wood and Stone 1994; Muir Wood 2002). Given the unavoidable shortcomings of the FE method, an approximate simplified scaling method (Anastasopoulos et al. 2007) is employed.

The constitutive model capability to reproduce soil behavior has been extensively validated through: (a) qualitative comparisons with numerous published experimental data (Horsfield 1977; Cole and Lade, 1984) and earlier case histories (Slemmons, 1957; Brune and Allen, 1967; Taylor et al., 1985); (b) semi-quantitative comparisons with case histories from the 1999 earthquakes of Kocaeli and Turkey (Anastasopoulos & Gazetas, 2007a,b; Faccioli et al., 2008); and (c) through quantitative blind predictions of centrifuge model tests (Anastasopoulos et al., 2009).

2.2.3. Validation of the Numerical Methodology: uniaxial push-tests on buried pipes

A wealth of research documents may be found on the estimation of pipe-soil resistance to one-directional loading. As early as 1977, Audibert & Nyman systematically investigated the restraint provided by soil, against the horizontal displacement of steel pipes. Their findings were further complemented by the experimental work of Trautmann and O'Rourke [1985], Hsu [1993], Calvetti et al. [2004], Turner [2004], Hsu et al. [2006], Di Prisco et al. [2006], Karimian et al. [2006], Wijewickreme et al. [2014], covering a wide range of pipe diameters and overburden ratios in both dry and partially saturated sand specimens. Capalletto et al. [1998], Paulin et al. [1998], Honegger [1999], Anderson [2005] and Wijewickreme et al. [2009] performed a series of field tests on pipes in cohesive and granular material to measure their pull-out capacity (axial resistance) and compared the findings with the simplified formulas suggested by ASCE [1984], ALA [2001] and PRCI [2004]. In all experiments the same interesting trend was observed: in dense and dry materials the actual axial capacity of the pipeline was found to be significantly higher than the one calculated when based on guidelines, while in loose materials the results were somehow closer.

Since a very important issue in the design of pipelines is the potential upheaval buckling, much effort was also placed on exploring the upward soil restraint (i.e upward p-y springs). Drained conditions have been assumed in the works of Trautmann et al (1985), Bransby et al. (2001), Chin et al. (2006), Cheuk et al (2008), while saturated soils under drained and undrained conditions were studied by White et al. (2001), Palmer et al. (2003), Schupp et al. (2006), Bransby & Ireland (2009), Williams et al. (2013). Experimental data on the (downward) bearing capacity of buried pipelines may be found on the work of Nagaoka (2007).

Four excellent experimental series have been selected to benchmark the adopted numerical algorithm. In all tests, a pipe section buried within dry sand (of variable D_r%) is pushed towards one single direction until failure (defined as the full mobilization of bearing capacity mechanism).

Lateral Push-Tests

Trautmann & O'Rourke (1985) performed large-scale tank experiments investigating the pipeline behavior under lateral movement. The steel pipe had a diameter of D = 102 mm, while the soil filling consisted of Cornell Dry sand, at three different densities: 0, 45 and 80% corresponding to φ_p values of 31^o, 36^o 44^o respectively. The pipe embedment depth (H/D) was also varied parametrically taking values H/D = 3.5, 5.5 and 8.

Fig. 2.5 illustratively compares the experimental response with that predicted by the finite element model (a snapshot of which is displayed in **Fig. 2.5d**). The Numerical parameters employed in the FE analyses are listed in Table 1. It is clarified that the values of the assumed shear strain parameters (γ_y, γ_p, γ_{res}) have been directly derived by direct shear tests of the respective sand specimens. For the estimation of the dilation angle ψ, the Bolton (1986) expression is followed, according to which

$$\psi = (\varphi_p - \varphi_{res})/0.8 \tag{1}$$

Evidently, all three tests were replicated very satisfactorily. The numerical model captured efficiently all attributes of the force-displacement response for all cases examined: maximum soil resistance, gradual yielding of soil, and the softening behavior of the dense sand were successfully reproduced by the numerical simulation. Some discrepancies are detected in the loose sand experiments at relatively large displacements where the analysis slightly under-predicts the measured response. This may be attributed to the densification of sand in front of the pipe, a phenomenon that cannot be captured by the FE analysis.

Vertical Push Tests

Cheuk et al (2008) conducted a series of verftical pullout tests of pipe sections in two sand specimens: fine loose sand (*FL)* (D_r = 30%) and fine dense sand (*FD*) (D_r = 90%). The pipe model was of diameter *D* = 100 mm, length *L* = 75.5 mm, and in all four tests it was placed at embedment depth *H/D* = 3. **Fig. 2.6** presents the measured response along with the FE predictions. Unfortunately no direct shear test was available; as such the *γ* values of the previous test series were assumed (**Table 2.2**). The comparison is again satisfactory. The numerical methodology predicts correctly the maximum resisting force as well as the post-peak decay. Yet, the numerical model underestimates the quasi-elastic stiffness of the system. This could be attributed to three main factors or a combination thereof. First, the simulation of the pipe-soil contact using interface elements unavoidably introduces a certain degree of elasticity in the system that is absent in the natural problem. Second, the constitutive model assumes a linear elastic response with a secant elastic modulus corresponding to the yield point (a rather large deformation), which naturally underestimates the actual modulus. Finally, it is generally accepted that the experimental simulation of a soil-structure system at extremely small displacements may rarely be flawless as it encompasses unavoidable inaccuracies (for example a small inevitable slack in the machinery may conceal the real force-displacement behavior). Yet, the numerical methodology proves capable of predicting the maximum force, the displacement where this force occurs, as well as the degradation of the restraining force as the pipe tends to emerge to the surface.

Push-Down Tests

Nagaoka [2007] conducted centrifuge tests of pipeline segments pushed into the soil until bearing capacity was reached. The model pipe corresponds to a prototype pipe of diameter *D* = 0.4 m and length *L* = 18.8 m placed within dry Fontainebleau sand of relative density D_r = 60% at two embedment ratios, *H/D* = 3.5 and *H/D* = 7. The agreement between the experimental and the numerical results is quite satisfactory, both in terms of stiffness and maximum soil resistance (**Fig. 2.7**).

Pull-Out Tests

Wijewickreme et al. (2009) conducted a series of full-scale pullout tests of pipes placed within dry Fraser River sand of relative density D_r = 75% and 20%. All tests were performed on a sand-blasted steel pipe segment with an outside diameter *D* = 457 mm (18 in) and a 12.7 mm (0.5 in) wall thickness. The pipe was placed at normalized burial depth *H/D* = 2.5 for dense sand specimens and *H/D* = 2.7 in loose sand tests. Soil laboratory testing described in Karimian (2006) indicated a peak friction angle of approximately φ_p =

45^o and a constant volume friction angle of 33^o for the dense sand, while the peak friction angle for the loose sand was measured as φ_p = 39^o. The interface friction angle between the sand-blasted steel and the Fraser River sand was also measured, yielding an interface φ_p of 36^o and 33^o for the dense sand and loose sand respectively, which drops to 31^o at large strains for both materials. To account for this exact interface response in the numerical modeling, an exponential decay law was assumed describing the softening behavior of the interface strength. All numerical model parameters are listed in Table 3. A view of the pull-out curve for both sand sediments is displayed in **Fig. 2.8** which reveals an excellent comparison between the analytical and the experimental behavior. Degradation of the interface strength appears to be taking place at small displacement (of the order of 0.05 m); consequently, this is a behavior that should be accounted for in the analysis of pipelines subjected to permanent ground displacements, where the forces acting on the pipeline result in it being pulled (or pushed) axially.

2.2.4. Numerical Modelling of Pipeline: 4-point bending tests on pipe segments

The adopted methodology should accurately capture the structural response of a steel pipe. The scientific community has put substantial effort on the experimental investigation of the bending response of pipes with special interest in the development of critical strain limit criteria to prescribe failure [e.g Stephens et al. (1991), Dorey et al. (2000), Zimmerman et al. (2004), Schaumann et al. (2005), Van Es et al. (2014)]. A set of three experiments from the experimental series of Van Es et al. (2014) is selected herein as a benchmark for our numerical simulations. The testing program consisted of 15 full scale four point bending tests on spirally and longitudinally welded pipes. The steel tubes were of outer diameter approximately D = 1070 mm and of D/t ratio ranging from D/t = 65 to D/t = 118. The steel grade varied between grades X52, X60 and X70. **Fig. 2.9a** presents an overview of the test setup (adopted by van Es (2014)). The tests monitored the applied load, the pipeline displacement and the average curvature over the middle section. An overview of the setup of the three selected tests is presented in Table 4. The pipe is modeled with shell elements of reduced integration with 48 elements around the circumference of the pipe of longitudinal dimension d_{FE} = 25 mm. To avoid any divergence from the actual configuration, the exact support set-up was mimicked in every detail: the pipe is restrained by two straps that are connected to a beam which is free to rotate.

The results of our numerical simulation are presented in **Fig. 2.9b** and **Fig. 2.9c**. Evidently the numerical model replicates correctly (for all three tubes geometries) the experimentally measured bending response of the pipeline all the way from the elastic region up to failure.

2.3. Numerical simulation of buried pipelines subjected to dip-slip faulting

The scope of this section is to recognize the basic mechanisms of a pipeline subjected to normal and reverse faulting. As an illustrative example, let us consider an infinitely long pipeline of outer diameter D = 40" (=1.016 m) and thickness t = 0.562" (=14.3 mm) covered by a soil layer of depth H_{cover} = 1.2 m (**Fig. 2.10**). The pipeline is embedded within dry sand material of small relative density and of low strength (φ = 30^o and ψ = 0^o) –typical backfill conditions for pipeline trenches. It is crossed either by a normal or by a reverse fault. In both cases the intersection angle between the pipe axis and the fault strike is 90^o. The normal fault has a dip angle of 60^o, while the reverse fault has a dip angle of 30^o. A first set of analyses is performed assuming zero internal pressure (p = 0)

2.3.1. Failure modes

Buried pipelines have proved to be vulnerable to permanent ground-induced actions, and under strong fault-induced displacements a buried steel pipeline is expected to develop severe deformation beyond the elastic limit. To quantify the pipeline performance using "allowable stress" criteria would not be appropriate. Rather, in such an adverse loading it is reasonable to only require from the pipeline to be able to fulfill its main design requirement: safety against loss of containment. Therefore, the pipe performance should be addressed in terms of limit ("failure") states based on strain associated with a failure that potentially leads to loss of containment. Failure states may be described in terms of: (a) tensile strain that may cause the pipe wall to rupture, whether it originates from stretching or bending (**Fig. 2.11a**), (b) local buckling of the pipe wall due to excessive compression or bending (**Fig. 2.11b**) or (c) excessive distortion of the cross-section due to bending, termed ovalization (**Fig. 2.11c**). To ensure safety against these types of failure the following criteria are recognized:

(a) The maximum tensile strain should be lower than a limit value. This limit value varies among the current codes. According to the EN 1998–4 Eurocode provisions for seismic-fault-induced actions on buried steel pipeline and by the seismic provisions of ASCE MOP 119 for buried water steel pipelines, the maximum tensile strain should be limited to 3%. The ASME B31.8 for the design of gas transmission and distribution piping systems permits a maximum strain of 2% regarding a design for stress greater than yield. The EN 1993-4 for the design of steel pipelines also introduces the concept of limiting tensile strain, a limit strain which is not a material property but a limitation dependent on the deformation capacity of the pipe wall with its welds; the value 0.5% is recommended. In the following analyses all these criteria are considered.

(b) Local buckling should be avoided. The buckled area is associated with significant strain concentration which, in case of repeated loading, may lead to development of fatigue cracks which will impose a serious threat to structural integrity of the pipeline (Dama et al (2007), Das et al (2008)). Hence, compressive deformation should be limited to buckling initiation. In our case, the buckling initiation is defined straight from the outcome.

(c) Excessive ovalization of the pipe section should be avoided. Following the Dutch specification NEN 3650, the decrease of the pipe diameter should always be maintained below 15%.

2.3.2. Normal faulting: key mechanisms of deformation

Fig. 2.12 presents the deformation of the pipeline in the vicinity of the fault. **Fig. 2.12a** shows the deformed pipeline with superimposed stress contours for fault displacement δ_{fault} = 2 m (scale factor = 3). The pipeline bends in response to the differential vertical displacement of its two ends, acquiring a characteristic double-curvature deformation. Signs of intensive distress are visible (red color) in the immediate vicinity of the fault trace: on the top side of the pipe segment within the footwall and at the bottom side of the pipe segment within the hanging wall. **Fig. 2.12b** plots the axial strain distribution along the top and the bottom centerline. Clearly, the entire pipeline is under tension (since the pipeline is stretched under the imposed fault elongation). Yet, near the fault trace, this stretching is combined with a quite significant bending action that for this particular configuration affects a length of l_b = 70 m ($l_{b,m}$ = 45 m within the footwall and $l_{b,s}$ = 25 m within the hanging wall). Under this combined action, tensile straining is maximized at the top side of the pipe Beyond this length, the pipe appears to be stressed exclusively due to stretching (the axial strains at the top and at the bottom of the section are equal).

Based on this observation three regions of distinctively different behavior can be recognized and are graphically depicted in **Fig. 2.13a**. A central region at the vicinity of the fault trace where the pipe is stressed due to bending and stretching (**region I**). Consider a section at the pipeline-fault intersection point (point O) and for reasons of simplicity instead of the soil, the pipeline dislocates with respect to the final position of the soil (after all the cause of distress is the relative movement between the pipeline and the soil) as indicated in **Fig. 2.13b**. The pipe segment within the hanging wall is subjected to an upward vertical dislocation $\delta_{z,1}$, an elongation $\delta_{x,1}$ and a rotation ϑ (due to the continuity of the pipeline). The shear force and bending moment caused by $\delta_{z,1}$ and ϑ are counterbalanced by the development of the soil reactions $p_{z,1}$. Eventually, there comes a point where the shear force and bending moment are practically 0 (point A). Likewise, the shear force and bending moment developed in the pipe segment within the footwall due to the vertical deflection $\delta_{z,2}$ and the rotation ϑ is balanced by the subgrade reactions and are effectively cancelled out at the point B. Since the subgrade reactions are much larger than the reaction to upward movement, a small length is sufficient for the accommodation of the shear force and bending moment within the stationary block. As a result, the curvature of the segment there is larger, and in return the axial strains are larger. This justifies the location of the critical section, which in the case of normal faults will invariably be located in the stationary block and close to the fault trace.

While the effect of bending is limited within the segment AB, the axial dislocation of the pipeline affects a much larger area (noted as *region II* and *region III* in the two blocks of the fault, generating shear tractions along the pipe-soil interface. Since the amplitude of these stresses is quite low, being controlled by the typically small burial depth and the friction coefficient of the pipe-soil interface (which is of the order of 0.5), quite a large length is required to balance the imposed axial dislocation.

The pipeline response within region I is summarized in **Fig. 2.14**. **Fig. 2.14a** presents the deformed pipe with axial strain contours, for various magnitudes of fault offset δ_{fault}. Naturally, the axial straining along the pipe increases with increased fault displacement. Ultimately, the entire section is yielding. At that point a neck forms and the pipeline enters an unstable state in which any additional strain is localized in this weakened zone.

Fig. 2.14b presents the evolution of maximum tensile strain along the pipe versus the imposed fault offset δ_{fault}. If the $\varepsilon_{x,max}$ = 0.5% failure criterion of "limit plastic strain" is assumed, the pipeline would accommodate a $\delta_{fault} \approx 1.5$ m. Relaxing the criterion to $\varepsilon_{x,max}$ = 2%, the pipeline margins drastically increase to $\delta_{fault} \approx 3.65$ m, while the adoption of the $\varepsilon_{x,max}$ = 3% criterion makes no difference ($\delta_{fault} \approx 3.7$ m), since the two latter criteria correspond both to strains associated with the formation of the neck.

Fig. 2.15 summarizes the response of the pipeline segment under pure tension (region III in particular). As already explained, the axial component of the fault dislocation affects a much larger length than the transversal one. This length is depicted in **Fig. 2.15a** where the axial strain distribution along the pipeline is presented. The mobilized pipeline length increases linearly with the imposed fault displacement up to the point of the neck formation. Observe the distribution right before (δ_{fault} = 3.5 m) and after neck formation (δ_{fault} = 4 m); when the pipeline starts necking the additional stresses concentrate on the neck while the rest of the pipeline remains unaffected. **Fig. 2.15b** presents the distribution of shear tractions along the pipe-soil interface for the same fault displacement magnitudes. It is interesting to note that indeed a very local phenomenon such as the abrupt displacement at the fault plane may affect a total pipeline length up to 2000 m (1000 m on each side of the fault). Notice also that for small values of offset the frictional capacity of the interface (≈ 8 kPa) is reached (and hence the pipe slipped) in only half of the affected length; as the offset increases a larger and larger part of the total affected length has undergone slippage, and the elastic reaction is limited to only about 20% of that length. **Fig. 2.15c** shows the evolution of the axial force at point B, the boundary of the central 3D response segment (region I). This axial force (N_B) may be seen as the restraining force at the end of region I. In other words, focusing on the vicinity of the fault while omitting the pipeline response at larger distance may lead to inaccurate simulation: introducing a fixity at the boundaries of region I ($N_B \rightarrow \infty$) would lead to an unrealistically unfavorable behavior, while leaving the pipe free (N_B = 0) would lead to a severe underestimation of the developed tensile strains.

2.3.3. Reverse faulting: key stressing mechanisms

In this section, the example pipeline is subjected to reverse faulting. For a fault offset δ_{fault} = 0.5 m **Fig. 2.16** presents the deformed pipeline with the stress contours accompanied with the distribution of axial strains along the top and bottom centerline. As with the normal fault, the pipeline bends to accommodate the imposed vertical displacement. In this case, however, the axial component of the fault tends to squeeze the pipeline, imposing significant compression. The critical section that tends to attract higher compressive strains, lies within the moving block. As in the case of the normal fault, the mostly distressed area (experiencing combined bending and compression) is concentrated within a limited zone around the fault trace; $l_{b,m}$ = 19 m within the hanging wall and $l_{b,s}$ = 22 m within the footwall.

Fig. 2.17 focuses on the near-field pipe response. **Fig. 2.17a** presents the deformed pipe with the axial strain contours for four values of fault offset δ_{fault} (scale factor = 5). As δ_{fault} increases, compressive strains are starting to concentrate at the bottom side of the highly bended section until the pipe wall wrinkles. For even larger displacements, wrinkling is evolved to buckling until the entire section is crushed under the extremely high compressive strains.

The evolution of local buckling of the pipe wall is presented in more detail in **Fig. 2.17b**, where the deformed pipe segment in the vicinity of the critical section is presented with superimposed axial strain contours. The initially uniform distribution of strains transforms into a "wavy" distribution as the axial strains increase and localize, thus creating the characteristic ripples. With further increase of the imposed displacement, one of the ripples becomes dominant and concentrates any additional compressive strain leading to the formation of a wrinkle and ultimately to the folding of the pipe wall. **Fig. 2.17c** shows the distribution of axial strains at the compressive side of the segment, depicting the initiation of local buckling. Notice that from δ_{fault} = 0.72 m onward, the strain distribution along most of the length freezes and any additional compressive strain is accumulated in the dominant ripple. This pattern, indicates local buckling initiation and denotes pipeline failure.

As would have been expected, the pipe, being a thin-walled structure, is quite vulnerable to the compressive actions induced by the reverse faulting. Therefore, pipeline failure is accelerated and the safety margins are substantially decreased compared to those for normal faulting; the formation of local buckling causes the collapse of the pipeline strength, hinders the **Fig. 2.18** summarizes the pipeline response in the footwall along the far-field region. Similarly with the normal fault, the axial component of fault displacement affects a much larger length than the lateral one. For this specific numerical example, this length extends to 600 m from fault trace. The readers should observe the relief from axial strain (**Fig. 2.18a**) and the reversal of its direction on the pipe-soil interface (**Fig. 2.18b**) for fault offset of δ_{fault} = 1 m. This behavior is a clear indication that as the critical section snaps due to local buckling, the pipe regains some of the imposed displacement, causing relief and development of negative skin friction. **Fig. 2.18c** presents the force-displacement response at the boundary of the near field, depicting vividly the collapse of the segment strength due to local buckling.

2.3.4. Concluding remarks

The two examined examples revealed that the fault-induced displacements do affect a quite significant length of a buried pipeline. For pipelines subjected to normal faulting, this length can reach up to 1000 m from the fault-pipeline intersection, while for reverse faulting this length is about 600m Within this length however, the pipeline is not stressed uniformly (**Fig. 2.19**). At the vicinity of the fault-trace (near-field) the pipeline experiences intense bending (to accommodate the vertical fault offset), while it is also stretched or compressed due to the axial component of the normal or reverse fault. Beyond this region (i.e. in the 'far field') the effect of bending is eliminated and the pipeline sustains pure stretching or compression.

Taking advantage of these different mechanisms, we apply a two-part numerical methodology that allows the simulation of large pipeline lengths without seriously hindering the efficiency of the numerical model. The near-field region is modeled in great detail employing with 3D non-linear FE algorithms. Thus, complex phenomena such as the fault-rupture propagation, the non-linear pipe-section behavior and the interplay between the pipe and the soil, maybe rigorously accounted for. Beyond this central 3D region the simulation of the problem is simplified to essentialy1-dimentional. Here, the pipeline is modeled with beam elements and soil reactions are simplistically represented by appropriate (non-linear) springs. By employing these "hybrid boundaries" for the representation of the far-field, we may increase the length of the simulation without excessively increasing the computational demand. In the following chapters, an exhaustive investigation is conducted to calibrate and validate the numerical methodology for both the "near-field" and the "far-field" response.

References

ALA (2001). *Guidelines for the design of buried steel pipes*, American Lifeline Alliance and ASCE, New York

American Society of Civil Engineers. Buried flexible steel pipe; design and structural analysis. In: Whidden WR, editor. ASCE manual of practice, MOP; 2009. p. 119.

American Society of Mechanical Engineers. Pipeline transportation systems for liquid hydrocarbons and other liquids, ANSI/ASME B31.4; 2006.

American Society of Mechanical Engineers. Gas Transmission and Distribution Piping Systems, ASME B31.8-2003, New York, New York, 2003.

Anastasopoulos, I., Gazetas, G., Bransby, M. F., Davies, M. C. R., & El Nahas, A. (2007). Fault rupture propagation through sand: finite-element analysis and validation through centrifuge experiments. *Journal of Geotechnical and Geoenvironmental Engineering*, *133*(8), 943-958.

Anastasopoulos I and Gazetas G (2007a), "Foundation-structure Systems over a Rupturing Normal Fault: Part I. Observations After the Kocaeli 1999 Earthquake," *Bulletin of Earthquake Engineering, 5(3)*: 253–275.

Anastasopoulos I and Gazetas G. (2007b), Behaviour of Structure–foundation Systems over a Rupturing Normal Fault: Part II. Analysis of the Kocaeli Case Histories," *Bulletin of Earthquake Engineering, 5(3)*: 277–301.

Anastasopoulos I., Gazetas G., Bransby M.F., Davies M.C.R., and El Nahas A. (2009), "Normal Fault Rupture Interaction with Strip Foundations", *Journal of Geotechnical and Geoenvironmental Engineering, ASCE, 135(3)*: 359-370.

Anderson, C., Wijewickreme, D., Ventura, C., & Mitchell, A. (2005). Full-scale laboratory testing of soil-pipe interaction in branched polyethylene pipelines. *Experimental Techniques*, 29: 33–37.

ASCE (1984). *Guidelines for the seismic design of oil and gas pipeline systems*. Committee on Gas and Liquid Fuel Lifelines, ASCE, New York.

Audibert, J. M., & Nyman, K. J. (1975). Coefficients of subgrade reaction for the design of buried piping. *Structural Design of Nuclear Plant Facilities* ASCE, 109-141.

Bransby, M. F., Newson, T. A., Brunning, P., and Davies, M. C. R. (2001). Numerical and centrifuge modeling of the upheaval resistance of buried pipelines. *Proc. 20th Int. Conf. on Offshore Mechanics and Arctic Engineering,* Rio de Janeiro, Brazil.

Bransby, M. F. & Ireland, J. (2009). Rate effects during pipeline upheaval buckling in sand. *Proc. ICE – Geotechical Engineering 1*62, No. 5, 247–256

Bray, J. D. (1990). "The effects of tectonic movements on stresses and deformations in earth embankments." Ph.D. dissertation, Univ. of California at Berkeley, Berkeley, Calif.

Bray, J. D., Seed, R. B., and Seed, H. B. (1993). "1*g* small-scale modeling of saturated cohesive soils." *Geotech. Test. J.*, 16(1), 46–53.

Bray, J. D., Seed, R. B., Cluff, L. S., and Seed, H. B. (1994a). "Earthquake fault rupture propagation through soil." *J. Geotech. Engrg.*, 120(3), 543–561.

Bray, J. D., Seed, R. B., and Seed, H. B. (1994b). "Analysis of earthquake fault rupture propagation through cohesive soil." *J. Geotech. Engrg.*, 120(3), 562–580.

Brune JN and Allen CR (1967), "A Low-stress-drop, Low Magnitude Earthquake with Surface Faulting, The Imperial, California, Earthquake of March 4, 1966," Bulletin of the Seismological Society of America, 57: 501–514.

Calvetti, F., di Prisco, C. & Nova, R., (2004), Experimental and Numerical Analysis of Soil-Pipe Interaction *Journal of Geotechnical and Geo-environmental Engineering*, 130, (No 12): 1292-1299.

Cappalleto A., Tagliaferri R., Giurlani G., Andrei G., Furlani G., & Scarpelli G. (1998). Field full scale tests on longitudinal pipeline-soil interaction. *Int. Pipeline Conference,* ASME Calgary, Alberta.

Cheuk, C. Y., White, D. J., & Bolton, M. D. (2008). Uplift mechanisms of pipes buried in sand. *Journal of Geotechnical and Geoenvironmental Engineering,* 134(2), 154-163.

Chin, E. L., Craig, W. H., & Cruickshank, M. (2006). Uplift resistance of pipelines buried in cohesionless soil. *Proc., 6th Int. Conf. on Physical Modelling in Geotechnics.* Ng, Zhang, and Wang, eds., Vol. 1, Taylor & Francis Group, London, 723–728.

Cole Jr, D. A., & Lade, P. V. (1984). Influence zones in alluvium over dip-slip faults. *Journal of Geotechnical Engineering*, *110*(5), 599-615.

Dama E, Karamanos SA, Gresnigt AM. (2007) Failure of locally buckled pipelines. *Journal of Pressure Vessel Technology,* ASME; 129(2):272–9.

Das S, Cheng JJR, Murray DW, & Nazemi N. (2008). Effect of monotonic and cyclic bending deformations on NPS12 wrinkled steel pipeline. *Journal of Structural Engineering*, ASCE, 134(12):1810–7.

Di Prisco C & Galli A. (2006). Soil–pipe interaction under monotonic and cyclic loads: experimental and numerical modeling. *Proc. 1st Euro-Mediterranean Symposium on Advances in Geomaterials and Structures,* Hammamet, Tunisia

Dorey, A. B., Murray, D. W., & Cheng, J. R. (2000, October). An experimental evaluation of critical buckling strain criteria. In *2000 3rd International Pipeline Conference* (pp. V001T01A011-V001T01A011). American Society of Mechanical Engineers.

EN 1993-4-3 (2007). Eurocode 3: Design of steel structures. Part 4-3: Pipelines. CEN, Brussels.

EN 1998-4 (2006). Eurocode 8: Design of structures for earthquake resistance. Part 4: Silos, tanks and pipelines. CEN, Brussels.

Erickson, S. G., Staryer, L. M., and Suppe, J. (2001). "Initiation and reactivation of faults during movement over a thrust-fault ramp: Numerical mechanical models." *J. Struct. Geol.*, 23, 11–23.

Faccioli, E., Anastasopoulos, I., Callerio, A., & Gazetas, G. (2008). Case histories of fault–foundation interaction. *Bulletin of Earthquake Engineering*, *6*(4), 557-583.

Honegger D.G. (1999) Field measurements of axial soil friction forces on buried pipelines. *Technical Council on Lifeline Earthquake Engineering Monograph,* 16, 703-710.

Horsfield, W. T. (1977). "An experimental approach to basement-controlled faulting." *Geol. Mijnbouw*, 56(4), 363–370.

Hsu T.W. (1993) Rate effect on lateral soil restraint of pipeline. *Soils and Foundations,* 33(4), 169-169.

Hsu T.W., Chen Y.J., & Hung W.C. (2006) Soil resistant to oblique movement of buried pipes in dense sand. *Journal of Transportation Engineering*, 132(2), 175-181.

Karimian, S. A. (2006). "Response of buried steel pipelines subjected to longitudinal and transverse ground movement". PhD thesis, University of British Columbia.

Karimian H., Wijewickreme D., and Honegger D.G. (2006), "Buried pipelines subjected to transverse ground movement: Comparison between full-scale testing and numerical modeling." Proceedings of the 25th International Conference on Offshore Mechanics and Arctic Engineering, Hamburg, Germany, 4-9 June 2006.

Lade, P. V., Cole Jr, D. A., & Cummings, D. (1984). Multiple failure surfaces over dip-slip faults. *Journal of Geotechnical Engineering*, *110*(5), 616-627.

Liang, J., & Sun, S. (2000). Site effects on seismic behavior of pipelines: a review. *Journal of pressure vessel technology*, *122*(4), 469-475.

Loukidis, D. _1999_. "Active fault propagation through soil." Thesis, School of Civil Engineering, National Technical Univ., Athens, Greece.

Muir Wood, D., and Stone, K. J. L. (1994). "Some observations of zones of localization in model tests on dry sand." *Localization and bifurcation theory for soils and rocks*, R. Chambon, J. Desrues, and I. Vardoulakis, eds., Balkema, Rotterdam, The Netherlands, 155–164.

Muir Wood, D. (2002). "Some observations of volumetric instabilities in soils." *Int. J. Solids Struct.*, 39, 3429–3449.

Nagaoka S. "The interaction of earthquake faults with foundations and pipelines," PhD thesis, University of Dundee, UK, 2007

Nakai, T., Muir Wood, D., and Stone, K. J. L. (1995). "Numerical calculations of soil response over a displacing basement." *Soils Found.*, 35(2), 25–35.

Nederlands Normalisatie-Instituut. Requirements for pipeline systems, NEN 3650, part-1: general, and part-2: steel pipelines; 2006.

O'Rourke, T. D., & Palmer, M. C. (1996). Earthquake performance of gas transmission pipelines. *Earthquake Spectra*, *12*(3), 493-527.

Palmer, A. C., White, D. J., Baumgard, A. J. et al. (2003). Uplift resistance of buried submarine pipelines: comparison between centrifuge modelling and full scale tests. Geotechnique 53, No. 10, 877–833

Pineda, O., & Ordaz, M. (2004, August). Influence of ground subsidence in the damage to Mexico City's primary water system due to the 1985 earthquake. In *XIII World Conference on Earthquake Engineering* (No. 2165).

Paulin M.J., Phillips R., Clark J.I., Trigg A., and Konuk I. (1998) "A full-scale investigation into pipeline-soil interaction" Proceedings, International Pipeline Conference, Calgary, AB, ASME, 779-779.

PRCI, (2004), "Guidelines for the Seismic Design and Assessment of Natural Gas and Liquid Hydrocarbon Pipelines, Pipeline Design, Construction and Operations", Edited by Honegger, D. G., and Nyman D. J., Technical Committee of Pipeline Research Council International (PRCI) Inc, October 2004

Roth, W. H., Sweet, J., and Goodman, R. E. (1982). "Numerical and physical modeling of flexural slip phenomena and potential for fault movement." *Rock Mech.*, 12, 27–46.

Schaumann, P., Keindorf, C., & Brüggemann, H. (2005, January). Elasto-plastic bearing behavior of steel pipes exposed to internal pressure and bending. In *The Fifteenth International Offshore and Polar Engineering Conference*. International Society of Offshore and Polar Engineers.

Schupp, J., Byrne, B. W., Eacott, N., Martin, C. M., Oliphant, J., Maconochie, A., and Cathie, D. (2006). "Pipeline unburial behaviour in loose sand." Proc., 25th Int. Conf. on Offshore Mechanics and Arctic Engineering, Hamburg, Germany, OMAE2006-92541.

Scott, R. F., and Schoustra, J. J. (1974). "Nuclear power plant sitting on deep alluvium." *J. Geotech. Engrg. Div.*, 100(4), 449–459.

Shibuya, S., Mitachi, T., and Tamate, S. (1997). "Interpretation of direct shear box testing of sands as quasisimple shear." *Geotechnique*, 47(4), 769–790.

Slemmons DB (1957), "Geological Effects of the Dixie Valley-fairview Peak, Nevada, Earthquakes of December 16, 1954," Bul. of the Seism. Soc. of America, 47(4): 353–375.

Stephens, D.R., Olson, R.J., Rosenfeld, M.J. (1991) "Topical Report on Pipeline Monitoring – Limit State Criteria" NG18 Report No. 188

Stone, K. J. L., and Muir Wood, D. (1992). "Effects of dilatancy and particle size observed in model tests on sand." *Soils Found.*, 32(4), 43–57.

Taylor CL, Cline KM, Page WD and Schwartz DP (1985), "The Borah Peak, Idaho earthquake of October 28, 1983 – Surface Faulting and Other Phenomena," Earthquake Spectra, 2(1): 23–49.

Trautmann C.H., and O'Rourke T.D. (1985) "Lateral force – displacement response of buried pipe." Journal of Geotechnical Engineering, ASCE, Reston, VW, Vol 111, No 9, pp 1077 – 1092.

Trautmann, C. H., O'Rourke, T. D., and Kulhawy, F. H. (1985). "Uplift force-displacement response of buried pipe." Journal of Geotechnical Engineering., 111(9), 1061–1076.

Turner JE. Lateral force–displacement behavior of pipes in partially saturated sand. MS thesis, Cornell University, Ithaca, NY; 2004.

Uzarski J and Arnold C. "Chi-Chi, Taiwan, Earthquake of September 21, 1999, Reconnaissance Report," *Earthquake Spectra, The Professional Journal of the EERI*, 17(Supplement A), 2001

Van Es, S. H. J., Gresnigt, A. M., Kolstein, M. H., & Bijlaard, F. S. K. (2014, August). Strain based design of spirally welded pipes, local buckling in 4-point bending. In *The Twenty-fourth International Ocean and Polar Engineering Conference*. International Society of Offshore and Polar Engineers.

Walters, J. V., and Thomas, J. N. (1982). "Shear zone development in granular materials." *Proc., 4th Int. Conf. on Numerical Methods in Geomechanics*, Vol. I, Edmonton, Canada, 263–274.

White, R. J., Stone, K. J. L., and Jewel, R. J. (1994). "Effect of particle size on localization development in model tests on sand." *Proc., Inst. Centrifuge Conf.*, C. F. Leung, F. H. Lee, and T. S. Tan, eds., Balkema, Rotterdam, The Netherlands, 817–822.

White, D. J., Barefoot, A. J., and Bolton, M. D. (2001). "Centrifuge modeling of upheaval buckling in sand." Int. J. Physical Modeling in Geotechnics, 2(1), 19–28.

Wijewickreme D., Karimian H., and Honegger D.G. (2009). "Response of buried steel pipelines subjected to relative axial soil movement" Canadian Geotechnical Journal, 46: 735-752.

Wijewickreme D., Monroy M., Nyman D.J., and Honegger D.G. (2014). "Response of buried pipelines subjected to ground displacements under different trench backfill conditions" Proceedings of the 10th U.S. National Conference on Earthquake Engineering, Anchorage, Alaska, 2014.

Williams, E. S., Byrne, B. W. & Blakeborough, A. (2013). Pipe uplift in saturated sand: rate and density effects. Geotechnique 63, No. 11, 946–956.

Zimmerman, T. Timms, C., Xei, J., Asante, J. (2004) "Buckling resistance of large diameter spiral welded linepipe:" *Proceedings of International Pipeline Conference,* Calgary, Canada

Figures

of Chapter 2

Test id	*D (m)*	*H/D*	D_r *(%)*	φ_{peak} *(deg)*	φ_{res} *(deg)*	ψ_{peak} *(deg)*	γ_{yield}
23	102	3.5	80	44	35	11.5	0.008
24	102	5.5	80	44	35	11.5	0.008
25	102	8.0	80	44	35	11.5	0.008
27	102	3.5	45	36	36	6	0.02
46	102	5.5	45	36	36	6	0.02
51	102	8.0	45	36	36	6	0.02
18	102	3.5	0	31	31	1	0.03
20	102	5.5	0	31	31	1	0.03
21	102	8.0	0	31	31	1	0.03

Table 2.1. Experimental configuration and properties of the sand for the transversal push experiments of Trautmann and O'Rourke (1985).

Test id	*D (m)*	*H/D*	D_r *(%)*	φ_{peak} *(deg)*	φ_{res} *(deg)*	ψ_{peak} *(deg)*	γ_{yield}
FD	100	3.0	92	52	39	25	0.01
FL	100	3.0	30	39.9	39.9	9.9	0.03

Table 2.2. Experimental configuration and properties of the sand for the vertical upward pull experiments of Cheuk et al (2008).

Test id	D (mm)	H/D	D_r (%)	φ_{peak} (deg)	φ_{res} (deg)	ψ_{peak} (deg)	γ_{yield}	φ_p^{int}	φ_{res}^{int}
AB–3	457	2.5	75	45	35	15	0.01	36	31
AB–5	457	2.7	20	39	-	10	0.02	33	31

Table 2.3. Experimental configuration and properties of the sand for the longitudinal pullout experiments of Wijewickreme et al. 2009

Test id	D (mm)	t (mm)	D/t	Grade	σ_y (MPa)
T1D9	1066	16.4	65.1	X70	550
T2D11	1067	9	118.3	X60	400
T11D7	1068	12.9	82.8	X52	350

Table 2.4. Experimental configuration and for the four-point bending tests of Van Es et al. 2014

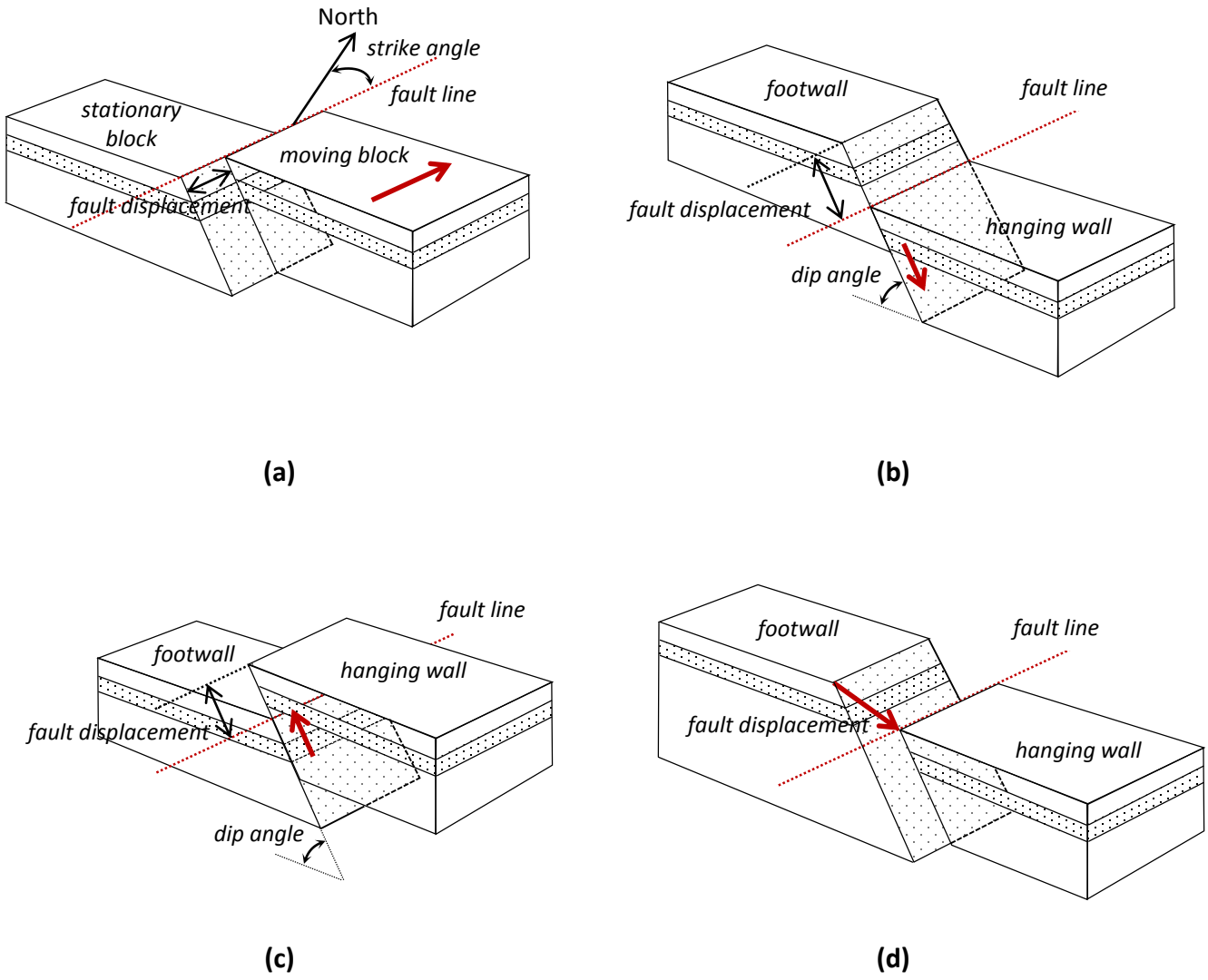

Fig. 2.1. Types of faults and terminology: (a) strike slip fault, (b) normal and (c) reverse fault, and (d) oblique fault

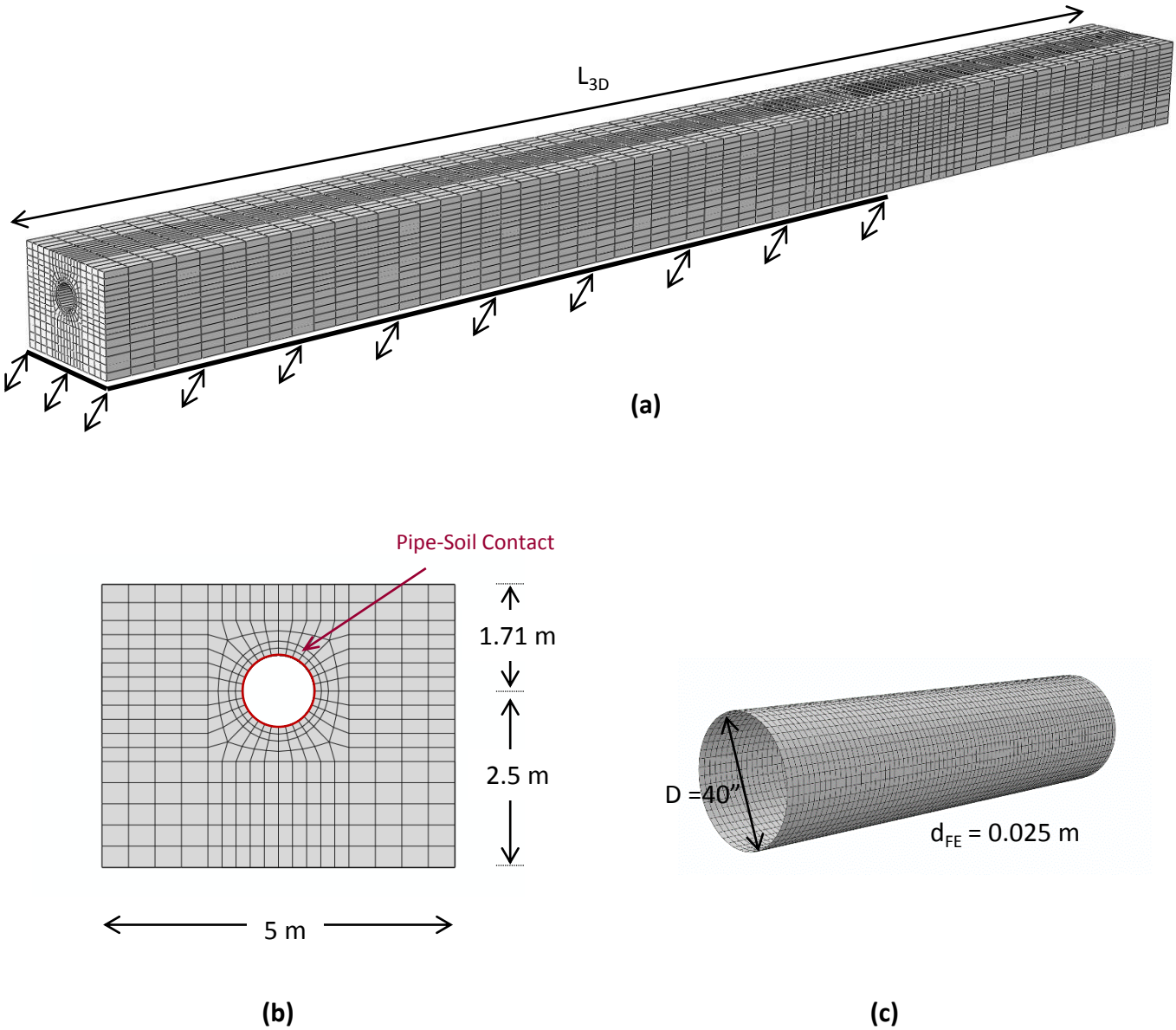

Fig. 2.2. Numerical simulation of the ‘near-field’. (a) a 3D view of the FE configuration. (b) a vertical section (c) detail of the pipeline mesh.

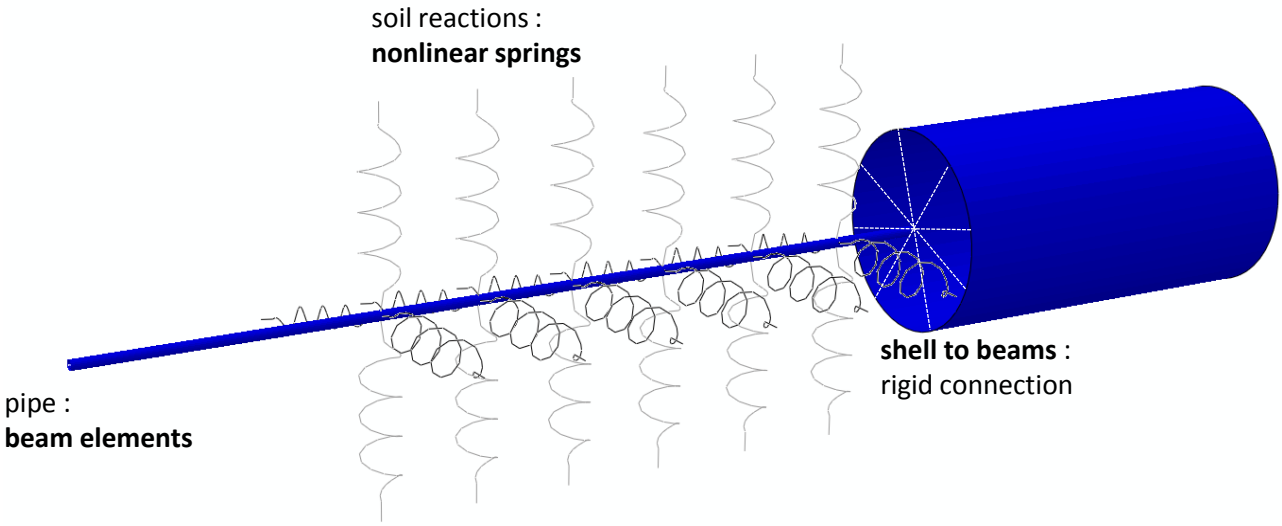

(a)

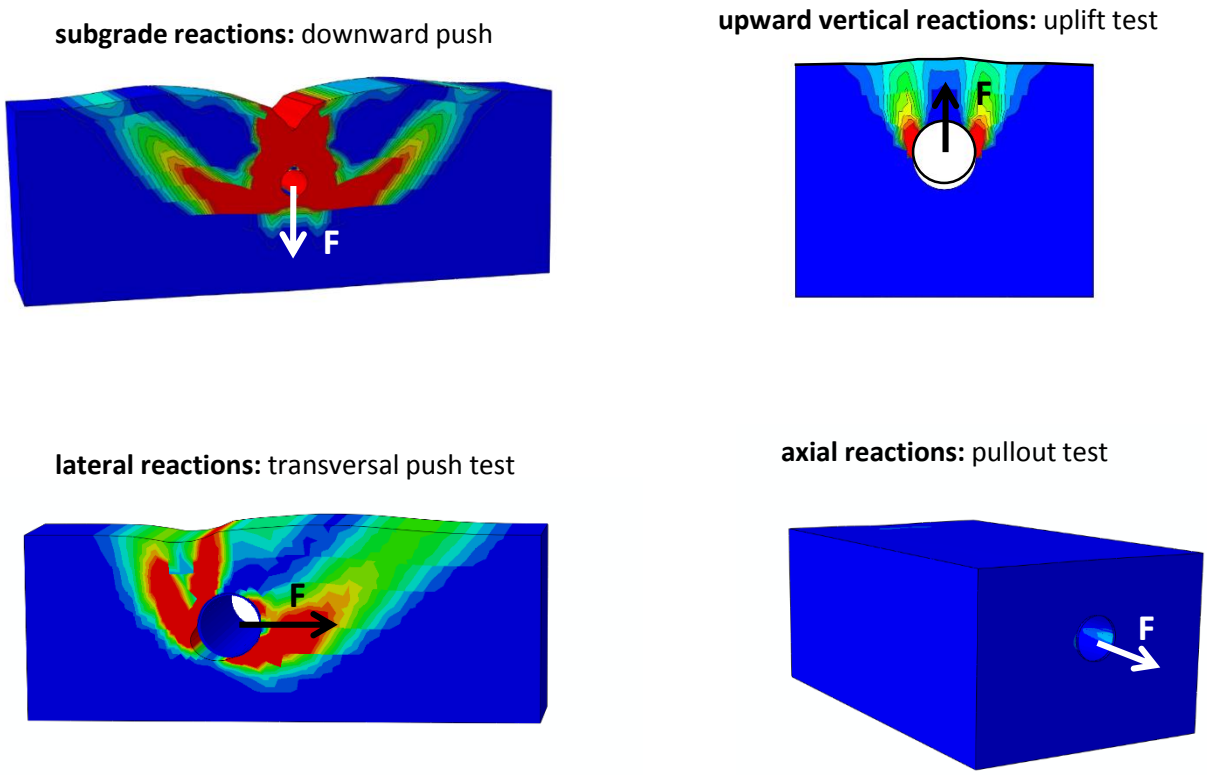

(b)

Fig. 2.3. (a) The 'far field' simulation : the numerical model at distance from the fault trace: the pipe is modeled with beam elements and the soil is replaced by appropriate non-linear springs. (b) Calibration of soil spring through the uniaxial push-test of the pipe: deformed models with superimposed plastic strain contours.

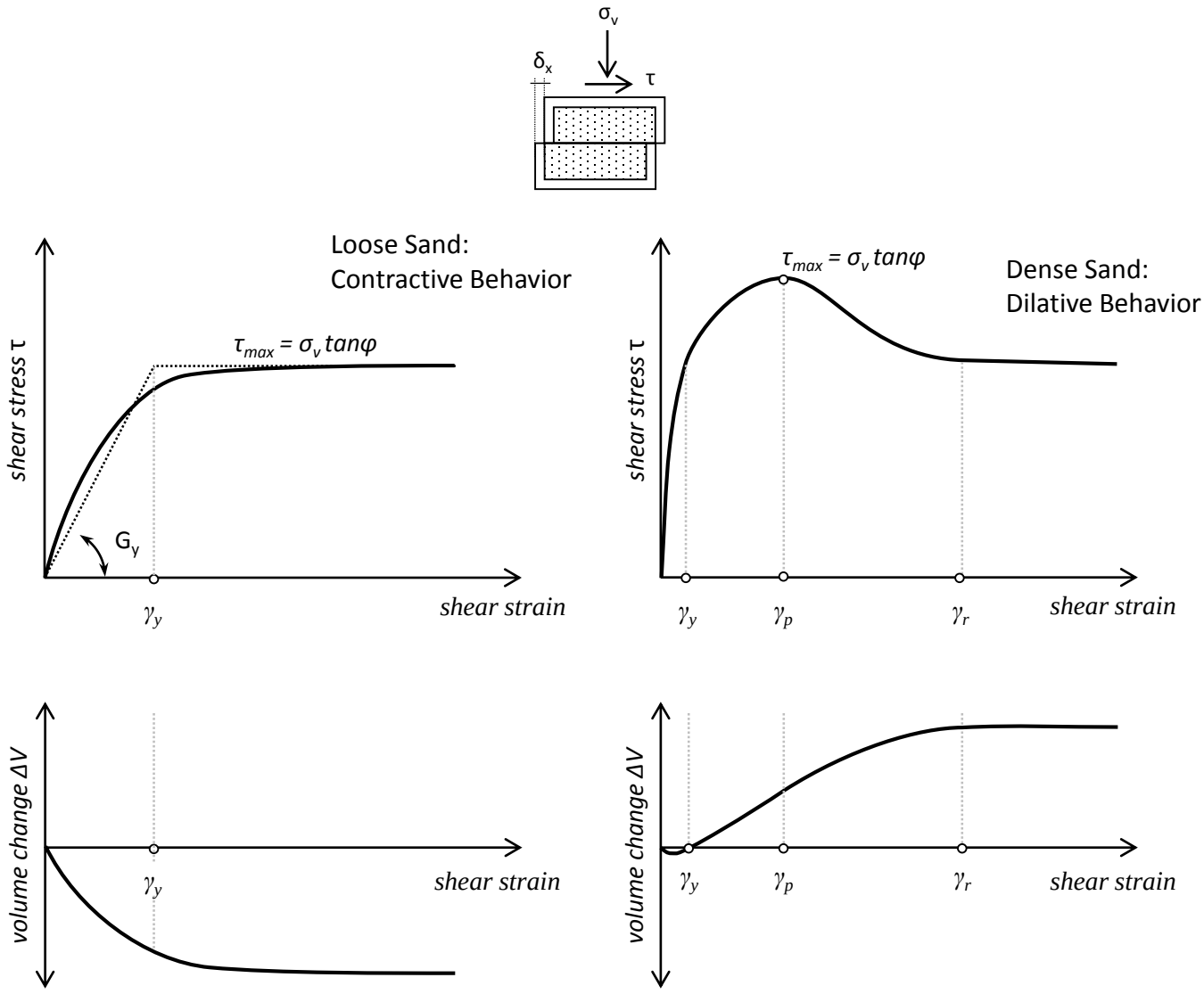

Fig. 2.4. Direct Shear Test on Loose (left) and Dense (right) sand specimens: the characteristic strains γ_y, γ_p, γ_r are denoted.

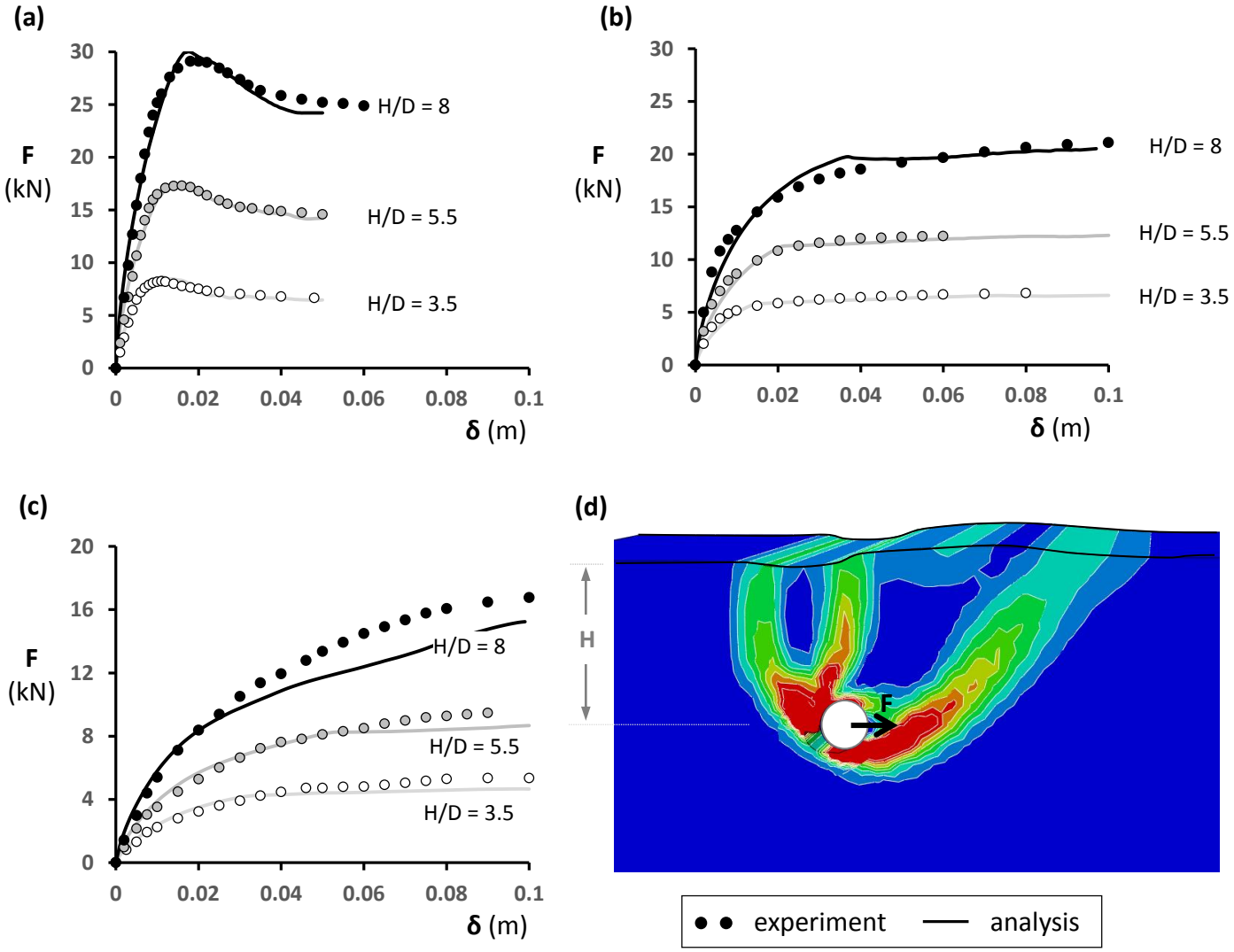

Fig. 2.5. Validation of the numerical methodology: Simulation of the *lateral push* experiments of Trautmann & O'Rourke (1985) for sand density **(a)** Dr = 80%, **(b)** Dr = 45% and **(c)** Dr = 0%. **(d)** View of the deformed numerical model (at the instant of δ = 0.04 m of lateral displacement of the pipe) with superimposed plastic strain contours (snapshot refers to : Dr = 80% and H/D = 3.5, D=0.102m).

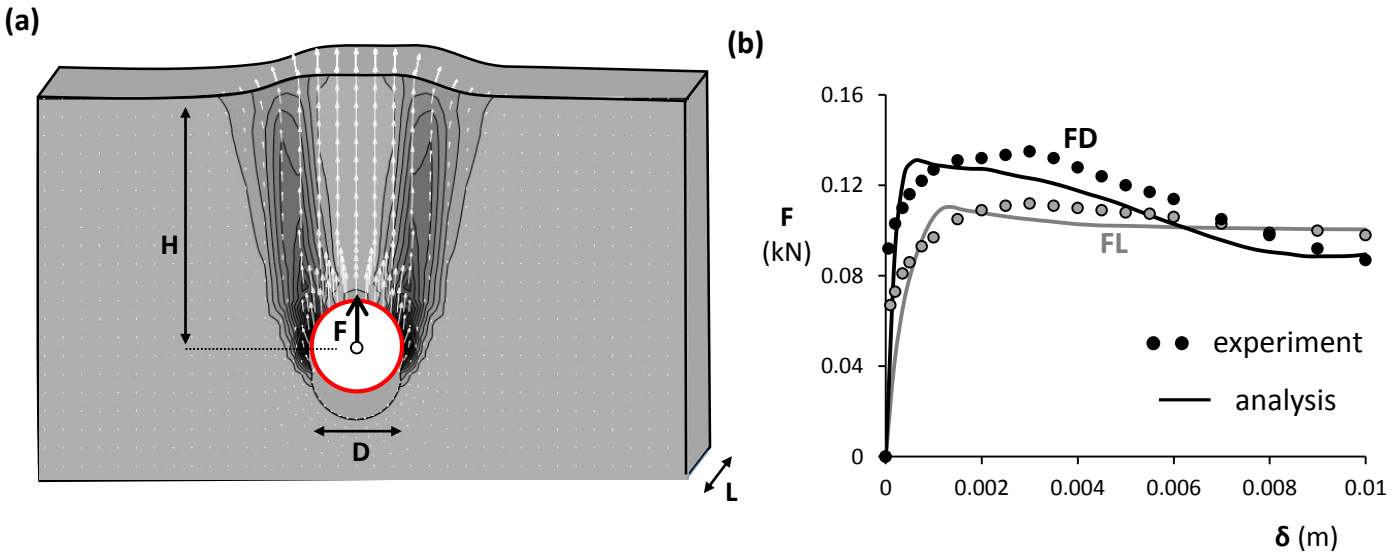

Fig. 2.6. Validation of the numerical methodology: Simulation of the *upward pull* experiments of Cheuk et al (2008) : **(a)** View of the deformed numerical model (at the instant of U = 0.01 m of vertical displacement of the pipe) with superimposed plastic strain contours (snapshot refers to fine dense sand experiment); **(b)** the numerically predicted F-δ curves are plotted against the experimental data.

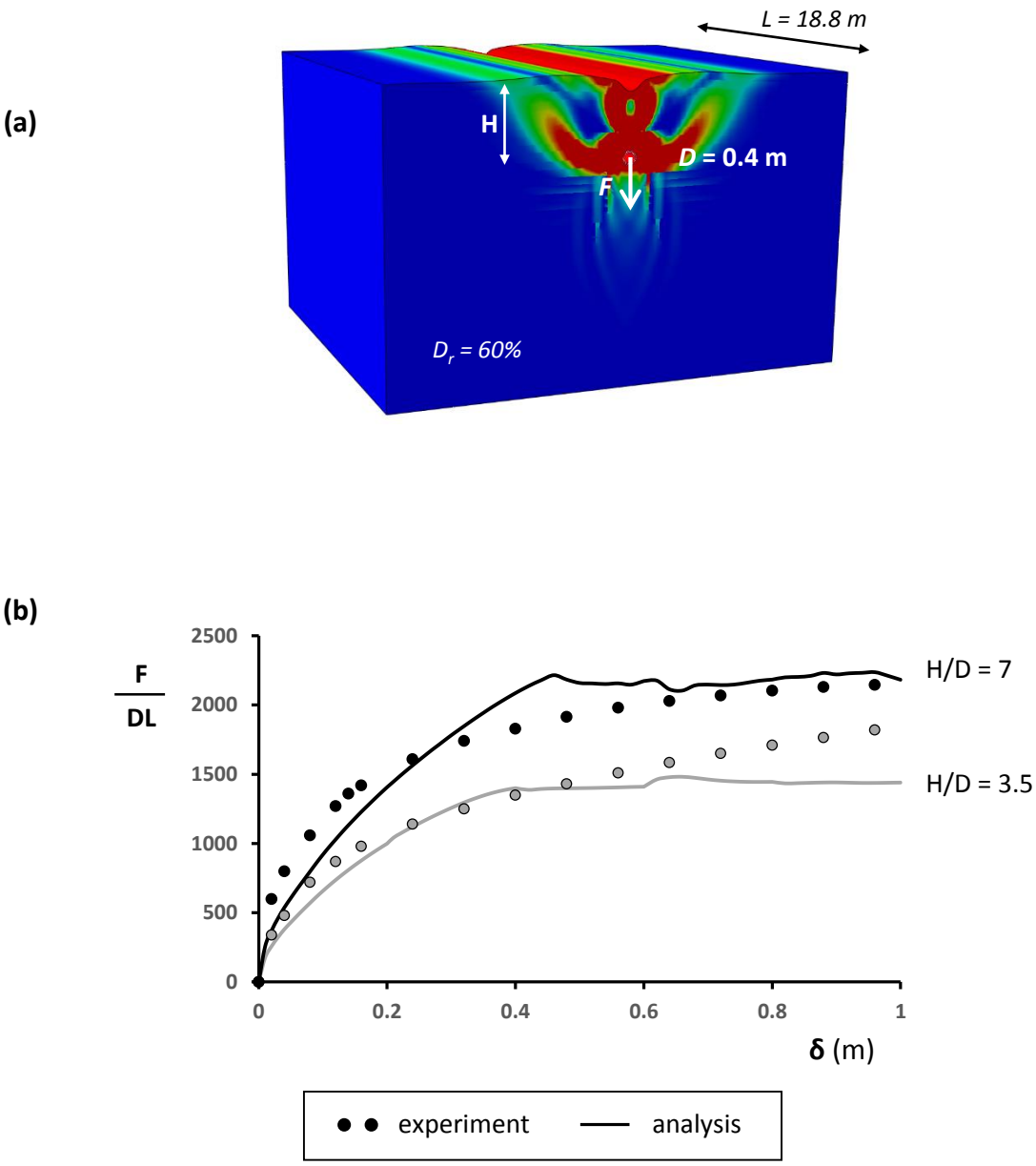

Fig. 2.7. Simulation of the downward push experiments of Nagaoka (2008); (a) deformed mesh of the model used with plastic strain contours, (b) comparison between the numerical prediction and the experimental results

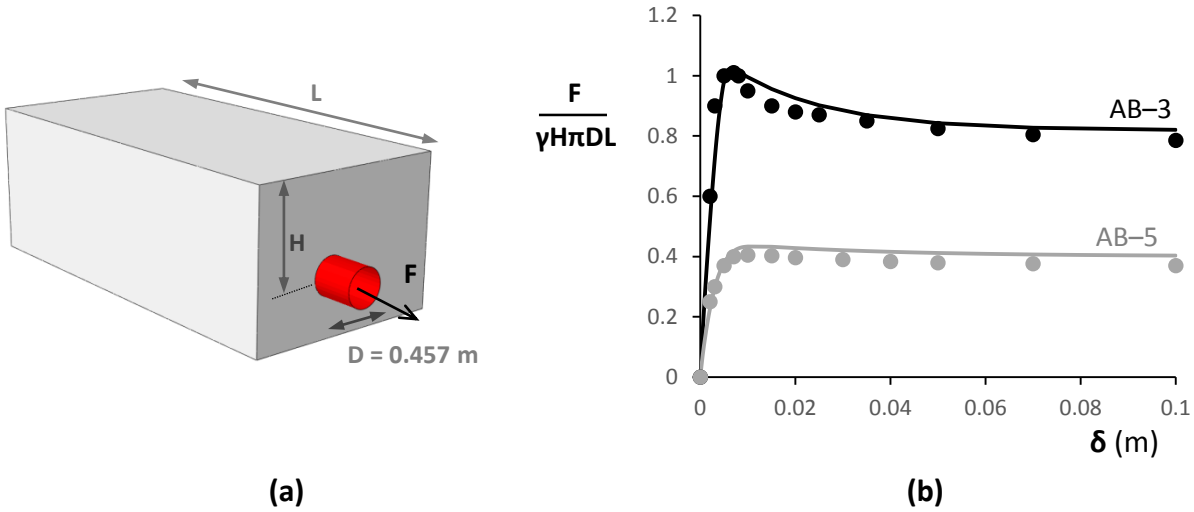

Fig. 2.8. Simulation of the downward push experiments of Wijewickreme et al (2009); (a) the numerical model used in the analyses, (b) comparison between the numerical prediction and the experimental results

(a)

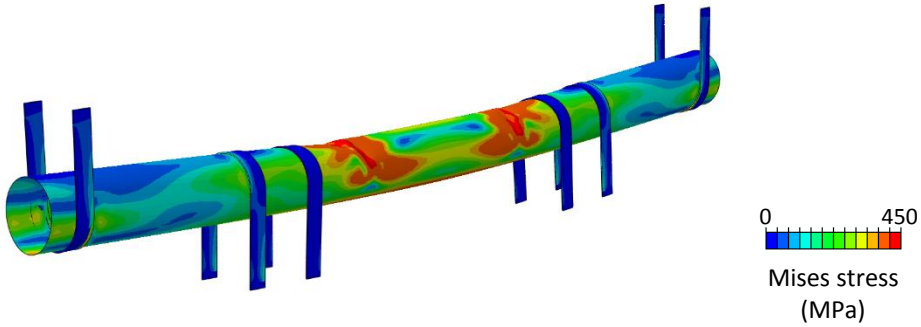

(b)

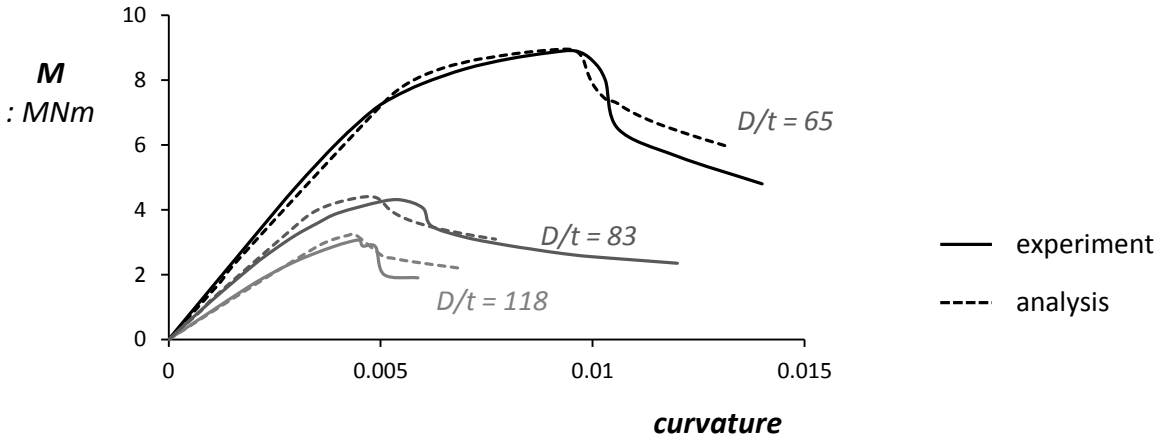

(c)

Fig. 2.9. Simulation of the four-point bending tests on steel pipe of Van Es et al. (2014): (a)experimental setup, (b) deformed mesh of the numerical model with stress contours and (c) comparison between the numerical prediction and the experimental results.

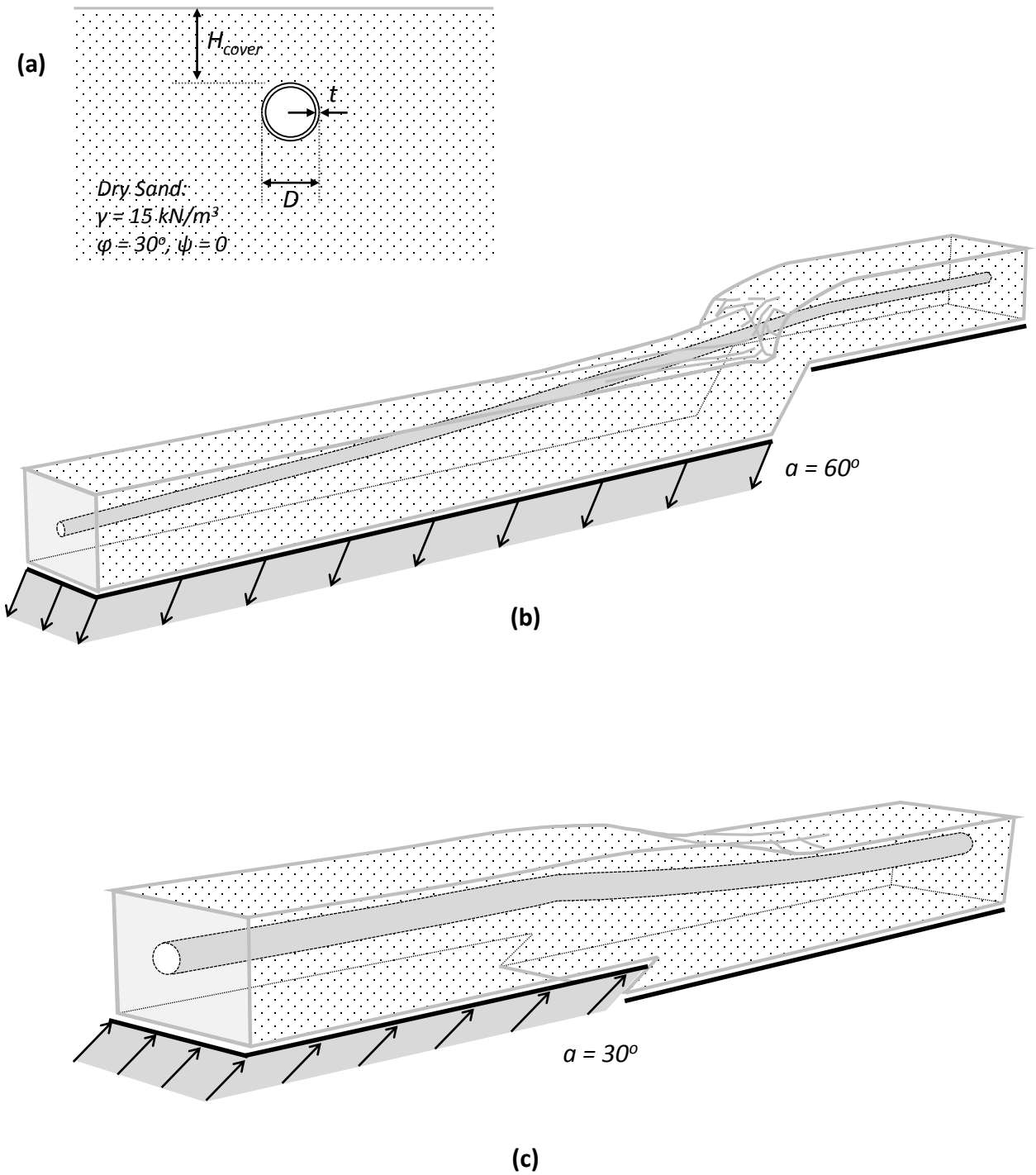

Fig. 2.10. Problem Statement: an infinitely long pipeline [D=40", t=0.5", H_{cover}=1.2 m], buried in loose dry sand subjected (a) to normal fault and (b) to reverse fault.

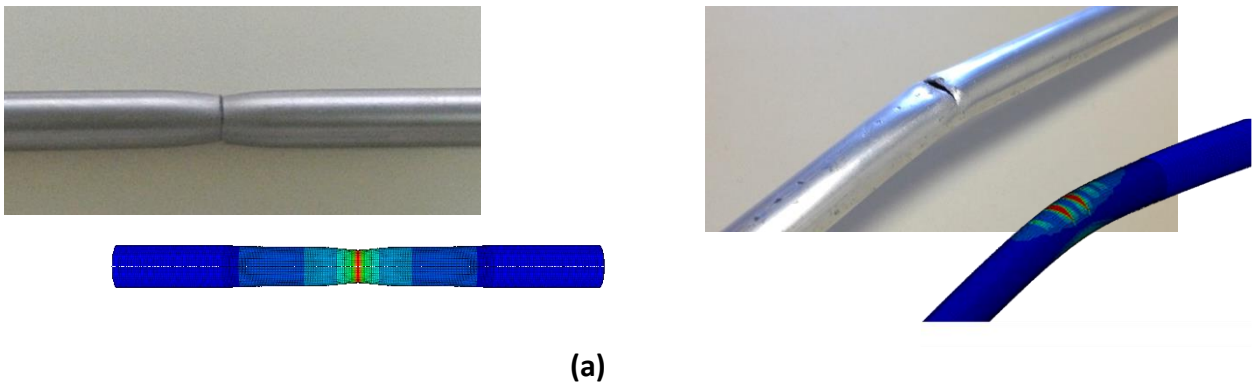

(a)

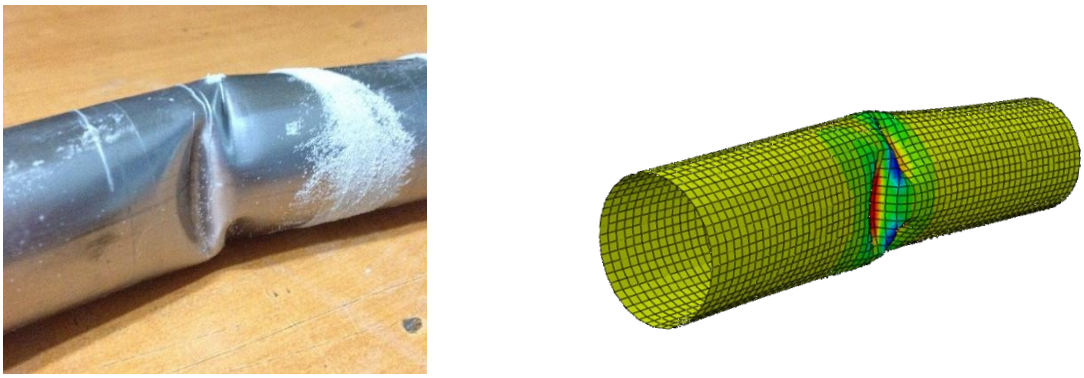

(b)

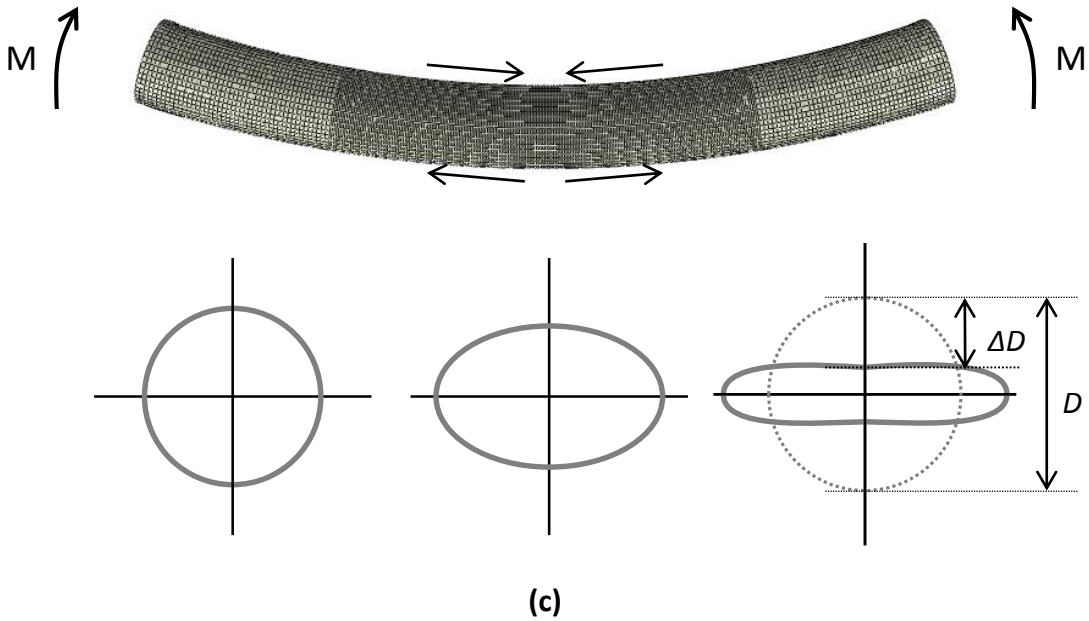

(c)

Fig. 2.11. Prevailing modes of failure of a steel pipeline: (a) rupture due to excessive tensile strains, (b) local buckling of the pipe wall due to excessive compressive strains, and (c) excessive distortion of the cross section (ovalization) due to bending.

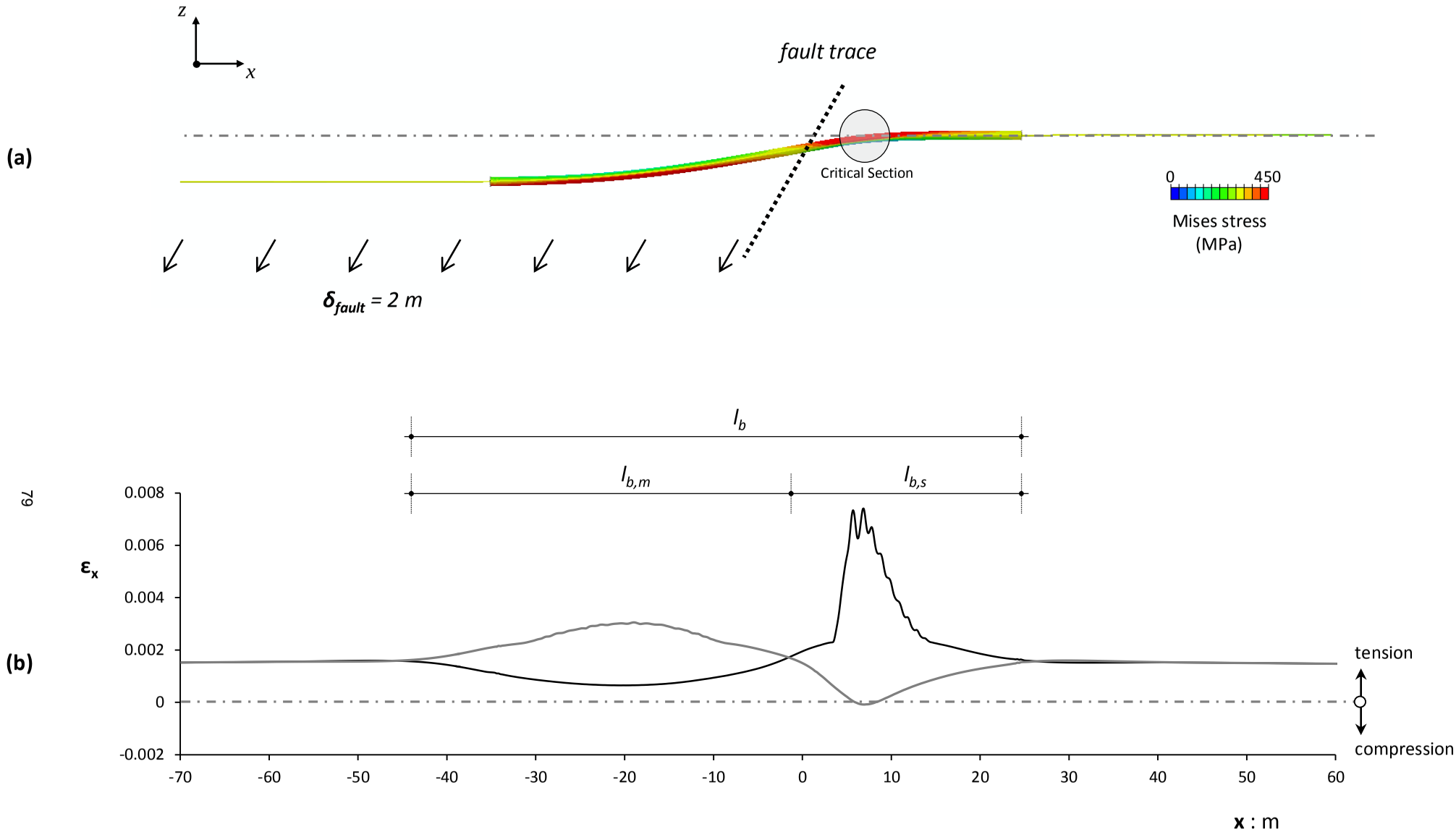

Fig. 2.12. Pipeline subjected to normal fault: (a) deformed mesh of the pipeline at the vicinity of the fault with superimposed stress contours (scale factor=3) and (b) axial strain distribution along the top and bottom centerline for fault offset δ_{fault} = 2 m.

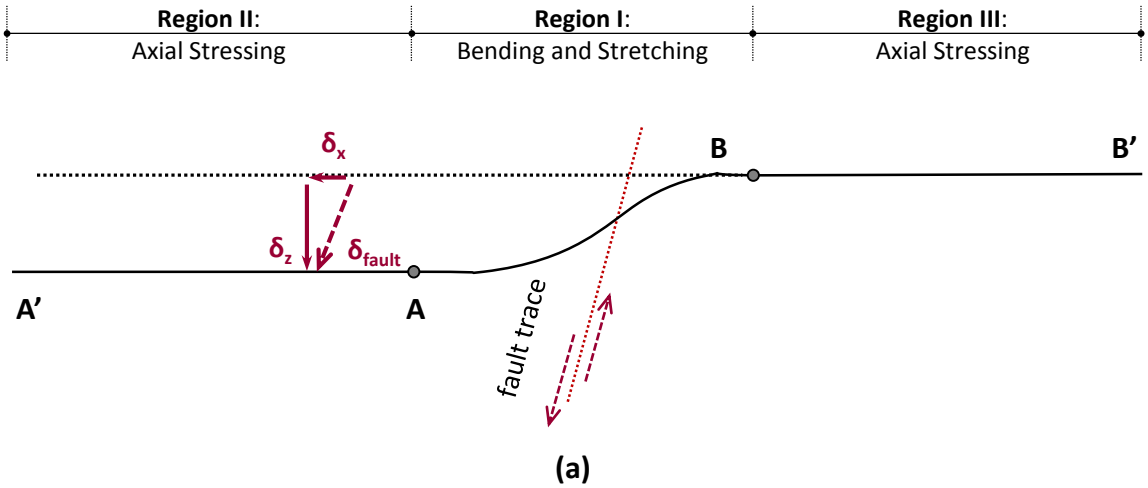

(a)

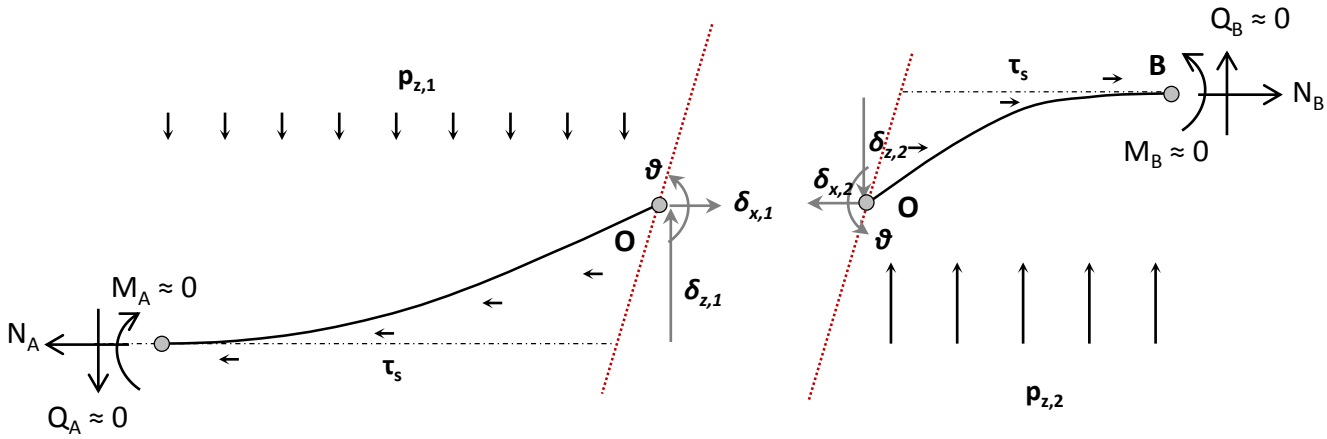

(b)

(c)

Fig. 2.13. Identification of the key mechanisms of a buried pipeline subjected to normal faulting: (a) the three stressing regions; (b) pipeline stressing along the 'near field' and (c) at the 'far field'.

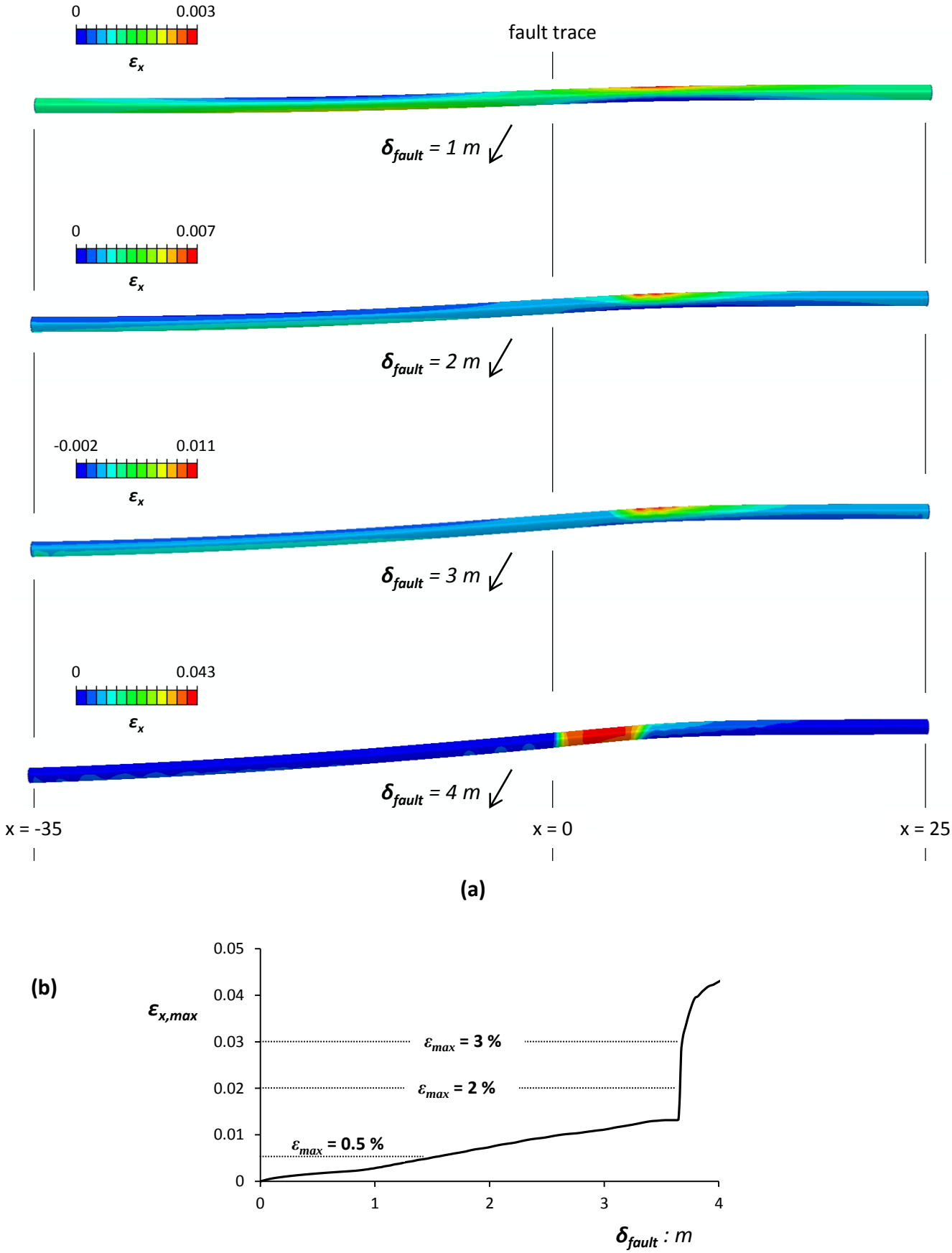

Fig. 2.14. Pipeline response at the "near field": (a) deformed mesh of the pipe with axial strain contours for various magnitudes of fault offset; (b) evolution of the maximum tensile strain along the pipe with the increase of the fault offset.

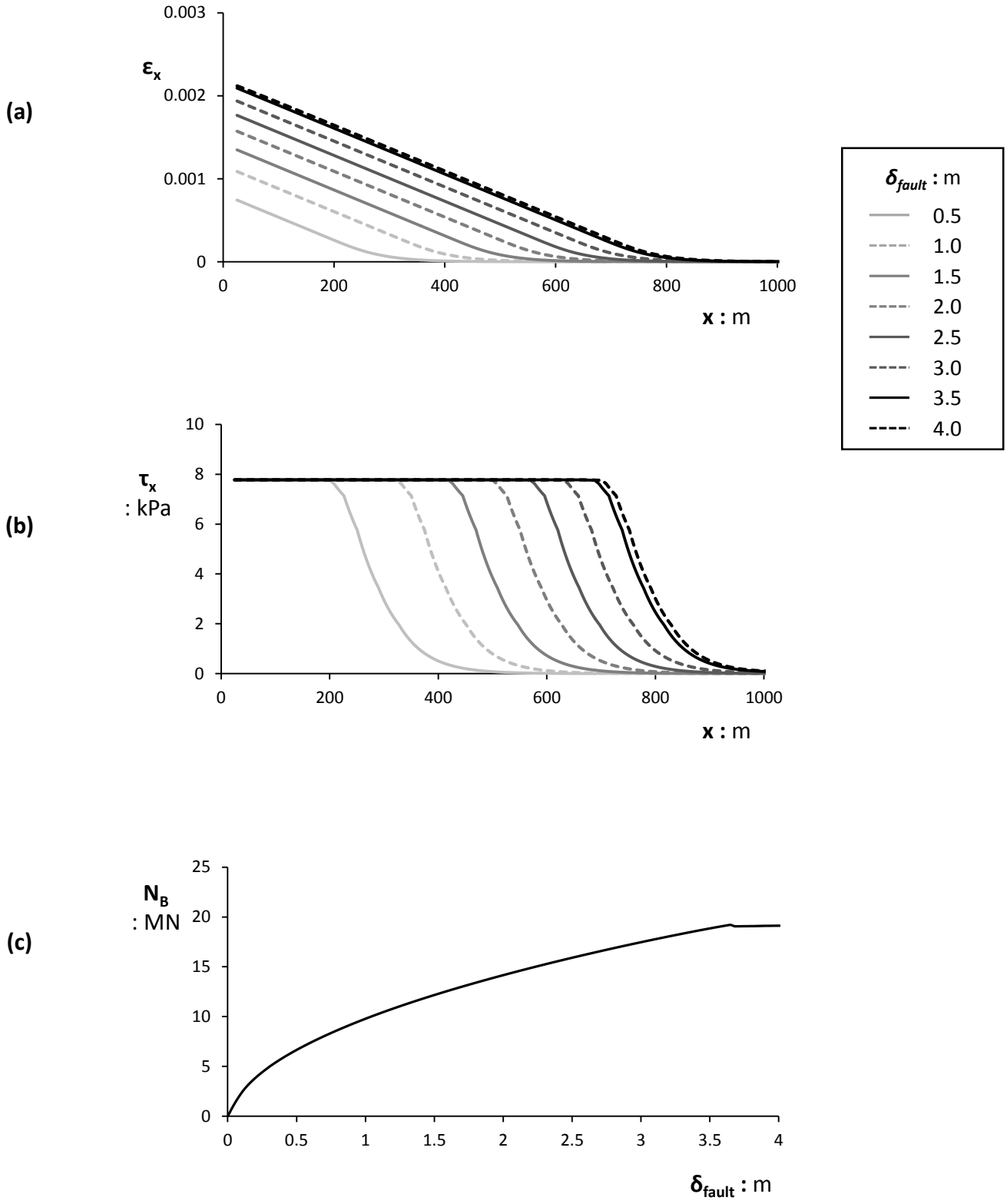

Fig. 2.15. Pipeline response in the 'far field': (a) axial strain distribution along the pipeline and (b) distribution of shear stresses at the pipe-soil interface for various fault offsets; (c) evolution of the axial force at point B (end boundary of the 'near-field' region) with fault offset.

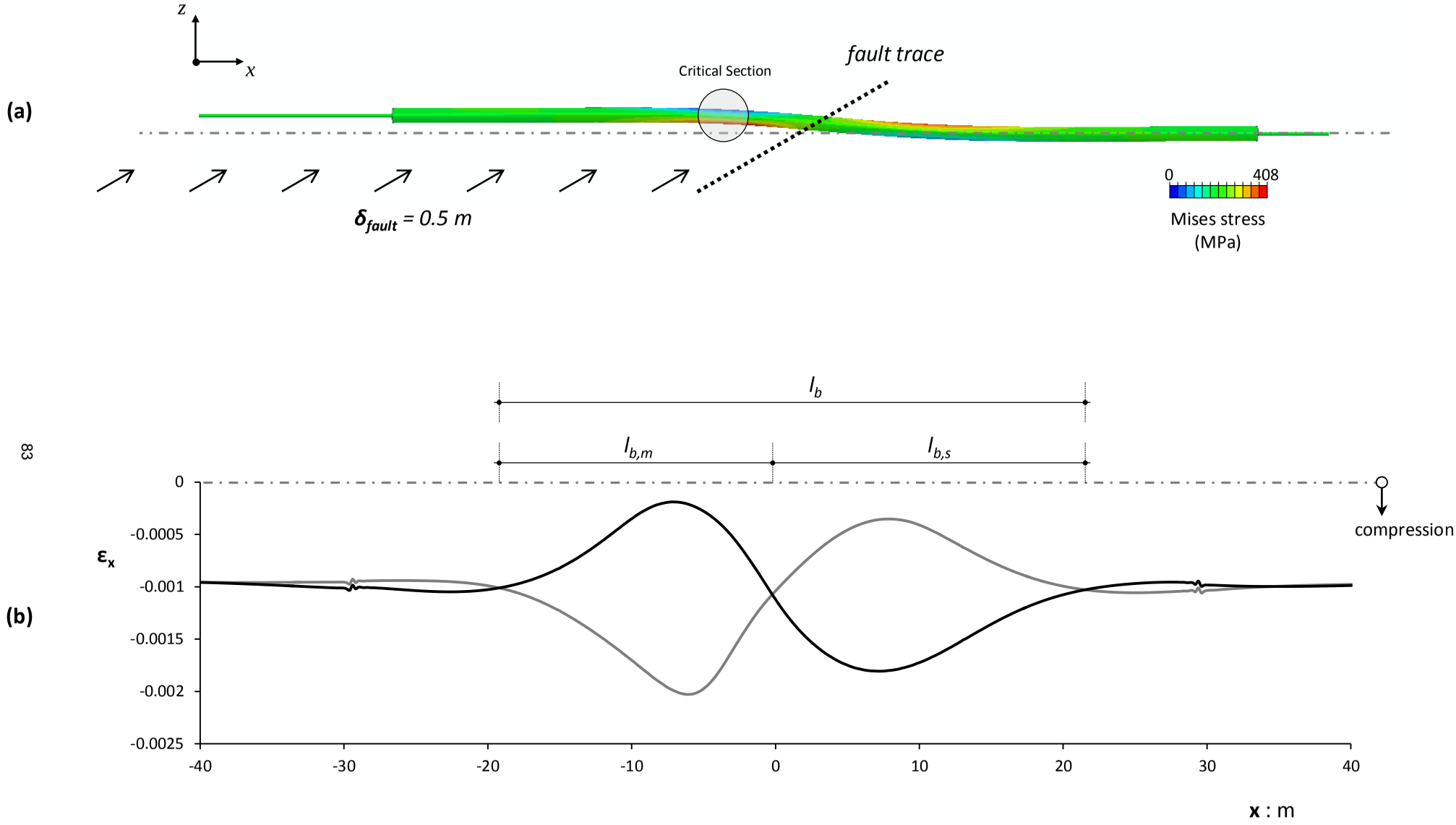

Fig. 2.16. Pipeline subjected to reverse fault: (a) deformed mesh of the pipeline at the vicinity of the fault with superimposed stress contours (scale factor=5) and (b) axial strain distribution along the top and bottom centerline for fault offset δ_{fault} = 0.5 m.

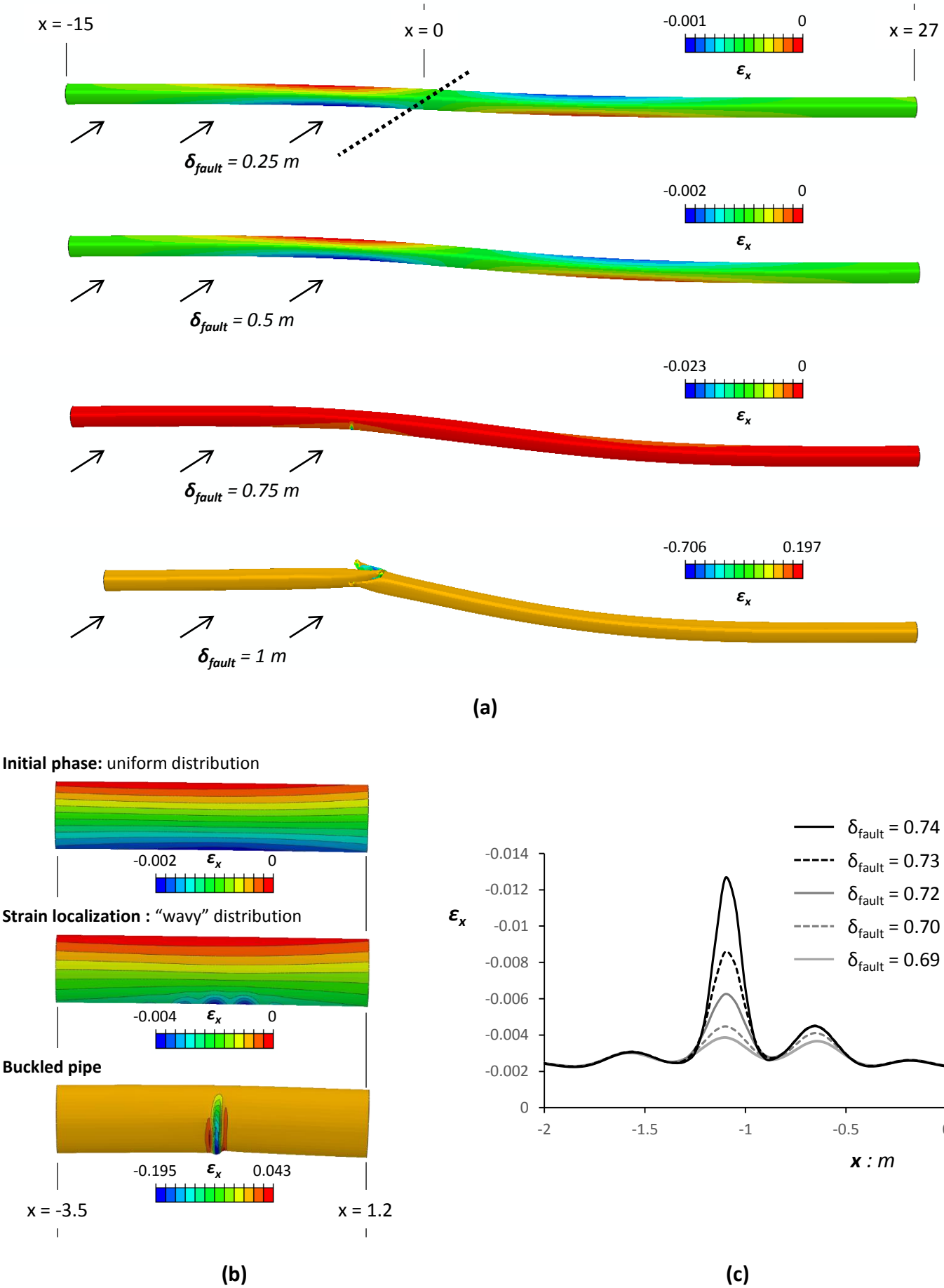

Fig. 2.17. Pipeline subjected to reverse fault: "near-field" response. (a) Deformed mesh of the pipe with axial strain contours for various magnitudes of fault offset (scale factor 5). (b) Deformed pipe segment in the vicinity of the critical section (scale factor 1) with axial strains depicting the evolution towards local buckling; (c) axial strain distribution at the compressive side of the pipe in the vicinity of the critical section.

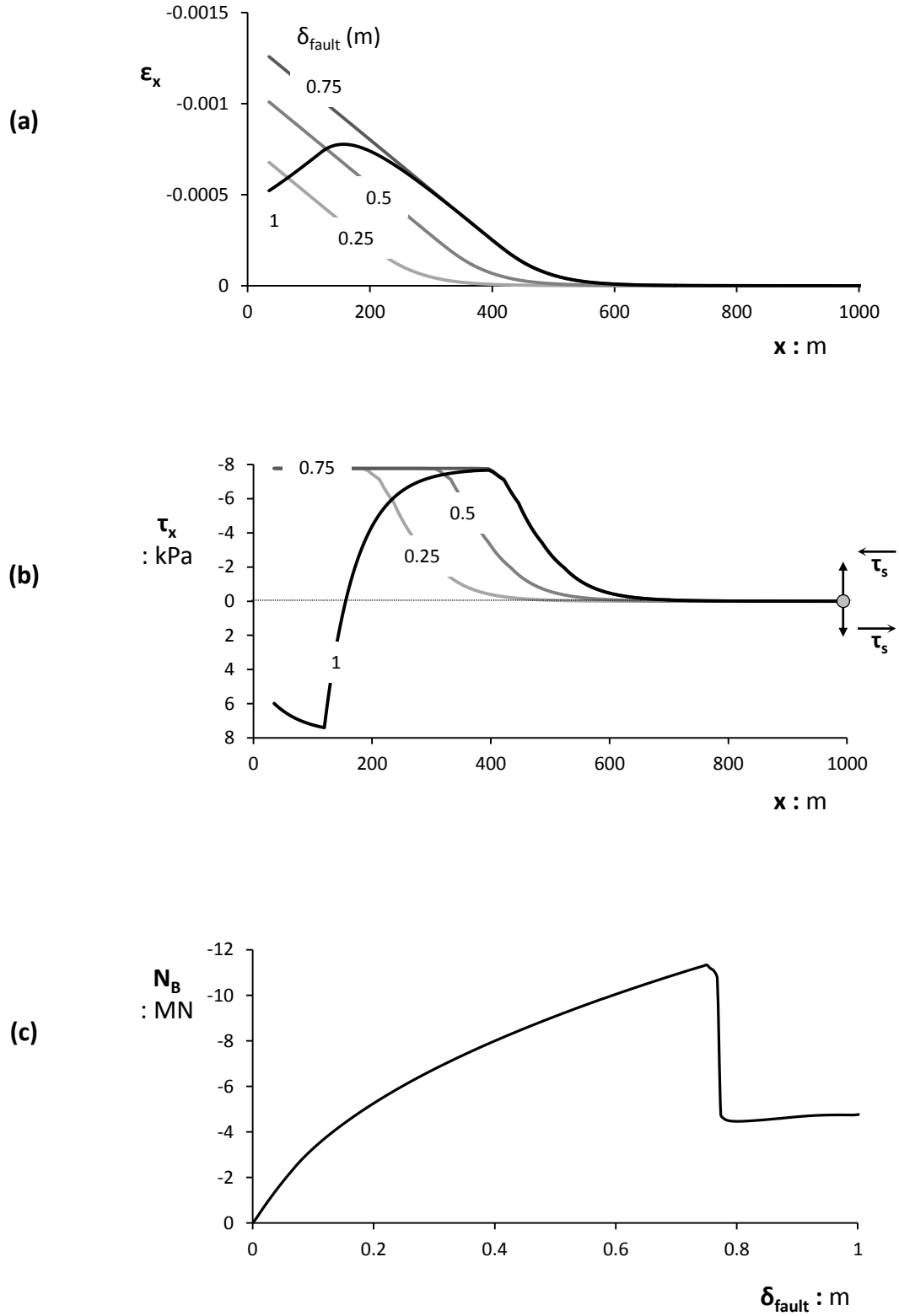

Fig. 2.18. Pipeline subjected to reverse fault: "far-field" response. (a) Axial strain distribution along the pipeline for various fault offset magnitudes. (b) Distribution of the shear stresses developed on the pipe-soil interface for the same fault offset magnitudes; (c) evolution of the axial force at point B (end of the central 3D-response region) with increasing fault offset.

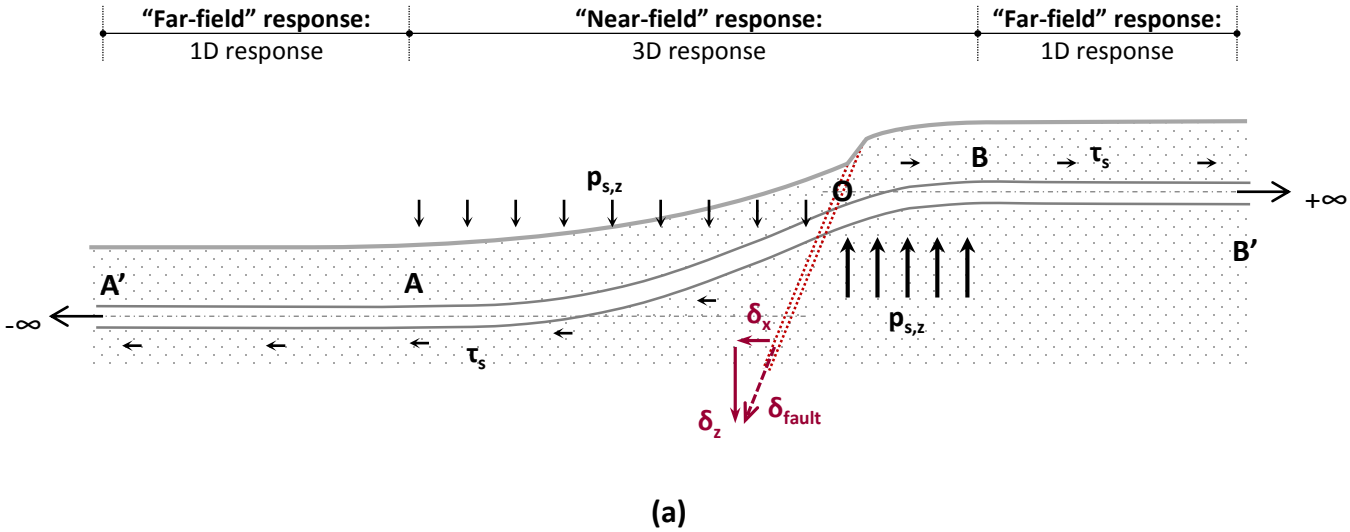

(a)

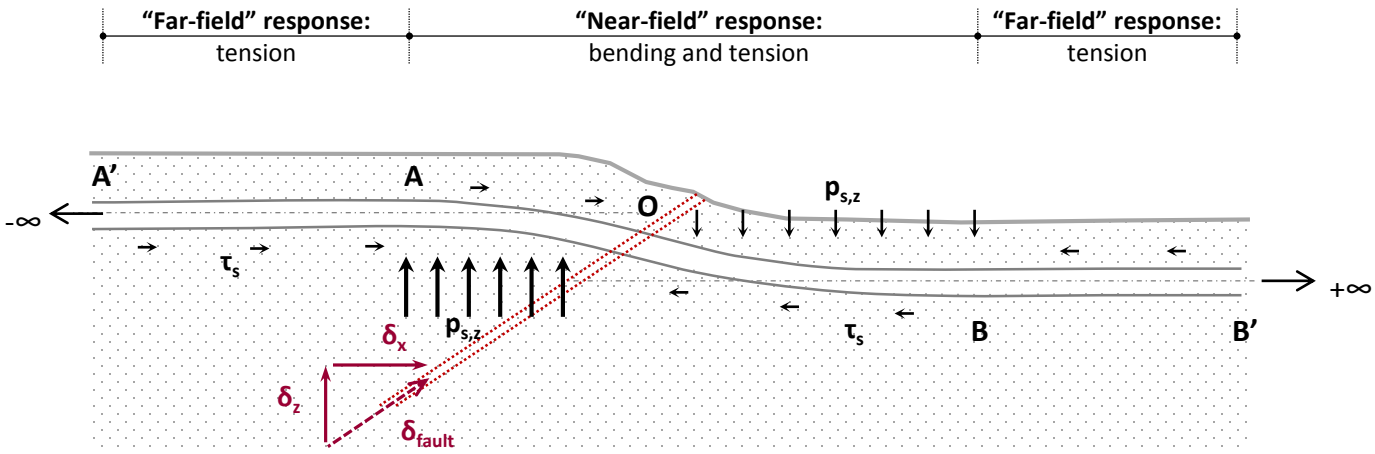

(b)

Fig. 2.19. Buried pipeline subjected to (a) normal and (b) reverse faulting. Three regions of distinctively different response may be recognized: a central region at the vicinity of the fault trace where the response is three-dimensional ("near-field" response), and two regions beyond the central one, within the footwall and within the hanging wall, where the pipe response is essentially one-dimensional ("far-field" response).

Chapter 3

Near-field response: Experimental Simulation of a buried pipe subjected to dip-slip faulting

3.1. Near-field response: an experimental investigation

This chapter studies the near-field response of a pipeline subjected to dip-slip faulting. Near the rupture zone, the soil deforms to accommodate the bedrock offset which forms a steplike landform. The pipeline on the other hand, resists the imposed displacement through its bending stiffness. Therefore, at the vicinity of the fault plane the pipe is subjected to a combined axial (tensile in case of normal faults and compressive in cases of reverse faults) and bending straining. **Fig. 3.1** presents schematically the deflection of a very long pipeline subjected to normal faulting. Beyond a narrow area in the vicinity of the fault, the relatively flexible pipeline eventually complies with the deformed soil pattern. Thus, the distress due to bending concentrates only in this limited length (denoted herein as l_b). It is in this length that the pipe may develop excessive tensile strains (or compressive strains in case of a reverse fault) and it may ultimately fail.

Hence, a numerical methodology aiming to simulate the pipeline response subjected to dip-slip faulting should place emphasis on accurately accounting for all the complicated phenomena occurring in this specific length. To this end, a series of experiments were conducted at the Laboratory of Soil Mechanics of National Technical University of Athens serving a dual purpose: firstly, to shed light on this near-field response of pipes subjected to dip-slip faulting, and secondly to provide a benchmark for the validation of our numerical tools.

3.2. Experimental Setup and Procedure

Simulation of the 'near-field' response should replicate precisely all possible fault rupture–soil–pipeline interaction phenomena, the inelastic response of materials (steel-soil), the rupture propagation through the upper soil strata, the geometric nonlinearities between the pipeline and the surrounding soil (i.e. sliding or loss of contact). To address these requirements, the experimental series was divided in three stages (presented in detail in **Fig. 3.2**). In the first stage, the rupture propagation was studied without the presence of a pipe, to focus on the nonlinear behavior of the soil during rupture

propagation. In the second stage the pipe–soil interaction problem was investigated parametrically. The reduced scale of the experiments introduced a number of scaling inconsistencies (refer to subsequent paragraphs of this Chapter) that impeded the experimental simulation of an actual fault-pipeline interaction problem. Thus we aimed for an experiment at least qualitatively similar to reality. To this end, a number of pipes of various diameter and thickness were subjected to normal and reverse fault movements to conclude with the most representative setup of an actual pipe–soil interaction problem. In other words, we were looking for a set-up where the model pipe was bending (rather than rotating) under the fault-induced displacements exhibiting the characteristic double-curvature deformation. The response of the pipe was not recorded during the experiment but its residual deformation was scanned after the end of the test using laser displacement transducers. Finally, in the third stage, the experiments with the most representative setups were repeated in order to measure in detail the pipeline staining using strain gauges along the pipeline length.

In this experimental series, no attempt was made to restrain the pipes axially. However, this choice was made in view of simplicity since on the one hand, fixing the pipes at the footwall and hanging wall boundaries would unacceptably affect the pipe behavior, while on the other hand adding an axial restrain such as a spring at both ends would add to complexity of the numerical analyses (regarding the restrain force, the connection between the spring and the pipe etc.).

The fault rupture box

This experimental series was conducted utilizing the Fault-Rupture Box of the NTUA Laboratory of Soil Mechanics (**Fig. 3.3**). This custom built apparatus has been designed to simulate quasi-static fault rupture propagation and Fault Rupture–Soil–Structure Interaction. It comprises a stationary and a movable part, which can move downwards or upwards to simulate normal or reverse fault conditions. The movable part is connected to a servo-mechanical screw-jack actuator, which can generate a maximum stroke of 20 mm in both directions. The dip angle α can be adjusted from 45^o to 90^o. For this experimental series, the dip angle was maintained at a=45^o, which is a reasonable value for both normal and reverse faults. The internal longitudinal dimension of the Fault Rupture Box is 2.65 m, its depth is 0.9 m, while the out-of-plane dimension is 0.9 m.

The soil material

Dry Longstone sand, an industrially produced fine and uniform quartz sand with d_{50} = 0.15 mm and uniformity coefficient $C_u = d_{60}/d_{10}$ = 1.42, are used in the experiments. The void ratios at the loosest and

densest state have been measured as e_{max} = 0.995 and e_{min} = 0.614, and the specific weight of the solids as G_s = 2.64. The respective gradation curve is shown in **Fig. 3.4a**.

Material and strength characteristics of the sand, as derived through a series of laboratory tests, documented in Anastasopoulos et al., (2010). The soil samples are placed within the Fault Rupture Box by dry pluviation with an electronically controlled sand raining system designed to produce soil samples of controllable relative density D_r (**Fig. 3.4b**). Two relative densities were selected for the purposes of this experimental series, D_r = 90 % and D_r = 60 %.

The pipe models

The pipe models were selected from a range of commercially available pipes. Three pipe materials were tested: (i) thick-walled steel pipes consisted of AISI Type 304 stainless steel, (ii) thick walled aluminum pipes consisted of Aluminum 6036 and (iii) thin-walled steel pipes of stainless steel grade AISI Type 444. The pipe specimens were also subjected to uniaxial tension tests to confirm stiffness-strength characteristics (**Fig. 3.5**).

Instrumentation

In order to record the pipe response within the soil, strains along the pipe were measured using 12 strain gauges. The strain gauges were 10 mm long, with resistance of 120 Ω and were temperature compensated (**Fig. 3.6a**). During the instrumented experiments they were placed at characteristic locations along the crown of the pipe (as shown in **Fig. 3.6b**), apart from one experiment, where they were placed in pairs, one on the crown and the other at the pipe invert. Each strain gauge was coated with scotch tape to protect the gauges from being dragged along by the moving soil around the pipe. The residual deformation of the pipe after the end of each experiment is scanned with laser displacement transducers. Laser displacement transducers were also used to measure the permanent ground deformation (**Fig. 3.7**). Finally, visual data were obtained using high definition cameras.

3.3. Presentation of the experimental results

Stage 1: Free field rupture propagation

Rupture propagation through the dense sand layers of relative density D_r = 90% was explored for normal and reverse fault types. **Fig. 3.8** portrays snapshots of rupture propagation process for various magnitudes of vertical base displacements δ_{vert}. Initially, the dislocation of the moving base provokes an

almost vertically propagating rupture. However, as revealed in the next snapshots, this is nothing but a localized secondary rupture attributed to the brittleness of the material that fails to accommodate the deformation in a quasi-elastic manner in this specific area. This localized rupture unfortunately conceals the main rupture until it finally emerges at the surface, for vertical bedrock dislocation δ_{vert} = 12 mm. By increasing the imposed bedrock displacement to more than δ_{vert} = 20 mm we may observe the development of a secondary antithetic rupture. This secondary rupture reaches the surface at δ_{vert} = 26 mm. As the bedrock displacement increases further, deformation accumulates along these two ruptures, without any additional change on the rupture pattern. Between the primary and secondary rupture a clear gravity graben is formed.

Snapshots for reverse faulting are presented in **Fig. 3.9**. Contrary to the normal fault loading, the soil deposit exhibits a more ductile behavior, accommodating the dislocation at its base in a quasi-elastic manner up to approximately δ_{vert} = 15 mm. At this point a clear shear band is formed that eventually reaches the surface at a δ_{vert} = 25 mm. Of particular interest is the fact that the rupture bends significantly towards the footwall as it propagates towards the surface. This should be attributed to scale effects: as it will be shown later on in detail, as the overburden stresses tend to zero the effective friction and dilation angle of the sand catapults. As a result, the bending of the rupture path that (for a given dip angle at the soil base) is a function of the dilation angle (Anastasopoulos et al. 2008) becomes more intense.

Experiments on a looser soil profile were also employed. This profile consists of Longstone sand placed within the Fault Rupture Box at relative density of D_r=60%. Results for the loose sand scenario are portrayed in **Fig. 3.10**. In comparison with the denser soil profile the rupture emerges at the surface for a significantly larger bedrock dislocation (approximately δ_{vert}=35 mm).

Stage 2: Preliminary soil-pipeline tests

During these preliminary tests, various parameters were tested to select the configuration that would produce the most useful results, i.e. results that are in qualitative consistency with how we expect a real pipeline to respond when subjected to normal or reverse fault movement. Amidst the parameters under investigation were the pipe diameter and material, the interface condition between pipe and soil, and the burial depth within the fault rupture box.

The main conclusions drawn from this group of experiments can be summarized in the following.

- To achieve similitude of the soil–pipeline interaction forces (i.e. same stiffness and strength ratio between the experiment and the prototype), the pipe should be placed at "realistic" cover depths. Consider the case where the model pipe is placed at a reduced (according to the scale) depth (e.g. 1 to 2 times the diameter which is rather common for hydrocarbon transportation pipelines). Since the experiments are performed in 1 g, the stiffness and strength of the sand is drastically decreased with the decrease of the depth. To maintain the same ratio of pipe to soil stiffness a decrease of the pipe stiffness analogous to the decrease of the soil stiffness should be considered. **Fig. 3.11a** shows the inadequacy of the configuration according to which metal pipes are placed at small depth). In that case, flexible materials such as plastic should be adopted for the pipe, however, it was a basic requirements for these experiments to be performed on metal pipes. Hence, depths larger than 0.5 m were necessary to be realistic.
- The pipes of diameter 50 mm did not exhibit the desired response, mainly when subjected to normal fault. The larger the pipe diameter, the larger length is needed for the pipe to be effectively fixed within the hanging wall in order to bend rather than simply rotate. Because of the limited fault rupture box dimensions, there is an upper bound to the pipe diameter that can be used.
- The friction coefficient of the interface between the pipe and the soil did not appear to play an important role on the pipe performance. The pipe length within the fault rupture box proves to be too small for the shear stresses on the interface to produce a substantial axial force.
- The more flexible aluminum pipe appears to be far more compliant to the imposed displacement compared to the steel pipe; a favorable attribute that solved many problems arising from the limited length of the box (**Fig. 3.11b**).

Stage 3: Fully instrumented (soil-pipeline) tests

In this set of experiments we have tested the most efficient setups (of Stage 2) fully recording the pipe response. Eight (8) experiments were performed on steel and aluminum thick-walled pipes of diameter D = 10 mm and thickness t = 1 mm, and on steel thin-walled pipes with D=35 mm and thickness t = 0.5 mm. Among these, the results of the thick-walled aluminum pipe subjected to normal and reverse fault and the results for the steel thin-walled pipe subjected to normal and reverse fault are presented herein.

Fig. 3.12 summarizes the results of the experiment #21. An aluminum pipe of diameter D = 10 mm and thickness t = 1 mm was buried at depth z = 550 mm within dense sand of relative density D_r = 90%, and it was subjected to **normal** faulting. **Fig. 3.12a** shows a picture of the pipe after the completion of the experiment and its removal from the rupture box. Although much of the elastic part of the deformation was regained after the pipe was unearthed, the characteristic double curvature deformation is still evident. **Fig. 3.12b** and **Fig. 3.12c** present the strain distribution along the crown of the pipe as it was measured for various magnitudes of fault offset. **Fig. 3.12b** refers to vertical fault offsets from h=5 mm to δ_{vert}=30 mm (showing results for all the fault offsets in between those two with a step of 5 mm), while **Fig. 3.12c** refers to larger vertical fault offsets (from δ_{vert} =30 mm to δ_{vert} =100 mm with a step of 10 mm). The pipe bends under the fault-induced displacements, acquiring the characteristic double-curvature deflection. The top side of the maximum curvature point within the hanging wall is under compression (negative axial strains), while the top side of the respective point within the footwall is under tension (positive axial strains). Between those two points, the one within the hanging wall is significantly more stressed. The length within which the pipe bends to accommodate the differential displacement is about l_b = 800 mm.

Fig. 3.13 presents the respective results for the experiment #22, where a similar aluminum pipe buried in dense sand is subjected to **reverse** faulting. **Fig. 3.13a** shows the residual deformation of the pipe after the completion of the test. **Fig. 3.13b** and **Fig. 3.13c** present the axial strains measured on the crown of the pipe during the experiment for various magnitudes of fault displacement. Compared to normal fault experiment, the strain distribution is reversed: the top side of the maximum curvature point within the hanging wall is under tension while the respective point within the footwall is under compression. As expected, the most distressed point is the one within the hanging wall, since it is stressed by the reaction of the underlying soil (as opposed to the maximum curvature point within the footwall that is stressed by the reaction of the overlying soil). The pipe is bended within a smaller length (compared to the normal fault case) l_b=700 mm –an indication that its relative stiffness is reduced when subjected to reverse faulting, leading to a more compliant response and to increased vulnerability.

Fig. 3.14 presents the pipe response during the experiment #23, where an aluminum pipe of D=10 mm and thickness t=1 mm was buried in medium dense sand of D_r=60% and was subjected to reverse fault. **Fig. 3.14a** presents a picture of the deformed pipe after the experiment, while **Fig. 3.14b** and **Fig. 3.14c** present the strain measurement along the pipe crown for various magnitudes of fault offset. It is interesting to notice the increase of the pipe relative stiffness compared to the case where it is buried in

dense sand, as it is expressed by the increase of the length where the pipe bends in order to accommodate the vertical differential displacement (from $l_b \approx 700$ mm to $l_b \approx 900$ mm).

Pipes of smaller diameter were expected to achieve enhanced fixity conditions at the two ends of the pipe (at least concerning the vertical displacement degree of freedom). Yet, such pipes inevitably come with small *D/t* ratios that are not representative of real pipelines. In order to investigate the response of pipes of larger *D/t* ratios steel pipes of diameter $D = 35$ mm and thickness $t = 0.5$ mm were selected. The *D/t* ratio of the latter allows for the development of structural instability phenomena, with particular emphasis on local buckling. **Fig. 3.15** summarizes the response of the thin-walled pipe buried in dense sand of $D_r = 90\%$ and subjected to normal fault (experiment #25). As expected, the pipe hardly exhibits a double curvature deformation, with the strains developing on the curvature point within the footwall lying within the elastic range (observe **Fig. 3.15b** for the strains measurements at the crown). Nonetheless, due to bending at maximum curvature point the pipe has buckled at the bottom (compressive) side (**Fig. 3.15a**). **Fig. 3.16** presents a summary of the response of the same pipe buried in dense sand and subjected to reverse faulting. The pipe in this case appears to be much more compliant to the imposed differential displacement than in the case of normal fault as it is depicted in **Fig. 3.16a**. The two maximum curvature points are evident, with the pipe having buckled at the compressive side of both points. **Fig. 3.16b** presents the axial strain distribution along the crown of the pipe for various magnitudes of fault offset. It is interesting to observe that the effective pipe length $l_b \approx 1500$ mm, normalized with the pipe diameter yields $l_b/D \approx 40$, which is substantially smaller than the respective normalized length of the aluminum pipe of diameter $D = 10$mm subjected to normal fault in the same sand $l_b/D \approx 700$mm/10mm = 70, despite the fact that the aluminum pipe is more flexible than the steel pipe. This is an evidence that the length of the "near-field" response is affected by the *D/t* ratio, and in fact, it decreases with the increase of the *D/t* ratio.

3.4. Numerical Simulation of the Laboratory Experiments

The presented experimental results are used herein to validate our numerical methodology developed for the representation of the near-field response. Two representative experiments (from the group of the fully instrumented experiments), are simulated: the thin-walled steel pipe subjected to normal and reverse fault (experiments #25 and 26). The experiments are simulated at laboratory scale. Details of the numerical model are presented in **Fig. 3.17**. The entire length and height of the soil

deposit is simulated, while in the transversal direction the boundaries are placed at distance 10 times the diameter to avoid any boundary-related effects. The pipe is finely meshed with element size of d_{FE}=1 mm along the critical regions.

In order to accurately capture the evolution of rupture propagation and the creation of the shear band, a nonlinear constitutive model with Mohr-Coulomb failure criterion and strain softening (described in detail in Chapter 3) is employed. The constitutive model parameters are calibrated to replicate the behavior of Longstone sand during direct shear testing for various levels of vertical effective stress σ_v varying from 15 to 300 kPa. **Fig. 3.18a** presents the results of these direct shear tests and the comparison with the finite element prediction. The direct tests also revealed a strong dependence of the mobilized friction and dilation angle on the effective stress level (**Fig. 3.18b**). The measured peak and residual internal friction angle of the dense sand specimens were increasing as the vertical effective stress decreased: for small stresses (σ_v<15 kPa) the mobilized friction angle goes well above φ=50°.

For small-scale experiments, where the depth of the soil deposit is low, the simulation of this behavior is crucial. In our test series, the maximum soil depth was a mere 0.65 m. Considering a density ρ = 1.6 kg/m^3, the maximum initial vertical stress at the bottom of the rupture box is σ_v = 10.2 kPa. Unfortunately, the exact properties of the sand at such small stresses could not be measured experimentally with the available testing apparatus (the minimum possible vertical stress is σ_v = 15 kPa). Therefore, the strength properties of the sand are extrapolated from the measured values assuming a power function dependency as follows:

$$\varphi_{peak}(\sigma_v) \approx 70.8\sigma_v^{-0.131} \quad (1)$$

$$\varphi_{res}(\sigma_v) \approx 54.5\sigma_v^{-0.10} \quad (2)$$

Presentation of the Results

The 3D finite element captures nicely the rupture propagation in the case of normal faulting (experiment #25), as illustrated in **Fig. 3.19**. **Fig. 3.19a** presents a comparison of the rupture propagation during the experiment with the numerical prediction. The bottom row shows the deformed mesh of the numerical model with plastic strain contours depicting the rupture formation and propagation at representative magnitudes of vertical offset *h*. On the top of each snapshot, a picture of the experiment at the same fault offset is presented for comparison. The numerical methodology predicts quite accurately all the mechanisms observed during the experiment: the practically vertical rupture for small bedrock displacements (δ_{vert} < 10 mm), the appearance of the main rupture and its emergence to the

surface at δ_{vert} = 15 mm, and finally the generation of an antithetic rupture and the formation of the graben for δ_{vert} = 25 mm. As demonstrated by **Fig. 3.19b** the numerical methodology also succeeds in predicting the actual magnitude and spatial distribution of ground settlement.

The numerical simulation of the pipeline response is also quite successful. **Fig. 3.20** compares the numerically predicted pipe response with the measured response during the experiment. As depicted in **Fig. 3.20a** the overall deformation pattern of the pipeline is nicely captured, while the numerical model even predicts the exact location and shape of local buckling. The numerical strain distribution at the top of the crest of the pipe is successfully compared to the measured strains in **Fig. 3.20b** (with the small exception of the overprediction of the peak strain at δ/D = 2). The good overall agreement verifies the appropriateness of our numerical methodology to rigorously simulate the complex pipeline-soil interaction under normal faulting.

The numerical results for the simulation of the reverse faulting (experiment #26) are presented in **Figs. 3.21-3.22**. As previously, **Fig. 3.21a** portrays the numerically predicted rupture propagation, and compares it with the experimental behavior. The replication of the experiment is fairly precise: the rupture path is closely captured along with the magnitude of bedrock displacement that provokes fault trace emergence in the ground surface. **Fig. 3.21b** shows the comparison of the displacement distribution along the surface which further justifies for appropriateness of the numerical simulation. Most importantly, the numerical methodology captures the distress of the pipe. Proof is presented in **Fig. 3.22a** where the deformed pipe mesh is visually compared to the actual deformed pipe after the experiment, and in **Fig. 3.22b** where the numerical axial strain distribution along the crown of the pipe is compared to the strain measurements. Evidently, the numerical model predicts the location of the two maximum curvature points, the formation of local buckling at these two points, and the overall strain distribution along the entire pipe length.

3.5. Conclusions

A series of experiments were conducted using the Fault-Rupture Box of the Laboratory of Soil Mechanics on pipes subjected to normal and reverse faulting. The main scope of these experiments was to provide the necessary data for the validation of the numerical methodology proposed for the description of the 'near-field' response of pipelines subjected to fault-induced displacements. Indeed the numerical predictions compare very well to the experimental results for both normal and reverse

fault. The evolution of fault rupture propagation as well as the pipeline distress are captured in great detail.

References

Anastasopoulos I., Georgarakos T., Georgiannou V., Drosos V., Kourkoulis R. (2010), "Seismic Performance of Bar-Mat Reinforced-Soil Retaining Wall: Shaking Table Testing versus Numerical Analysis with Modified Kinematic Hardening Constitutive Model", *Soil Dynamics & Earthquake Engineering, 30*(10): 1089–1105.

Anastasopoulos I., Gerolymos N., Gazetas G., and Bransby M. F. (2008), "Simplified approach for design of raft foundations against fault rupture. Part I : Free-field", *Earthquake Engineering and Engineering Vibration*, 7: 147–163

Figures

of Chapter 3

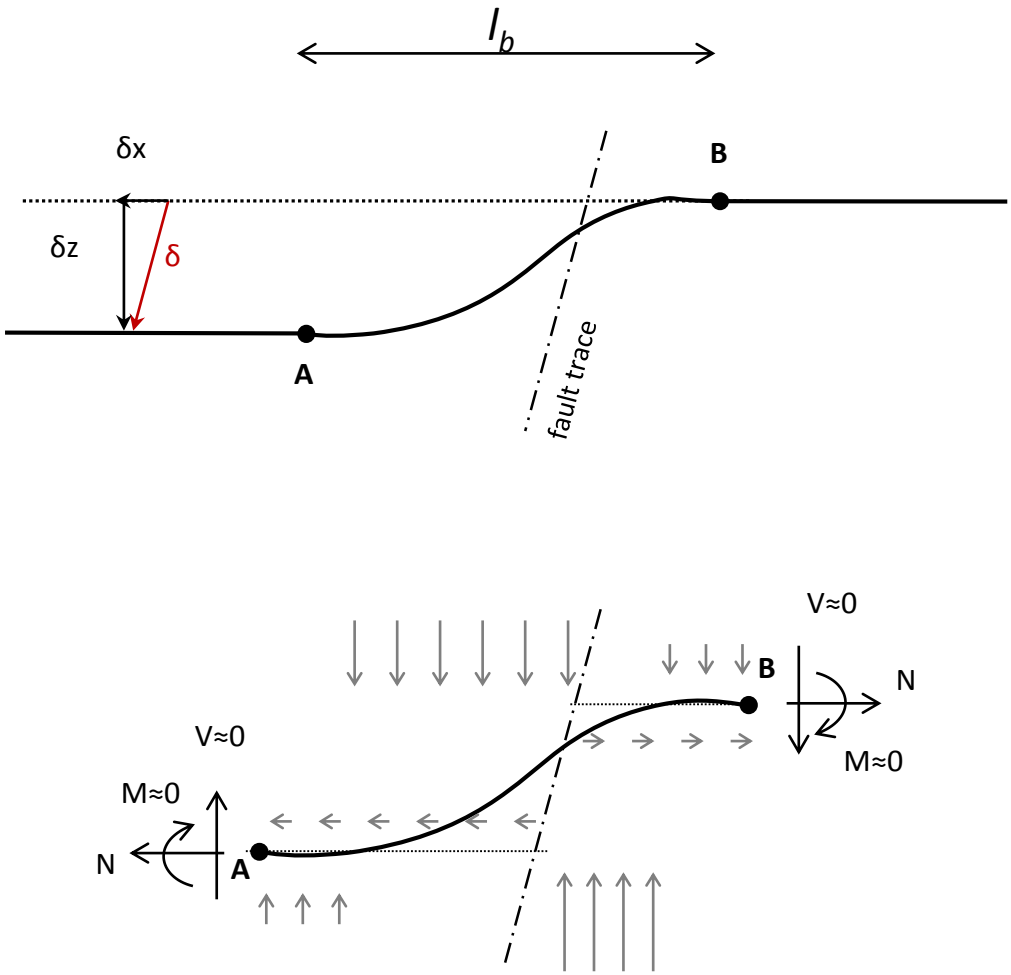

Fig. 3.1. Stressing of an infinitely long pipeline subjected to normal faulting. Near the fault plane the soil acquires a step-like deformation, while the pipe resists to this deformation with its bending stiffness.

exp #	*fault type*	D_r	*pipe material*	*D x t (mm x mm)*	*z (mm)*
free field rupture propagation tests					
1	normal	90 %	-	-	-
2	reverse	90 %	-	-	-
3	reverse	60 %	-	-	-
preliminary tests					
4	normal	90 %	AISI Type 304 stainless steel	50 x 1.5	-100
5	normal	90 %	AISI Type 304 stainless steel	30 x 1	-100
6	normal	90 %	Aluminum 6036	50 x 1.5	-100
7	normal	90 %	AISI Type 304 stainless steel	50 x 1.5	-550
8	normal	90 %	AISI Type 304 stainless steel	30 x 1	-550
9	normal	90 %	Aluminum 6036	50 x 1.5	-550
10	normal	90 %	AISI Type 304 stainless steel	20 x 1	-300
11	normal	90 %	AISI Type 304 stainless steel	20 x 1	-550
12	normal	90 %	AISI Type 304 stainless steel	10 x 1	-550
13	normal	90 %	AISI Type 304 stainless steel	10 x 1	-300
14	normal	90 %	Aluminum 6036	22 x 1	-300
15	normal	90 %	Aluminum 6036	22 x 1	-550
16	normal	90 %	Aluminum 6036	10 x 1	-550
17	reverse	90 %	AISI Type 304 stainless steel	10 x 1	-550
18	reverse	90 %	Aluminum 6036	10 x 1	-550
fully instrumented tests					
19	normal	90 %	AISI Type 304 stainless steel	10 x 1	-550
20	reverse	90 %	AISI Type 304 stainless steel	10 x 1	-550
21	normal	90 %	Aluminum 6036	10 x 1	-550
22	reverse	90 %	Aluminum 6036	10 x 1	-550
23	reverse	60 %	Aluminum 6036	10 x 1	-550
24	reverse	60 %	Aluminum 6036	10 x 1	-550
25	normal	90 %	AISI Type 444 stainless steel	35 x 0.5	-550
26	reverse	90 %	AISI Type 444 stainless steel	35 x 0.5	-550

Fig. 3.2. Experimental pipe-faulting interaction investigation : Table of Experiments

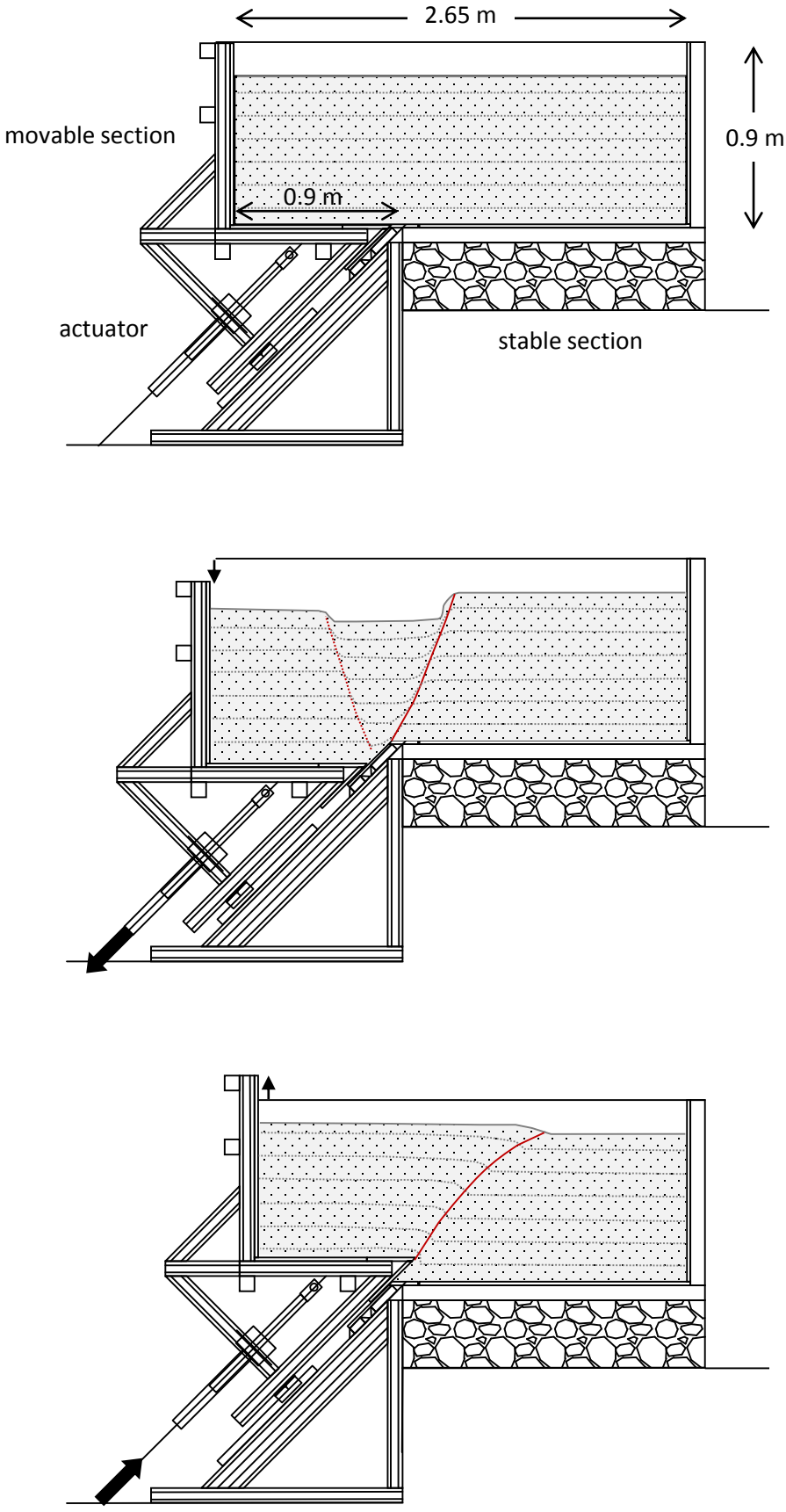

Fig. 3.3. The Fault Rupture Box of the Laboratory of Soil Mechanics. This apparatus is used to simulate quasi-static fault rupture propagation.

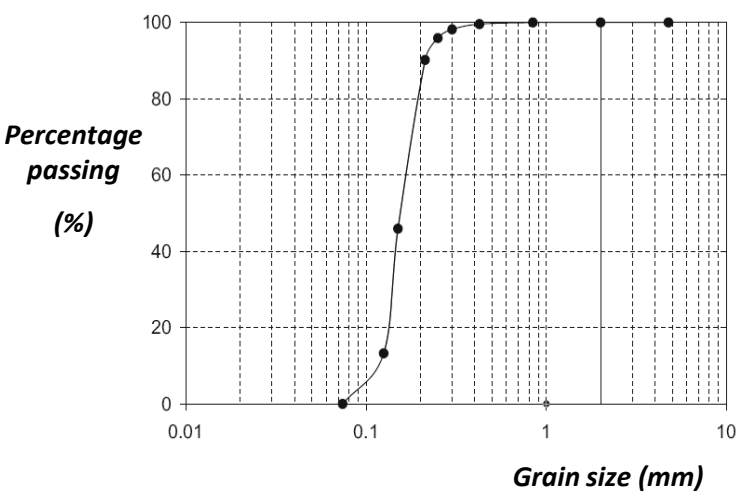

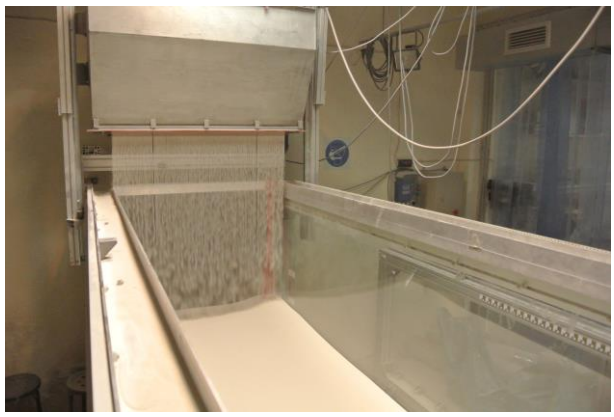

(a) **(b)**

Fig. 3.4. (a) The gradation curve of the Longstone sand used in the experiments. (b) The electronically controlled sand raining system used to produce soil samples of controllable relative density.

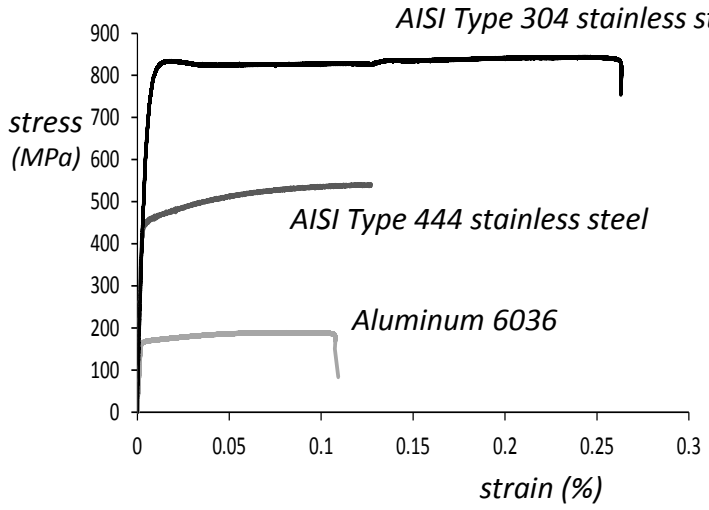

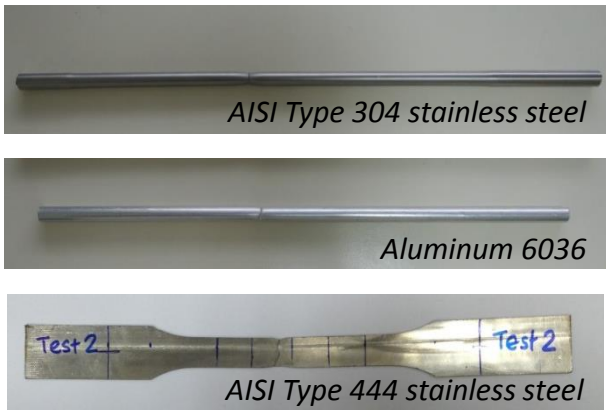

(a) **(b)**

Fig. 3.5. Specimens from pipes were subjected to uniaxial tension tests in order to accurately measure the stress–strain relation. (a) The stress–strain relation derived from uniaxial tensile tests. (b) View of the three specimens after the tests.

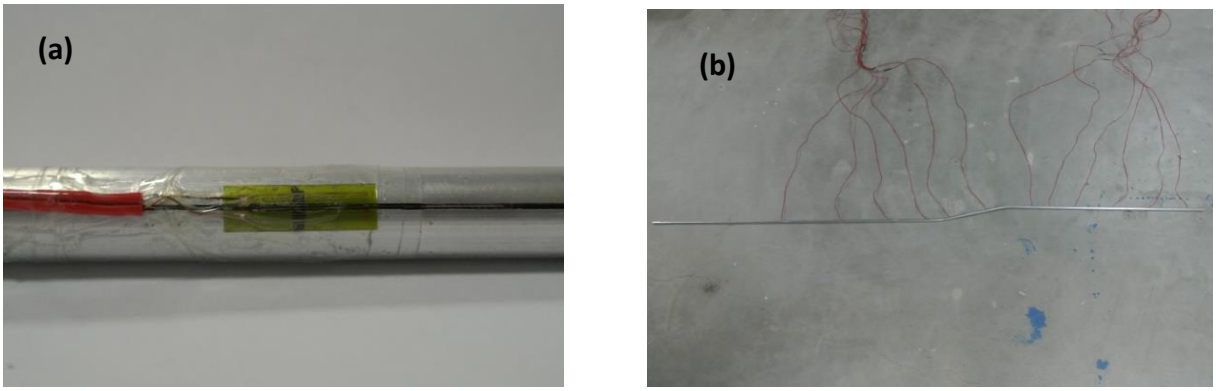

Fig. 3.6. (a) Close photo of one of the strain gauges used in this experimental series to measure strains along the pipe. (b) In all cases but one, all the strain gauges were placed at characteristic locations along the pipe crown.

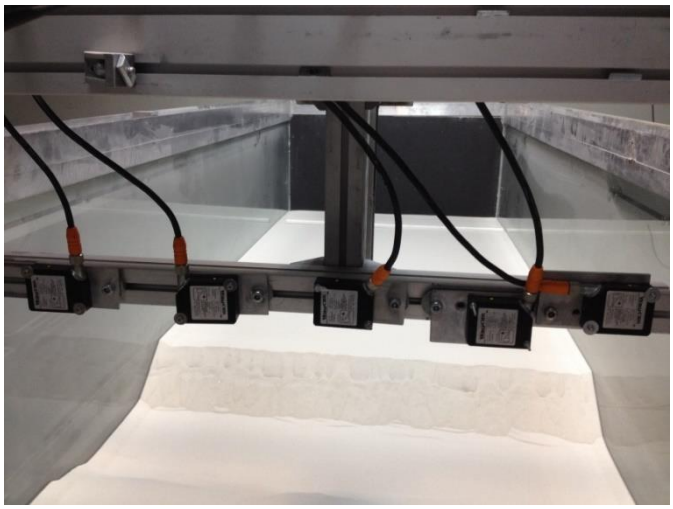

Fig. 3.7. Measurement of permanent ground deformation: five laser displacement transducers are implemented to scan the surface.

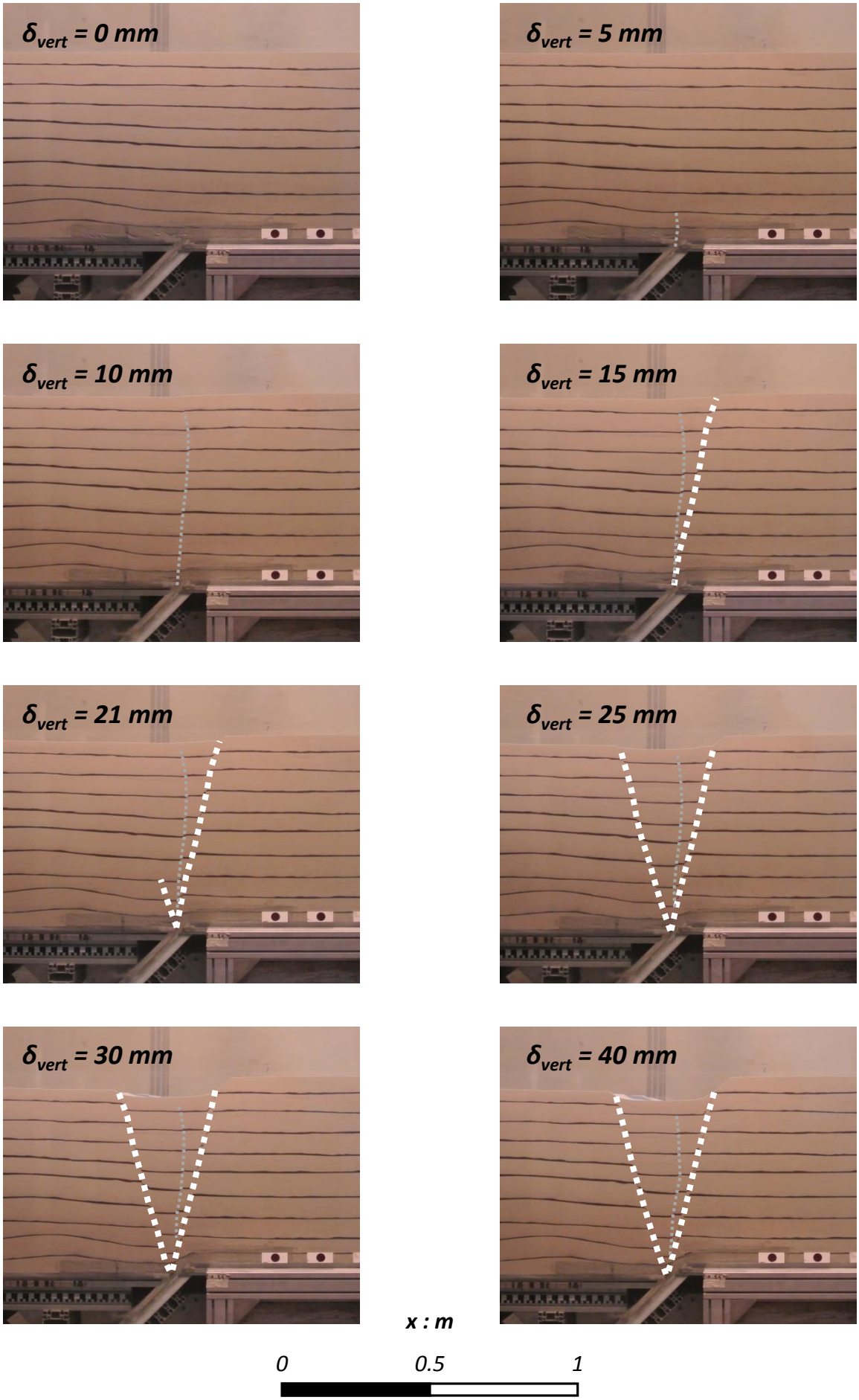

Fig.3.8. Snapshots of normal fault rupture propagation through dense sand (D_r = 90%).

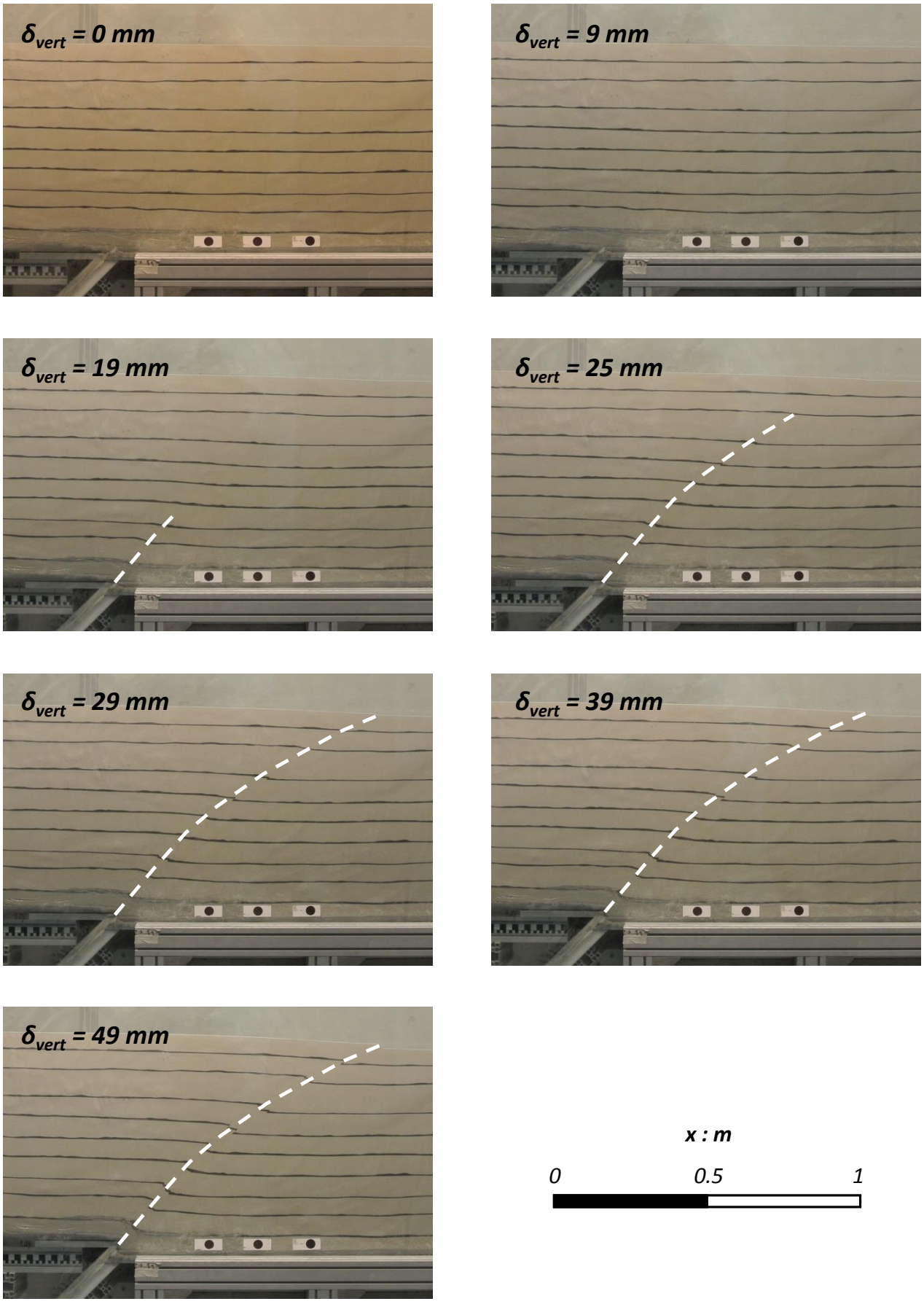

Fig. 3.9. Snapshots of reverse fault rupture propagation through dense sand (D_r = 90%).

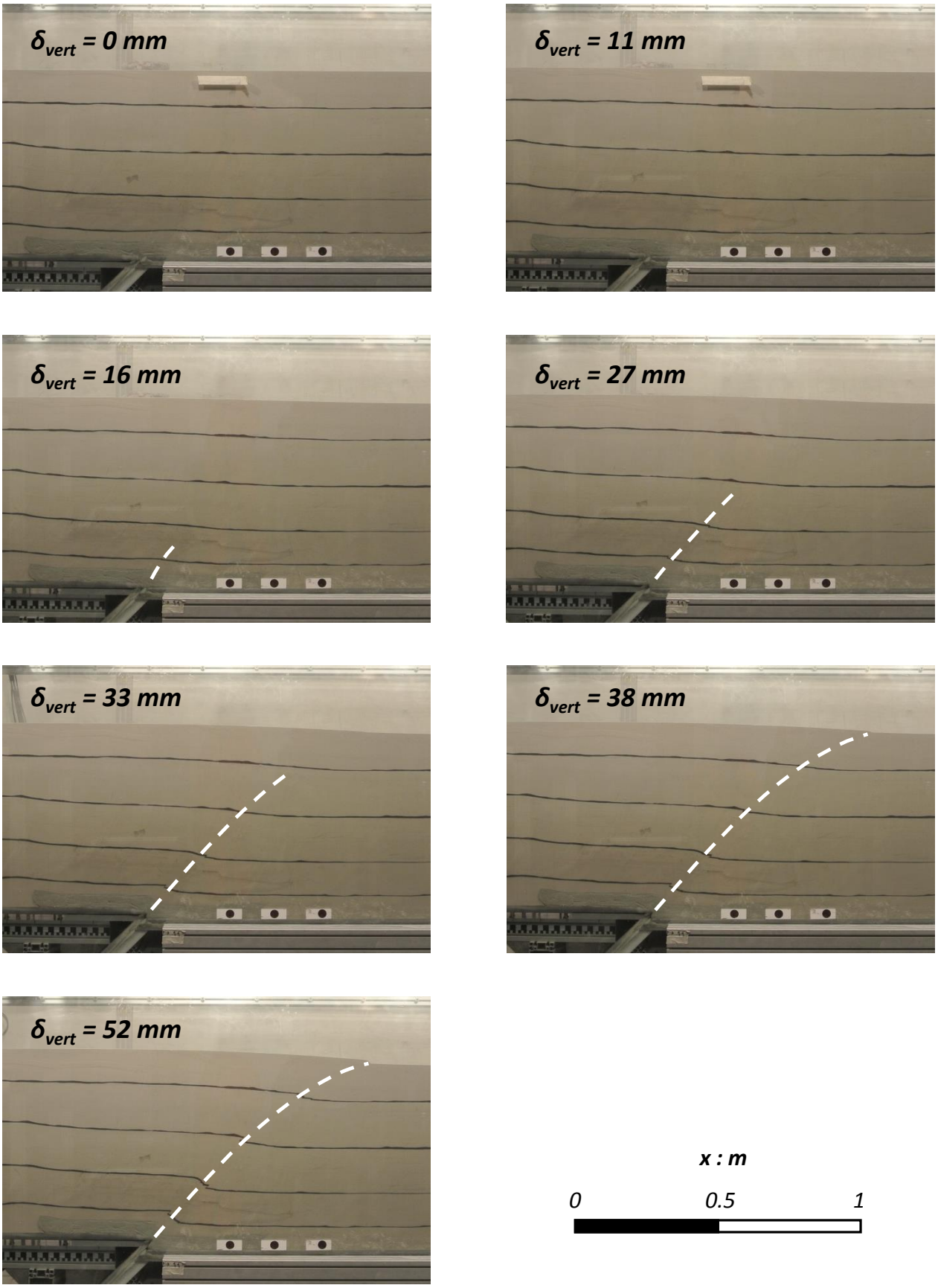

Fig. 3.10. Snapshots of reverse fault rupture propagation through medium dense sand (D_r = 60%).

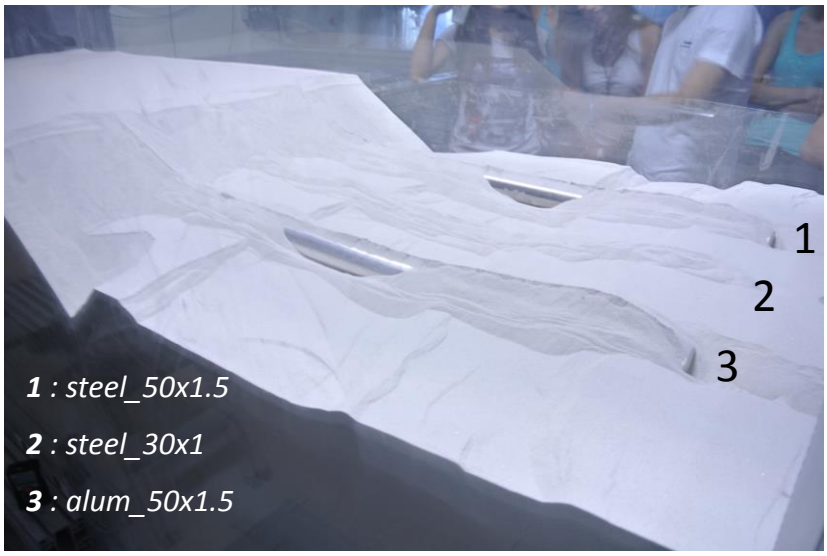

(a)

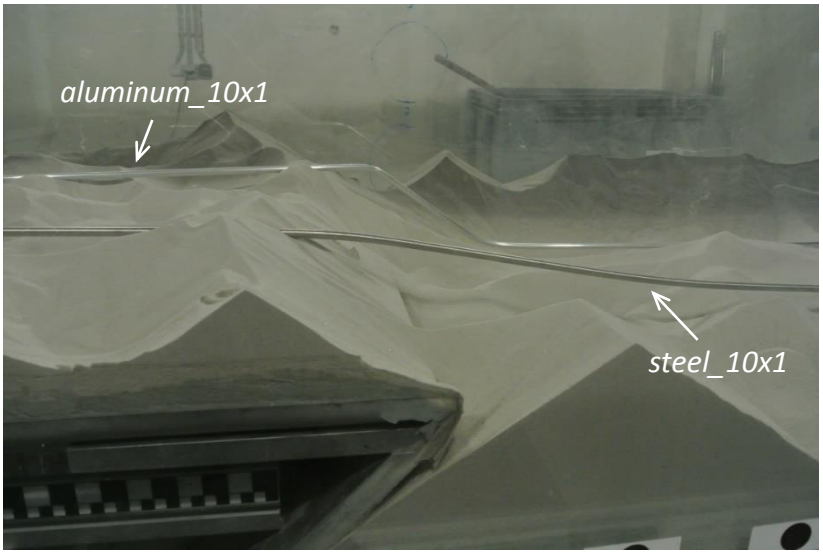

(b)

Fig. 3.11. Pictures from the preliminary test series : (a) Picture of the deformed pipes placed at depth equal to 2 ÷ 3 times the diameter. This configuration proves that the pipes should be placed at larger depths to achieve realistic soil-pipeline interaction forces. (b) Picture of the preliminary test where the effect of the pipe material is investigated (Aluminum 6036 pipe vs AISI Type 304 stainless steel pipe).

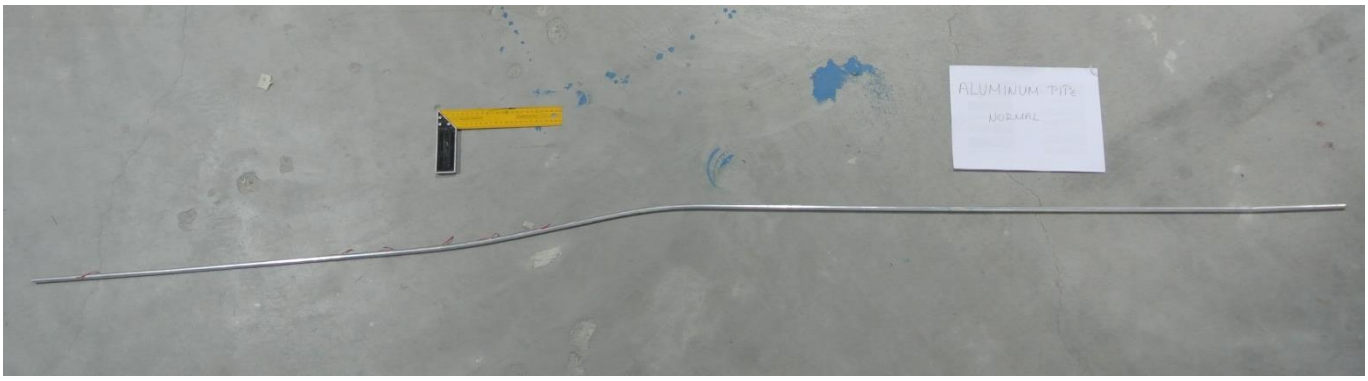

(a)

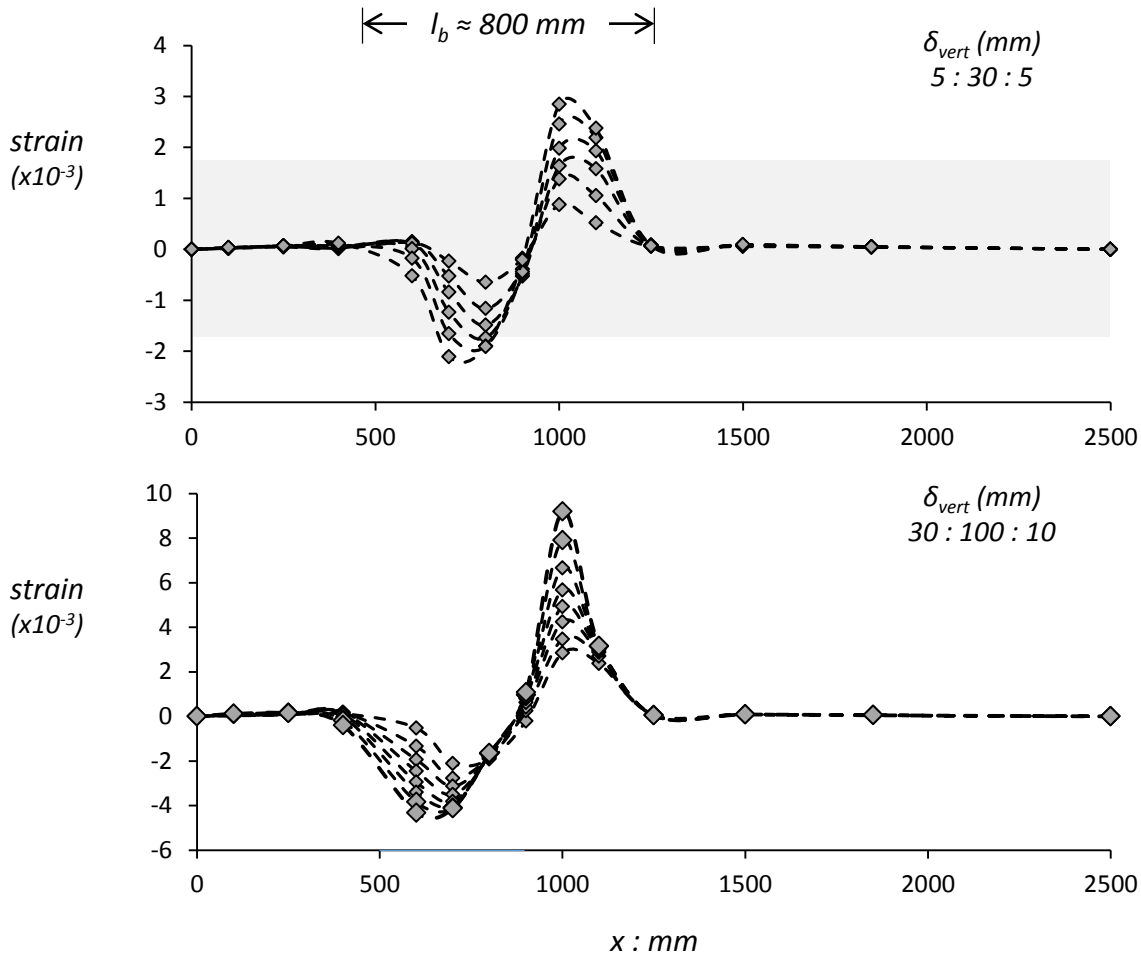

(b)

Fig. 3.12. (a) Residual deformation of the aluminum pipe subjected to normal fault of total vertical offset δ_{vert} = 150 mm. (b) Strain distribution along the crown of the aluminum pipe of diameter D = 10 mm and thickness t = 1 mm embedded in sand of relative density D_r = 90 % subjected to normal faulting for various magnitudes of vertical fault offset.

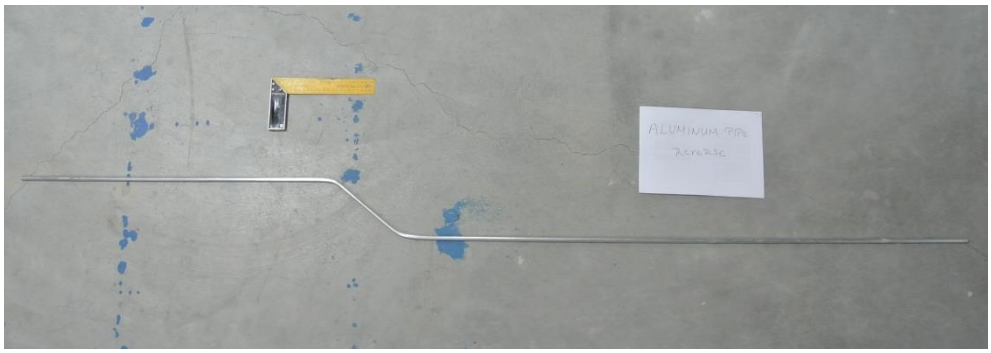

(a)

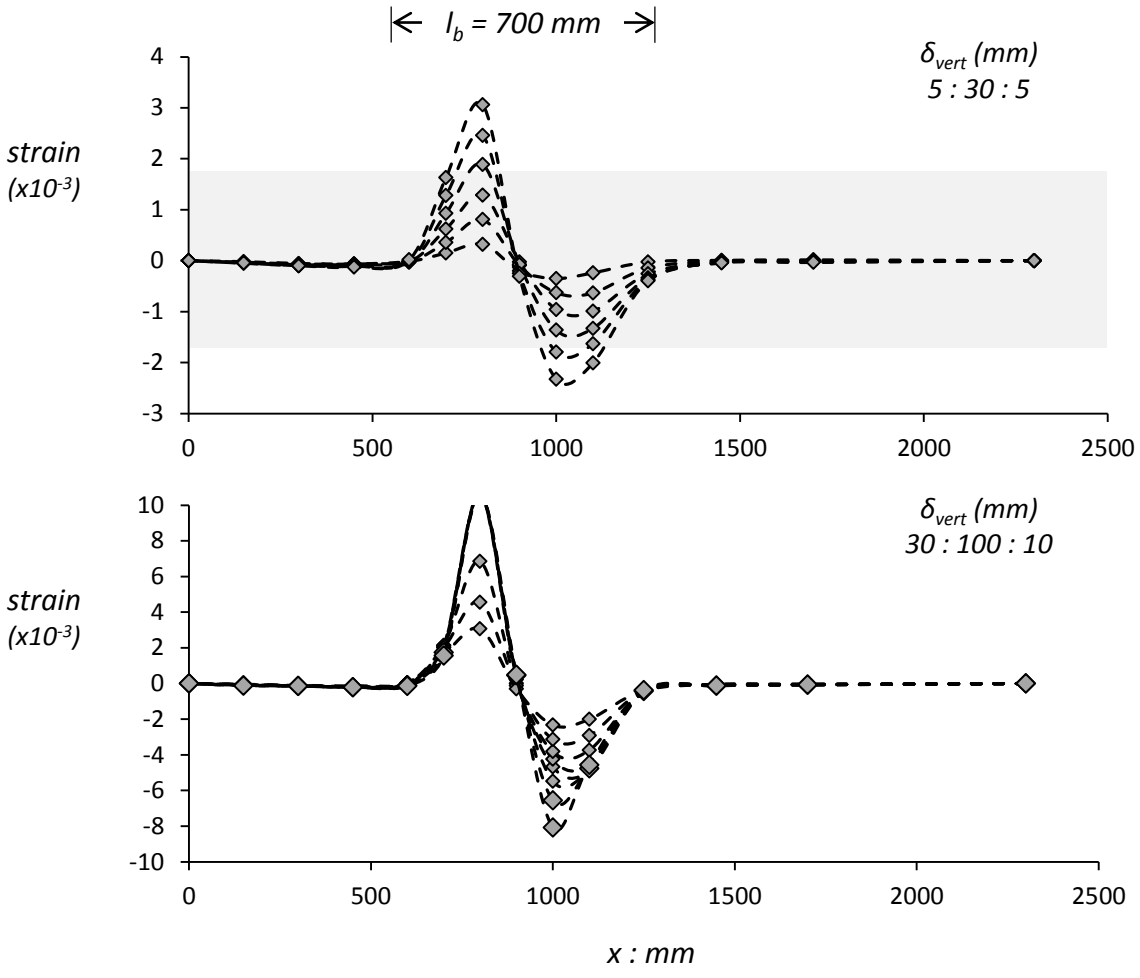

(b)

Fig. 3.13. (a) Residual deformation of the aluminum pipe subjected to reverse fault of total vertical offset δ_{vert} = 150 mm. (b) Strain distribution along the crown of the aluminum pipe of diameter D = 10 mm and thickness t = 1 mm embedded in sand of relative density D_r = 90 % subjected to reverse faulting for various magnitudes of vertical fault offset.

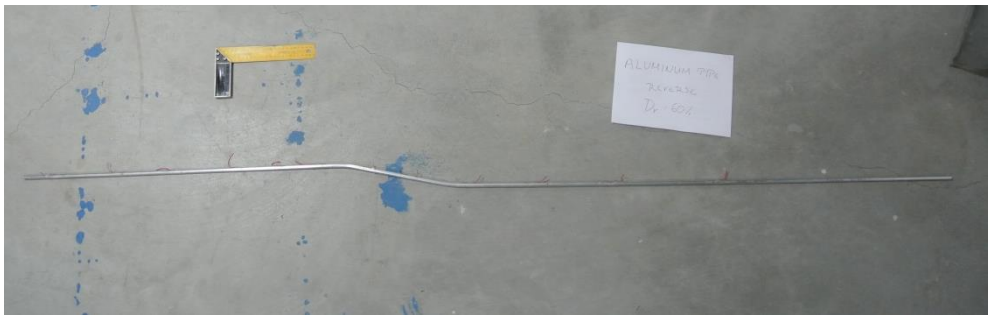

(a)

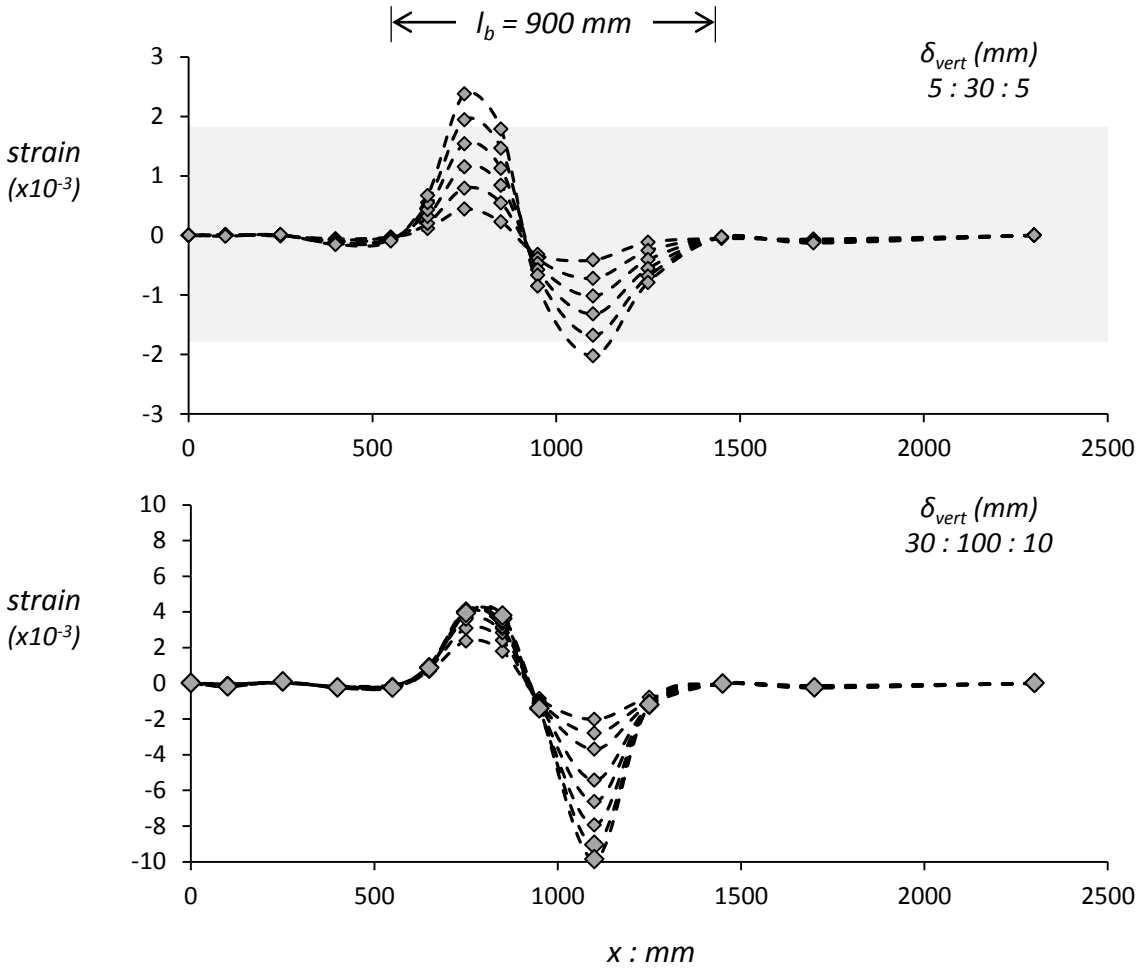

(b)

Fig. 3.14. (a) Residual deformation of the aluminum pipe embedded within sand of relative density D_r = 60 % and subjected to normal fault of total vertical offset δ_{vert} = 100 mm. (b) Strain distribution along the crown of the aluminum pipe of diameter D = 10 mm and thickness t = 1 mm embedded in sand of relative density D_r = 60 % and subjected to reverse faulting for various magnitudes of vertical fault offset.

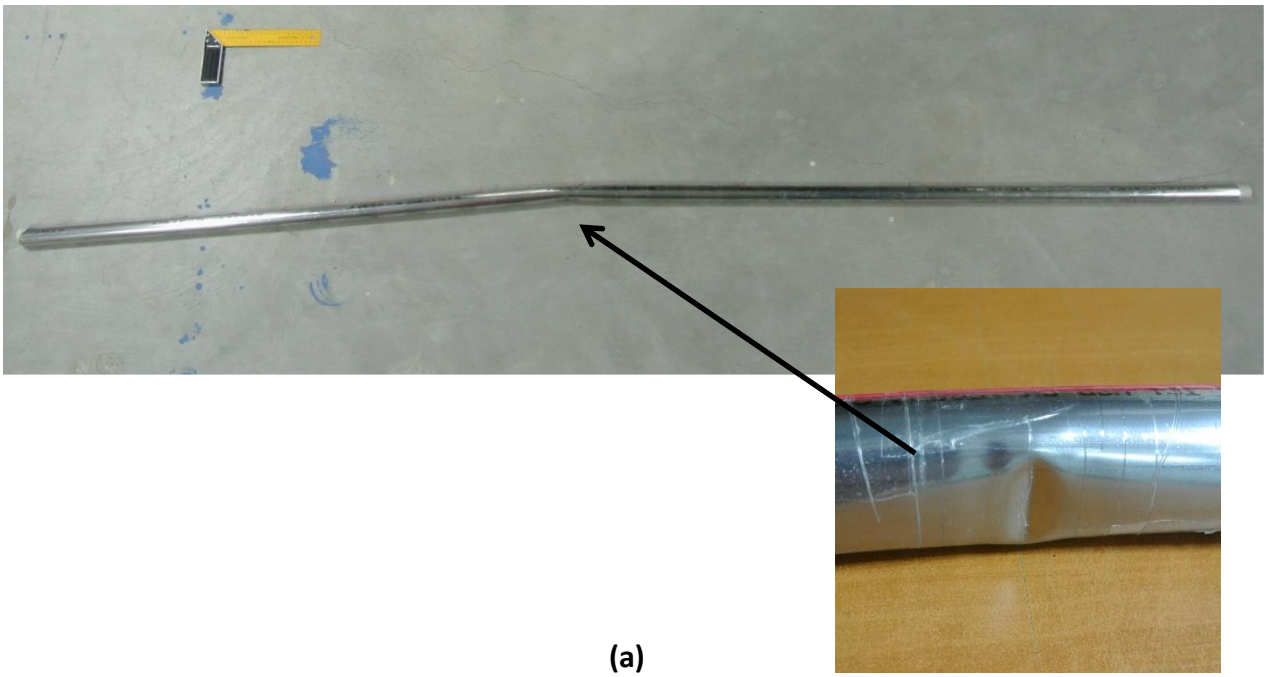

(a)

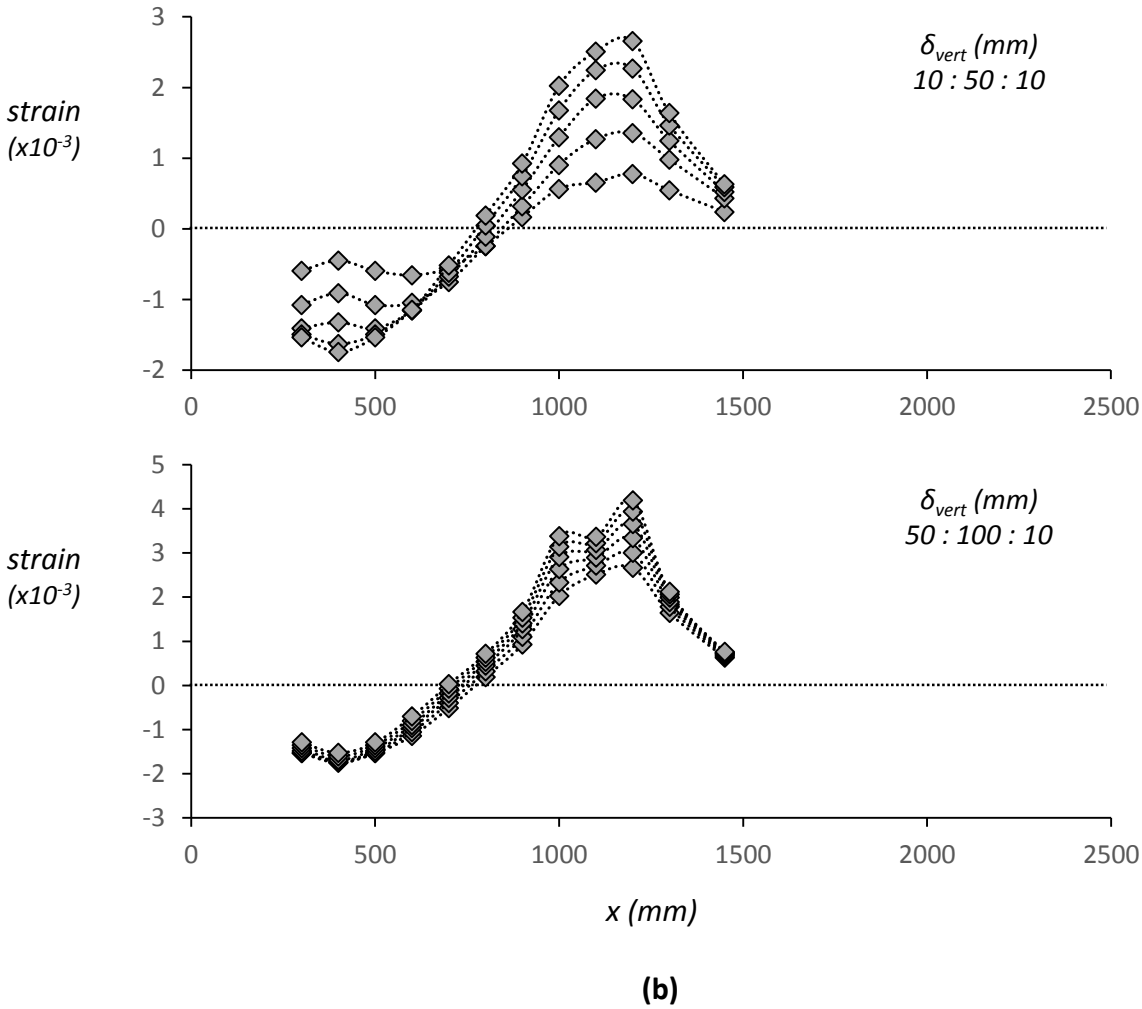

(b)

Fig. 3.15. (a) Residual deformation of the thin-walled steel pipe subjected to normal fault of total vertical offset δ_{vert} = 150 mm. (b) Strain distribution along the crown of the steel pipe of diameter D = 35 mm and thickness t = 0.5 mm embedded in sand of relative density D_r = 90 % subjected to reverse faulting for various magnitudes of vertical fault offset.

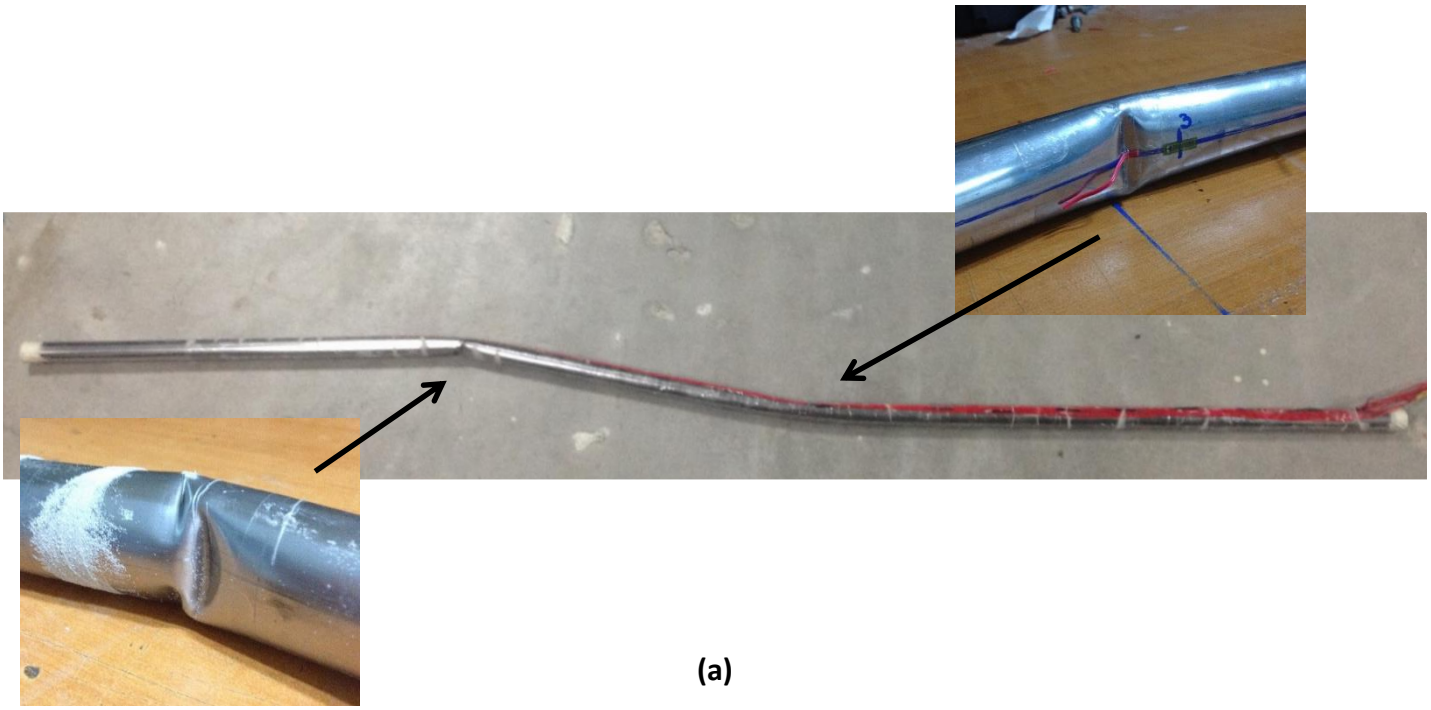

(a)

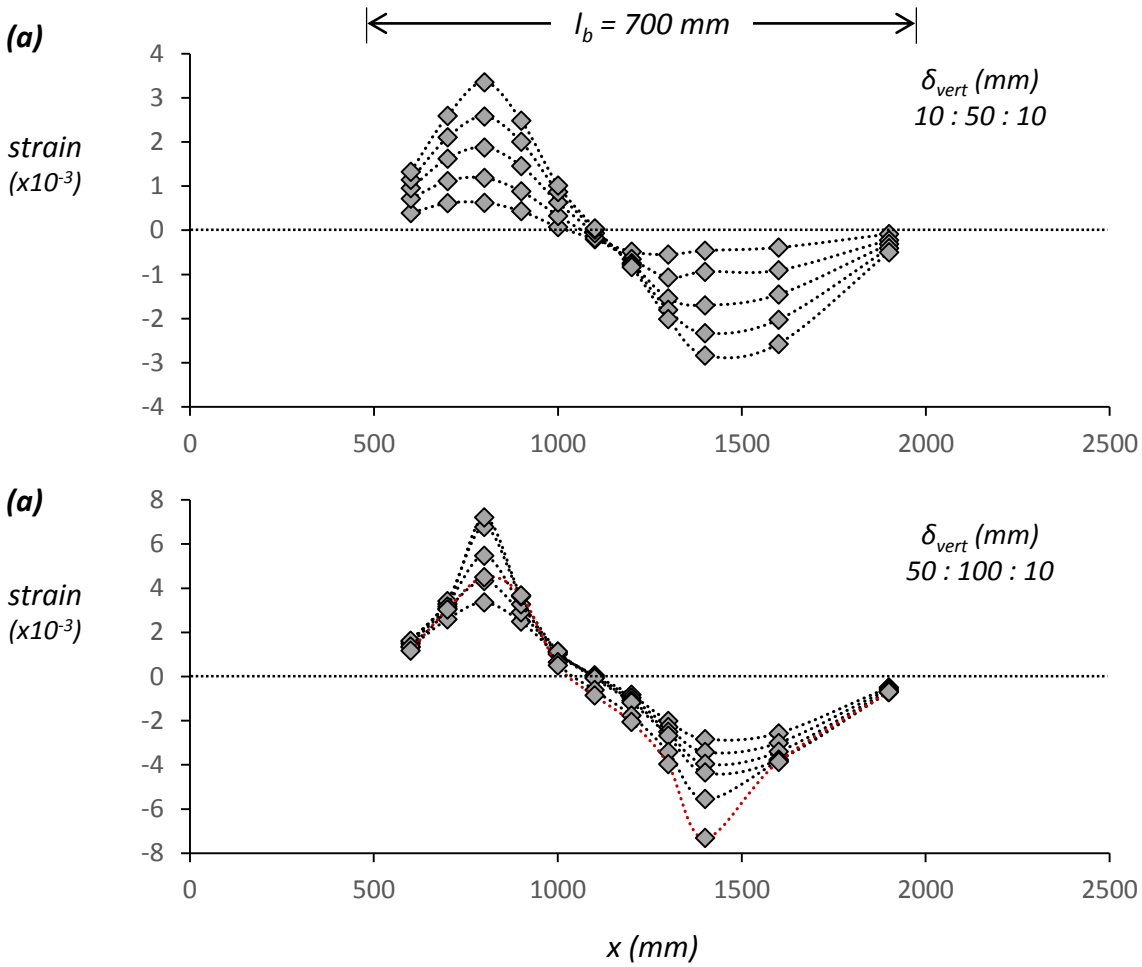

(b)

Fig. 3.16. (a) Residual deformation of the thin-walled steel pipe subjected to reverse fault of total vertical offset δ_{vert} = 150 mm. (b) Strain distribution along the crown of the steel pipe of diameter D = 35 mm and thickness t = 0.5 mm embedded in sand of relative density D_r = 90 % subjected to reverse faulting for various magnitudes of vertical fault offset.

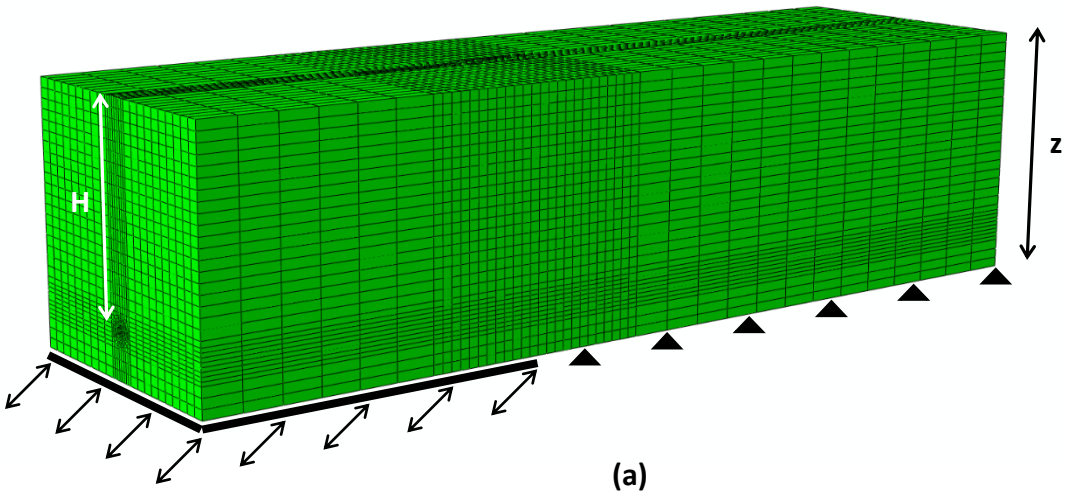

(a)

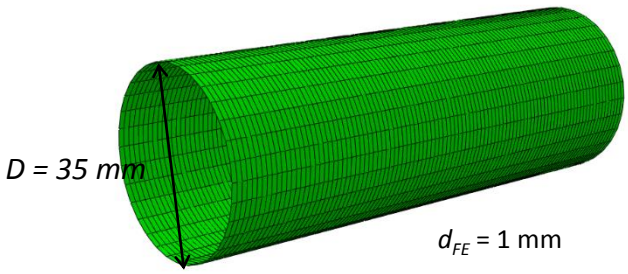

(b)

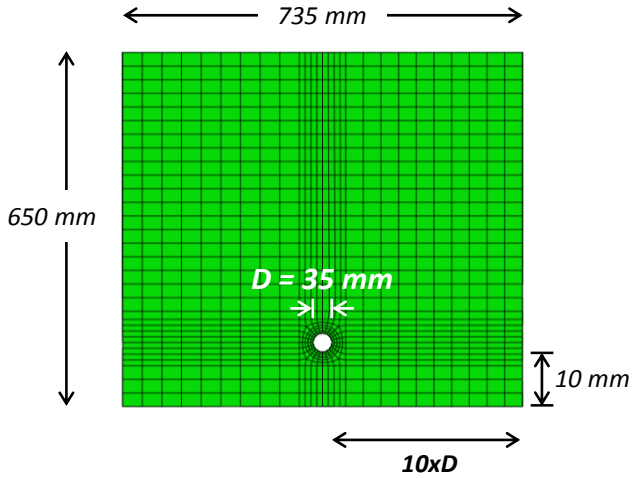

(c)

Fig. 3.17. Details of the numerical model used to simulate the experiments #25 and #26. (a) 3D view of the mesh of the model. (b) The mesh of the pipe at the critical regions. (c) Cross section of the model depicting the dimensions of the model and the location of the pipe.

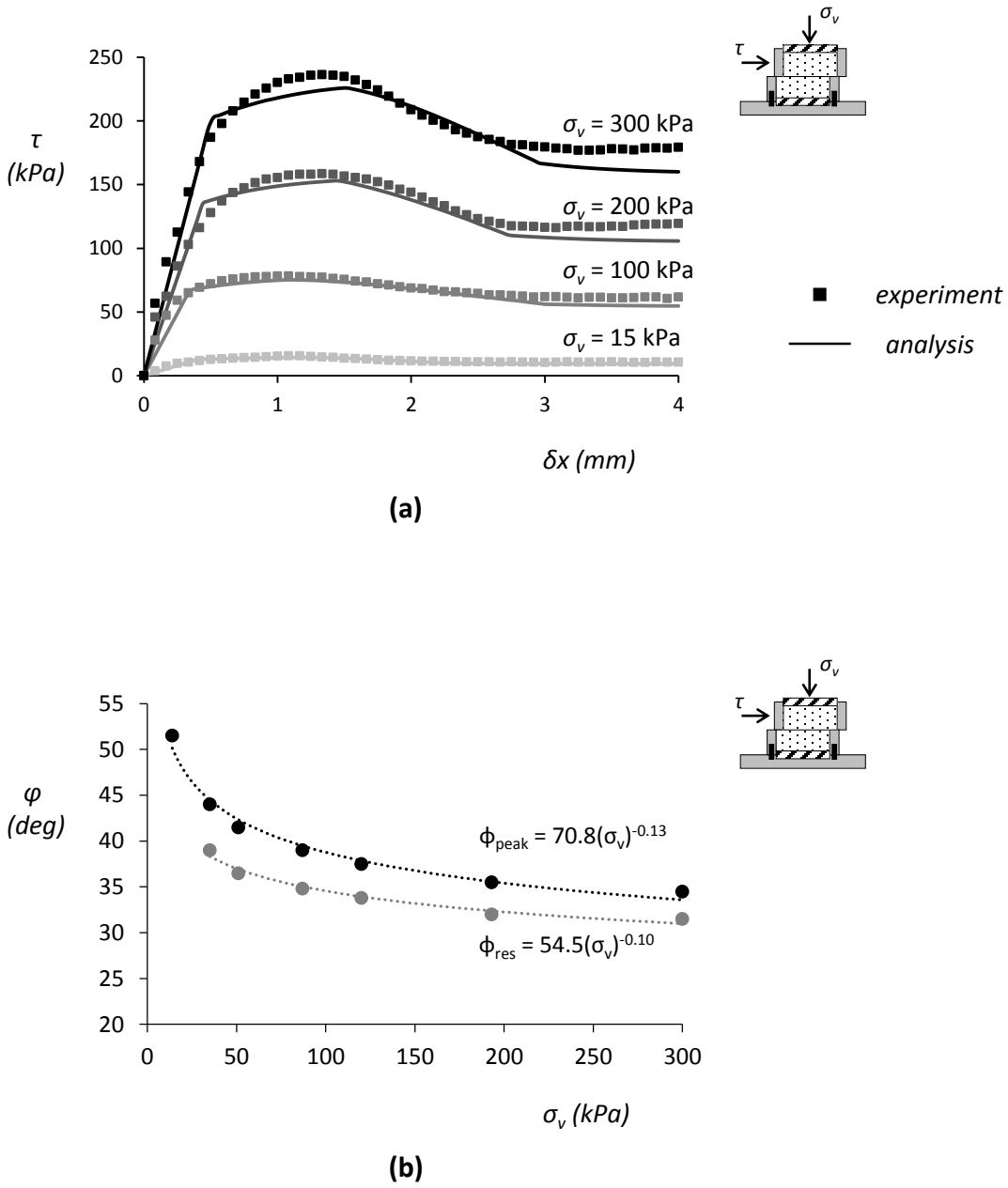

Fig. 3.18. (a) Direct shear tests results of the Longstone sand at Dr=90% and numerical simulation of these results. (b) The dependence of the peak and residual friction angle on the stress level.

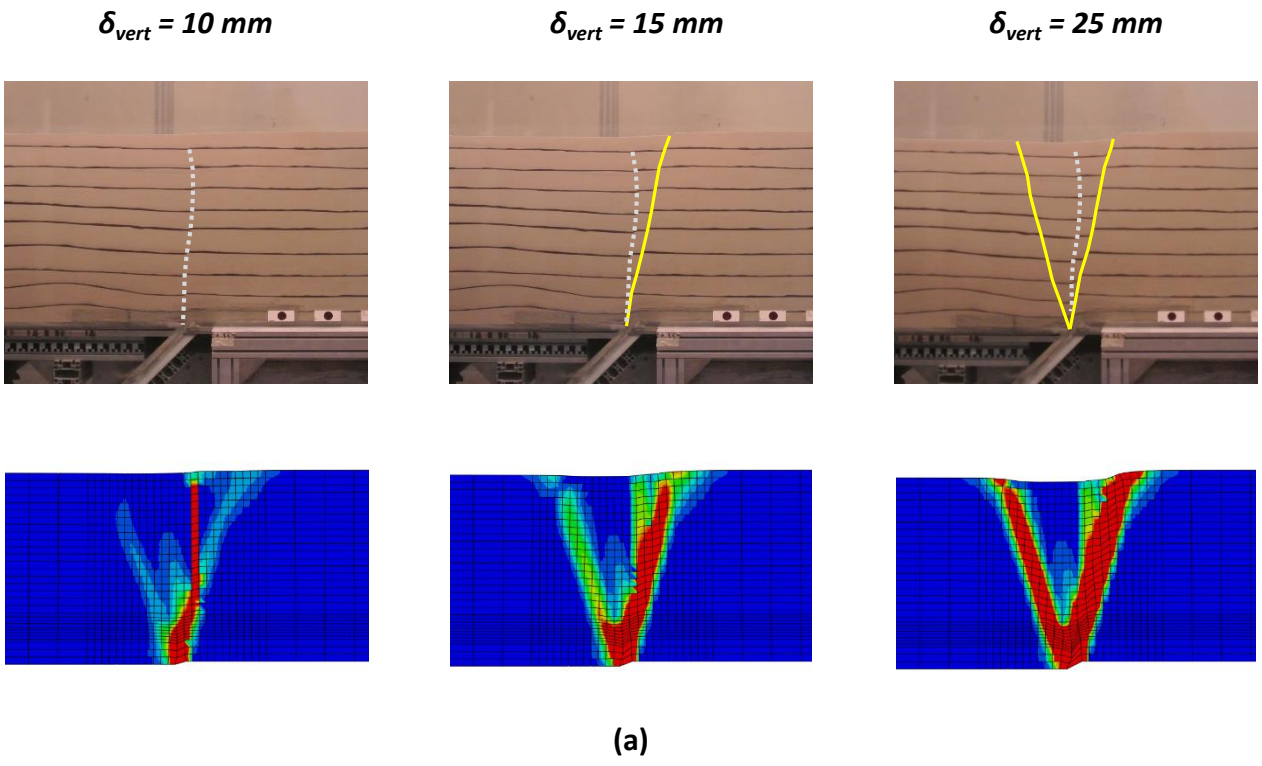

(a)

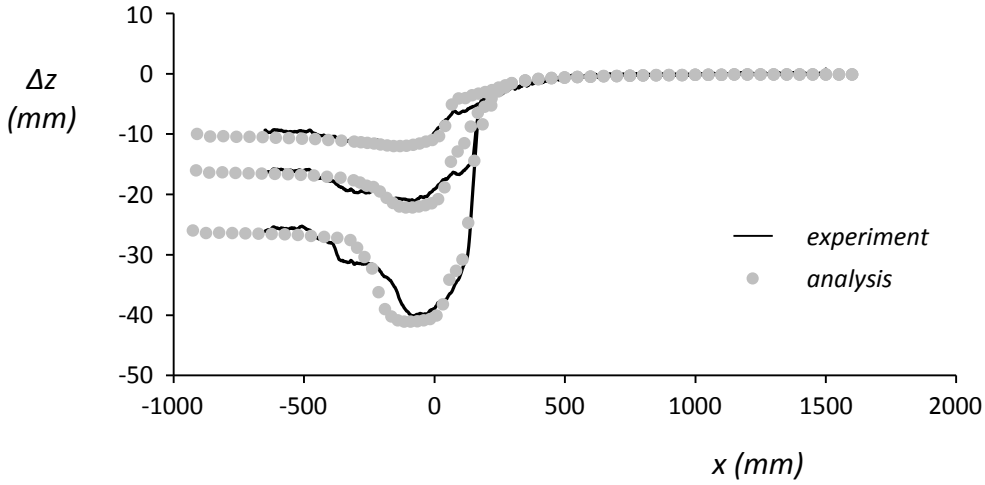

(b)

Fig. 3.19. Numerical Predictions are compared to Experimental Data for the case of a dense sand deposit subjected to normal fault: (a) evolution of rupture propagation with increased levels of fault offset (b) distribution of vertical ground surface offset.

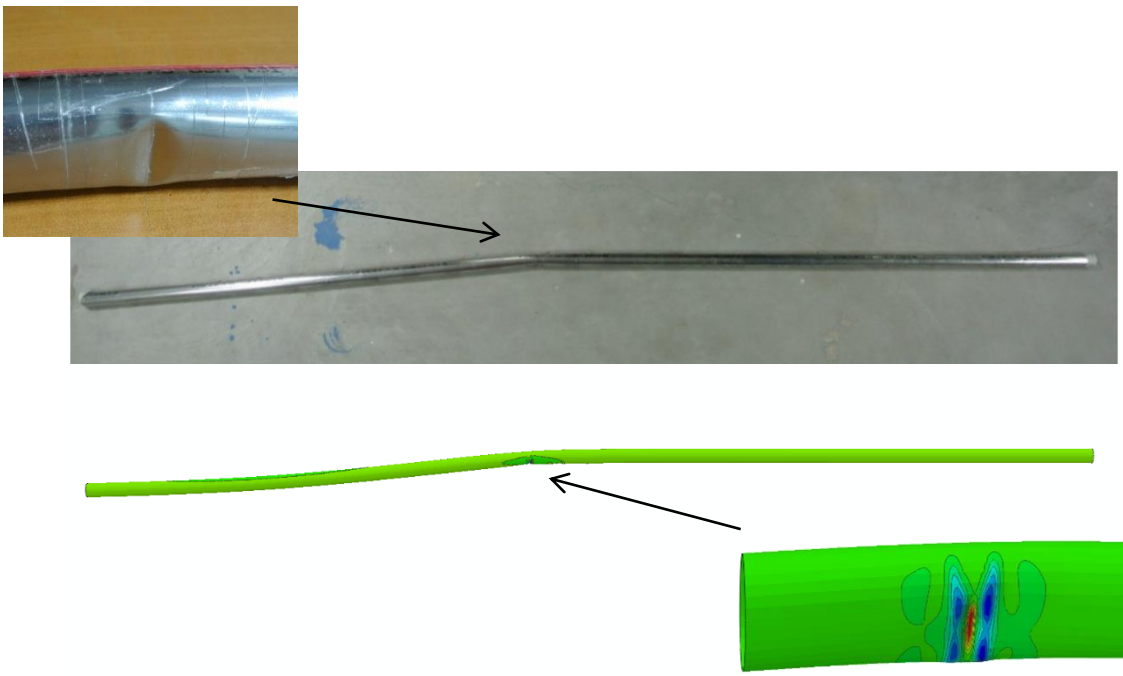

(a)

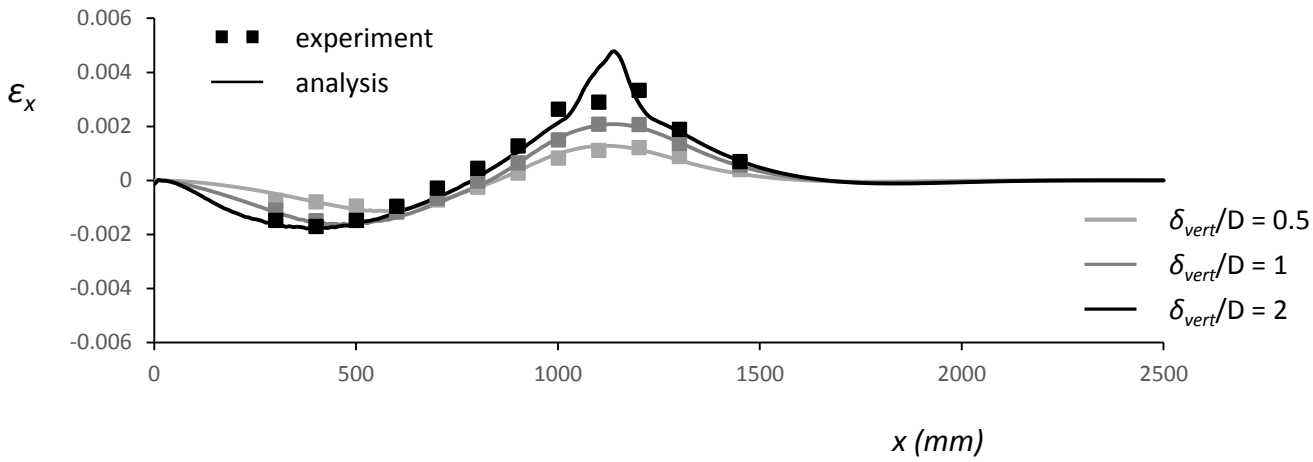

(b)

Fig. 3.20. Numerical reproduction of Experiment #25 : (a) The deformed pipe shape is compared with the shape of the deformed pipe upon completion of the experiment. (b) Strain distribution along the pipe crown

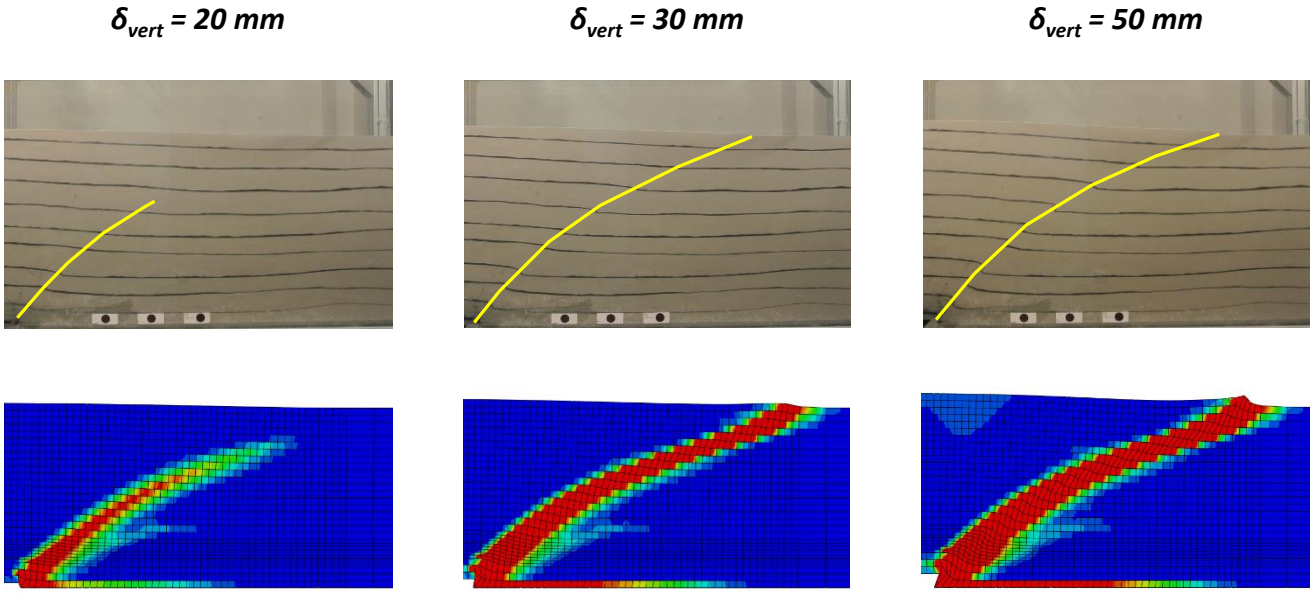

(a)

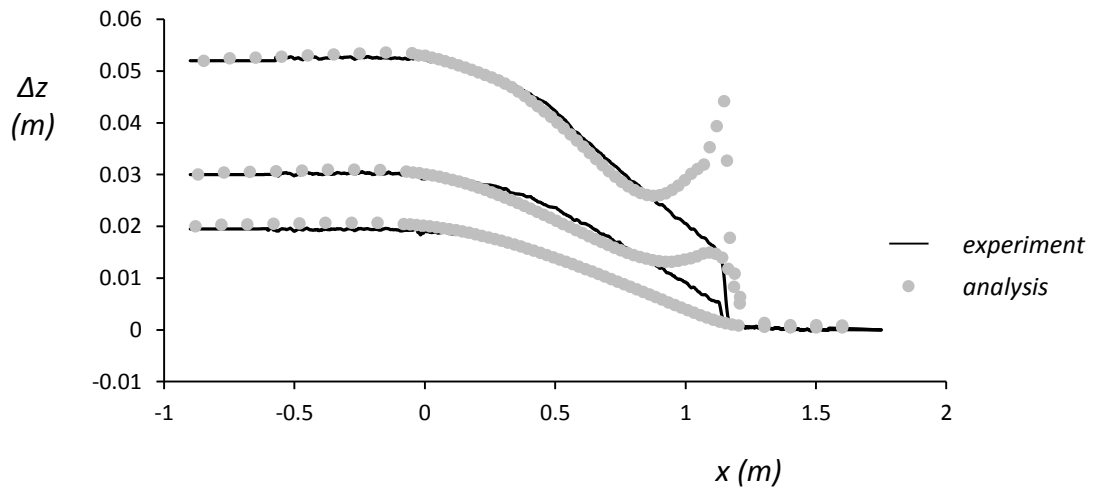

(b)

Fig. 3.21. Numerical Predictions are compared to Experimental Data for the case of a dense sand deposit subjected to reverse fault: (a) evolution of rupture propagation with increased levels of fault offset (b) distribution of vertical ground surface offset.

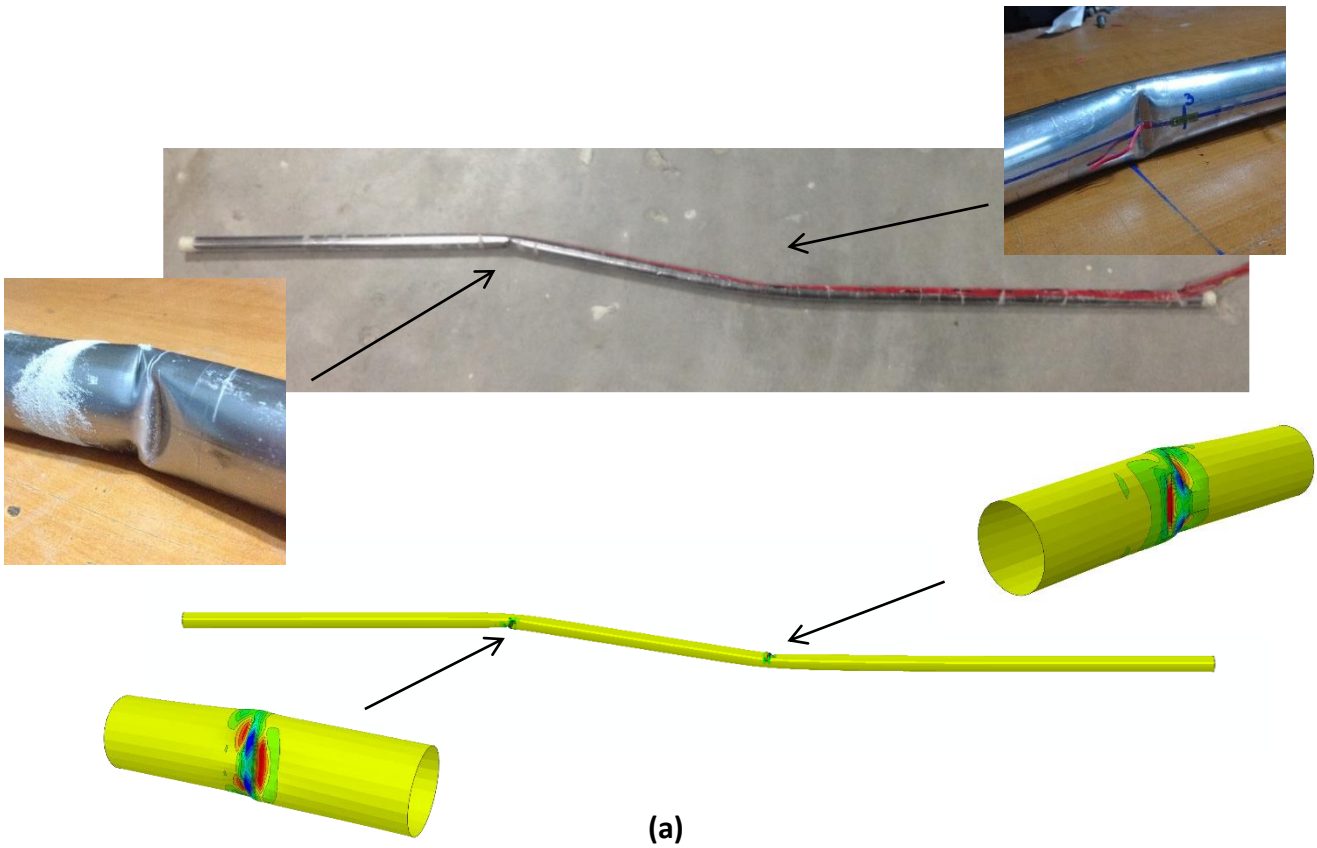

(a)

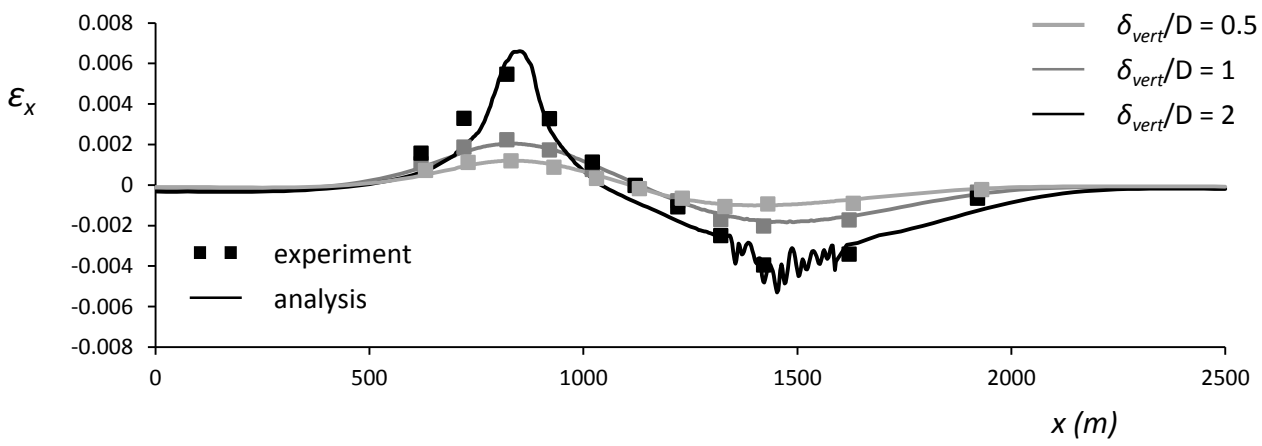

(b)

Fig. 3.22. Numerical reproduction of Experiment #26 : (a) The deformed pipe shape is compared with the shape of the deformed pipe upon completion of the experiment. (b) Strain distribution along the pipe crown

Chapter 4

Far-field Response: Pull-out resistance of buried pipelines and insights into the role of soil dilatancy

4.1 Introduction

The previous chapter outlined the pipeline response at the 'near-field' (i.e. at the vicinity of the rupturing fault). Along the 'near-field' area the pipeline deforms to accommodate the oblique fault fracture. The latter imposes normal and parallel (to the pipeline axis) deformations over a pipeline length (denoted as AB in **Fig. 4.1**) causing significant bending stressing and axial stretching. The length of Segment AB (which is expected to undertake this coupled bending-stretching loading) is relatively small, since the flexible pipeline eventually complies with the step-like ground deformation pattern. Outside of the 'near-field' region, (i.e., termed herein as 'far-field'), the pipeline experiences purely axial loading over an extended length (segments A'A and BB' of **Fig. 4.1**).

This far-field' response introduces flexibility at the two ends of the 'near-field' segment influencing the overall pipeline performance: the stiffer the axial pullout response, the larger the tensile strains at the vicinity of the fault and the higher the possibility of pipeline fracture. In this Chapter, attention is drawn to the truthful representation of the pipeline response in the "far-field. The Chapter starts by presenting some new data on the pull-out resistance of buried pipelines into dilative soils followed by the description and validation of a simplified numerical procedure to address the experimental findings. The Chapter concludes with a discussion on the effect of this 'far-field' response on the overall pipeline performance.

4.2 Pull-out tests of buried pipelines on dilative sands: New Findings

Code provisions (e.g. ALA 2001, PRCI 2004, IITK-GSDMA 2007) recommend the representation of soil-pipeline interaction under pull-out loading by means of discrete axial elastic-perfectly plastic soil springs. The ultimate 'pull-out' resistance of the latter (for non-cohesive soils) is described by **Eq. (1)** :

$$F_{max} = \pi D H \gamma \frac{1+K_0}{2} tan\delta \quad (1)$$

where *D* is the pipe outside diameter, *H* the depth to pipe centerline, *γ* the effective unit weight of the soil, K_o the coefficient of horizontal earth pressure "at rest" and δ the interface angle of friction between

the pipe and the soil. Evidently, the ultimate pull-out resistance is assumed to be controlled by the magnitude of soil stresses acting on the pipeline at rest conditions (i.e. before the initiation of any pull-out displacement). In a recent amendment of PRCI (2009), the "at rest" lateral earth pressure coefficient K_o of **Eq. 1** is replaced by an effective coefficient of horizontal earth pressure coefficient K_{eff} which varies from K_o (for loose soils) to values as high as 2 (for dense dilative soils). Yet, no further details/recommendations are provided on the calculation of this effective coefficient nor on its dependency on the dilation angle of the soil.

Besides, scarce experimental evidence on pull-out tests of buried pipelines [Singhal (1980), Colton, J. et al. (1982), Capalletto et al. (1998), Honegger (1999)] denote a rather interesting finding: the maximum axial load of pipes embedded in dense sands may be significantly higher than that predicted by **Eq. 1**. The same trend was also observed in the full-scale axial pullout tests of Paulin et al (1998) and the work of Anderson (2005) on straight and branched buried HDPE pipes in loose and dense sand. The recent full-scale pull-out experiments of Wijewickreme et al (2009) allowed the measuring of soil stresses during the pull-out testing (**Fig. 4.2a**). Results from this last experimental work demonstrated that although the measured axial soil resistance of a pipeline buried in loose sand was quite close to prediction of **Eq.1**, the peak values of axial pullout resistance for pipes buried in dense sand was several-fold higher (**Fig. 4.2b**). To provide some numbers, for an example test case of a pipeline with outer diameter D = 18", buried at H = 1.15 m (depth to the pipe centerline) in a soil deposit of dense sand with $\varphi = 45^o$ and γ = 16 kN/m^3 ,the experimental value of the peak pull-out resistance was measured at 26 kN/m, which is more than double the code provision of $T_{max} = 12.43$ kN/m for the exact same problem.

The authors attributed this discrepancy to the distribution of normal stresses around the pipe. Indeed, experimental measurements suggest that during the pull-out, soil pressure increases substantially overly exceeding the 'at rest' earth pressure (described by the coefficient K_o). For the particular example an 'effective' pressure coefficient of K_{eff} *equal to* 1.8 has been measured.

The axial response of buried steel pipelines was also investigated in the framework of the European Project GIPIPE (GIPIPE, 2015). Steel pipes of outer diameter D=8.625" were subjected to full-scale pullout tests (**Fig. 4.3a**). The pipes were buried in dense sand at depth H=0.75 m (surface to pipe centerline). The small-stress friction angle of the sandy deposit was measured at $\varphi = 50^o$. As in the case of Wijewickreme et al experiments, the measured pull-out resistance was F_{max} = 11.5 kN/m, while the code provision suggested a mere F_{max} = 4.3 kN/m (**Fig. 4.3b)**. In order to account for the increased pull-out resistance a horizontal earth pressure coefficient of K = 2.3 should have been assumed.

4.3 A Step-wise numerical procedure: Description & Validation

The aforementioned experiments suggest that the distribution of normal stresses acting on the pipe-soil interface is considerably increased during pullout tests. A tentative explanation is portrayed in **Fig. 4.4**. As the pipe is pulled axially, the soil resists to the pipeline movement through shearing forming a thin shear-zone around the pipe. In case of dilative soils, this shear-zone tends to expand radially. Yet, the expansion is constrained by the pipe and the surrounding soil. This constrained dilatancy provokes excessive normal stresses $\Delta\sigma_n$ along the pipe periphery. The latter are responsible for increased values of pull-out capacity evident in the experiments of dense sand.

To account for such small-strain effects in conventional FE modeling a simplified step-by-step numerical methodology is introduced, which may be described by the flowchart of **Fig. 4.5.**

Step 1: *Estimate the volumetric expansion (δz) of the shear zone*

The formation of shear zone between the pipe and the surrounding soil during a pull-out experiment is assumed to be mechanically analogous to the formation of a shear band during a direct shear test of a soil element (**Fig. 4.6**). If so the vertical displacement $\delta_{z,DST}$ measured during the direct shear test is assumed to express the expected volumetric expansion at the pipe-soil interface (if it was not bounded by the surrounding soil).

Step 2: Estimate the normal stresses σ_n on the pipe

A cavity expansion test is performed in which the nodes of the pipe section are assumed to displace (radially) outwards by $\delta_{z,DST}$ /2 and the average normal stress $\sigma_{n,aver,target}$ acting on the pipe perimeter is calculated (**Fig. 4.8**). Clearly the calculated stresses would be controlled by the assumed (secant) shear modulus of the soil – a complication resulting from the assumption of an elastoplastic M-C criterion. To address this problem, an *elastic cavity expansion* analysis precedes so as to determine the average shear strain *γ* that develops within the width of the shear zone (**Fig. 4.7a**). The latter, following the Vardoulakis and Graf (1985) suggestion[1], is considered to be equal to 16 times the mean particle size d_{50}. Having defined the average γ, the secant shear modulus G (to be utilized in the actual cavity expansion analysis)

[1] The width of the shear band is a point of friction among researchers. Roscoe (1970) and Bridgewater (1980) argued that the shear band is 10 times the mean particle size d_{50} , while the micro-scale particle image velocimetry (PIV) observations of DeJong et al. (2006) suggested that the thickness of shear band is approximately 5 - 7 particle diameters

is estimated following the shear modulus degradation curve proposed by Oztoprak and Bolton (2013) (**Fig. 4.7b**)

$$\left(\frac{G}{G_0}\right) = 1/\left[1 + \left(\frac{\gamma-\gamma_e}{\gamma_r}\right)^a\right] \quad (2)$$

where G_0 is the elastic (maximum) shear modulus, γ is the shear strain, γ_e is the elastic threshold strain beyond which the shear modulus falls below its maximum, γ_r is the characteristic reference shear strain at which $G/G_0 = 0.5$, and a is the curvature parameter.

Step 3: *Select an equivalent horizontal earth pressure coefficient K_{equiv}* model *that yields the target average normal stress*

The K_{equiv} should yield the average $\sigma_{n,aver,target}$ along the pile periphery. This implies that, a 3D FE model should be constructed (as that presented in **Fig. 4.10**) comprising the pipeline and the surrounding soil. After that an initial static analysis is performed assuming that the 'at rest' earth pressure is equal to the K_{equiv}. Admittedly, by just assuming an increased K_{equiv} value we are not replicating the actual stress distribution along the pipe circumference (**Fig. 4.9**), but we do manage to correctly capture the increased magnitude of the *average* normal stress (which is eventually controlling the peak axial resistance of the pipe).

Step 4: *Perform a pullout test to calculate the non-linear force-displacement curve*

To realistically simulate the interface condition between the steel pipe and the surrounding soil special-purpose contact elements are introduced that allow the pipe to slide on the ground. In sand deposits, the maximum mobilized shear resistance τ_{max} at the pipe-soil interface is a function of the frictional coefficient μ and the normal stress (i.e, $\tau_{max} = \mu\,\sigma_n$). Yet, in dilative soils the friction coefficient μ is not constant: it starts at a peak value $\mu_{peak} = tan\delta = tan(f*\varphi_{peak})$, where φ_{peak} is the peak friction angle of the surrounding soil, and f is a coefficient that depends on the roughness of the pipe wall (f = 0.8 for rough steel) and as the axial displacement increases it gradually drops to a residual value where $\mu_{res} = tan(f*\varphi_{res})$, where φ_{res} is the residual friction angle of the soil. Normally the transition of μ from peak to residual conditions follows an exponential decay law as follows:

$$\mu(\delta_x) = \begin{cases} \mu_{peak}, & \delta_x < \delta_{x,peak} \\ \mu_{res} + \left(\mu_{peak} - \mu_{res}\right)e^{-\lambda\left(\delta_x - \delta_{x,peak}\right)}, & \delta_{x,peak} < \delta_x < \delta_{x,res} \\ \mu_{res}, & \delta_x > \delta_{x,res} \end{cases} \quad (3)$$

To incorporate this non-constant μ value in our FE analysis, a user-defined subroutine has been introduced that correlates μ to δ_x according to Eq. 3.

Finally, in order to derive the non-linear force-displacement curve (F-δ), a monotonically increasing axial displacement δ is applied at the one end of the pipe and the evolution of resistance (per unit length) with displacement is recorded.

4.4 Validation of the proposed methodology

Application to the Wijewickreme et al (2009) experiments

The proposed 4-Step methodology is applied herein to numerically capture the pull-out resistance measured by *Wijewickreme et al (2009)* experiments (**Fig. 4.11**). As evidenced by the direst shear test results of **Fig. 4.11a**, the sandy deposit demonstrates a clearly dilative behavior: after attaining an initial peak resistance (corresponding to a φ_{peak} = 45^o), the soil specimen dilates until reaching a critical state (corresponding to φ_{res} = 36^o) at which shear deformation continuous in the absence of any volumetric change (i.e. $\delta_{z,DST}$ remains constant at 0.75 mm which corresponds to a dilation angle of $\psi = asin(dy/dx) \approx$ 15^o). During the second step, the pipe is subjected to a radial displacement of $\delta_{z,DST}$. The latter produces an average shear strain of $\gamma_{aver,target}$ = 0.39%, which for a secant shear modulus of 0.96 G_o. (according to Oztoprak & Bolton (2013)) yields an average normal stress (around the pipe) of $\sigma_{n,aver,target}$ = 26.7 kPa . For such an increased σ_n to develop, an equivalent horizontal earth pressure coefficient of K_{equiv} = 1.9 needs to be assumed. This value of K_{equiv} is incorporated into a final analysis, in which the pile is monotonically pulled-out from the sand deposit and the reaction F is recorded. A comparison between the experimentally measured and the numerically predicted force-displacement curve is presented in **Fig. 4.11d**.Evidently the two curves compare extremely well.

Application to the GIPIPE full-scale experiments (2015)

The GIPIPE pull-out experiments are serving as a second benchmark problem for the proposed methodology (**Fig. 4.12**). Similar to the previous case the direct shear test results present a peak friction angle of φ_{peak} = 48^o, a residual friction angle of φ_{res} = 35^o and specimen height increase of $\delta_{z,DST}$ = 0.75 mm. By assuming a pipe diameter expansion of $\delta_{z,DST}$, an average shear strain of $\gamma_{aver,target}$ = 0.82% is developed corresponding to an average normal stress around the pipe of $\sigma_{n,aver,target}$ = 20.6 kPa. Accordingly, for this average soil stress to develop a K_{equiv}=2.4 is required. By assuming this value of K_o in the Step 4 of the

proposed methodology the force –displacement curve of **Fig. 4.12d** is attained which apparently compares very nicely to the one measured during the actual experiment.

4.5. The effect of the dilation on the pipeline response

Up to this point we have demonstrated that:

(i) In dip-slip faulting the far-field response of a pipeline is practically uniaxial and therefore it may be described by a pull-out force-displacement curve

(ii) The pull-out response of pipes embedded in dense or loose sand is very different. In dense sand the constraint of the tendency of the soil to dilate generates an increased stress distribution, hence, increasing the pull-out resistance of the system. Not dilatant loose sand does not experience this effect.

(iii) We have proposed and validated a procedure that incorporates direct shear results into a non-linear 3D FE analysis to estimate the pull-out performance of pipelines accounting for dilation.

In this paragraph we are answering the following question: "How important is the incorporation of dilation phenomena to the pipeline performance under dip-slip faulting?". For a qualitative answer, refer to the plot of **Fig. 4.13** which portrays the soil reaction to the axial movement of a 36" diameter pipe for a dense sand of $\varphi_{peak} = 40^o$. Two cases are considered: the solid curve accounts for a dilation of $\psi = 10^o$ (following the previously described procedure) while the dashed line corresponds to the code suggestion (where the dilatancy of soil is practically ignored). Apparently, the dilatant curve is the larger and hence in far-field conditions the axial deformation of the pipeline is more restricted in dense soil. This restrain generates axial stresses of higher amplitude along the entire pipeline length. Eventually these higher stresses may result in pipeline failure at an earlier stage (i.e. at lower faulting displacement compared to the case of a non-dilative soil). The following set of analyses aims to quantify the importance of such dilation phenomena on the performance of a pipeline.

The numerical example (**Fig. 4.14)** refers to an infinitely long hydrocarbon transportation pipeline, with outer diameter $D = 36"$ and thickness $t = 0.5"$, buried at $H_{cover} = 1$ m. The pipeline is assumed to cross an active normal fault with a dip angle of 60^o (perpendicularly to the pipeline axis). The properties of the embedment vary parametrically to account for different soil conditions. In particular, three dry sands profiles are considered with friction angle $\varphi = 45^o$, $\varphi = 40^o$ and $\varphi = 35^o$ representing a very dense, a rather dense and a quite loose formation. For each friction angle a broad range of dilation angles are assumed, varying from $\psi = 0^o$ to $\psi = 25^o$. Following the proposed step-wise procedure, the axial force-displacement

response of the pipe is calculated for all the examined sand deposits (**Figs 4.15-4.17**). The latter is prescribed into the nonlinear law of the axial springs of the far-field model.

Pipeline performance

As shown in Chapter 3, when a pipeline is crossed by a normal fault, excessive tensile strains are expected to develop in the vicinity with the fault intersection. As the faulting displacement increases, so do the tensile strains until an ultimate point is reached where pipe fracture is eminent. The definition of that point is a matter of approach: according to EN 1993-4 for the design of steel pipelines ε_{max} = 0.5% , while a less strict approach adopted by other codes such as the EN 1998–4 provisions for seismic-fault-induced actions on buried steel pipeline defines pipeline tensile failure at ε_{max} = 3% .

Fig. 4.18 correlates the amplitude of critical faulting displacement (δ_{crit}) to the dilation angle (ψ) of the sandy deposit. Observe that as the dilation angle increases the safety margins of the pipeline decrease substantially. For example, in case of a dense sand deposit with friction angle φ = 45°, the normalized fault displacement that is expected to provoke pipeline rupture decreases from δ_{crit}/D = 0.74 for a non-dilative soil to δ_{crit}/D = 0.6 for a dilation angle of ψ = 25°. The same trend is also observed for the looser deposits. In fact, if the pipeline is embedded in a non-dilative sand of φ = 40°, a normalized critical displacement of δ_{crit}/D = 0.95 would have been required to provoke failure, while if the same deposit had a dilation angle of ψ = 20° the critical normalized displacement would have dropped to 0.77.

The negative impact of dilation on the pipeline safety margins is even more evident if the ε_{max} = 3% failure criterion is adopted (**Fig. 4.18b**). In this scenario, for a non-dilative sand of friction angle φ = 35°, the pipeline may safely accommodate up to δ_{crit}/D = 3.44; this value drops sharply to δ_{crit}/D = 2.55 when a ψ = 15° is assumed.

A clear pattern is revealed: *in normal faulting conditions, pipeline performs better in non-dilative rather than dilative soils*. Therefore, the tendency of sands towards dilation should be accounted for in the design of a pipelines. Failing to do so could lead to an overestimation of the actual safety margins until failure.

4.6. Design Recommendations on the K_{eff}

As previously stated, Code provisions have only recently recognized the dependence of pipeline pull-out resistance on the dilative characteristics of the embedment soil. This is reflected in the amendment of PRCI (2009), where the "at rest" lateral earth pressure coefficient K_o of **Eq. 1** is replaced by an *effective horizontal earth pressure coefficient* K_{eff}. Although the code suggest that the amplitude of K_{eff} is expected

to vary quite substantially from loose to dense soil profiles, no further recommendations are provided on its calculation nor on its dependency on the dilation angle of soil.

To bridge this gap, we have performed a rather thorough parametric study for pipelines of varied dimensions (D = 8" ÷ 48"). and burial depths (H_{cover} ranges between 1 m which is the minimum cover for pipelines transporting Liquid Petroleum Gas according to ASME B31.4-2002 to the most commonly adopted solution of H_{cover} = 1.5 m)[2]. The examined geometries are tested for a variety of soil scenarios (for both dilative and non-dilative soils), and the effective lateral earth pressure coefficient K_{eff} is calculated. The soils under consideration are dry sands. Namely, three sands with $\varphi = 45^o$, $\varphi = 40^o$ and $\varphi = 35^o$ are considered and correlated to a variety of dilation angles ($\psi = 5^o \div 25^o$) covering a range from heavily to mildly dilative soils.

For every possible combination of soil, pipe and burial depth, the aforementioned step-wise procedure is followed and the K_{equiv} is derived. **Fig. 4.19**, **5.21** and **4.23** present the properties of each soil under consideration, as well as the results of the numerically performed direct shear tests. The estimated K_{equiv} for all assumed geometries and soils is presented (in tabulated form) in **Figs 4.20**, **5.22** and **4.24**.

A closer look on the collective results, reveals some interesting insights:

- As evidenced by **4.25a** the cover depth H_{cover} does not seem to affect the magnitude of K_{equiv} (at least for the cover depths encountered in common practice for hydrocarbon transportation pipelines).
- The diameter of the pipe does influence the developed stresses at the pipe periphery and accordingly the attained K_{equiv} : the larger the pipe diameter the lower the K_{equiv}. An indicative example is presented in **Figure 4.25b,** where two pipeline diameters are considered**:** a pipe of diameter D = 20" and another of D = 48''. Both pipes are buried in a dense sand profile of $\phi = 45^o$ at a depth of H_{cover} = 1.5 m. Evidently, for a given dilation angle ψ, larger normal stresses are developed around the smaller pipe. The latter are associated with increased values of K_{equiv}.

References

American Lifelines Alliance. Guidelines for the design of buried steel pipes, ASCE, New York (2001)

Anderson, C., Wijewickreme, D., Ventura, C., & Mitchell, A. (2005). FULL-SCALE LABORATORTY TESTING OF SOIL-PIPE INTERACTION IN BRANCHED POLYETHYLENE PIPELINES. *Experimental Techniques, 29(2)*, 33-a37.

[2] The smaller pipes of D=8" and 20" are combined with a smaller cover depth to represent water transportation pipelines.

ASME B31-4 (2002). Pipeline Transportation Systems for Liquid Hydrocarbons and Other Liquids. Code for Pressure Piping, B31 an American National Standard.

Bridgwater, J. (1980). On the width of failure zones. Geotechnique, 30(4), 533-536.

DeJong, J. T., White, D. J., & Randolph, M. F. (2006). Microscale observation and modeling of soil-structure interface behavior using particle image velocimetry. *Soils and foundations, 46*(1), 15-28.

Cappelletto, A., Tagliaferri, R., Giurlani, G., Andrei, G., Furlani, G., & Scarpelli, G. (1998). Field full scale tests on longitudinal pipeline-soil interaction. In *PROC INT PIPELINE CONF IPC, ASME, FAIRFIELD, NJ,(USA), 1998*, (Vol. 2, pp. 771-778).

Colton, J. D., Chang, P. H. P., & Lindberg, H. E. (1982). Measurement of dynamic soil-pipe axial interaction for full-scale buried pipelines. *International Journal of Soil Dynamics and Earthquake Engineering, 1*(4), 183-188.

European Commission, Directorate-General for Research and Innovation (2015), "*Safety of buried steel pipelines under ground-induced deformations (GIPIPE)*", ISBN: 978-92-79-54040-0

Honegger, D. G. (1999). Field Measurement of Axial Soil Friction Forces on Buried Pipelines. In *Optimizing Post-Earthquake Lifeline System Reliability* (pp. 703-710). ASCE.

Honegger, D.G. and Nyman, D.J., (2004). "Seismic design and assessment of natural gas and liquid hydrocarbon pipelines", Pipeline Research Council International, Inc., No. L51927.

IITK-GSDMA (2007), Guidelines for seismic design of buried pipelines. Indian Institute of Technology, Kanpur

Karimian, S. A. (2006). "Response of buried steel pipelines subjected to longitudinal and transverse ground movement". PhD thesis, University of British Columbia.

Paulin M.J., Phillips R., Clark J.I., Trigg A., and Konuk I. (1998) "A full-scale investigation into pipeline-soil interaction" *Proceedings, International Pipeline Conference, Calgary,* AB, ASME, 779-779.

Oztoprak, S., & Bolton, M. D. (2013). Stiffness of sands through a laboratory test database. *Géotechnique, 63*(1), 54-70.

Roscoe, K. H. (1970). The influence of strains in soil mechanics. *Geotechnique*, 20(2), 129-170.

Singhal, A. C. (1980) "Experiments of pipeline joints." American Society of Mechanical Engineers, n 80-C2/PVP-70, 5p.

TO, P. T. A. P. (2009). Guidelines for Constructing Natural Gas and Liquid Hydrocarbon Pipelines Through Areas Prone To Landslide and Subsidence Hazards.

Wijewickreme, D., Karimian, H., & Honegger, D. (2009). Response of buried steel pipelines subjected to relative axial soil movement. *Canadian Geotechnical Journal, 46*(7), 735-752.

Vardoulakis, I. and Graf, B. (1985). Calibration of constitutive models for granular materials using data from biaxial experiments. Geotechnique 35, 299-317.

Figures

of Chapter 4

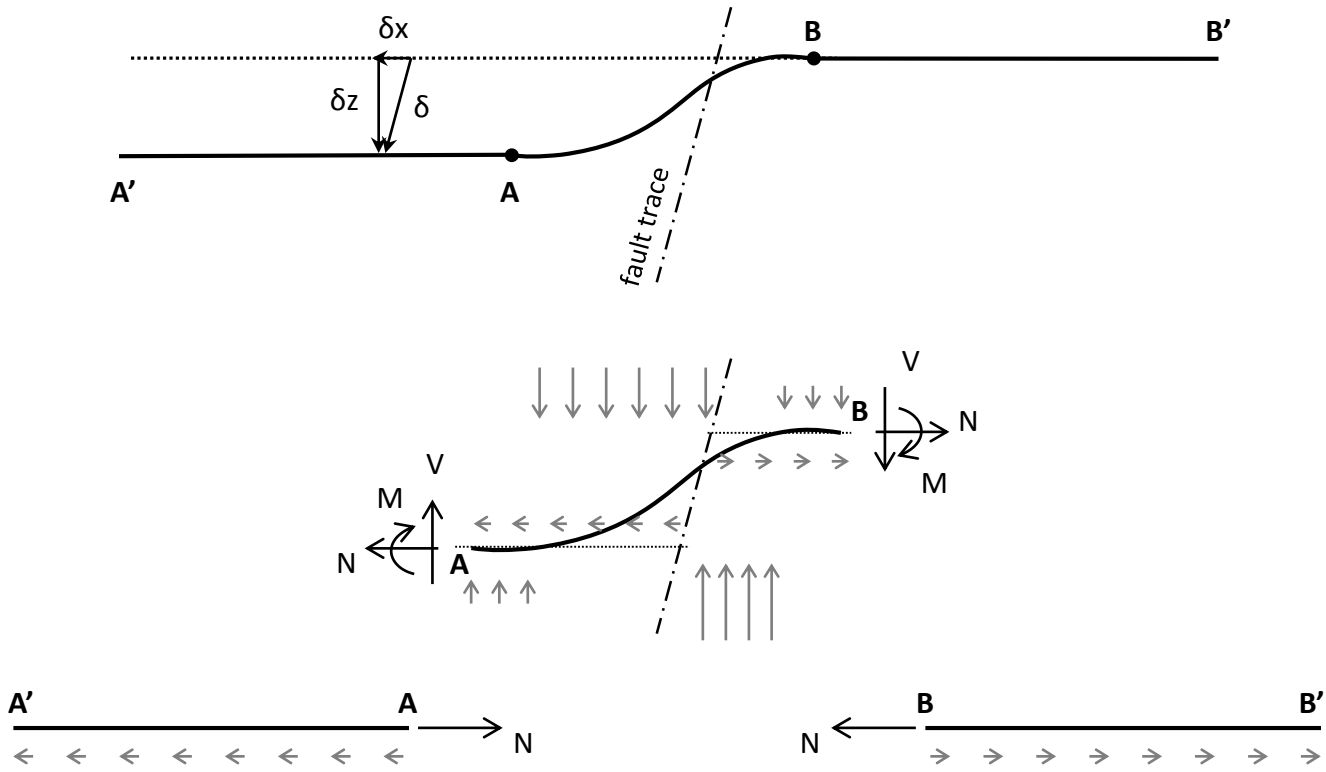

Figure 4.1. Structural behavior of an infinitely long pipeline subjected to normal faulting. Three regions can be recognized based on the type of stressing of the pipe: a central region at the vicinity of the fault trace where the pipe is stressed due to bending and stretching (segment AB), and two regions beyond the central segment where the stressing of the pipe is practically exclusively due to stretching (segments A'A and BB').

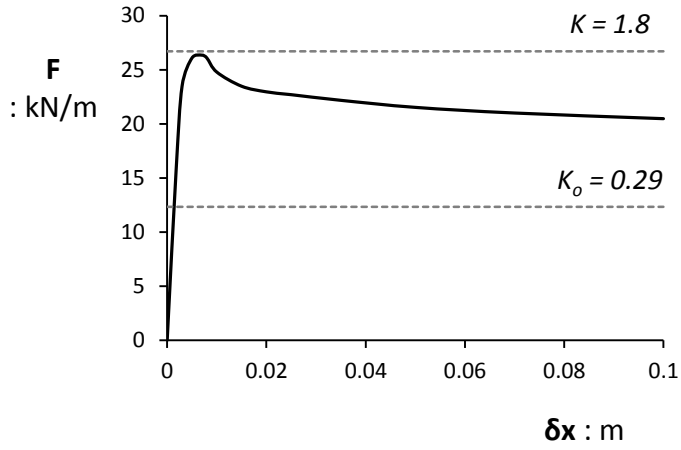

(a) **(b)**

Figure 5.2. The pullout test of Wijewickreme et al (2009): (a) photo of the experimental setup and (b) the measured force-displacement curve.

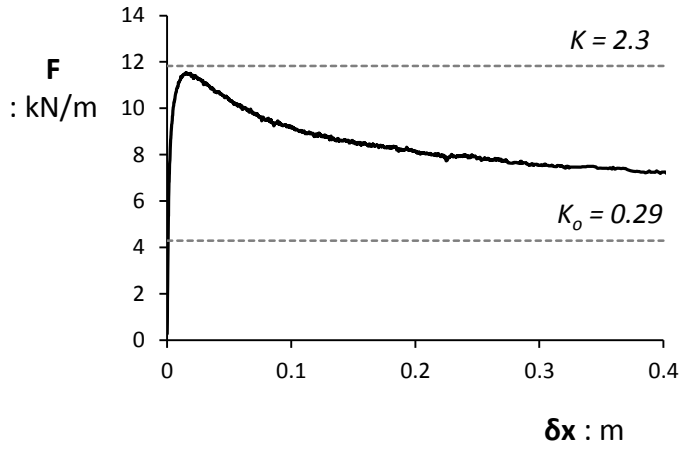

(a) **(b)**

Figure 4.3. The pullout test of the GIPIPE project (20015): (a) photo of the experimental setup and (b) the measured force-displacement curve.

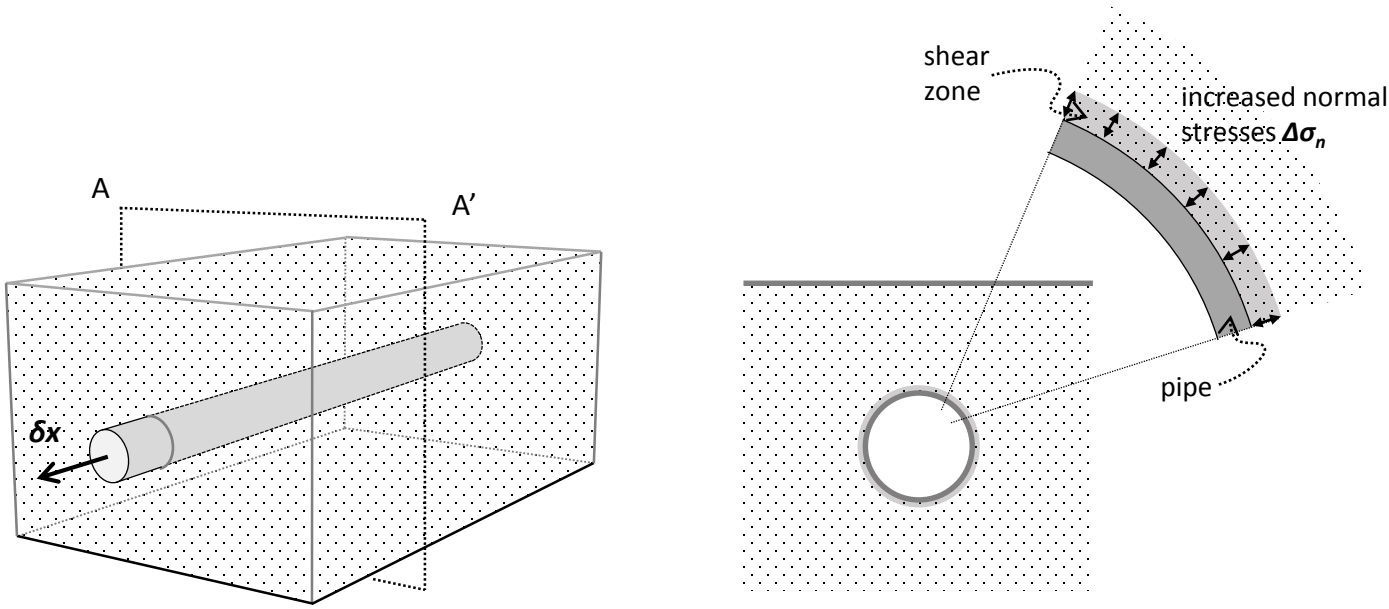

Figure 4.4. During axial movement of the pipe, the overall normal soil stresses on the pipe during pullout increases substantially in comparison with the initial values. This increase is attributed to the constrained dilation of the thin shear zone.

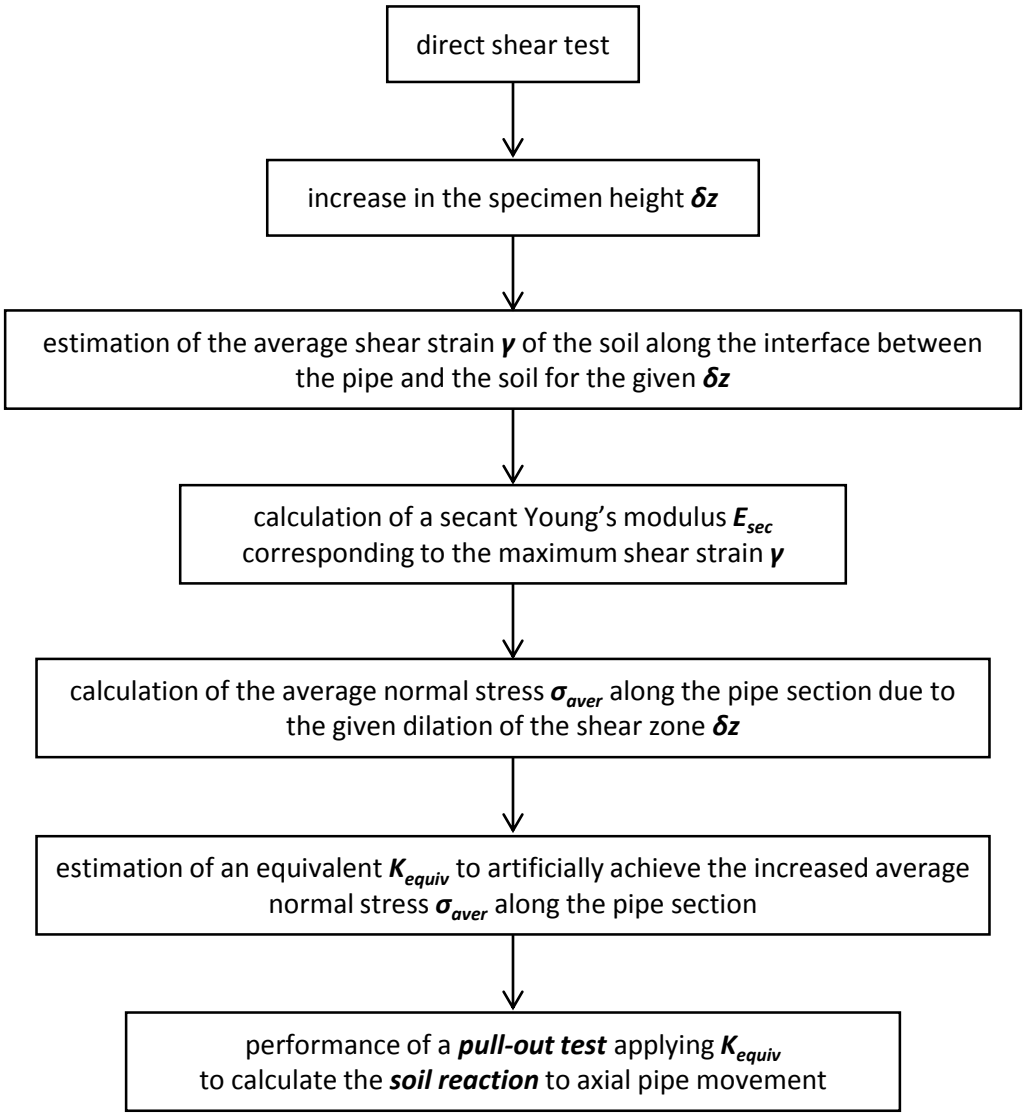

Figure 4.5. Flowchart presenting the steps of the finite element methodology used to calculate the soil reaction to axial pipe movement.

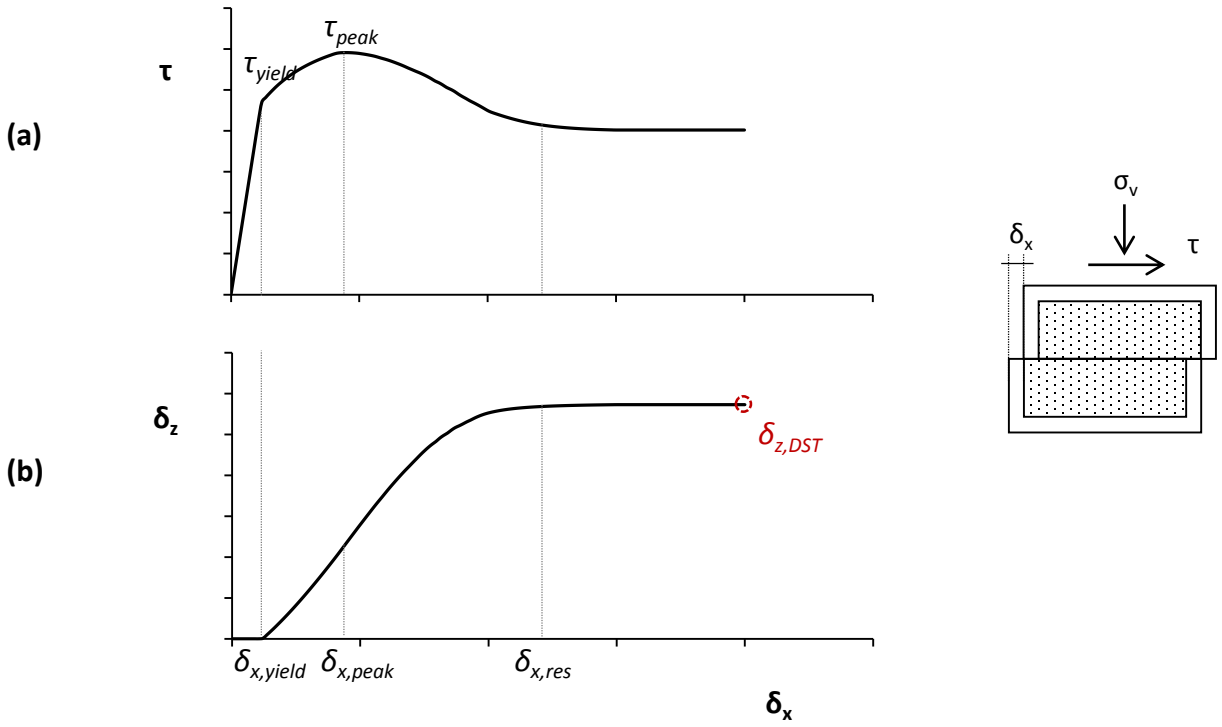

Figure 4.6. Step 1: The expansion of the shear zone (if it was not bounded by the outer soil) is estimated through direct shear testing. (a) A typical stress - displacement curve and (b) a vertical displacement - horizontal displacement curve for a dilative soil.

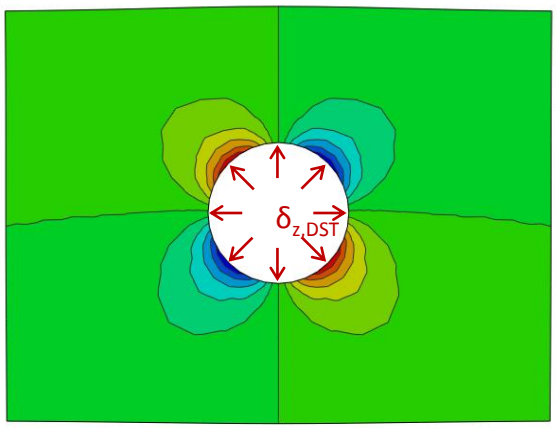

(a)

$$\left(\frac{G}{G_0}\right) = 1/\left[1+\left(\frac{\gamma-\gamma_e}{\gamma_r}\right)^a\right]$$

$$\gamma_r(\%) = 0.009\, ln\left(\frac{p'}{p_a}\right) + 0.037$$

$$\gamma_e(\%) = 8x10^{-5}\, ln\left(\frac{p'}{p_a}\right) + 0.007$$

$$p' = \frac{\sigma_1+\sigma_2+\sigma_3}{3}$$

$$p_a = 100\ kPa$$

$$a = 0.88$$

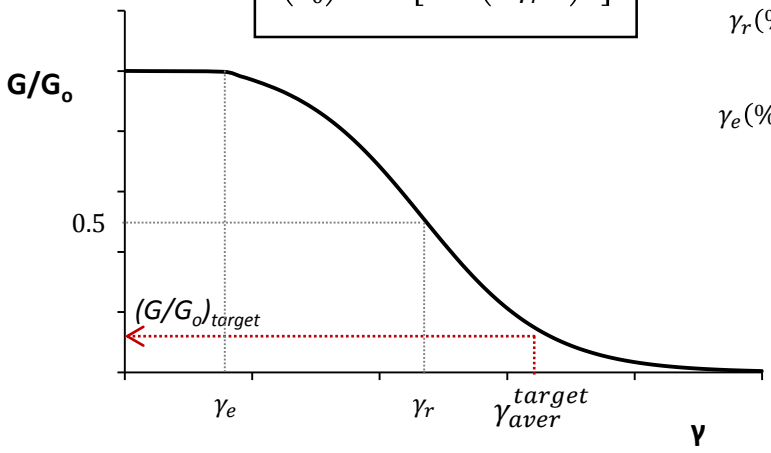

(b)

Figure 4.7. Step 2: Calculation of the appropriate (secant) shear modulus. (a) distribution of shear strains at the soil for an increase in the pipe diameter by δ. (b) The shear modulus degradation curve proposed by Oztoprak and Bolton (2013).

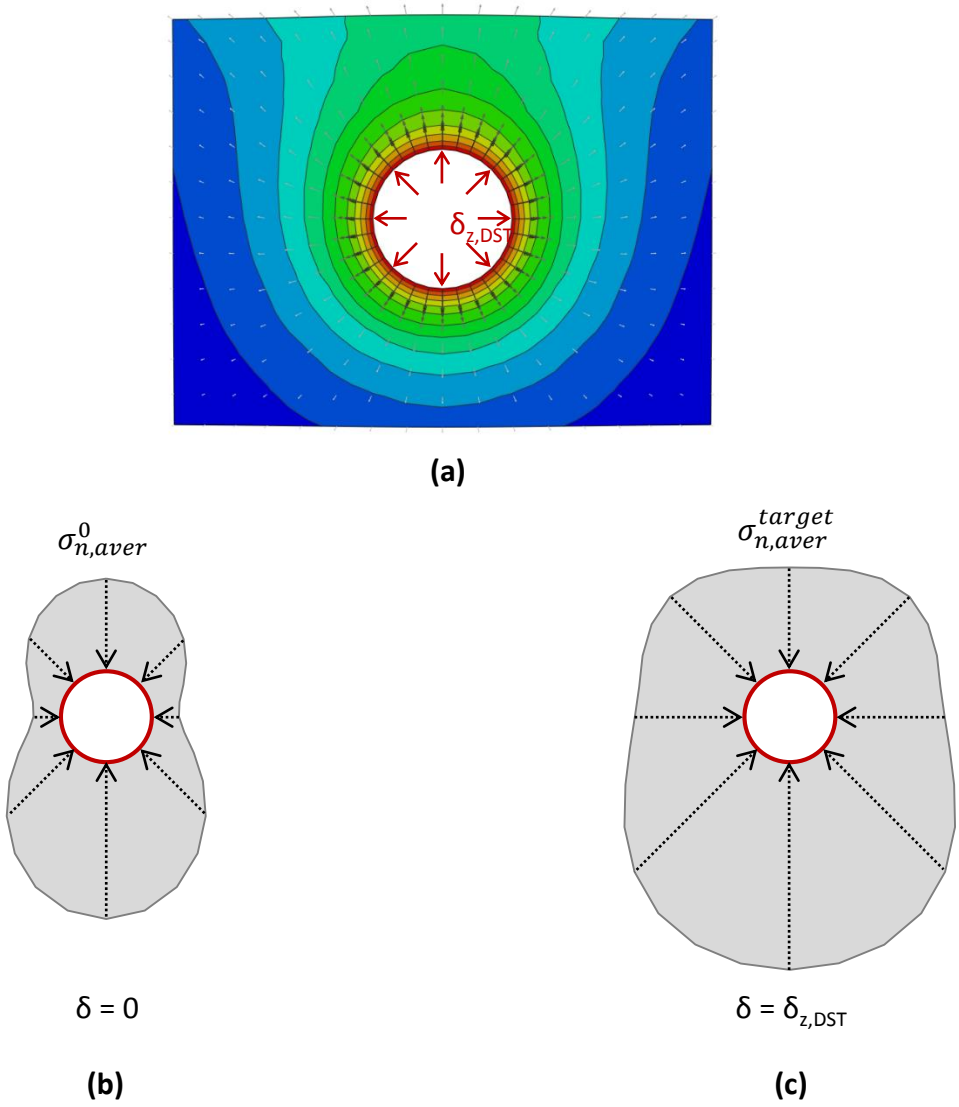

Figure 4.8. Step 2: A radial expansion analysis is used to simulate the increased normal stresses around the pipe during pullout. (b) The initial normal stresses distribution and (c) the increased stresses for radial expansion equal to the vertical expansion of the direct shear test specimen.

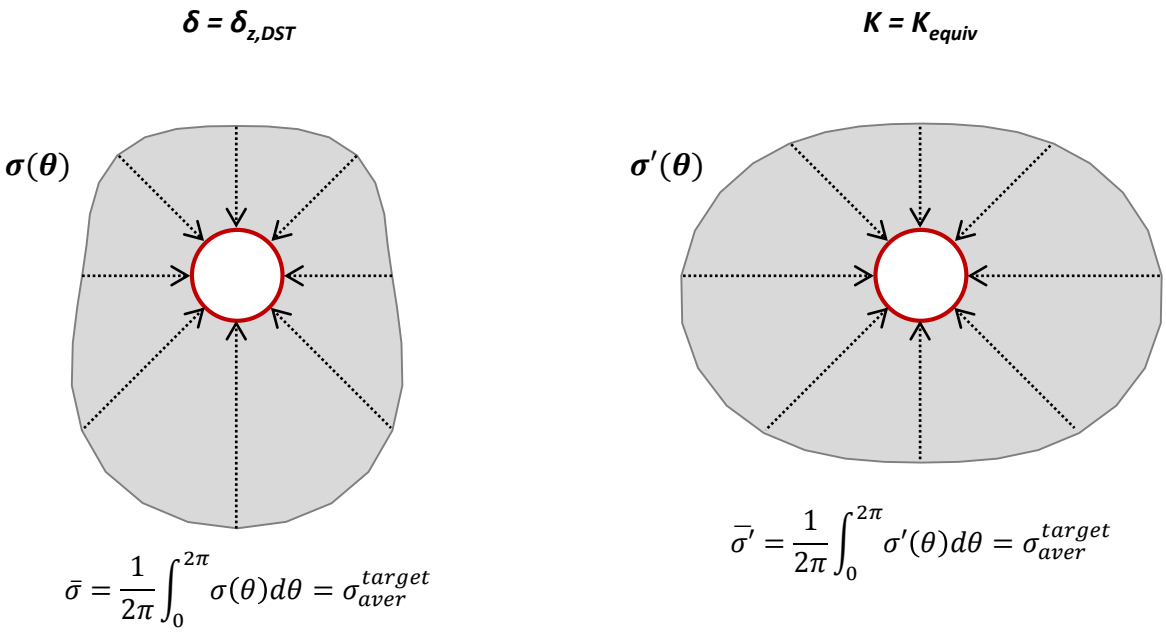

Figure 4.9. Step 3: An equivalent horizontal earth pressure coefficient K_{equiv} is selected that yields the target average normal stress $\sigma_{aver,target}$ on the pipe. The goal is to replicate the magnitude of the average normal stress not the actual stress distribution.

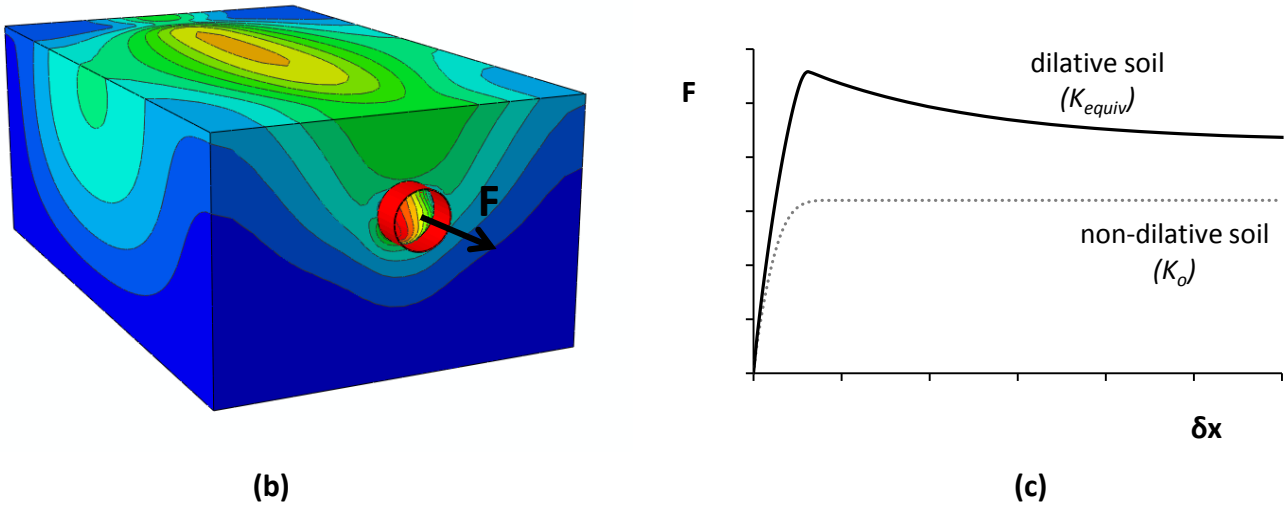

Figure 4.10. Step 4: Numerical calculation of the actual force-displacement behavior of the pipe subjected to axial relative displacement. (a) The deformed mesh of a typical model used for the pullout test. (b) A typical force-displacement curve for a dilative soil compared to the respective curve of a non-dilative soil.

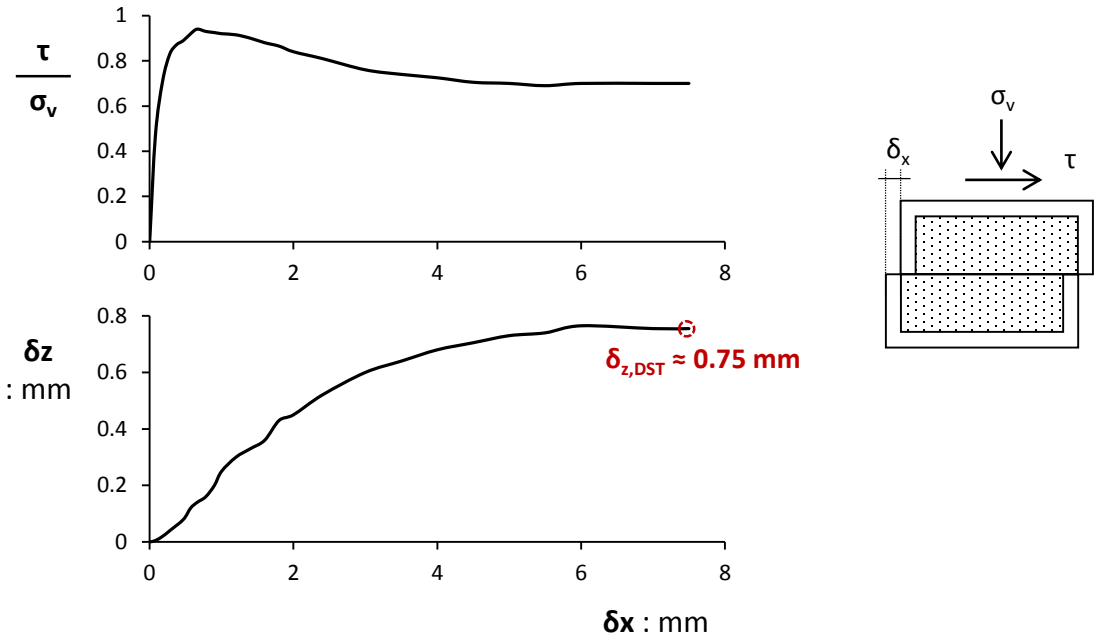

(a)

$\delta_{z,DST}$ (mm)	$\gamma_{aver,target}$ (%)	$(G/Go)_{target}$ (%)	$\sigma_{aver,target}$ (kPa)	K_{equiv}
0.75	0.39	3.4	26.7	1.90

(b)

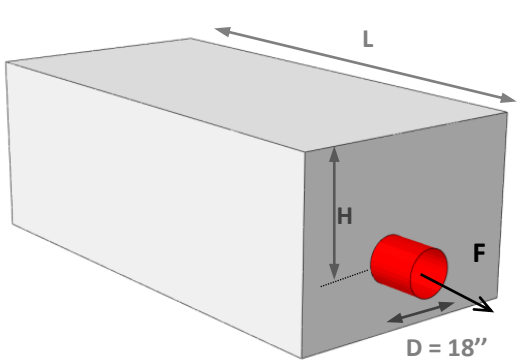

(c)

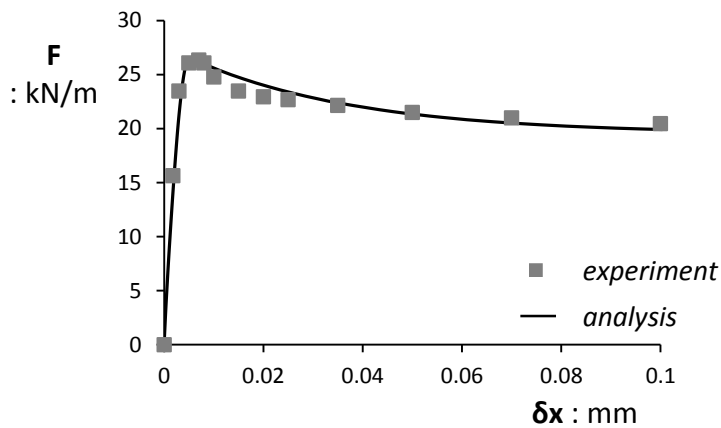

(d)

Figure 4.11. Validation of the proposed procedure against the pullout experiment performed by Wijewickreme et al (2009). (a) Direct shear tests of the sand used in the experiments, conducted at relative density and overburden stress similar to the experiments (Karimian 2006). (b) Summary of the outcome of each step of the procedure. (c) The geometry of the numerical model used to replicate the pullout test. (d) Comparison between the measured during the experiments and the numerically predicted force-displacement curve.

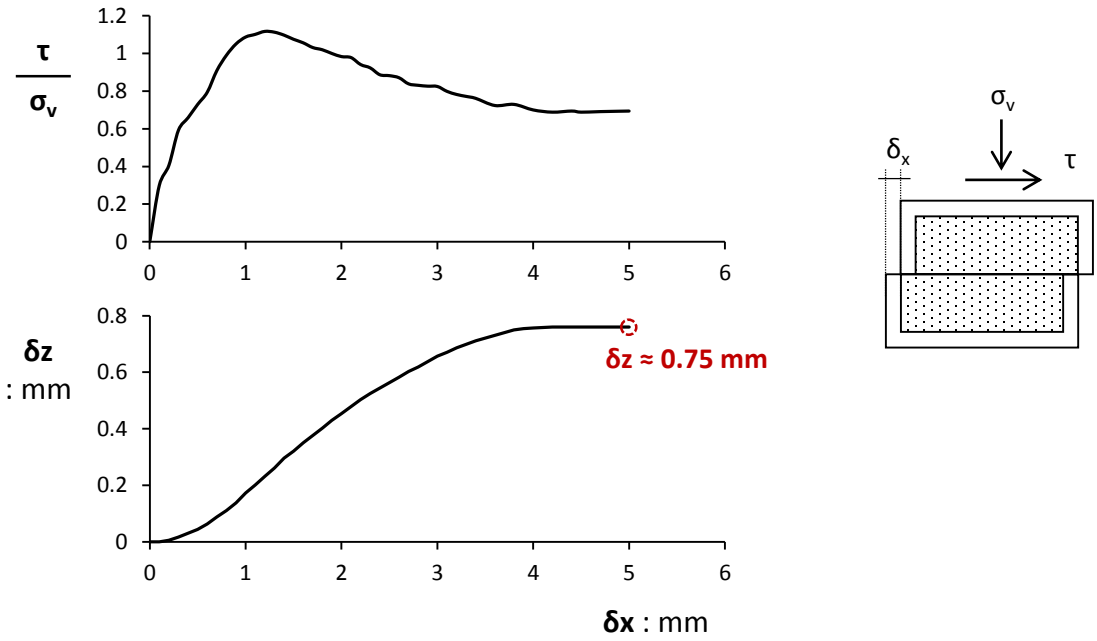

(a)

$\delta_{z,DST}$ (mm)	$\gamma_{aver,target}$ (%)	$(G/Go)_{target}$ (%)	$\sigma_{aver,target}$ (kPa)	K_{equiv}
0.75	0.82	4.1	20.6	2.4

(b)

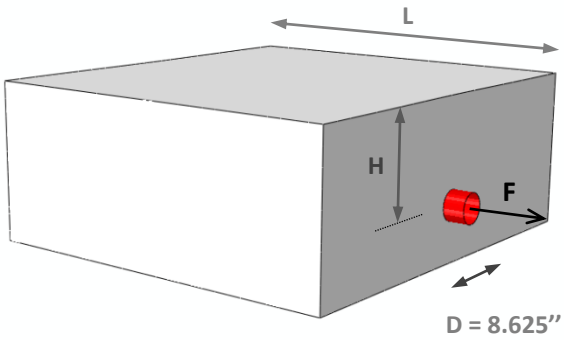

(c)

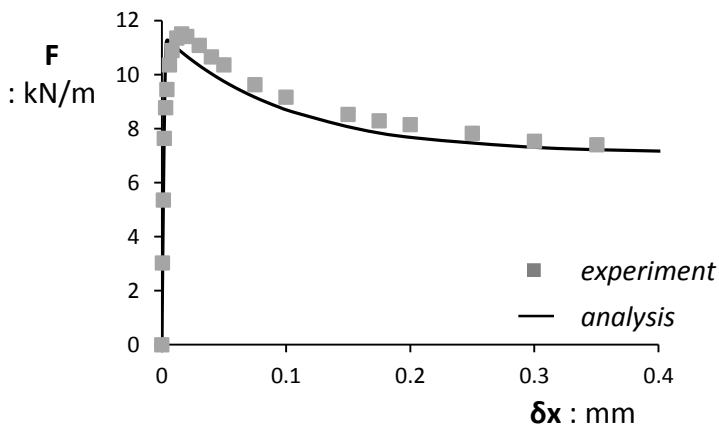

(d)

Figure 4.12. Validation of the proposed procedure against the pullout experiment performed in the framework of the GIPIPE project (2015). (a) Direct shear tests of the sand used in the experiments, conducted at relative density and overburden stress similar to the experiments. (b) Summary of the outcome of each step of the procedure. (c) The geometry of the numerical model used to replicate the pullout test. (d) Comparison between the measured during the experiments and the numerically predicted force-displacement curve.

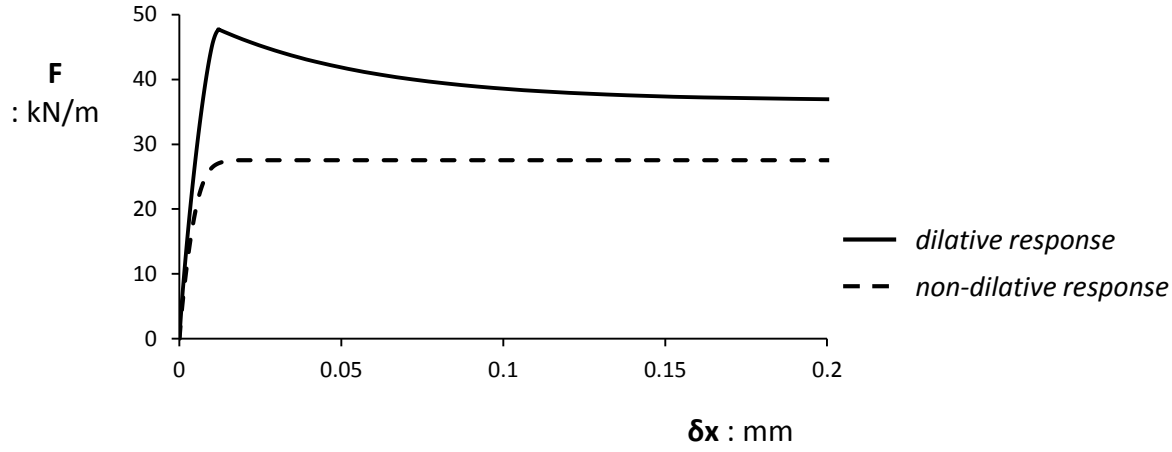

Figure 4.13. Soil reaction to axial movement of a 36" diameter pipe within a sandy soil deposit of φ_{max} = 40° ignoring and accounting for the effect of dilation.

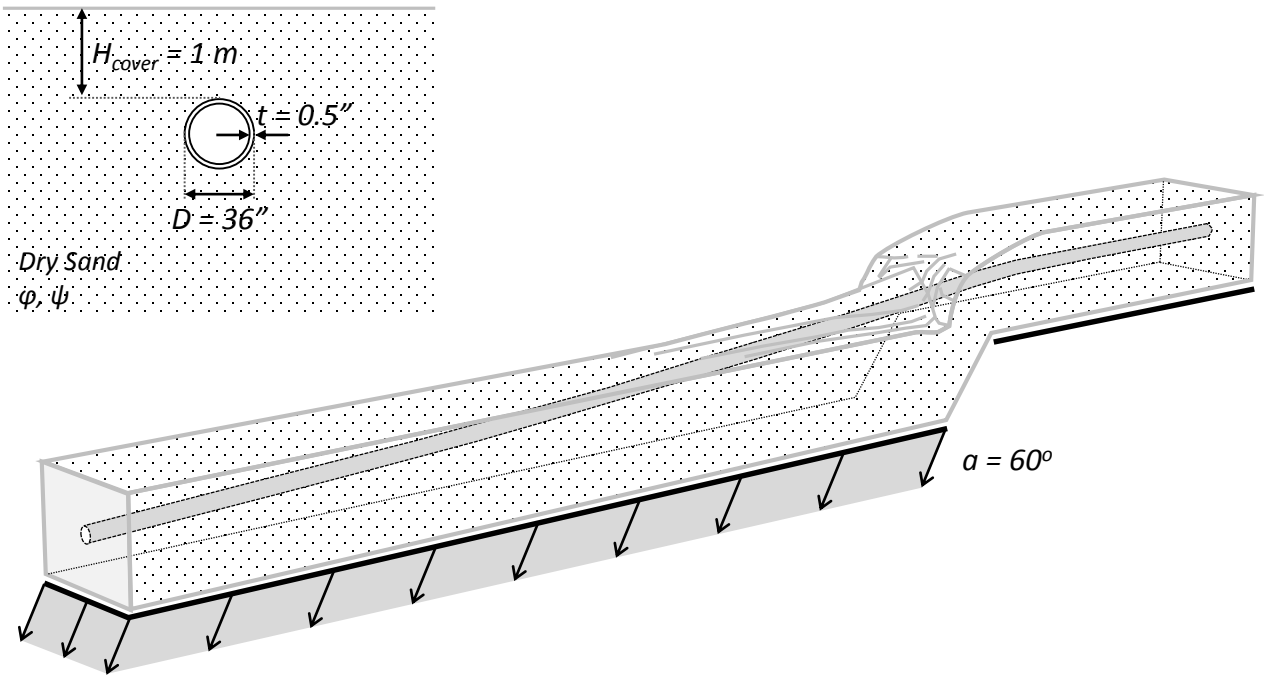

Figure 4.14. In order to investigate the effect of the dilative behavior of the soil on the overall pipeline performance an example is used: an infinitely long pipeline (D=36", t=0.5", H_{cover}=1 m), buried in dry sand is subjected to normal fault perpendicular to its axis (dip angle α=60°). A range of soil properties (combinations of friction angle ϕ, and dilation angle ψ) are considered.

φ (deg)	ψ (deg)	φ_{res} (deg)	γ_{yield}	γ_{peak}	γ_{res}	$\delta_{z,DST}$ (mm)	K_{equiv}
45	25	35	0.01	0.025	0.09	1.15	1.73
45	20	35	0.01	0.025	0.09	0.92	1.66
45	15	35	0.01	0.025	0.09	0.70	1.57
45	10	35	0.01	0.025	0.09	0.46	1.45
45	5	35	0.01	0.025	0.09	0.23	1.25
45	0	-	0.01	-	-	-	0.293

(a)

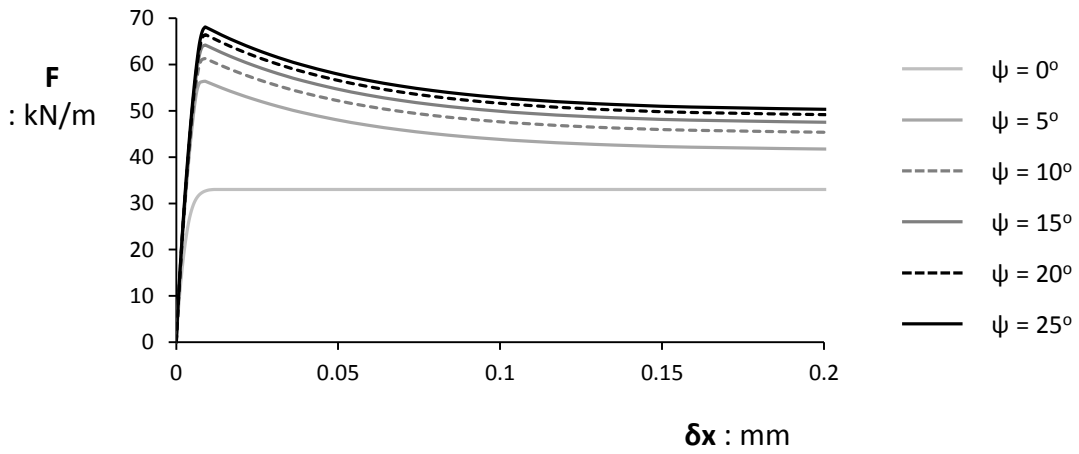

(b)

Figure 4.15. Details for the soil for the case of friction angle ϕ=45°. (a) Table with the properties of the sand, the vertical expansion during direct shear testing and the appropriate K_{equiv} required to describe the increase in the normal stresses acting on the pipe during axial pullout. (b) Soil reaction to axial relative movement of the pipe for the various dilation angles under consideration.

φ (deg)	ψ (deg)	φ_{res} (deg)	γ_{yield}	γ_{peak}	γ_{res}	$\delta_{z,DST}$ (mm)	K_{equiv}
40	20	32	0.017	0.035	0.10	0.93	1.50
40	15	32	0.017	0.035	0.10	0.71	1.43
40	10	32	0.017	0.035	0.10	0.46	1.33
40	5	32	0.017	0.035	0.10	0.23	1.17
40	0	-	0.017	-	-	-	0.357

(a)

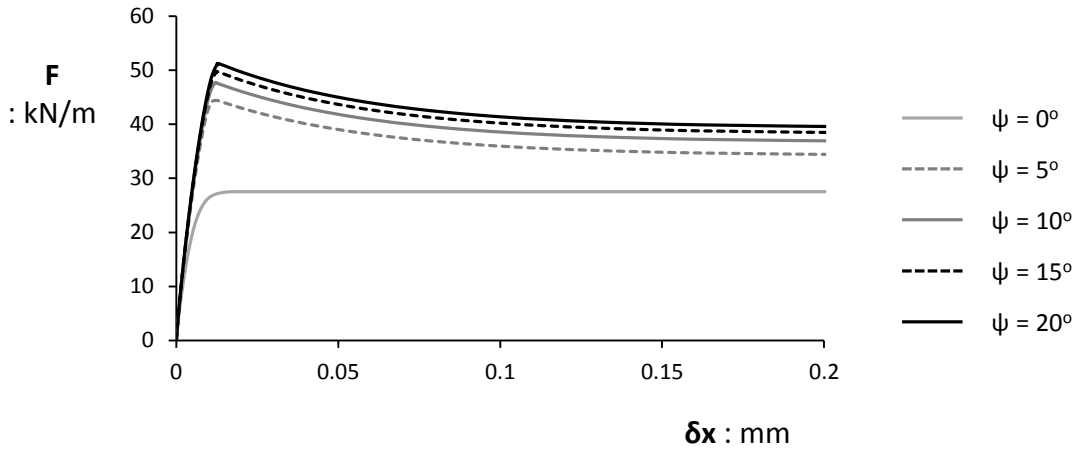

(b)

Figure 4.16. Details for the soil for the case of friction angle ϕ=40°. (a) Table with the properties of the sand, the vertical expansion during direct shear testing and the appropriate K_{equiv} required to describe the increase in the normal stresses acting on the pipe during axial pullout. (b) Soil reaction to axial relative movement of the pipe for the various dilation angles under consideration.

φ (deg)	ψ (deg)	φ_{res} (deg)	γ_{yield}	γ_{peak}	γ_{res}	$\delta_{z,DST}$ (mm)	K_{equiv}
35	15	30	0.023	0.04	0.11	0.73	1.34
35	10	30	0.023	0.04	0.11	0.49	1.26
35	5	30	0.023	0.04	0.11	0.24	1.12
35	0	-	0.023	-	-	-	0.426

(a)

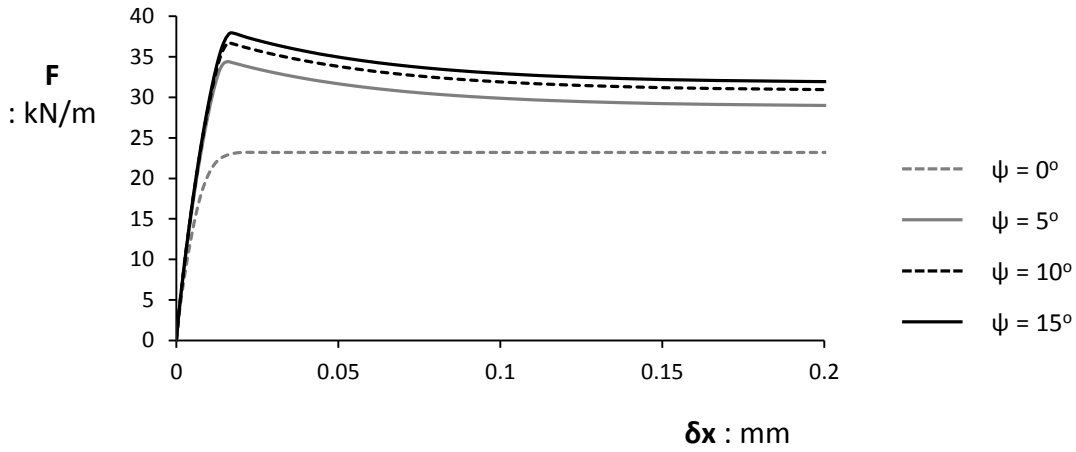

(b)

Figure 4.17. Details for the soil for the case of friction angle ϕ=35°. (a) Table with the properties of the sand, the vertical expansion during direct shear testing and the appropriate K_{equiv} required to describe the increase in the normal stresses acting on the pipe during axial pullout. (b) Soil reaction to axial relative movement of the pipe for the various dilation angles under consideration.

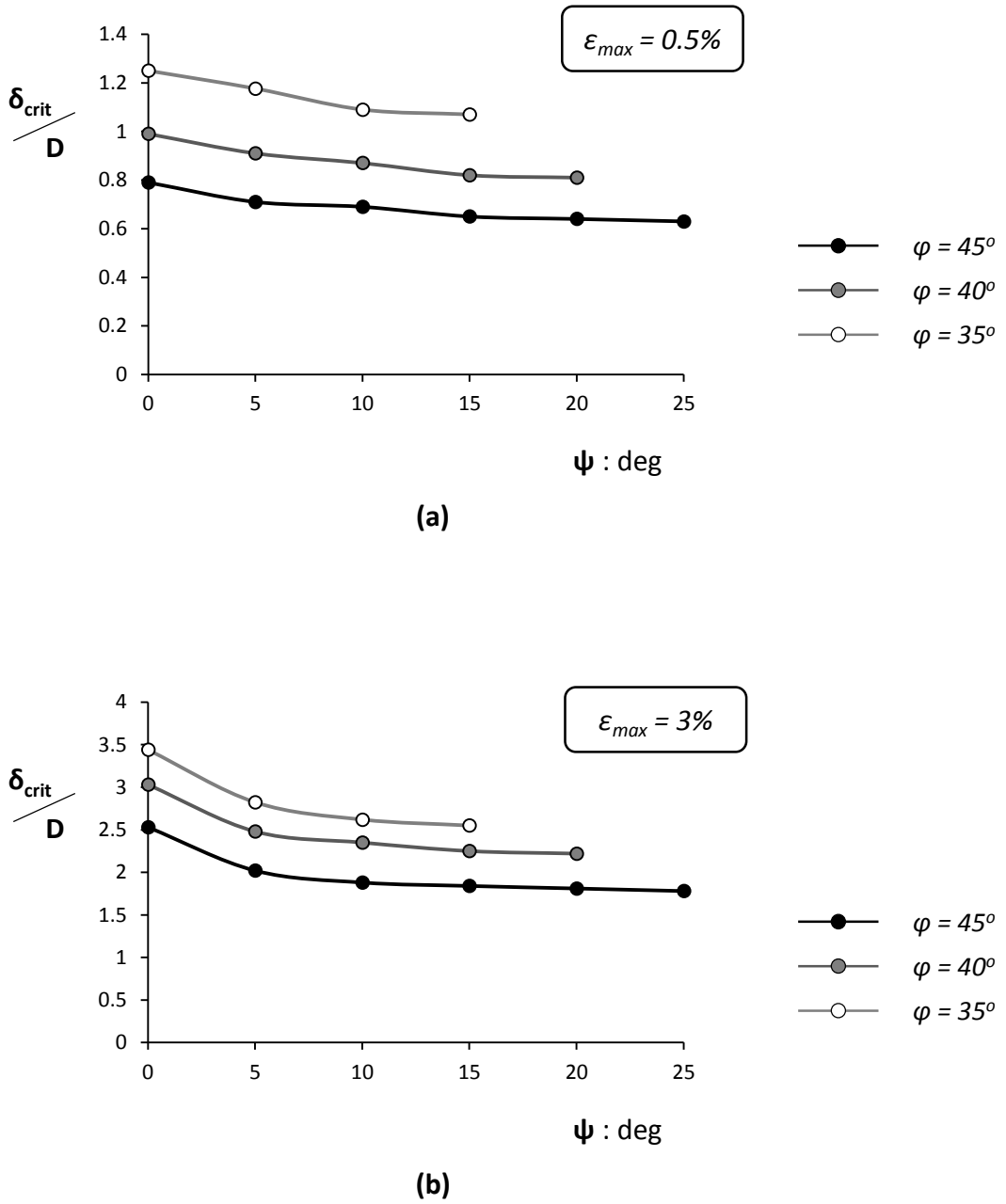

Figure 4.18. The effect of the soil dilation on the overall pipeline performance. The critical fault displacement that leads the pipeline to failure normalized with the pipe diameter considering as tensile failure criterion (a) the maximum tensile axial strain ε_{max} = 0.5% and (b) ε_{max} = 3%.

φ_{peak} (deg)	φ_{res} (deg)	δ_{xyield} (mm)	δ_{xpeak} (mm)	δ_{xres} (mm)	D (mm)
45	35	0.5	1.25	4.5	50

(a)

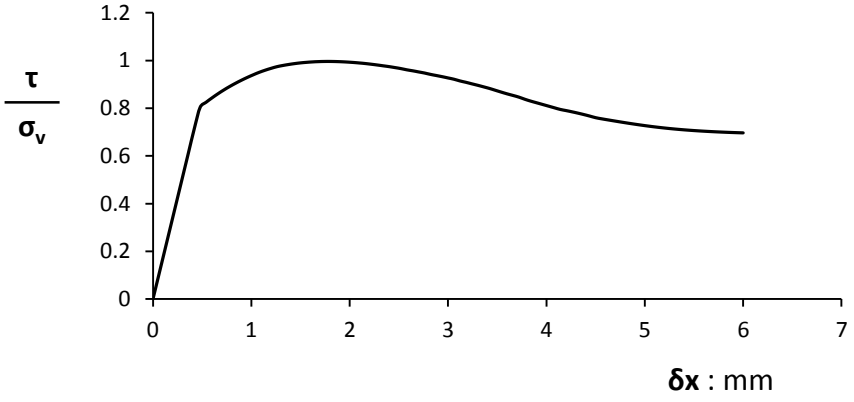

(b)

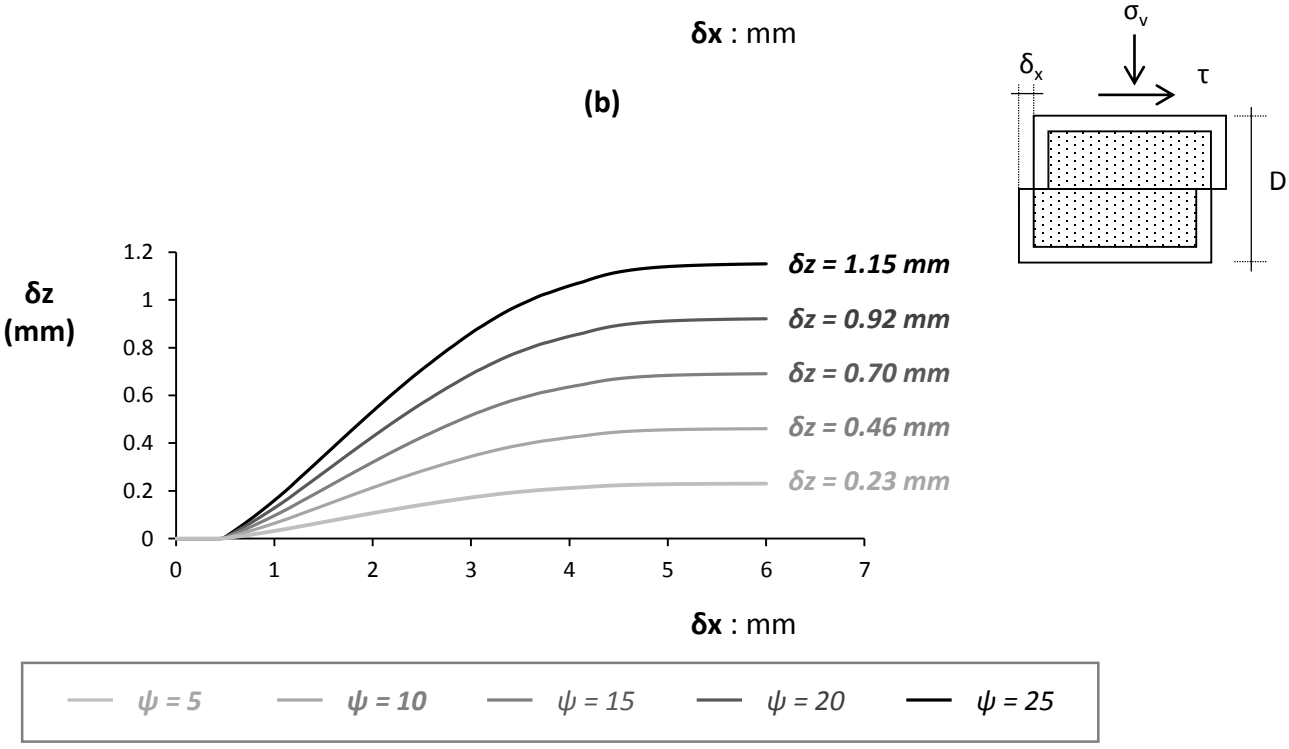

(c)

Figure 4.19. Results from the numerically conducted direct shear tests of the sand of friction angle ϕ=45o. (a) Summarizing table with the direct shear tests results. (b) Normalized shear stress-displacement curve. (c) Increase in the specimen height with horizontal displacement

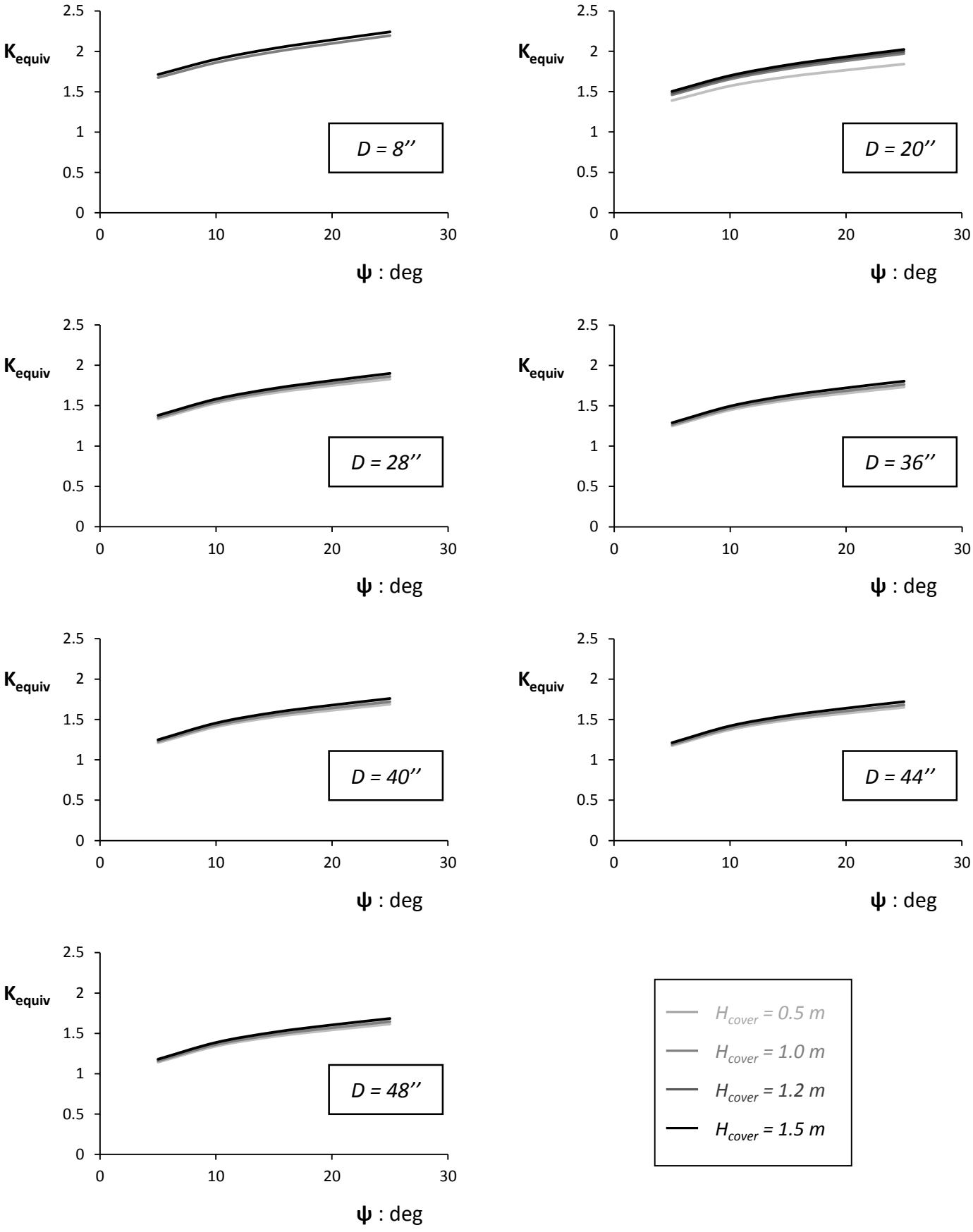

Figure 4.20. Charts with the appropriate K_{equiv} to be used for the calculation of the maximum soil resistance to axial relative movement of the pipe, when the surrounding soil is sand of friction angle ϕ=45^{o}. Pipe diameter from D=8" to 36".

φ_{peak} (deg)	φ_{res} (deg)	δ_{xyield} (mm)	δ_{xpeak} (mm)	δ_{xres} (mm)	D (mm)
40	32	0.85	1.75	5	50

(a)

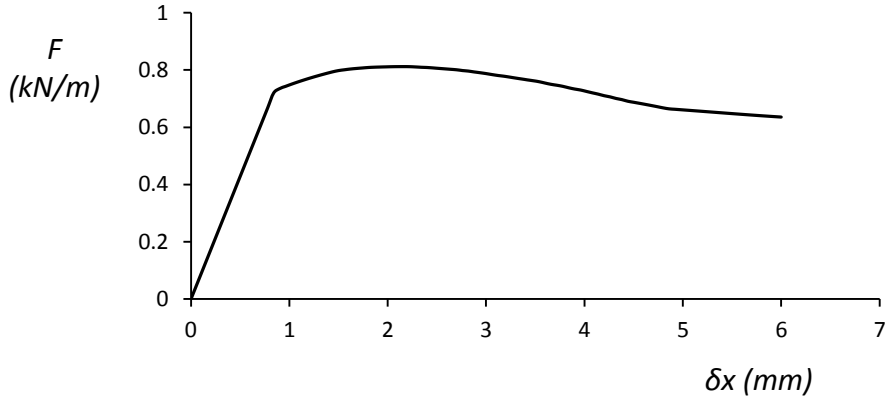

(b)

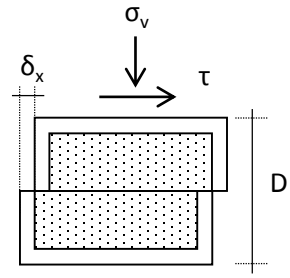

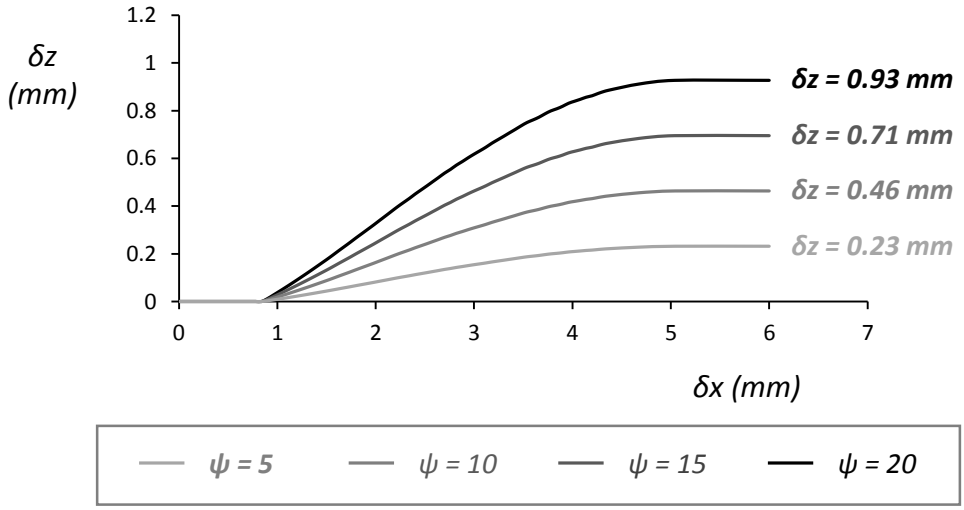

(c)

Figure 4.21. Results from the numerically conducted direct shear tests of the sand of friction angle ϕ=40^o. (a) Summarizing table with the direct shear tests results. (b) Normalized shear stress-displacement curve. (c) Increase in the specimen height with horizontal displacement

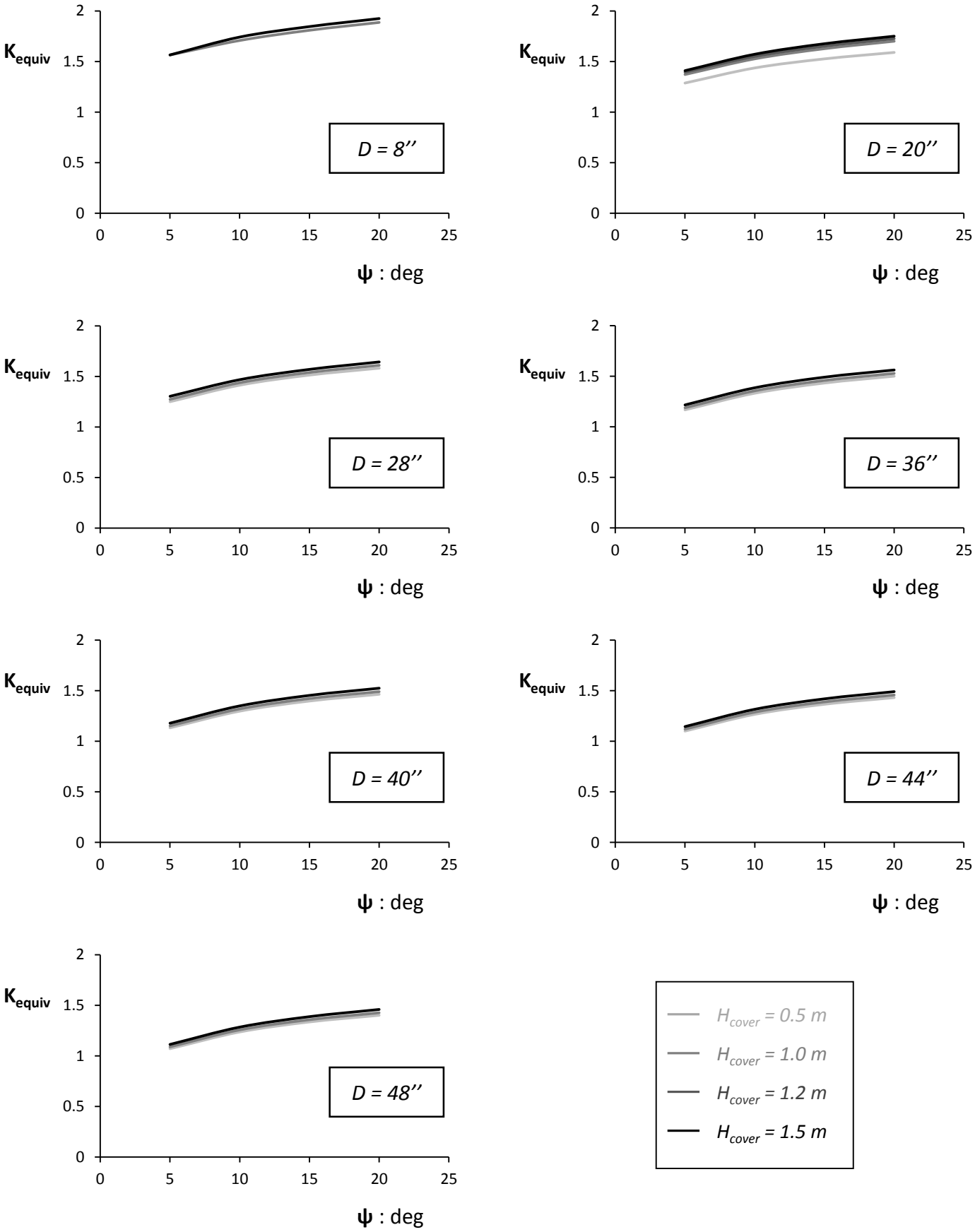

Figure 4.22. Charts with the appropriate K_{equiv} to be used for the calculation of the maximum soil resistance to axial relative movement of the pipe, when the surrounding soil is sand of friction angle ϕ=40^{o}. Pipe diameter from D=8" to 36".

φ_{peak} (deg)	φ_{res} (deg)	δ_{xyield} (mm)	δ_{xpeak} (mm)	δ_{xres} (mm)	D (mm)
35	30	1.15	2	5.5	50

(a)

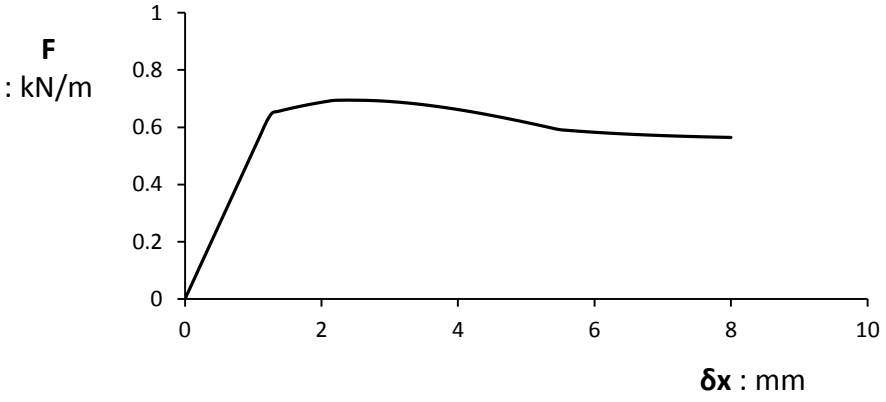

(b)

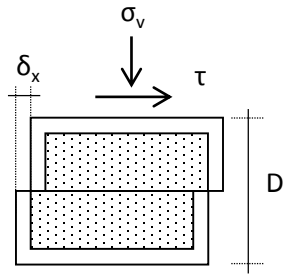

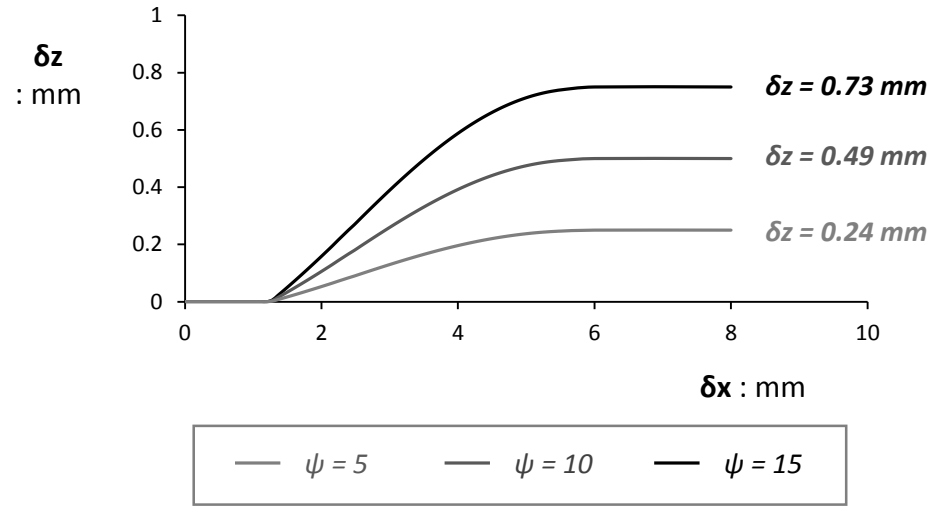

(c)

Figure 4.23. Results from the numerically conducted direct shear tests of the sand of friction angle ϕ=35^{o}. (a) Summarizing table with the direct shear tests results. (b) Normalized shear stress-displacement curve. (c) Increase in the specimen height with horizontal displacement

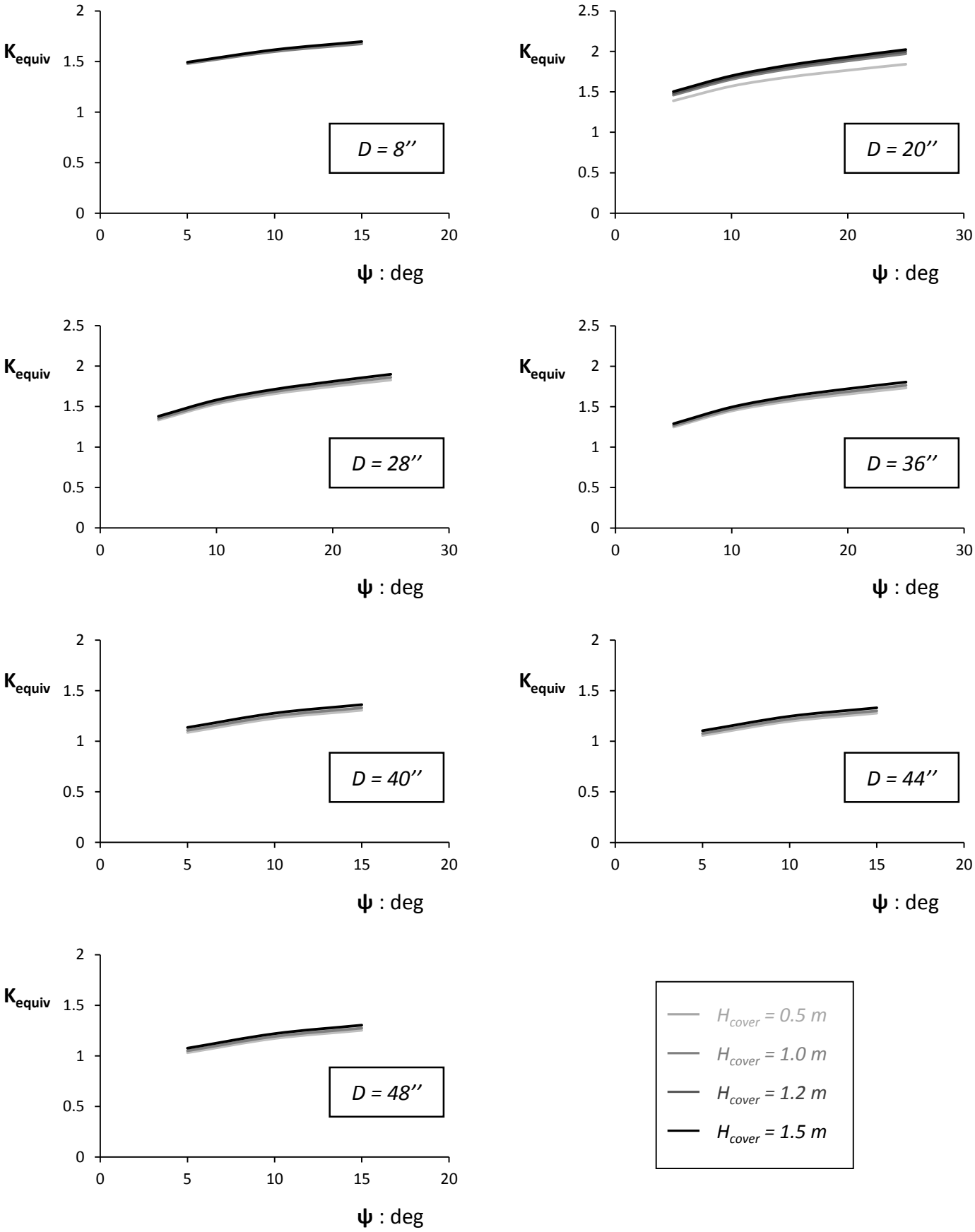

Figure 4.24. Charts with the appropriate K_{equiv} to be used for the calculation of the maximum soil resistance to axial relative movement of the pipe, when the surrounding soil is sand of friction angle ϕ=35^{o}. Pipe diameter from D=8" to 36".

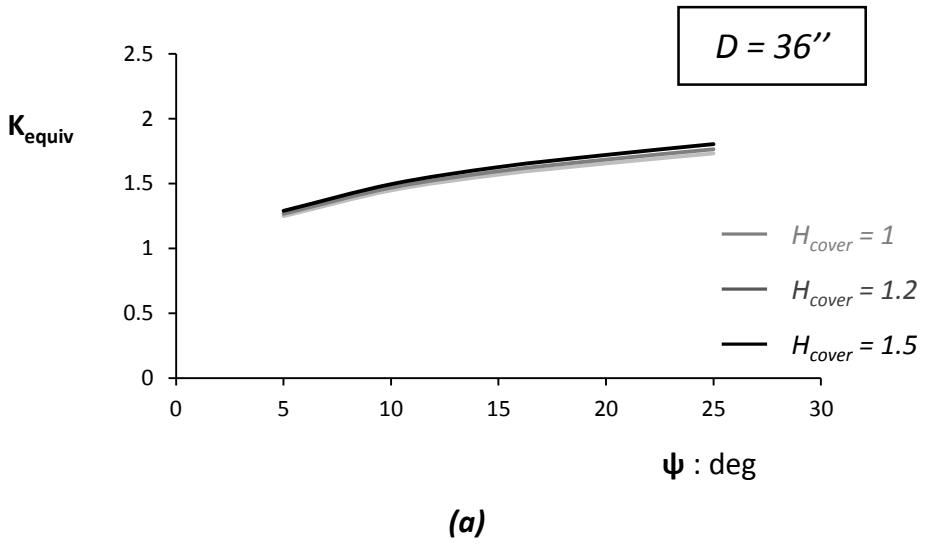

(a)

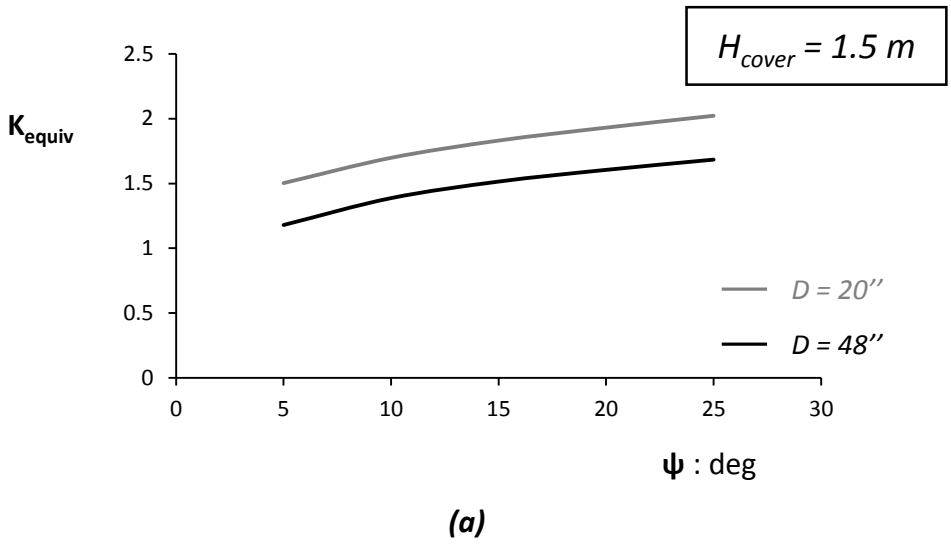

(a)

Figure 4.25. (a) The influence of the burial depth of the pipe on the appropriate $K_{o,equiv}$. (b) The influence of the pipe diameter on the appropriate $K_{o,equiv}$.

Chapter 5

Pipeline performance under dip-slip faulting

5.1. Introduction

In the previous chapters a finite element methodology was conceived to realistically simulate the response of buried continuous pipelines subjected to dip slip faulting. The methodology was based on the distinctively different response of the pipe in the vicinity of the fault ("near-fault" response) and at large distance from it ("far-field" response). The methodology was extensively validated against physical testing for both the "near-fault" and the "far-field" response. Having gained confidence in the numerical methodology, in this chapter we utilize it with the scope of (a) gaining an insight of the performance of a variety of pipes commonly used for the transportation of hydrocarbons subjected to normal and reverse faulting, and (b) to investigate the effect of some of the most influential factors of the problem. To this end, a parametrical study is performed to pinpoint the effect of the soil strength and stiffness, the dip angle of the fault and of the internal pressure on the pipeline response.

5.2. Performance of buried pipelines subjected to normal faulting

The effect of the soil strength

To begin with, the effect of the soil strength and stiffness on the pipeline response subjected to normal faulting is examined using an illustrative example. An infinitely long continuous pipeline of diameter D = 40" and thickness t = 0.562" is considered. The pipeline is made of steel X65 (σ_y = 450 MPa) and it is buried within the soil with a cover depth of H_{cover} = 1.2 m (the depth of the pipe top centerline). **Fig. 5.1** schematically presents the studied problem. The properties of the surrounding soil are parametrically accounted for: four non-cohesive soils are selected to cover a range of soils from very loose to very dense sand. The properties of the four sands are summarized in **Table 5.1**, where the results of hypothetical direct shear tests of the four sands are also presented. Based on these results, the axial force-displacement curves are calculated using the methodology presented in chapter 5. As shown in chapter 5, the accurate calculation of the axial soil restrain accounting for the effect of dilation is fundamental for the realistic simulation of the "far-field" response. **Fig. 5.2** presents the axial restrain curves for each of the four sands.

Fig. 5.3 summarizes the response of the pipeline when it is embedded in sand of φ=40°. **Fig. 5.3a** presents the axial strain evolution with the fault imposed displacement δ_{fault} at two characteristic points at the top side of the critical pipe segment (denoted as point A and point B). As explained in Chapter 3, the critical segment is the one at the vicinity of the fault-pipeline intersection within the footwall, since this is where the combined bending moments and tensile stresses due to stretching maximize (at the point of maximum curvature, which in this case is the point A). The axial strain evolution is accompanied by the deformed mesh of the critical pipe segment with superimposed axial strain contours for representative magnitudes of δ_{fault}. The pipeline responds elastically for fault offsets up to 0.5 m (highlighted as region I). During this time, the strain distribution is uniform both at the top and at the bottom side of the pipe segment. As the pipe enters the plastic regime, the strain accumulation ratio is increased (region II). The tensile strains tend to localize at point A (maximum curvature point). Ultimately there comes a point where necking is formed starting in point B which lies closer to the pipe-fault intersection. The whole section at point B is under yielding, resulting in drastic decrease in its stiffness; strains localize thus at this specific section rendering the pipe susceptible to rupture due to abrupt increase of tensile strains (region III). The transition from plastic response to necking is of particular interest. Before the formation of the neck, the increase in the maximum tensile strain is attributed to the combined stretching and bending. Therefore, the maximum tensile strain is located at the point of maximum curvature. In contrast, after the formation of the neck, the increase of strains is attributed to stretching, as advocated by the location of the neck which is closer to the pipe-fault intersection where the axial strains due to stretching are higher. As the prevailing loading mechanism shifts from the combined bending and stretching to exclusively stretching, the point of maximum tensile strain is transferred from point A to B. During this translation of the maximum strain point from A to B, the strain increase at point A comes to halt creating a temporary plateau. **Fig. 5.3b** presents the distribution of the tensile strains at the top side of critical pipe segment for the fault displacements shown in **Fig. 5.3a**.

Expectedly, the pipe response is qualitatively similar for the rest of the sands under consideration. **Fig. 5.4a** presents the maximum tensile strain evolution curve (the maximum of the two curves corresponding to point A and point B shown in **Fig. 5.3a**) for the four sands under consideration. In all four cases the elastic response is followed by an increase in the strain accumulation rate as the pipe is forced into its plastic regime. In the ensuing the appearance of a plateau marks the onset of necking that ultimately leads to an unstable condition. Though qualitatively similar, the effect of the relative stiffness between the pipe and the soil appears to play a crucial role in the magnitude of the pipe distress. As reasonably expected, the increase in the soil strength and stiffness leads to larger strain accumulation rate. The pipe is forced

to more severe bending and stretching as the vertical and axial soil reactions increase with the increase of the soil strength; the rate of strain accumulation increases with the increase of the soil strength, while the maximum axial strain at the onset of necking also becomes larger. **Fig. 5.4b** presents the fault offsets that correspond to the failure criteria adopted by the codes: maximum tensile strain of (a) $\varepsilon_{x,max}$ = 0.5%, (a) $\varepsilon_{x,max}$ = 2% and (a) $\varepsilon_{x,max}$ = 3%. The decrease of the critical fault offset with the increase in the friction angle vividly depicts the vulnerability of buried pipelines to stiff soils. However, there is another interesting point we need to comment on. During necking, the axial stiffness of the pipeline tends to zero: a small increase in the imposed displacement may result in an abrupt increase of the developed strain (unstable state) that may lead to wall rupture. Consequently, the onset of necking is a state that should be avoided during the design of pipelines subjected to normal fault-induced displacements. Considering the three failure criteria, the $\varepsilon_{x,max}$ = 3% criterion does not protect from the formation of necking in any of the examined cases. The $\varepsilon_{x,max}$ = 2% failure criterion protects in cases of stiff soils where the development of tensile strains due to bending and stretching is already substantial before the formation of necking. However, it fails to help the designer to avoid the necking formation for more compliant soils. Finally, the $\varepsilon_{x,max}$ = 0.5% failure criterion results in allowable fault displacements smaller than those that lead to necking, yet it proves quite conservative. Conclusively, the onset of necking should be also adopted as failure state and should be avoided during the design. Apart from the classical maximum tensile strain failure criteria, the designer should check for the formation of a neck.

The effect of the cover depth

In the analyses configuration examined in the previous, an additional parameter is added: the burial depth. The 40" diameter pipe is buried in the four sands of varying strength and stiffness with varying burial depth, which in this case is expressed by the depth of the cover between the top of the pipe and the ground level (cover depth): (a) H_{cover} = 1 m, (b) H_{cover} = 1.2 m and (c) H_{cover} = 1.5 m. For hydrocarbon transportation pipelines these values are very common, since the smaller H_{cover} = 1 m roughly corresponds to the minimum cover depth allowed (36" according to U.S. Code of Federal Regulations Title 49 part 195), and cover depths larger than H_{cover} = 1.5 m are rarely encountered in practice since they would demand deep excavations. As summarized in the table of **Fig. 5.5a**, the cover depths H_{cover} = 1 m, 1.2 m and 1.5 m yield *H/D* ratios of *H/D* = 1.48, 1.68 and 1.98 respectively. **Fig. 5.5b, 5.5c and 5.5d** summarize the critical fault offsets as calculated with the $\varepsilon_{x,max}$ = 0.5%, $\varepsilon_{x,max}$ = 2% and $\varepsilon_{x,max}$ = 3% respectively. As reasonably expected, the increase of the depth of the cover leads to a decrease of the safety margins, since the larger depths lead to larger confinement stresses. Since the soil profiles considered consist of non-cohesive

materials, the increase in the confinement stresses results in an increase in the strength and stiffness of the soil, and consequently in the decrease of the pipeline relative stiffness.

The effect of the dip angle

Back to the scenario of the 40" pipeline being buried at cover depth H_{cover} = 1.2 m. The surrounding soil is the dry sand of friction angle φ = 40° considered before. In this chapter the active fault that intersects with the pipeline is of unknown dip angle, hence the dip angle is parametrically accounted for. A wide range of angles is considered, with a minimum dip angle of a = 15° (very mild inclination that is unrealistic for a normal fault) and a maximum dip angle of a = 75°. **Fig. 5.6** presents the performance of the pipeline subjected to the faults of the various angles. In **Fig. 5.6a** the maximum tensile strain evolution is presented for the six cases of dip angle examined. In all cases the pipe accumulates strain due to the combined action of stretching and bending. Ultimately, the pipes fail due to necking. The fault with the mildest inclination appears to have the most detrimental effect on the pipe: a fault displacement of δ_{fault} = 1.1 m is sufficient to cause necking, while for the steeper fault rupture δ_{fault} = 3.7 m are needed to have the same result. From the pipeline response with respect to the angle of the displacement two important conclusions can be drawn. **Fig. 5.6b** presents the fault offset that leads to first yield (development of maximum tensile strain $\varepsilon_{x,max} = \varepsilon_{yield}$ = 0.225%) and to maximum tensile strain $\varepsilon_{x,max}$ = 0.5% (the more strict failure criterion met in the existing codes). The pipe appears to yield first when subjected to normal fault of dip angle a = 45°, while as the dip angle increases towards 90° or decreases towards 0°, a larger fault displacement is required to cause yielding. The same goes for the $\varepsilon_{x,max}$ = 0.5% curve: it has a minimum at a = 45° while it increases towards 90° and 0°. At 45°, the horizontal displacement δx and the vertical displacement δz are of the same magnitude, while as the dip angle increases or decreases the difference between the magnitude of δx and δz increases (large δx and small δz at small angles and large δz and small δx at large dip angles). Thus, the two curves shown in **Fig. 5.6b** illustrate a well-defined trend: the more intense the conjunction of the horizontal displacement component (that imposes tension on the pipe) with the vertical displacement component (that is responsible for the pipe bending), the more unfavorable the pipe response gets. The second interesting finding from the results of the pipe response with respect to the dip angle of the fault becomes apparent if we plot the strain evolution against the horizontal component of the displacement δx (instead of the total displacement δ_{fault}) as shown in **Fig. 5.6c**. As vividly depicted in this figure, pipe failure (necking) occurs at practically the same magnitude of δx, signifying that necking should be attributed almost exclusively to the development of excessive tensile forces rather than the combined stretching and bending which is responsible for $\varepsilon_{x,max}$ until the onset of necking.

The effect of the internal pressure

In general, transmission pipelines are rarely without internal pressure. The only periods that they will remain without pressure is the construction stage and possible maintenance periods, which are but a small fraction of the structure lifetime. In this part, the effect of the internal pressure on the pipe response and on the resulting safety margins is examined. An example is used: the D = 40" pipe used in the previous buried at H_{cover} = 1.2 m within the dry sand of $\varphi = 40^o$ is subjected to a normal fault intersecting at 90^o. In this case the pipe is considered to operate at the maximum design pressure p_{max} = 9 MPa calculated by the expression:

$$p_{max} = 0.72*(2\ \sigma_y\ t/D)$$

Fig. 5.7 offers a direct comparison of the response of the pipe with and without internal pressure, presenting the maximum tensile strain evolution with the increase in the fault displacement. Along with the strain evolution, the deformed mesh of the critical pipe segment is also presented with superimposed axial strain contours. The comparison between the non-pressurized and the pressurized pipe reveals a number of distinctively different behaviors. Firstly, the pressurized pipe yields under smaller fault displacement, namely $\delta_{fault} \approx 0.4$ m compared to the respective $\delta_{fault} \approx 0.5$ m for the non-pressurized pipe. Secondly, when in its plastic regime, the pressurized pipe accumulates plastic strain at significantly larger rate than the non-pressurized pipe. Thirdly, the maximum strain evolution curve for the pipe under internal pressure exhibits a plateau; the critical pipe segment keeps on accommodating additional fault offset (i.e. developing additional curvature) without increasing the maximum observed tensile strain $\varepsilon_{x,max}$. This response (which is reminiscent of the plastic hinging mechanism) is unique for the pressurized pipe. Ultimately, as with the non-pressurized pipeline the increase in the axial force due to the horizontal displacement of the fault becomes critical and leads to necking of a section closer to the pipe-fault intersection.

The above unique characteristics of the pressurized pipe response should be attributed to the reduced moment capacity due to the simultaneous action of the internal pressure. The initially straight pipe is stressed due to the soil actions, as the soil deforms due to the rupturing fault. The soil action transversal to the pipe axis causes the pipe to bend and ultimately to fail at the points of maximum curvature. For the sake of simplicity, let's assume that the imposed fault displacements of the same magnitude lead to the development of approximately the same soil transversal actions on the pipe and therefore, practically the same bending moment on the critical pipe segment for both the pressurized and the non-pressurized pipes. **Fig. 5.8a** presents in qualitative terms the influence of the internal pressure on the moment – curvature behavior of a straight pipe, according to the EN1993-4-3 Eurocode. For a straight pipe under

pure bending moment without any other action, there is an initially elastic response up to the yield moment capacity $M_y^{p=0}$ where the first yielding occurs followed by a gradual stiffness degradation up to the plastic moment capacity $M_{pl}^{p=0}$, where the entire section experiences yielding. As vividly depicted in this diagram, under the simultaneous action of the internal pressure the respective yield moment $M_y^{p\neq0}$ and plastic moment capacity $M_{pl}^{p\neq0}$ decreases. Under this decreased yield moment capacity $M_y^{p\neq0}$ the faster first yielding of the pressurized pipe is therefore to be expected.

Fig. 5.8a is also quite enlightening for the interpretation of the second distinctive behavior of the pressurized pipe: the substantial increase in the plastic strain accumulation rate. Consider a bending moment demand M larger than yield moment capacity of both the non-pressurized $M_y^{p=0}$ and the pressurized pipe $M_y^{p\neq0}$. This bending moment M leads to the development of a larger curvature (and therefore strain) for the pressurized pipe. In fact, for every M larger than both yield moment capacities the pressurized pipe is further into its plastic regime than the non-pressurized pipe and is associated with a reduced stiffness. Hence, an increase ΔM of the same magnitude (which is attributed to an increase in the fault displacement) causes a larger step of curvature and therefore strain $\Delta\varepsilon_{x,max}$ thus justifying the increased plastic strain accumulation.

The reduced bending capacity of the pressurized pipe depicted in **Fig. 5.8a** is indirectly responsible for the third unique characteristic, the quasi-plastic hinging response. The reduced value of the plastic moment capacity $M_{pl}^{p\neq0}$ combined with the increase in the plastic strain accumulation rate (due to decrease in $M_y^{p\neq0}$) lead to the exhaustion of the plastic moment capacity of the pressurized pipe at a substantially smaller displacement than the non-pressurized pipe. As a result, when the plastic moment capacity is reached, no rise in the maximum axial strain is observed, only a stress redistribution. This redistribution of stress is depicted in **Fig. 5.8b**, where the axial strain distribution along the tensile side of the critical segment is presented for various representative fault displacements. This wavy distribution consists of three prominent spikes, where tensile strains localize. The maximum values of these spikes initially increase with the increase of the fault displacement. For displacements larger than $\delta_{fault} \approx 1$ m, the maximum values barely increase. In contrast, the increase in the imposed displacement causes the "widening" of the spike located at $x = 4$ m; the work of the additional displacement is dissipated by the mobilization of a larger area – a stress redistribution. In contrast, this quasi-plastic-hinging response is not observable in the non-pressurized pipe for two reasons: the plastic strain accumulation rate is smaller while the plastic moment capacity is larger. Hence, the pipe fails due to necking first, before reaching the plastic moment capacity.

Arguably, the most characteristic feature of the pressurized pipe response (as depicted in **Fig. 5.7**) is the differentiation of the strain distribution. The non-pressurized pipe develops a rather uniform axial strain distribution, that when entering the plastic regime localizes around the maximum curvature point (see **Fig. 5.7a**). In stark contrast, for the pressurized pipe the initially uniform strain distribution transforms into a "wavy" distribution when the yield capacity is exceeded; there is not a single maximum point, rather there are a number of maxima in the form of successive spikes along the tensile side of the critical pipe segment (see **Fig. 5.7b**). This peculiar behavior should be attributed to second order phenomena. In particular, as the pipe enters its plastic regime the developed curvature becomes considerable. As a result of this bending, the length of the two outer fibers change, with the one under compression shrinking and the one under tension stretching as schematically shown in **Fig. 5.9a**. At the same time, the internal pressure *p* produces a theoretical upward force when integrated along the top (tensile) side and a respective downward force when integrated along the bottom (compressive) side. For the initially straight pipe these two forces cancel each other (they are of the same magnitude and of opposite sign). However, as the curvature of the pipe segment increases, there is a divergence between the length of the tensile and that of the compressive fiber. Now, the internal pressure integrated along the top side yields a larger force than when integrated along the bottom side. Hence, due to change in the geometry, the curved pipe "experiences" an internal pressure p' acting only on the tensile side that tends to reduce its curvature. Moreover, the magnitude of this parasitic pressure is proportional to the difference in the length of the two opposite sides (i.e. the segment curvature). The existence of *p'* is indicated by the fact that it tends to straighten a number of sections along the curved segment. **Fig. 5.9b** shows the curved critical pipe segment with axial strain contours with and without internal pressure (a scale factor of 20 has been imposed). It is in these sections that the strain localizes yielding the characteristic wavy distribution.

Structural performance of buried pipelines subjected to normal faulting

In this part, the results already shown and described are enhanced to encompass pipes for various geometries of particular interest. The loading case remains the intersection of the pipeline with an active normal fault, with the fault strike normal to the pipeline axis (as graphically shown in **Fig. 5.10a**). Maintaining a sense of realism, the cover depths that are accounted in this extended study are H_{cover} = 1 m, 1.2m and 1.5 m (**Fig. 5.10b**). Since this study focuses on hydrocarbon transportation pipelines, the results are expanded to account for pipes of medium large to large diameters (D = 28", 36", 40" and 48"). In order for the results to have a practical value, the closest commercially available thickness is selected

for each pipe to yield a *D/t* ratio of about 70 which is very common in practice. **Fig. 5.10c** presents a table with the geometrical characteristics of the four tubes considered in the analyses. Finally, the properties of the soil is also parametrically accounted for, with the soil properties shown in **Fig. 5.10d**.

To begin with, **Fig. 5.11** presents the results for the performance of the pipes assuming they operate without pressure. **Fig. 5.11a** presents the maximum axial strain evolution considering a cover depth of H_{cover} = 1 m, while **Fig. 5.11b** and **Fig. 5.11c** present the respective results for H_{cover} = 1.2 and H_{cover} = 1.5 m. The evolution of the pipe distress (expressed through the maximum tensile strain) is correlated with the fault displacement δ_{fault} normalized with the pipe diameter *D*. The pipes under consideration appear to exhibit similar behavior in terms of normalized fault displacement δ_{fault}/D, provided that the cover depth is the same and that the soil is of the same strength and stiffness. This normalization of the response of the different pipes is depicted in the safety margins considering the three tensile failure criteria for the pipes buried at cover depth H_{cover} = 1 m (**Fig. 5.12**), H_{cover} = 1.2 m (**Fig. 5.13**) and H_{cover} = 1.5 m (**Fig. 5.14**). In the same manner, the response of the pressurized pipes is presented in **Fig. 5.15** to **Fig. 5.18**. In **Fig. 5.15** the evolution of the maximum tensile strain is plotted against the imposed normalized fault displacement δ_{fault}/D. For all the pressurized pipes examined, the response of the pipe can be assorted in the four regions explained in the previous: the initial mild strain accumulation (elastic response) is followed by a significant increase in the axial strain development as the pipe enters its plastic regime; the pipe exhausts its plastic bending moment capacity and the maximum tensile strain accumulation curve forms a plateau. Ultimately, the prevailing stressing mechanism alters and the pipe fails due to excessive stretching at the proximity of its intersection with the fault rupture. As with the non-pressurized pipes the increase in the soil strength and stiffness has a detrimental effect on the pipe response. The same stands for the increase in the cover depth. Aggregating the results by soil strength and stiffness (indicated by the friction angle ϕ) and by the cover depth H_{cover} reveals a remarkably similar behavior of the four pipes under consideration in terms of normalized displacement δ_{fault}/D. This similitude in the performance of the pipes is also portrayed in the safety margins considering the three tensile failure criteria. **Fig. 5.16** summarizes the critical fault displacement assuming each of the failure criteria for the pressurized pipes that are buried at H_{cover} = 1 m, while **Fig. 5.17** and **Fig. 5.18** present the respective results for H_{cover} = 1.2 m and 1.5 m.

5.3. Performance of buried pipelines subjected to reverse faulting

Following the same procedure as in the case of normal faulting, in this part the performance of buried pipelines is examined subjected to reverse faulting. A set of the numerical analyses is performed considering the same pipes as before, three cover depths (H_{cover} = 1 m, 1.2 m and 1.5 m) and the four non-cohesive soil profiles used in the previous. This time the pipes are considered to cross a reverse fault normal to their axes that is expected to produce displacements at dip angle a = 30°. The values of the parameters used in this parametrical investigation are presented in **Fig. 5.19**. Finally, the effect of the internal pressure is also accounted for considering two alternatives: (a) the pipes are under no internal pressure and (b) the pipes operate at the maximum of their design pressure which is approximately p_{max} = 9 MPa for all pipes.

Fig. 5.20 presents the response of the non-pressurized pipes for all the soil profiles and cover depths considered. The evolution of the maximum compressive strain along the pipe is shown with the increase in the fault offset δ_{fault} normalized with the diameter D. In all the examined cases, the pipes fail due to local buckling: the combined action of compression and bending moment due to the horizontal and vertical dislocation of the hanging wall results in the development of large compressive strains at the maximum curvature point within the hanging wall. These strains lead the pipe to yielding, and subsequently to the formation of local buckling due to the thin-walled nature of the pipes. During buckling, an increase in the fault offset leads to an abrupt increase in the developed strains (unstable condition). Despite the minor divergence in the metaplastic response (which should be attributed to the minor differences in the D/t ratios of the pipes, but is of little interest anyway, since the pipeline is considered to have failed), the response of the pipes of different diameter proves to be quite similar in terms of normalized fault displacement δ_{fault}/D, provided that the strength and stiffness of the soil as well as the depth of the cover are the same. This similitude in the response of the pipes is further advocated by **Fig. 5.21** that summarizes the normalized critical fault displacement that causes the onset of local buckling of the non-pressurized pipes.

Fig. 5.22 isolates from the ensemble of the results those that refer to the 40” diameter pipe. Thus, three failures lines are plotted corresponding to the normalized critical fault offsets for different depths of soil cover H_{cover}. As with the normal fault, the increase of the cover depth leads to a rise of the respective overburden stresses and a subsequent increase in the soil strength and stiffness. Hence, the relative stiffness of the pipe decreases reducing the fault offset it can safely accommodate.

The effect of the dip angle

To investigate the effect of the dip angle of the reverse fault distressing the pipe, an example is used: the 40" diameter is buried within the sand of $\varphi = 30^o$ at depth $H_{cover} = 1.2$ m. The angle of the dislocation of the hanging wall is unspecified, and therefore the dip angle is parametrically considered in the analyses, ranging from 15^o to 75^o (possibly unrealistic for a reverse fault). In all the examined cases the pipe buckles locally due to the combination of compression and bending moment. **Fig. 5.23a** presents the fault displacement that leads to first yielding of the pipe as well as the displacement that leads to the onset of local buckling as a function of the dip angle of the fault. First let's focus on the response up until yielding. As with the normal fault, the displacement that causes first yielding minimizes when the dip angle is 45^o, while as the dip angle increases towards 90^o or decreases towards 0^o the required displacement to cause yielding increases. Similarly with the effect of dip angle of the normal fault, the more intense the conjunction of the horizontal displacement component (that imposes compression on the pipe) with the vertical displacement component (that is responsible for the pipe bending), the more unfavorable the pipe response gets. This behavior is not reflected on the fault displacement that leads to buckling. If this behavior was also valid during the onset of local buckling we would expect a convex curve with a minimum at $a = 45^o$. Rather, the critical fault offsets are smaller than expected for dip angles less than 45^o and larger than expected for dip angles larger than 45^o. The root of this shift in the response lies in the metaplastic response of the pipe. The first yielding curve refers to fault offsets that by definition result to the same axial strain ($\varepsilon_x = \varepsilon_{yield} = 0.00225$) for all dip angles. Yet, it appears that this is not the case for the buckling curve. In particular, **Fig. 5.23b** shows the values of the compressive strain at the moment of buckling initiation as a function of the dip angle of the normal fault. These values are extracted in a consistent manner: the minimum axial strain at the compressive side of the critical section at the moment when the axial strain distribution along the compressive side "freezes" and any additional strain localizes at the dominant ripple that start dislocating outwards forming the characteristic bump of the local buckling. This figure illustrates the dependence of the critical compressive strain on the fault dip angle. Hence, if we consider the performance for $a = 45^o$ as a reference point, for smaller angles the local buckling will occur "faster", while for larger angles the onset of local buckling will be delayed. This behavior should be accounted responsible for the small but noticeable deviation of the failure line from the expected.

At the bottom of this behavior lies the effect of the compressive force on the metaplastic response of the pipe. Let's consider a pipe segment that is under significant bending leading to the development of significant compressive plastic strains at the bottom side. In the case of a thin-walled pipe, the pipe segment will not be able to develop its fully plastic bending since there will be a point where the

compressive wall will develop a tendency for transversal displacement (local buckling). If this pipe segment is at the same time under compression, then the Poisson effect (the phenomenon in which a material tends to expand in directions perpendicular to the direction of compression) will add to the tendency for outward dislocation (**Fig, 5.24a**). The synergy of those two mechanisms deteriorate the metaplastic deformation capacity of the pipe: the larger the compression is the smaller plastic strain the pipe can develop before buckling locally.

The effect of the internal pressure

In the following, the effect of the internal pressure on the response of buried pipelines subjected to reverse faulting is investigated. **Fig. 5.25** presents the normalized critical fault offsets δ_{fault}/D that lead to local buckling initiation for the pressurized pipes ($p_{oper} = p_{max}$). The results refer to the four pipes under consideration as well as the four soil profiles and the three cover depths. The analyses refer to reverse faulting with a strike perpendicular to the pipe axis and with dip angle $a = 30^o$.

Contrary to what we would intuitively expect, the presence of the internal pressure is not deterrent to the formation of local buckling, while in fact has a detrimental impact on the pipeline performance. **Fig. 5.26** compares the performance of the non-pressurized 40" pipe buried at H_{cover} = 1.2 m with that of the fully pressurized pipe for the four sandy profiles under consideration. The decrease in the safety margins against local buckling with the increase of the pressure is substantial (of the order of 50%). Decrease of the critical fault offset with internal pressure was also observed in pressurized pipes subjected to compressive strike-slip faults by Vazouras et al. (2012). Although contrary to expectations that would call for an increased stability of the cross section with the presence of internal pressure and therefore increased resistance to local buckling, this behavior has a reasonable explanation. Let's consider the non-pressurized pipe at first: under the effect of the fault-induced compressive force, the critical pipe segment tends to radially expand (Poisson effect). With the increase in this compressive force (and under the simultaneous action of bending moment), the critical pipe segment will buckle locally exhibiting the characteristic bump that in this case will have an outward direction: since local buckling is a bifurcation phenomenon, the buckle will be in the most vulnerable direction. **Fig. 5.27a** presents the deformed pipe segment for a non-pressurized pipe showing the outward buckle. The simultaneous action of the internal pressure adds to the tendency for outward expansion, facilitating the formation of an outward buckle and rendering the pipe more vulnerable to local buckling. **Fig. 5.27b** schematically presents strength decreasing mechanisms. Macroscopically, the influence of the internal pressure is vividly depicted in the interaction relation for the combination of axial force in terms of *Ar* (axial force A to axial tensile resistance

Ay) and bending moment *Mr* (bending moment *M* to the plastic moment M_p) for internal pressure p = 0 and p = 9 MPa (**Fig. 5.27c**). This relation introduced by Mohareb (2002) is based on the fully plastic capacity of the pipe, and for the combination of axial force, bending moment and internal pressure takes the following form:

$$M_r = \sqrt{1 - \frac{3}{4}p_r^2} * cos\left\{\frac{\frac{\pi}{2}(A_r - \frac{1}{2}p_r)}{\sqrt{1 - \frac{3}{4}p_r^2}}\right\}$$

This relation is based on the fully plastic capacity of the pipe, and therefore it is used herein only qualitatively to show the effect of internal pressure on the pipe capacity. As vividly depicted in the left quadrant (space of combined compression and bending), the failure envelop shrinks spectacularly for p = 9 MPa, yielding combinations of compressive forces and bending moments substantially smaller than the respective for p = 0. Notice that were the pipe section able to acquire its full plastic moment capacity, this bending moment resistance would drop to 60% of the non-pressurized pipe even without any compressive force. Although in our case the pipe will buckle before reaching its fully plastic moment capacity, the trend of the diminished moment capacity still stands. In addition, the compression capacity also drastically decreases. Since the imposed loading has a dominant compressive component, this degradation of the compression capacity with the increase of the internal pressure also plays an important role. **Fig. 5.27d** presents the increase in the axial force on the pipe with the increase in the fault displacement for the non-pressurized and the pressurized pipe, vividly depicting the trend of substantially decreasing compression capacity with the increase of the internal pressure.

5.4. Concluding remarks

In this chapter a substantial number of numerical analyses was performed considering buried pipelines subjected to normal and reverse fault. A range of pipes commonly used in the hydrocarbon transmission industry was selected. Four representative non-cohesive soil profiles were selected to account for the change in the soil strength and stiffness. Three characteristic cover depths were accounted for. This numerical study serves the purpose of gaining an insight on the performance of buried pipelines subjected to normal and reverse faulting and to conclude with a realistic estimation of the safety margins that could be used as a benchmark for more simplified analyses. The set of results illustrated that the response of the pipes is qualitatively and quantitatively similar in terms of normalized fault offset δfault/D provided

they refer to the same soil profile and the same cover depth. Further examination of the results brought to light some interesting findings:

- The neck formation due to excessive stretching of a pipe subjected to normal faulting is correlated with an abrupt increase in the tensile strain (unstable condition). There are cases where the maximum tensile strain failure criteria fail to account for the neck formation. Hence, the designer should consider pipe necking a separate failure criterion.
- The presence of internal pressure differentiates significantly the behavior of a pipeline subjected to normal faulting. The yield moment capacity as well as the plastic moment capacity decrease. As a result a smaller fault displacement is needed to cause first yielding, while the plastic strain accumulation rate increases significantly. A pipe under significant internal pressure will reach its plastic moment capacity before necking exhibiting a plastic hinging similar response. Finally, the axial strains along the tensile side of critical pipe segment acquire a wavy distribution due to second order effects.
- The effect of the internal pressure on a pipeline subjected to reverse faulting is also unfavorable: it reduces both the compression and bending capacity of the pipe.
- The synergy of bending moment and axial force appears to affect the metaplastic deformation capability of the pipe. With the increase of the compressive axial force the pipe was found to be less capable to deform within its plastic regime: local buckling occurred at smaller compressive axial strain.

References

Mohareb, M. (2002). Plastic interaction relations for pipe sections. *Journal of engineering mechanics, 128(1)*, 112-120.

Vazouras, P., Karamanos, S. A., & Dakoulas, P. (2012). Mechanical behavior of buried steel pipes crossing active strike-slip faults. *Soil Dynamics and Earthquake Engineering, 41*, 164-180.

Comité Européen de Normalisation. Eurocode 3, Part 4-3: Pipelines. CEN EN 1998-4, Brussels, Belgium; 2006.

Figures
of Chapter 5

φ (deg)	φ_{res} (deg)	ψ (deg)	δ_{xyield} (mm)	δ_{xpeak} (mm)	δ_{xres} (mm)	δ_z (mm)	ρ (Mg/m^3)
45	35	15	0.5	1.25	4.5	0.70	1.8
40	32	10	0.85	1.75	5.0	0.46	1.7
35	30	5	1.15	2.0	5.5	0.24	1.6
30	30	0	1.5	-	-	-	1.5

Table 5.1. Properties of the sand materials considered in the parametric study.

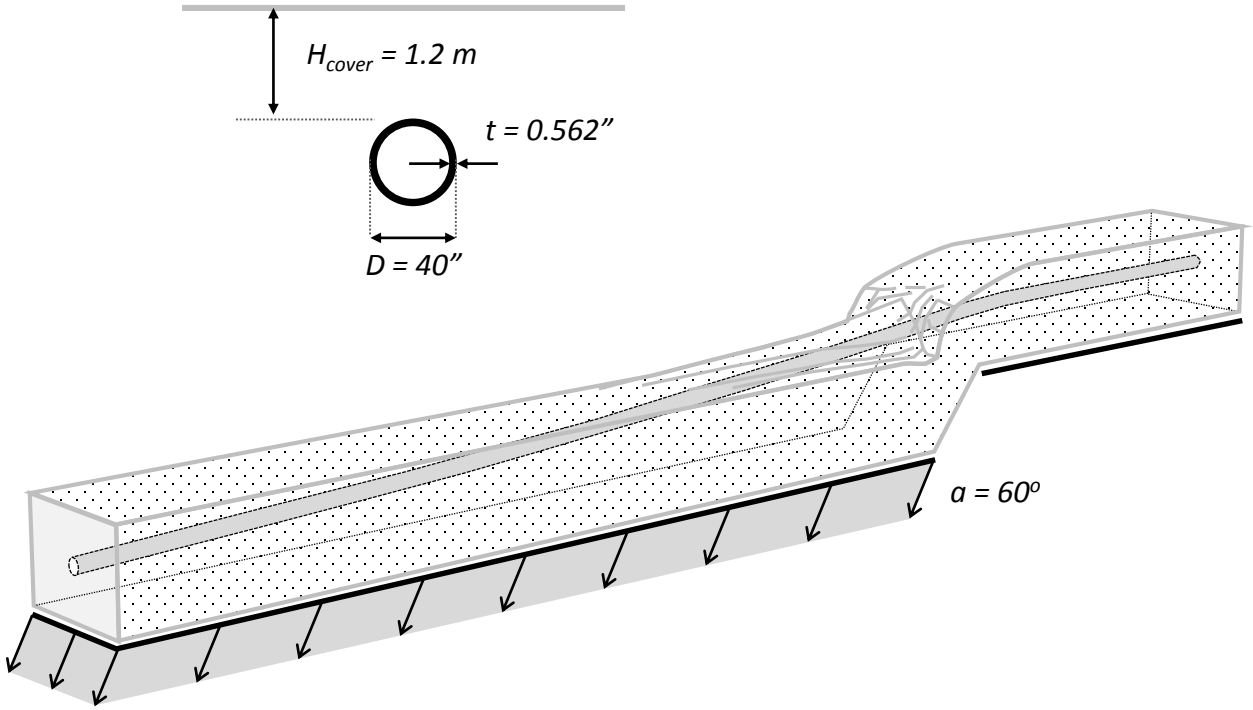

Fig. 5.1. The studied problem: a continuous pipeline [D=40”, t=0.562”, steel X65], buried at H_{cover} 1.2 m, crosses perpendicularly an active normal fault of dip slip a=60º. The response of the pipeline is examined with respect to the properties of the soil.

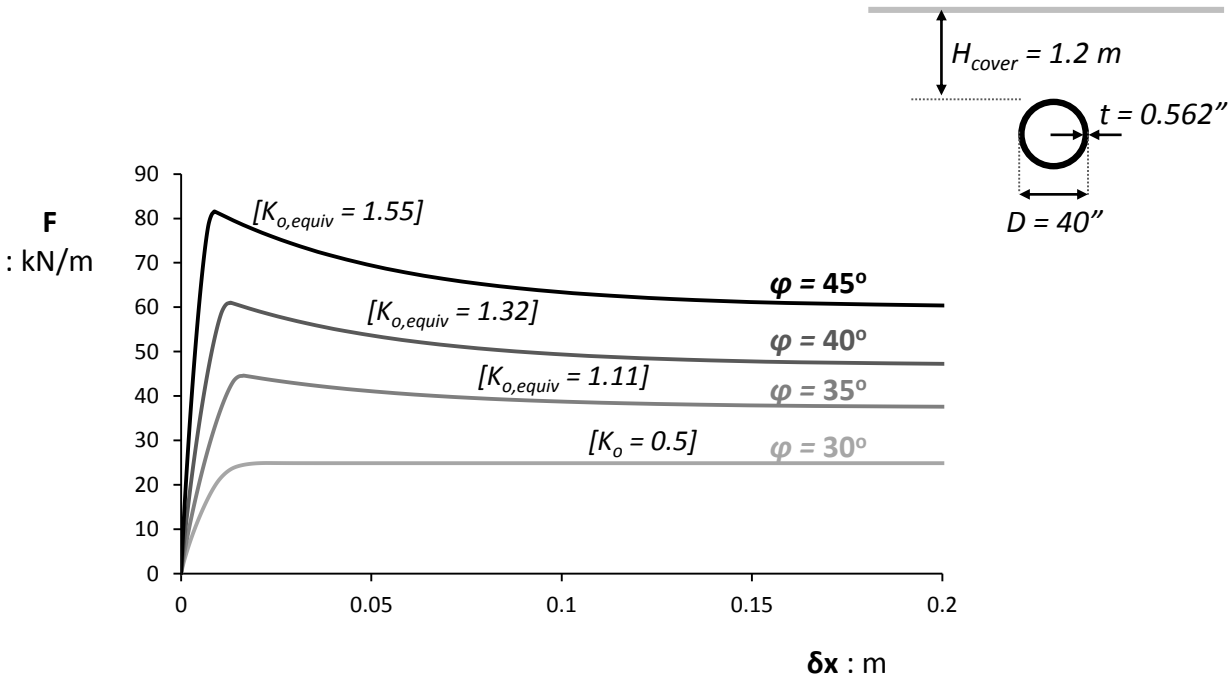

Fig. 5.2. Axial force-displacement curves accounting for the effect of dilation for the sands considered in the parametric study.

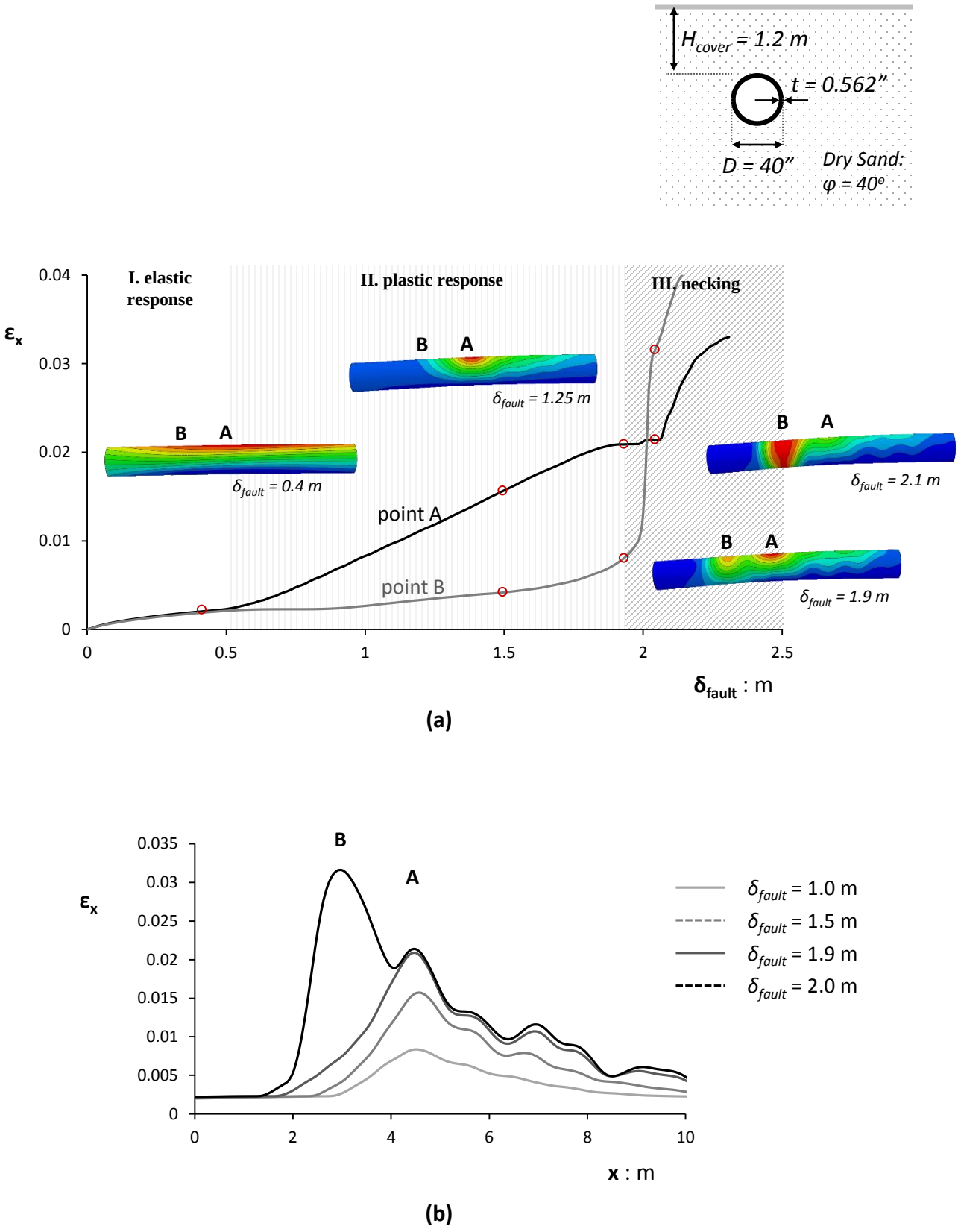

Fig. 5.3. Pipeline response subjected to normal faulting: 40” pipe buried at H_{cover}=1.2 m within sand of φ=40°. (a) Evolution of axial strains at two characteristic points on the top side of the critical pipe segment, accompanied with the deformed mesh of the critical pipe segment with superimposed axial strain contours. (b) Axial strain distribution at the top of the critical pipe segment for various characteristic fault offsets.

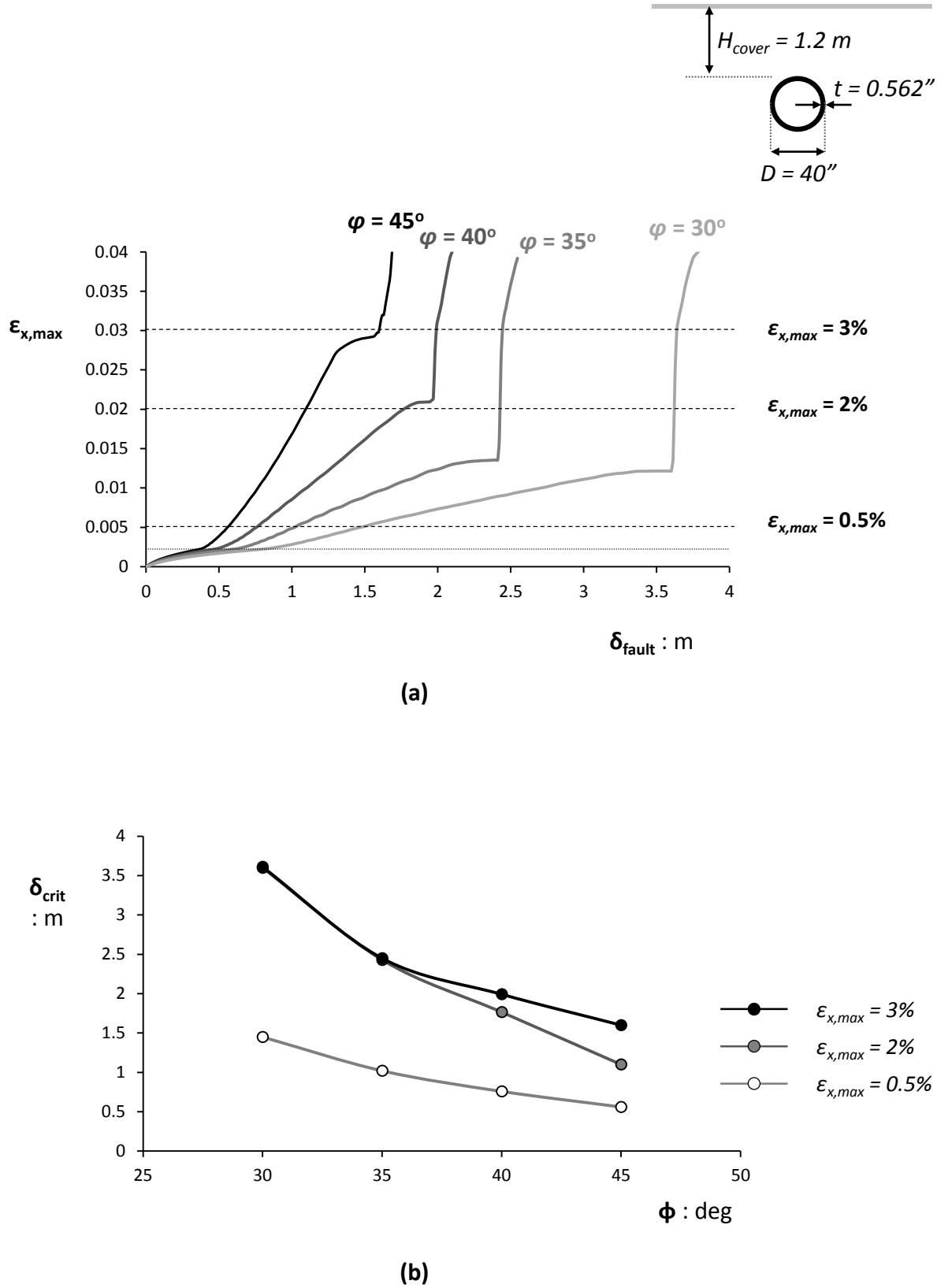

Fig. 5.4. Response of the 40” pipeline subjected to normal faulting for the four soils under consideration: (a) evolution of the maximum axial strain along the pipe with the increase of the fault displacement; (b) critical fault displacement correlated with the soil strength (all three failure criteria are considered).

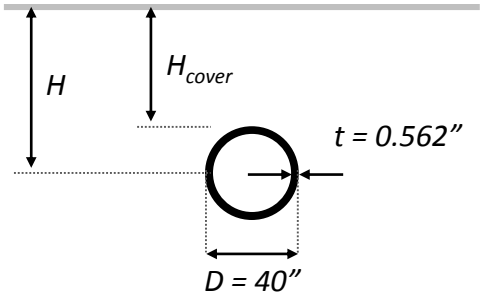

H_{cover} (m)	D (m)	H (m)	H/D
1.0	1.016	1.508	1.48
1.2	1.016	1.708	1.68
1.5	1.016	2.008	1.98

(a)

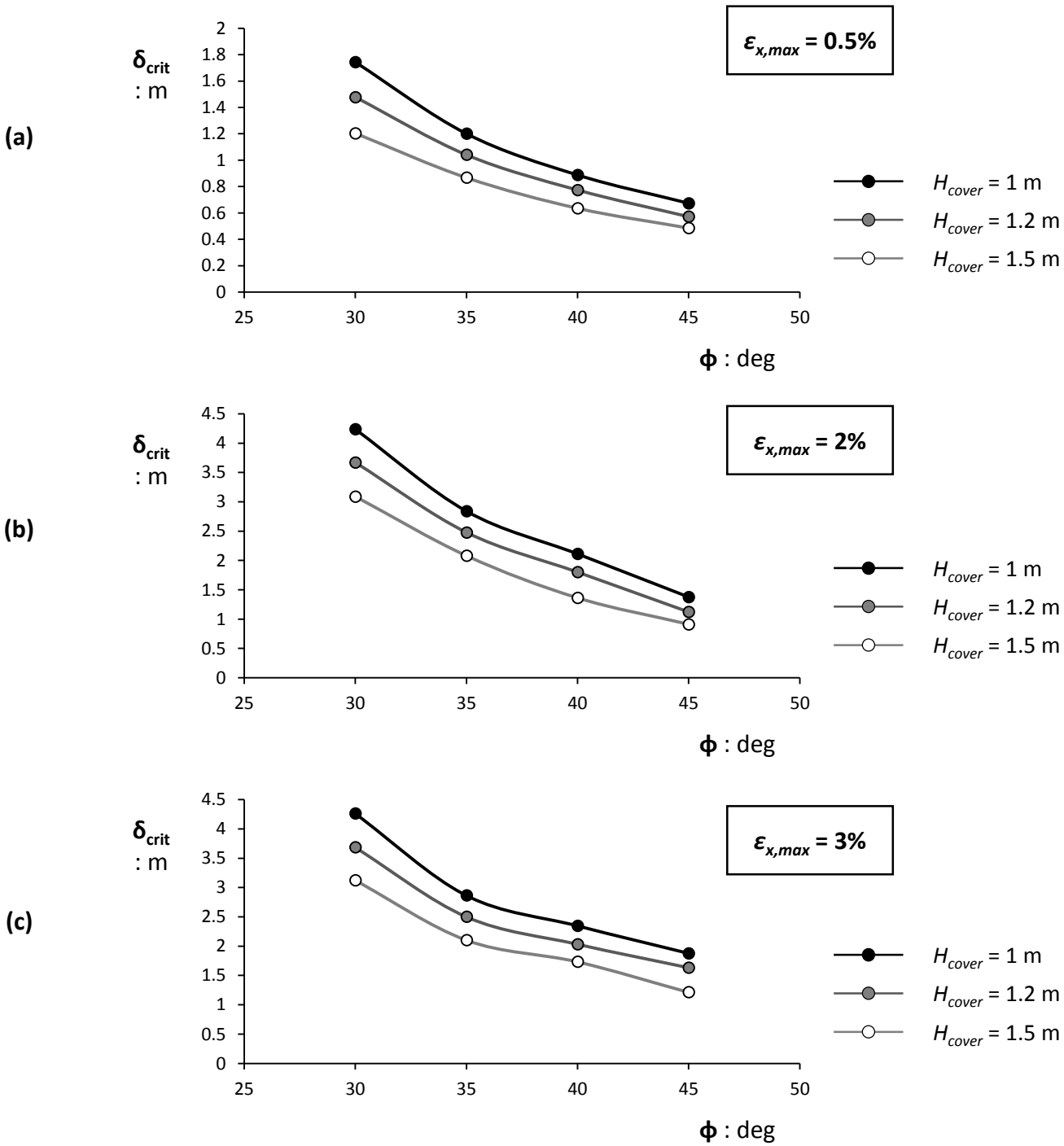

Fig. 5.5. The effect of the burial depth on the response of the 40” pipeline subjected to normal faulting. (a) Table with the considered cover depths. Critical fault displacement correlated with the soil friction angle for the three cover depths examined considering the failure criterion of (a) $\varepsilon_{x,max}$=0.5%, (b) $\varepsilon_{x,max}$=2%, and (c) $\varepsilon_{x,max}$=3%.

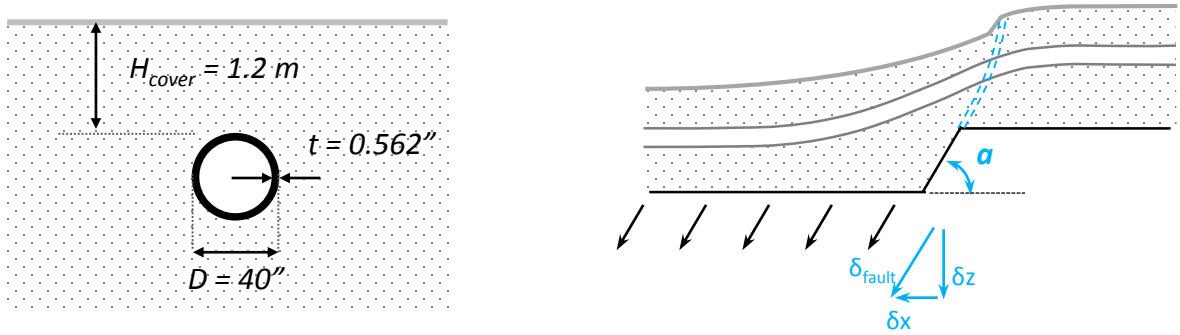

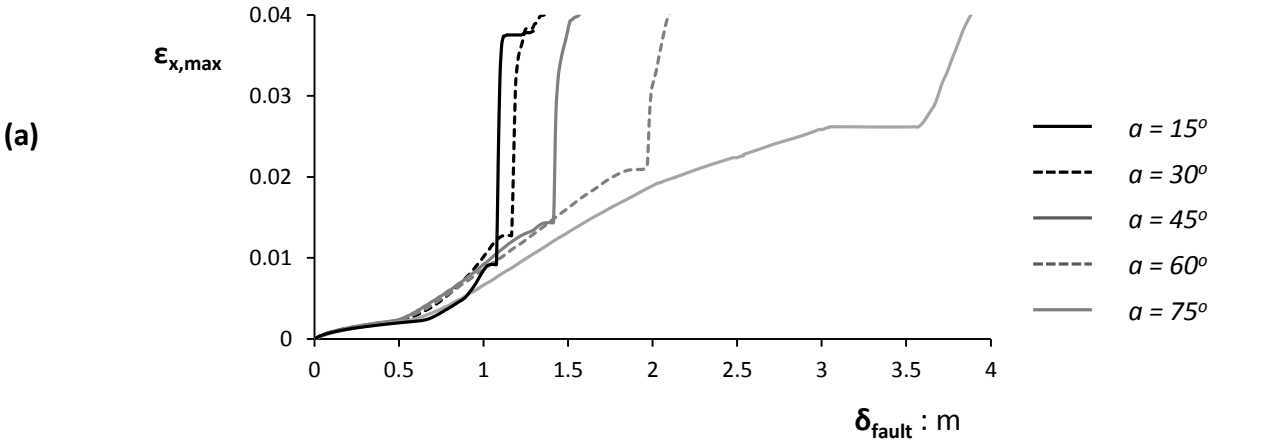

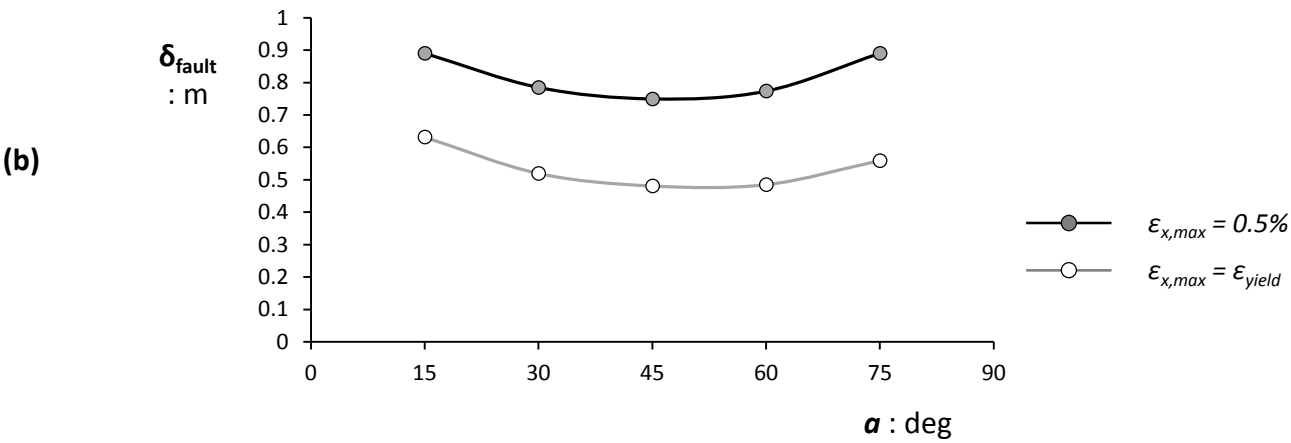

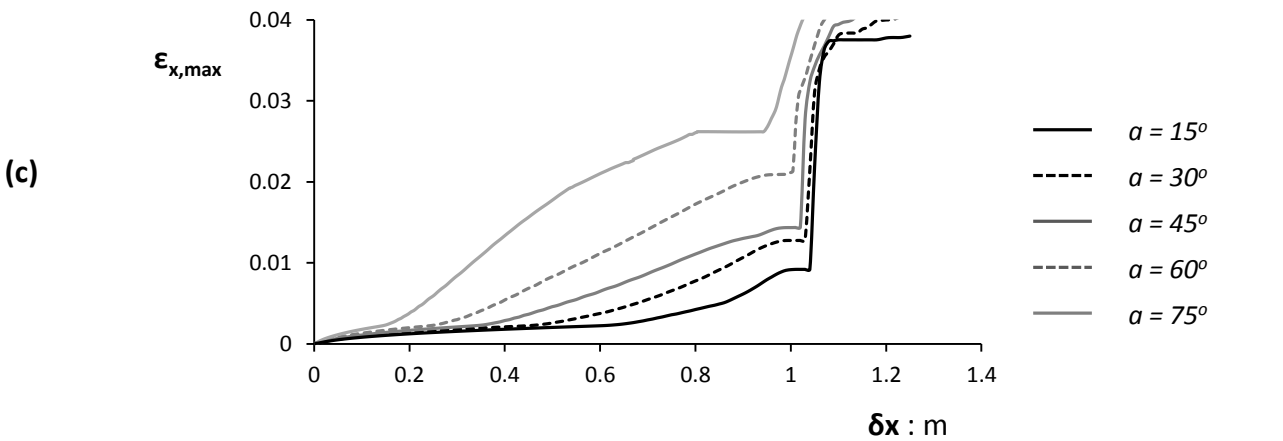

Fig. 5.6. The effect of the fault dip angle. The 40” pipeline is buried at cover depth H_{cover} = 1.2 m within sand of φ=40º and it is subjected to normal fault of dip angle ranging from α=15º to α=75º. Evolution of maximum axial strain with the increase of fault displacement magnitude δfault. (b) fault displacement that causes first yield and the development of $\varepsilon_{x,max}$=0.5% as a function of the dip angle. (c) Evolution of maximum axial strain with the increase of the horizontal component of the fault displacement δx.

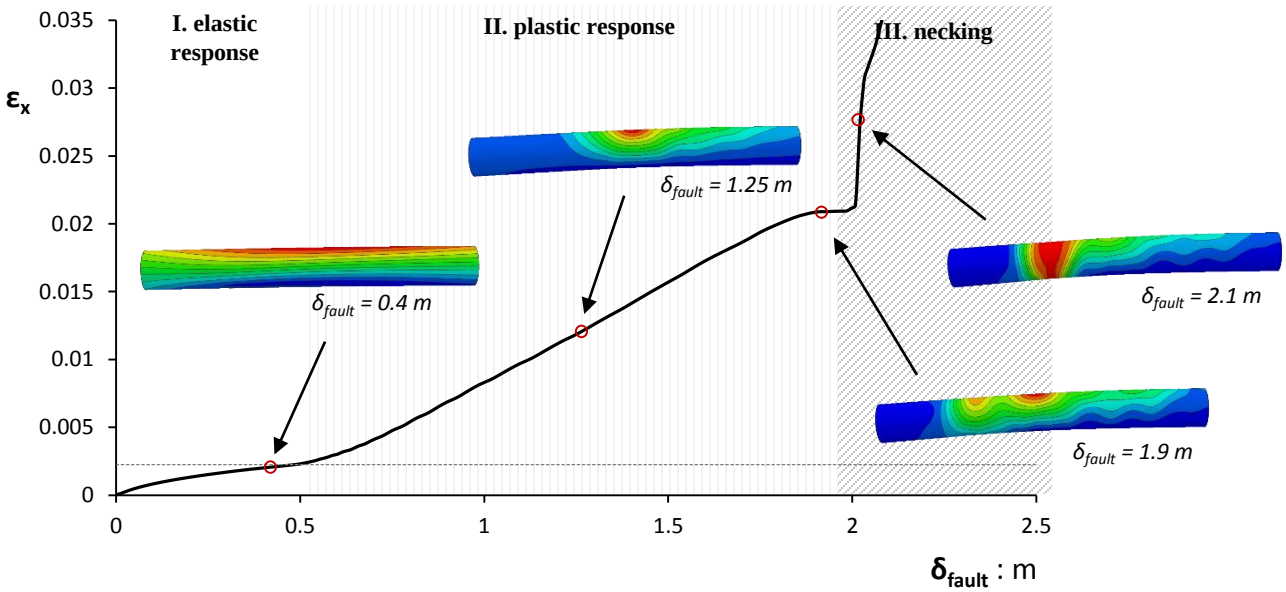

(a)

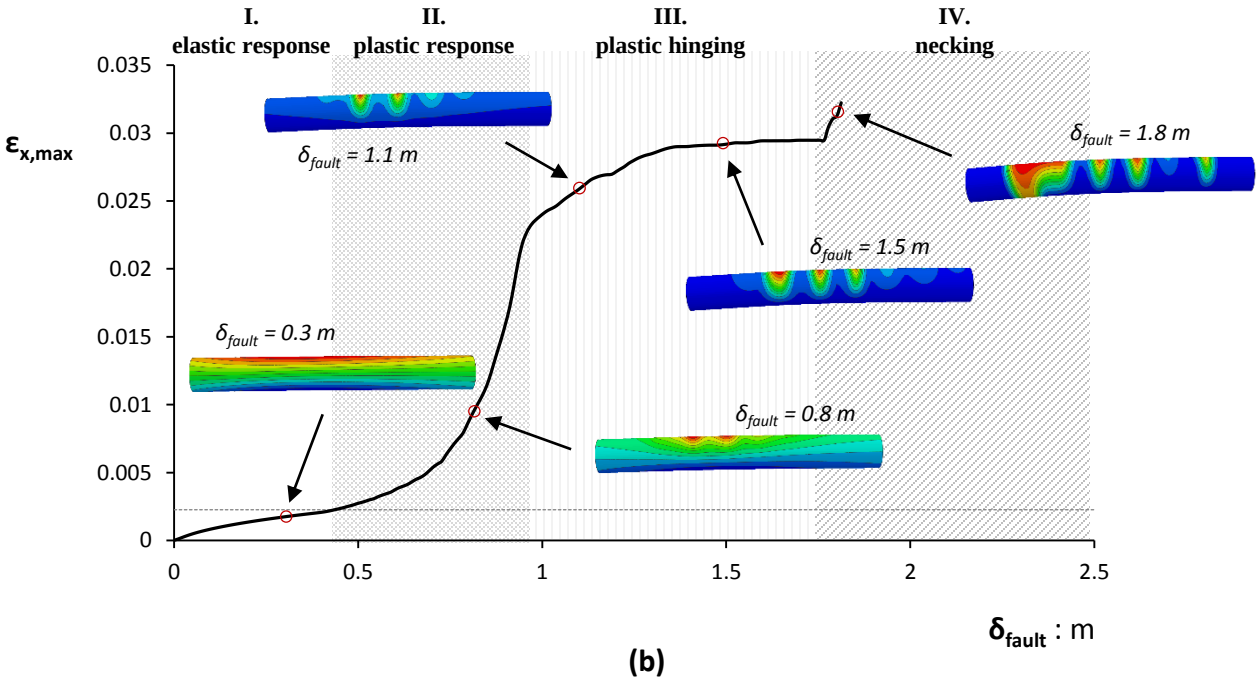

(b)

Fig. 5.7. The effect of internal pressure on the pipeline response subjected to normal faulting: 40" pipe buried at H_{cover}=1.2 m within sand of φ=40°. Evolution of maximum axial strain on the top side of the critical pipe segment with the increase of the fault displacement, accompanied with the deformed mesh of the critical pipe segment with superimposed axial strain contours. (b) p = 0 and (b) p = 9 MPa.

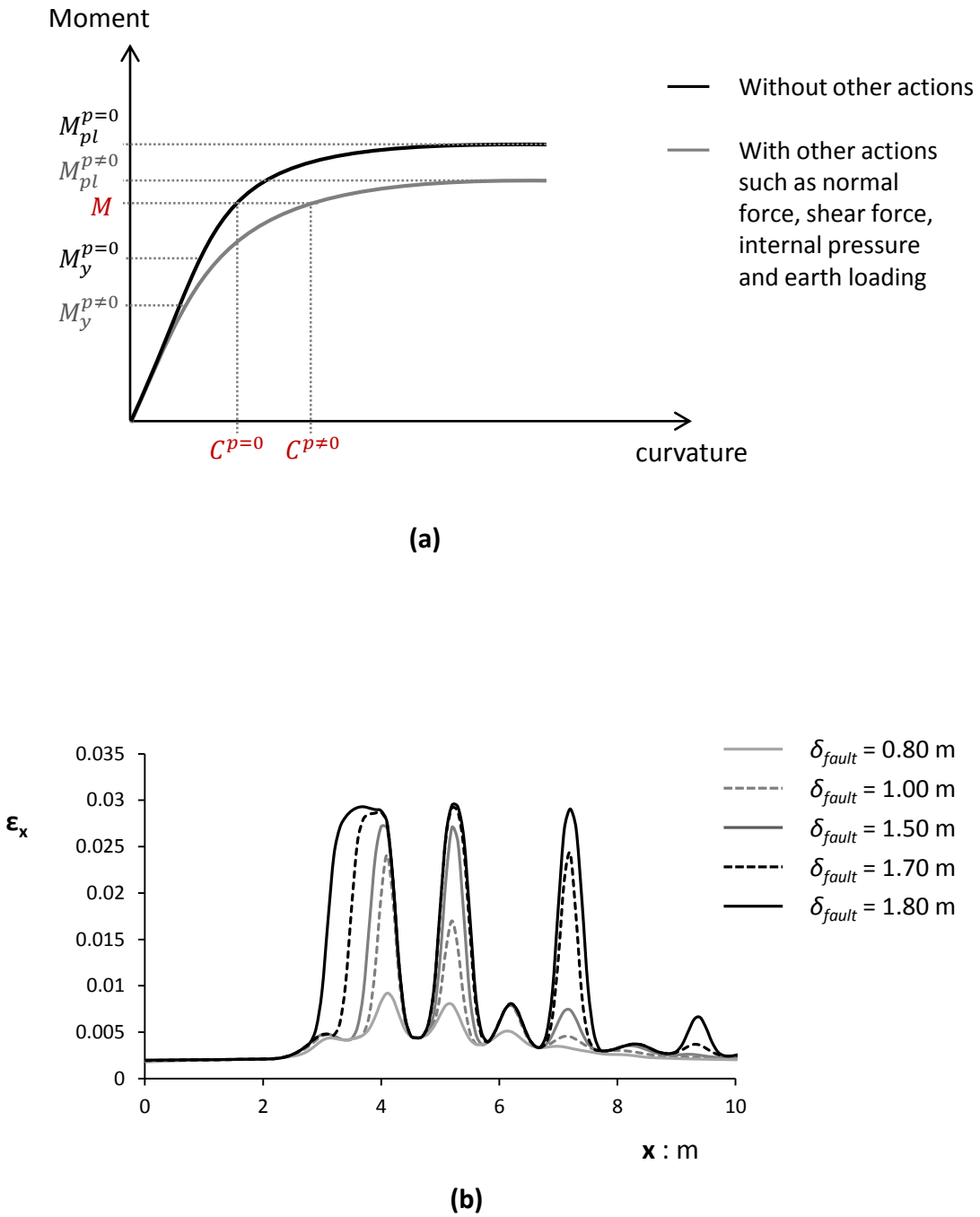

Fig. 5.8. (a) The moment – curvature diagram of a straight pipe according to the EN 1993-4-3 Eurocode, exhibiting the effect of various actions on the pipe. (b) Axial strain distribution at the top of the critical pipe segment for various characteristic fault offsets.

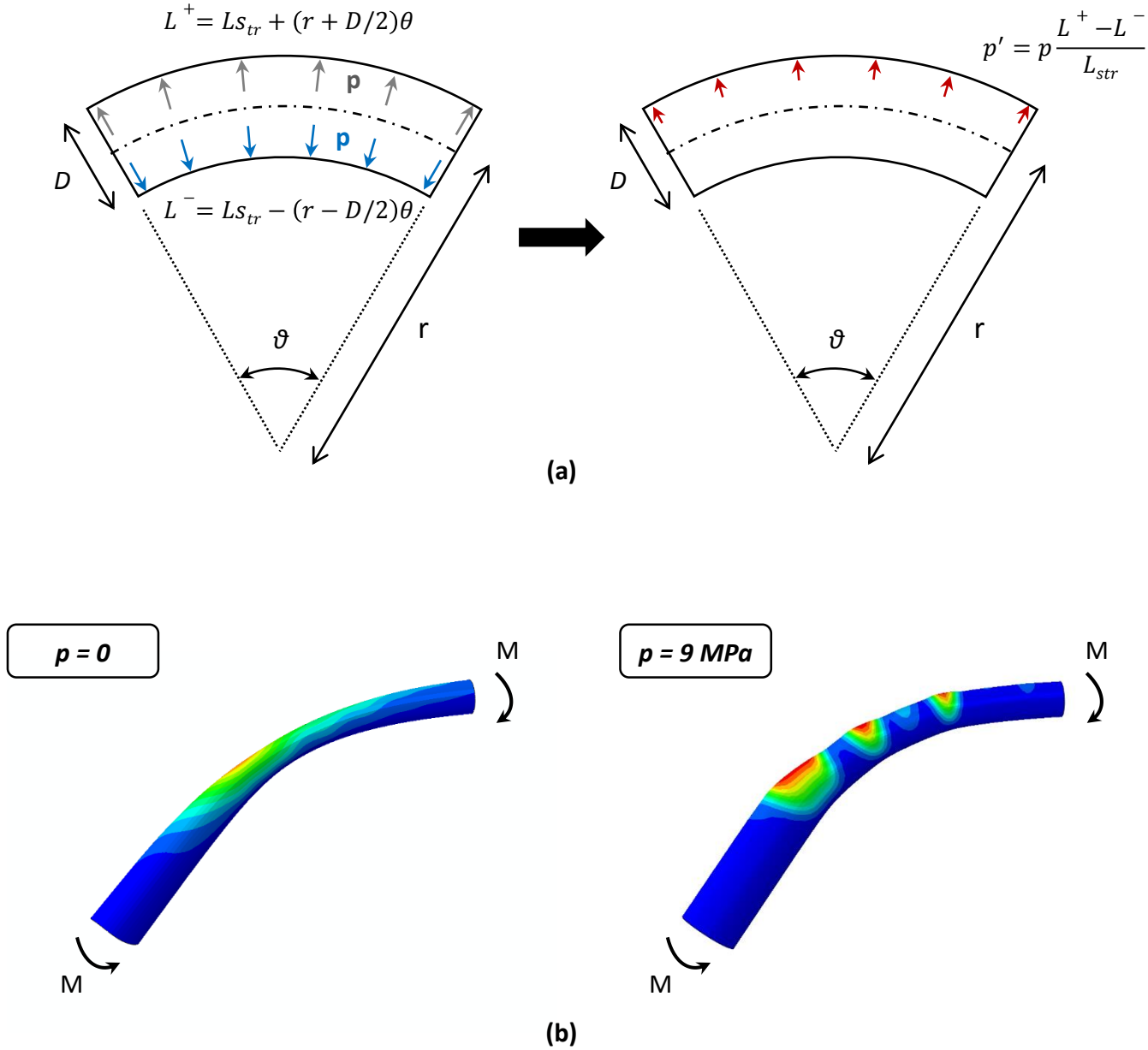

Fig. 5.9. (a) Due to change in the geometry (2nd order effects) a parasitic pressure p' is generated that tends to reduce the pipe segment curvature. (b) This parasitic pressure manifests itself through "straightening" a number of sections along the curved segment, causing strain localization and yielding the characteristic "wavy" strain distribution.

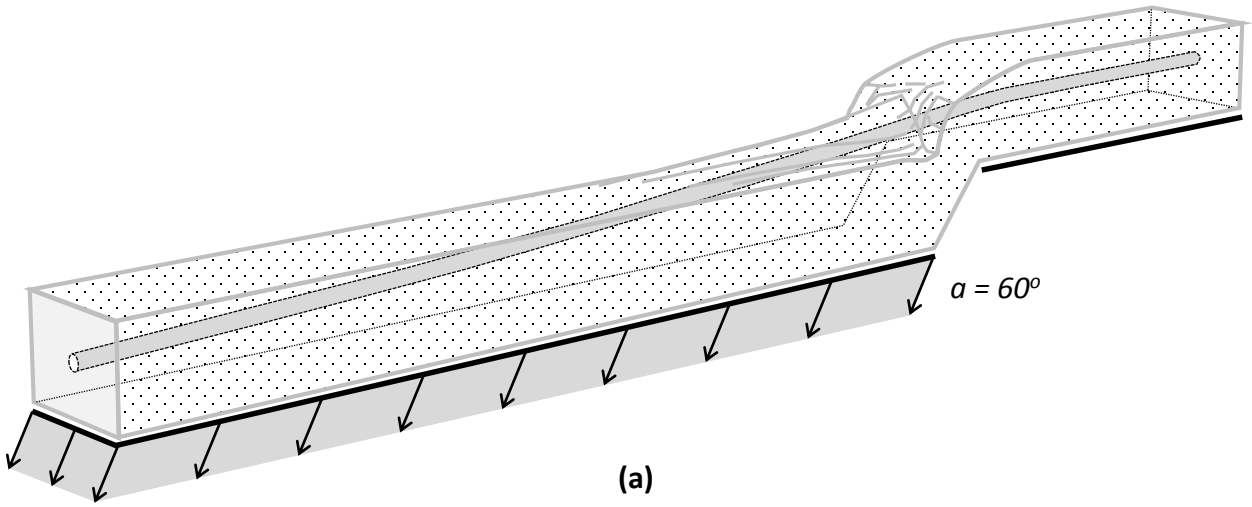

(a)

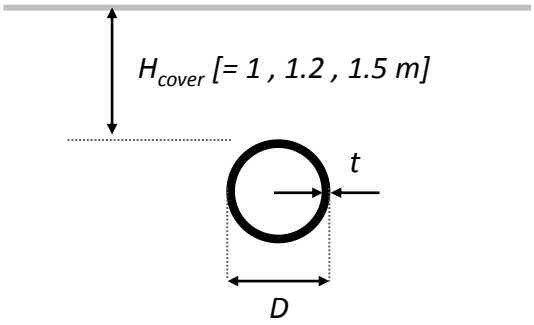

(b)

D *(in)*	***t*** *(in)*	***D/t***
28	0.375	74.7
36	0.5	72
40	0.562	71.2
48	0.688	69.8

(c)

φ *(deg)*	φ_{res} *(deg)*	ψ *(deg)*	δ_{xyield} *(mm)*	δ_{xpeak} *(mm)*	δ_{xres} *(mm)*	δ_z *(mm)*	ρ *(Mg/m³)*
45	35	15	0.5	1.25	4.5	0.70	1.8
40	32	10	0.85	1.75	5.0	0.46	1.7
35	30	5	1.15	2.0	5.5	0.24	1.6
30	30	0	1.5	-	-	-	1.5

(d)

Fig. 5.10. Parametrical investigation of pipelines subjected to normal faulting. (a) The pipeline crosses perpendicularly a normal fault of dip angle α = 60°. (b) The cover depths considered in the study. (c) The geometrical characteristics of the tubes under consideration. (d) The properties of the soil profiles under consideration.

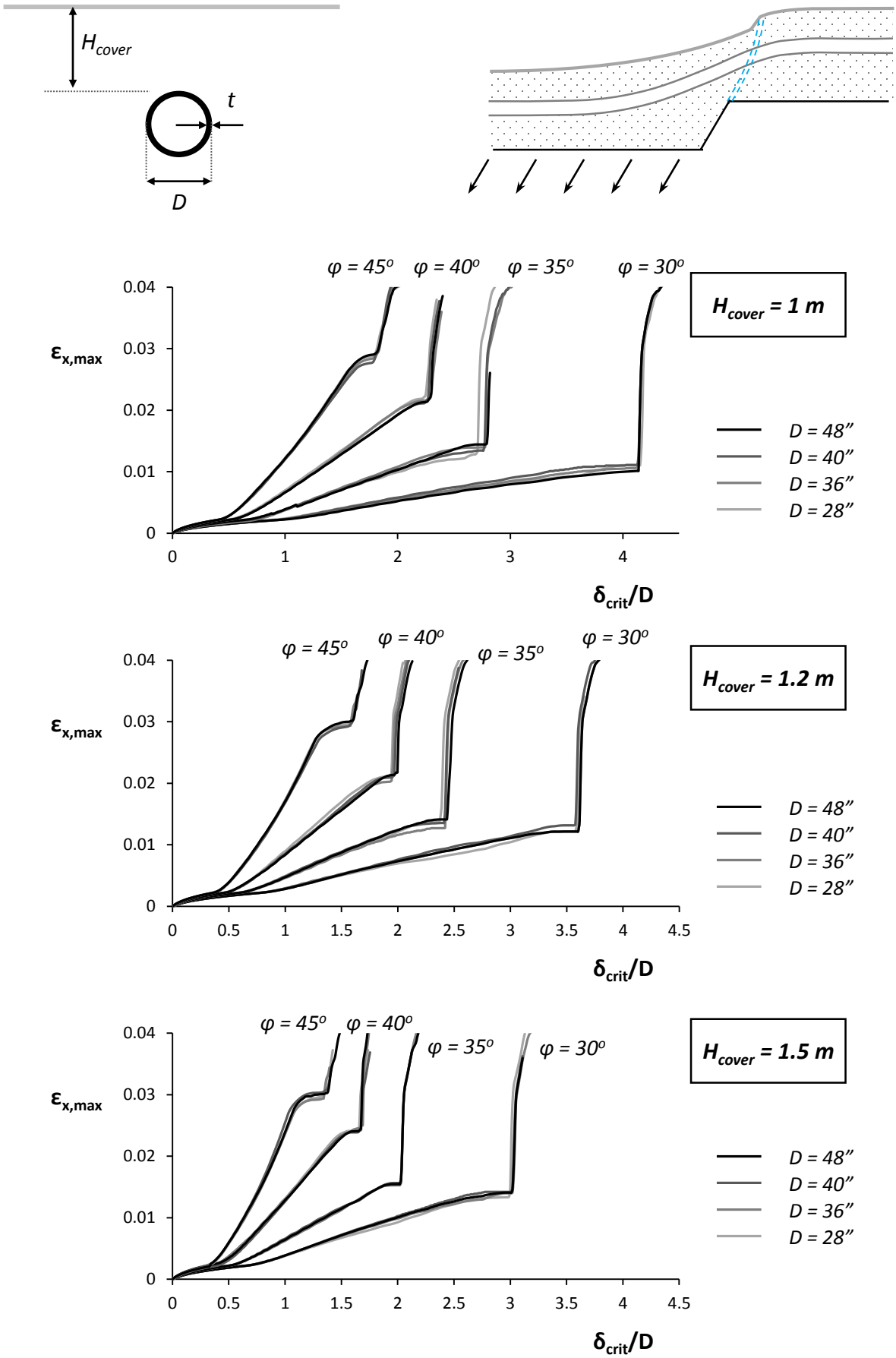

Fig. 5.11. Results of the parametric study for the non-pressurized pipelines subjected to normal faulting: evolution of maximum axial strain along the pipe for the pipes buried at (a) H_{cover}=1 m, (b) H_{cover}=1 m and (c) H_{cover}=1.5 m

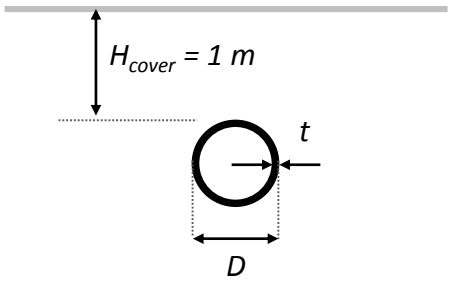

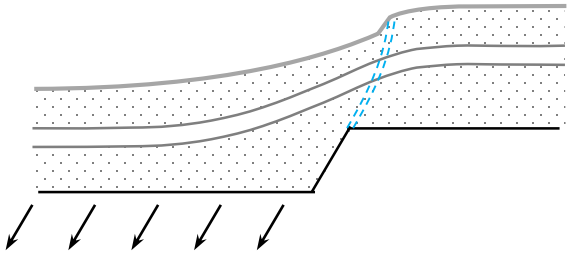

(a)

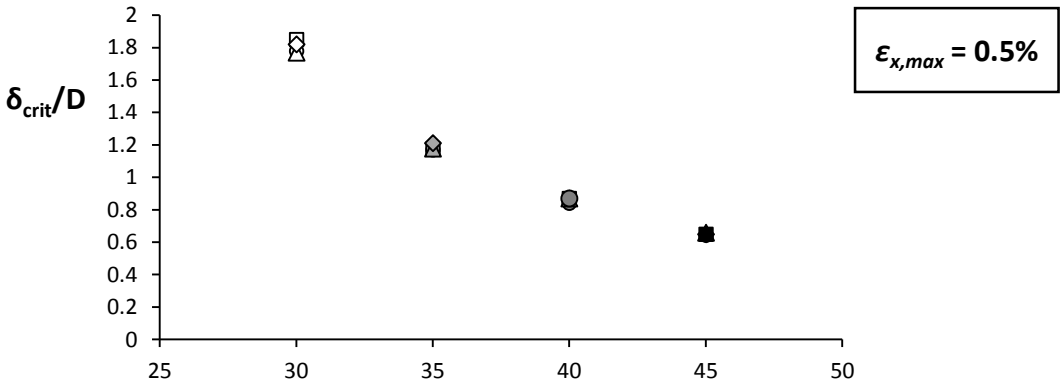

(b)

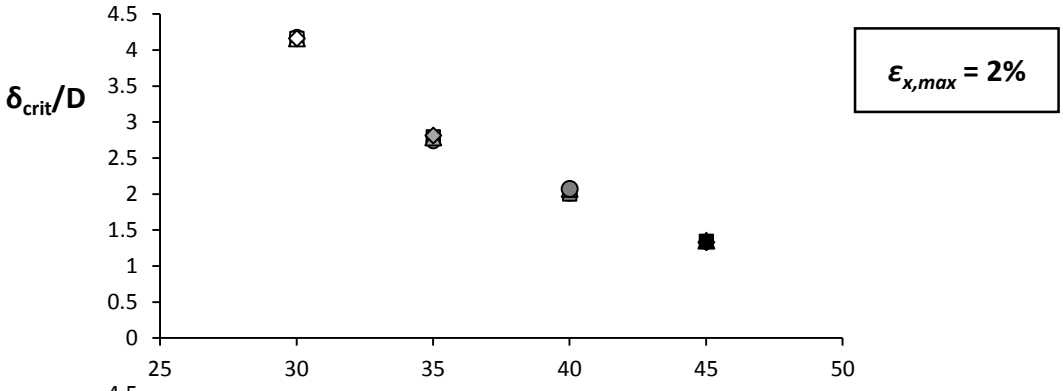

(c)

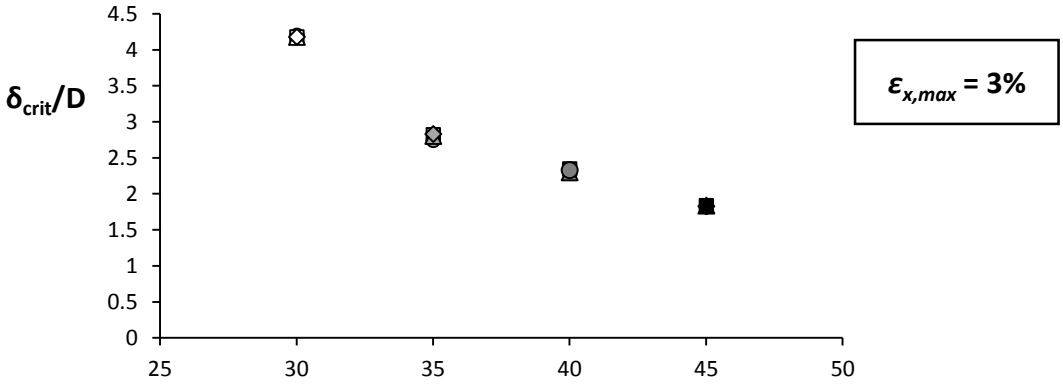

ϕ : deg

○ *D = 28″_φ = 30º*	● *D = 28″_φ = 35º*	● *D = 28″_φ = 40º*	● *D = 28″_φ = 45º*
□ *D = 36″_φ = 30º*	■ *D = 36″_φ = 35º*	■ *D = 36″_φ = 40º*	■ *D = 36″_φ = 45º*
△ *D = 40″_φ = 30º*	▲ *D = 40″_φ = 35º*	▲ *D = 40″_φ = 40º*	▲ *D = 40″_φ = 45º*
◇ *D = 40″_φ = 30º*	◆ *D = 40″_φ = 35º*	◆ *D = 40″_φ = 40º*	◆ *D = 40″_φ = 45º*

Fig. 5.12. Non-pressurized pipes buried at depth H_{cover}=1 m, subjected to normal faulting: normalized critical fault displacement δ_{fault}/D corresponding to failure criterion (a) $\varepsilon_{x,max}$=0.5%, (b) $\varepsilon_{x,max}$=2% and (c) $\varepsilon_{x,max}$=3%.

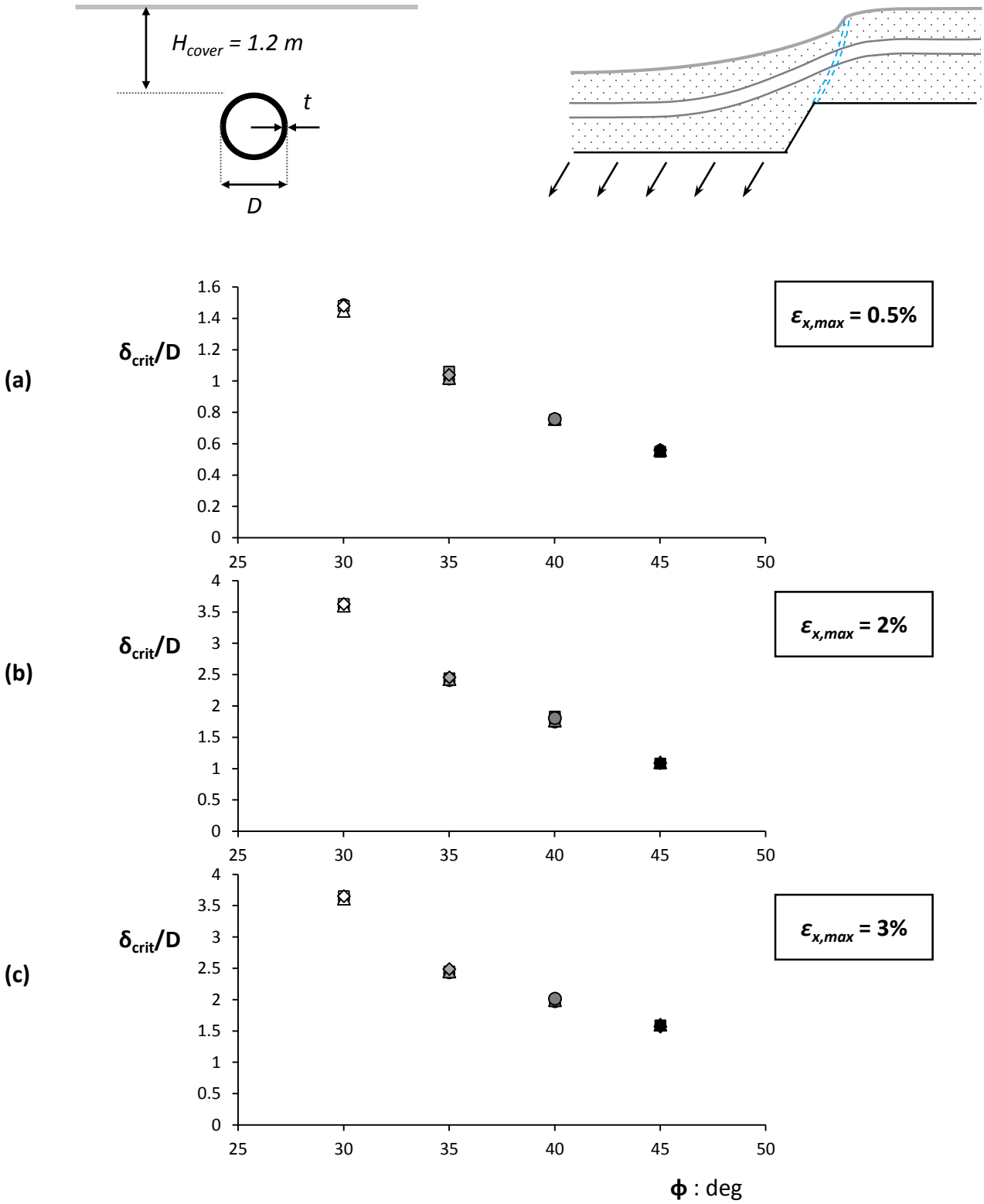

Fig. 5.13. Non-pressurized pipes buried at depth H_{cover}=1.2 m, subjected to normal faulting: normalized critical fault displacement δ_{fault}/D corresponding to failure criterion (a) $\varepsilon_{x,max}$=0.5%, (b) $\varepsilon_{x,max}$=2% and (c) $\varepsilon_{x,max}$=3%.

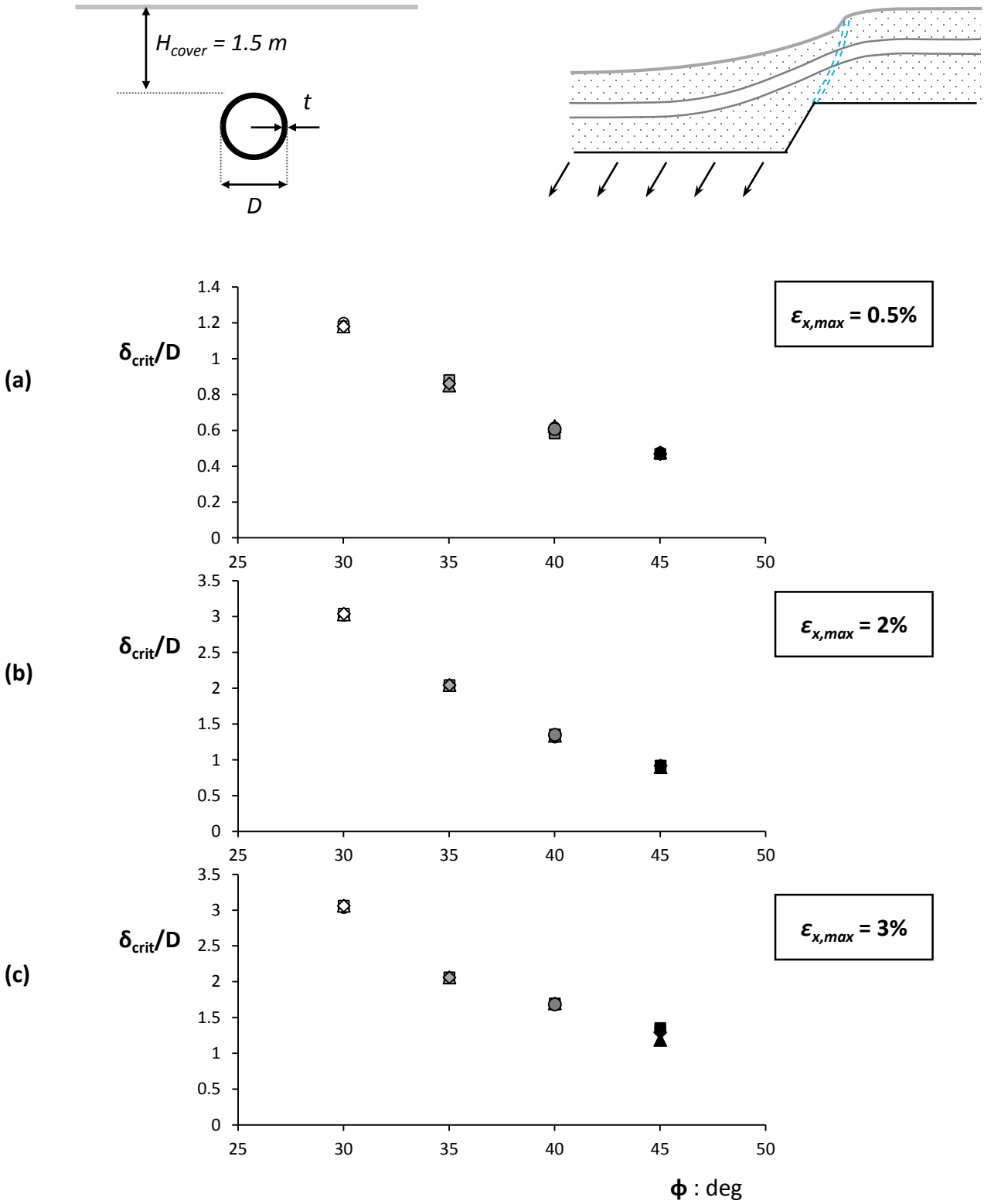

Fig. 5.14. Non-pressurized pipes buried at depth H_{cover}=1.5 m, subjected to normal faulting: normalized critical fault displacement δ_{fault}/D corresponding to failure criterion (a) $\varepsilon_{x,max}$=0.5%, (b) $\varepsilon_{x,max}$=2% and (c) $\varepsilon_{x,max}$=3%.

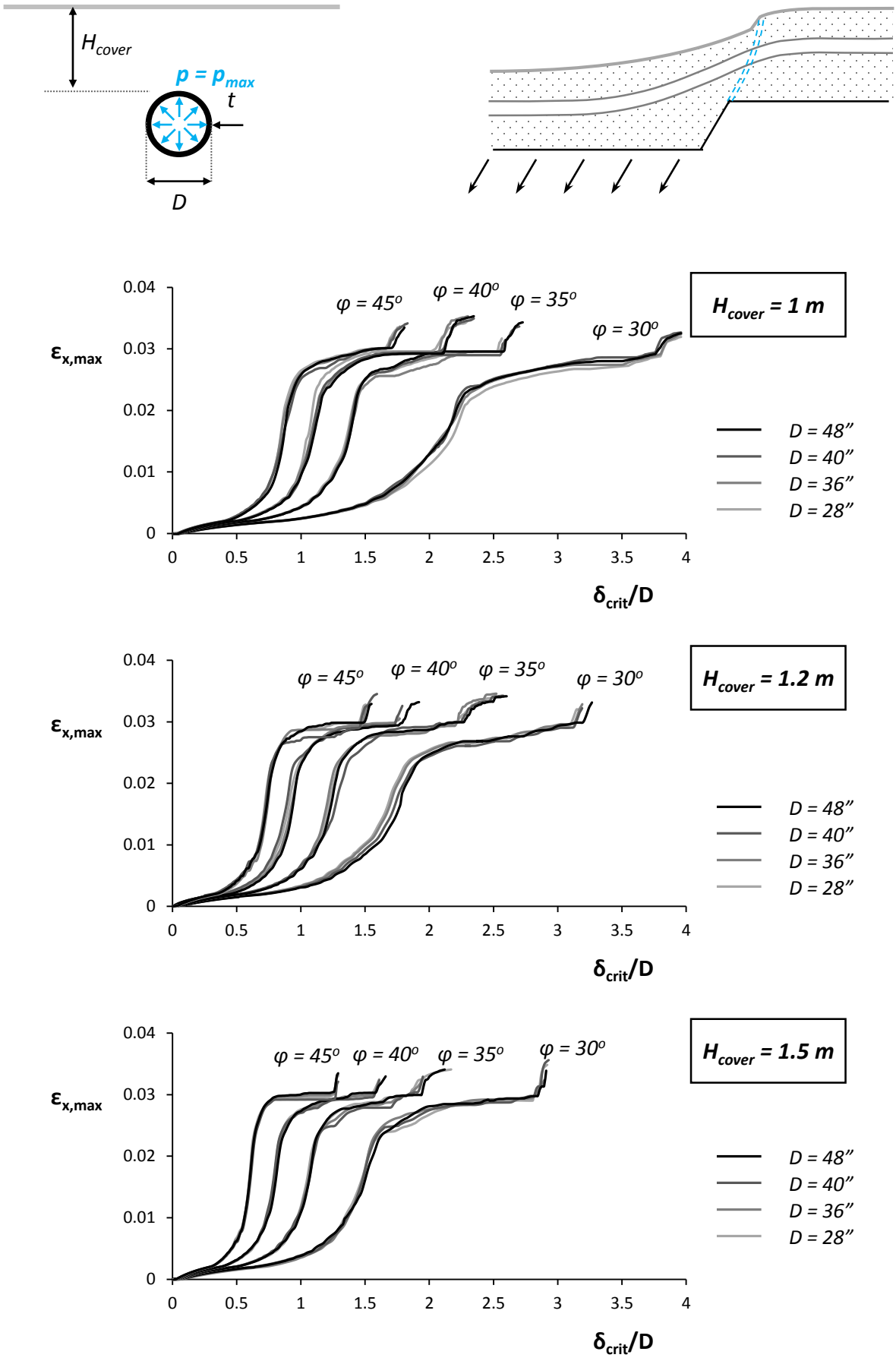

Fig. 5.15. Results of the parametric study for the pressurized pipelines (p=p_{max}) subjected to normal faulting: evolution of maximum axial strain along the pipe for the pipes buried at (a) H_{cover}=1 m, (b) H_{cover}=1 m and (c) H_{cover}=1.5 m

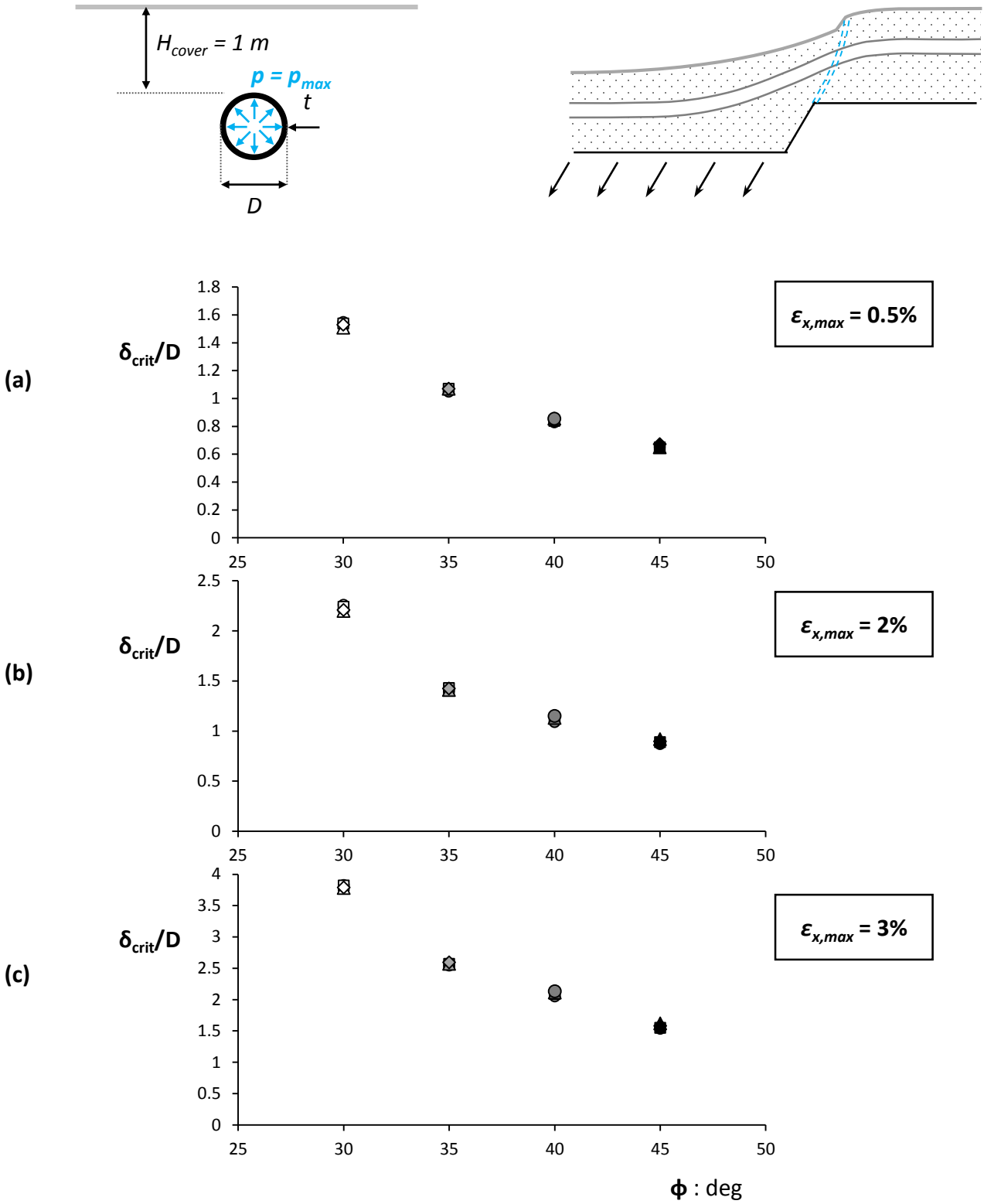

Fig. 5.16. Pressurized pipes buried at depth H_{cover}=1 m, subjected to normal faulting: normalized critical fault displacement δ_{fault}/D corresponding to failure criterion (a) $\varepsilon_{x,max}$=0.5%, (b) $\varepsilon_{x,max}$=2% and (c) $\varepsilon_{x,max}$=3%.

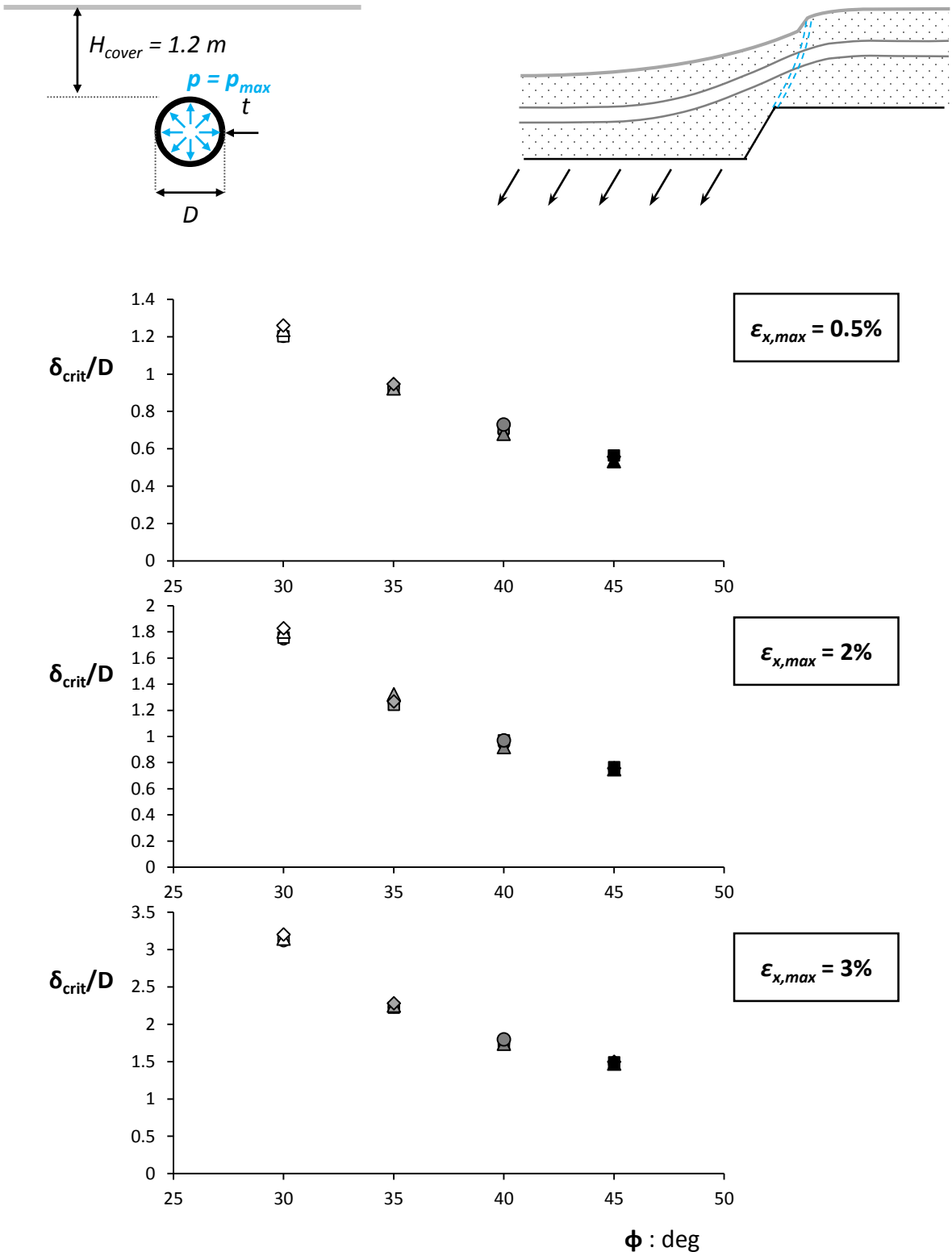

Fig. 5.17. Pressurized pipes buried at depth H_{cover}=1.2 m, subjected to normal faulting: normalized critical fault displacement δ_{fault}/D corresponding to failure criterion (a) $\varepsilon_{x,max}$=0.5%, (b) $\varepsilon_{x,max}$=2% and (c) $\varepsilon_{x,max}$=3%.

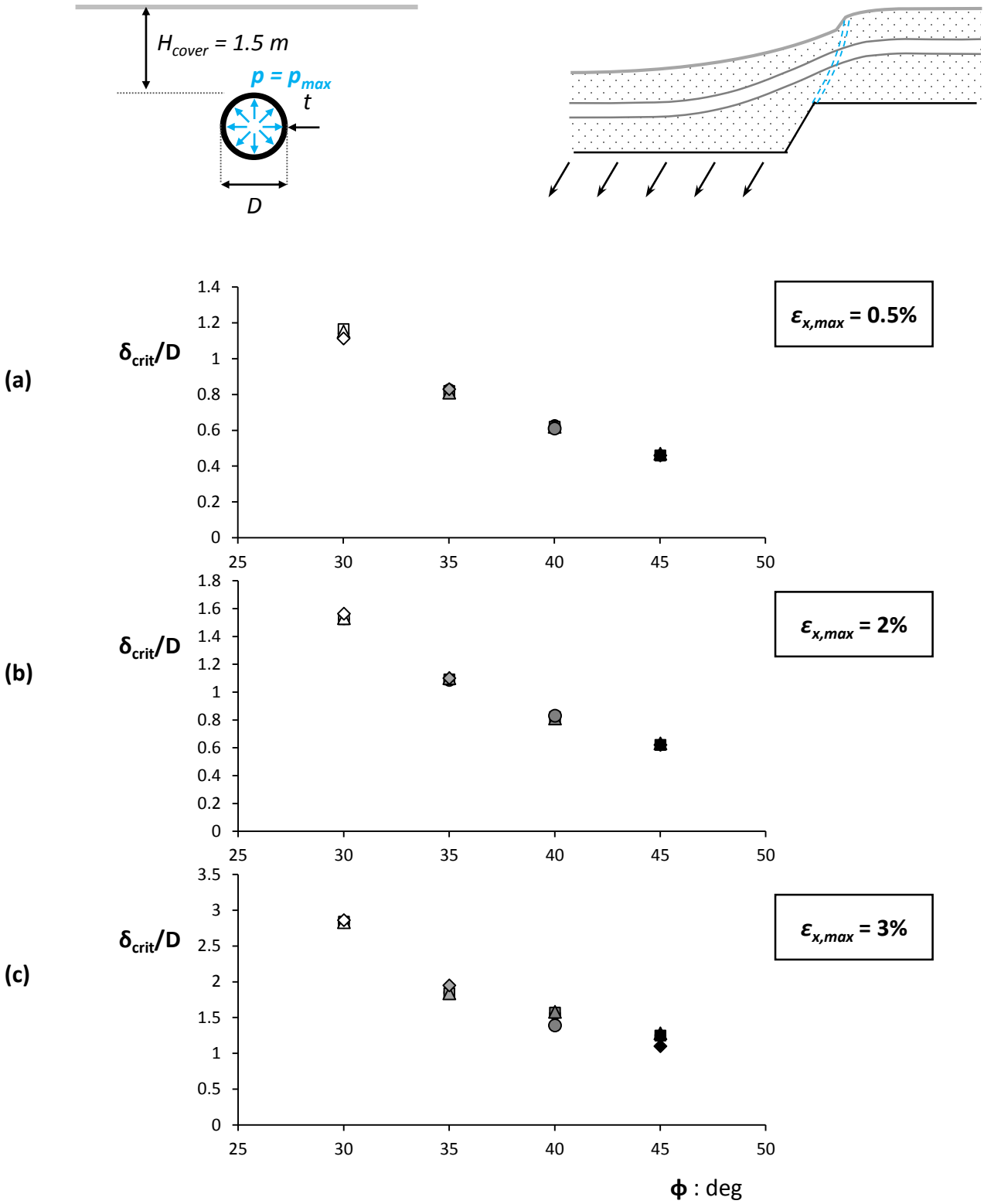

Fig. 5.18. Pressurized pipes buried at depth H_{cover}=1.5 m, subjected to normal faulting: normalized critical fault displacement δ_{fault}/D corresponding to failure criterion (a) $\varepsilon_{x,max}$=0.5%, (b) $\varepsilon_{x,max}$=2% and (c) $\varepsilon_{x,max}$=3%.

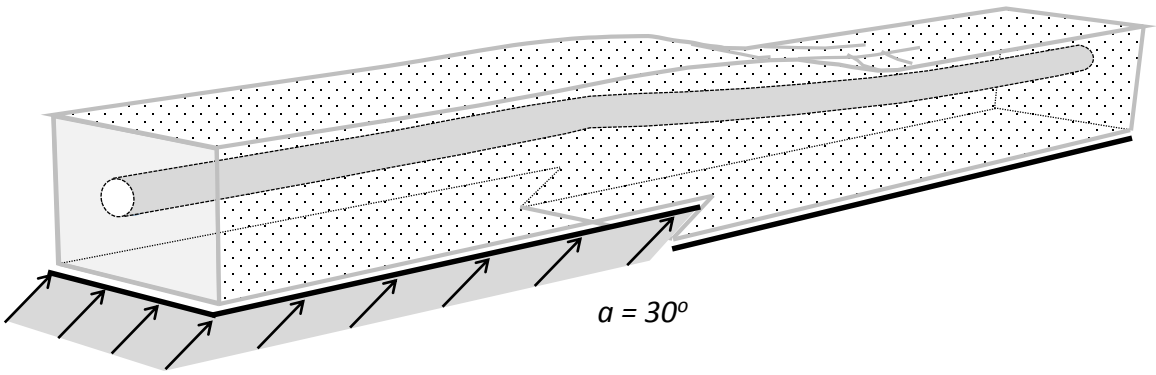

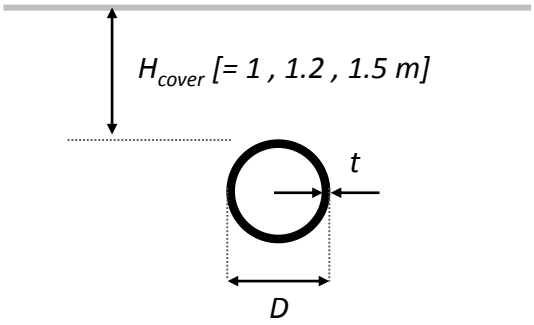

(a)

D *(in)*	***t*** *(in)*	***D/t***
28	0.375	74.7
36	0.5	72
40	0.562	71.2
48	0.688	69.8

(b)

φ *(deg)*	φ_{res} *(deg)*	ψ *(deg)*	δ_{xyield} *(mm)*	δ_{xpeak} *(mm)*	δ_{xres} *(mm)*	δ_z *(mm)*	ρ *(Mg/m³)*
45	35	15	0.5	1.25	4.5	0.70	1.8
40	32	10	0.85	1.75	5.0	0.46	1.7
35	30	5	1.15	2.0	5.5	0.24	1.6
30	30	0	1.5	-	-	-	1.5

(c)

Fig. 5.19. Parametrical investigation of pipelines subjected to reverse faulting. (a) The pipeline crosses perpendicularly a reverse fault of dip angle α = 30°. (b) The cover depths considered in the study. (c) The geometrical characteristics of the tubes under consideration. (d) The properties of the soil profiles under consideration.

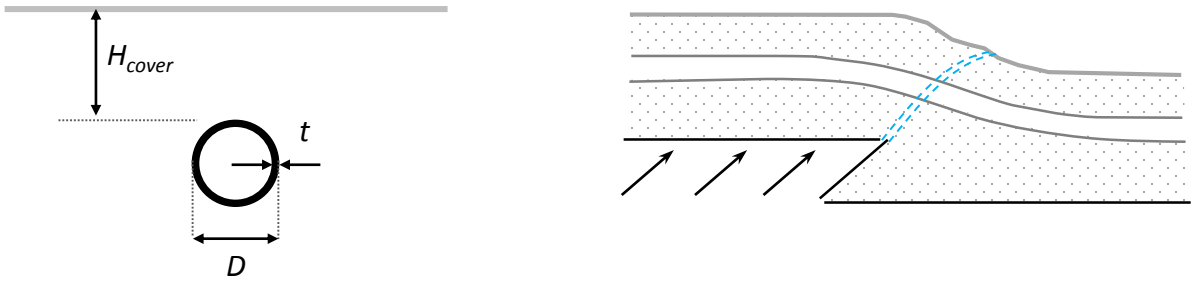

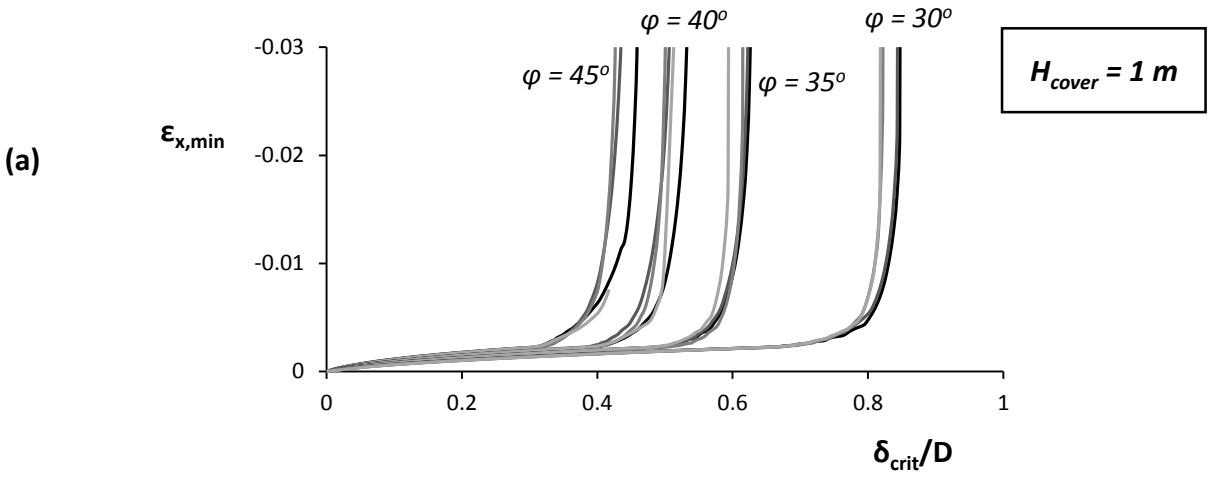

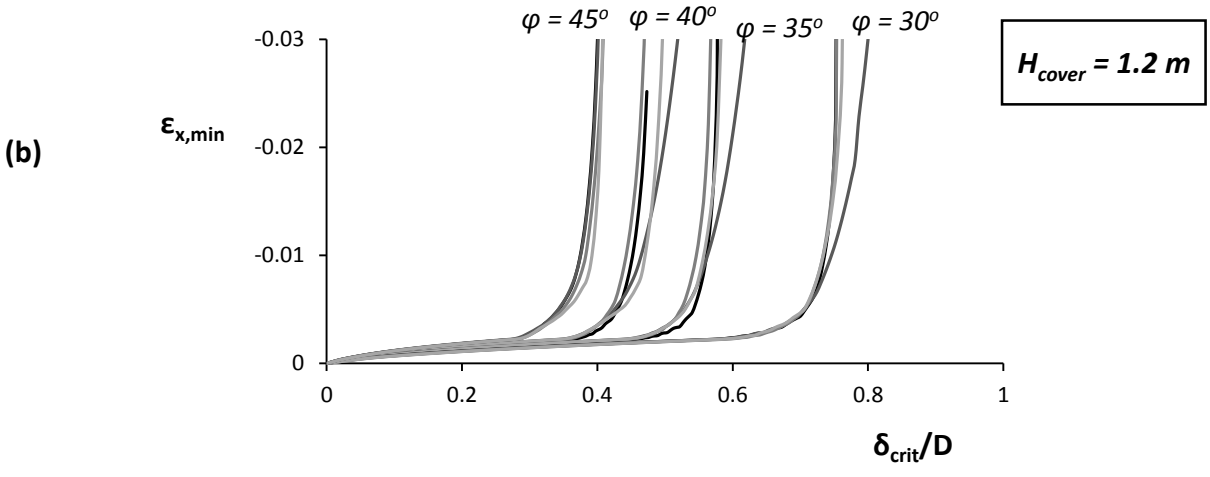

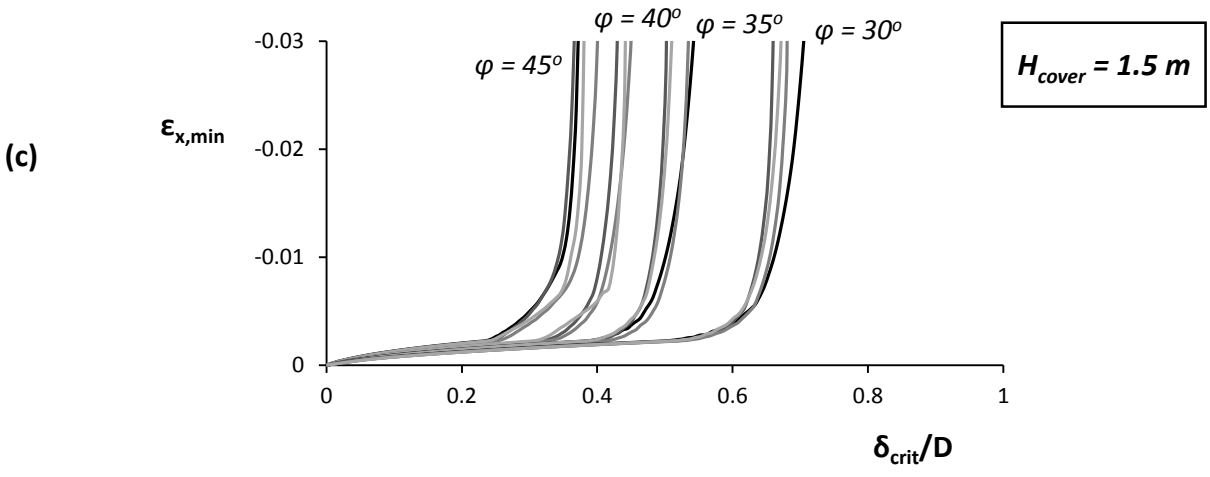

Fig. 5.20. Results of the parametric study for the non-pressurized pipelines subjected to reverse faulting: evolution of minimum axial strain (compressive) along the pipe for the pipes buried at (a) H_{cover}=1 m, (b) H_{cover}=1 m and (c) H_{cover}=1.5 m

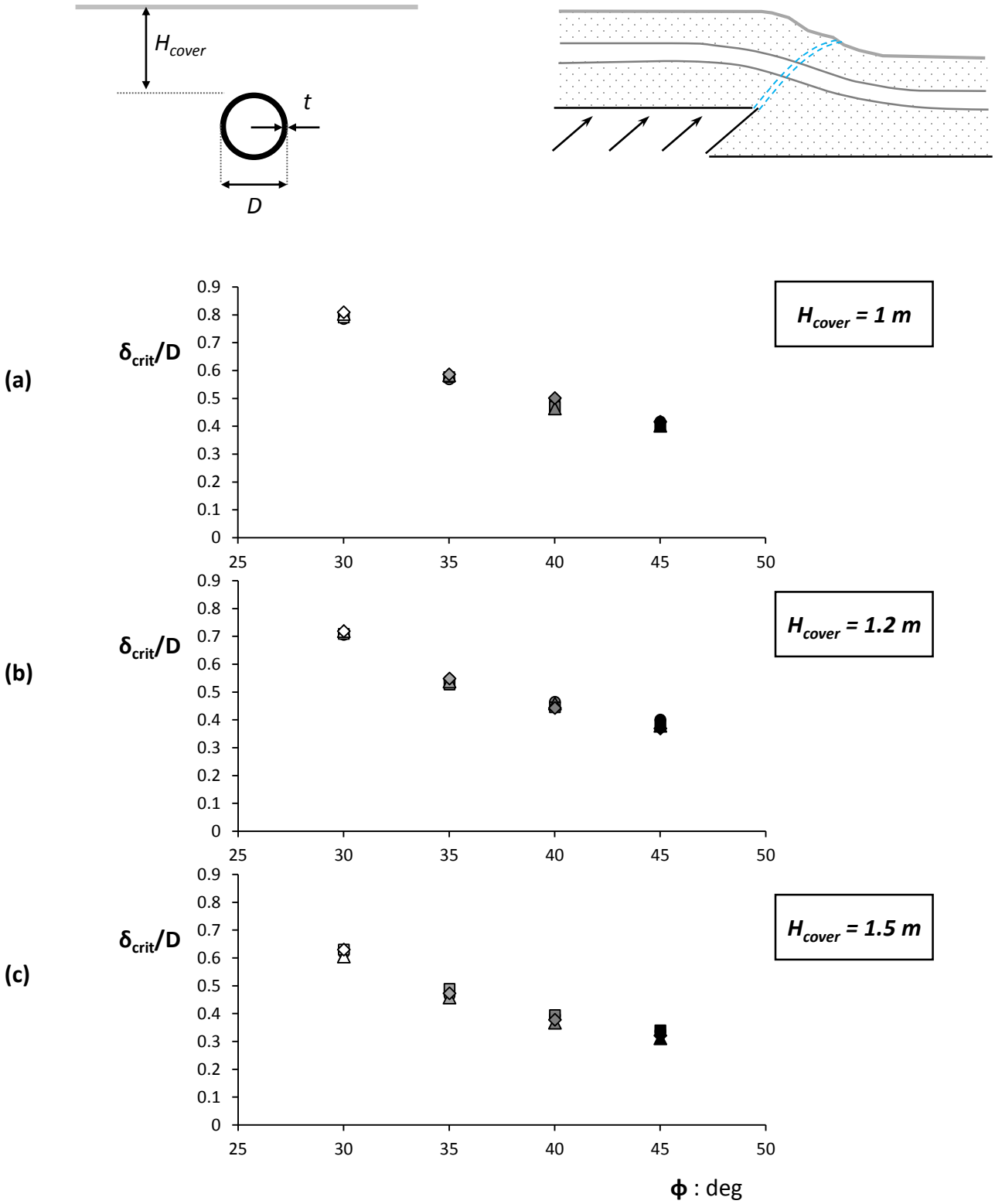

Fig. 5.21. Non-pressurized pipes subjected to reverse faulting: normalized critical fault displacement δ_{fault}/D corresponding to buckling initiation for the pipes buried at (a) H_{cover}=1 m, (b) H_{cover}=1.2 m and (c) H_{cover}=1.5 m.

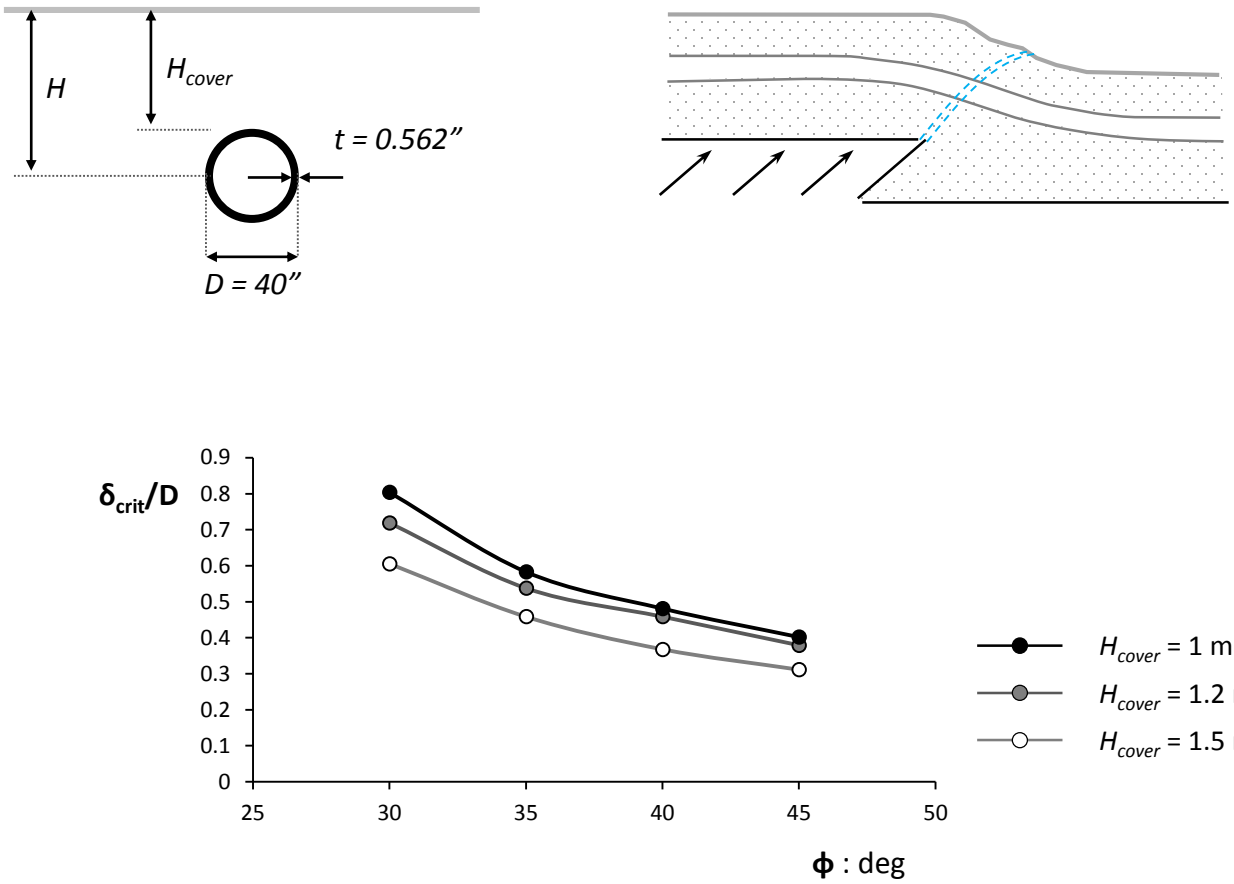

Fig. 5.22. The effect of the burial depth on the response of the 40” pipeline subjected to reverse faulting: Normalized critical fault displacement correlated with the soil friction angle for the three cover depths examined.

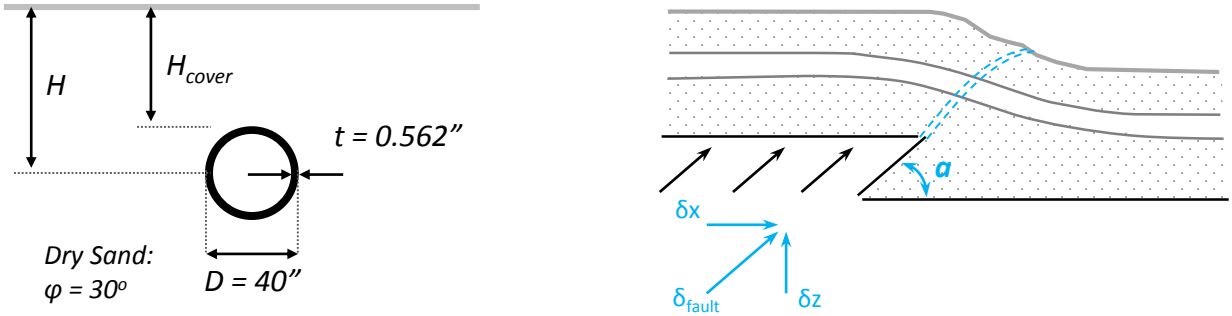

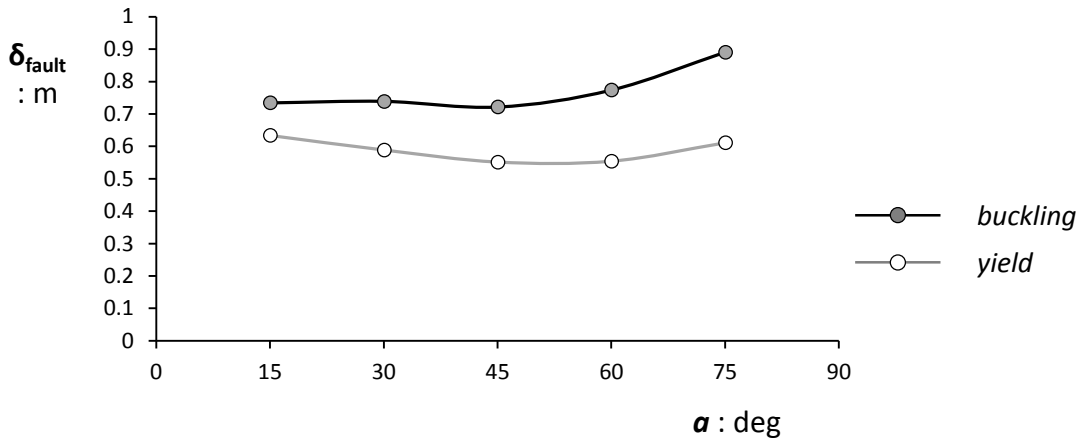

(a)

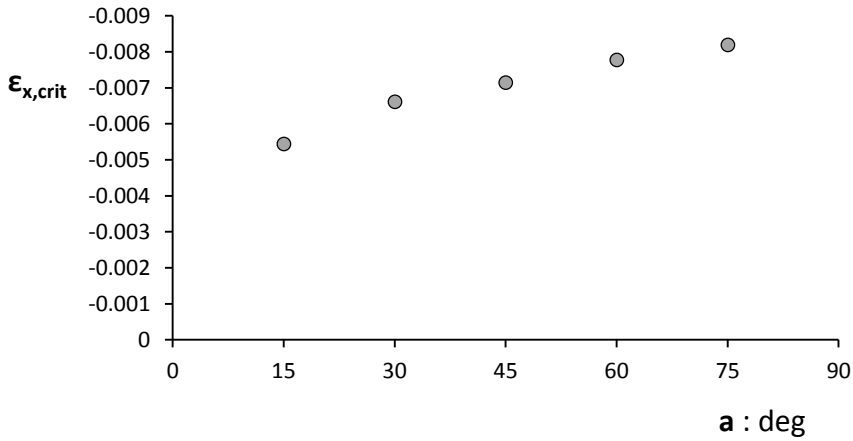

(b)

Fig. 5.23. The effect of the fault dip angle. The 40” pipeline is buried at cover depth H_{cover} = 1.2 m within sand of φ=30° and it is subjected to reverse fault of dip angle ranging from α=15° to α=75°. (a) Fault displacement that causes first yield and buckling initiation as a function of the dip angle. (b) Minimum axial strain at the moment of buckling initiation as a function of the dip angle.

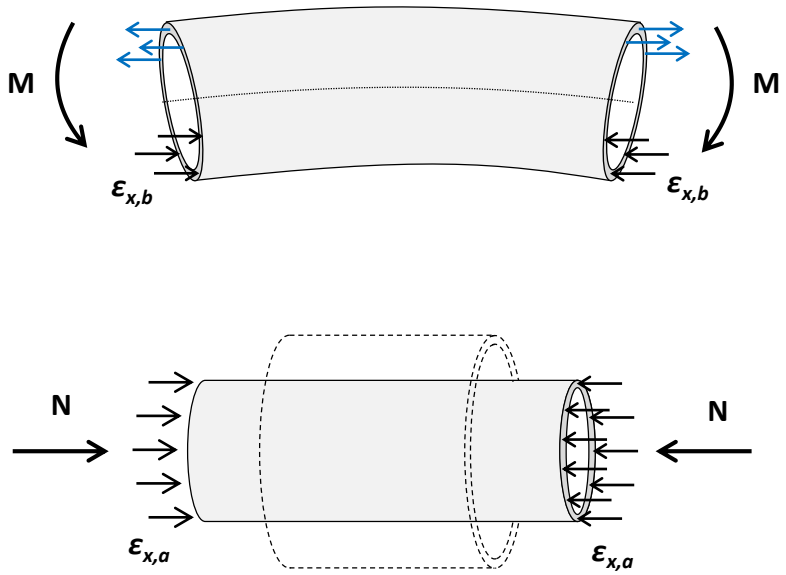

Fig. 5.24. (a) The expansion of the pipe cross-section due to compression and the transversal dislocation of the pipe wall due to buckling are two competitive mechanisms: (b) the combination of these two mechanisms result in deterioration of the pipe metaplastic deformation capacity leading to decrease of the critical compressive strain (strain associated with local buckling initiation).

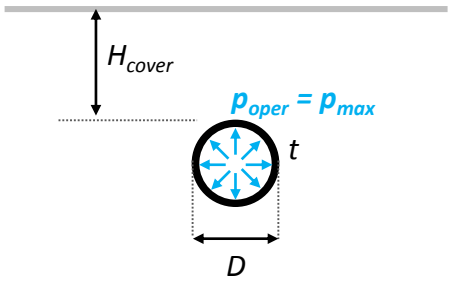

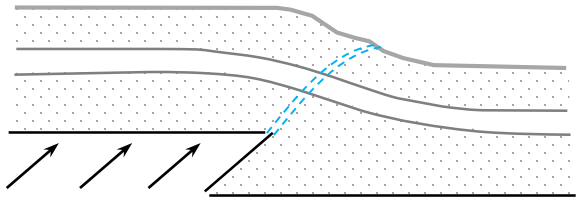

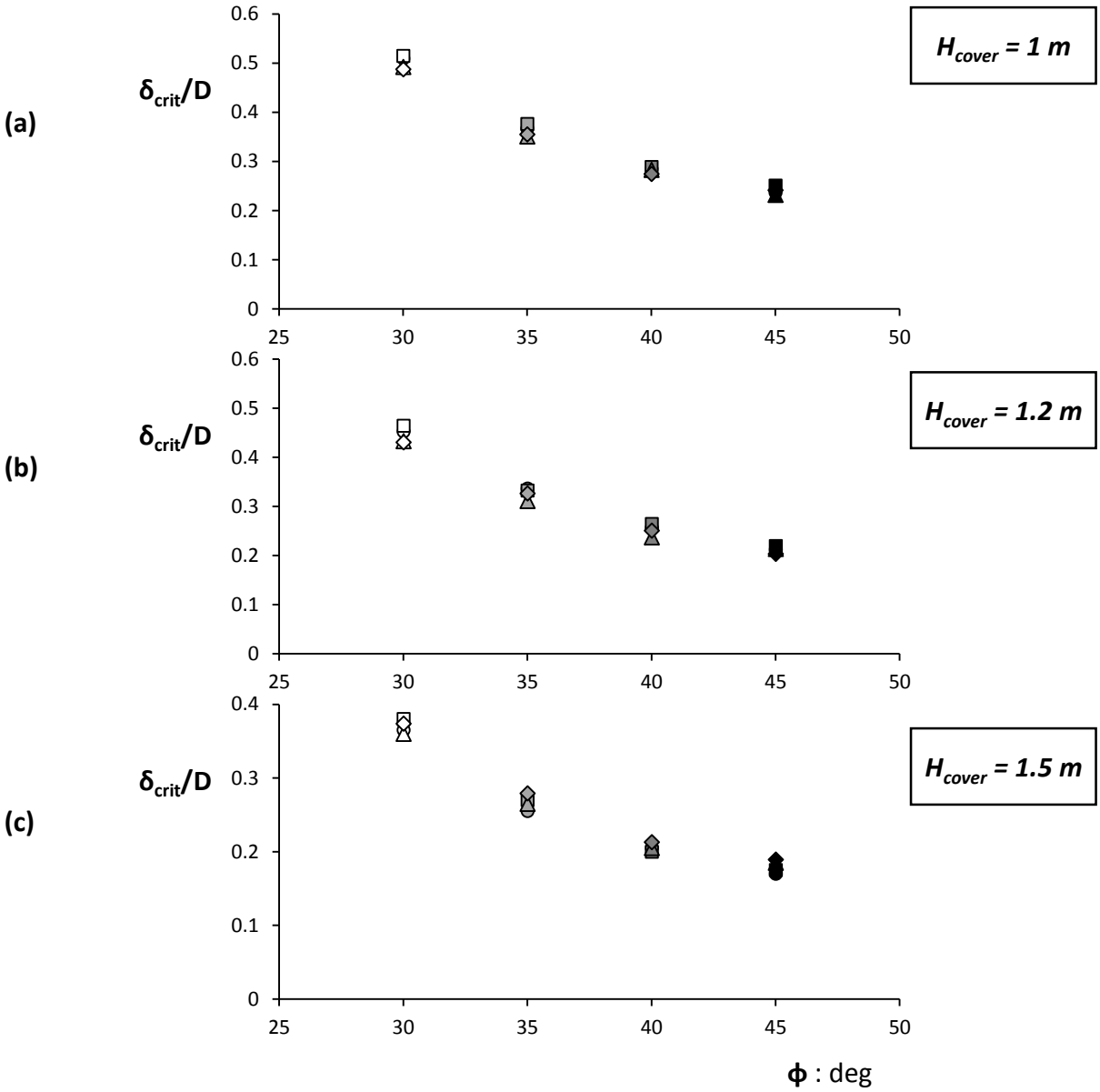

○ $D = 28''\_\varphi = 30^o$	● $D = 28''\_\varphi = 35^o$	● $D = 28''\_\varphi = 40^o$	● $D = 28''\_\varphi = 45^o$
□ $D = 36''\_\varphi = 30^o$	■ $D = 36''\_\varphi = 35^o$	■ $D = 36''\_\varphi = 40^o$	■ $D = 36''\_\varphi = 45^o$
△ $D = 40''\_\varphi = 30^o$	▲ $D = 40''\_\varphi = 35^o$	▲ $D = 40''\_\varphi = 40^o$	▲ $D = 40''\_\varphi = 45^o$
◇ $D = 48''\_\varphi = 30^o$	◆ $D = 48''\_\varphi = 35^o$	◆ $D = 48''\_\varphi = 40^o$	◆ $D = 48''\_\varphi = 45^o$

Fig. 5.25. Pressurized pipes subjected to reverse faulting: normalized critical fault displacement δ_{fault}/D corresponding to buckling initiation for the pipes buried at (a) H_{cover}=1 m, (b) H_{cover}=1.2 m and (c) H_{cover}=1.5 m.

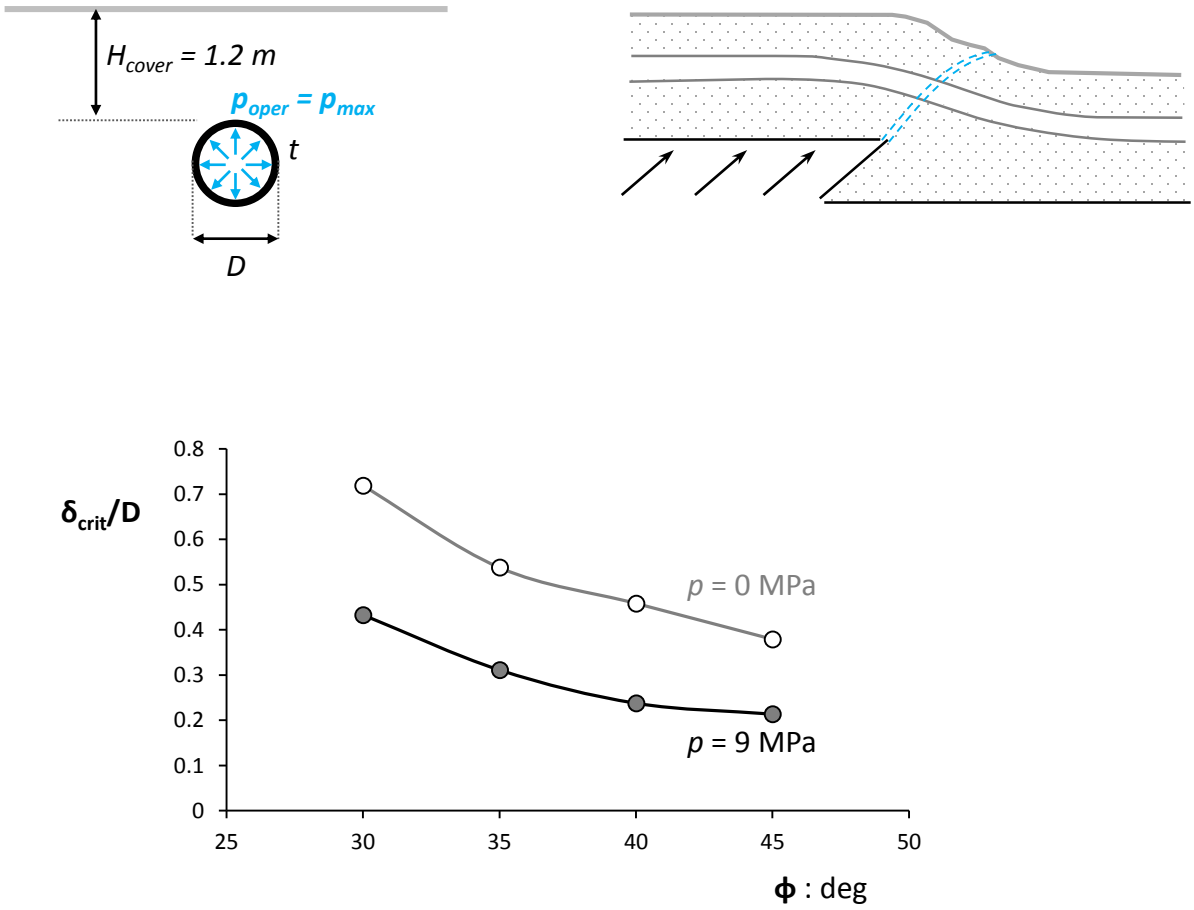

Fig. 5.26. The effect of the internal pressure on the pipe response subjected to reverse faulting: 40" pipe buried at H_{cover}=1.2 m. Normalized critical fault displacements as a function of the soil strength for the pipe without internal pressure and with p = 9 MPa.

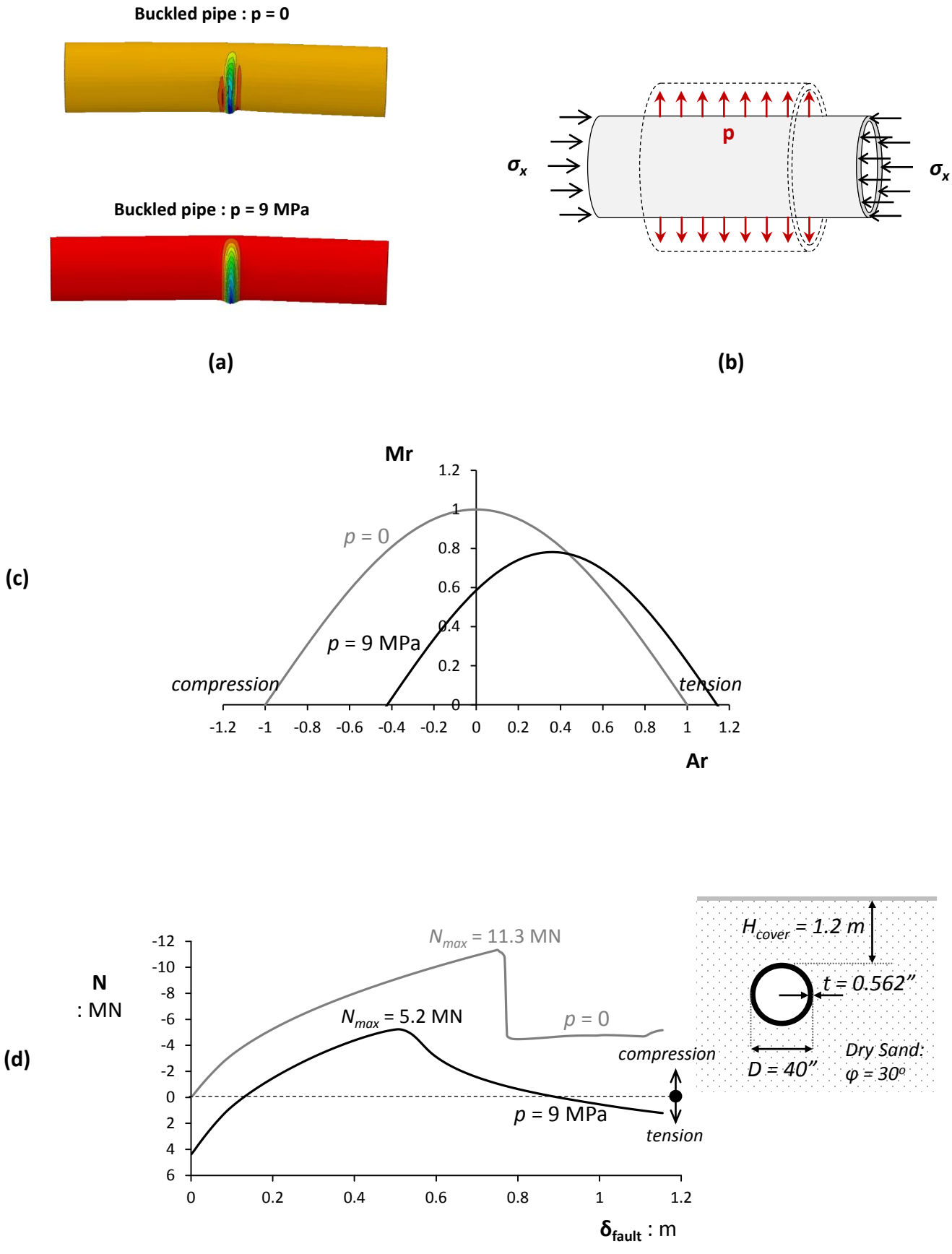

Fig. 5.27. (a) Due to significant compression both pressurized and non-pressurized pipes buckle outwards. (b) The simultaneous action of the internal pressure adds to the tendency for radial expansion resulting in a more unstable and prone to buckling cross-section. (a) Failure envelopes for the non-pressurized pipe and for the pipe under pressure p = 9 MPa for a combination of axial force and bending moment after Mohareb (2002). (b) Axial force of the pipe at the boundaries of the "near-field" model with the increase of the imposed fault displacement.

Chapter 6

Buried Pipelines subjected to landslide-induced actions

6.1. Introduction

Among the various types of permanent ground displacement, the effects of landslide occurrence on a pipeline concentrates the interest from a designer's point of view. Not only because of the higher frequency of occurrence compared to other types of permanent ground deformation that almost take place exclusively during a seismic event of significant intensity (fault rupture, lateral spreading), but also because of the typically very long pipelines (e.g. hundreds of miles for hydrocarbon transmission pipelines) that unavoidably cross many precarious slopes in their route. Determining the behavior of pipelines subjected to landsliding is a great challenge and remains a matter requiring further research. The current state of practice addresses the pipeline-landslide interaction in a rather simplifying manner. As with any Permanent Ground Deformation (PGD) problem, a Winkler-type beam-on-spring methodology is assumed. The soil is often idealized by non-linear discrete soil springs (acting in the axial, lateral, upward, downward direction), while the landslide movement is represented as a set of displacements applied to the free- nodes of the respective springs [Jibson & Keefer (1993); Gantes et al. (2008)]. Notwithstanding the practical value of Winkler-type methodologies, the latter are as accurate as the assumed p-y springs formulations, while they completely ignore any load transfer effects between the adjacent soil springs. For design purposes, the elastic perfectly plastic (p-y) formulations suggested by ALA (2001) and PRCI (2004) are commonly adopted, although recent research findings are questioning their appropriateness. Phillips et al. (2004), Yimsiri et al. (2004), Guo (2005), Hsu et al. (2006), Cocchetti et al. (2009), Daiyan et al. (2009, 2010) and Pike & Kenny (2011) systematically estimated (both numerically and experimentally) the oblique pipeline-soil capacity (i.e. under axial-lateral and lateral-vertical displacement) and concluded that the bearing mechanisms under combined loading are strongly coupled; as such it may be inaccurate to replace soil by independent uniaxial p-y springs.

In this chapter, an original Finite element methodology is introduced that allows the study of the coupled landslide-pipeline problem in a rigorous manner. The proposed methodology realistically accounts for the soil behavior (the complex movement of the dislocating soil, the coupling of oblique loading), for the nonlinear response of the pipeline and especially of any possible fitting components (including any instability phenomena such as buckling), and for any interaction phenomena between the

pipe and the soil. The proposed finite element methodology is utilized to predict the response of a pipeline subjected to landslide-induced actions considering two representative cases: (i) the axis of the pipeline is parallel to the soil movement and (ii) the pipeline is perpendicular to the soil movement. Scope of this study is to enhance our understanding on the mechanics governing the soil-landslide interplay, highlight the potential failure modes of the pipeline and provide evidence on the importance of the detailing (i.e. location and geometry of fitting components (elbows and bends)) on the actual capacity of the pipeline-soil system.

6.2. Analysis methodology

Landslide simulation requires modeling of soil of the order of several hundred meters while on the other hand the pipe diameter is of the order of 1-2 meters. In order to model all possible structural instability phenomena (e.g. local bucking, excessive ovalization of the pipe section etc.), an extremely fine mesh discretization is required. Hence, preserving the same mesh requirements to the surrounding soil would have shaped an enormous mesh of millions of finite elements that is computationally unattractive. To overcome this obstacle, an original two-step procedure is introduced and schematically described in **Fig. 6.1** for the case of pipeline axis parallel to the soil movement.

The "global" model

In the first step, a "global" model is employed to simulate the evolution of soil movement during the landslide event. The output of this first-step is a set of displacement vectors to be assigned as boundary conditions at the respective soil nodes of the subsequent step. Here, the pipeline presence is tactically ignored – a reasonable assumption for landslides geometries with an out-of-plane dimension significantly larger than the pipeline diameter. Evidently, in this global model the mesh requirements are manageable while a relatively coarse mesh (as that of **Fig. 6.1a**) is considered appropriate to model the evolution of the landslide movement.

The "local" model

In the second step, an extremely fine "local" model is introduced comprising the pipeline and portion of the surrounding soil. Here, the landslide action is introduced as 3-d displacement vectors (calculated by the "Global" model) assigned at the bottom and lateral nodes of the local model. [To handle the incompatibility between the coarse mesh of the Global model and the fine mesh of the local model, a

simple mathematical mapping formulation has been developed]. The pipeline distress is later estimated as a function of the soil-movement amplitude.

6.3. Pipeline axis normal to the slope crest

As an illustrative example, in this part we numerically investigate the structural performance of a buried steel pipeline subjected to a rotationally evolving landslide. A sketch of the problem under consideration is presented in **Fig. 6.2**. A typical hydrocarbon transportation pipeline crosses a slope prone to failure. The pipeline axis is straight in plan view and crosses perpendicularly the slope crest. It is manufactured of grade X65 steel (σ_y = 450 MPa), has an outer diameter of D = 36 in, thickness t = 12.7 mm. A soil layer of H = 1.5 m is enclosed between the pipe crown and the ground surface (**Fig. 6.2b**). To accommodate the change in direction, cold bending elbow segments are introduced whose radius is R = 40D (where D is the pipe diameter) (**Fig. 6.2c**). The slope is initially in precarious static equilibrium: a soil mass termed "unstable" soil is considered hazardous for sliding along a potential sliding surface, termed "weak zone". The rest of the slope consists of healthier soil that is not prone to sliding, termed "stable" soil. Failure being imminent: at any external triggering the unstable soil will slide along the weak zone evolving in the form of a rotational landslide. Two landslide scenarios are considered (**Fig. 6.3**) assuming to distinct "weak zones". According to the first scenario, only a part of the slope mobilizes and therefore called "shallow" landslide scenario. The slope fails at the vicinity of the slope crest (point O) and the sliding surface propagates up to 15 m from the slope foot (point B_1). A second scenario is also considered where the entire slope fails, termed "deep" landslide scenario. The sliding surface extends from point O all the way to 9 m beyond the slope foot (point B_2).

6.3.1. Description of the numerical model

The structural performance of the pipeline subjected to the example landslide scenarios is explored using the aforementioned analysis methodology. In **Fig. 6.4a** a view of the Global model of Step 1 (of the decoupled methodology presented) is presented for the shallow landslide scenario. The stable soil (below the weak zone) is modeled as dense sand, with Young's modulus $E_2 \approx 17$ MPa and $\gamma = 20$ kN/m^3 that follows the M-C criterion with stain-softening behavior. For the definition of the latter the following material properties are assumed: $\varphi_p = 45^o$, $\varphi_{res} = 37^o$, $\psi = (\varphi_p - \varphi_{res})/0.8 = 10^o$, $\gamma_y = 0.01$, $\gamma_p = 0.03$ and $\gamma_{res} = 0.07$.

On the other hand, the soil on top of the weak zone (i.e. the sliding mass) is considered as loose sand, consisting of deposits from a previous landslide event. The loose sand has a unit weight $\gamma = 17$ kN/m^3 and

Young's modulus equal to $E \approx 4.5$ MPa. The loose material does not exhibit softening behavior and as such, a peak friction angle of $\varphi = 34^o$, a dilation angle of $\psi = 5^o$ and a $\gamma_y = 0.03$ are assumed. For the simulation of the weak zone, a row of elements of reduced stiffness and strength (E_r = 3 MPa and $\varphi_r = 30^o$) is considered.

The landslide is artificially triggered by progressively reducing the strength of these elements during the analysis step time. Note that all results stem from static analyses and hence any time reporting (t=1,2,3 etc) hereafter refers to analysis step count and not to actual time units. **Fig. 6.4b** presents snapshots of the deformed mesh with superimposed displacement contours of the free field problem highlighting the onset (t = 1), the evolution (t=2), and the deposition (t=4) of the landslide. Note that as the sliding mass runs downslope it keeps accelerating under the effect of gravity, while the displacements increase exponentially.

To predict the pipeline response to the imposed landslide-induced actions the local model is employed, presented in **Fig. 6.5**. The pipe is modeled with four-noded reduced integration shell elements, using a total of 48 elements along its circumference, with a longitudinal dimension limited down to d_{FE} = 2.5 cm within the regions of maximum distress. The realistic simulation of the interface condition between the steel pipe and the surrounding soil calls for the use of special-purpose contact elements. The latter allow the pipe to slide on the ground, while the maximum mobilized shear resistance τ_{max} is a function of the frictional coefficient μ. In this study μ has been considered equal to 0.5. As with the fault-induced displacements, the far-field response of the pipeline should be realistically accounted for. In the same manner as before, the far-field response is simulated with "hybrid" boundaries, with the soil reactions being simulated with nonlinear springs, while the pipeline in the respective area with beam elements. The spring properties are appropriately calibrated through uniaxial push tests.

A soil layer of thickness d' is assumed to be enclosed between the pipe periphery and the location of the prescribed soil movements. Understandably, the thickness of this local soil (d'), should be small enough to facilitate computational efficiency, but large enough to ensure that the soil-pipe interaction is appropriately captured. To estimate this optimum thickness, a simple "test-model" is introduced (**Fig. 6.6**). The test model comprises two segments, a stable and a moving part. The stable part mimics the pipeline segment that is anchored within the soil, while the moving part represents the area of the pipe (close to the landslide toe) that is forced to move outwards (i.e. in the z direction). In this illustrative test model, the axial soil displacement (u_x) is tactically ignored, since it is irrelevant to the estimation of the minimum allowable thickness d'. Therefore only vertical soil displacements in the z direction are prescribed along the bottom side of the moving part (leaving the top boundary free to move). To assess

the minimum required dimension *d'*, two alternative configurations are comparatively tested: an 'adequately small' local model '3D Model' where *d'* = 3*D*, and a rigorous model '10D Model' (but computationally not as efficient), where *d'* = 10*D*. The two alternative local models are compared in terms of ground deformations along the pipe-axis and bending distress (monitored by the maximum axial stain recorded along the pipe). Evidently, the two models respond quite closely. The 3D model tends to over-predict the pile distress by 15% compared to the accurate 10D model; a reasonable compromise between accuracy in results and computational efficiency (**Fig. 6.7**). This finding justifies the adoption of a small and efficient local model, where d'=3D. This local model will be used in the next section for the parametric study.

Inevitably, under the extreme displacements caused by a landslide, a buried steel pipeline is expected to develop severe deformation. Considering the adversity of the loading, it is reasonable to only expect of the pipeline to satisfy its fundamental requirement: safety against leakage. Therefore, rupture of the pipe wall should be avoided, whether caused by excessive tension or collapse of the cross section due to compression or bending. To assess the pipeline performance the following failure criteria are identified:

(a) The maximum tensile strain should be lower than a limit value of ε_{max} = 3% to avoid rupture due to tension. This value is an upper bound adopted by the EN 1998–4 provisions for seismic-fault-induced actions on buried steel pipeline and by the seismic provisions of ASCE MOP 119 for buried water steel pipelines

(b) Local buckling should be avoided. The buckled area is associated with significant strain concentration which, in case of repeated loading, may lead to development of fatigue cracks which will impose a serious threat to structural integrity of the pipeline (Dama et al (2007), Das et al (2008)).

(c) Excessive ovalization of the pipe section should be avoided. Following the Dutch specification NEN 3650, the decrease of the pipe diameter should always be maintained below 15%.

6.3.2. Pipeline behavior subjected to soil movement parallel to its axis: understanding the mechanics

Shallow landslide scenario

A first set of results is presented in **Fig. 6.8** corresponding to the pipeline experiencing the shallow landslide scenario. The deformed mesh of the pipeline is presented in **Fig. 6.8a** with superimposed stress contours (a scale factor of 5 has been applied to render the results more comprehensible). Results are presented for the instant when the soil at the vicinity of the landslide toe (point B_1) is displaced by U_{soil} = 2 m; a quite severe landslide event has occurred. It is evident that the pipe is extensively deformed under

the soil actions originated from the rotational movement of the sliding mass. The latter may be analyzed in two components: an axial and a normal to the pipe axis displacement (**Fig. 6.8b**). The axial component tends to drag the pipeline downslope, inducing tension near the landslide crown and compression near the landslide toe. Yet, the axial forces transmitted onto the pipeline are bounded by the low strength of the pipe-soil interface (described by a friction coefficient μ = 0.5) and as such the axial distress of the pipe appears not to be critical for the pipeline safety. On the contrary, the normal component of the soil movement causes significant stressing on the pipe. Near the landslide crown (area A') the (perpendicular to the pipe axis) relative soil displacement is negative (i.e. drags the pipe downwards), while close to the toe of the landslide, the soil moves upwards ($u_{s,2a}$ >0) carrying the pipe along. Since the pipeline is not free to follow the soil movement but is rather fixed at the crest and at the toe within the stable ground, it unavoidably bends; bending is positive at Region A' and negative at Region A. Moreover, since the subgrade pressure is much greater than that produced by the overlying soil (i.e. the downward soil reactions are much higher than the upward reactions), the pipeline is more distressed near the toe of the landslide in Area A. Although signs of yielding (depicted in red color) are visible near the crest of the slope (in the anchoring region beyond the slope crest and in region A'), the pipeline appears to have failed near the landslide toe (region A). In fact, the pipeline appears to have buckled under the extreme bending due to subgrade reactions. **Fig. 6.9** focuses on the stressing of the pipe segment at the vicinity of the critical section (highlighted in **Fig. 6.9a**). The initially uniformly distributed compressive strains (**Fig. 6.9b**) at the bottom side of the segment have localized in two distinctive points (ripples) with the increase of the imposed bending. For further increase, one of the two ripples becomes dominant, concentrates any additional stresses and ultimately transforms into the distinctive pipe wall folding of the local buckling. The distribution of the compressive strains at the bottom side of this pipe segment is presented in **Fig. 6.9c**, vividly depicting the localization of strains and the formation of local buckling. For U_{soil} = 1.6 m the appearance of the two ripples is evident (two maxima in the strain distribution), while for U_{soil} = 1.75 m the buckling of the pipe wall is evident (further increase in the imposed displacement is concentrated on the two maxima points while the rest of the strain distribution remains constant). Failure of the pipeline is considered the when the ripples that will form the local buckling are clearly formed, for U_{soil} = 1.6 m.

Deep landslide scenario

In the previously examined landslide scenario, the weak zone was assumed to cross the pipe at its straight part - in an area that lies at some distance from the bottom bend. This section investigates the pipe response when a more extended landslide scenario, termed "deep landslide scenario", is triggered

(**Fig. 6.3**, blue line). In this scenario, the entire slope fails. The landslide crown remains at point O, but the sliding plane emerges at the ground surface at the left side of the slope tow (point B_2 at x = - 9 m).

A view of the deformed pipeline for the two landslide scenarios under consideration is presented in **Fig. 6.10**. The loading mechanisms in the deep scenario (**Fig. 6.10a**) and in the shallow scenario (**Fig. 6.10b**) are similar: the pipe is being dragged downwards at the landslide crown area while it is pushed upwards at the toe area, with the pipe segment near the landslide toe experiencing the most severe stressing. However, there is one substantial difference. While in the shallow scenario the pipe wall collapses inwards due to excessive bending, in the deep scenario, buckling is manifested through crushing of a whole section (for both buckled points) indicating a simultaneous substantial compressive force. The reason behind this behavior lies in the geometry of the 'anchoring' area within the stable part of the slope. As depicted in **Fig. 6.10a**, when subjected to the shallow landslide scenario the area of maximum distress (maximum deflection point) is preceded by an area that lies in the stable soil and experiences a counterbalancing bending moment. The length of this area is what is commonly termed effective "fixity length". For the shallow scenario, the "fixity" is implemented within the straight part of the pipe, which is not the case for the deep scenario. Here, the point of maximum deflection moves closer to the elbow element (**Fig. 6.10b**). Inevitably, the pipe segment that will react to that bending is the elbow itself. Due to its concave geometry, the elbow does not only bend but also is significantly compressed, since the drag force of the soil translates into a significant axial force in the rotated axis of the bend. The combination of bending and significant compression leads to local buckling (in the form of a whole section being crushed) at the wall of the elbow element within the anchoring region (instead of only at the maximum deflection region).

The evolution of local buckling at the elbow section is graphically depicted in **Fig. 6.11**. **Fig. 6.11a** portrays the critical pipe segment before and after buckling. **Fig. 6.11b** plots the progressive growth of axial strains as a function of landslide movement. Note that for soil displacement of the order of U_{soil} = 1.10 m, any additional strain is concentrated on the two peaks, leaving the rest of the compressive side unaffected. This is the moment when the pipe is considered to have failed.

6.3.3. The effect of the internal pressure

A pipeline will be without internal pressure only during construction and possible maintenance. For the vast majority of its lifetime the pipeline will operate under internal pressure. Ignoring the simultaneous action of the internal pressure may be acceptable for a preliminary analysis or when the scope is to identify the basic response mechanisms. However, to assess the performance of the pipeline and estimate the safety margins against a possible landslide occurrence, the analysis should also account

for the effect of the internal pressure. The pipeline under consideration is designed for a maximum operating pressure p_{max} = 9 MPa based on the formula:

$$p_{max} = 0.72*[(2\sigma_y\, t)/D]$$

In the following, the effect of this pressure on the pipeline performance is investigated.

Fig. 6.12 presents as comparison of the pipeline response subjected to the shallow landslide scenario between the non-pressurized and the pressurized pipeline, focusing on the pipe segment around the critical section. The deformed pipe segment is presented for various magnitudes of soil displacement, superimposed with axial strain contours. In both cases the pipe bends as it is forced to dislocate upwards by the moving soil. This bending manifests through tensile axial strains at the top side of the pipe and through compressive strains at the bottom side. In contrast with the non-pressurized pipe however, the pressurized pipe appears to be able to accommodate very large displacements without the occurrence of local buckling. In this case, the internal pressure has a stabilizing effect on the tendency of the pipe wall to collapse inwards. Yet, the presence of the internal pressure affects the pipe in another way: the pipe wall is pushed outwards increasing the hoop strains. It proves that for the pressurized pipe, apart from the axial (longitudinal) strains, the increase in curvature results in a significant increase in the hoop strains. In fact, the latter prove to increase at a larger rate than the axial strains. **Fig. 6.13a** presents the deformed pipe segment around the critical section for soil displacement U_{soil} = 3 m, this time with contours of hoop strain. It appears that although the axial strains at the same moment (see Fig. 12) are within limits (i.e. no buckling occurrence and tensile strains < 3%), the developed tensile hoop strains have lead the pipeline to failure. **Fig. 6.13b** presents the distribution of hoop strains around the critical section for various magnitudes of soil displacement. Notice that the maximum tensile strains are encountered at the bottom side of the pipe that is under compressive longitudinal strains. As depicted in **Fig. 6.13c** where the evolution of the maximum tensile hoop strains is correlated with the imposed soil displacement, the pipeline fails at U_{crit} = 2.6 m; a significant increase in the safety margins compared to the non-pressurized pipeline (U_{crit} = 1.10 m).

The internal pressure has a similar effect on the pipeline subjected to the deep landslide scenario. This effect is depicted in **Fig. 6.14** and **Fig. 6.15**. **Fig. 6.14** presents the evolution of the axial (longitudinal) strains at the bottom elbow. Again, the presence of the internal pressure has opposes the tendency for local buckling. Notice that for U_{soil} = 1.5 m the pressurized pipe has not buckled contrary to the one without pressure. As with shallow landslide scenario, the internal pressure causes a significant increase in the hoop strains with the increase in the curvature (**Fig. 6.15**). The maximum tensile hoop strains are encountered

again at the side that is under compressive axial strains (top side of the pipe). Ultimately, the tensile hoop strains exceed the limit of εmax = 3% at U_{crit} = 1.25 m.

6.4. Pipeline axis parallel to the slope crest

In the present section, the pipeline is placed parallel to the slope crest, and therefore, a potential mobilization of the soil mass will occur perpendicular to the pipe. As an illustrative example, the same pipe as before is selected (steel X65, D = 36", t = 0.5", p_{design} = 9 MPa, H_{over} = 1.5 m). The axis of the straight pipeline is parallel to the slope crest and it is located at the middle of the slope (x = 35) as depicted in **Fig. 6.16a**. The deep landslide scenario is selected as a possible scenario of soil mobilization. As opposed to the case where the pipe axis is normal to the slope crest, in this case the out-of-plane shape and extent of the landslide is of great interest. To this end, two landslide scenarios are considered. It is assumed that the 2D section depicted in **Fig. 6.16a** corresponds to the middle cross section of the landslide. According to the first landslide scenario the sliding surface extends to 20 m from the middle section at both sides. With a total width of d = 40 m (graphically depicted in **Fig. 6.16b**) this scenarios represents an extensive landslide termed "broad" landslide scenario. A second scenario is considered where the total width of the sliding mass d = 20 m, representing a more limited soil mobilization termed "narrow" landslide scenario.

The scale inconsistency problem still remains, therefore the decoupled methodology is also applied here. **Fig. 6.17** schematically presents the two steps of the methodology, the analysis in the global level and subsequently the focus on the pipeline-landslide interaction in local level. **Fig. 6.18** presents details of the numerical model used to simulate the pipeline-landslide interaction. Taking advantage of the problem symmetry, half of the landslide and the pipe are modeled. The near-field 3D model extends to a total length L_{tot} = 50 m from the plane of symmetry (the middle section of the landslide). Beyond the 3D model, hybrid boundaries are used to account for the far-field response of the pipe. In this case, the boundaries of the soil prism extend to 5D in the direction of the soil movement.

6.4.1. The effect of the landslide extent to the pipeline response

Broad landslide scenario

Fig. 6.19 presents results assuming that the broad landslide scenario has occurred. In **Fig. 6.19a** the 3D deformed mesh of the near-field model is presented with displacement contours for soil displacement at the boundaries of the soil prism of the magnitude of U_{soil} = 2 m. Subjected to this substantial displacement the pipe is significantly stressed as depicted in **Fig. 6.19b** where the deformed pipe is presented with stress

contours. The pipe bends to accommodate the differential lateral displacement, receiving the characteristic double curvature deformation pattern. Consequently, strain concentration is observed at the points of maximum curvature, as it is shown in **Fig. 6.19c** where the axial strain distribution along the two normal to the soil movement direction generators. Three regions of distinctive behavior can be recognized. A region at a distance from the end of the landslide where the pipe is practically fixed within the stable soil and therefore, is practically unaffected by the displacing soil. A second region can be recognized where the pipe practically complies with the imposed displacement and the pipe distress can be summarized in the axial stressing due to stretching. Finally, between these two regions, there lies a third one where the pipe accommodates the imposed differential displacement through bending. This is the region of maximum stressing and ultimately failure. The fundamentals of the pipe response are schematically presented in **Fig. 6.20**. The length of the region A (pointed in the figure as l_b, while the component of l_b that lies within the stable soil is pointed as $l_{b,s}$ and the respective that lies within the moving soil as $l_{b,m}$) is a characteristic of the pipe-soil interaction. In other words, no matter how larger the width of the sliding mass d would be, the length where the pipe responds through bending would be the same. Consulting **Fig. 6.19c**, l_b can be estimated about 30 m, while $l_{b,s}$ and $l_{b,m}$ are approximately 15 m each.

Fig. 6.21 summarizes the response of region A assuming that the pipe is without pressure. As the pipe segment bends due to the differential lateral displacement at its ends, the cross section of the pipe distorts (ovalization). This distortion is more intense at the points of maximum curvature. Ultimately, the pipe diameter decreases more than the allowed $f = \Delta D/D = 15\%$, and the pipeline is considered to have failed at $U_{soil} = 3.55$ m.

Limited landslide scenario

It is mentioned in the previous that the length l_b within which the pipe responds through bending is a characteristic of the pipe-soil interaction, and therefore, no matter how larger the width of the sliding mass would be, this length would remain the same. Consequently, no major divergence in the pipe performance is expected. What about the case where the landslide becomes narrower? In particular, the previous discussion showed that a certain distance $l_{b,m}$ within the moving soil is needed for the pipe to accommodate the differential displacement at the two ends. What would be the effect on the pipe response if the width of the sliding mass was less than the required? To answer this question a second landslide scenario is assumed termed “narrow” landslide scenario, according to which the sliding mass extends to $d/2 = 10$ m from the middle section (a length that is smaller than the $l_{b,m} = 15$ m).

A comparison of the pipe behavior subjected to the two landslide scenarios is presented in **Fig. 6.22**. For the "broad" scenario (**Fig. 6.22a**) and for the "narrow" scenario (**Fig. 6.22b**) the deformed pipe is presented with superimposed stress contours as well as the distribution of axial strains along the two most stressed generators for soil displacement U_{soil} = 1 m. As expected, when subjected to the "narrow" landslide scenario, the available length is not enough for the pipe to receive the deformation pattern indicated by its relative stiffness. Moreover, the middle cross section is forced to retain perpendicularity with the soil movement direction due to symmetry. The combination of the two results in a development of curvature at the middle section larger than that of the maximum curvature points according to the "broad" scenario. Consequently, for the same soil displacement the developed axial strains are larger in for the "narrow" scenario compared to the "broad" scenario.

Ultimately, the strains localization at the middle cross section leads to local buckling of the compressive side of the pipe. **Fig. 6.23** presents the evolution of local buckling at the critical section. As depicted in the deformed mesh of the pipe with superimposed axial strain contours, the initially uniform distribution of compressive strains, transforms into a wavy distribution as the strains increase, resulting finally in the characteristic wall folding of the local buckling. The onset of buckling can be monitored by the evolution of maximum compressive axial strain with the increase of the imposed displacement (**Fig. 6.23b**). As attested by the abrupt increase in the strain accumulation rate, buckling occurs at U_{soil} = 1. 35 m.

6.4.2. The effect of the internal pressure

Having identified the principals of pipeline response subjected to soil movement normal to its axis, in this section the effect of the internal pressure is investigated, assuming that the pipe operates under the pressure for which it is designed for (p =9 MPa). **Fig. 6.24** summarizes the performance of the pressurized pipeline experiencing the "broad" landslide scenario. **Fig. 6.24a** presents the axial strains developed along the pipe for soil displacement U_{soil} = 2 m. Although, the developed axial strains are significant, no tensile failure is observed ($\varepsilon_{x,max}$ < 3%) nor local buckling is visible (despite the large compressive strains $\varepsilon_{x,min}$ = -0.035). At the same time however, the pipe proves to be significantly distressed at the cross section plane, since the hoop strains developed exceed the limit tensile strain εmax = 3 % (**Fig. 6.24b**). Once again, the increase in the section curvature results in significant increase in the hoop strains, with the maximum hoop strain located at the side where compressive axial strains develop (**Fig. 6.24c** presents the distribution of hoop strains around the critical cross section). **Fig. 6.25** quantifies the safety margins of the pressurized pipeline subjected to the "broad" landslide by correlating the evolution of maximum tensile

hoop strain with the increase in the soil displacement. The developed hoop strain meets the failure criterion of ε_{max} = 3% at U_{soil} = 1.35 m.

Similar is the effect of the internal pressure when the pipe experiences the "narrow" landslide scenario. Although the presence of the internal pressure seems to delay the manifestation of local buckling (observe in **Fig. 6.26a** that for U_{soil} = 1.5 m there is no evidence of local buckling), the developed hoop strain for the dame soil movement (**Fig. 6.26b**) leads the pipeline to failure. In particular, as attested in **Fig. 6.27** the developed tensile hoop strain leads the pipe to failure for soil displacement U_{soil} = 1.05 m.

6.5. Design insights

Admittedly, the previous discussion is non-exhaustive and examines but a few possible scenarios of pipeline-landslide interaction. Yet, a few conclusions can be drawn regarding the fundamental response mechanisms that can be universally applied and should be taken into account at the design.

From the investigated cases, it becomes apparent that the shape, the geometry and the extent of the mobilized soil mass is a crucial factor affecting the pipeline response. The example of the pipeline with axis parallel to the slope crest subjected to the "broad" and the "narrow" landslide scenario is quite representative. The decrease in the extent of the landslide results in altering the pipeline response mechanisms and in the drastic decrease of the safety margins. **Fig. 6.28** compares the performance of the pressurized pipeline subjected to these two landslide scenarios. When the "broad" scenario is activated the pipeline will be able to accommodate 1.35 m of displacement before failure due to excessive tensile hoop strains. Yet, designing the pipeline based on this scenario would prove unsafe. If the "narrow" landslide scenario activates, the pipe would rupture at earlier stage (U_{crit} = 1.05). Conclusively, the exact geometry and shape of the mobilized soil mass and the distribution and direction of the soil displacement may be decisive in assessing the pipeline vulnerability. Thus, all possible landslide geometries should be considered before concluding on the worst-case scenario regarding the pipeline design.

An equally important element in the design of pipelines against landslide induced actions is the presence of elbows. These fitting components prove to be the most vulnerable parts of the pipeline, and in cases of landslides that affect them, they will determine whether the pipe endures or fails. The elbow at the slope foot is particularly susceptible to the combination of bending and compression. A pipeline crossing perpendicularly the slope crest is an illustrative example of such a behavior (**Fig. 6.29**). If the "shallow" landslide scenario mobilizes the bottom elbow remains practically intact and the pipeline will be able to accommodate soil displacements of the order of 2.6 m (considering internal pressure p = 9

MPa). However, if the mobilized soil mass affects the bottom elbow (as with the "deep" landslide scenario), the pipeline safety margins are halved (U_{crit} = 1.25 m). It becomes apparent that special attention should be paid to the design of the bends, while the pipeline analysis should account for possible landslide scenarios that affect them.

The examined cases also highlight the significant effect of the internal pressure on the pipeline performance. Taking into account the simultaneous action of the internal pressure, the calculated safety margins substantially change. On the one hand, the internal pressure has a stabilizing effect on the cross section distortion (counterbalancing the inward collapse of the pipe wall when under extreme bending or eliminating the tendency of the cross section to ovalize). On the other hand, it provokes severe hoop strains with the increase of the section curvature. Hence, the internal pressure can prove favorable or detrimental. Representative example of favorable effect of the internal pressure is the case where a pipeline with axis normal to the slope crest experiences the "shallow" landslide scenario (**Fig. 6.30a**). Ignoring the presence of the internal pressure the pipeline safety margins would be of the order of U_{crit} = 1.6 m, with the pipeline failing due to local buckling, while accounting for the simultaneous action of internal pressure the pipeline does not buckle, but rather fail due to excessive tensile hoop strains at U_{crit} = 2.6 m. In stark contrast, the effect of the internal pressure proves highly detrimental in the case of a pipeline parallel to the slope crest experiencing the "broad" landslide scenario (**Fig. 6.30b**). The non-pressurized pipeline can accommodate a spectacular U_{crit} = 3.55 m before failing due to excessive ovalization. Yet, the same pipeline operating under the design pressure can only accommodate a mere 1.35 m of soil displacement before failing due to excessive tensile hoop strains. Conclusively, it is evident the pipeline analysis should account for the simultaneous action of the internal pressure for which it is designed. Moreover, the analysis method should provide accurate modeling of the nonlinear response of the pipe cross-section accounting for possible cross-section distortion and the increase in hoop strains with the increase in the curvature.

In this chapter, only the cases of pipelines parallel and normal to the slope crest were considered. These two cases are but the two extremes among numerous possible pipeline-slope crest intersection angles. The pipeline may cross a slope at any given angle between 0o (parallel to slope crest) and 90o (normal to slope crest). Yet, for all the possible intersections angles, the pipeline response is expected to be a combination of the two extreme cases examined herein. Therefore, for any intersection angle the sliding soil displacement can be analyzed in:

(a) A normal to the pipe component that will induce bending at the plane of the slope (lateral), similar to that of a pipeline parallel to the slope crest (see **Fig. 6.20**).

(b) A parallel to the pipeline axis component that will induce tension near the landslide crest and compression near the landslide toe

(c) A normal to the pipeline axis that will induce bending at the vertical plane (downward or even upward in case of a rotational slide), similar to that of a pipeline perpendicular to the slope crest (see **Fig. 6.8**).

The pipeline response is expected to consist of the spatial combination of the above three components. Of course, if the landslide affects any of the elbows, the induced bending of these element is expected to play a vital role in the pipeline performance, particularly the "closing" of the bottom bend.

References

American Lifelines Alliance. Guidelines for the design of buried steel pipes, ASCE, New York (2001)

American Society of Civil Engineers. Buried flexible steel pipe; design and structural analysis. In: Whidden WR, editor. ASCE manual of practice, MOP; 2009. p. 119.

Cocchetti, G., Prisco, C., Galli, A., and Nova, R. (2009). "Soil-pipeline interaction along unstable slopes: a coupled three-dimensional approach. Part 1: Theoretical formulation", Can. Geotech. J., 46:1289-1304.

Comite Europeen de Normalisation. Eurocode 8, part 4: silos, tanks and pipelines, CEN EN1998-4. Brussels, Belgium; 2006.

Daiyan, N., Kenny, S., Phillips, R., and Popescu, R. (2009). "Parametric study of lateral-vertical pipeline/soil interaction in clay, 1st Int./1st Eng. Mechanics and Materials Specialty Conf., St. John's, NL, Canada.

Daiyan, N., Kenny, S., Phillips, R., and Popescu, R. (2010). "Numerical investigation of oblique pipeline/soil interaction in sand", 8th Int. Pipeline Conf., Calgary, Alberta, Canada.

Dama E, Karamanos SA, Gresnigt AM. Failure of locally buckled pipelines. Journal of Pressure Vessel Technology, ASME 2007; 129(2):272–9.

Das S, Cheng JJR, Murray DW, Nazemi N. Effect of monotonic and cyclic bending deformations on NPS12 wrinkled steel pipeline. Journal of Structural Engineering, ASCE 2008;134(12):1810–7.

Gantes, C.J., Bouckovalas, G.D., and Koumousis, V.K., "Slope Failure Verification of Buried Steel Pipelines", 10th International Conference on Applications of Advanced Technologies in Transportation, Athens, Greece, May 27- 31, 2008.

Guo, P. (2005). "Numerical modeling of pipe-soil interaction under oblique loading." J. of Geotech. and Geoenviron. Eng., ASCE, 131(2): 260-268.

Hsu T.W., Chen Y.J., and Hung W.C. (2006) “Soil resistant to oblique movement of buried pipes in dense sand.” Journal of Transportation Engineering, 132(2), 175-181.

Jibson, R.W. and Keefer, D.K., (1993), “Analysis of the Seismic Origin of Landslides: Examples from the New Madrid Seismic Zone,” Geological Society of America Bulletin, April, Vol. 105, pp. 521-536.

Nederlands Normalisatie-Instituut. Requirements for pipeline systems, NEN 3650, part-1: general, and part-2: steel pipelines; 2006.

Phillips, R., Nobahar, A., and Zhou, J. (2004). Combined axial and lateral pipe-soil interaction relationship, 5th Int. Pipeline Conf., Calgary, Alberta, Canada.

Pike, K., Seo, D., and Kenny, S. (2011). “Continuum modelling of ice gouge events: Observations and assessment”, Arctic Technology Conf., Houston, TX, USA.

PRCI, (2004), “Guidelines for the Seismic Design and Assessment of Natural Gas and Liquid Hydrocarbon Pipelines, Pipeline Design, Construction and Operations”, Edited by Honegger, D. G., and Nyman D. J., Technical Committee of Pipeline Research Council International (PRCI) Inc, October 2004

Yimsiri, S., Soga, K., Yoshizaki, K., Dasari, G.R., and O'Rourke, T.D. (2004). “Lateral and upward soil-pipeline interactions in sand for deep embedment conditions”, J. of Geotech. and Geoenviron. Eng., ASCE, 130(8): 830-842.

Figures

of Chapter 6

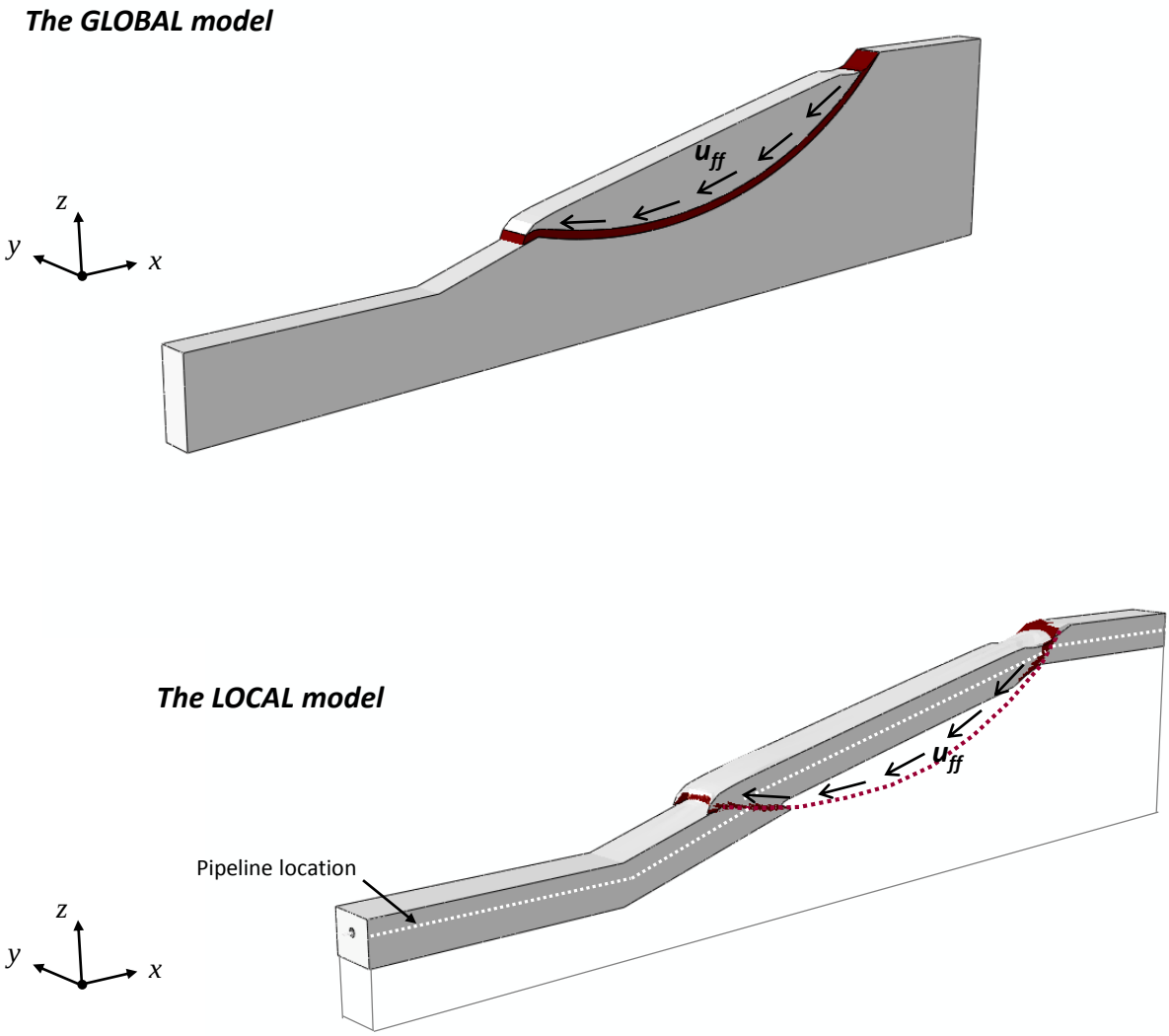

Figure 6.1. Outline of the proposed 2-step numerical methodology: the vectors of soil movement u_{ff} estimated by the analysis of the GLOBAL Model are assumed at the bottom, and lateral boundaries of the LOCAL model to estimate the induced pipeline distress.

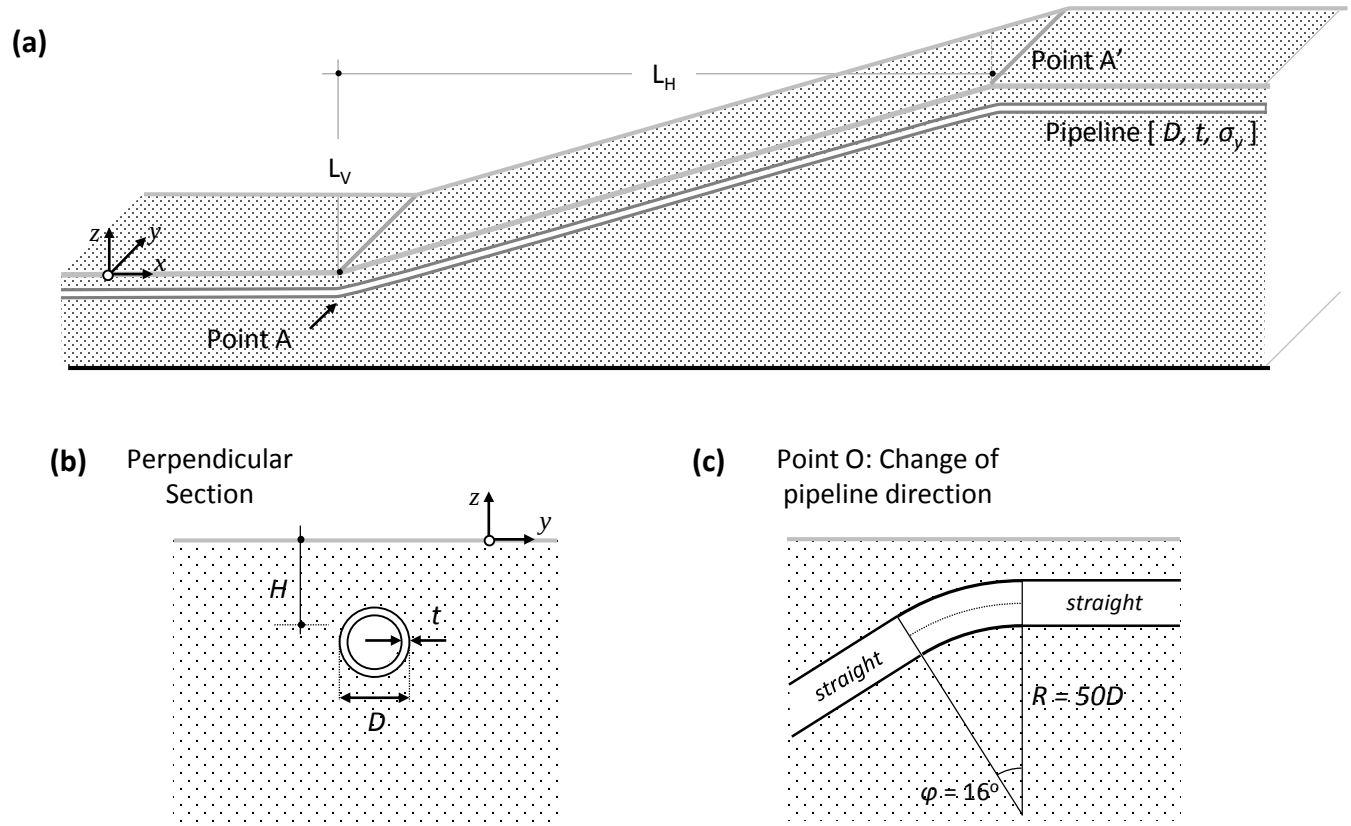

Figure 6.2. The studied example: pipeline axis normal to the slope crest. **(a)** 3D sketch slope and the pipeline; **(b)** view of a typical cross-section; **(c)** geometry of the fitting element at Point A (i.e. at the slope crest).

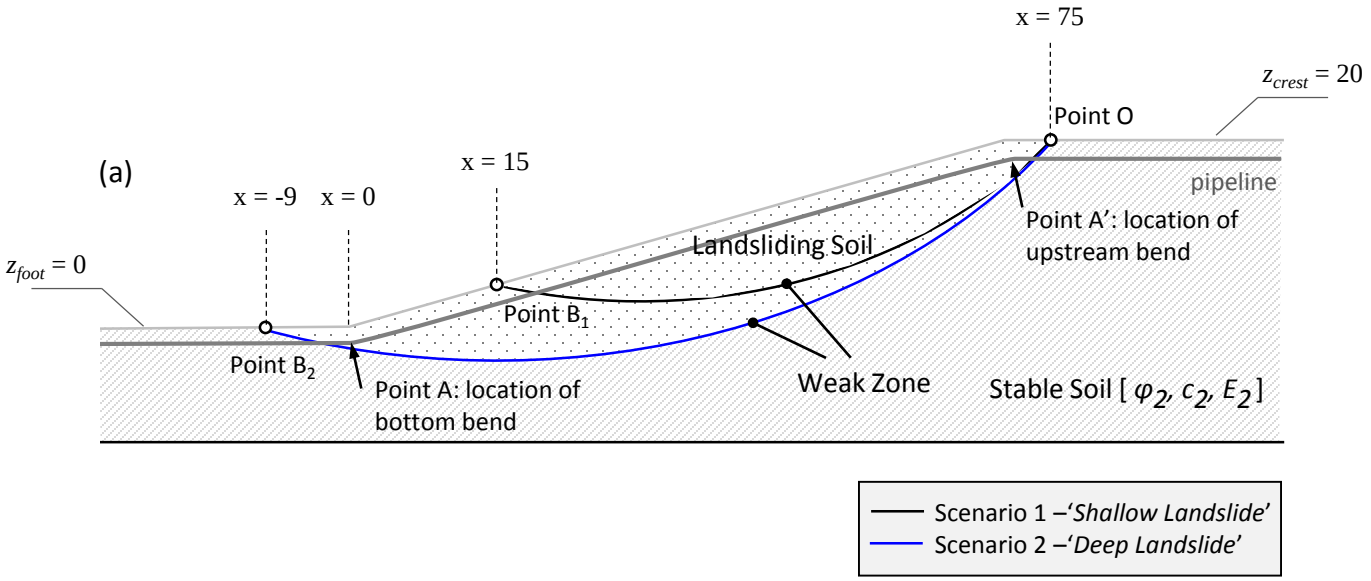

Figure 6.3. The two landslide scenarios that are considered in the analysis.

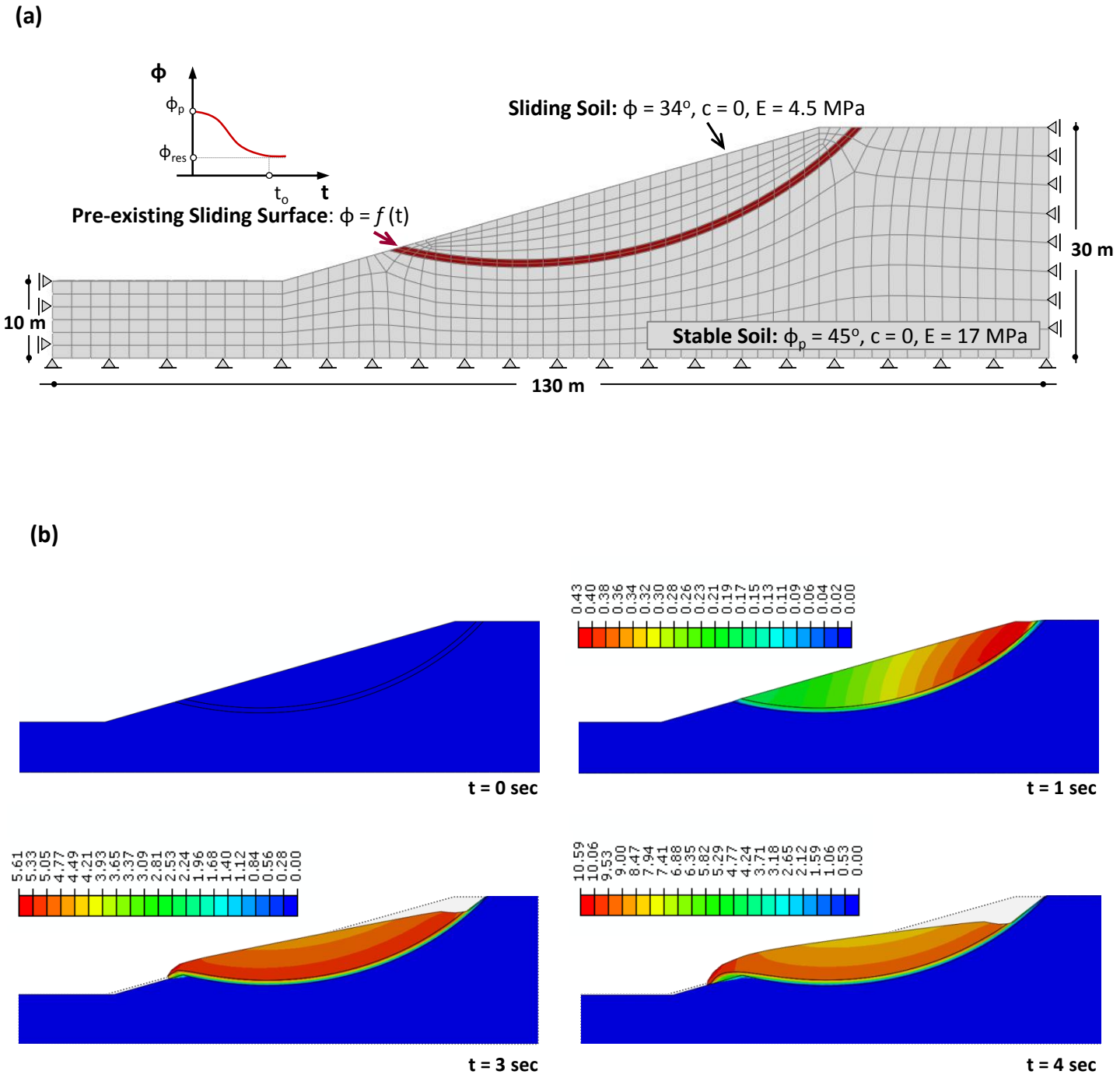

Figure 6.4. (a) The plane strain free-field (ff) model and **(b)** snapshots of the deformed mesh with vectors of displacements, at four characteristic instants: *triggering, evolution and deposition of the landslide.*

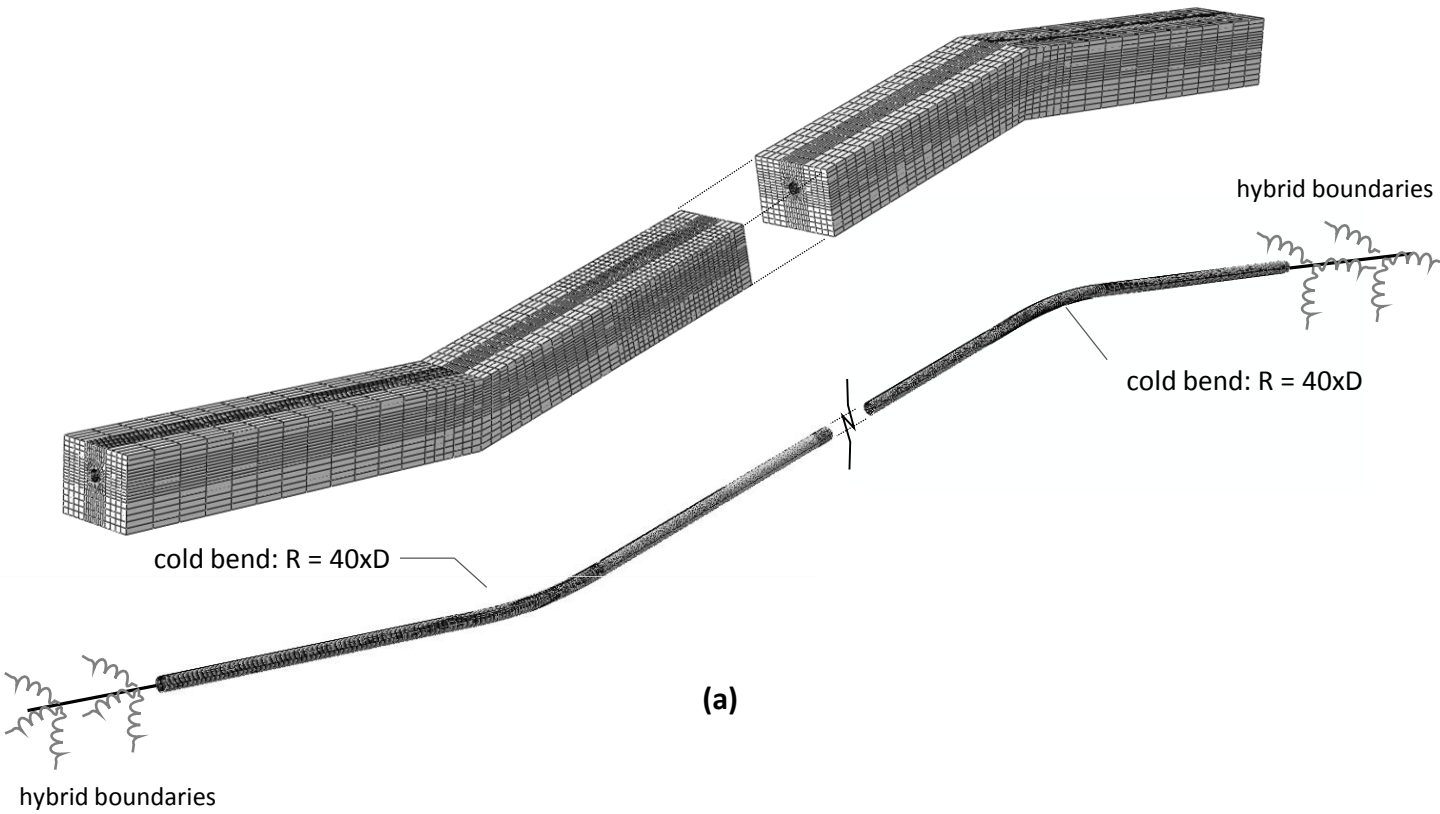

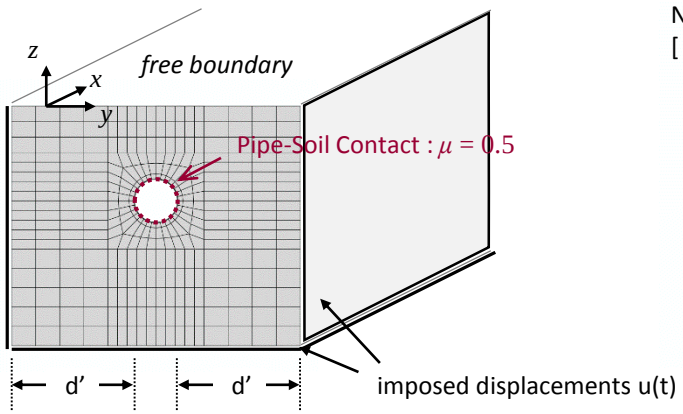

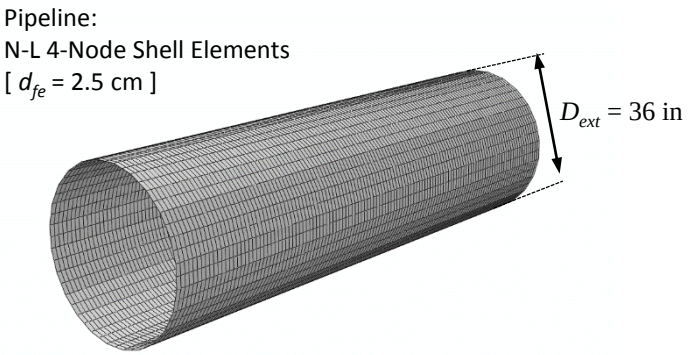

Figure 6.5. The local Model : **(a)** view of the mesh of the soil prism and of the pipeline **(b)** the cross-section of the analyzed system, **(c)** a closer view of a typical pipe segment.

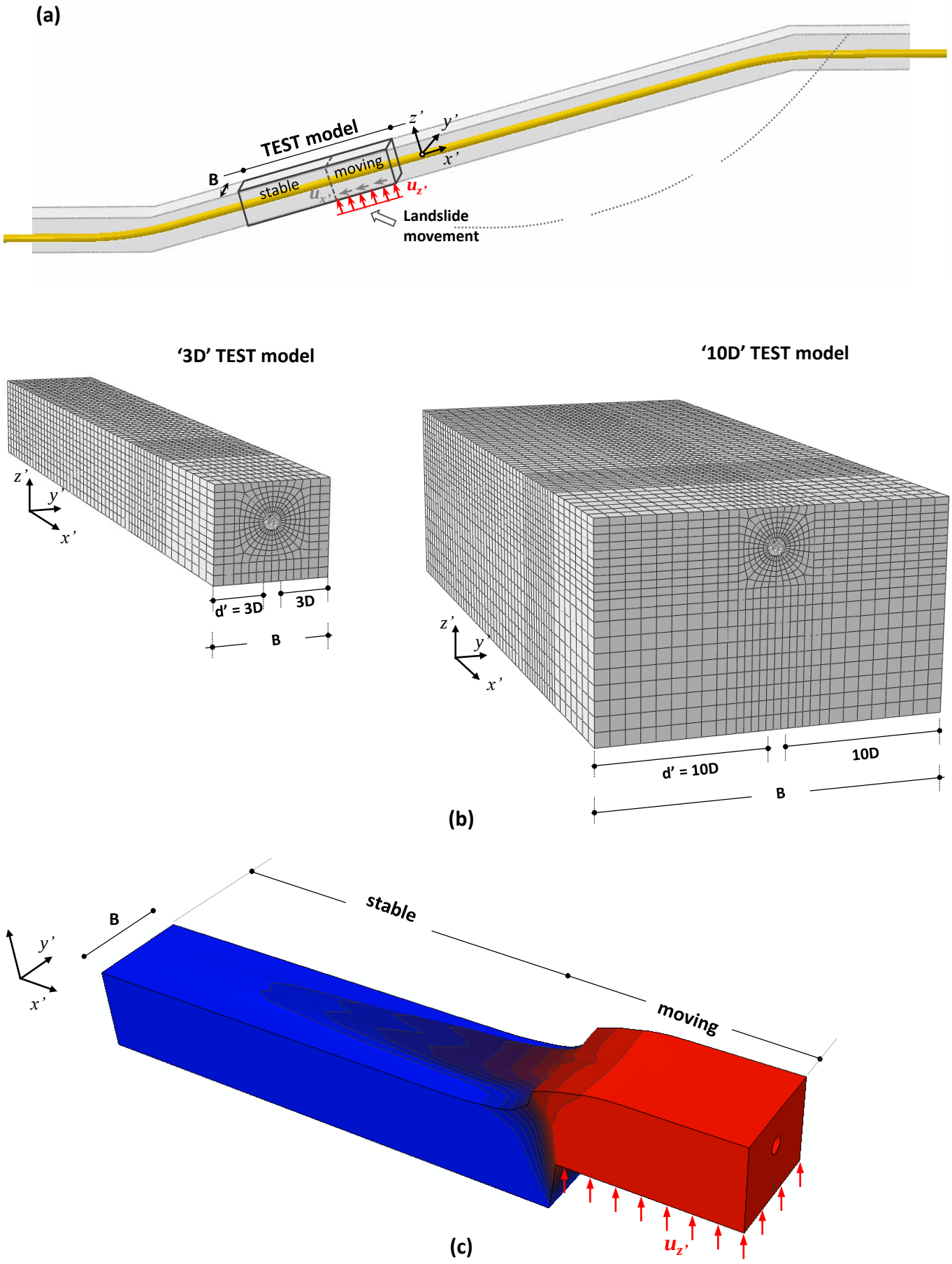

Figure 6.6. (a) Definition of the TEST model; **(b)** the '3D' and the '10D' alternatives; **(c)** view of the deformed mesh of the TEST model after the application of the $u_{z'}$ displacement.

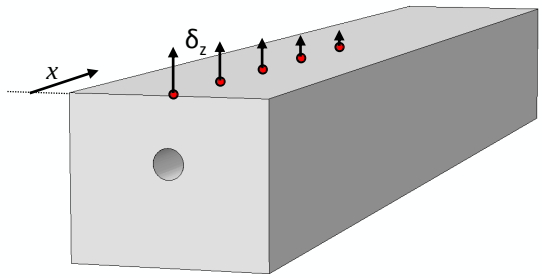

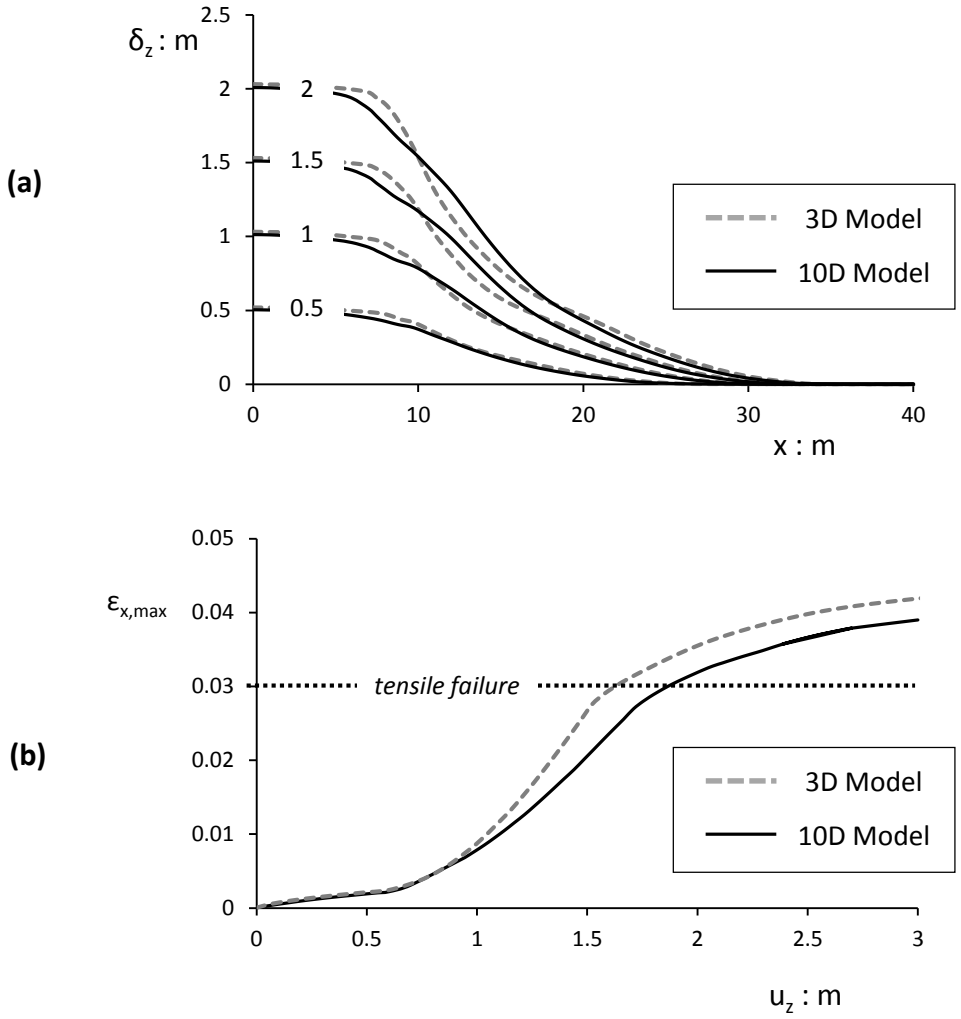

Figure 6.7. Comparison of results for the two models: Evolution of **(a)** vertical ground displacement δz along the pipe axis and **(b)** maximum axial stain with increasing imposed displacement u_z.

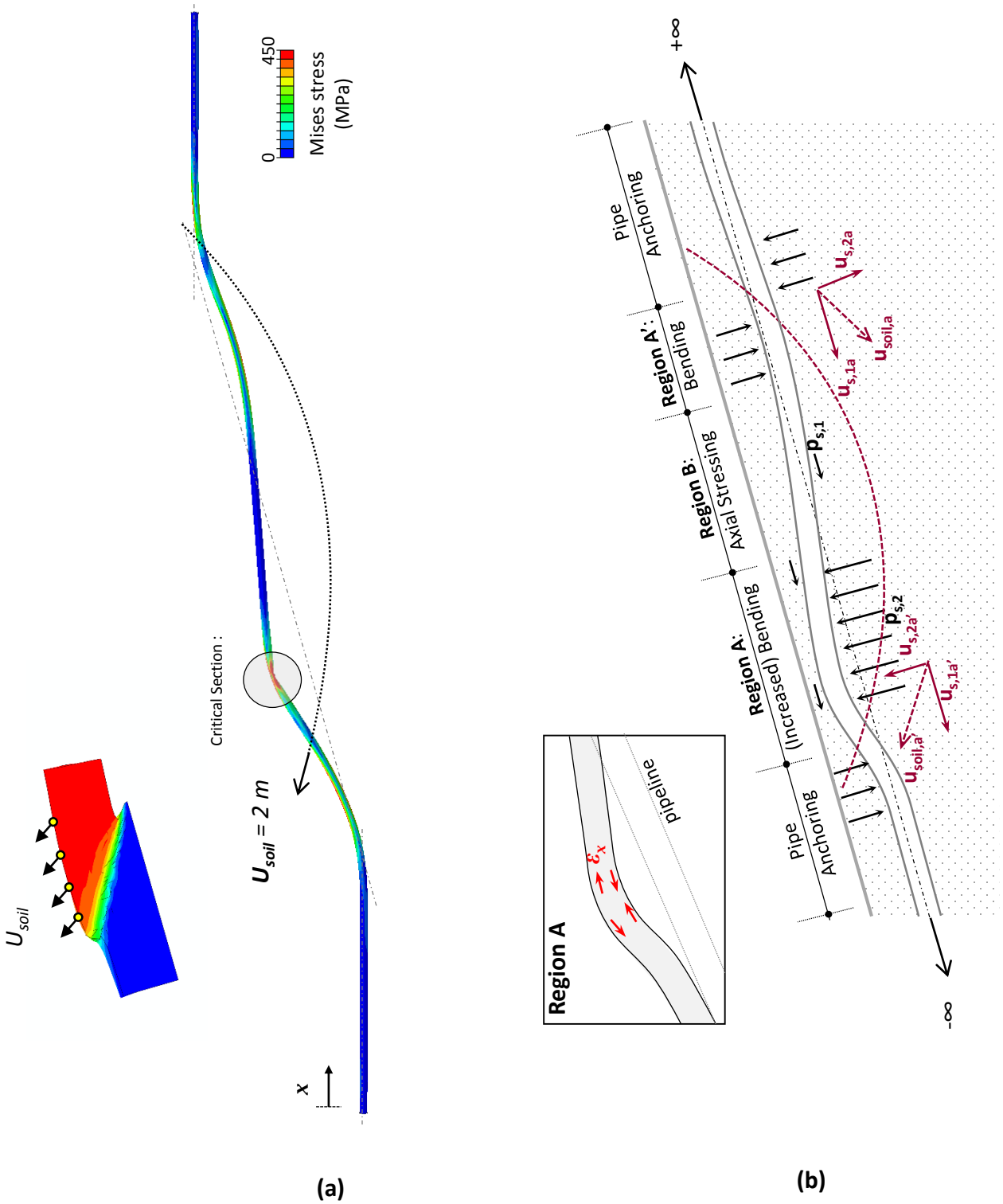

Figure 6.8. Pipeline subjected to the "shallow" landslide scenario: **(a)** Deformed pipeline with superimposed Mises stresses (red sections experience most intense bending); **(b)** schematic illustration of the key stressing mechanisms along the pipe axis.

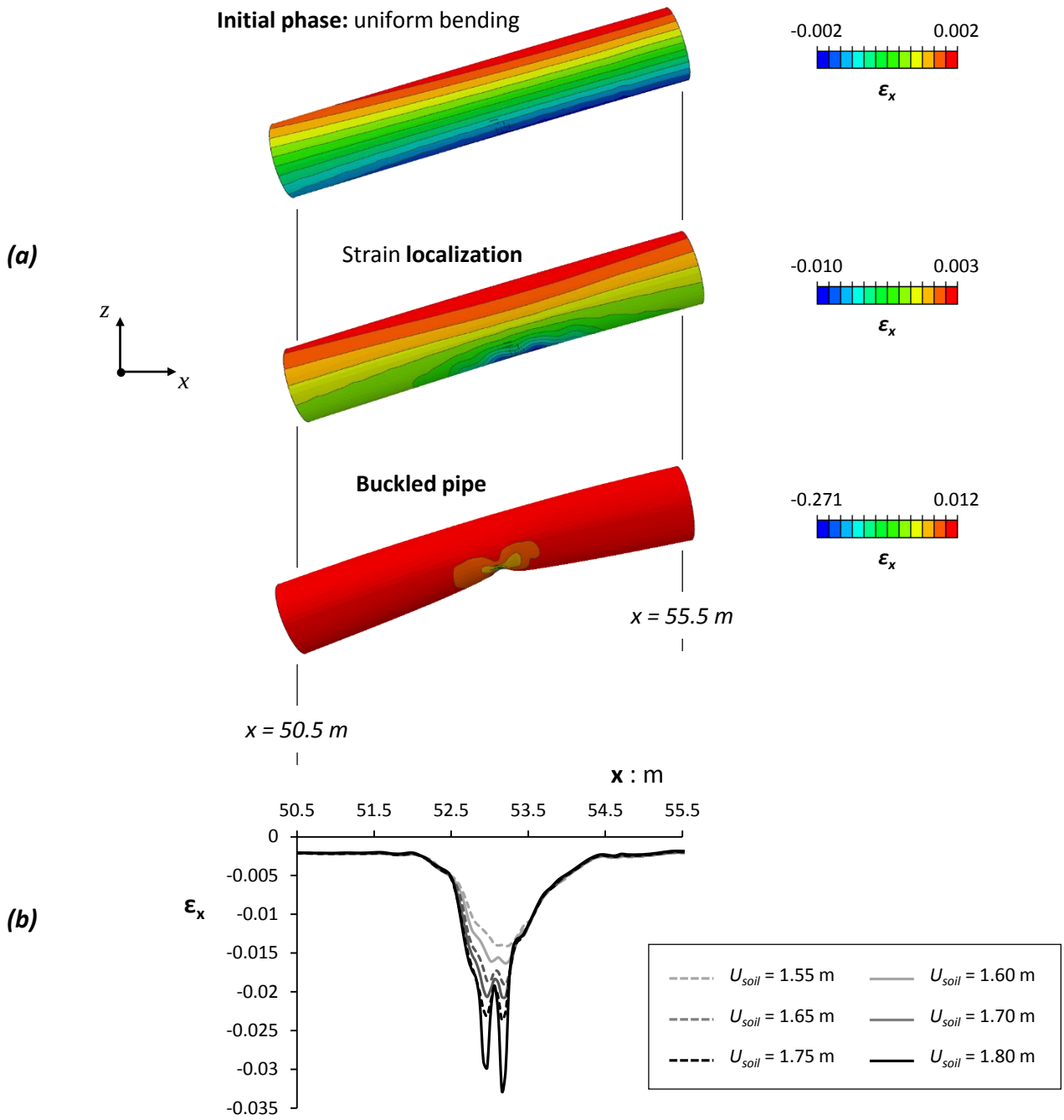

Figure 6.9. Pipeline subjected to the "shallow" landslide scenario: **(a)** contours of axial strain along the critical region of the pipeline depicting buckling evolution; **(b)** evolution of axial strain on the compressive side of the critical region.

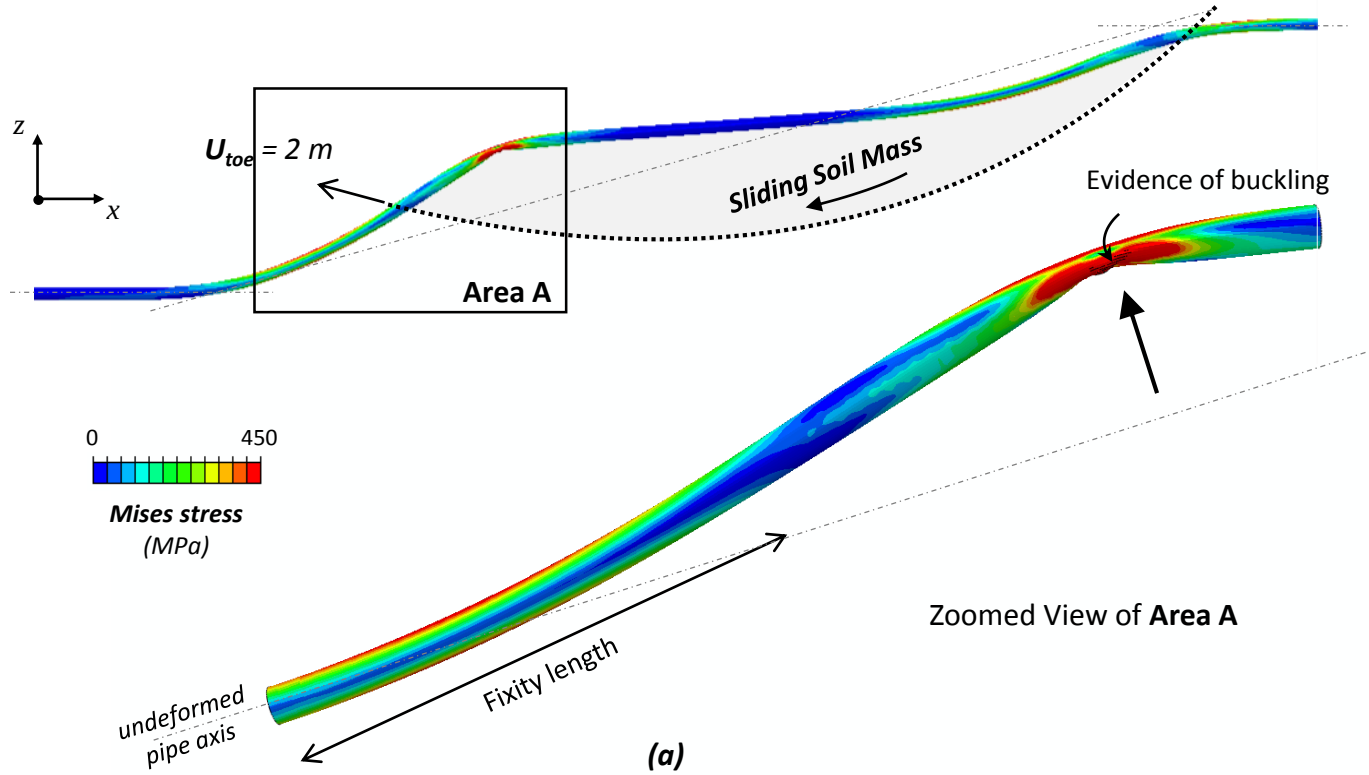

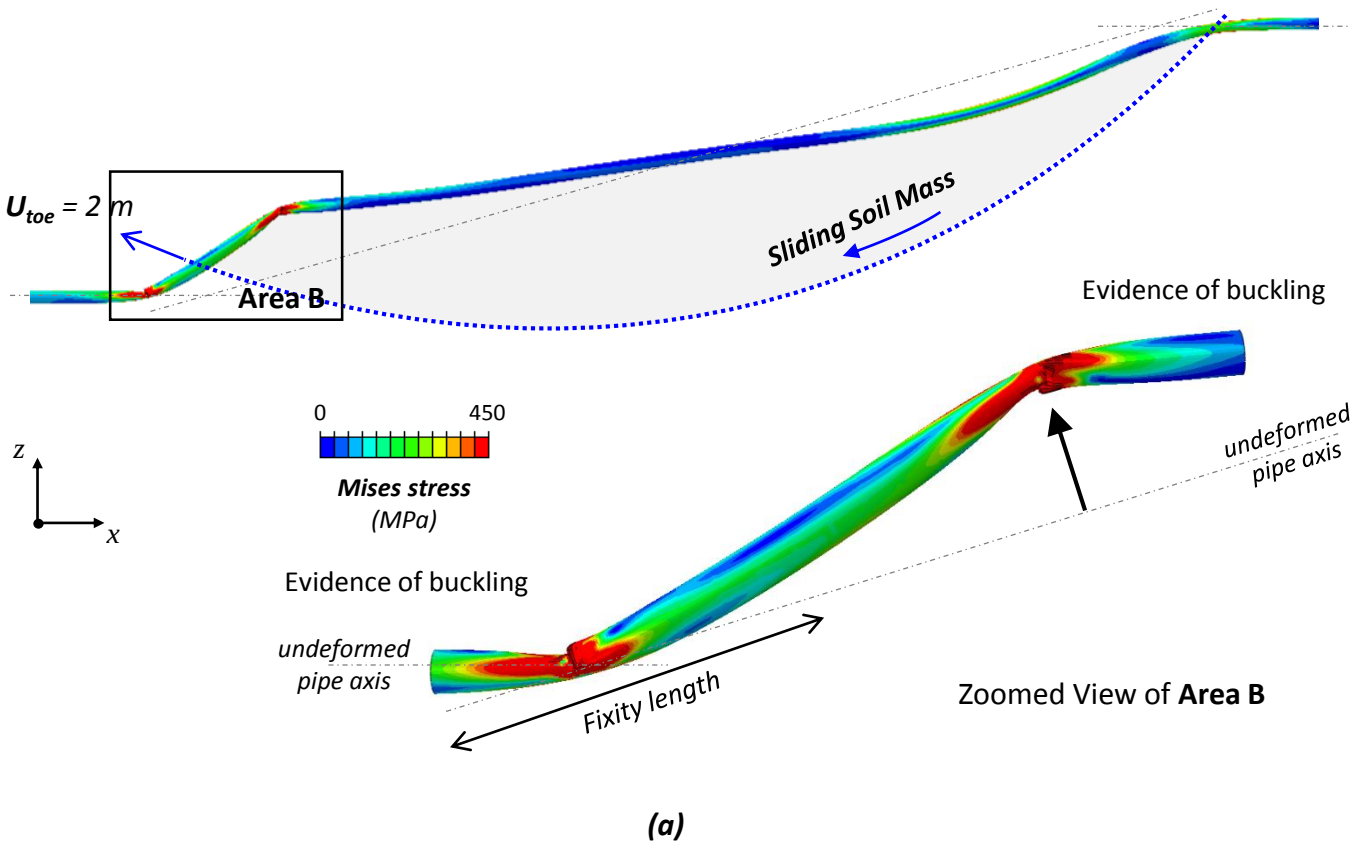

Figure 6.10. Pipeline subjected **(a)** to the "shallow" and **(b)** to the "deep" landslide scenario: deformed pipeline at the instant of U_{toe} = 2 m.

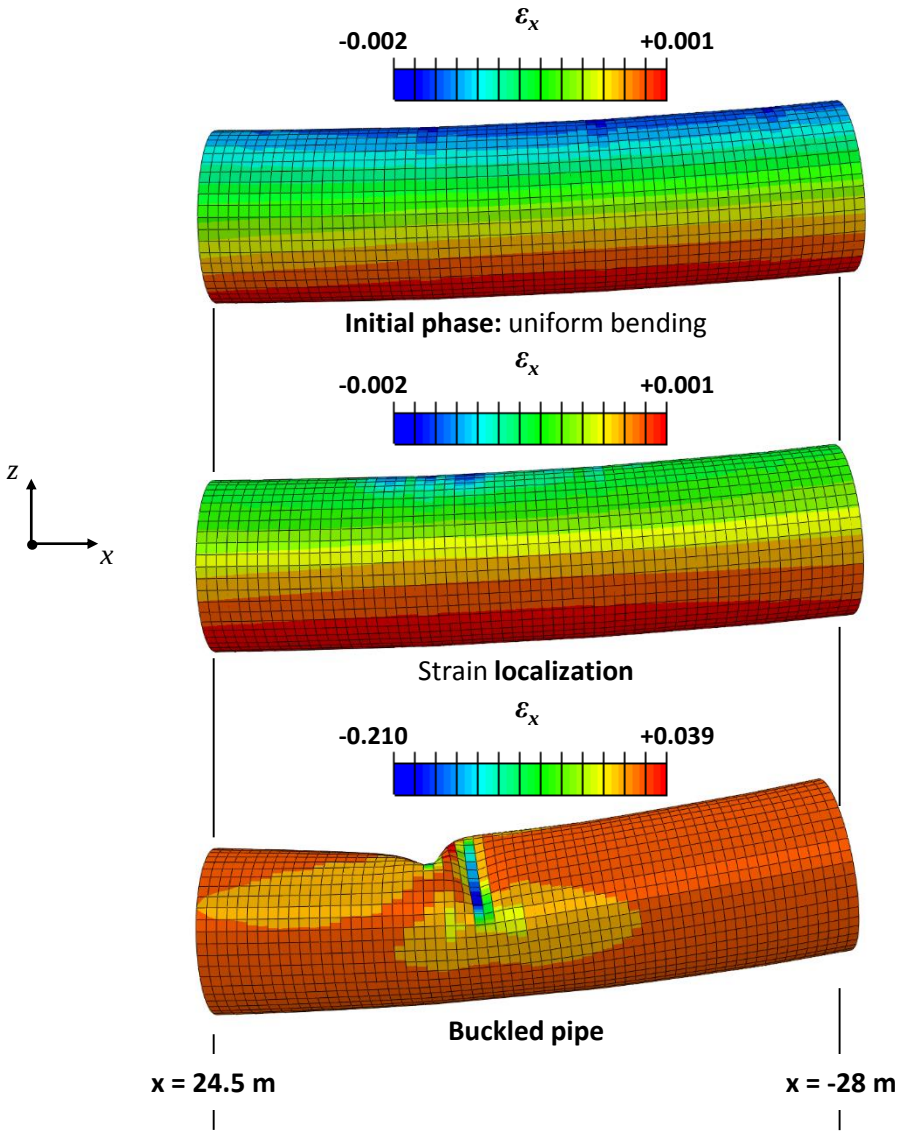

(a)

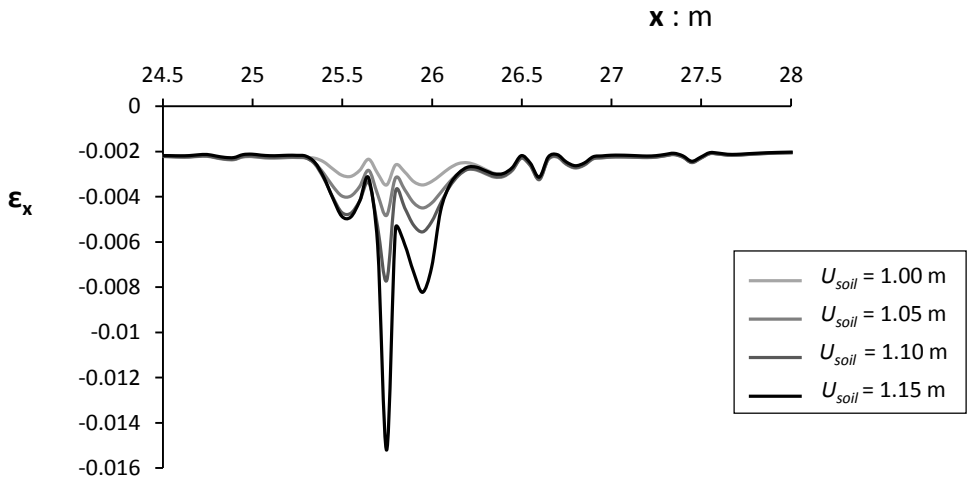

(b)

Figure 6.11. Pipeline subjected to the "deep" landslide scenario: **(a)** Contours of axial strain along the critical region of the pipeline depicting buckling evolution. **(b)** Evolution of axial strain on the compressive side of the critical region.

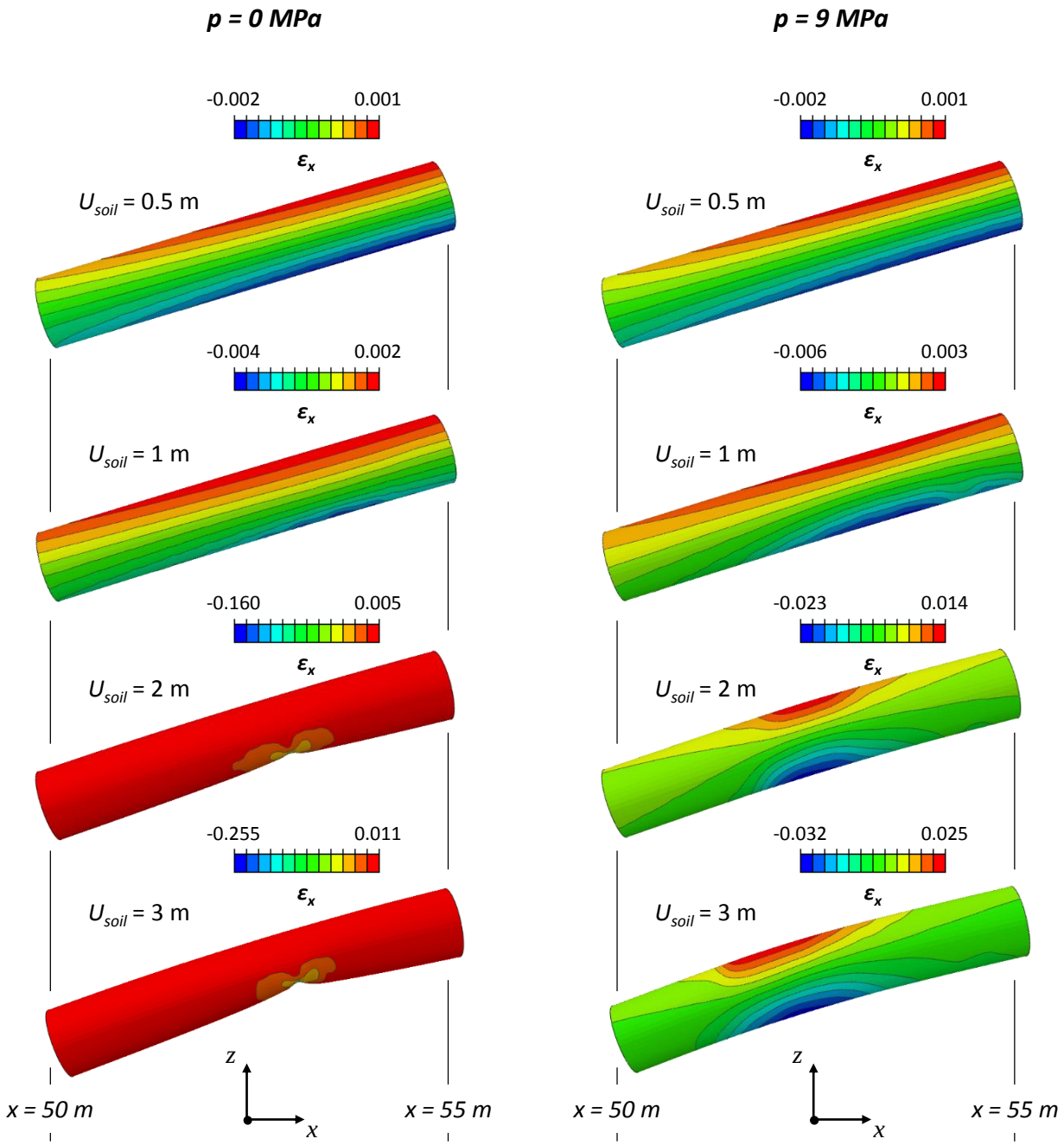

Figure 6.12. Pipeline performance with and without internal pressure subjected to the “shallow” landslide scenario: evolution of axial strain at the pipe segment at the vicinity the critical region.

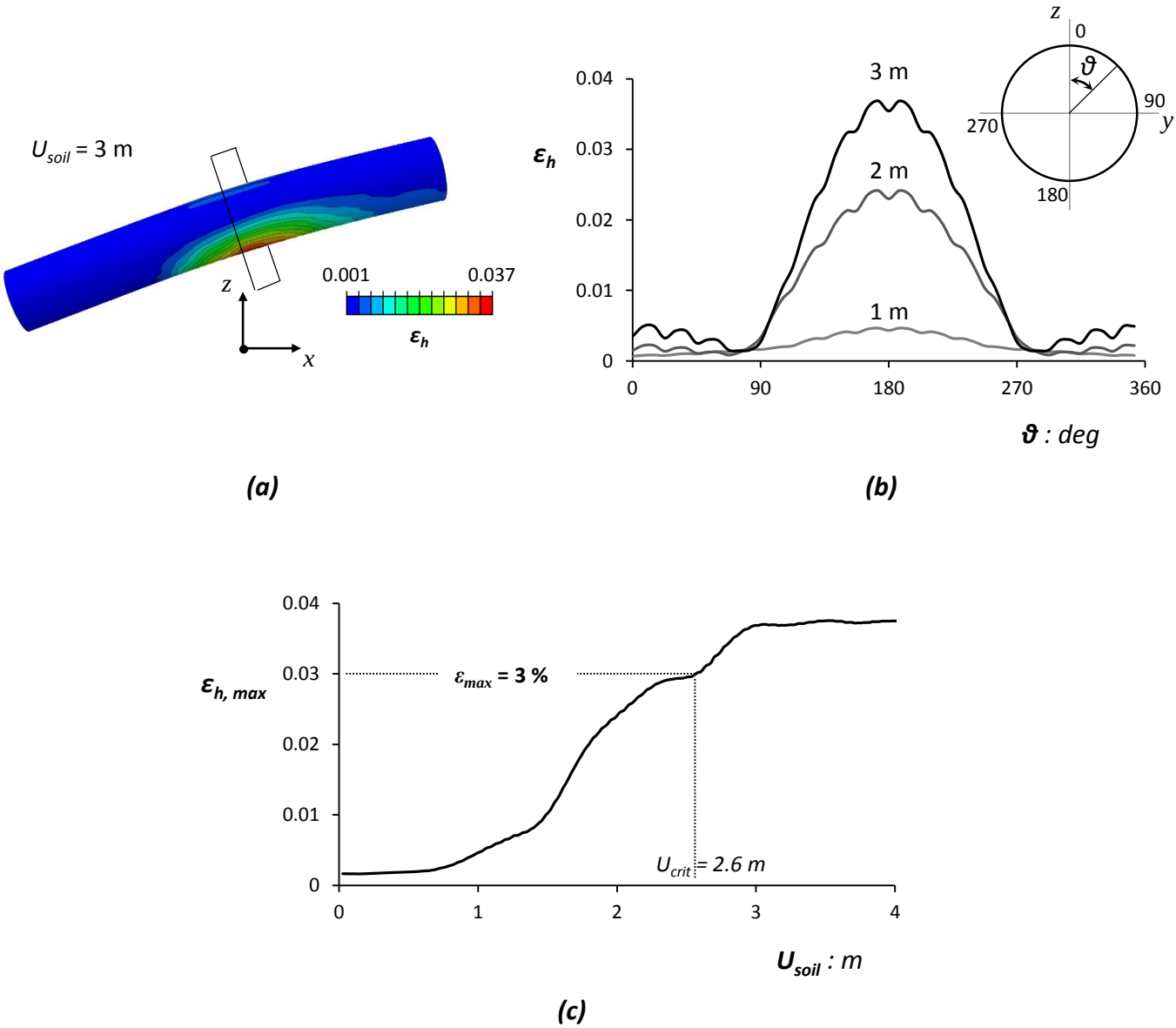

Figure 6.13. Pipeline performance with internal pressure subjected to the "shallow" landslide scenario: **(a)** hoop strains at the pipe at the vicinity of the critical section, **(b)** hoop strain distribution at the critical section, and **(c)** evolution of maximum hoop strain with the increase of the imposed soil displacement.

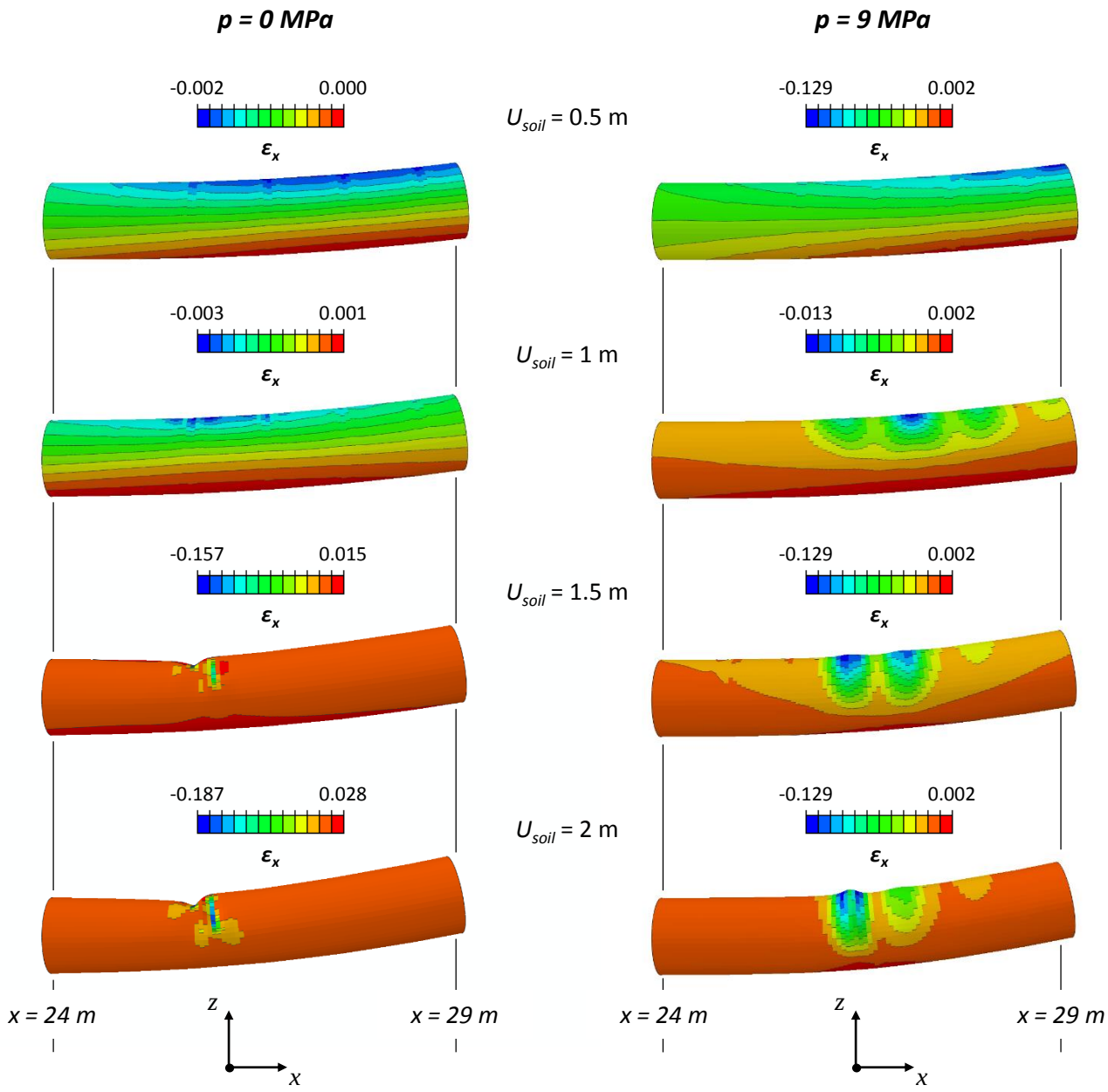

Figure 6.14. Pipeline performance with and without internal pressure subjected to the "deep" landslide scenario: evolution of axial strain at the pipe segment at the vicinity the critical region (bottom elbow).

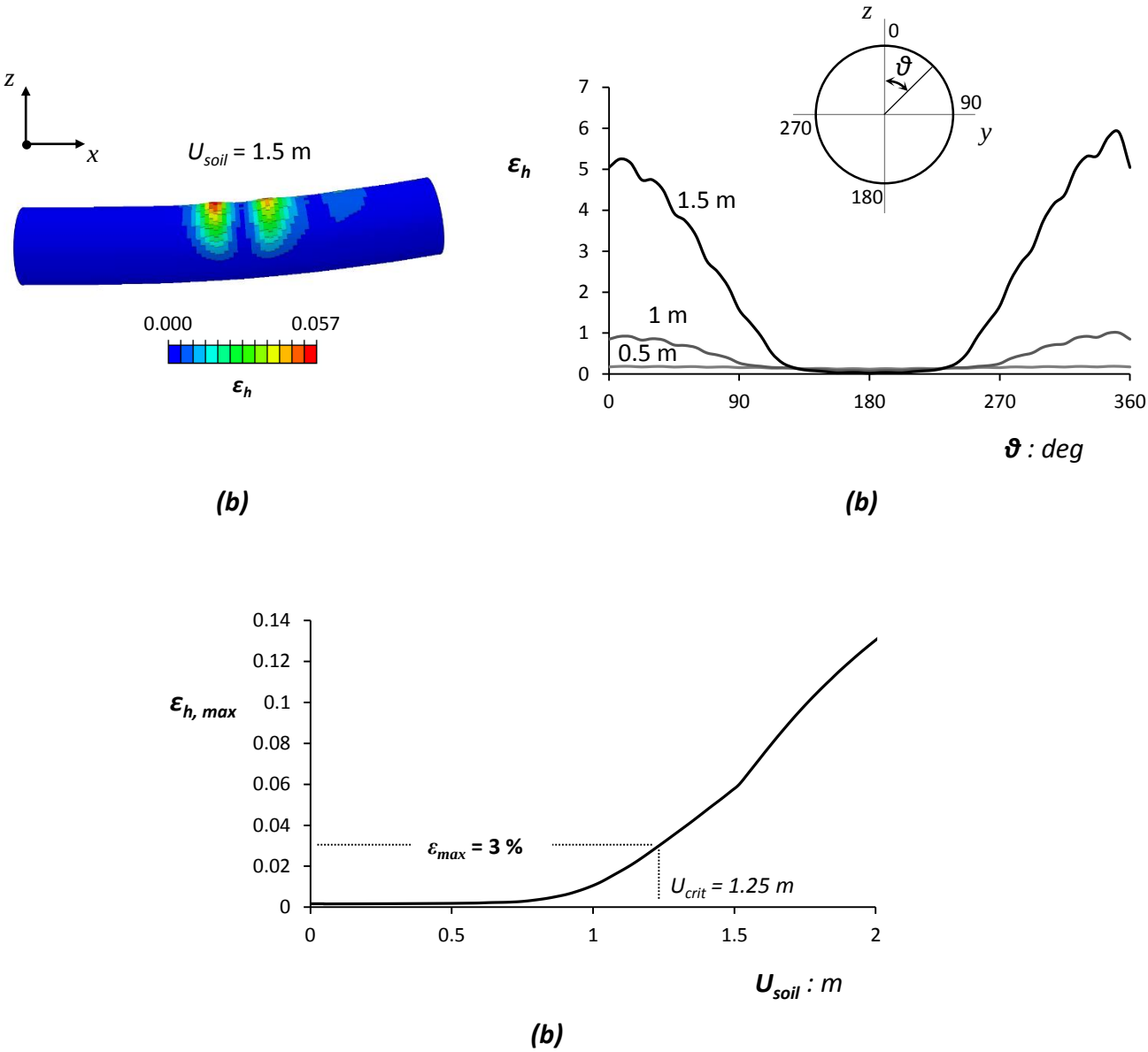

Figure 6.15. Pipeline performance with internal pressure subjected to the "deep" landslide scenario: **(a)** hoop strains at the pipe at the vicinity of the critical section, **(b)** hoop strain distribution at the critical section, and **(c)** evolution of maximum hoop strain with the increase of the imposed soil displacement.

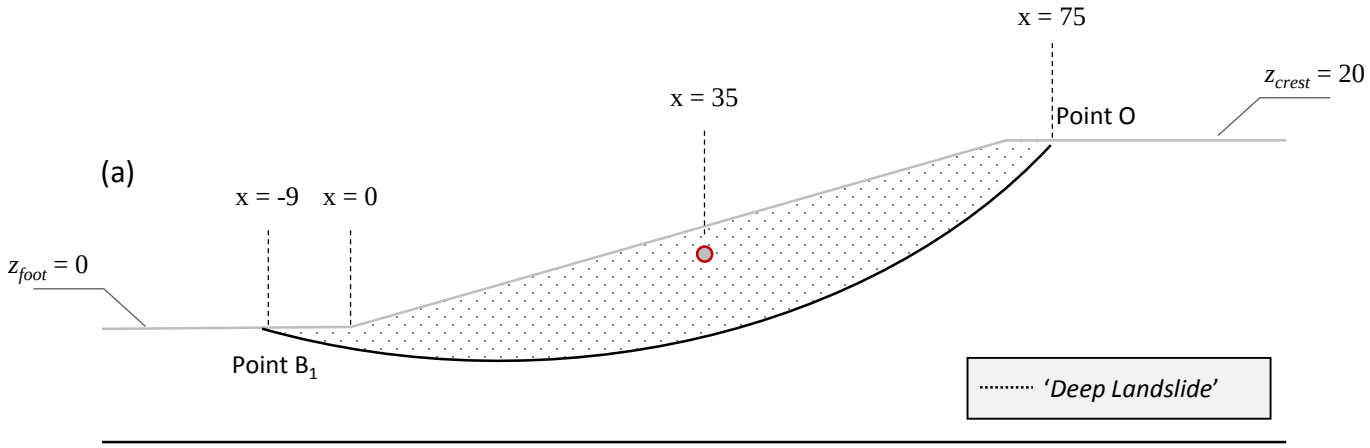

(a)

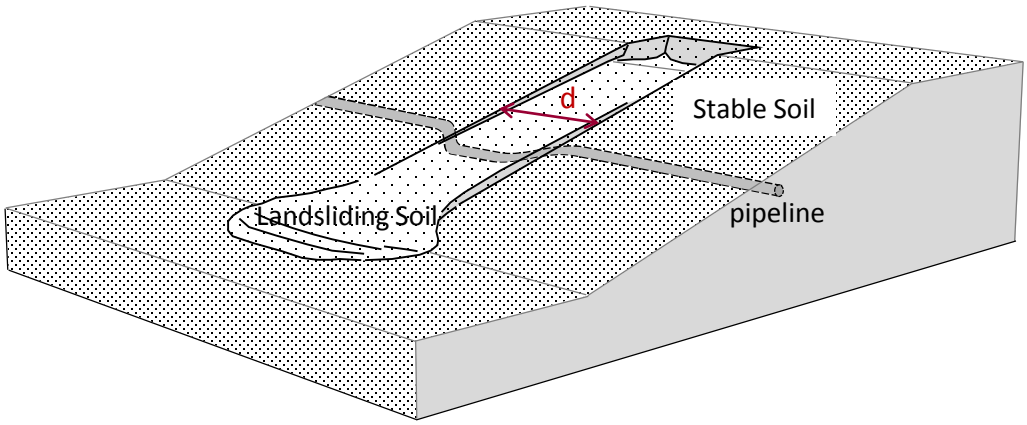

(b)

Figure 6.16. The studied example: pipeline axis parallel to the slope crest. (b) The middle section of the considered landslide geometry highlighting the location of the pipeline. (c) The width of the sliding soil mass *d* is parametrically considered resulting in two landslide scenarios: one with *d* = 20 m termed "broad" landslide scenario and one with *d* = 10 m, termed "narrow" landslide scenario.

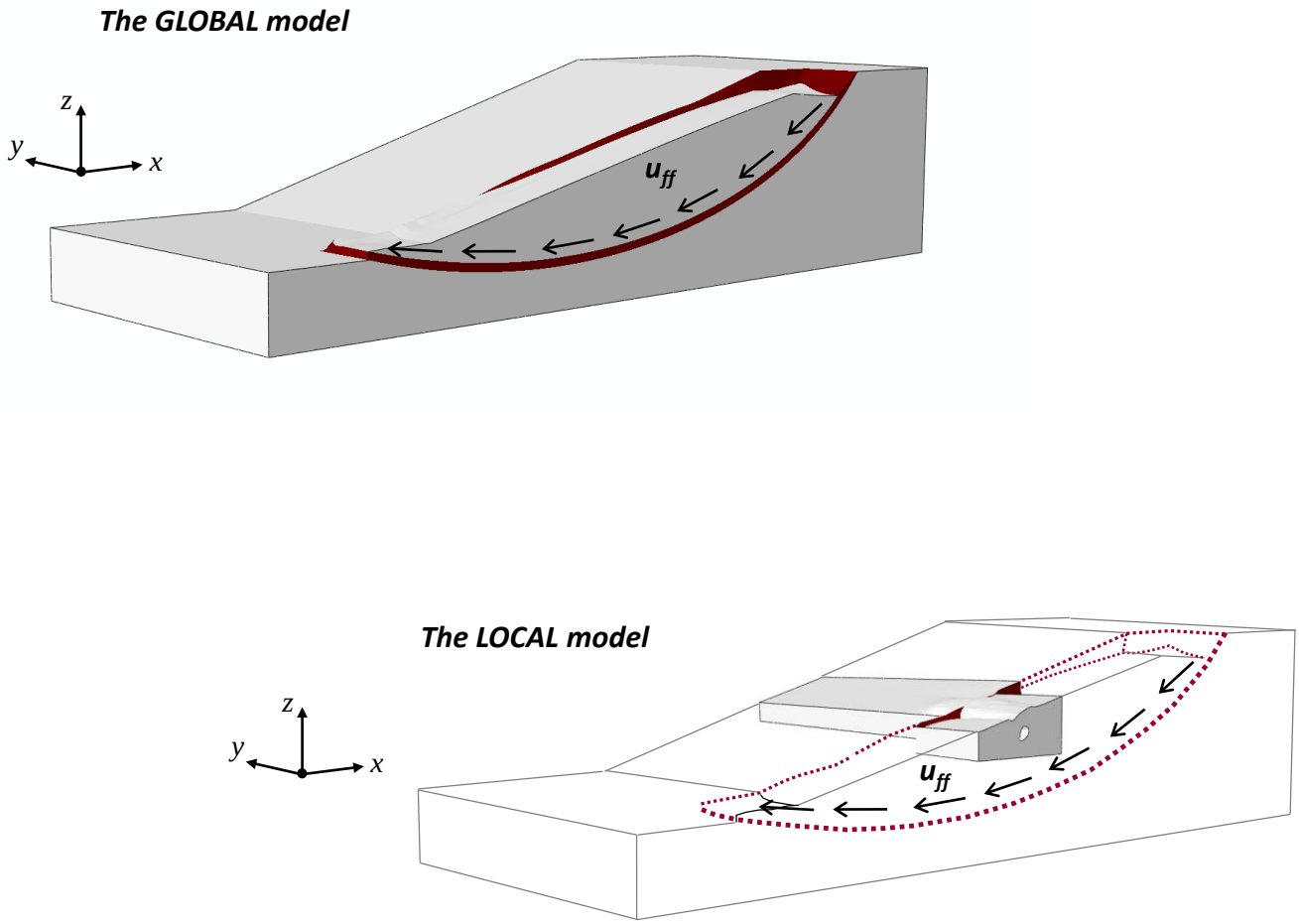

Figure 6.17. Outline of the proposed 2-step numerical methodology for the case of the pipeline parallel to the slope crest: the vectors of soil movement u_{ff} estimated by the analysis of the GLOBAL Model are assumed at the bottom, and lateral boundaries of the LOCAL model to estimate the induced pipeline distress.

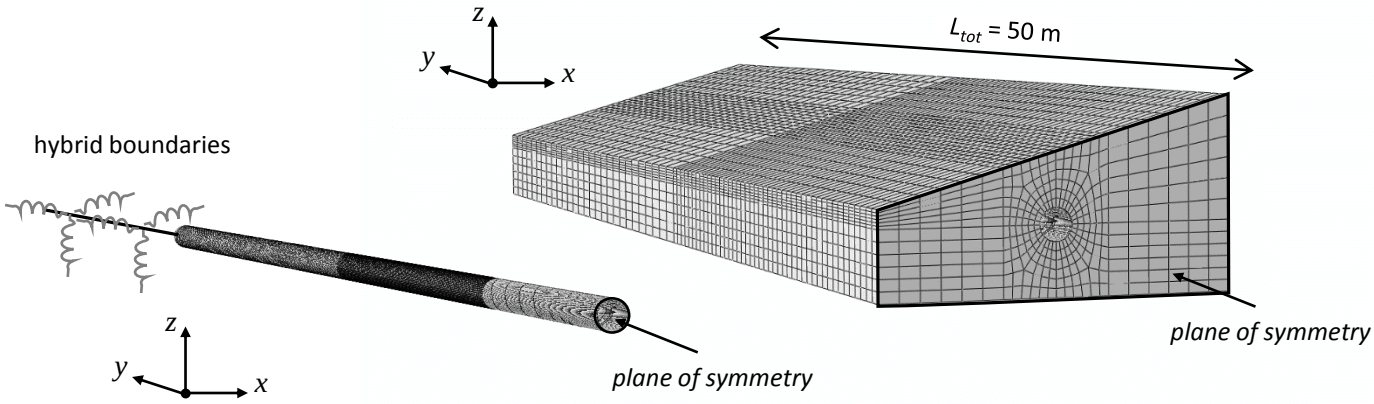

(a)

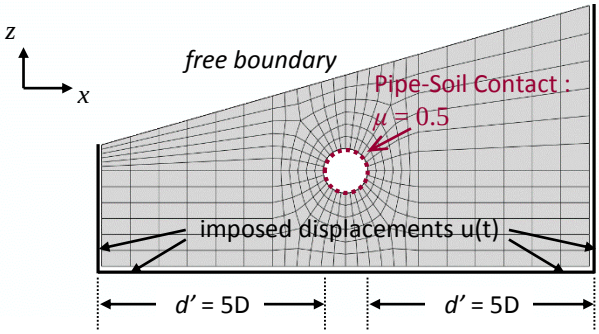

(a)

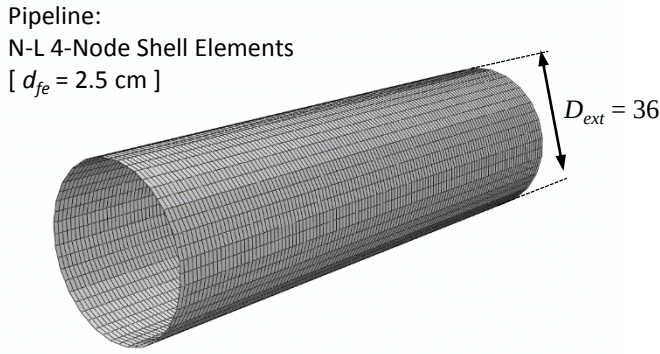

(a)

Figure 6.18. Details of the local Model : **(a)** view of the mesh of the soil prism and of the pipeline **(b)** the cross-section of the analyzed system, **(c)** a closer view of a typical pipe segment.

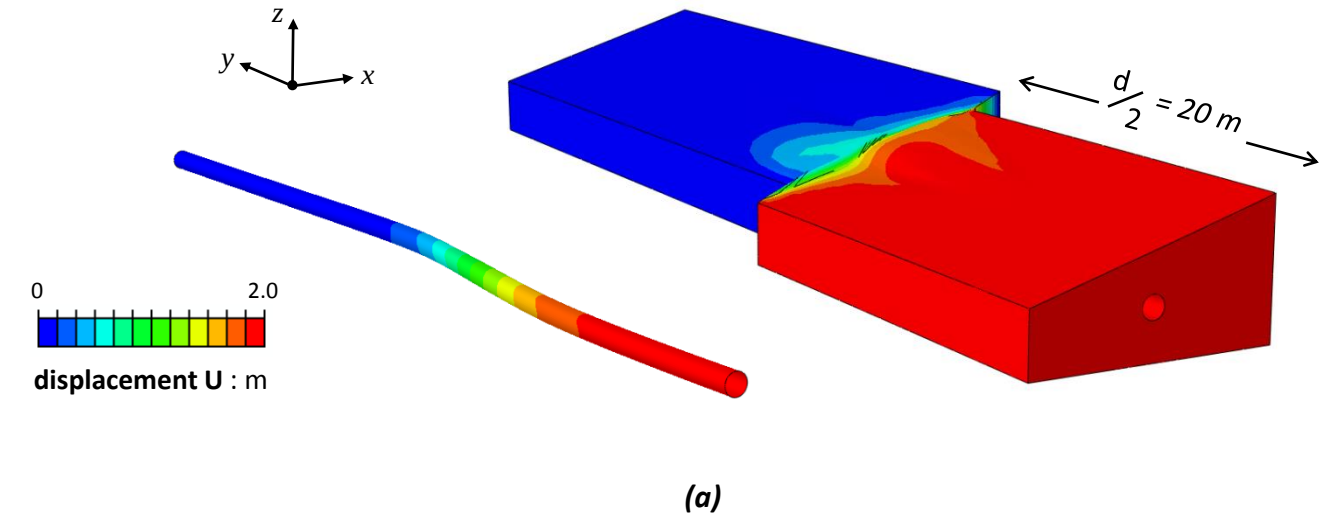

(a)

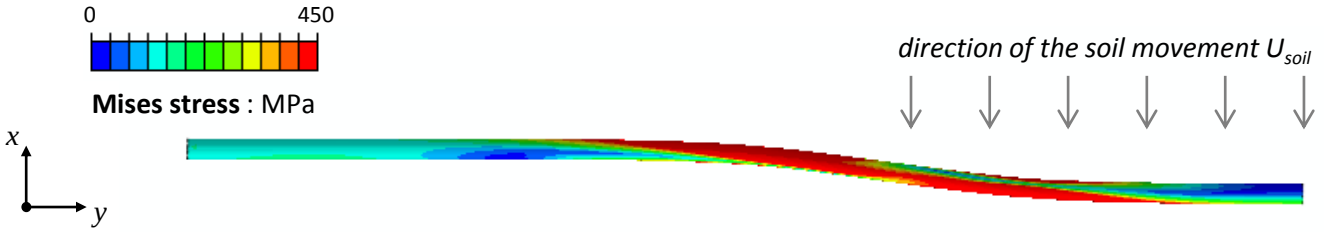

(c)

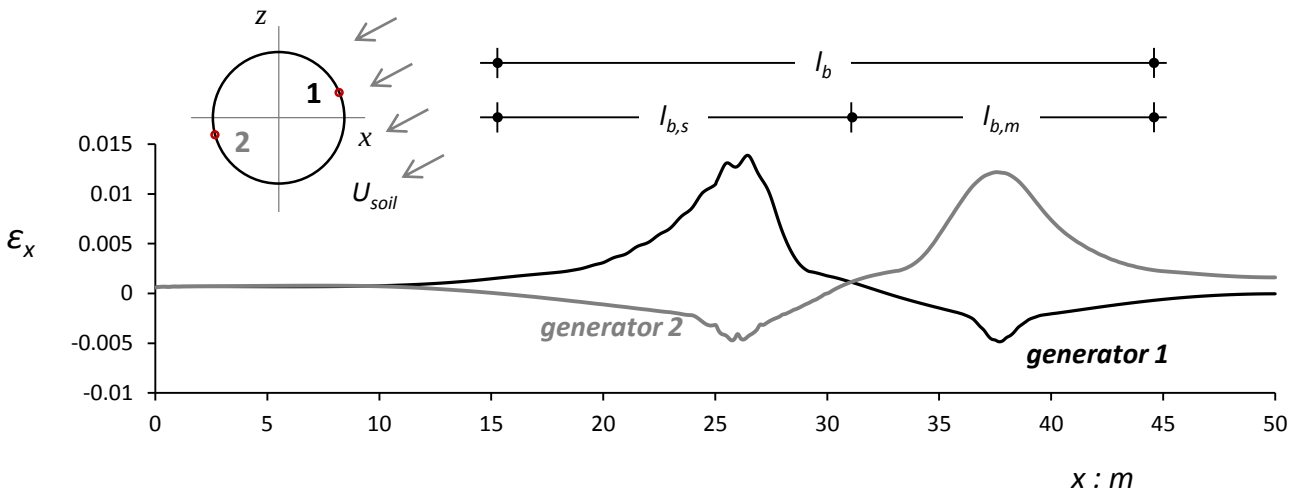

(c)

Figure 6.19. Pipeline subjected to the "broad" landslide scenario: **(a)** Deformed mesh of the pipeline and of the soil prism around it with superimposed displacement contours for 2 m of soil displacement. **(b)** Deformed mesh of the pipeline with Mises stresses (red sections experience most intense bending) at the same displacement; **(c)** Distribution of axial strains along the two most stressed generators at the same displacement.

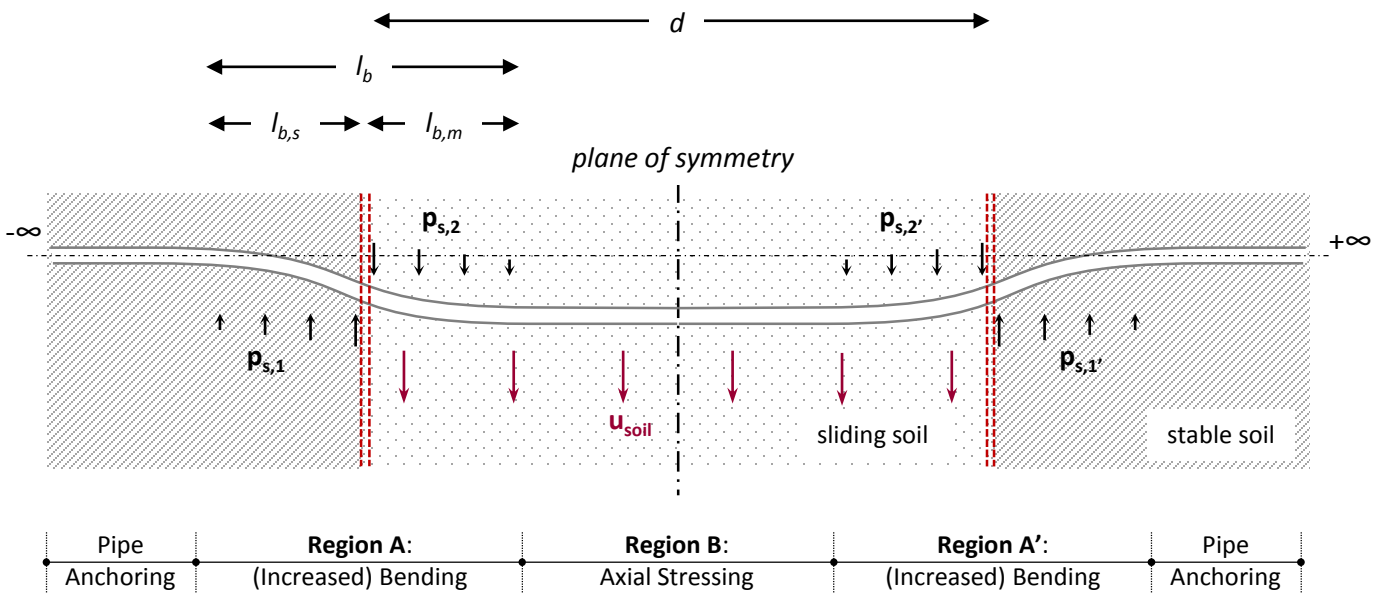

Figure 6.20. Pipeline subjected to landslide actions normal to its axis: schematic illustration of the key stressing mechanisms along the pipe axis.

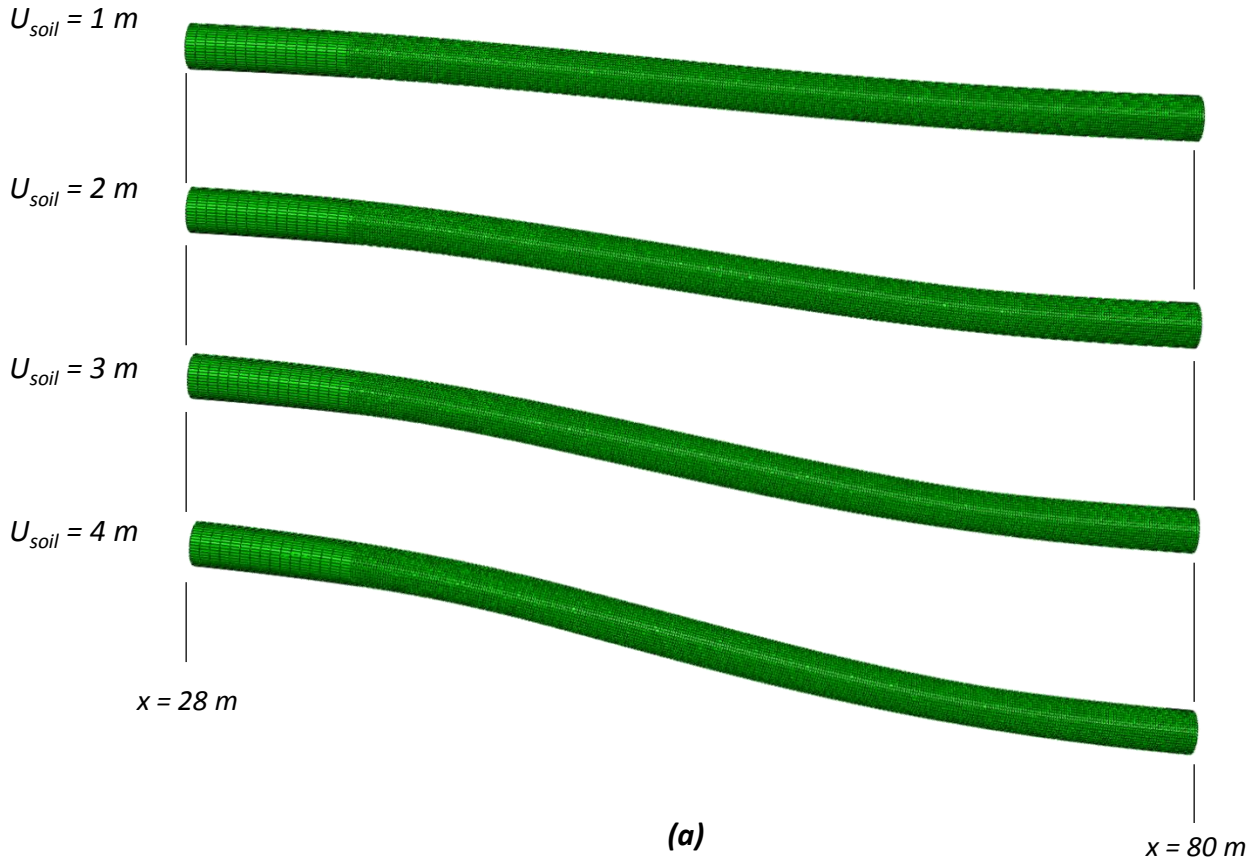

(a)

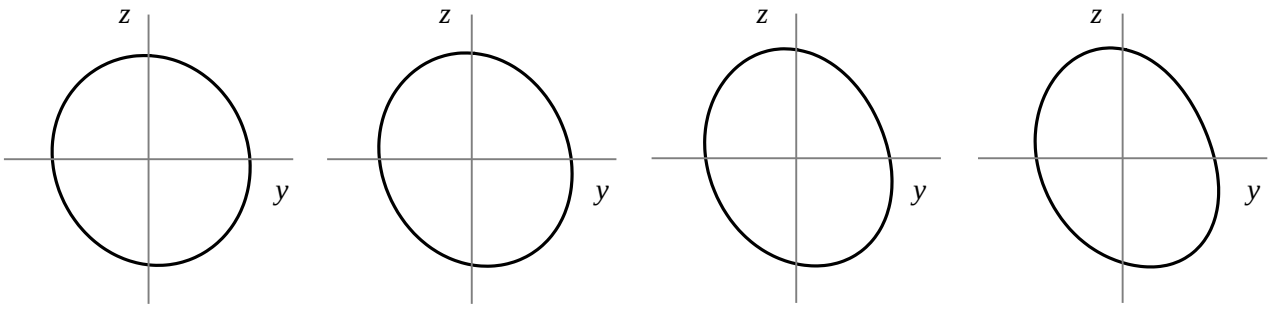

(b)

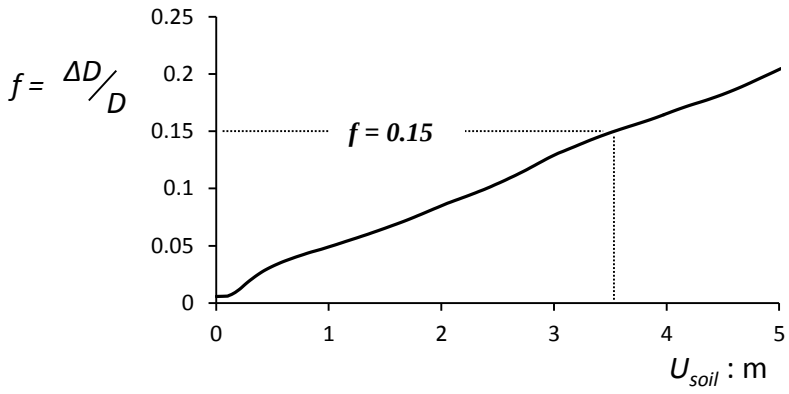

(c)

Figure 6.21. Pipeline subjected to the "broad" landslide scenario: **(a)** Deformed mesh of the pipeline within the region of intense bending; **(b)** Distortion of the cross-section for various magnitudes of soil displacement; **(c)** Evolution of the ovalization factor *f* with the increase of soil displacement.

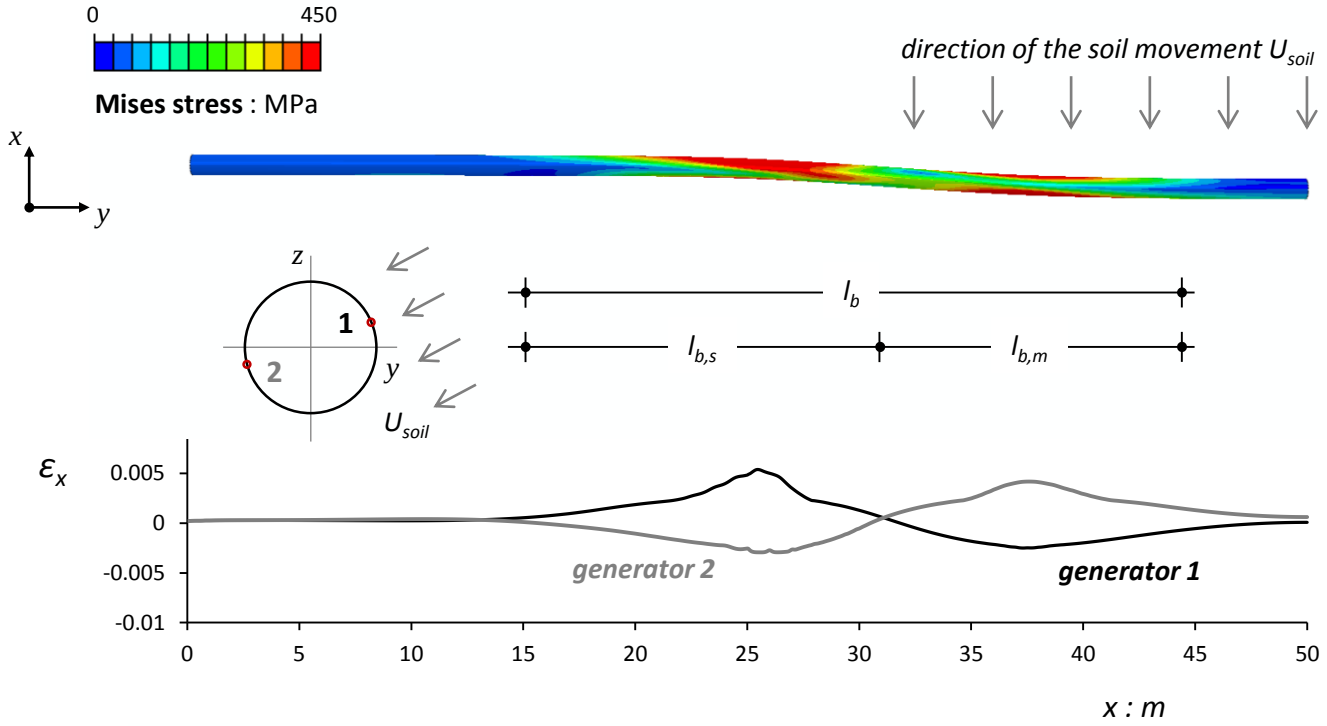

(c)

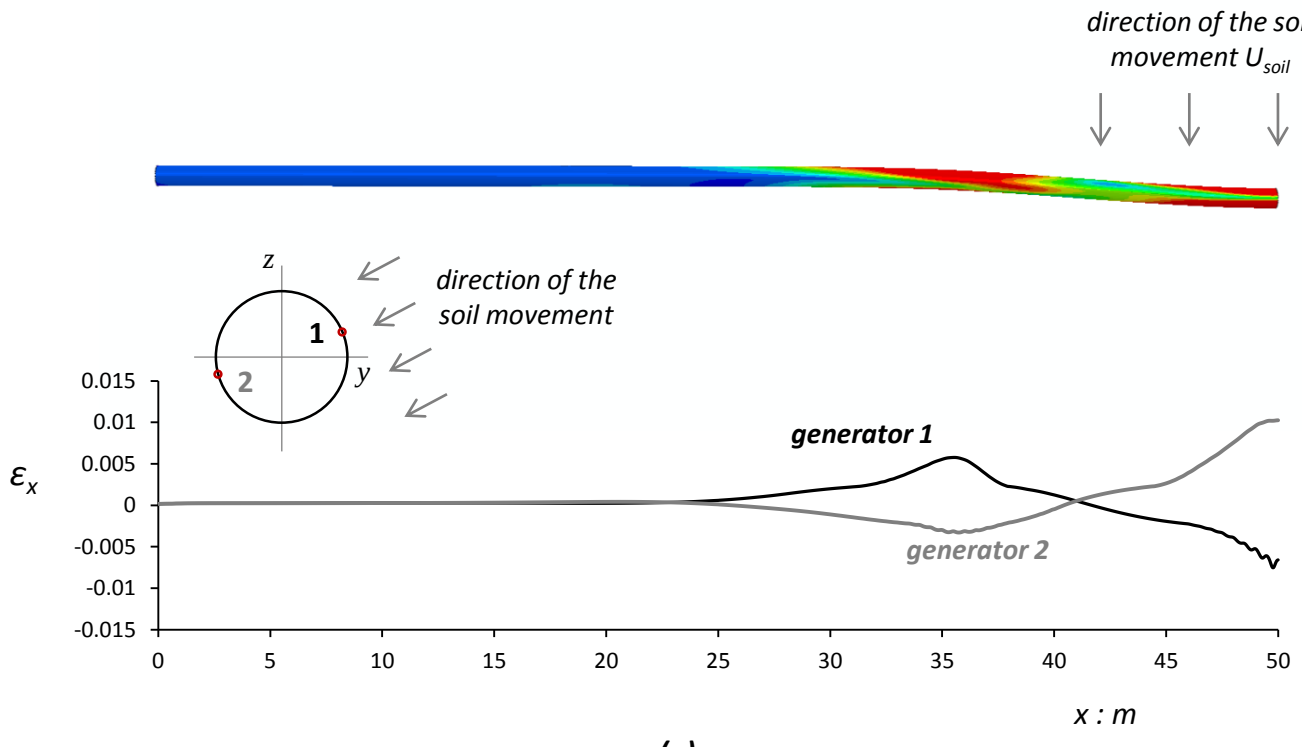

(a)

Figure 6.22. Pipeline subjected **(a)** to the "broad" and **(b)** to the "narrow" landslide scenario: deformed pipeline and axial strain distribution along the two most stressed generators at the instant of U_{toe} = 1 m.

(a)

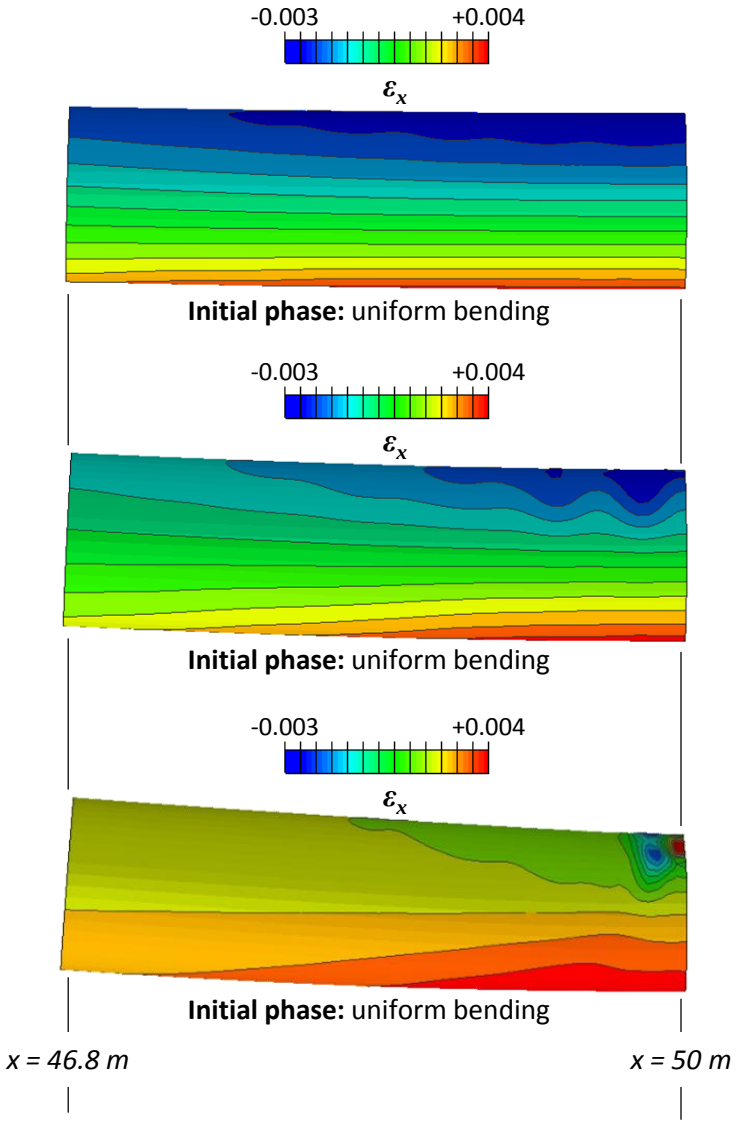

(b)

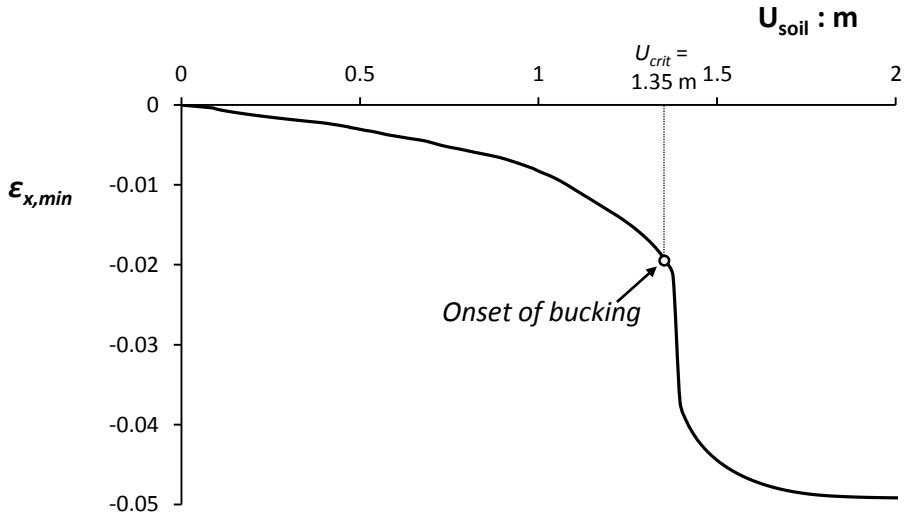

Figure 6.23. Pipeline subjected to the "narrow" landslide scenario: **(a)** Contours of axial strain along the critical region of the pipeline depicting buckling evolution. **(b)** Evolution of minimum axial strain on the compressive side of the critical region with the increase of the imposed soil displacement.

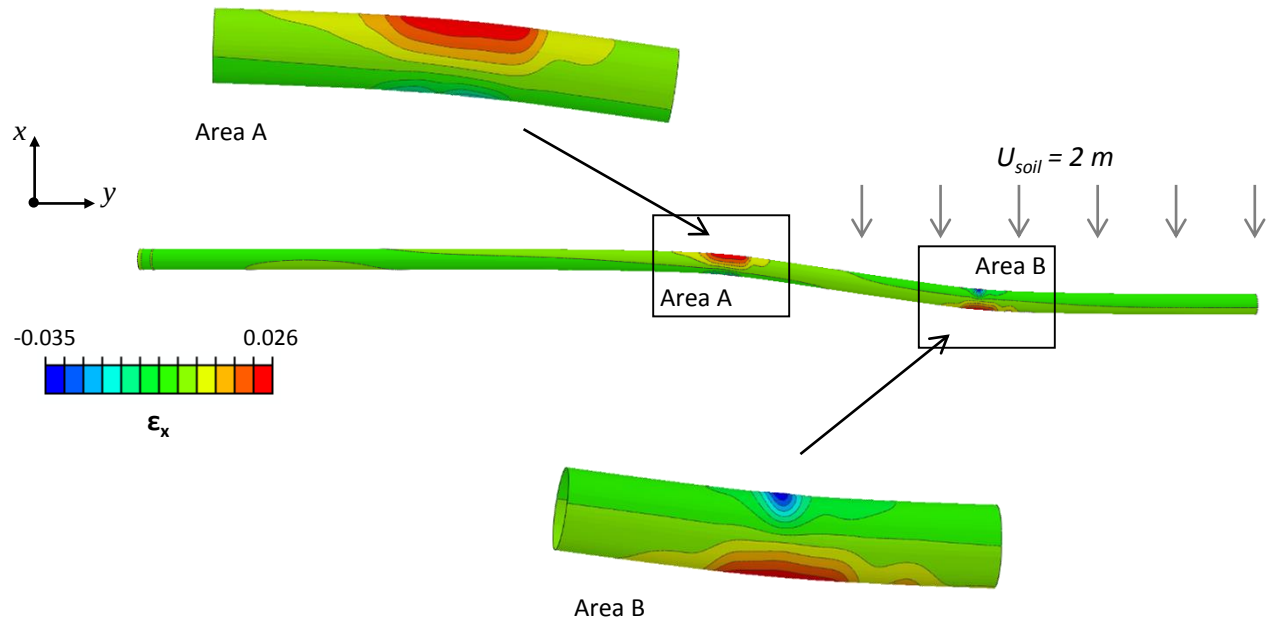

(a)

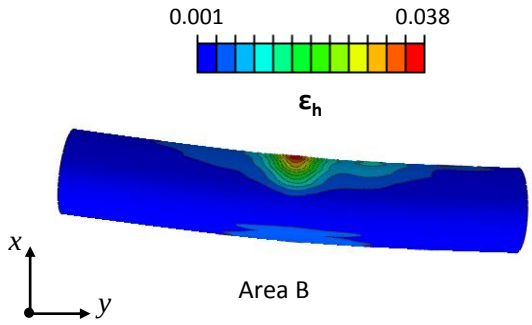

(b)

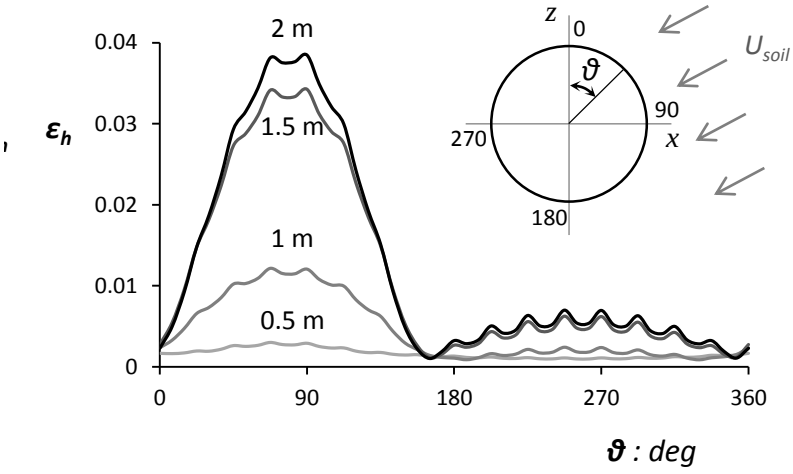

(c)

Figure 6.24. Pipeline performance with internal pressure subjected to the "broad" landslide scenario: **(a)** Deformed pipeline with superimposed axial strains at the instant of U_{soil} = 2 m; **(b)** hoop strain distribution at the critical section at the same instant; **(c)** Distribution of hoop strains at the critical section for various magnitudes of soil displacement.

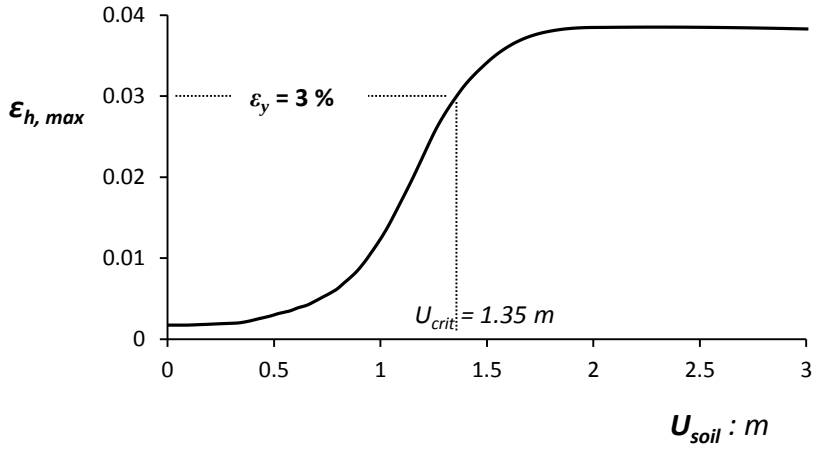

Figure 6.25. Pipeline performance with internal pressure subjected to the "broad" landslide scenario: evolution of the maximum hoop strain with the increase of the imposed soil displacement.

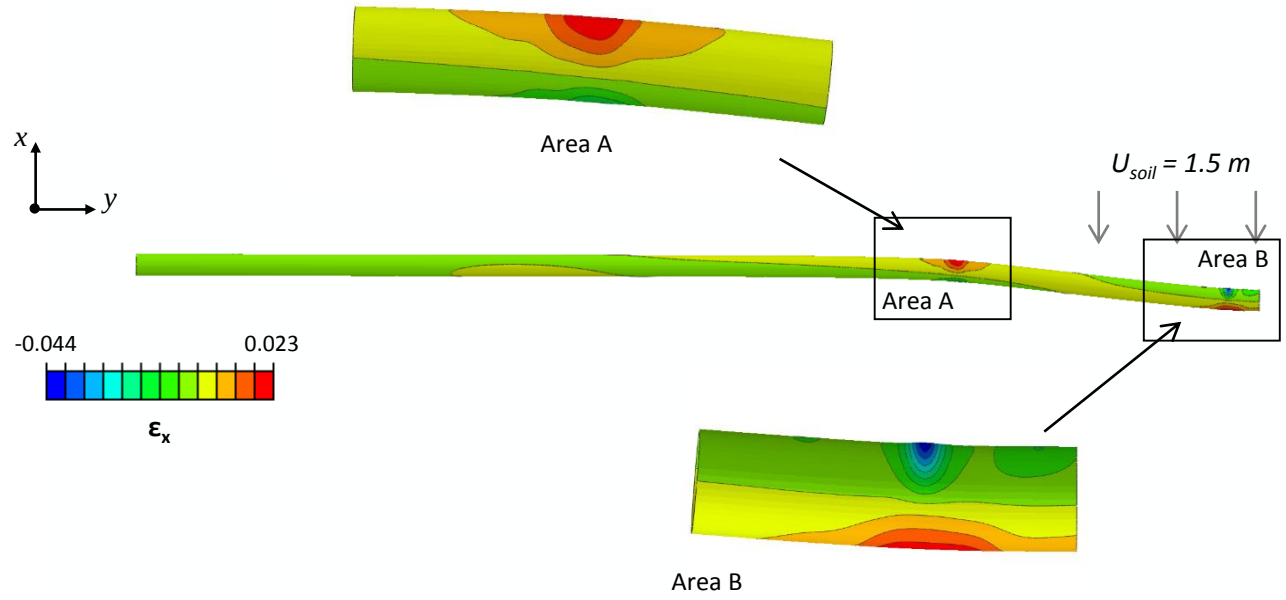

(a)

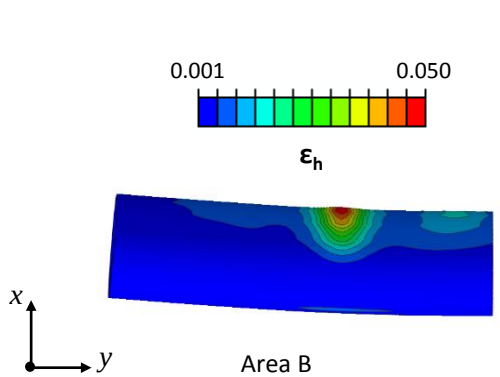

(b)

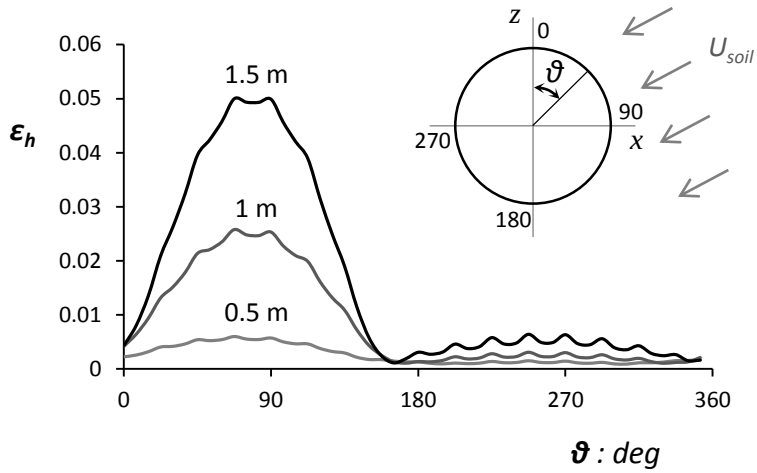

(b)

Figure 6.26. Pipeline performance with internal pressure subjected to the "narrow" landslide scenario: **(a)** Deformed pipeline with superimposed axial strains at the instant of U_{soil} = 1.5 m; **(b)** hoop strain distribution at the critical section at the same instant; **(c)** Distribution of hoop strains at the critical section for various magnitudes of soil displacement.

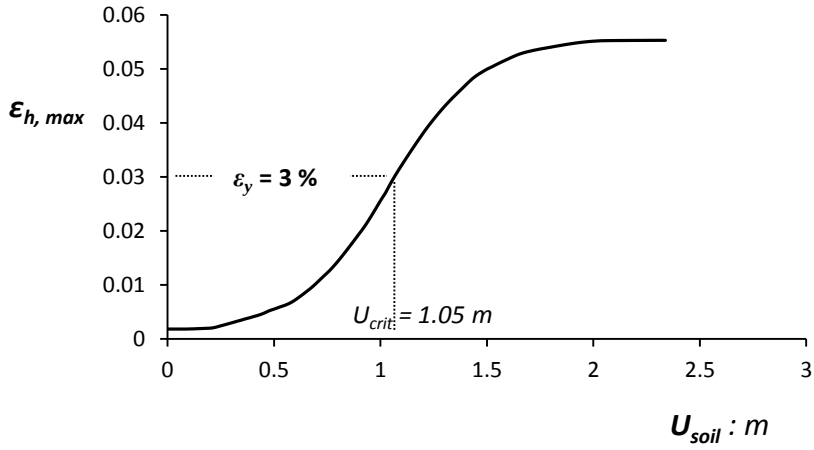

Figure 6.27. Pipeline performance with internal pressure subjected to the "narrow" landslide scenario: evolution of the maximum hoop strain with the increase of the imposed soil displacement.

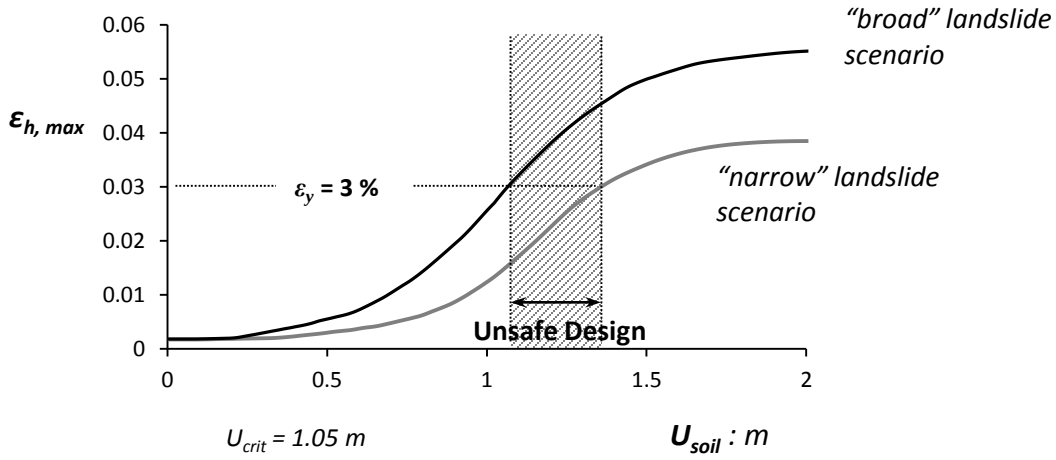

Figure 6.28. The effect of the landslide extent on the performance of the pipeline: evolution of maximum hoop strain with the increase of the imposed soil displacement for the pressurized pipeline subjected to the "broad" and the "narrow" landslide scenarios.

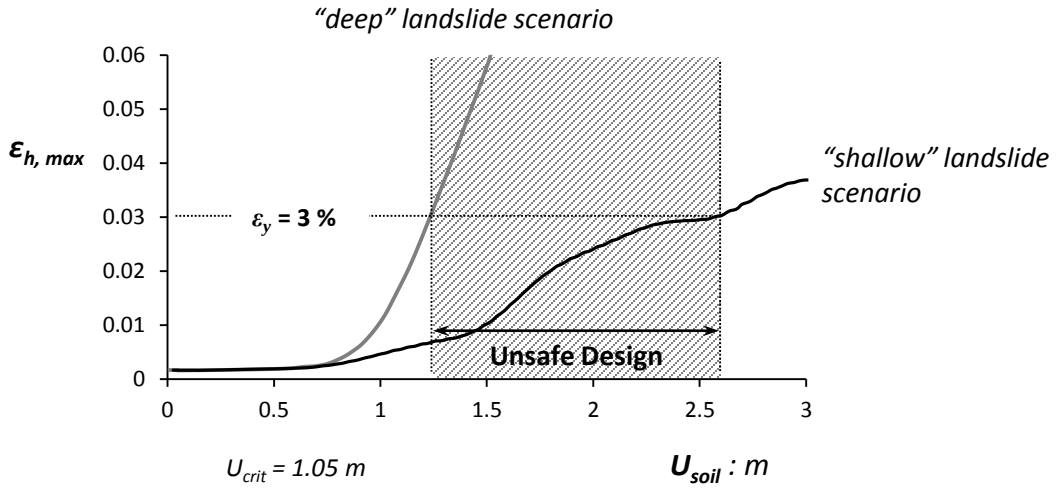

Figure 6.29. The effect of the elbows on the performance of the pipeline: evolution of maximum hoop strain with the increase of the imposed soil displacement for the pressurized pipeline subjected to the "shallow" and the "deep" landslide scenarios.

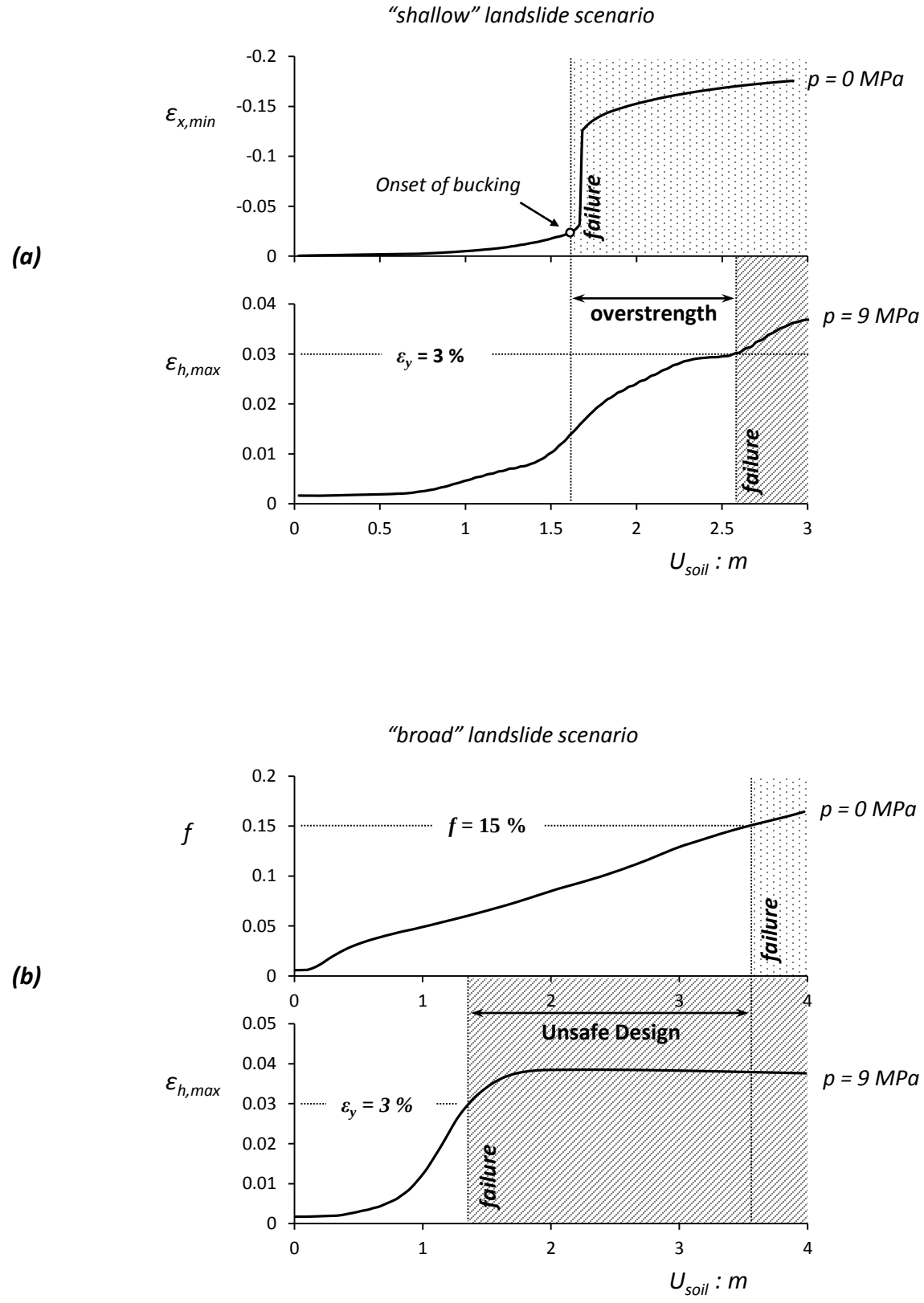

Figure 6.30. The effect of the internal pressure on the performance of the pipeline: (a) favorable effect on the performance of the pipeline normal to the slope crest subjected to the "shallow" landslide scenario; (b) detrimental effect on the performance of the pipeline parallel to the slope crest subjected to "broad" landslide scenario.

Chapter 7

Design Considerations

7.1 Problem statement

In the framework of this doctoral thesis a rigorous numerical methodology was proposed, validated and employed to describe the response of buried steel pipelines subjected to large ground deformations (be it the normal/reverse seismic faulting or landslides). Instead of a closure, in this last chapter, we aim to conduct a forward comparison between our FE methodogy and current state-of-practice procedures for characteristic example test cases.

The State-of-Practice

The current practice decomposes the pipe-soil interaction problem into an equivalent 'beam on springs' model, in which soil reactions are accounted as individual uniaxial non-linear springs acting in all principal directions (axial, lateral, upwards, downwards). The ground deformation pattern is applied to the bottom nodes of the springs and the resulting strains along the pipeline are calculated. To assure the structural integrity of the pipe, the calculated strains should remain within prescribed limits. Understandably, the efficiency of this numerical procedure greatly lies upon the robust estimation the soil springs reactions as well as the ground deformation pattern at the pipeline axis. For the former case the American Lifelines Alliance (ALA, 2001) and some recent code directives (PRCI 2004, IITK-GSDMA 2007,) are prescribing the use of semi-empirical widely accepted elastic-perfectly plastic formulas as follows:

- Axial soil springs

$T_U = \pi D \alpha c + \pi D H \gamma \frac{1+K0}{2} \tan\delta$ and

Δ_t (*displacement at* T_u) = 3 – 5 mm for sands or Δ_t = 8 – 10 mm for clays

- Vertical uplift springs

$Q_u = N_{cv} c D + N_{qv} \gamma H D$ and

Δ_{qu} (*displacement at* Q_u) = 0.01H-0.02 =H < 0.1 D for sands *or* Δ_{qu} = 0.1 H-0.2 H < 0.2D for clays

- Vertical Bearing Soil Springs

$Q_d = N_c\ c\ D + N_q\ \gamma\ H\ D + N_\gamma\ \gamma\ D^2 / 2$

Δ_{qd} (displacement at Q_d) = 0.1D for granular soils and Δ_{qd} =0.2 D for cohesive soils

- Lateral soil springs

$P_u = N_{ch}\ c\ D + N_{qh}\ \gamma\ H\ D$

Δ_P (displacement for P_u) = 0.04 (H + D / 2) <0.1 D – 0.15 D

where ϕ the internal friction angle of the soil; c the soil cohesion; H the depth to pipe centerline; D the pipe diameter

For the latter case, that of ground deformation pattern, no particular direction is described. In case of seismic faults, the most straightforward procedure would be to assume a step-line pattern (with offset equal to the fault offset displacement). While for a strike-slip fault that would be absolutely precise, this is not the case for normal or reverse faults propagating within compliant soils. Here87, the rupture path is not a simple extension of the plane of the fault in the base rock: phenomena such as “diffraction” and “bifurcation” substantially alter the propagation path and the offset pattern/magnitude. Therefore, before applying the simplified ‘beam on springs’ procedures an initial free-field fault propagation analysis (i.e. without the pipeline) should be conducted in order to estimate the actual dislocation pattern in the pipeline location. Whilst, this fault propagation analysis is not code material — it requires implementation of strain softening models into FE algorithms — ignoring it would imply extremely unfavorable conditions for the pipeline and ultimately a quite conservative design. To lift this point of friction in the comparisons of the next paragraphs, all ‘beam-on-springs’ models are preceded by a free-field fault propagation analysis.

Two different level of comparison have been conceptualized; in all of them the rigorous FE methodology is compared to a specific ‘beam-on-springs’ model with the following attributes:

(a) **Type A Comparison:** the non-linear springs are derived by FE push tests. With this class of tests, we are comparing two models (the rigorous 3D FE model and a Winkler type model) that are perfectly equivalent in terms of soil reactions, in order to isolate phenomena associated with spring to spring interaction etc.

(b) **Type B Comparison:** All non-linear springs follow API (2001) recommendations. This class of tests is a forward comparison between the current state of practice and the proposed methodology.

7.2 Buried pipeline subjected to normal faulting

Pipeline with zero internal pressure

The problem under consideration is schematically presented in **Fig. 7.1**. The steel pipeline (steel grade X65) has an outer diameter of D=40" and thickness t=0.562" and it is buried within a layer of loose dry sand of friction angle φ=30^o at depth H_{cover}=1.2 m. The pipeline crosses an active normal fault with a strike perpendicular to the pipe and dip angle a=60^o. The bedrock lies at depth 15 m.

Implementation of the Rigorous FE Methodolgy

Firstly, the response of the pipe is studied using the rigorous 3D continuum methodology. The near-field response of the pipe is analyzed in 3D, while the far-field response is simulated using 1D elements, following the recommendations of Chapters 4 and 5. The deformed mesh of the 3D model is presented in **Fig. 7.2a** corresponding to a fault offset of δ_{fault}=4 m. The deformed mesh of the soil is displayed with superimposed displacement contours; the step-like deformation at the base turns to a far smoother distribution at the surface, while the tendency of the pipe to emerge from the soil is evident as the sand flows around it. The deformed mesh of the pipe with superimposed axial strain contours for the same fault offset is also portrayed. The pipe takes the characteristic double-curvature shape to accommodate the vertical differential displacement of its two ends. As the pipe is forced further within its plastic regime, the concentration of strains at the maximum curvature point within the stable soil prevails. Ultimately, there comes a fault displacement (i.e., δ_{fault} = 2.5 m) that causes an entire section to yield; from that point on any additional strain is concentrated within this section resulting an abrupt increase in the developed strains until the formation of a clear neck (**Fig. 7.2b)**.

Type A Comparison

In the 'beam-on-springs' approach the pipeline is simulated with beam elements (in particular, pipe elements that account for the hoop stress across the cross-section) while discrete nonlinear springs are used to simulate the soil reaction in each orthogonal direction (**Fig. 7.3a**). The imposed ground deformation is materialized by dislocating the appropriate support nodes of the springs. As mentioned previously, to render the results of the two methods comparable, the support nodes of the springs are dislocated in the exact same manner to those of the full 3D model (as shown in **Fig. 7.3b**) to correctly capture the propagation of rupture within the assumed soil layer.

Following the definitions of the preceding paragraph, in the Type A Comparison, the force-displacement response of the soil springs is calibrated through numerical uniaxial push tests in each principal direction

the results of which are shown in **Fig. 7.4**. The results of the simplified analysis are summarized in **Fig. 7.5**. In **Fig. 7.5a** the axial strain distribution along the top and bottom centerline is presented for three representative fault offsets. As expected, the pipeline response is indeed in qualitative agreement with the full 3D model. As previously, the maximum tensile strain is initially located in the maximum curvature point within the stable soil, while as the imposed dislocation increases the maximum straining is transferred to a neighboring section (close to pipe-fault intersection) experiencing excessive stretching (**Fig. 7.5b)**.

Fig. 7.6 compares the response of the pipeline predicted by the rigorous 3D analysis and by the simplified Winkler-type analysis in terms of maximum tensile strain developed along the top and bottom centerline. Evidently, within the elastic range (up to δ_{fault}≈0.7 m), the maximum tensile strains predicted by both models are practically the same. However, as the imposed dislocation increases, the simplified model appears to overestimate the maximum tensile strain developed along the top centerline, while it successfully predicts the maximum strain along the bottom centerline. At this point, the maximum strain of the top centerline is located in the maximum curvature point, and it is attributed to pipeline bending because of the underlying soil reactions. A possible overestimation of the bearing soil reaction (assumed in the Winkler Model) would explain this slight strain overestimation. This observation, whilst not easy to explain, is the main point of criticism for the use of Winkler-type models: by representing soil reactions with discrete springs, the transfer of loads between adjacent springs and the interaction between the various loading components cannot be properly accounted. Building upon this statement, recent findings have highlighted a strong coupling between the vertical and horizontal loading (e.g. Di Prisco et al. 2006, Cocchetti et al. 2008, Hodder and Cassidy 2010, Tian et al. 2011) which cannot be ignored. In our particular case, the soil at the vicinity of the fault is in active mode which greatly reduces its bearing capacity. Similar trends have been reported in the experimental study of Ha et al. 2008, where the measured peak resistance of the underlying soil where found to be much lower, about 1/8 of the theoretical value proposed by ASCE.

For increased level of fault dislocation, the two models tend to converge predicting the ultimate tensile failure of the pipeline at a δ_{fault}≈3.6 m (still though the simplified model forecasts failure at a slightly earlier stage). Here, the differences are attributed to an overestimation of the magnitude of axial soil restrain. Clearly, the Winkler-model ignores the decrease of axial capacity caused by the formation of gaps between the subsiding soil and the reacting pipe.

Overall the Type A Comparison is rather satisfactory: **the Winkler-model successfully predicts the response at relatively small displacements as well as the ultimate tensile failure of the pipeline.** Some minor differences do exist that result in a slightly conservative (and thus safer) design.

Pipeline with non-zero internal pressure

The analyses are repeated considering that the pipe operates under internal pressure p_{oper}=9 MPa. **Fig. 7.7** summarizes the response of the pipe predicted by the sophisticated 3D analysis and the simplified Winkler-type model. Contrary to the p=0 case, the trends are reversed with the simplified model underestimating the maximum tensile strain developed in the top centerline of the pipe. This behavior exposes the main drawback of representing non-solid structures (such as pipes) with beam elements. According to beam theory, sections of a beam are not allowed to deform in their own plane; yet this criterion cannot not hold true for non-solid cross-sections experiencing intense straining. In this case the response of the structure in the plane of its cross-section is non-negligible resulting in a much softer behavior that cannot be represented by beam theory. As a result, (assuming a failure criterion of $\varepsilon_{x,max}$=2%) the simplified model predicts pipeline failure at δ_{fault}≈3 m while the rigorous 3D model predicts failure at a much lower fault offset of δ_{fault}≈2 m. In **Figure 7.8** we are attempting to further elucidate the deficiencies of beam theory by comparing the axial strain distribution along the top and bottom centerline of the pipe predicted by the two models. At relatively small fault offsets up to δ_{fault}≈1 m the comparison is quite close. As the fault offset increases, the axial strain distribution (of the 3D pipeline) starts following a wavy pattern (result of strain localization at a number of neighboring sections). Initially there is one dominant spike (in the sense that stains are peaking at a specific section), but as imposed displacement increases the straining on the pipeline is redistributed and more spikes are “mobilized”. This very behavior indicates that this particular pipe segment has reached its ultimate capacity and any further displacement will be accommodated in a ductile manner. Clearly, these highly non-linear phenomena may not be correctly captured by means of beam elements. Hence, **the simplified models overestimate the bending resistance of pipe (at large deformations) and predict smaller strains resulting ultimately in an unsafe design.**

Type B Comparison

In this class of tests the rigorous 3D methodology is compared to the current design practice. As such a new Winkler-type model is constructed employing the code-specified (by ALA, 2001) nonlinear springs of

the introductory paragraph. Before commenting on the pipeline response, in **Fig. 7.9a** we are first comparing the predictions of the two methodologies in terms of soil reactions to uniaxial displacements. Evidently, the ALA 2001 analytical expressions slightly underestimate the bearing and uplift soil resistance, while there is a rather satisfactory agreement in terms of axial soil resistance. Moreover, the bearing and axial response is notably stiffer according to ALA2001 formulas.

The pipeline response (portrayed by means of evolution of maximum tensile strain at the top and bottom centerline) is displayed in **Fig 7.9(b)**. For this example test case, the 3D model predicts failure at a δ_{fault}≈3.7 m (i.e., instant at which the axial strain reaches the limit value of $\varepsilon_{x,max}$=2 %), while the simplified ALA 2001 model assess a critical fault offset of δ_{fault}≈2.7 m; a quite conservative prediction. Needless to say, that the inaccurate estimation of the bearing spring stiffness combined with the overall deficiencies of the Winkler-type models (discussed previously) are responsible for substantially **overestimating the actual pipeline straining resulting in a very conservative (and thus expensive) design.**

Pipeline buried into dilative Soil

The same infinitely long steel pipeline (D=40", t=0.562", H_{cover}=1.2 m) is buried now within a layer of relatively dense sand of friction angle φ=40^o and dilation angle ψ=10^o and as previously is subjected to a normal fault of dip angle α=60^o. A comparison of the soil reactions (ALA formulations against FE calculations) is offered in **Fig. 7.10a**. In this case, and although the bearing and uplift response are adequately approximated by the ALA, the axial soil reaction is severely underestimated. This very underestimation is attributed to sand dilation; a phenomenon that is totally ignored by code provisions. As thoroughly discussed in Chapter 5, the soil surrounding the pipeline resists to the axial pipe movement through shearing, forming a thin shear-zone around the pipe. In case of dilative soils, this shear-zone tends to expand radially but is constrained by the pipe and the surrounding soil. This constrained dilatancy provokes additional normal stressing along the pipe periphery andleads to increased pull-out capacity. This behavior is accounted for in the 3D model while it is totally ignored by the ALA 2001 provisions. The outcome is depicted in **Fig. 7.10b** where the maximum tensile strain along the bottom and top centerline of the pipe is presented considering both methodologies. As the 3D model takes into account this increased axial soil restraint, it predicts failure (in terms of necking formation) at an earlier stage than the simplified model (2m instead of 2.5 m). Yet, even this overestimation is overshadowed by the overall conservatism of the simplified model rendering the the predictions of the ALA simplified model still on

the safe side: according to ALA pipeline failure is expected at a fault offset of δ_{fault}≈1.5 m, while the 3D FE model suggests a δ_{fault}≈2 m.

7.3 Buried pipeline subjected to reverse faulting

The exact same pipeline examined previously (D=40", t=0.562", H_{cover}=1.2 m) is now subjected to reverse faulting (**Fig. 7.11**). The pipe is buried within loose sand (φ=30^o) and it crosses an active fault with a dip slip of a=45^o at the bedrock level ($z_{bedrock}$=-15 m). **Fig. 7.12** presents the deformed mesh of the 3D model: the soil is shown with displacement contours for fault offset δ_{fault}=1 m while the pipe is portrayed with superimposed stress contours for the same offset depicting the stress concentration around the buckled area.

The results of the proposed 3D Methodology are compared to the Winkler type Models (Type A and B) in **Fig. 7.13a.** It is observed that within the elastic range the results of the three models are practically identical. As the fault offset increases the 3D model calculations start to deviate substantially from the predictions of the simplified models, while the latter two continue to compare quite well. Finally, at δ_{fault}≈0.8 m (corredponding to ε_c=-0.0035) the pipeline enters an unstable state (a finite increase in the imposed displacement results in a massive increase in the developed strain), known as local buckling. Evidently, the beam elements of the simplified approach may not directly simulate the onset of local buckling. Instead the designer should correlate the ability of the section to undergo plastic deformation to the developed curvature (expressed by the developed compressive strain). This correlation is made through the limit strain ε_c (critical buckling strain). A number of researchers have experimentally investigated the plastic deformation capacity of cylindrical shells [e.g. Jirsa et al. (1972), Reddy (1979), Tugcu and Schroeder (1979), Gresnigt, (1986), Kyriakides and Shaw (1987), Fowler (1990), Kyriakides & Ju (1991), Van Foeken and Gresnigt (2001), Zimmerman et al. (2004), Schaumann et al. (2005), Van Es et al. (2014)], and several relationships have been published for the estimation of the this critical buckling strain ε_c. Here we are using the experimentally derived formulas by Gresnigt 1986 that has been also adopted by the CSA Z662, which correlate the critical buckling strain to the pipeline hoop stress (σ_h) as follows:

$$\varepsilon_c = 0.5\left(\frac{t}{D}\right) - 0.0025 + 3000\left(\frac{\sigma_h}{E}\right)^2 \quad (7.1)$$

where σh depends on the level of internal pressure p:

$$\sigma_h = \begin{cases} \frac{pD}{2t},\ if\ \frac{pD}{2t\sigma_y} \leq 0.4 \\ 0.4\sigma_y,\ if\ \frac{pD}{2t\sigma_y} > 0.4 \end{cases} \quad (7.2)$$

By applying **Eq. 7.1** to our test case, the pipe is expected to exhaust its capacity at ε_c=-0.0045 (i.e. at larger strain compared to the 3D model prediction). A possible explanation of this difference is the inefficiency of **Eq. 7.1** (or any other similar equation in the literature) to accurately describe the buckling response of pipelines subjected to combined bending and axial loading. As explained in Chapter 6, the metaplastic deformation capacity of a circular section was found to depend on the axial force acting on the section: the presence of compressive force may render the pipe section more vulnerable to local buckling (i.e. decrease the critical compressive strain ε_c) due to the tendency of the section for outward expansion. **Overall, the simplified procedures tend to overpredict the maximum allowable fault displacement.** Namely, a δ_{fault}≈1 m compared to a δ_{fault}≈0.8 m predicted by the 3D FE model.

Pipeline with non-zero internal pressure

Contrary to the non-pressurized pipe, when assuming a pipeline operating at internal pressure p=p_{max} = 9 MPa the 3D model predictions and the simplified models compare quite well (**Fig. 7.13b)**. All three methods agree that the critical fault dislocation (which provokes local buckling) is in the order of δ_{fault}≈0.55 m corresponding to a ε_c=-0.0069 – as suggested by the application of Eq.8.1 and the numerical modelling of the pipeline section.

7.4 Concluding Remarks

The above non-exhaustive examples aimed to elucidate some of the deficiencies of the simplified beam-on-springs models to accurately predict the structural response of buried steel pipelines subjected to permanent ground displacements. The key conclusions may be summarized as follows:

- The Winkler-type foundation fails to account for the interaction of 'co-existing' loading types. Particularly in the case of normal faulting (where the bearing capacity of the soil decreases due to the

prevailing active conditions at the vicinity of the fault), the simplified procedures tend to overestimate the developed strain on the pipe and as a result to underestimate the maximum allowable fault offset.

- The simplified models overestimate the pipe stiffness when it operates under substantial pressure resulting in unsafe (non-conservative) results.
- Simplified models cannot simulate the initiation of local buckling. The latter is provided by literature expressions correlating the developed strain with the deformation capacity of the pipe. Hence, the simplified models are as accurate as the expressions adopted.
- The ALA 2001 analytical expressions fail to account for the increase in axial soil restraint in cases of dilative soil profiles resulting in non-conservative predictions for pipelines subjected to reverse faulting.

References

American Lifelines Alliance (ALA). (2001). "Guidelines for the design of buried steel pipe."

ASCE. American Society of Civil Engineers, (1984). "Guidelines for the seismic design of oil and gas pipeline systems. Committee on Gas and Liquid Fuel Lifelines." *Technical Council on Lifeline Earthquake Engineering, ASCE, New York*.

Canadian Standard Association. Oil and gas pipeline systems, CSA-Z662. Mississauga, Ontario, Canada; 2007.

Cocchetti, G., di Prisco, C., & Galli, A. (2008). Soil-pipeline interaction along active fault systems. *International Journal of Offshore and Polar Engineering, 18*(03).

Dash, S. R., & Jain, S. K. (2007). IITK-GSDMA Guidelines for seismic design of buried pipelines: provisions with commentary and explanatory examples. *National Information Center of Earthquake Engineering, Kanpur, India.*

di Prisco, C., & Galli, A. (2006). Soil-pipe interaction under monotonic and cyclic loads: experimental and numerical modelling. In *Proceedings of the First Euro Mediterranean Symposium in Advances on Geomaterials and Structures. Hammamet, Tunisia* (pp. 3-5).

Foeken, R.J. van, Gresnigt A.M. (1998). Buckling and collapse of UOE manufactured steel pipes. Report prepared for the Offshore and Onshore Design Applications Supervisory Committee of PRC International at the American Gas Association, Arlington, www.prci.com/publications.

Fowler, J.R. (1990). Recommended design procedures for offshore pipelines, *Seminar Proceedings Collapse of Offshore Pipelines*, February 20, 1990, AGA Catalogue No. L51646.

Gresnigt, A.M. (1986). Plastic design of buried steel pipelines in settlement areas, *HERON*, Vol. 31, no. 4.

Kyriakides, S. & Ju, G.T. (1992). Bifurcation and localization instabilities in cylindrical shells under bending – I. *Experiments, Int. J. Solids & Structures*, Vol. 29. pp. 1117-1142.

Kyriakides, S. & Shaw, P.K. (1987). Inelastic buckling of tubes under cyclic bending. *J. Pressure Vessel Technology*, *ASME*, Vol. 109, pp. 169-178.

Ha, D., Abdoun, T., O'Rourke, M., Symans, M., O'Rourke, T., Palmer, M., & Stewart, H. (2008). Buried Hdpe Pipelines Subjected to Normal Faulting-a Centrifuge Approach. *Canadian Geotechnical Journal, 45*, 1733-1742.

Hodder, M. S., & Cassidy, M. J. (2010). A plasticity model for predicting the vertical and lateral behaviour of pipelines in clay soils. *Géotechnique, 60*(4), 247-263.

Honegger, D.G. and Nyman, D.J., 2004, Seismic design and assessment of natural gas and liquid hydrocarbon pipelines, Pipeline Research Council International, Inc., No. L51927.

Jirsa, J.O., Lee, F.H., Wilhoit, J.C. & Merwin, J.E. (1972). Ovaling of pipelines under pure pressure. *Offshore Technology Conference*, OTC 1569.

Reddy, D.B. (1979). An experimental study of the plastic buckling of circular cylinders in pure bending. *Int. J. Solids and Structures*, Vol. 15, pp 669-685.

Schaumann, P., Keindorf, C., & Brüggemann, H. (2005, January). Elasto-plastic bearing behavior of steel pipes exposed to internal pressure and bending. In *The Fifteenth International Offshore and Polar Engineering Conference*. International Society of Offshore and Polar Engineers.

Tian, Y., & Cassidy, M. J. (2011). Pipe-soil interaction model incorporating large lateral displacements in calcareous sand. *Journal of Geotechnical and Geoenvironmental Engineering, 137*(3), 279-287.

Tugcu, P. & Schroeder, J. (1979). Plastic deformation and stability of pipes exposed to external couples. *Int. J. Solids & Structures*, Vol. 15. pp. 643-658.

Van Es, S. H. J., Gresnigt, A. M., Kolstein, M. H., & Bijlaard, F. S. K. (2014, August). Strain based design of spirally welded pipes, local buckling in 4-point bending. In *The Twenty-fourth International Ocean and Polar Engineering Conference*. International Society of Offshore and Polar Engineers.

Zimmerman, T. Timms, C., Xei, J., Asante, J. (2004) "Buckling resistance of large diameter spiral welded linepipe:" *Proceedings of International Pipeline Conference*, Calgary, Canada

Figures
of Chapter 7

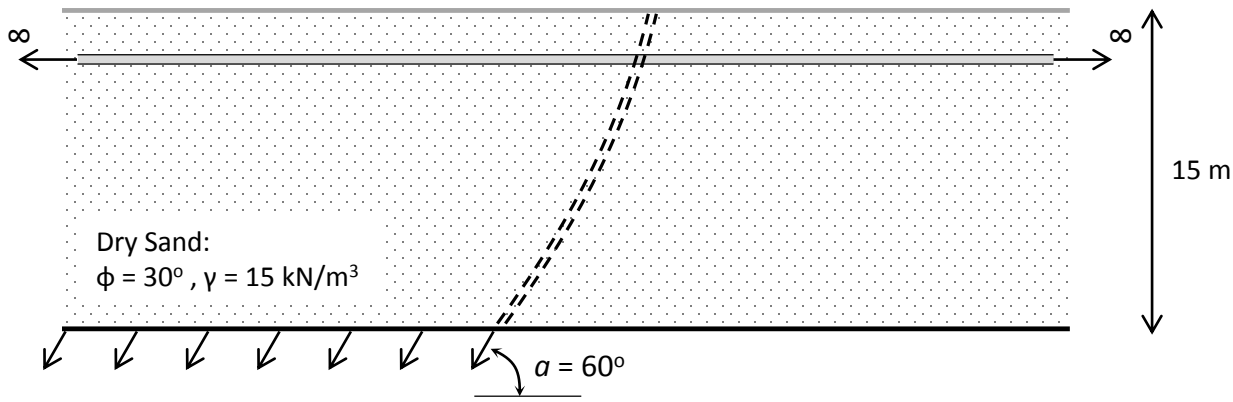

(a)

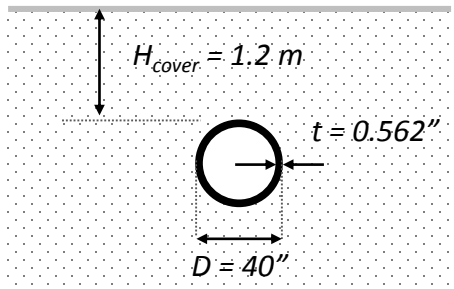

(b)

Fig. 7.1. The first benchmark problem: **(a)** an infinitely long pipeline buried in loose sand crosses a normal fault perpendicular to its axis with a dip slip a=60°, **(b)** the geometrical characteristics of the pipe and its cover depth.

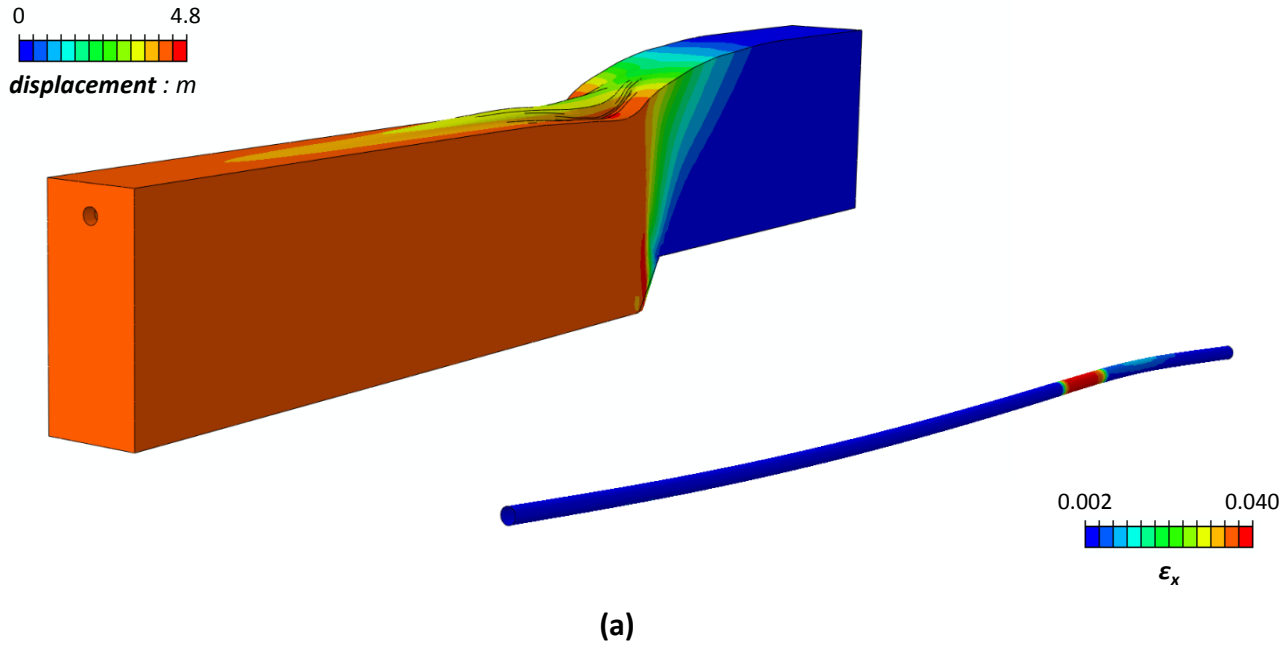

(a)

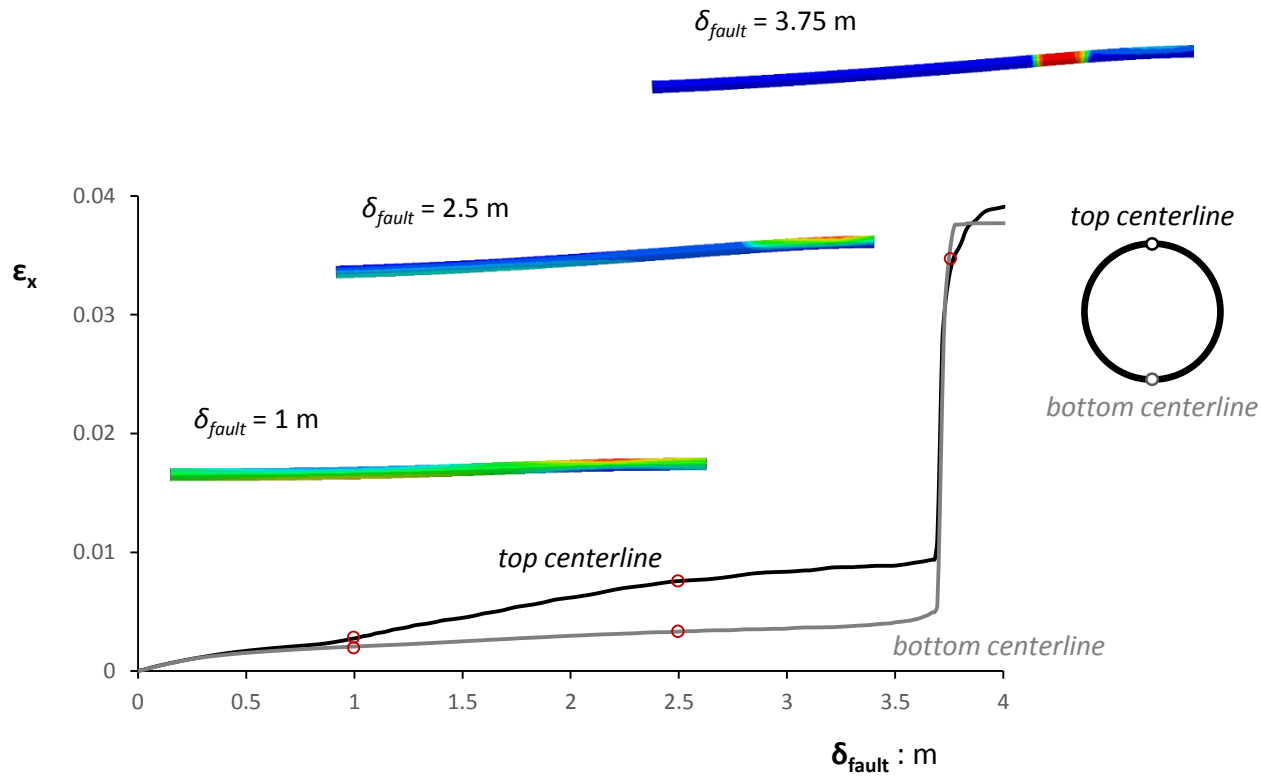

(b)

Fig. 7.2. Evaluation of the pipe response using the sophisticated 3D numerical methodology: (a) deformed mesh of the soil with superimposed displacement contours and of the pipe with axial strain contours. (b) evolution of the maximum tensile axial strain along the top and the bottom centerline with the increase of the fault offset.

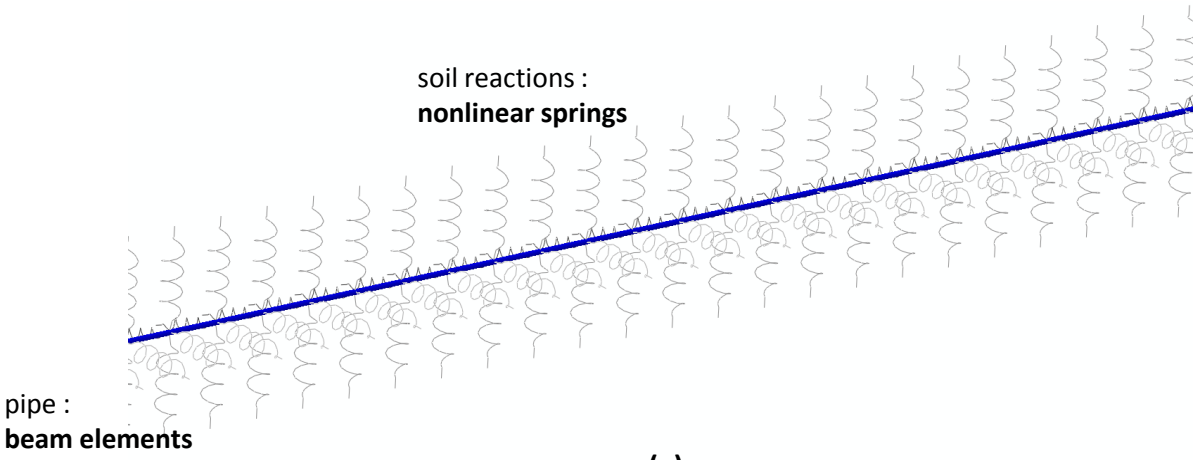

(a)

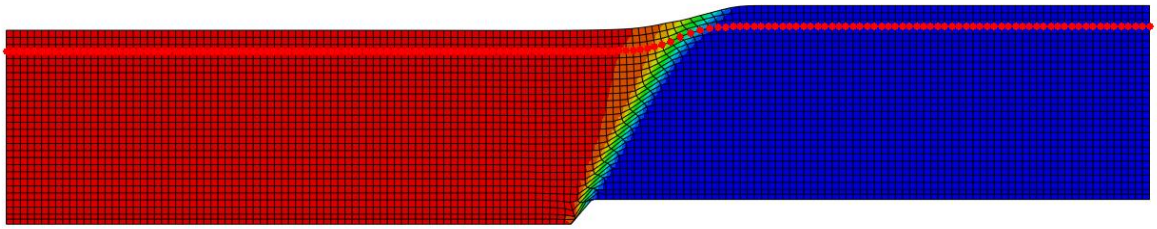

(b)

Fig. 7.3. Evaluation of the pipe response using simplified models: (a) the pipe is modeled with beam-type elements while the soil is modeled with discrete nonlinear springs in each orthogonal direction. (b) the fault-induced displacements are simulated by dislocating the spring support nodes following the results of the 3D model to account for the rupture propagation effects.

subgrade reactions: downward push

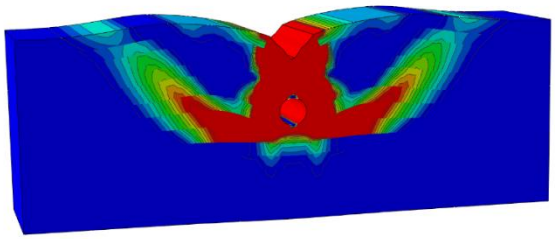

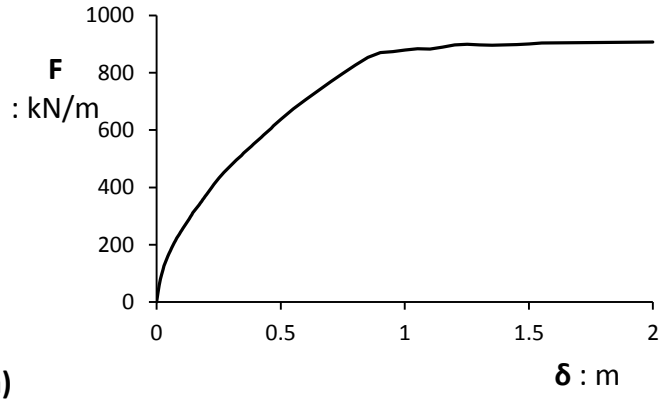

(a)

upward vertical reactions: uplift test

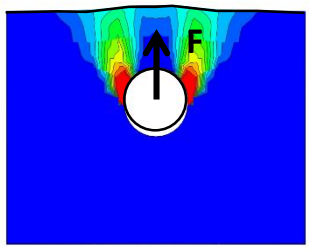

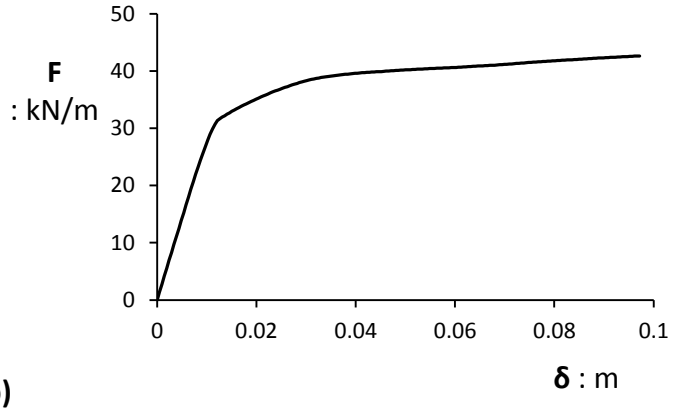

(b)

lateral reactions: transversal push test

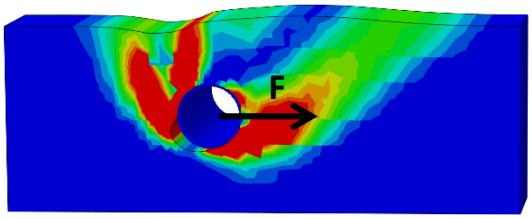

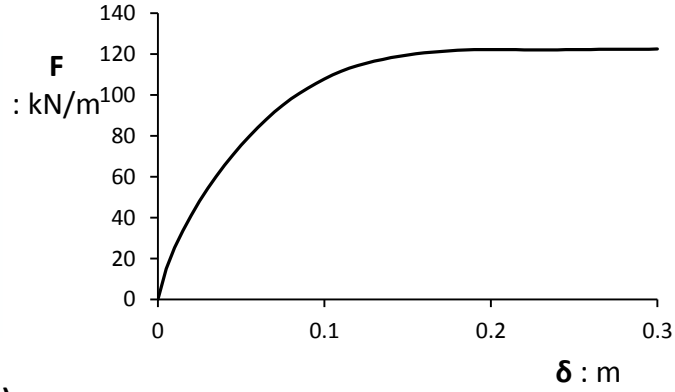

(c)

axial reactions: pullout test

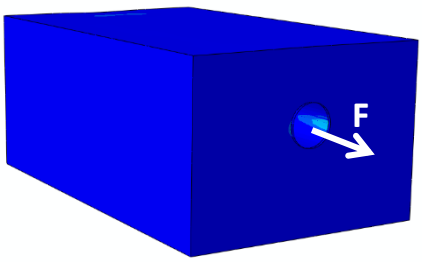

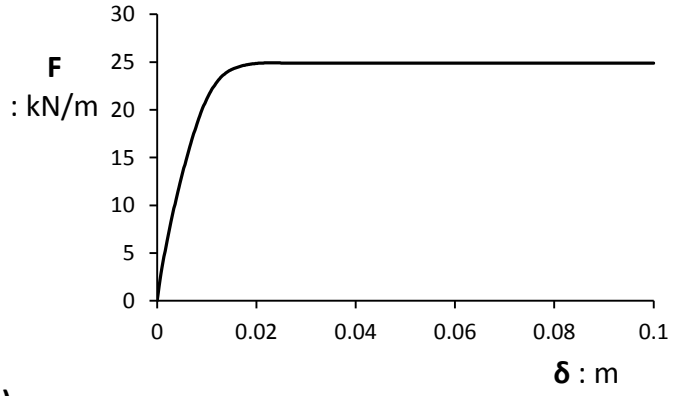

(d)

Fig. 7.4. The force-displacement response soil springs is calibrated against numerical uniaxial push tests: **(a)** downward push for the bearing capacity response, **(b)** uplift test for the restraint to upward vertical dislocation, **(c)** transversal push for the lateral reactions and **(d)** pullout test for the axial reactions.

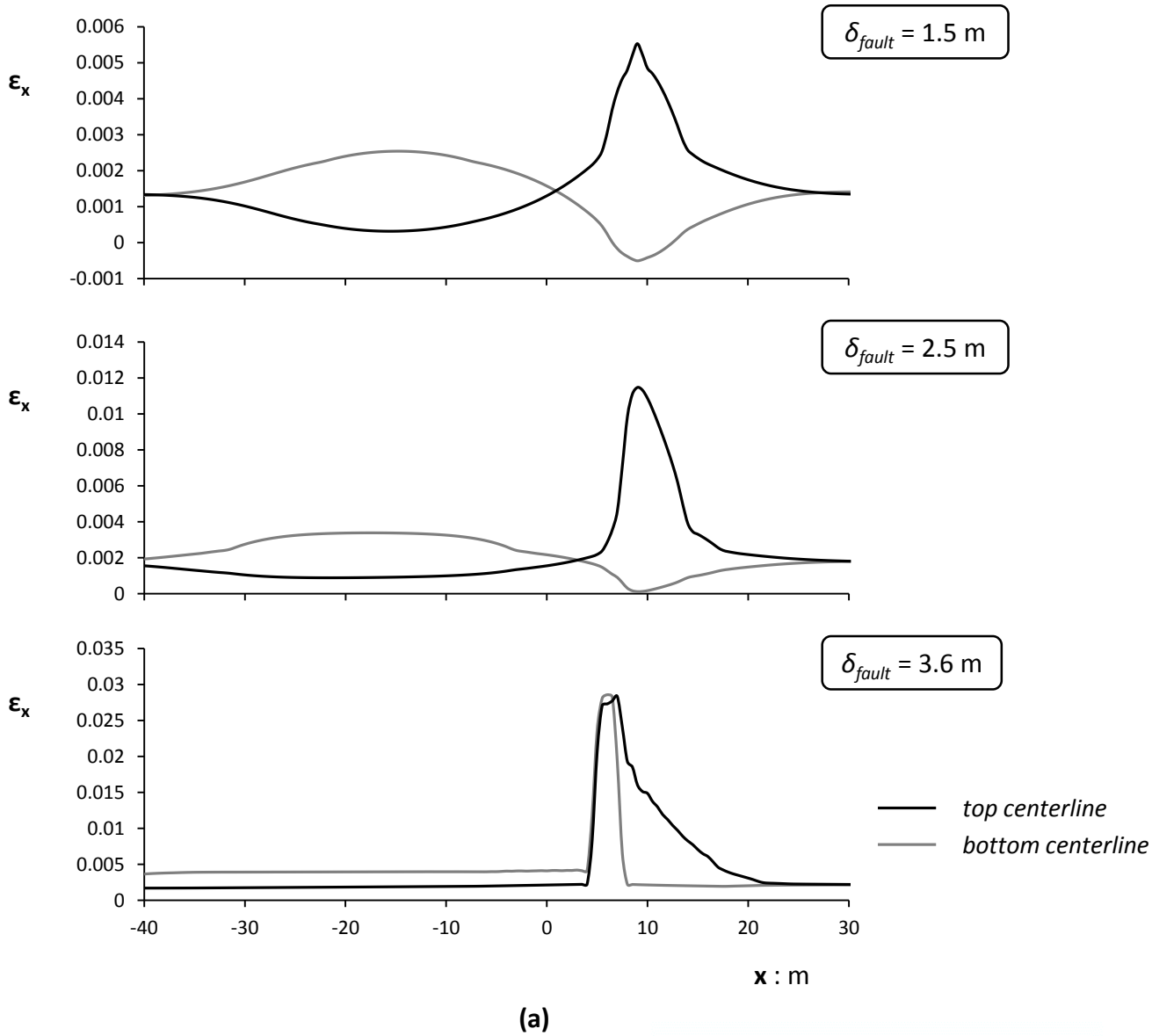

(a)

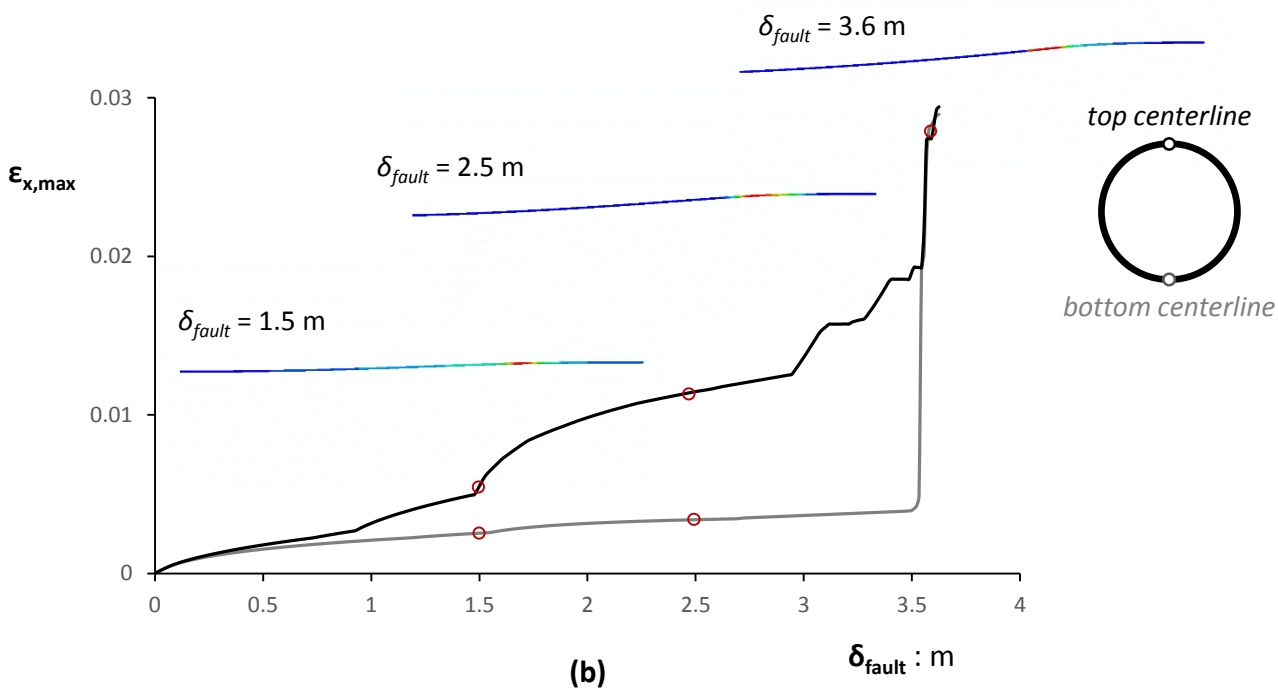

(b)

Fig. 7.5. The pipe response to normal faulting predicted by the simplified model. (a) axial strain distribution along the top and bottom centerline of the pipe for three representative fault offsets. (b) evolution of the maximum tensile axial strain along the top and the bottom centerline with the increase of the fault offset.

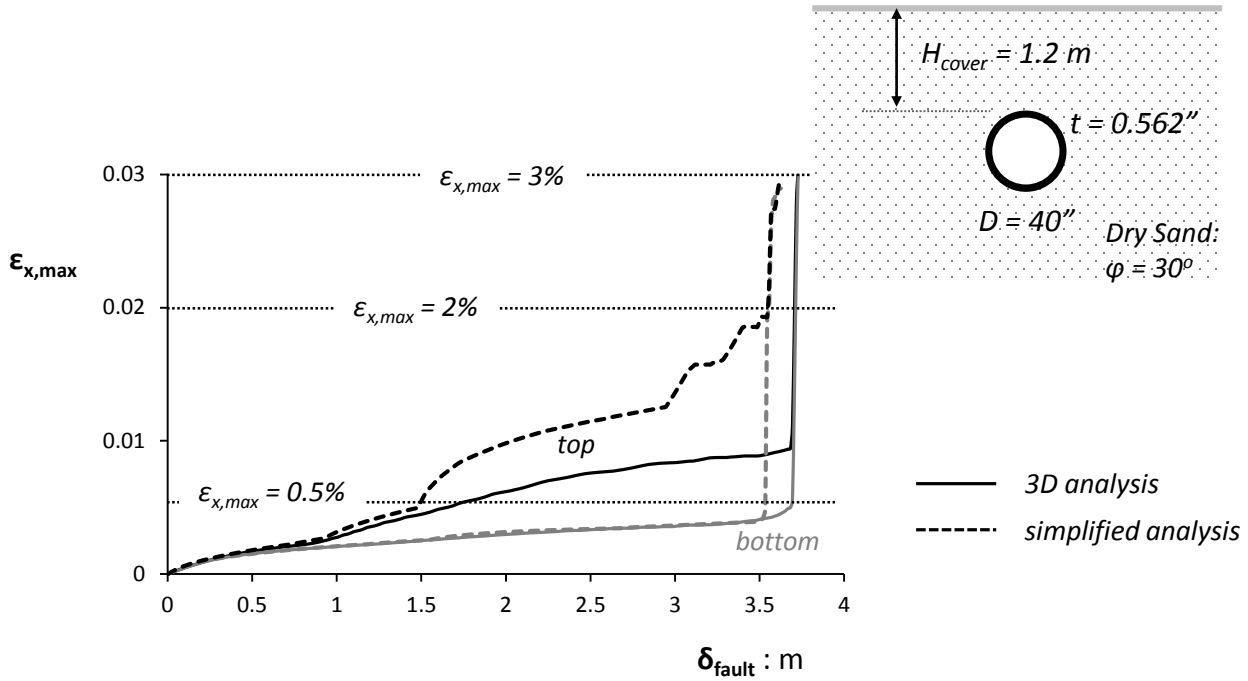

Fig. 7.6. Comparison between the prediction of the sophisticated 3D analysis and that of the simplified analysis for the pipeline buried in loose sand and subjected to normal faulting: evolution of the maximum tensile axial strain along the top and the bottom centerline with the increase in the fault offset.

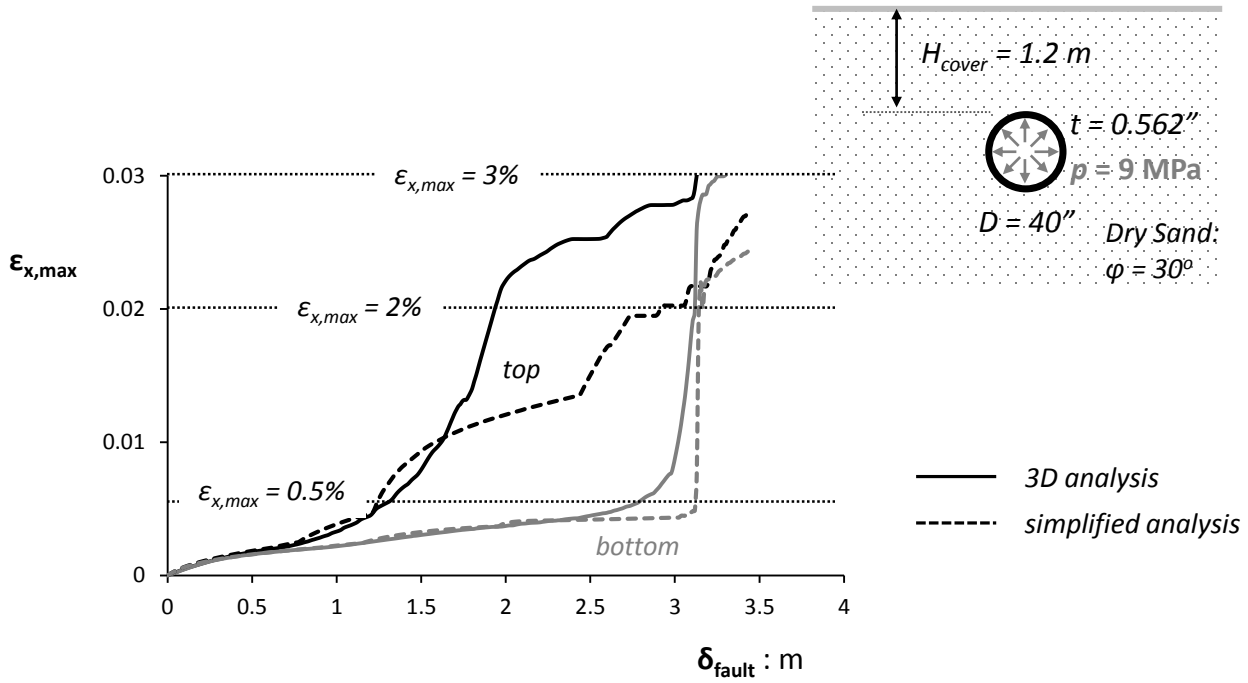

Fig. 7.7. Comparison between the prediction of the sophisticated 3D analysis and that of the simplified analysis for the pressurized pipeline buried in loose sand and subjected to normal faulting: evolution of the maximum tensile axial strain along the top and the bottom centerline with the increase in the fault offset.

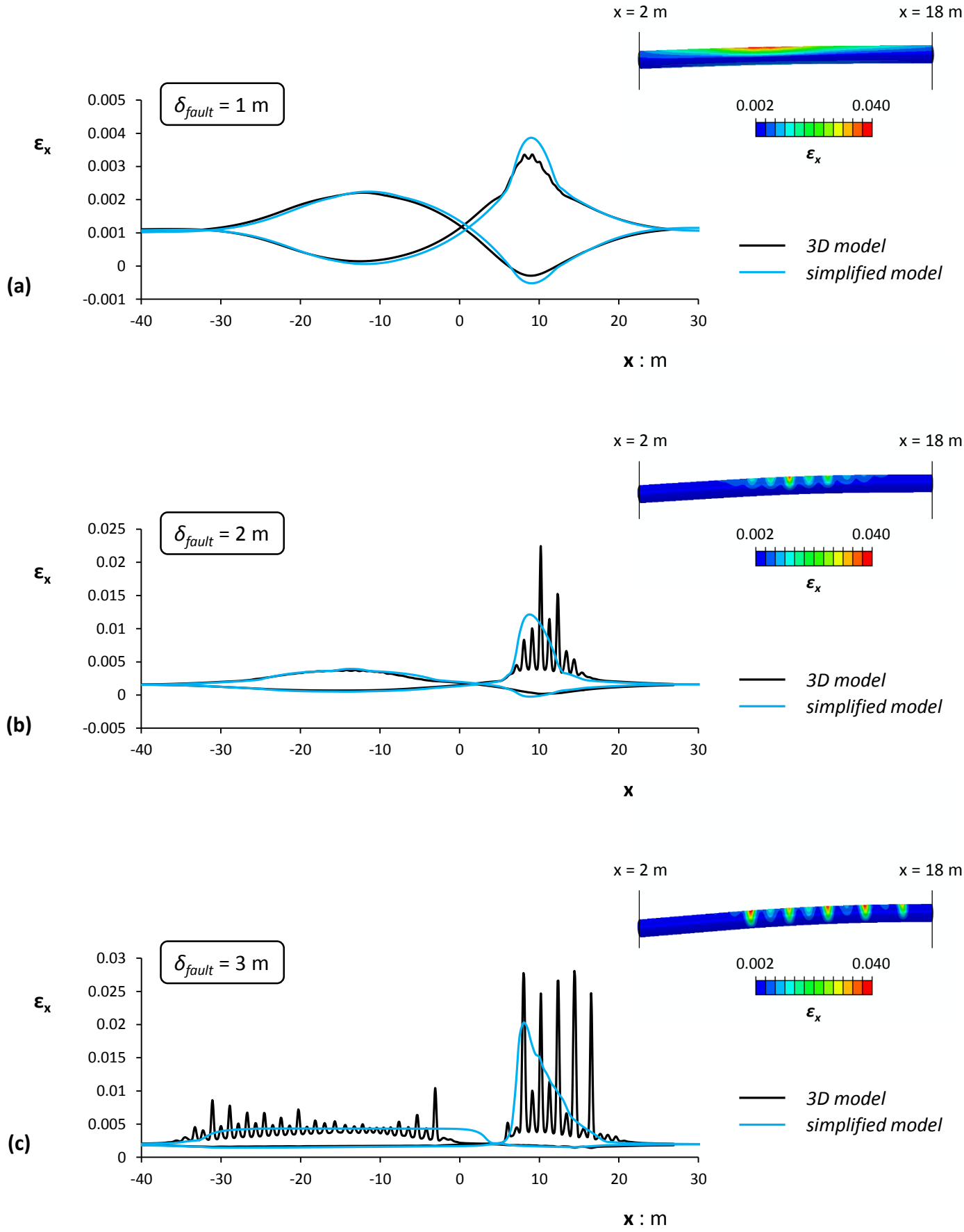

Fig. 7.8. Comparison between the prediction of the sophisticated 3D analysis and that of the simplified analysis for the pressurized pipeline buried in loose sand and subjected to normal faulting: axial strain distribution along the top and bottom centerline of the pipe for (a) δ_{fault}=1 m, (b) $\delta\delta_{fault}$=1 m and (c) δ_{fault}=3 m.

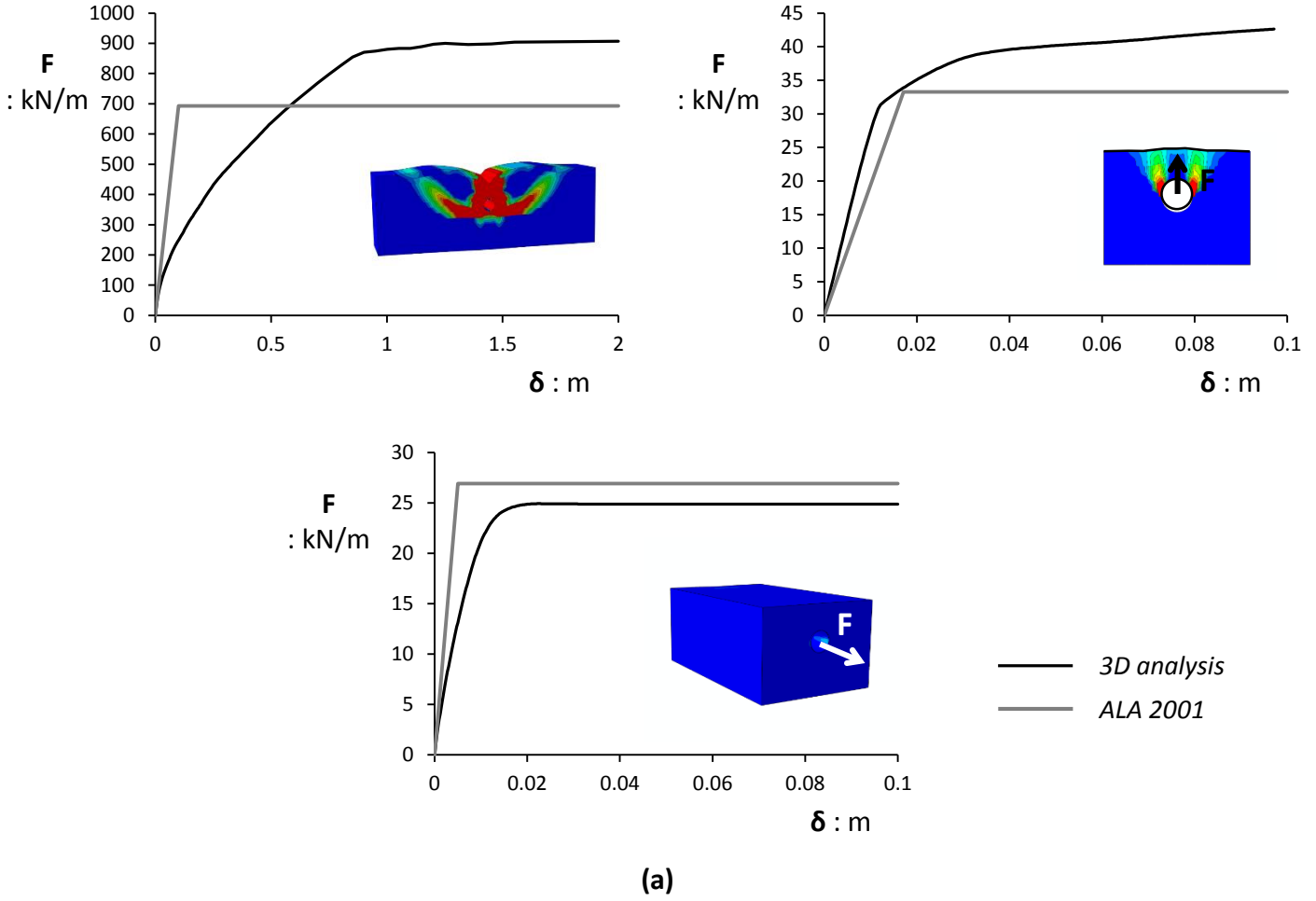

(a)

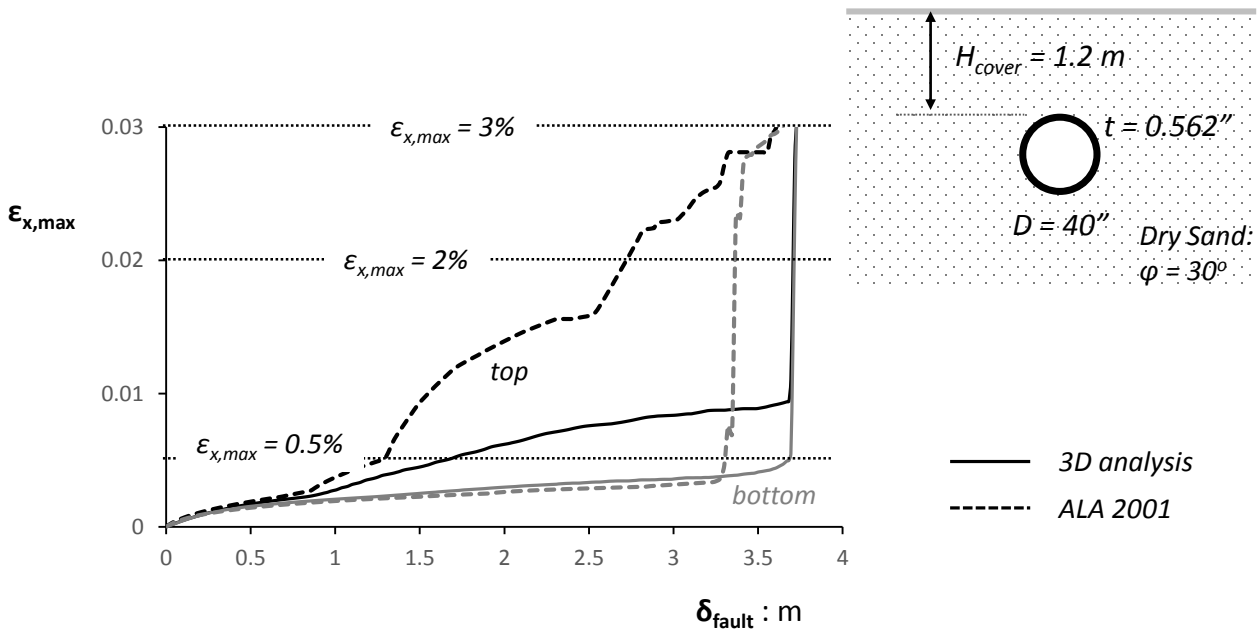

(b)

Fig. 7.9. (a) Soil reactions estimated by analytical expressions according to the ALA 2001 provisions compared to the results of uniaxial push numerical tests for loose sand (φ=30°). (b) The pipe response estimated by the simplified model with springs calibrated according to ALA 2001 as opposed to the response of the pipe predicted by the 3D model: maximum axial strain along the top and the bottom centerline.

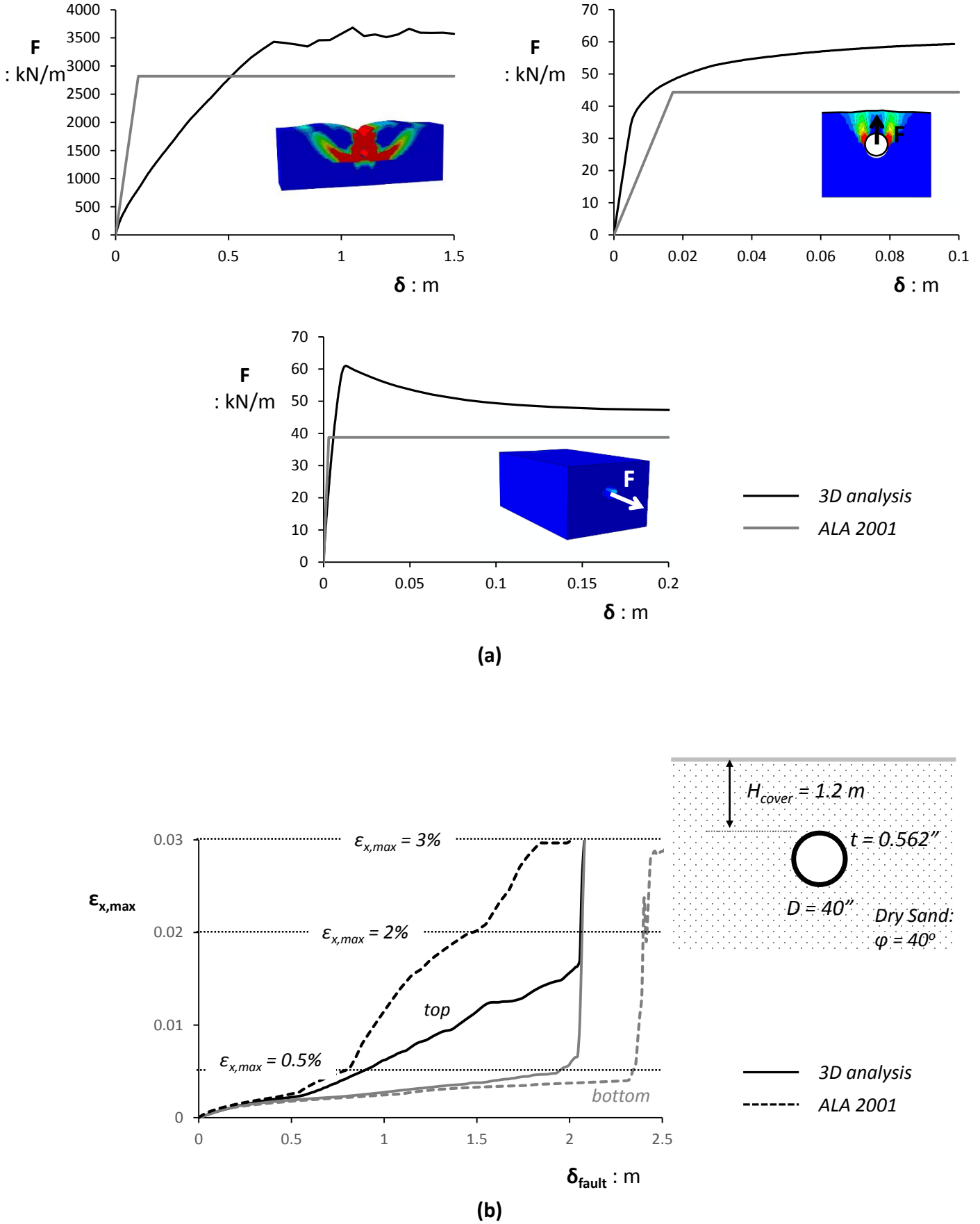

Fig. 7.10. (a) Soil reactions estimated by analytical expressions according to the ALA 2001 provisions compared to the results of uniaxial push numerical tests for dense sand (φ=40°, ψ=10°). (b) The pipe response estimated by the simplified model with springs calibrated according to ALA 2001 as opposed to the response of the pipe predicted by the 3D model: maximum axial strain along the top and the bottom centerline.

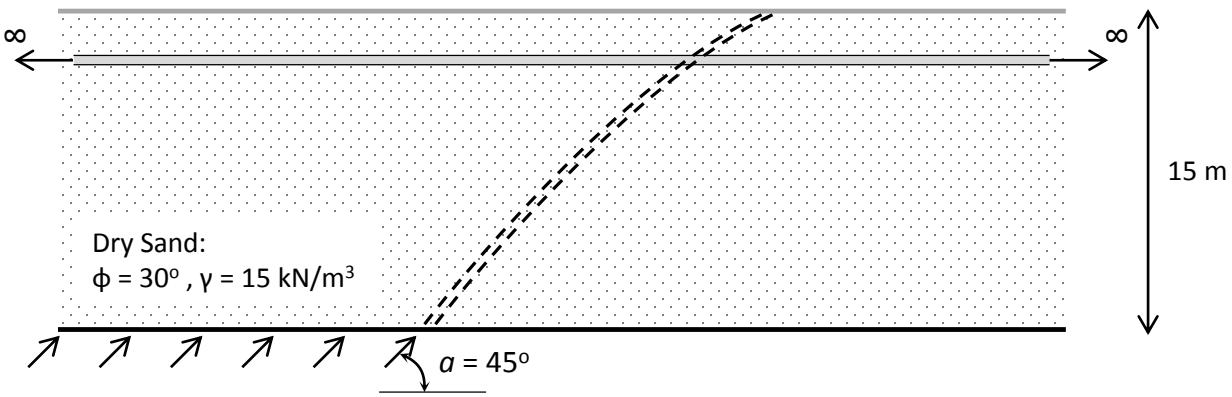

(a)

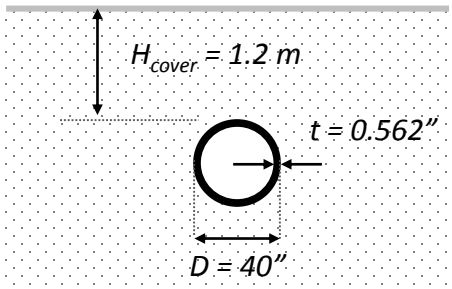

(b)

Fig. 7.11. The second benchmark problem: **(a)** an infinitely long pipeline buried in loose sand crosses a reverse fault perpendicular to its axis with a dip slip α=45°, **(b)** the geometrical characteristics of the pipe and its cover depth.

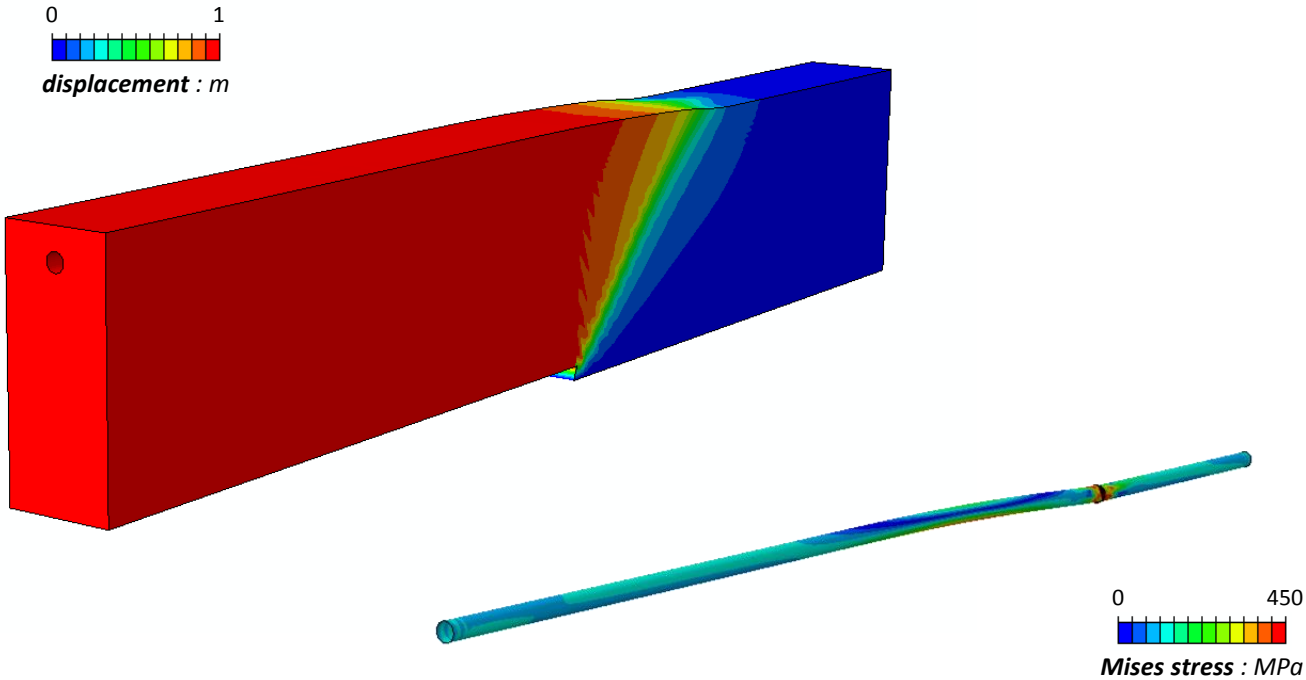

(a)

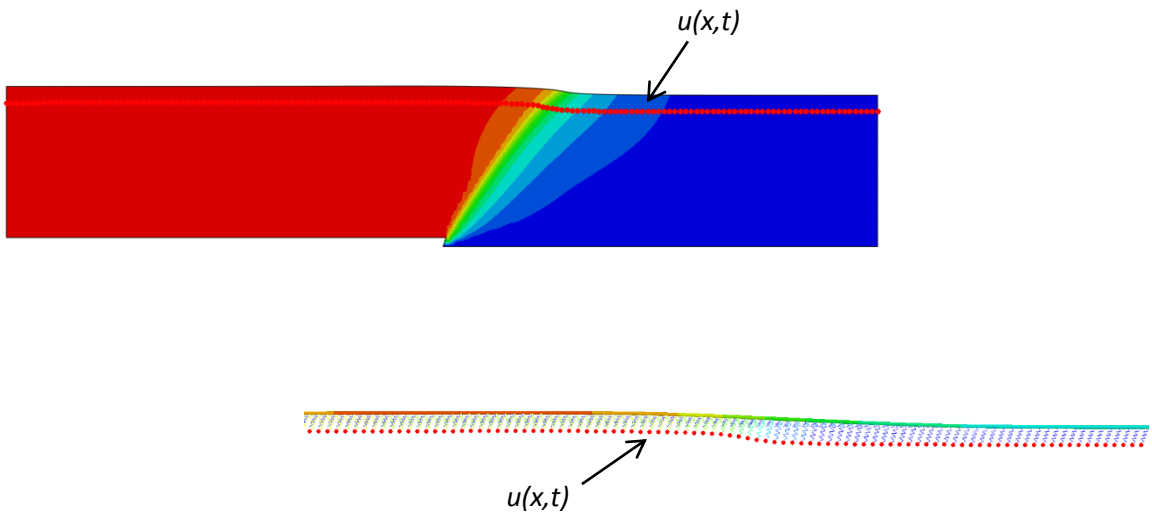

(b)

Fig. 7.12. **(a)** Evaluation of the pipe response using the sophisticated 3D numerical methodology: deformed mesh of the soil with superimposed displacement contours and of the pipe with stress contours. **(b)** Evaluation of the pipe response using a simplified model: to account for the rupture propagation related effects the displacement of the spring support nodes follows the distribution calculated by the 3D model.

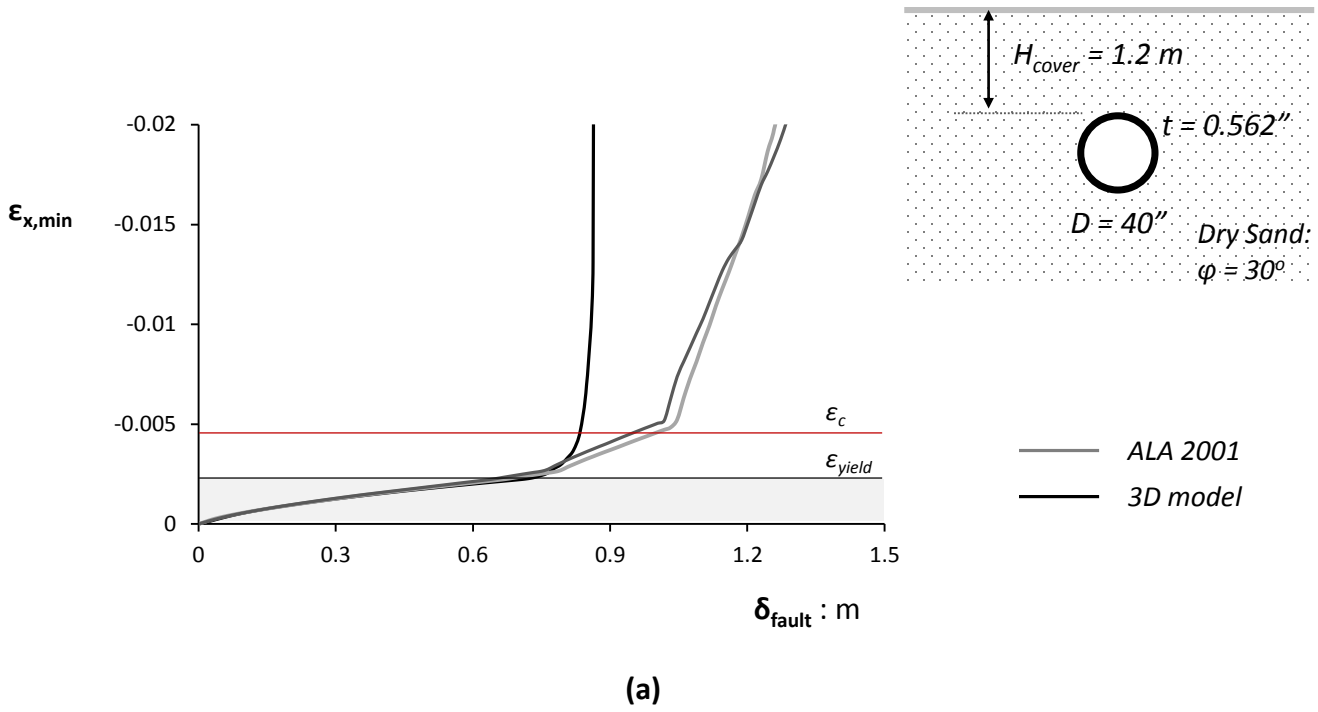

(a)

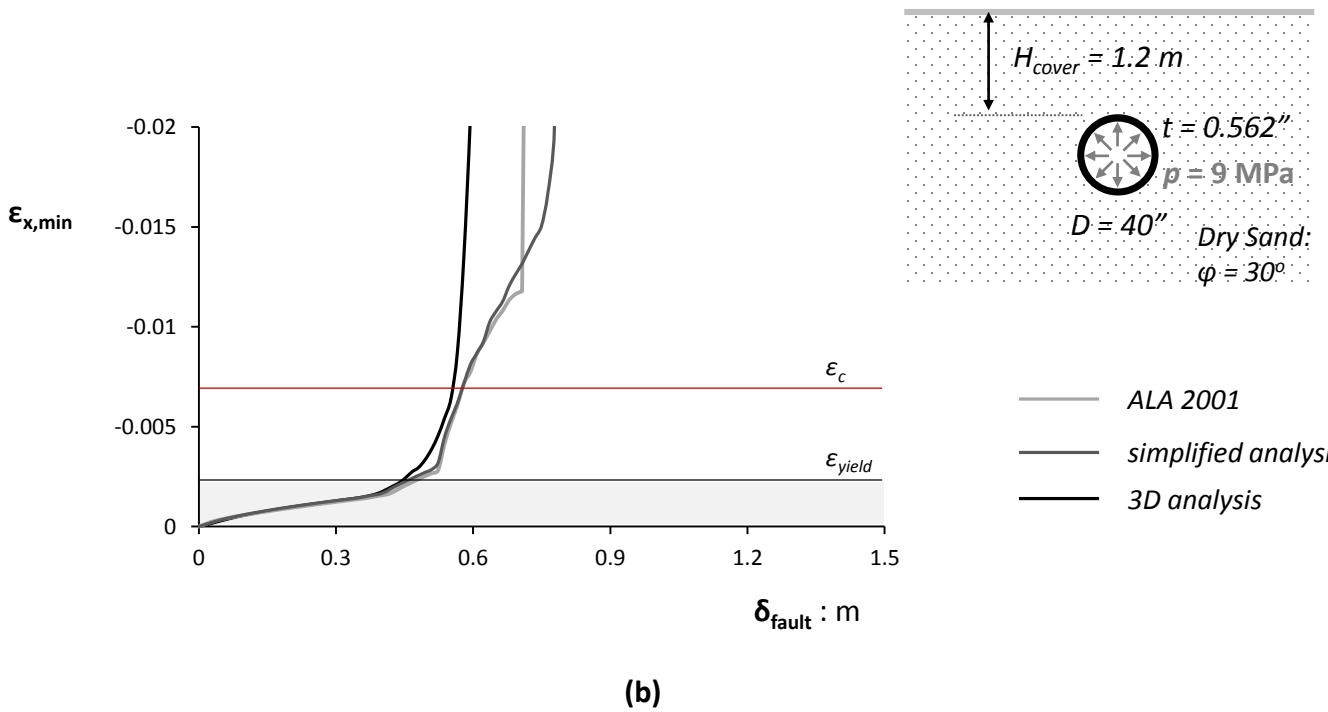

(b)

Fig. 7.13. Comparison of the pipe response predicted by the 3D model, the simplified model with springs calibrated against uniaxial numerical push tests (*simplified model*) and the simplified model with springs calibrated using the ALA 2001 analytical expressions (*ALA 2001*) **(a)** for the non-pressurized pipe and **(b)** for the pressurized pipe (p_{oper}=9 MPa): evolution of the minimum axial strain with the increase in the fault offset.